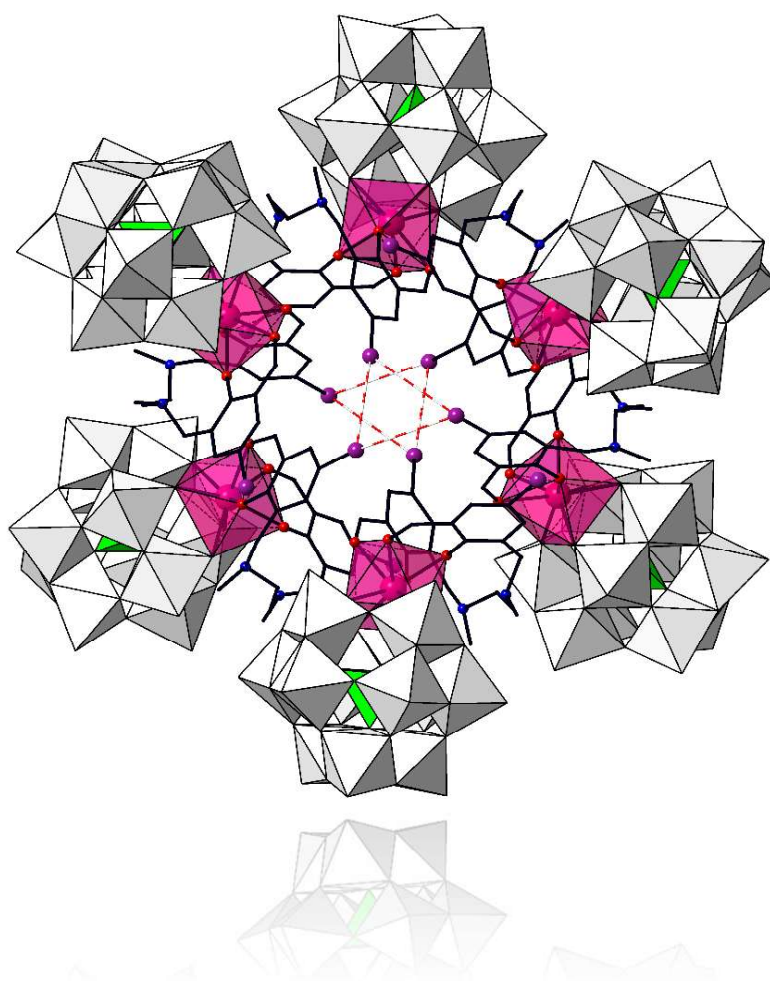


Polyoxometalate-Based Hybrids with 3d- and 4f-Metal Complexes Bearing Multidentate Organic Ligands

From Magnetoluminescent Molecular Species to
Extended Frameworks with Sorption Ability



Estibaliz Ruiz Bilbao

Ph.D Thesis

February 2023

eman ta zabal zazu



Universidad
del País Vasco

Euskal Herriko
Unibertsitatea

ZIENTZIA
ETA TEKNOLOGIA
FAKULTATEA
FACULTAD
DE CIENCIA
Y TECNOLOGÍA



Polyoxometalate-Based Hybrids with 3d- and 4f-Metal Complexes Bearing Multidentate Organic Ligands

From Magnetoluminescent Molecular Species to
Extended Frameworks with Sorption Ability

Memoria presentada por

Estibaliz Ruiz Bilbao

Para optar al grado de

Doctora por la Universidad el País Vasco / Euskal Herriko Unibertsitatea

Leioa, Febrero 2023

**TESI ZUZENDARIAREN BAIMENA TESIA
AURKEZTEKO**

**AUTORIZACIÓN DEL/LA DIRECTORA/A DE
TESIS PARA SU PRESENTACIÓN**

Zuzendariaren izen-abizenak /Nombre y apellidos del/la director/a:

BEÑAT ARTETXE ARRETXE

IFZ /NIF:

45668892-T

Tesiaren izenburua / Título de la tesis:

**Polyoxometalate-Based Hybrids with 3d- and 4f-Metal Complexes Bearing
Multidentate Organic Ligands - From Magnetoluminescent Molecular Species to
Extended Frameworks with Sorption Ability**

Doktorego programa / Programa de doctorado:

Ciencia y Tecnología de Materiales

Doktoregaiaren izen-abizenak / Nombre y apellidos del/la doctorando/a:

Estibaliz Ruiz Bilbao

Unibertsitateak horretarako jartzen duen tresnak emandako ANTZEKOTASUN TXOSTENA ikusita, baimena ematen dut goian aipatzen den tesia aurkez dadin, horretarako baldintza guztiak betetzen baititu.

Visto el INFORME DE SIMILITUD obtenido de la herramienta que a tal efecto pone a disposición la universidad, autorizo la presentación de la tesis doctoral arriba indicada, dado que reúne las condiciones necesarias para su defensa.

Tokia eta data / Lugar y fecha:

Leioa, a 9 de febrero de 2023

Sin. / Fdo.: **Beñat Artetxe Arretxe**

**TESI ZUZENDARIAREN BAIMENA TESIA
AURKEZTEKO**

**AUTORIZACIÓN DEL/LA DIRECTORA/A DE
TESIS PARA SU PRESENTACIÓN**

Zuzendariaren izen-abizenak /Nombre y apellidos del/la director/a:

LUIS M. LEZAMA DIAGO

IFZ /NIF:

30580768-Z

Tesiaren izenburua / Título de la tesis:

**Polyoxometalate-Based Hybrids with 3d- and 4f-Metal Complexes Bearing
Multidentate Organic Ligands - From Magnetoluminescent Molecular Species to
Extended Frameworks with Sorption Ability**

Doktorego programa / Programa de doctorado:

Ciencia y Tecnología de Materiales

Doktoregaiaren izen-abizenak / Nombre y apellidos del/la doctorando/a:

Estibaliz Ruiz Bilbao

Unibertsitateak horretarako jartzen duen tresnak emandako ANTZEKOTASUN TXOSTENA ikusita, baimena ematen dut goian aipatzen den tesia aurkez dadin, horretarako baldintza guztiak betetzen baititu.

Visto el INFORME DE SIMILITUD obtenido de la herramienta que a tal efecto pone a disposición la universidad, autorizo la presentación de la tesis doctoral arriba indicada, dado que reúne las condiciones necesarias para su defensa.

Tokia eta data / Lugar y fecha:

Leioa, a 9 de febrero de 2023



Sin. / Fdo.: **Luis M. Lezama Diago**

AUTORIZACIÓN DE LA COMISIÓN ACADÉMICA DEL PROGRAMA DE DOCTORADO

La Comisión Académica del Programa de Doctorado en **Ciencia y Tecnología de Materiales** en reunión celebrada el día **1** de **febrero** de **2023**, ha acordado dar la conformidad a la presentación de la Tesis Doctoral titulada:

Polyoxometalate-Based Hybrids with 3d- and 4f-Metal Complexes Bearing Multidentate Organic Ligands - From Magnetoluminescent Molecular Species to Extended Frameworks with Sorption Ability

dirigida por los Dres. **Beñat Artetxe Arertxe** y **Luis M. Lezama Diago** y presentada por Dña. **Estibaliz Ruiz Bilbao**

adscrito o adscrita al Departamento **Química Orgánica e Inorgánica**

En **Leioa** a **9** de **febrero** de **2023**

EL/LA RESPONSABLE DEL PROGRAMA DE DOCTORADO



Fdo.: **Luis M. Lezama Diago**

AUTORIZACIÓN DEL DEPARTAMENTO

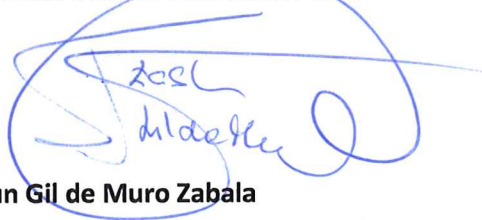
El Consejo del Departamento de **Química Orgánica e Inorgánica** en reunión celebrada el día **6 de febrero de 2023** ha acordado dar la conformidad a la admisión a trámite de presentación de la Tesis Doctoral titulada:

Polyoxometalate-Based Hybrids with 3d- and 4f-Metal Complexes Bearing Multidentate Organic Ligands - From Magnetoluminescent Molecular Species to Extended Frameworks with Sorption Ability

dirigida por los Dres. **Beñat Artetxe Arretxe** y **Luis M. Lezama Diago** y presentada por Doña. **Estibaliz Ruiz Bilbao** ante este Departamento.

En Leioa a **9 de febrero de 2023**

VºBº DIRECTORA DEL DEPARTAMENTO



Fdo.: **Izaskun Gil de Muro Zabala**

SECRETARIA DEL DEPARTAMENTO



Fdo.: **Mª Isabel Moreno Benítez**

ACTA DE GRADO DE DOCTOR O DOCTORA
ACTA DE DEFENSA DE TESIS DOCTORAL

DOCTORANDO/A DON/DÑA. **ESTIBALIZ RUIZ BILBAO**

TITULO DE LA TESIS: **Polyoxometalate-Based Hybrids with 3d- and 4f-Metal Complexes Bearing Multidentate Organic Ligands** - From Magnetoluminescent Molecular Species to Extended Frameworks with Sorption Ability

El Tribunal designado por la Comisión de Postgrado de la UPV/EHU para calificar la Tesis Doctoral arriba indicada y reunido en el día de la fecha, una vez efectuada la defensa por el/la doctorando/a y contestadas las objeciones y/o sugerencias que se le han formulado, ha otorgado por _____ la calificación de:
unanimidad ó mayoría

--

SOBRESALIENTE / NOTABLE / APROBADO / NO APTO

Idioma/s de defensa (en caso de más de un idioma, especificar porcentaje defendido en cada idioma):

Castellano _____

Euskera _____

Otros Idiomas (especificar cuál/cuales y porcentaje) _____

En _____ a _____ de _____ de _____

EL/LA PRESIDENTE/A,

EL/LA SECRETARIO/A,

Fdo.:

Fdo.:

Dr/a: _____

Dr/a: _____

VOCAL 1º,

VOCAL 2º,

VOCAL 3º,

Fdo.:

Fdo.:

Fdo.:

Dr/a: _____

Dr/a: _____

Dr/a: _____

EL/LA DOCTORANDO/A,

Fdo.: _____

ACKNOWLEDGEMENTS

En primer lugar, me gustaría agradecer a mis directores, los Dres. Beñat Artetxe y Luis Lezama, Profesor adjunto y Catedrático del Departamento de Química Orgánica e Inorgánica de la Facultad de Ciencia y Tecnología de la Universidad del País Vasco (UPV/EHU). Al primero por su continuo apoyo a lo largo de estos años, por haber confiado siempre en mí y haberme motivado a crecer como investigadora. Al segundo, por haberme acogido en su grupo de investigación y por su disposición y dedicación siempre que lo he necesitado. Gracias ambos por vuestra ayuda y esfuerzo diario y por haberme sabido guiar haciendo posible este trabajo.

Al Catedrático Juan M. Gutiérrez-Zorrilla, por haberme dado la oportunidad de unirme a su grupo de investigación cuando todavía era una estudiante de segundo de carrera. Agradecerle todas sus ideas que me han ayudado a avanzar con la tesis, por todo el conocimiento que ha conseguido transmitirme y, sobre todo, las risas y el enorme apoyo recibido en los incontables cafés juntos.

A la Dra. Leire San Felices, Dr. Aitor Larrañaga y Dr. Fco. Javier Sangüesa, por toda la ayuda proporcionada durante estos años. Su trabajo diario y su apoyo tanto laboral como personal han sido indispensables tanto para el desarrollo de este trabajo como para mi formación como investigadora. Asimismo, también me gustaría agradecer a los técnicos de los Servicios Generales de Investigación de la UPV/EHU, así como a todas las personas que han realizado medidas presentadas en este trabajo: Dr. Luis Lezama, Dra. Itziar Oyarzabal y Dr. Iñaki Orue por las medidas de susceptibilidad magnética, EPR y por haber sido un apoyo en todo lo relacionado con el magnetismo. Dra. Leire San felices por todas las medidas de difracción de rayos-X en monocristal. Dres. Aitor Larrañaga y Dco. Javier Sangüesa por las medidas de difracción de rayos-X en muestra policristalina. Al Dr. Santiago Reinoso, por su trabajo y ayuda en la distancia. Al Dr. José Ángel García, Catedrático del Departamento de Física Aplicada II de la UPV/EHU por ofrecerme su laboratorio de fotoluminiscencia. Dr. Luis Bartolomé por las medidas de análisis elemental, y a las Dras. Isabel Collado y Patricia Navarro por las medidas de $^1\text{H-NMR}$ y ESI-MS, respectivamente. Finally, to Dr. Debobrodo Sensharma and Dra. Shaza Darwish (University of Limerick, Ireland) for the gas and water vapor sorption experiments carried out.

I wish to express my gratitude to Prof. Mike Zaworotko for providing me the opportunity of join his research group at the University of Limerick, Ireland, for three months. I would also like to thank him for his support before, during and after my stay in Limerick. In the same way, I want to thank Julia Álvarez, Amrit, Parth, Vidit, Shaza, Debo, Julia, X.K., C.D., Meiyan, Catiúcia, Sam, Yassin, and all the group members for introducing me in the field of gas and water sorption as well as for their support and friendliness.

Agradecer especialmente a todos los compañeros de laboratorio, Janire (Uantre), Ángela, Asier, Corina y Laura por haber estado ahí cuando lo necesitaba y por todas esas risas tanto dentro como fuera del laboratorio. A Maite, Jon Pascal, Sandra, Aitor, Cristian, Mikel, Carlos S., Mikel R., Lia, Lorena, Estela y Carlos A., todos los compañeros de carrera

que empezamos juntos en este viaje y a todas esas personas que han ido entrando durante estos años y seguimos juntos al pie del cañón. Por todos esos congresos juntos y todos los viajes que nos han unido aún más. Habéis sido un gran apoyo.

A mis cuadrillas de Astrabudua, Barakaldo y Deusto, Miriam, Sheila, Sandra, Olatz, Arkaitz, Aketza, Irantzu, Ainara, Judit, Nerea, Lety eta Andrea, Markel, Alberto, Alain eta Tamara, Borja, Jaime, Txikito, Javi eta Esti. Y en especial, agradecerle a Julio por el apoyo diario, por su preocupación, por haber aguantado todas mis penurias incondicionalmente y haberme animado día a día a seguir y a poner todas mis fuerzas en este proyecto. Sin todos esos buenos momentos que me habéis dado, sin vuestras risas no lo hubiera logrado.

Por último, agradecer profundamente a mi familia: Ama eta Manu, Izeko eta Osaba, Amama eta Aitite, Alvaro, Alazne eta Alvarito, la familia que ahora tengo en Madrid, Borja, Ana y Sally, y la nueva familia que ha venido desde Sevilla, Iñigo, Lucia y Patri: por todo su apoyo y comprensión durante todos estos años y en especial en la pandemia. No sé cómo agradecereros todo lo que habéis hecho por mí, entre todos habéis hecho de esto una realidad.

A todos los que estuvieron ahí cuando lo necesitaba y a los que ya no pueden estar.
Eskerrik asko guztioi!

Estitxu Ruiz Bilbao

Dedicado al Aita

Always in my heart (1960–2012)

RESUMEN

Los polioxometalatos (POMs) son clústeres aniónicos formados por metal y oxígeno, que forman una clase de compuestos única debido a su complejidad estructural, y versatilidad topológica, electrónica y reactiva. Debido a estas características los POMs pueden mostrar importantes aplicaciones en diversos campos como el magnetismo, catálisis, ciencia de los materiales o biomedicina. La gran variedad estructural y composicional (Figura 1) de los POMs general estructural que van desde pequeños aniones dimetalatos, hasta estructuras con mayor nuclearidad que pueden llegar a mostrar tamaños similares a los de las proteínas. Los elementos que pueden actuar como metales *adenda* quedan restringidos a aquellos que presenten una combinación adecuada entre carga y radio iónico, así como la accesibilidad de los orbitales *d* vacantes y disponibles para la formación de enlaces π M–O. De este modo, los POMs están compuestos por metales de transición de los grupos 5 y 6 en sus estados de oxidación más elevados, generalmente; V^V , Mo^VI , W^VI . Desde un punto de vista estructural, los POMs se forman mediante condensación ácida de unidades poliédricas $\{MO_n\}$ ($n = 4-7$), en las que, comúnmente, el metal presenta un número de coordinación 6, con una geometría octaédrica. La condensación entre unidades octaédricas $\{MoO_6\}$ se da entre vértices, aristas o caras, de tal manera que, por poliedro, no queden más de dos átomos de oxígeno sin compartir.

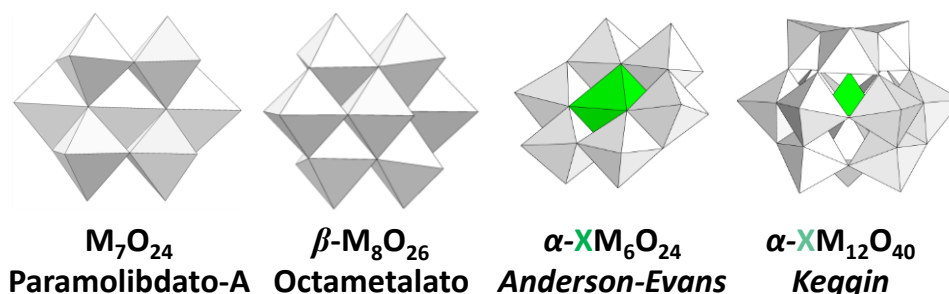


Figura 1. Representación de la variabilidad estructural de los POMs con algunos de los clústeres más comunes.

Además de la diversidad estructural presentada por los POMs, la funcionalización de estos clústeres amplía considerablemente su aplicabilidad, Esta derivatización se puede lograr fácilmente a través de rutas sintéticas convencionales y, por lo general, conduce a compuestos con propiedades que los grupos no funcionalizados no pueden exhibir. Tradicionalmente, se han utilizado dos estrategias principales para este propósito; la incorporación de centros metálicos 3d y/o 4f en especies lacunarias y; la derivatización orgánica de clúster POM inorgánicos, donde se distinguen; i) la combinación de polioxowolframatos lacunarios con organoderivados del grupo p como órganosililos, -estánilos, fosforilos o germilos; ii) la sustitución de los oxígenos superficies por ligandos N- u O-dadores; iii) la derivatización de POMs que contienen centros metálicos 3d o 4f con

ligandos orgánicos, o; iv) la coordinación de complejos metalorgánicos a la superficies del clúster.

Con respecto a estas dos últimas estrategias, este trabajo de investigación se centra en la síntesis de compuestos híbridos basados en POMs que contienen complejos metalorgánicos de metales 3d o 4f. El objetivo es, por una parte, i) evaluar la capacidad de iso- y hetero-polioxomolibdatos en combinación con complejos de metales de transición de ligandos tetraaza macrocíclicos coordinados a su superficie para generar redes híbridas extendidas; y por otra, ii) preparar sistemas moleculares híbridos mediante la derivatización orgánica a través de ligandos orgánicos compartimentales de POMs sustituidos con lantánidos. En el primer caso, los compuestos resultantes podrían exhibir una porosidad permanente asociada a funcionalidades interesantes como la adsorción selectiva de gases, así como la capacidad de experimentar transiciones estructurales tras la evacuación de las moléculas de disolvente. Los sistemas más apropiados también podrían exhibir la capacidad de experimentar transformaciones monocristal-a-monocristal provocadas por un determinado estímulo externo, de tal manera que permita monitorizar la ubicación de cada átomo específico a lo largo de la transición estructural. En el segundo caso, los centros lantánidos podrían exhibir propiedades luminiscentes, así como la relajación lenta de la magnetización, clave para la preparación de imanes moleculares para la computación cuántica o sistemas tipo qubit.

Los 26 nuevos compuestos que se describen en este estudio muestran características interesantes que van desde sus propiedades luminiscentes a la capacidad de adsorber gases de forma selectiva. El trabajo se ha dividido en dos partes bien diferenciadas: los Capítulos 2 y 3 abordan el estudio sistemático sobre la reactividad de isopolioxomolibdatos con complejos metalorgánicos de metales 3d y ligandos tetraaza macrocíclicos para dar lugar a estructuras híbridas extendidas. Además, el Capítulo 4 extiende este tipo de análisis a aniones tipo Anderson-Evans. Por otro lado, el capítulo 5 se centra en la funcionalización orgánica de polioxowolframatos lacunarios sustituidos con lantánidos, para dar lugar a compuestos moleculares con propiedades magneto-luminiscentes interesantes.

En los **Capítulos 2 y 3**, se presenta el estudio sistemático de la influencia del pH en el sistema sintético constituido por isopolioxomolibdatos y el complejo de cobre(II) con el ligando N4-macrocíclico cyclam, $\{\text{Cu}(\text{cyclam})\}^{2+}$ (cyclam = 1,4,8,11-tetraazacicotetradecano). Cuando la síntesis se realiza a pH básico (superior a 10), se obtiene el compuesto $[\text{Cu}(\text{cyclam})][\text{MoO}_4] \cdot 4\text{H}_2\text{O}$ (**MoCu**) que muestra una estructura con fuerte carácter monodimensional, formada por oxoaniones tetraédricos conectados a través de complejos octaédricos. Condiciones sintéticas similares también pueden dar lugar a otros análogos de oxoaniones/complejos metálicos $[\text{M}(\text{cyclam})][\text{XO}_4] \cdot n\text{H}_2\text{O}$ (X = Cr, V, Mo, W; M = Co, Ni, Cu, Zn) tal como se describe en el *Apéndice 1* (Figura 2). Por el contrario, las

condiciones de pH ácido facilitan una mayor condensación y, por lo tanto, se aísla la red robusta $[\text{Cu}(\text{cyclam})]_2[\gamma\text{-Mo}_8\text{O}_{26}] \cdot 1.5\text{H}_2\text{O}$, que está constituida por cadenas $[\text{Mo}_8\text{O}_{26}]_n^{4n-}$ unidas entre sí a través de las esferas de coordinación de los complejos $\{\text{Cu}(\text{cyclam})\}^{2+}$. La evaporación lenta de las disoluciones finales para las reacciones llevadas a cabo en condiciones de pH cercanas a la neutralidad (valores de pH en el rango de 6 a 9) dan inicialmente $\{[\text{Cu}(\text{cyclam})]_3(\kappa\text{-Mo}_8\text{O}_{27})\} \cdot 14\text{H}_2\text{O}$ (**1-Mo8**), cuyo complejo comportamiento termoestructural, así con sus interesantes propiedades de adsorción, merecen un capítulo aparte (**Capítulo 3**). Si se retira el **1-Mo8** del medio de reacción, se obtiene la red covalente tridimensional $\{[\text{Cu}(\text{cyclam})]_3(\text{Mo}_7\text{O}_{24})\} \cdot 15.5\text{H}_2\text{O}$ (**1-Mo7**) (Figura 2) como una fase cristalina pura, mientras que un segundo compuesto co-cristaliza a valores de pH entre 6 y 8, de fórmula $(\text{NH}_4)[\{\text{Cu}(\text{cyclam})\}_{2.5}(\text{Mo}_7\text{O}_{24})] \cdot 5.5\text{H}_2\text{O}$ (**1B-Mo7**). Las estructuras cristalinas de **1-Mo7** y **1B-Mo7** se han dilucidado mediante difracción de rayos X en monocristal. En ambas, los aniones heptamolibdato (paramolibdato A) se encuentran unidos mediante los complejos metalorgánicos, generando redes híbridas extendidas. Como ambas fases no se pueden distinguir visualmente bajo un microscopio óptico, solo describe la caracterización completa de **1-Mo7** que se lleva a cabo mediante análisis elemental (AE) y térmico (TGA/DTA), espectroscopia infrarroja (FTIR) y difracción de rayos X en polvo (PXRD). El estudio de PXRD a temperatura variable demuestra que **1-Mo7** es capaz de experimentar dos transformaciones consecutivas en estado sólido asociadas a la pérdida de las moléculas de disolvente presentes en los canales, para dar lugar a dos nuevas fases, la parcialmente deshidratada **2-Mo7** y la anhidra **3-Mo7**.

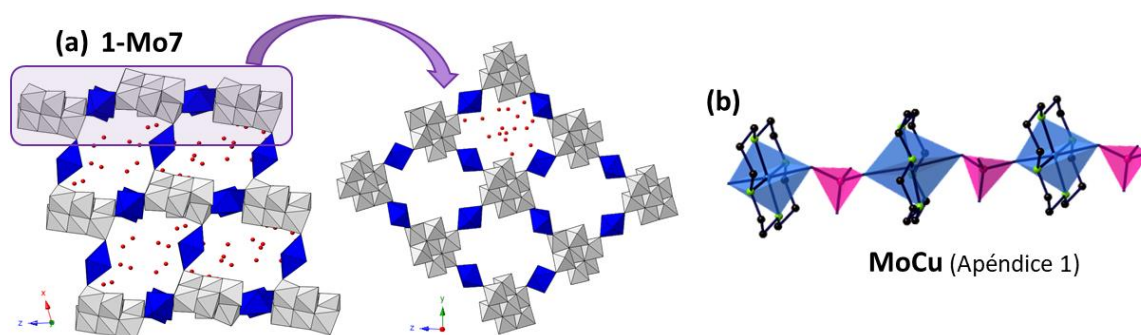


Figura 2. Representación de (a) el empaquetamiento cristalino presente en **1-Mo7** y (b) la estructura monodimensional formada a pH básico.

En el **Capítulo 3** se aborda la síntesis y caracterización completa del compuesto híbrido $\{[\text{Cu}(\text{cyclam})]_3(\kappa\text{-Mo}_8\text{O}_{27})\} \cdot 14\text{H}_2\text{O}$ (**1-Mo8**), cuya estructura está formada por aniones octamolibdato diferentes a los publicados hasta el momento $\{\kappa\text{-Mo}_8\text{O}_{27}\}$, unidos mediante complejos $\{\text{Cu}(\text{cyclam})\}^{2+}$. Cuando se calienta, el compuesto **1-Mo8** es capaz de experimentar dos transformaciones monocristal-a-monocristal promovidas térmicamente para dar lugar a dos nuevos compuestos anhidros, **2-Mo8** y **3-Mo8** (Figura 3). Estudios de XRD en monocristal demuestran que estas transiciones conllevan no solo modificaciones en el empaquetamiento cristalino debida a las modificaciones en las esferas de coordinación

de los complejos metalorgánicos, sino también la isomerización del anión octamolibdato. Por consiguiente, la migración de los centros metálicos en estado sólido, da lugar a dos nuevos clústeres, $\{\lambda\text{-Mo}_8\text{O}_{27}\}$ y $\{\mu\text{-Mo}_8\text{O}_{27}\}$, que tampoco se habían podido obtener antes mediante rutas sintéticas convencionales. La reversibilidad de estas transiciones ha sido estudiada, de tal forma que se observa que si se exponen los cristales de **3-Mo8** al aire, se genera una nueva fase hidratada (**4-Mo8**) que involucra la condensación de una molécula de agua adicional al anión octamolibdato para dar lugar al ya conocido anión $\{\gamma\text{-Mo}_8\text{O}_{26}(\text{OH})_2\}$. La deshidratación del compuesto **4-Mo8** resulta inicialmente en la fase anhidra **6-Mo8**, que exhibe parámetros de celda similares, mientras que seguidamente evoluciona a **3-Mo8**. Por el contrario, la fase anhidra **2-Mo8** revierte rápidamente para dar lugar a una última fase **5-Mo8** que presenta parámetros de celda similares, pero el mismo clúster $\{\kappa\text{-Mo}_8\text{O}_{27}\}$ que en **1-Mo8**, por lo que podría considerarse una especie intermedia en la transformación de **1-Mo8** a **2-Mo8**.

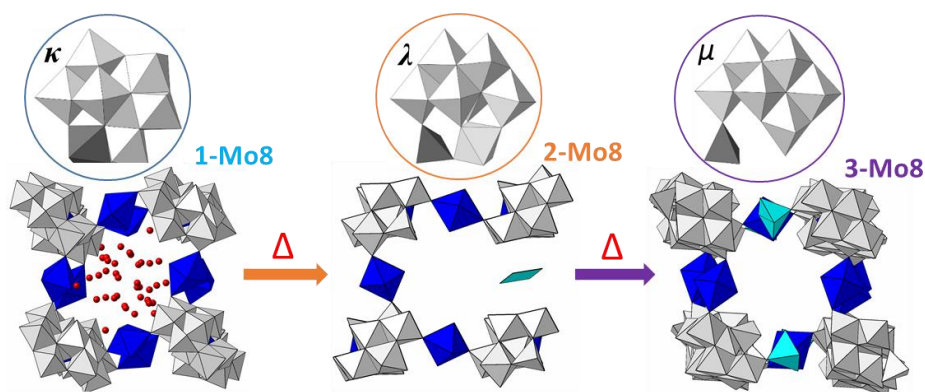


Figura 3. Representación esquemática de los cambios que conllevan las transiciones monocristal-a-monocristal inducidas térmicamente tanto en el empaquetamiento, como en la isomerización del polianión presente en **1-Mo8**.

Las tres fases anhidras generadas (**2-Mo**, **3-Mo** y **6-Mo8**) muestran microporosidad permanente tal y como se observa en los estudios de adsorción de N_2 y CO_2 gaseosos a baja temperatura. Por otro lado, también se ha estudiado la capacidad de adsorción de gases de estas fases, profundizando en las capacidades adsorptivas de **3-Mo8**, puesto que ha demostrado la habilidad de adsorber selectivamente C_2H_2 frente a C_2H_4 incluso en concentraciones muy bajas (1:99 ratio), así como de adsorber selectivamente C_2H_6 frente a C_2H_4 , presentando un comportamiento contrario al observado habitualmente para materiales porosos tipo MOF. Finalmente, los análisis de adsorción de vapor de agua están en buen acuerdo con las transiciones estructurales y muestran una alta ciclabilidad, así como, algunos de los valores más altos de absorción total publicados hasta la fecha para los sistemas basados en POMs. Las isothermas muestran una capacidad de adsorción abrupta al 20-30% de nivel de humedad relativa que podría ser potencialmente deseable para los dispositivos de control de humedad en espacios confinados.

Con respecto al **Capítulo 4**, la reacción entre aniones heptamolibdato y el complejo metalorgánico $\{\text{Cu}(\text{DMC})\}^{2+}$ (DMC = 1,8-dimetil-1,4,8,11-tetraazaciclotetradecano) en medio acuoso conlleva el reordenamiento del clúster para dar un nuevo polianión de fórmula $[\text{H}_4\text{CuMo}_6(\text{MoO}_3)_2\text{O}_{24}]^{6-}$ basado en un POM tipo Anderson-Evans al que se le unen dos unidades $\{\text{MoO}_4\}$ tetraédricas en cada una de las caras (Figura 4). El híbrido resultante presenta una red tridimensional porosa con canales interconectados, en los cuales, se sitúan las moléculas de agua de hidratación. Motivados por estos resultados, en la segunda parte de este capítulo se estudia la reacción entre polianiones tipo Anderson-Evans $[\text{H}_6\text{CrMo}_6\text{O}_{24}]^{3-}$ y complejos metalorgánicos $\{\text{Cu}(\text{DMC})\}^{2+}$ en diferentes medios de reacción. De este modo, en función de la presencia o ausencia de sales disueltas en el medio de reacción acuoso, se obtienen un total de 6 estructuras híbridas con dimensionalidades que varían desde cadenas híbridas, hasta estructuras extendidas. Cuando la síntesis se lleva a cabo en agua pura, se obtiene el híbrido $[\text{Cu}(\text{DMC})(\text{H}_2\text{O})][\{\text{Cu}(\text{DMC})\}_{0.5}\{\text{H}_6\text{CrMo}_6\text{O}_{24}\}] \cdot 10\text{H}_2\text{O}$ (**1-CrMo6**) con una estructura de un fuerte carácter monodimensional. Por el contrario, las reacciones en medios acuosos con alta fuerza iónica como el NaCl 1M conducen al ensamblaje de dos compuestos bidimensionales diferentes: $\text{Na}[\{\text{Cu}(\text{DMC})\}\{\text{H}_6\text{CrMo}_6\text{O}_{24}\}] \cdot 8\text{H}_2\text{O}$ (**1Na-CrMo6**) y $\text{Na}_2[\{\text{Cu}(\text{DMC})\}_{0.5}\{\text{H}_6\text{CrMo}_6\text{O}_{24}\}] \cdot 11,5\text{H}_2\text{O}$ (**1Na2-CrMo6**). Cuando la reacción se lleva a cabo en disoluciones acuosas de NaNO_3 o LiCl , se obtienen diferentes híbridos bidimensionales, que están constituidos por capas híbridas POM-metalorgánicas con las moléculas de agua de hidratación y contraiones ocupando espacios interlaminares. Estos son los compuestos $[\{\text{Cu}(\text{DMC})\}_2\{\text{H}_6\text{CrMo}_6\text{O}_{24}\}]\text{NO}_3 \cdot 5\text{H}_2\text{O}$ (**1NO3-CrMo6**) y $[\{\text{Cu}(\text{DMC})\}_2\{\text{H}_6\text{CrMo}_6\text{O}_{24}\}]\text{Cl} \cdot 5\text{H}_2\text{O}$ (**1Cl-CrMo6**), respectivamente. En un medio más insoluble como el KCl acuoso, cristaliza la sal puramente inorgánica la sal $\text{K}_3[\text{H}_6\text{CrMo}_6\text{O}_{24}] \cdot 6\text{H}_2\text{O}$ (**CrMo6**). Por último, el análisis termoestructural de las fases **1Na-CrMo6**, **1NO3-CrMo6**, **1NO3 CrMo6** mediante una combinación de análisis térmico y PXRD a temperatura variable, demuestra que el primero es capaz de experimentar dos transiciones de fase promovidas térmicamente, mientras que la deshidratación en la dos últimas no implica cambios drásticos en sus estructuras (comportamiento robusto).

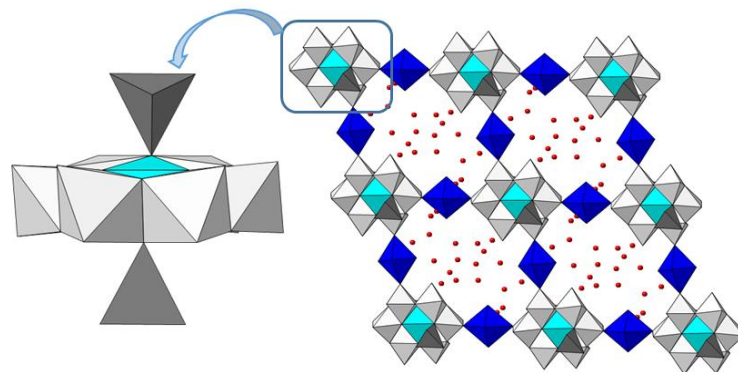


Figura 4. Representación del nuevo polianión $[\text{H}_4\text{CuMo}_6(\text{MoO}_3)_2\text{O}_{24}]^{6-}$, junto con la proyección de la capa híbrida en el empaquetamiento tridimensional formado por el oxoanión y complejos $\{\text{Cu}(\text{DMC})\}^{2+}$.

La segunda parte de este trabajo se encuentra recogida en el **Capítulo 5**, que tiene como objetivo la preparación de híbridos moleculares mediante la coordinación simultánea de ligandos orgánicos e inorgánicos sobre un centro metálico 4f. La estrategia sintética empleada consiste en la incorporación de complejos metalorgánicos basados en iones lantánidos y ligandos orgánicos de tipo base de Mannich, sobre polioxowolfratos monolacunarios $[\alpha\text{-SiW}_{11}\text{O}_{39}]^{8-}$ de tipo Keggin. Siguiendo este procedimiento, se han obtenido 10 compuestos isoestructurales (**1-Ln**) que presentan aniones híbridos de fórmula $[\text{Ln}(\text{H}_2\text{L})(\alpha\text{-SiW}_{11}\text{O}_{39})]^{5-}$ (Ln = Sm^{III} a Lu^{III}; H₂L = N,N'-dimetil-N,N'-bis(2-hidroxi-3-formil-5-bromobenzil)ethilen-diamina). Todas estas fases han sido caracterizadas mediante AE, FTIR, TGA/DTA y XRD tanto sobre muestra policristalina, como en monocristal. Estos compuestos moleculares tipo sándwich están formados por un ion Ln^{III} central que presenta una geometría de tipo prisma trigonal biaugmentado, tras la coordinación simultánea de los cuatro átomos de oxígeno pertenecientes al ligando orgánico y los cuatro oxígenos delimitando la vacante en la especie lacunaria. El entorno de coordinación N₂O₂ queda vacío en el ligando orgánica, de tal forma que permite que el ligando se pliegue, mostrando así una disposición que no se había visto hasta el momento (Figura 5). Asimismo, las propiedades fotoluminiscentes y magnéticas de estos compuestos se han estudiado en profundidad. Con respecto a la primera, la presencia de ligandos antena ha resultado efectiva en la activación de la emisión de los centros 4f para los compuestos que contienen Sm y Eu en el rango visible y para Er e Yb en el infrarrojo cercano. Los estudios de magnetización y susceptibilidad magnética a diferentes temperaturas y frecuencias, juntos con los experimentos de resonancia paramagnética electrónica, han permitido detectar comportamientos de relajación lenta de la magnetización en los derivados de Gd e Yb. Por consiguiente, el compuesto formado por Yb representa el primer POM que contiene lantánidos, capaz de comportarse como un material bifuncional magneto-luminiscente. Por último, la estabilidad en disolución de estos híbridos también se ha confirmado mediante experimentos de espectrometría de masas ESI-MS y resonancia magnética nuclear ¹H-NMR.

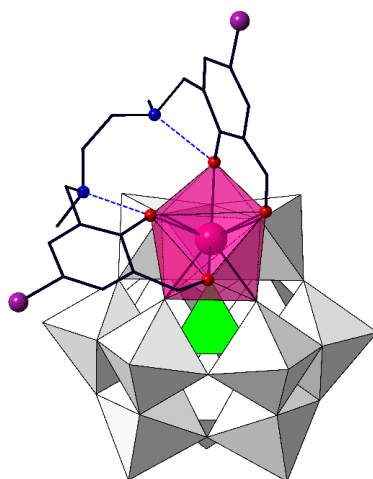


Figura 5. Representación del híbrido molecular $[\text{Ln}(\text{H}_2\text{L})(\alpha\text{-SiW}_{11}\text{O}_{39})]^{5-}$ presente en los compuestos **1-Ln** (Ln = Sm-Lu).

Table of contents

1. GENERAL INTRODUCTION

1.1. Polyoxometalates	3
1.1.1. Definition	3
1.1.2. Classification of POMs	6
1.2. The Keggin Anion and Derivatives	7
1.3. Metal-Substituted POMs	10
1.3.1. Lanthanide-containing POMs	11
1.3.2. Properties of lanthanide-containing POMs	13
1.4. Organic Functionalization of POMs	18
1.4.1. Organic derivatization of 3d- or 4f-metal substituted POMs	21
1.4.2. Grafting of transition metal complexes at POM surface	23
1.5. Porous POM-Metalorganic Hybrid Frameworks	24
1.5.1. Complexes of macrocyclic polyamines: cyclam and DMC	26
1.5.2. Single-Crystal-to-Single-Crystal transformation	30
1.6. Aim of the Work	34
1.7. References	37

2. THERMOSTRUCTURAL STUDIES IN HEPTAMOLYBDATE-METALORGANIC HYBRID FRAMEWORKS

2.1. Introduction	55
2.1.1. Heptamolybdate-metalorganic hybrids	56
2.2. Experimental Section	59
2.2.1. Synthesis	59
2.2.2. Single-crystal X-ray crystallography	60
2.3. Results and Discussion	61
2.3.1. Synthetic considerations	61
2.3.2. Thermostructural behavior of 1-Mo7	65
2.3.3. Crystal structure of 1-Mo7 and SCSC transformations	68
2.3.4. Crystal structure of 1B-Mo7	74
2.4. Conclusions	78
2.5. References	79

3. SEQUENTIAL SINGLE-CRYSTAL-TO-SINGLE-CRYSTAL ISOMERIZATIONS OF OCTAMOLYBDATE ANIONS WITHIN A MICROPOROUS HYBRID FRAMEWORK WITH SELECTIVE SORPTION PROPERTIES

3.1. Introduction	85
3.1.1. Octamolybdate-based hybrid compounds	87
3.2. Experimental Section	88
3.2.1. Synthesis	88
3.2.2. Single-crystal X-ray crystallography	89
3.2.3. Gas sorption and dynamic vapor sorption (DVS) experiments	90
3.3. Results and Discussion	91
3.3.1. Synthetic considerations	91
3.3.2. Thermostructural behavior	92
3.3.3. Crystal structure of 1-Mo8	94
3.3.4. SCSC transformations upon heating: isomerization of octamolybdate anions	97
3.3.5. Reversibility of the SCSC transformations	102

3.4. Water Vapor Sorption Properties _____	109
3.5. Gas Sorption Measurements _____	115
3.5.1. Multi-component adsorption selectivity _____	117
3.6. Conclusions _____	123
3.7. References _____	124

4. STRUCTURAL DIVERSITY IN POM-METALORGANIC HYBRIDS CONTAINING ANDERSON-EVANS ANIONS

4.1. Introduction _____	133
4.1.1. Anderson-Evans-based hybrid compounds _____	134
4.2. Experimental Section _____	136
4.2.1. Synthesis _____	136
4.2.2. Single-crystal X-ray crystallography _____	138
4.3. Results and Discussion _____	139
4.3.1. Synthetic considerations _____	139
4.3.2. Thermostructural behavior _____	143
4.3.3. Crystal structure of 1-CuMo8 _____	147
4.3.4. Crystal structure of 1-CrMo6 _____	150
4.3.5. Crystal structure of 1Na-CrMo6 _____	153
4.3.6. Crystal structure of 1Na2-CrMo6 _____	155
4.3.7. Crystal structure of 1NO3-CrMo6 _____	157
4.3.8. Crystal structure of 1Cl-CrMo6 _____	159
4.4. Conclusions _____	162
4.5. References _____	164

5. MONONUCLEAR LANTHANIDE-CONTAINING POLYOXOMETALATES WITH COMPARTMENTAL ORGANIC LIGANDS

5.1. Introduction _____	169
5.2. Experimental Section _____	172
5.2.1. Synthesis _____	172
5.2.2. Thermal analyses _____	175
5.2.3. Single-crystal X-ray crystallography _____	175
5.3. Results and Discussion _____	178
5.3.1. Synthetic considerations _____	178
5.3.2. Single-crystal X-ray diffraction _____	181
5.3.3. Photoluminescence properties _____	187
5.3.4. Magnetic properties _____	196
5.3.5. Solution stability _____	212
5.4. Conclusions _____	216
5.5. References _____	217

6. FINAL REMARKS AND FUTURE PERSPECTIVES

6.1. Final Remarks _____	225
6.2. Future Perspectives _____	227

APPENDICES

A.1. Monodimensional compounds based on group 6 tetraoxometalates and transition metal complexes of cyclam ligand _____	231
A.2. Materials and methods _____	253
A.3. Additional material of compounds included in Chapter 3 _____	265
A.4. Additional material of compounds included in Chapter 5 _____	271

General Introduction

- 1.1. Polyoxometalates
- 1.2. The Keggin anion and derivatives
- 1.3. Metal-substituted POMs
- 1.4. Organic functionalization of POMs
- 1.5. Porous POM-metalorganic hybrid frameworks
- 1.6. Aim of the work
- 1.7. References

ABSTRACT: *This chapter nicely illustrates the compositional, structural and electronic diversity of a family of anionic metal-oxo clusters known as polyoxometalates (POMs). These features make POMs unique compounds for being applied in fields like catalysis, magnetism, material science or biomedicine. Since the first pioneering studies by synthetic and structural chemists, this field has grown very quickly taking advantage from the rapid development of crystallography and single-crystal X-ray diffraction and currently, has become the focus of interdisciplinary research from areas such as physics, biology, biomedicine, materials science and theoretical chemistry. A brief introduction to the POM chemistry is given in this introductory chapter with strong focus on the Keggin structure. Moreover, the main derivatization methods are also described. These are the incorporation of transition-metal and/or lanthanide centers into the cluster skeleton and the organic functionalization of POMs. This considerably extends the catalogue of available species and allows the fine tuning of the desired electronic and redox properties for a given application. Special attention is given to luminescent and magnetic properties exhibited by lanthanide-containing POMs, as well as to extended networks based on transition-metal complexes of macrocyclic tetraamines grafted at POM surfaces, that are able to undergo single-crystal-to-single-crystal (SCSC) transformations triggered by external thermal stimuli. The last part of this chapter is completed with a brief description of the aim of the work, which is based on the synthetic approaches mentioned above.*

CHAPTER 1

1.1. POLYOXOMETALATES

1.1.1. Definition

Polyoxometalates (POMs) are a well-known family of anionic metal-oxygen nanoclusters that exhibit a wide compositional, structural, reactive and electronic versatility.¹ These characteristics make POMs unique compounds with a huge range of potential applications in fields like catalysis,² magnetism,³ material science⁴ and biomedicine.⁵ This inorganic family also exhibits a great variety of structures and compositions varying from small dimetalate anions to complex clusters with sizes comparable to those of proteins (Figure 1.1). It is commonly believed that the polyoxometalate chemistry was originated in 1826, when J. J. Berzelius reported the first polyoxometalate salt, the ammonium $[\text{PMo}_{12}\text{O}_{40}]^{3-}$ anion.⁶ However, almost 40 years before (1783) Juan José and Fausto Elhuyar had already synthesized a bitter, spicy and yellow salt which was later identified as $(\text{NH}_4)_{10}[\text{H}_2\text{W}_{12}\text{O}_{42}] \cdot 10\text{H}_2\text{O}$.⁷ Although POM chemistry has long been known, it was not until the 80's when research in this field started to grow very quickly. The first crystallographic determination of a POM cluster dates from 1933, when James F. Keggin reported the first structural evidence of the $\text{H}_3[\text{PMo}_{12}\text{O}_{40}] \cdot 5\text{H}_2\text{O}$ polyanion, nowadays known as *Keggin* anion after him.⁸ The fast expansion of POM chemistry in the last two decades makes it to be considered as one of the most active and dynamic fields within Inorganic Chemistry, which can be exemplified by the large number of books⁹ and published works and reviews in the last few years.¹⁰

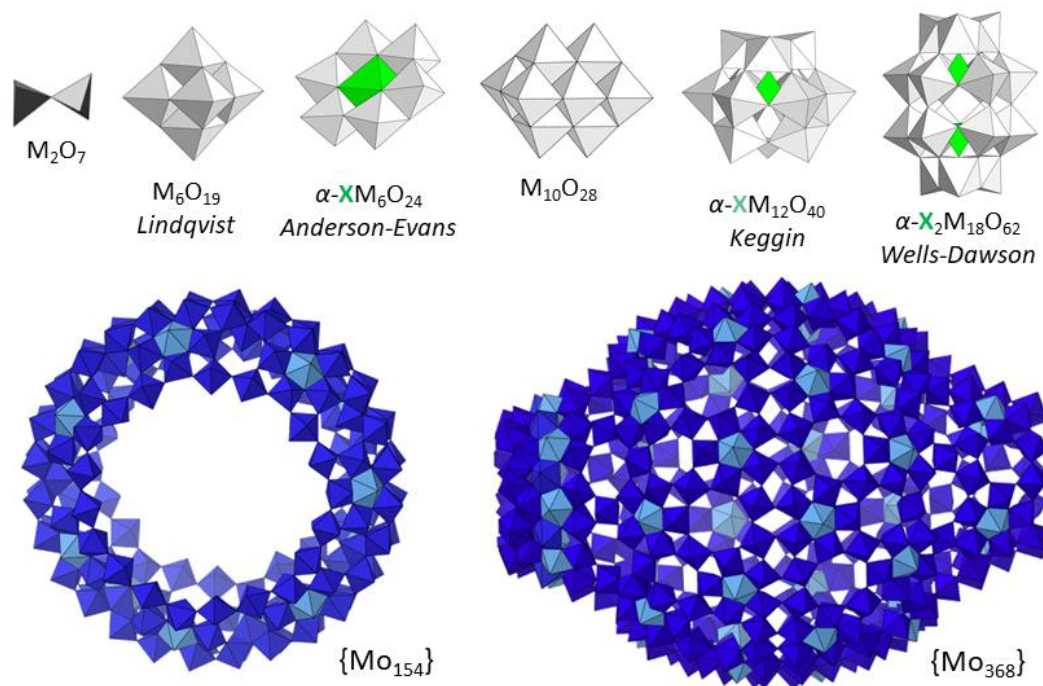


Figure 1.1. Structural diversity of POMs illustrated by a variety of clusters. Color code: $\{\text{MO}_x\}$, pale grey; $\{\text{XO}_x\}$, green; $\{\text{MoO}_6\}$ from $\{\text{Mo}_{154}\}$ Keplerate and $\{\text{Mo}_{368}\}$ “blue lemon”, dark blue; $\{\text{Mo}^{\text{V}}\text{O}_5\}$ units with pentagonal bipyramid geometry, cyan.

POMs are composed of early transition metals (M, so-called *addenda* metals) from groups 5 and 6 in their highest oxidation states, commonly V^V , Mo^VI and W^VI . The suitable combination between charge and ionic radius, as well as the accessibility of empty *d* orbitals available for electronic back-donation in the formation of M–O bonds, makes these metals appropriate to act as *addenda* atoms (Figure 1.2a). Moreover, POM clusters based on Nb or Ta have also been studied, and, while polyoxotantalates still represents an incipient field, the number of reports regarding isopolyoxoniobates have grown in the last two decades.¹¹ Regarding unconventional POMs, clusters based on noble metals such as polyoxopalladates, -platينات and -aurates has been isolated recently,¹² together with some other related families such as peroxy-actinyl species.¹³

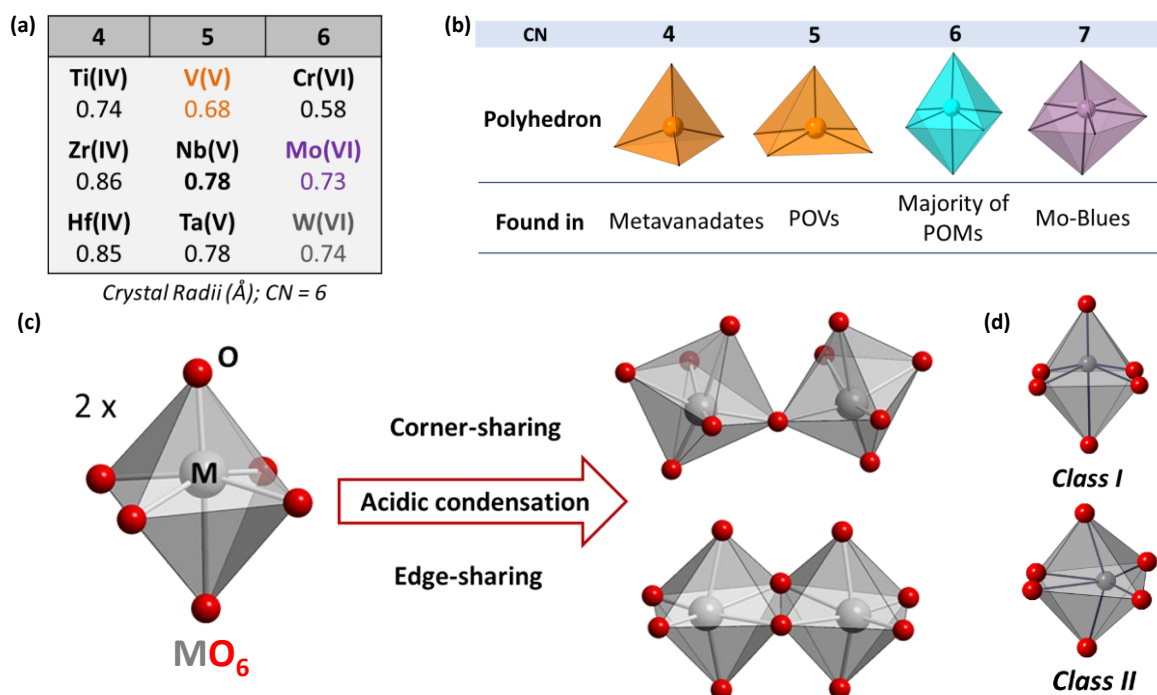


Figure 1.2. (a) Crystal radii for metal ions (Coordination Number = 6) from groups 4, 5 and 6 in their highest oxidation states; (b) Most common coordination polyhedra for *addenda* metals (POV = polyoxovanadates); (c) Schematic representation of the two common linkages-modes between $\{MO_6\}$ octahedra, and; (d) Representation of $\{MO_6\}$ coordination polyhedra for *class I* and *class II* POMs.

From the structural point of view, POMs are formed by the acidic condensation of a variable number of $\{MO_n\}$ polyhedra ($n = 4-7$), in which the *addenda* metal commonly shows an octahedral geometry ($n = 6$), and less frequently tetrahedral ($n = 4$) and square-pyramidal ($n = 5$). Some Mo^VI and W^VI can also occupy a seven-coordinated $\{O=M(O_6)\}$ environment (Figure 1.2b), which allows the assembly of giant POM architectures such as $\{Mo_{132}\}$ Keplerates, the $\{Mo_{154}\}$ big wheel, or the $\{Mo_{368}\}$ “hedgehog” or “blue lemon”, among others.¹⁴ Condensation of $\{MO_6\}$ subunits occurs favorably by either corner- or edge-sharing in such a way that no more than two oxygen atoms of the polyhedra are left unshared (Lipscomb’s principle) to avoid the dissociation of the cluster by minimizing the

strong trans-effect of the terminal M–O bonds (Figure 1.2c).¹⁵ Electrostatic repulsion between metal centers on POM anions cannot be denied; therefore, corner-sharing among octahedra is expected to be more frequent than edge-sharing, as it separates the metal centers more efficiently. On the contrary, the edge-sharing linkage reduces the number of terminal oxide ions and hence, it stabilizes the system to a greater extent than corner-sharing. Face-sharing condensation is not commonly found, as the *addenda* metals are too close to each other.

The oligomerization is not infinite because the polarization of the central metal towards the outer oxygen atoms, as well as vacant and accessible *d* orbitals of the *addenda* metals allow the formation of terminal M=O double bonds, avoiding the condensation of additional octahedra. Each metal center located in a MO₆ environment is displaced towards terminal oxygen atoms because of the participation of *d* orbitals in the π M–O bond. This way, two types of polarizations can be distinguished; towards one terminal oxygen atoms (*class I*) and towards two terminal oxygen atoms located in relative *cis* configuration (*class II*) (Figure 1.2d). The main difference between these two polyoxoanions resides in their electronic properties. Since the LUMO orbital for the first class has a non-bonding nature, they can be easily and reversibly reduced under certain chemical, electrochemical and/or photochemical methods. This leads to the formation of mixed-valence “blue” or “brown” species, which can be reversibly reduced under mild conditions and with no significant alterations of the POM skeleton. In contrast, *class II* POMs possess anti-bonding LUMO orbitals, which makes the reduction of these species irreversible and much more complicated.¹⁶

Properties of the POM anions, including their size, shape, composition, or redox behavior, among others, can be easily custom-fitted by defining the synthetic parameters. However, despite this wide structural and compositional diversity, most POMs exhibit some common features:¹

- a. They usually show high charge, size and symmetry, as well as high thermal and solution stability.
- b. The preparation of POM clusters highly dependent on a number of variables such as, concentration of reactants, pH, presence of additional ligands, counterions employed, ionic strength of the media, temperature or pressure, among others. Furthermore, several studies developed in aqueous solution demonstrate that for a given pH value, there are many POM species coexisting together. For that reason, the species that are isolated in a certain pH do not need to be the predominant, but the less soluble.
- c. POM salts containing alkali counterions are usually soluble in water, whereas organic counterions confer solubility on organic solvents.

1.1.2. Classification of POMs

Depending on their composition, POM are traditionally classified into two main groups (Figure 1.3):

Isopolyoxometalates (isoPOMs) with the general formula $[M_mO_y]^{n-}$. Clusters from this group are exclusively constituted by *addenda* metals and oxygens. Most of the structures of iso-POMs are derived from the parent $M_{10}O_{28}$ decametalate cluster, which is formed by the condensation of ten edge-sharing $\{MO_6\}$ octahedra arranged in an ideal D_{2d} symmetry.¹⁷ The most common iso-POMs are generated *via* elimination of octahedral units from the parent clusters including β - M_8O_{26} octametalate, M_7O_{24} heptametalate (also known as paramolybdate-A) and the M_6O_{19} hexametalate (so-called Lindqvist structure) anions.¹⁸ IsoPOMs generally display high charges and strong basic oxygen surfaces, able to be used as building blocks. Furthermore, it is worth mentioning the $H_2W_{12}O_{42}$ polyanion (paratungstate-B), which is formed from the rearrangement of $[W_7O_{24}]^{6-}$ paratungstate-A in solution instead of deriving from the $M_{10}O_{28}$ decametalate.¹⁹ Poly- and metavanadates are also included within this group.²⁰

Heteropolyoxometalate (heteroPOMs): Clusters from this group show the general formula $[X_xM_mO_y]^{n-}$, as they are not only composed by transition metals and oxygen, but also additional elements known as heteroatoms (X). Unlike the *addenda* metals, the heteroatom does not show any specific restrictions as many of the elements on the periodic table can act as heteroatoms with exception of noble gases. These specially include a variety of transition metals and *p*-block elements, which can exhibit coordination number between 4 and 12. As a result of their high solution stability, heteropolyoxometalates are the most explored group within the POM chemistry. Through the removal of octahedra, addition of new polyhedra and relative rotation of some building blocks, the vast majority of heteroPOM structures can be originated from the following three parent clusters displaying high symmetry; the $\{XM_{12}O_{40}\}$ Keggin structure that exhibits an ideal T_d symmetry, the $\{XM_{12}O_{38}\}$ cluster with a O_h symmetry and the Dexter-Silverton structure $\{XM_{12}O_{42}\}$ with a I_h symmetry.

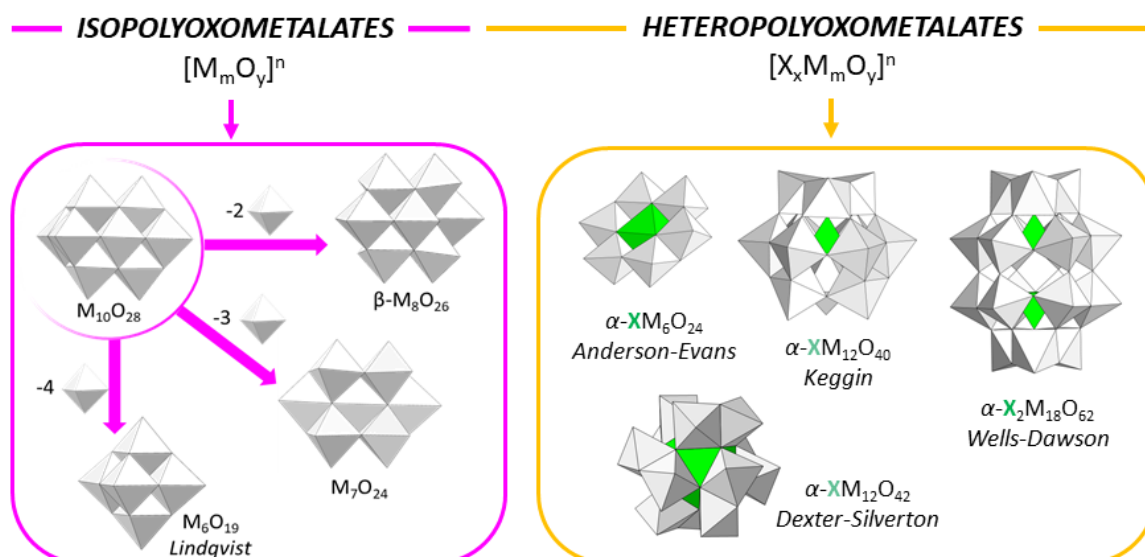


Figure 1.3. Polyhedral representation of some iso- and heteroPOM archetypes.

1.2. THE KEGGIN ANION AND DERIVATIVES

Keggin anions with the general formula $[XM_{12}O_{40}]^{n-}$ ($M = Mo^{VI}, W^{VI}$; $X = P^V, As^V, Si^IV, Ge^IV, B^{III}, Al^{III}, Fe^{III}, Co^{II}$, among others) are one of the most studied class of heteroPOMs, because their great compositional variability together with high solution and thermal stability makes them useful for a plethora of applications including catalysis (either in classical acid- / redox-catalysis or, photo- and electrocatalysis) and electrochemical energy storage systems, among others.²¹ The redox capacity of these clusters mainly depend on the *addenda* metal, in such a way that Mo-based Keggin anions are more easily reduced than their W-based counterparts.²² This fact is clearly exemplified by the $[PMo_{12}O_{40}]^{3-}$ “electron sponge”, which could *a priori* incorporate up to 24 electrons after a super-reduction process that involves the formation of metal-metal bonds.²³ Reduction processes do not imply significant structural changes and they are usually associated with the protonation of bridging oxygen atoms. Thus, Keggin-type POMs can act as both proton and electron reservoirs simultaneously.

The α -Keggin-type structure is constituted by four $\{M_3O_{13}\}$ trimers, which are formed by three edge-sharing $\{MO_6\}$ octahedra, that are linked to each other and to the central $\{XO_4\}$ tetrahedron through corner-sharing in an ideal T_d symmetry. Regarding group V metals, the $[XNb_{12}O_{40}]^{16-}$ heteroniobates ($X = Si, Ge$) have been recently prepared as isolated clusters²⁴, whereas related examples for vanadium only include mixed addenda-metal (V/Mo or V/W) clusters and the bicapped α -Keggin-type $[PV_{14}O_{42}]^{9-}$ species.²⁵ Keggin-type heteropolyanions exhibit five structural isomers, known as *Baker-Figgis* isomers (Figure 1.4). These result from the 60° rotation of one (β), two (γ), three (δ) or four (ϵ)

M_3O_{13} trimers from the parent α -Keggin anion. The α and β isomers are the most stable, because they do not show any edge-sharing linkage between M_3O_{13} trimers. The α , β and γ isomers of Keggin-type tungstosilicates can be readily synthesized and have been successfully characterized in both solution and solid state.²⁶ Nevertheless, the δ isomer structure has only been observed for the aluminum-based $[(AlO_4)Al_{12}(OH)_{24}(H_2O)_{12}]^{7+}$ cationic cluster,²⁷ and the $[H_2W_4V_8(VO_4)O_{33}(C_6H_{13}NO_3)]^{5-}$ anion, which is stabilized with a tripodal organic ligand.²⁸ Reports containing ε -Keggin-type building block as independent cluster are limited to a few examples such as the lanthanide stabilized $[\varepsilon-PMo_{12}O_{36}(OH)_4\{Ln(H_2O)_4\}_4]^{4+}$ phosphomolybdate series (Ln = La to Sm)²⁹ and the aluminium $[MO_4Al_{12}(OH)_{24}(H_2O)_{12}]^{n+}$ (M = Al, Ga, Ge) polyoxocations. It should be highlighted that although α and β isomers could show *a priori* a similar stability, it has been proved that the latter isomer (as for γ , δ and ε) is transformed into the α form in aqueous solution.³⁰

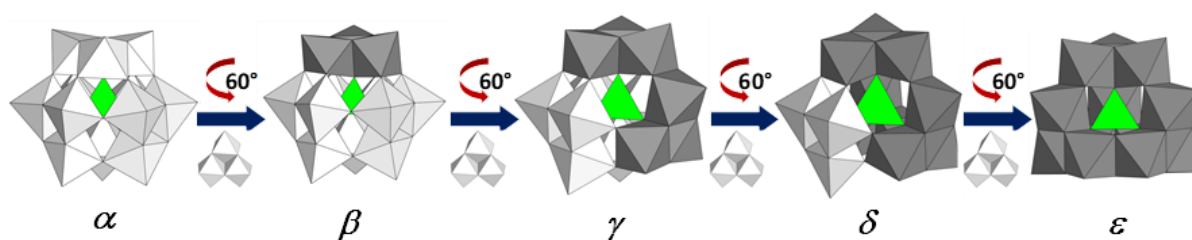


Figure 1.4. Baker-Figgis isomers of the Keggin-type structure. Rotated trimers are depicted in dark grey.

Although the plenary Keggin-type species are stable in aqueous solution, basification of the medium leads to the rupture of M–O bonds, which implies the loss of a variable number of MO_6 octahedra. These clusters present vacant sites within the inorganic cluster skeleton and they are known as *lacunary* species. Different lacunary species can be obtained from the parent plenary $\{\alpha-XM_{12}O_{40}\}$ Keggin anion. From the α -isomer, mono- $\{XM_{11}O_{39}\}$ and trivacant $\{XM_9O_{34}\}$ species can be generated upon elimination of one or three octahedra, respectively. The α - XM_9O_{34} anion shows two different isomers named as A- α or B- α depending on whether the removed $\{MO_6\}$ octahedra belongs to a $\{M_3O_{13}\}$ edge-sharing trimer or to a $\{M_3O_{15}\}$ corner-sharing triad, respectively. Similar trilacunary species can be isolated for the β -isomer. However, the lower symmetry of $\{\beta-XM_{12}O_{40}\}$ allows three different monolacunary species to be formed depending on the position of the vacant site. The vacant position in the β_1 derivative is located in the triad opposite to the 60° rotated trimer, whereas for the β_2 and the β_3 forms it lies at the central belt and the rotated trimer, respectively. Up to date, only the dilacunary $\{\gamma-XM_{10}O_{36}\}$ species has been isolated from the γ -isomer, in which two edge-sharing octahedra from the two rotated trimers are removed. Chemical equilibria of Keggin-type tungstosilicates in water solution are depicted in Figure 1.5, which illustrates the complexity of the pH-dependent interconversion pathways between plenary and lacunary POMs.

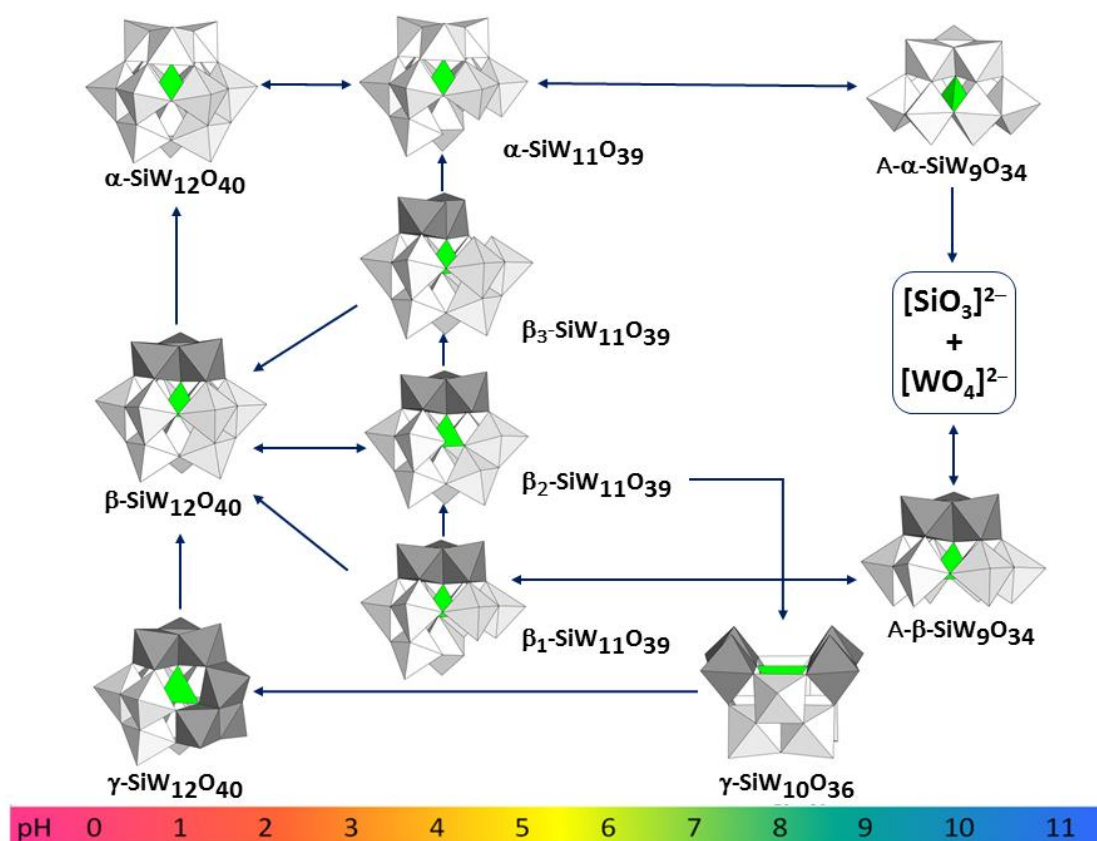


Figure 1.5. Scheme of the chemical equilibria between different plenary and lacunary Keggin-type tungstosilicates. Color code: $\{WO_6\}$, pale grey; $\{SiO_4\}$, green; rotated trimers are depicted in dark grey.

All the ten species represented can be prepared and isolated as alkaline salts from mixtures of silicate and tungstate sources depending on the pH, by following the procedures reported by Téze & Hervé.²⁶ Furthermore, for some specific heteroatoms like As^{III} , Sb^{III} , Te^{IV} or Se^{IV} , the presence of a lone pair of electrons precludes the full closure of the Keggin shell, so that only B- XW_9O_{33} trivacant species can be formed.³¹ In some cases, lacunary species can undergo further condensation reactions in water to lead to new heteroPOM derivatives. For instance, one of the most remarkable examples is given by the $X_2M_{18}O_{62}$ Wells-Dawson cluster, which is constituted by two A- α - XM_9O_{34} ($X = P^V, As^V, S^{VI}$) trilacunary units sharing corners through the belt $\{MO_6\}$ octahedra in an ideal D_{3h} symmetry.³² Different isomeric forms and lacunary species are also known for the Wells-Dawson type anion. For example, the β isomer comprises one A- α and one A- β trilacunary Keggin-type building blocks, whereas the γ form contains two β units.³³ Two types of monolacunary species can be obtained from the plenary α form, so called α_1 and α_2 depending on whether the removed octahedron belongs to a belt or cap positions, respectively.³⁴ Trilacunary $\{\alpha-X_2M_{15}O_{56}\}$ units can be readily prepared by the removal of a cap trimer, whereas polylacunary species like the hexavacant $\{\alpha-X_2M_{12}O_{48}\}$ are obtained after the removal of four belt $\{MO_6\}$ units and one additional center from each cap.³⁵ The latter building block is found in the $[P_8W_{48}O_{184}]^{40-}$ macrocycle³⁶ and Preyssler-type $[NaP_5W_{30}O_{110}]^{14-}$ anions.³⁷

1.3. METAL-SUBSTITUTED POMs

Besides structural diversity displayed by POMs, the incorporation of additional functionalities to these molecular architectures considerably broadens the catalogue of available metal-oxo frameworks. This derivatization can be easily achieved via conventional synthetic routes and it usually leads to compounds with properties that unfunctionalized clusters cannot exhibit. Lacunary polyoxotungstates are effective in stabilizing arrays of d- and f-metal centers, because they can act as inorganic ligands towards electrophilic transition metal and lanthanide ions through the oxygen atoms delimiting their vacant sites. This ability has resulted in an enormous catalogue of metal-substituted POMs, which usually show additional properties brought by the presence metal atoms such as magnetism, Lewis acidity, luminescence...³⁸ The chemistry of these clusters is dominated by polyoxotungstates, in such a way that a large number of species ranging from simple entities to giant structures have proved to result from the incorporation of 3d or 4f metals to the available catalogue of lacunary species. In the last decade several heterometallic POMs containing 3d and 4f centers simultaneously have also been synthesized.³⁹

Several topologies and nuclearities of 3d-metal containing polyoxotungstates can be obtained following synthetic strategies that range from simple solution approaches to more extreme solvothermal routes. The simplest examples are those in which 3d metal centers occupy the vacant position of lacunary Keggin and Wells-Dawson species to regenerate the plenary cluster skeleton.⁴⁰ In contrast, monomeric structures are scarcely found in literature when reacting trilacunary anions with 3d metals and dimeric sandwich-type POMs are obtained instead, which comprise a variable number of metal atoms in central belt positions. Weakley-type architectures with the general formula $[M_4(H_2O)_2(B-\alpha-XW_9O_{34})_2]^{n-}$ ($X = Si, Ge, P, As^V$) or $[M_4(H_2O)_2(\alpha-X_2W_{15}O_{56})_2]^{n-}$ ($X = P, As^V$) trap a central $M_4O_{14}(H_2O)_2$ ($M = Mn$ to Zn) rhomblike core,⁴¹ whereas A-type trilacunary fragments can encapsulate a triangle of three first row transition metal cations, which complete their octahedral spheres with two coordination water molecules, to produce $[M_3(H_2O)_6(A-\alpha-XW_9O_{34})_2]^{12-}$ ($X =$ traditionally P , but occasionally Si) Knoth-type sandwich POMs⁴². Similarly, the presence of a lone-pair of electrons in the heteroatom precludes the closure of the Keggin shell and thus, only B-type trilacunary species can be formed. In this sense, the 3d-metal directed assembly of two $\{B-\alpha-XW_9O_{33}\}$ units results in Hervé-type sandwich-species with the general formula $[(M(H_2O))_3(B-\alpha-XW_9O_{33})_2]^{n-}$, in which the three square-pyramidal metals in belt position exhibit one terminal water molecule per each center.⁴³ In contrast, Krebs-type⁴⁴ species with the general formula $[(M(H_2O)_3)_2(WO_2)_2(XW_9O_{33})_2]^{n-}$ ($M = Zn, Ni, Co^{II}, Fe^{III}$ or Mn^{II} , and X accounts for Sb^{III} or Bi^{III}) are formed from the association of two $\{B-\beta-XW_9O_{33}\}$ units connected *via* two inner *cis*- $\{WO_2\}$ and outer $\{M(H_2O)_3\}$ moieties (Figure 1.6).

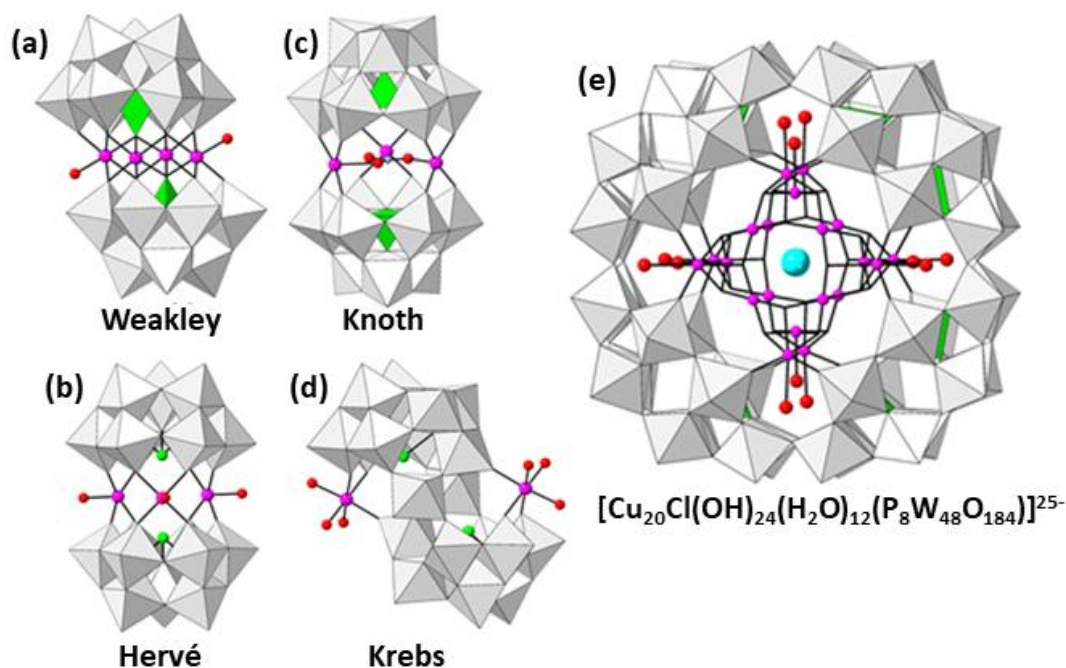


Figure 1.6. Molecular structures of representative examples of 3d-metal substituted POMs: (a) $[\text{Co}_4(\text{H}_2\text{O})_2(\text{GeW}_9\text{O}_{34})_2]^{12-}$ (Weakley); (b) $[\{\text{Cu}_3(\mu\text{-NO}_3)\}\{\text{PW}_9\text{O}_{34}\}_2]^{13-}$ (Knoth); (c) $[\{\text{Cu}(\text{H}_2\text{O})\}_3(\text{BiW}_9\text{O}_{33})_2]^{12-}$ (Hervé); (d) $[\{\text{Co}(\text{H}_2\text{O})_3\}_2(\text{WO}_2)_2(\text{SbW}_9\text{O}_{33})_2]^{10-}$ (Krebs), (e) $[\text{Cu}_{20}\text{Cl}(\text{OH})_{24}(\text{H}_2\text{O})_{12}(\text{P}_8\text{W}_{48}\text{O}_{184})]^{25-}$. Color code: 3d-metals, pink spheres; Cl ion, blue sphere; N, dark blue sphere.

Besides the archetypical, dimeric sandwich type anions, the huge variety of 3d-metal substituted POMs that can accommodate up to 40 transition metal centers has been regularly reviewed.⁴⁵ On the other hand, owing to their large size, oxophilic character and high coordination numbers (usually higher than 7), lanthanide ions have been successfully incorporated into lacunary polyoxotungstate fragments leading to a large variety of assemblies which extends from dimeric Peacock-Weakley type species to giant, complex architectures (Figure 1.7). For this reason, together with the different properties that a 4f-metal substituted POMs can show (e.g. luminescence, magnetism, catalysis), these 4f-containing species have been studied in depth.⁴⁶

1.3.1. Lanthanide-containing POMs

Peacock and Weakley described the first family of lanthanide-containing POMs in 1971, namely the series $[\text{Ln}(\text{W}_5\text{O}_{18})_2]^{9-}$ (Ln = lanthanide(III) ion).⁴⁷ These species consist of two monolacunary Lindqvist type POMs encapsulating a 4f metal ion in an eight-coordinated square-antiprismatic $\text{LnO}_4(\text{O}_4')$ fashion. Since then, all the sandwich-type clusters formed by a lanthanide ion trapped between two monolacunary fragments have been known as Peacock-Weakley type anions after them. Besides decatungstate-based sandwich-type species, structural characterization of only a few other types of lanthanide-containing isoPOMs has been reported to date.⁴⁸ In contrast, a wide range of Peacock-Weakley-type POMs containing Keggin or Wells-Dawson monolacunary units have been

reported, including the $\{\text{Ln}(\alpha\text{-XW}_{11}\text{O}_{39})_2\}$ ($X = \text{Si}^{\text{IV}}, \text{P}^{\text{V}}, \text{As}^{\text{V}}$),⁴⁹ $\{\text{Ln}(\beta_2\text{-SiW}_{11}\text{O}_{39})_2\}$ ⁵⁰ or $\{\text{Ln}(\alpha\text{-P}_2\text{W}_{17}\text{O}_{61})_2\}$ ($\alpha = \alpha_1, \alpha_2$)⁵¹ families. Although lanthanide-substituted monomeric species were identified in solution in related early works, these usually form chains or dimers in solid state.⁵² In addition to Peacock-Weakley species, some other lanthanide-containing dimeric POMs are known. These are based on di- or trilacunary Keggin or Wells-Dawson⁵³ units and include Knoth-type POMs incorporating 4f metals.⁵⁴ Only a few examples of trimeric lanthanopolyoxotungstates are found in the literature,⁵⁵ whereas tetrameric species represent a large group where almost all members display dilacunary Keggin type POMs or trilacunary units with lone-pair containing heteroatoms such as As^{III} or Sb^{III}. Francesconi's $[(\text{Eu}_2\text{PW}_{10}\text{O}_{38})_4(\text{W}_3\text{O}_{14})]^{30-}$ anion⁵⁶ could be considered as a representative example of the second group. Higher nuclearity has also been observed in crown-shaped $\{\text{K}[\text{Eu}(\text{H}_2\text{O})_2(\alpha\text{-AsW}_9\text{O}_{33})_6]\}$ hexameric assemblies⁵⁷ and the largest lanthanide-containing $\{[\text{W}_{14}\text{Ce}^{\text{IV}}\text{O}_{61}](\text{W}_3\text{Bi}_6\text{Ce}^{\text{III}}_3(\text{H}_2\text{O})_3\text{O}_{14})[\alpha\text{-BiW}_9\text{O}_{33}]_3\}_2$ tungstobismuthate reported to date.⁵⁸

The larger size of 4f ions compared to 3d metals usually prevents their full incorporation in lacunary frameworks as *addenda* atoms, and therefore, additional sites are available in the coordination sphere of the lanthanide centers for further derivatization. Even if the largest polyoxotungstate architectures known in terms of the number of tungsten atoms, that is the $[\text{Mn}_{40}\text{P}_{32}\text{W}_{224}\text{O}_{888}]^{144-}$ anion,⁵⁹ has been obtained by employing first row transition metal linkers, the combination of lanthanide atoms with dilacunary $\{\text{GeW}_{10}\text{O}_{38}\}$ or trilacunary $\{\text{B-As}^{\text{III}}\text{W}_9\text{O}_{33}\}$ units has also led to several gigantic metal-oxo frameworks. In 1997, the $[\text{As}_{12}\text{Ce}_{16}(\text{H}_2\text{O})_{36}\text{W}_{148}\text{O}_{524}]^{76-}$ anion⁶⁰ was synthesized by Pope and co-workers and it constituted the largest polyoxotungstate known until 2010. This anion incorporates twelve $\{\text{B-}\alpha\text{-AsW}_9\text{O}_{33}\}$ subunits, four monolacunary Lindqvist-type $\{\text{W}_5\text{O}_{18}\}$ subunits and sixteen Ce centers linked by extra tungstate groups in a disc-shaped assembly with ideal D_{2d} symmetry. Similar gigantic POMs, the $[\text{Ce}_{20}\text{Ge}_{10}\text{W}_{100}\text{O}_{376}(\text{OH})_4(\text{H}_2\text{O})_{30}]^{56-}$ and $[\text{Gd}_8\text{As}_{12}\text{W}_{124}\text{O}_{432}(\text{H}_2\text{O})_{22}]^{60-}$ can be both described as dimeric entities composed of two halves related by an inversion center. The pentameric half of the former dumbbell-shaped POM comprises five $\{\beta\text{-Ce}_2\text{GeW}_{10}\text{O}_{38}\}$ subunits linked to each other by the coordination sphere of Ce atoms,⁶¹ whereas hexameric halves in the latter POM are composed of six $\{\text{AsW}_9\text{O}_{33}\}$ and two $\{\text{Gd}_2\text{W}_4\}$ building blocks.⁶² Since 2010, the giant crown-shaped $[\text{K}_7\text{Ce}_{24}\text{Ge}_{12}\text{W}_{120}\text{O}_{444}(\text{OH})_{12}(\text{H}_2\text{O})_{64}]^{52-}$ has been the last member of the family of giant lanthanide-containing polyoxometalates,⁶³ nevertheless two giant Ln₃₀-containing POMs have been recently reported. The high nuclear $\{\text{Ln}_{30}\text{Ge}_{12}\text{W}_{107}\text{O}_{420}(\text{OH})_2(\text{H}_2\text{O})_{14}\}$ cluster is formed by the assembly of 10 dilacunary Keggin type POWs, in which two $\beta(4,11)$ subunits located at the two opposite vertices of the giant cluster, are linked through eight dilacunary α -Keggin anions (four $\alpha(1,5)$ and four $\alpha(1,8)$).⁶⁴ Related works involve the use different lanthanide ions, alkaline cation directed assemblies, interesting solution behavior, as well as magnetic and luminescent studies.⁶⁵

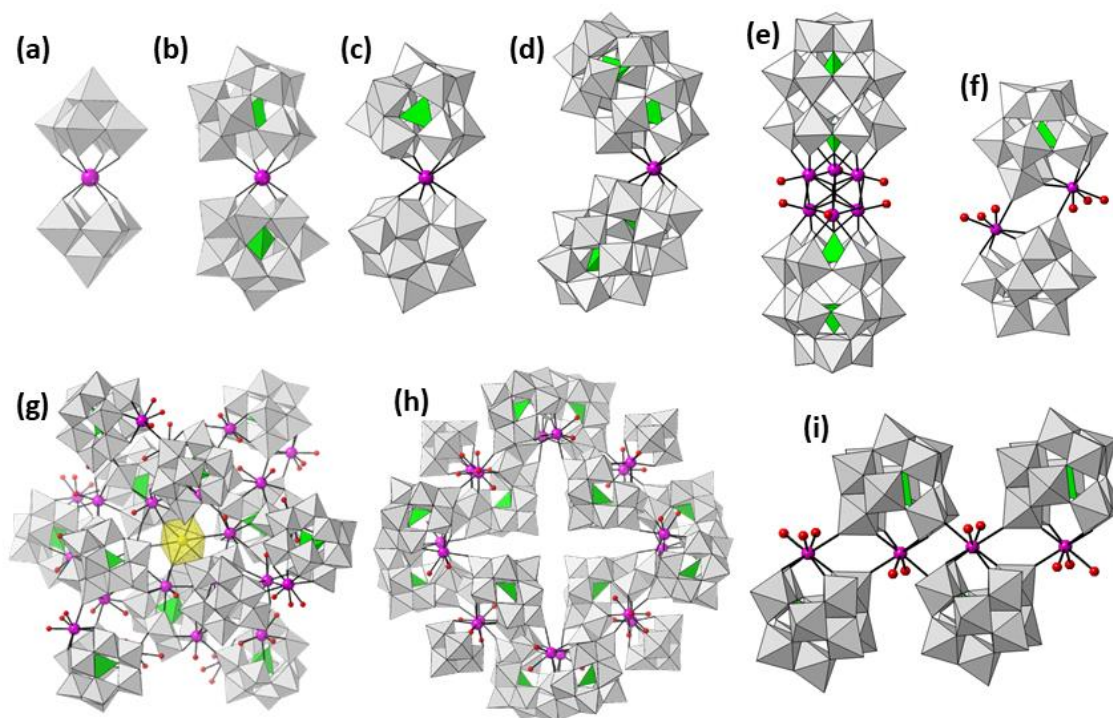


Figure 1.7. Representative structures of lanthanide-containing POMs. (a) $[\text{Ln}(\text{W}_5\text{O}_{18})_2]^{9-}$; (b) $\{\text{Ln}(\alpha\text{-XW}_{11}\text{O}_{39})_2\}$; (c) $A\text{-}\{\text{Ln}(\beta_2\text{-SiW}_{11}\text{O}_{39})_2\}$; (d) $\{\text{Ln}(\alpha_2\text{-P}_2\text{W}_{17}\text{O}_{61})_2\}$; (e) $[\{\text{Yb}_6\text{O}(\text{OH})_6(\text{H}_2\text{O})_6\}(\text{P}_2\text{W}_{15}\text{O}_{56})_2]^{14-}$; (f) $[\{\text{Ln}(\text{H}_2\text{O})_3(\alpha\text{-PW}_{11}\text{O}_{39})_2\}_2]^{6-}$; (g) $[\text{K}_7\text{Ce}_{24}\text{Ge}_{12}\text{W}_{120}\text{O}_{444}(\text{OH})_{12}(\text{H}_2\text{O})_{64}]^{52-}$; (h) $[\text{As}_{12}\text{Ce}_{16}(\text{H}_2\text{O})_{36}\text{W}_{148}\text{O}_{524}]^{76-}$; (i) zig-zag $\{\text{Ln}(\text{H}_2\text{O})_2(\alpha\text{-XW}_{11}\text{O}_{39})\}_\infty$ chains.⁶⁷ Color code: Ln, pink; K, yellow polyhedra.

1.3.2. Properties of lanthanide-containing POMs

Extensive work has been carried out in this field due to the interesting structural and physicochemical properties that lanthanide-containing POMs might show, including their role as Lewis acid catalysts, magnetism or luminescence.⁴⁷ In spite of their structural simplicity, small mono- or dimeric species have also attracted enormous interest because of their outstanding properties. For instance, Ln-containing POMs with accessible coordination sites can behave as effective and recoverable Lewis acid catalysts with enhanced selectivity.⁶⁸ The high coordination numbers and flexible coordination geometries of lanthanide ions allow the presence of accessible and labile coordination sites, which confers the system with the capacity to activate organic substrates and acts as Lewis acid catalyst. Many Ln-POMs have been reported to act as efficient Lewis catalysts for different reactions including reduction of nitriles, cyanosilation of aldehydes and ketones, Diels-Alder reactions, among others.⁶⁹ Some recent studies take advantage of the Lewis acid character of 4f metals with the Lewis base behavior of oxygen-rich POM surfaces to design efficient bifunctional catalysts.⁷⁰ In addition, their catalytic role in hydrolysis reactions with strong biological implications such as phosphoesterase or protease activity have also been addressed.⁷¹ Nonetheless, similar to that observed for classical coordination

complexes, the study of optical and magnetic properties dominates the field of 4f-metal-containing metal-oxo clusters.

Magnetic properties

Another field of research with high dynamism within the family of Ln-based compounds is molecular magnetism. The intrinsic large magnetic anisotropy together with large ground-state spin values displayed by rare-earth metal ions under certain ligand fields, accompanied by the rigidity and insulating ability of POMs as ligands have been proved to result in molecular systems showing slow relaxation of the magnetization. Different 4f-containing POMs have been reported to behave as effective single-ion or single-molecule magnets (SIMs or SMMs) or spin qubits in recent years; this may pave their way for being applied in high-density memory-storage/sensor devices, spintronics or quantum computing. When it comes to Ln-substituted POMs with SMM behavior,⁷² they exhibit some advantages in comparison to classical coordination complexes: (i) lacunary POM ligands show higher thermal and chemical stability both in solution and in the solid state; (ii) the rigidity of the ligand can result in highly symmetric environments for the 4f centers, or even force unusual geometries such as the 5-fold C_5 symmetry;⁷³ (iii) their large size and diamagnetism ensures magnetic isolation over the neighboring species. The use of low nuclearity 4f metal complexes represents a suitable approach to design systems with slow relaxation of magnetization, in which magnetization reversal is retained by the presence of an energy barrier. In this regard, different series of Peacock–Weakley-type assemblies in which Ln centers with square antiprismatic geometry are trapped between lacunary fragments, i.e., $[\text{Ln}(\text{W}_5\text{O}_{18})_2]^{9-}$ ($\text{Ln}^{\text{III}} = \text{Tb}, \text{Dy}, \text{Ho}, \text{and Er}$), $[\text{Er}(\beta_2\text{-GeW}_{11}\text{O}_{39})(\alpha\text{-GeW}_{11}\text{O}_{39})]^{13-}$, and $[\text{Ln}(\beta_2\text{-SiW}_{11}\text{O}_{39})_2]^{13-}$ ($\text{Ln}^{\text{III}} = \text{Dy}, \text{Ho}, \text{Er}, \text{and Yb}$), have displayed slow relaxation of the magnetization.⁷⁴ The high coherence of the $[\text{Ho}(\text{W}_5\text{O}_{18})_2]^{9-}$ molecular qubit should be mentioned, as well as the chemically controlled reversible switching of the SMM behavior for POM-based systems.⁷⁵

The 4f electrons are located in inner orbitals, which are shielded by fully occupied 5s and 5p electrons. This lowers the effects from surrounding ligands, making them to be less affected by an external ligand field in comparison to 3d metal centers. Conversely, the spin-orbit coupling is much stronger in lanthanide ions, since it is larger than crystal field effects. Figure 1.8 provides a description of the energy levels on a 4f-ion considering electron-electron interactions, spin-orbit couplings (J levels) and crystal-field splitting effects (M_J sub-levels).

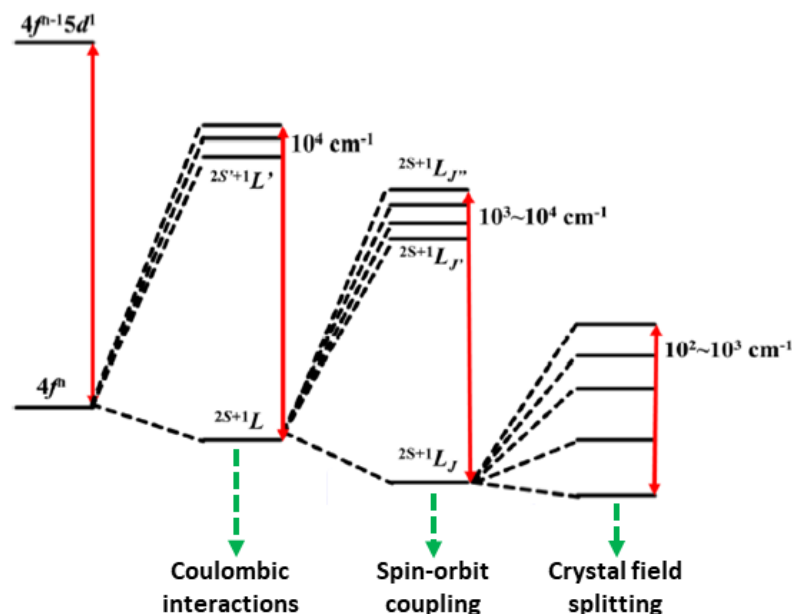


Figure 1.8. Energy splitting diagram of the sublevels of the lanthanide ions.

The slow magnetic relaxation (or hysteresis) comes from the combination of two main factors: i) a strong magnetic anisotropy that leads to a high-spin ground state well separated from the excited levels and; ii) a large axial anisotropy (D). These two factors generate a thermal barrier that prevents the reversal of the magnetization, also known as the *energy barrier* (U). In this way, in the absence of external magnetic field ($H_z = 0$), the ground states own the same energy and are equally populated. Thus, the system does not present any magnetization (Figure 1.9a). On the contrary, in the presence of strong external field ($H_z \neq 0$), one of the sublevels is stabilized in comparison to the other, and the spin of the molecules is oriented in the same direction as the applied field, populating the stabilized sublevel (Figure 1.9b). Then, when the external magnetic field is removed, the ground state reaches again a double degenerate state, and the magnetization of the systems tends to relax and return to the initial equilibrium state, losing the magnetization ($M = 0$) (Figure 1.9c). However, it is necessary to overcome the energy barrier to relax. If the temperature is below the blocking temperature (T_B), the magnetization is blocked in one of its orientations; therefore, it returns very slowly to the initial equilibrium, exhibiting this way magnetic hysteresis.⁷⁶ This is why SMM behavior is only observed at very low temperatures.

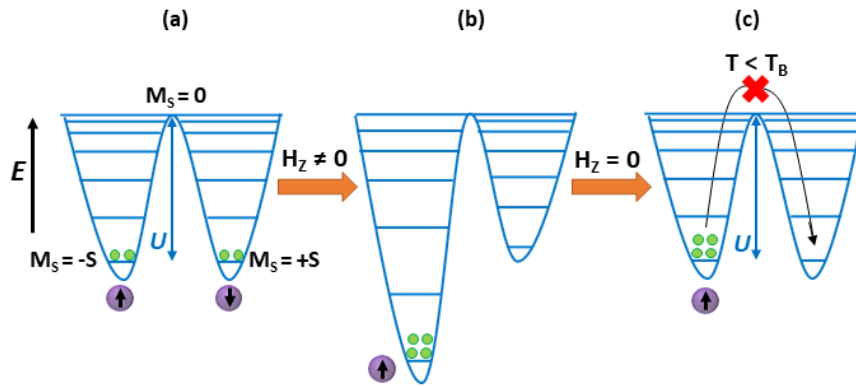


Figure 1.9. Schematic representation of the orientation of the magnetization: (a) in equilibrium in absence of magnetic field; (b) in the presence of an external field, and; (c) blocking of the magnetization in the absence of external field and when $T < T_B$.

The three common relaxation mechanisms are those taking place through spin-phonon coupling processes (Figure 1.10a):⁷⁷ i) a **direct process** in which the spin is relaxed by emitting a single phonon with the same energy as the difference between the M_S sublevels in the ground state; ii) **Raman process**, in which the spin absorbs a phonon with a certain frequency (ω_1), and reaches a virtual excited state from which it quickly relaxes emitting a new phonon of ω_2 . Thus, the overall energy transferred is the difference between the absorbed and the emitted phonon; and iii) **Orbach process**. It is a two-stage process in which a phonon (ω_3) is absorbed by a direct process, making a spin to jump to a higher excited level. From this excited state, the system is relaxed emitting a second phonon (ω_4). Therefore, the spin is indirectly transferred from an excited state to a ground level by passing through a second excited state.

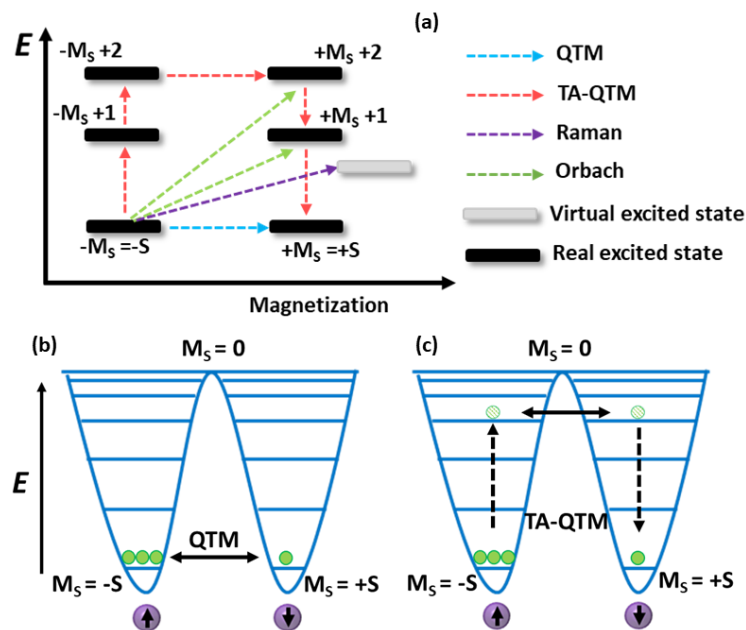


Figure 1.10. (a) Scheme of: Raman, Orbach, QTM and TA-QTM relaxation processes, together with a more detailed representation of the inversion of magnetization due to (b) QTM effect, (c) TA-QTM effect.

Moreover, there is an additional relaxation process occurring between the M_S sublevels of the doubly degenerate ground state without the need of overcoming the energy barrier. This is called the **Quantum Tunneling mechanism (QTM)** (Figure 1.10b). Sometimes the relaxation pathways can be combined, and QTM occurs between excited states. This process is known as **Thermally Assisted Quantum Tunneling of Magnetization (TA-QTM)** (Figure 1.10c). When this process occurs, there is an effective thermal energy barrier (U_{eff}), which is lower than the expected thermal activation barrier. The most common strategies to overcome QTM consist on magnetically diluting the samples with diamagnetic ions, or applying an external *dc* (direct current) magnetic field that breaks the degeneracy of the M_S sublevels and the thermally activated relaxation process are favored.

Photoluminescent properties

With regard to optical properties, parity forbidden (Laporte's rule) 4f–4f transitions of Ln ions can result in bright photoluminescence in the visible to near-infrared (NIR) region if suitable antenna ligands are used. It is well-known that energy transfer from strongly absorbing ligands to emitting centers can populate excited states giving rise to intense and sharp emission bands. The excitation of these antenna ligands is followed by an energy transfer from the ligand to the excited levels of the metal center and the subsequent characteristic emission of the lanthanide ion (Figure 1.11). Analogous to the behavior of coordination complexes bearing ligands which usually contain aromatic groups,⁷⁸ POMs can sensitize 4f metal ions via $O \rightarrow M$ ($M = Mo, W$) ligand-to metal charge-transfer (LCMT) states.⁷⁹ Multidentate organic moieties or lacunary POM fragments can also block coordination sites to avoid the emission quenching originating from coordinated aqua ligands. These facts can lead to sharp and monochromatic emission bands and relatively long luminescence lifetimes for Sm, Eu, Tb and Dy species in the visible region or for Nd, Er and Yb in the near infrared (NIR). Lanthanide ion complexes that emit in the visible region are widely used in biomedical applications and imaging of cells and tissues, among other applications.⁸⁰ However, systems that emit in the NIR region show interesting applications in optical and electronic devices, especially for biological applications as sensors.⁸¹ It is worth mentioning the $[Eu(W_5O_{18})_2]^{9-}$ anion reported by Yamase and Sugeta,⁸² which constitutes the most applied POM in the construction of functional materials.⁸³ Chemically-controlled switching of the emission and enhanced photoluminescent properties have been achieved by supporting this cluster into multiple surfaces or thin films, as well as nanoparticles of different matrices such as polysaccharides, silica, or surfactants.⁸⁴

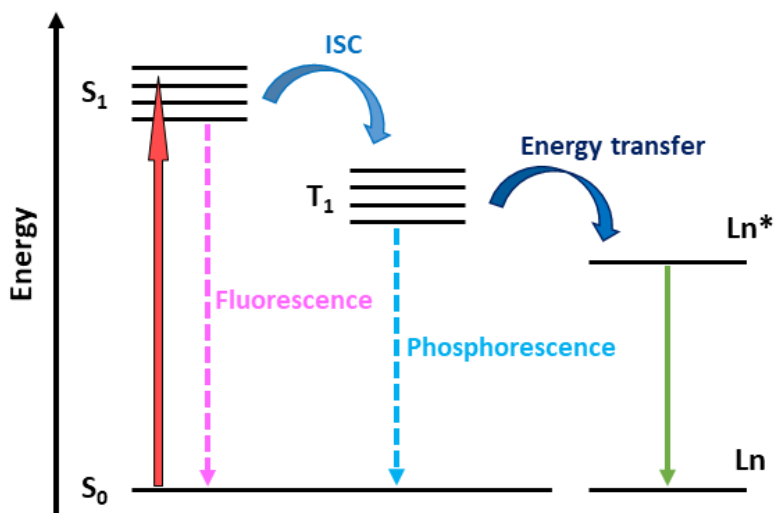


Figure 1.11. Simplified Jablonsky diagram for the antenna effect in a lanthanide complex (ISC = Intersystem Crossing radiationless process).

1.4. ORGANIC FUNCTIONALIZATION OF POMs

POM clusters are ideal candidates to be used as active molecular entities in functional materials due to their inherent features (e.g. high solution and thermal stability, high acidity, and versatile redox properties). This way, the organic functionalization of POMs represents a key factor for these clusters to be suitably incorporated into matrixes like polymers or carbon nanotubes, and also to interact with diverse surfaces (e.g. silica, silicon, gold, alumina, graphite) or metallic nanoparticles.⁸⁵ This strategy might pave their way for the fabrication of new multifunctional devices (e.g. immobilized catalysts, photoactive systems for energy production, electron storage systems). However, it usually requires elaborated organic functions that can only be achieved via multistep synthetic work on preformed hybrid POM platforms.⁸⁶ The combination of organic functions with inorganic oxo-clusters can also lead to the designs of photocatalysts, luminescent systems, or photochromic materials. Two different classes of POM-based organic-inorganic hybrids can be distinguished attending to the type of interaction between the two components. The first class gathers all the systems in which electrostatic interactions, hydrogen bonds, or Van der Waals forces are established between the organic and inorganic fragments. Regarding the second class of POM-based hybrids, the organic and inorganic moieties are linked via strong covalent bonds. In this sense, different synthetic methods have been developed for the covalent attachment of organic groups to inorganic POM skeletons that are studied in depth. In this sense, different synthetic methods have been developed for the covalent attachment of organic groups to inorganic POM skeletons.⁸⁷

One of the most extensively explored routes consist in combining lacunary polyoxotungstates with *p-block organoderivatives*. These are predominantly organosilyl, -

phosphoryl and -stannyl moieties, but also -germyl, -arsenyl and -stibyl groups can play this role (Figure 1.12). The nucleophilic character of the oxygen atoms delimiting the vacant site is significantly higher than those from the plenary anion, which facilitates the union with electrophilic groups. Two main strategies can be followed to incorporate custom-designed organic moieties into POM systems. The first approach consists in preparing the desired organic molecule, followed by its reaction with polyoxoanions. In the second strategy, the organic function exhibits a reactive pendant group, which is first incorporated into the vacant site of the cluster. Since the first description of a series of organosilyl derivatives $[\text{SiW}_{11}\text{O}_{39}\{\text{O}(\text{SiR})_2\}]^{4-}$ ($\text{R} = \text{C}_2\text{H}_5, \text{C}_6\text{H}_5, \text{NC}(\text{CH}_2)_3, \text{C}_3\text{H}_5$) in 1979, a large variety of organic functions have been incorporated into monolacunary Keggin or Wells-Dawson-type structures. The resulting molecular hybrid POMs can contain up to two organosilyl groups or one dimeric μ -oxo-bridged $(\text{RSi})_2\text{O}$ unit per vacant site.⁸⁸ Moreover, from two to four organo-groups can be anchored in the larger lacunae of di- or trilacunary Keggin units.⁸⁹ In contrast, only a few works describe the functionalization of POMs with organogermlyl moieties.⁹⁰

Organophosphonate groups have been widely used for the functionalization of Strandberg-type polyoxomolybdates, lacunary polyoxotungstates derived from the Keggin and Wells-Dawson structures or diverse polyxovanadates.⁹¹ The fact that functionalization can be monitored by means of ^{31}P -NMR spectroscopy is a major advantage for the characterization of organophosphonate-derivatives. Similarly, organotins constitute another interesting group, as they show some noticeable advantages like; the high stability of the Sn-C bond in aqueous media, and the similar ionic radius between Sn^{IV} and M^{VI} ($\text{M} = \text{Mo}, \text{W}$), which facilitates the inclusion of the organotin fragments into lacunary sites. Dimethyltin (SnMe_2) moieties were employed in combination with polylacunary POM frameworks leading to outstanding structures such as the dodecameric $[\{\text{SnMe}_2(\text{H}_2\text{O})\}_{24}\{\text{SnMe}_2\}_{12}(\text{A-XW}_9\text{O}_{34})_{12}]^{36-}$ ($\text{X} = \text{P}, \text{As}$) ball-shaped anion.⁹² Kortz's group is also the responsible for the handful of reports on organo-antimony POM derivatives.⁹³

Another strategy to covalently attach organic groups to the POM skeleton involves the **replacement of shell O atoms** with O- or N- donor ligands, as exemplified by trisalkoxo capped Anderson-Evans clusters, Lindqvist-type polyoxovanadates or $[\text{H}_4\text{P}_2\text{V}_3\text{W}_{15}\text{O}_{62}]^{5-}$ anions (V_3 -Wells-Dawson) as well as by organoimido/diazenido derivatives of Lindqvist-type molybdates (Figure 1.12). During the last decade, an impressive work has been carried out in the organic functionalization of Anderson-Evans anions with trisalkoxide ligands.⁹⁴ Ligand substitution usually takes place over the two triangular faces of the $\{\text{XO}_6\}$ octahedron (δ isomer with ideal D_{3d} symmetry). Occasionally, two μ_3 -O oxygen atoms from the $\{\text{XO}_6\}$ unit and one μ_2 -O from the $\{\text{M}_6\text{O}_{18}\}$ ring are substituted. In this case, the less frequent χ isomer with ideal C_{2h} symmetry is obtained.⁹⁵ It is also worth highlighting the recent reports on the

organic derivatization of the bent β isomer of the Anderson-Evans anion⁹⁶ together with the scarce successful attempts for the functionalization of polyoxotungstates.⁹⁷ Moreover, single-side and asymmetric functionalization for δ isomers have been achieved by Wei's and Cronin's groups, respectively.⁹⁸

Preparation of trisalkoxo-functionalized species is also well-described in the case of mixed addenda V_3 -Wells-Dawson anions.⁹⁹ The use of bridging ligands has resulted in hybrids with very diverse conformation (dumbbell-, triangular-, dendrimer-shape), which can self-assemble into vesicles in aqueous solutions.¹⁰⁰ Furthermore, this structure allows not only the direct derivatization with trisalkoxo ligand, but also the covalent attachment of small organic molecules showing amide and diol groups.¹⁰¹ Similarly, trisalkoxo type ligands have also been used to prepare Lindqvist-type hexavanadates difunctionalized in *trans* fashion.¹⁰² In contrast, only one example of the *cis*-functionalization have been published to our knowledge.¹⁰³ Regarding the N-donor ligands, since the first organoimido derivative of the Lindqvist-type molybdate,¹⁰⁴ this family of hybrid POMs has experienced a vast growing. In this context, a wide range of mono- and di-organimoimido derivatives have been synthesized¹⁰⁵ following the efficient synthetic process described by Peng and coworkers.¹⁰⁶ A recent study has demonstrated that not only terminal oxo ligands, but also bridging O atoms can be replaced with these ligands.¹⁰⁷ In contrast to organoimido derivatives, functionalization with organodiazenido-type molecules have been comparatively less studied.¹⁰⁸

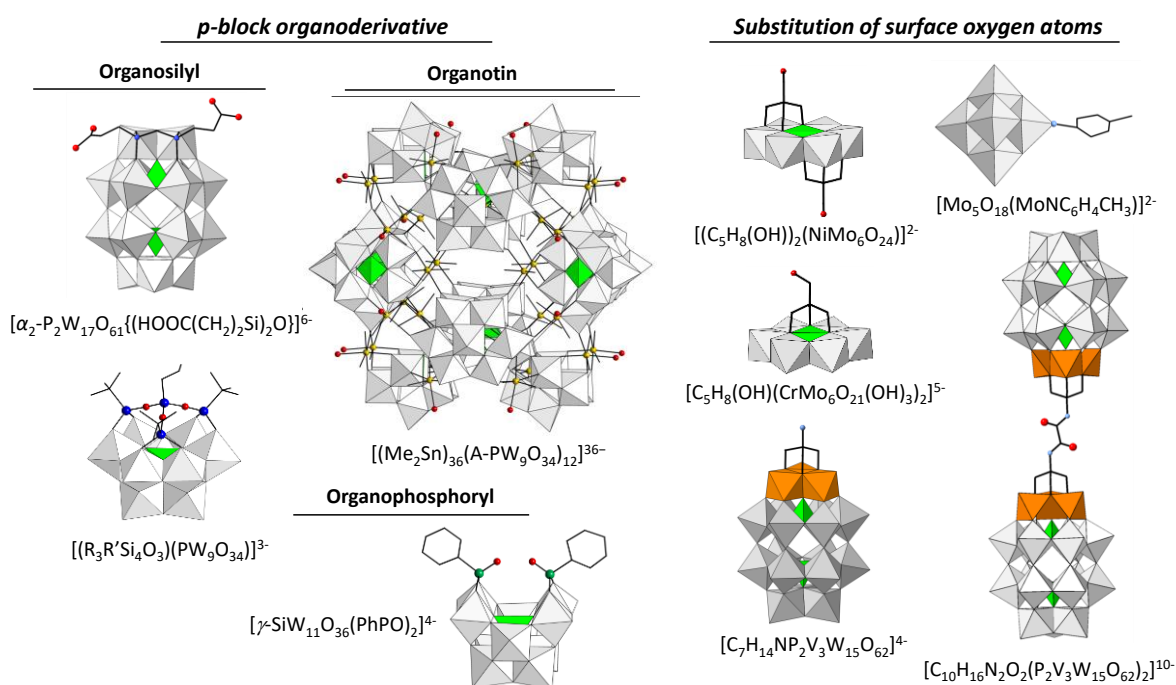


Figure 1.12. Representative examples of hybrid POMs bearing *p*-block organoderivatives (R = C₄H₁₂; R' = C₃H₇; Ph = phenyl; Me = Methyl), and those in which surface O-atoms are replaced by organic fragments. Color code: N, light blue; for *p*-block elements: Si, dark blue; P, green; Sn, yellow.

CHAPTER 1

Furthermore, transition metal or lanthanide complexes bearing organic ligands can be linked to POMs either by their coordination to surface O atoms or by their incorporation into the vacant positions of lacunary anions. The resulting structures can exhibit i) discrete, molecular hybrid entities when ligands with no bridging ability are coordinated to metal substituted POMs or the surface-appended metal complexes act as antenna group; and ii) extended hybrid systems when bridging ligands are coordinated to suitable metal substituted POMs or surface-appended metal complexes play a bridging role between contiguous clusters.

1.4.1. Organic derivatization of 3d- or 4f-metal substituted POMs

As mentioned in the previous section, the incorporation of transition metals or lanthanides into vacant polyoxoanions is one of the oldest and most studied reactions in POM chemistry. Organic ligands can be effectively coordinated to these additional metal centers of suitable POM anions leading to organic-inorganic hybrids. There are three main strategies for the organic functionalization of these clusters. The first approach involves the replacement of labile solvent molecules (e.g. acetone, acetate anions, water molecules) coordinated to exposed metal centers. A second route implies the reaction of metal complexes bearing organic ligands with lacunary polyoxotungstates, whereas the third strategy consists in simpler one-pot procedures by simultaneously mixing the appropriate oxoanion, with the 3d/4f-metal salt and the organic ligand together.

Regarding the first route, this strategy seems to be the less used so far, due to the difficulty of finding solution stable POM precursors with accessible metal centers. Steric effects and repulsion between anionic ligands and POMs make complexation of exposed metal centers in POM clusters challenging. Overall, negatively charged and bulky ligands will react less favorably than small neutral ligands. The first studies in this approach were carried out through the substitution of the water molecule of a 3d-metal-substituted Keggin-type $[M(H_2O)(XM_{11}O_{39})]^{n-}$ polyanion with the N-donor ligands pyridine and imidazole derivatives.¹⁰⁹ In a similar way, N-donor ligands (e.g. pyridine, imidazole or pending ethylenediamine) have been used for the substitution of coordinated water molecules on Weakley- $[M_4(H_2O)_2(XW_9O_{34})_2]^{n-}$ and Hervé-type $[M_3(H_2O)_3(XW_9O_{33})_2]^{n-}$ sandwich POMs.¹¹⁰ Besides these examples, the reactivity of Krebs-type $[M^II(H_2O)_3]_2(WO_2)_2(SbW_9O_{33})_2]^{10-}$ tungstoantimonates towards planar and aromatic N,O chelating ligands has been systematically studied very recently, because this anion exhibits up to three accessible and labile water molecules per external belt metal center.¹¹¹

Pope prepared POM hybrids through the second approach for the first time. Those include ethylenediamine chelated Co centers encapsulated between two $\{PW_9O_{34}\}$ or $\{PW_{10}O_{38}\}$ lacunary Keggin units or lacunary hexamolybdates.¹¹² This strategy also allows

the incorporation of chiral organic ligands in such a way that the resulting compounds display potential applications in asymmetric catalysis, nonlinear optical materials and applied biology, among others.¹¹³ Following this route, Hill's group reported two enantiomerically pure compounds by mixing a divacant Wells-Dawson anions with Zr-based metalorganic complexes containing tartrate or malate ligands.¹¹⁴ Some other authors opted for one-pot procedures. In this sense, Rousseau and coworkers synthesized multi-transition-metal containing species to which organic ligands bearing carboxylate groups were coordinated by the reaction between trilacunary Keggin-type units, an excess of 3d metal source and carboxylate ligands under mild conditions.¹¹⁵ Some examples are represented in Figure 1.13.

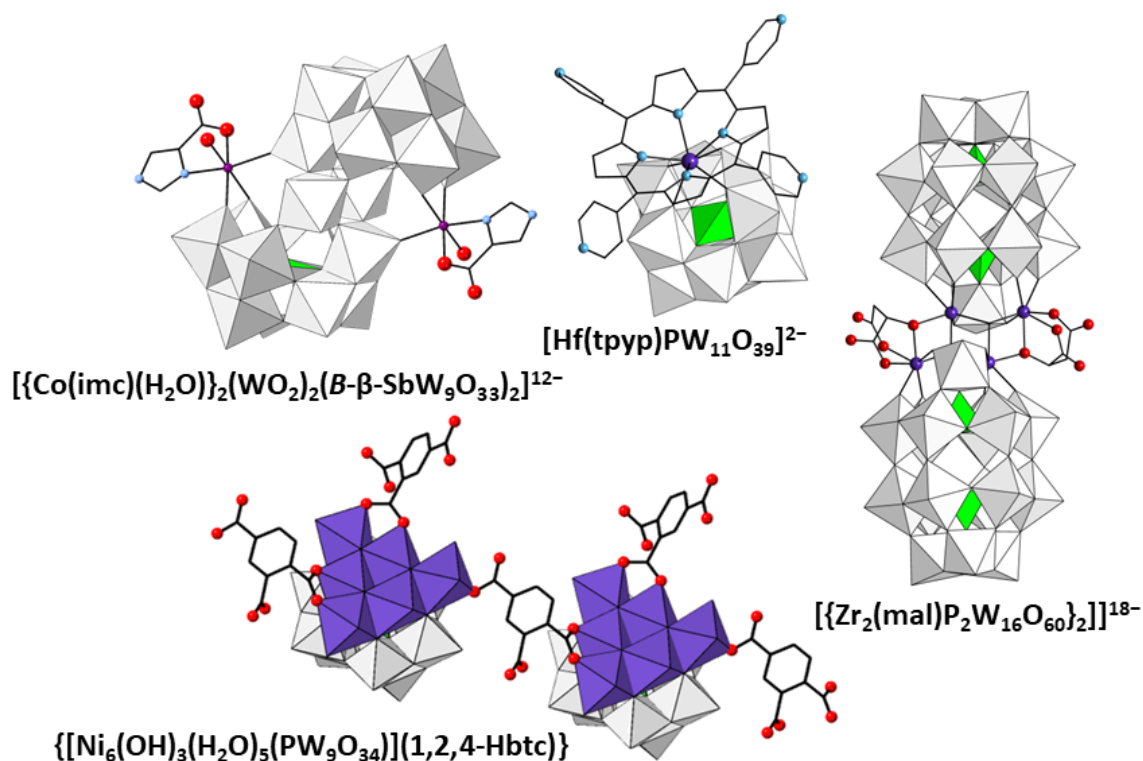


Figure 1.13. Representative examples of organic functionalization on 3d-metal containing POMs. Ligands: imc = imidazolecarboxylate; tpyp = meso-tetra-(4-pyridil)-porphyrine; btc = benzenetricarboxylate; mal = malate. Color code = 3d metals, purple balls or polyhedra.

Alternatively, other groups have also considered hydrothermal techniques for accommodating organic ligands into 3d metal containing POM structures. In this case, Yang and coworkers lead to the formation of extended and porous POMOF (POLYoxometalate-Metal-Organic-Framework) networks, in which $\{\text{Ni}_6\text{PW}_9\text{O}_{34}\}$ building blocks were interconnected by bridging carboxylate ligands.¹¹⁶ Nevertheless, in some occasions the isolation of transition metal complexes instead of the desired POM hybrid is achieved due to the high affinity that some metals present towards some specific organic ligands. Finally,

it should be mentioned that only few studies have been reported about organically functionalized POMs in organic solvents.¹¹⁷

Concerning 4f metal substituted POMs, most of the species with the exception of Peacock-Weakly type polyanions usually show several available coordination positions. Additionally, the oxophilic nature of the lanthanide centers make carboxylic acids suitable ligands for such ligand replacement. However, the negative charge of both carboxylate groups and POM anions together with the steric hindrance that a given POM could produce make direct functionalization challenging. These drawbacks have been overcome by using small chelating ligands in a large excess,¹¹⁸ or even by selecting positively charged POMs such as the tetra-lanthanide-capped and mixed-valence ϵ -Keggin-type phosphomolybdates.¹¹⁹ These examples are further commented in Chapter 5.

1.4.2. Grafting of transition metal complexes at POM surface

Several groups including ours have studied the synthesis of hybrid species via grafting of d-metal complexes at POM surfaces to incorporate additional catalytically or magnetically active centers to the system. *Decoration* can result in molecular hybrid-POMs or extended structures depending on the nature of the organic ligand (Figure 1.14). In the last decades, a huge number of structures synthesized by hydrothermal methods have been reported.¹²⁰ This work started by Zubieta and co-workers, which first focused on polyoxomolybdates / -vanadates, and later expanded their studies to -tungstates.¹²¹ More recently, the systematic studies carried out by our group included both mild bench conditions and harsher hydrothermal syntheses. Initially, the copper(II)-monosubstituted Keggin-type tungstosilicate $[\text{SiW}_{11}\text{O}_{39}\text{Cu}(\text{H}_2\text{O})]^{6-}$ was reacted with dinuclear cationic complexes $[\{\text{Cu}(\text{phen})(\text{H}_2\text{O})_2\text{OAc}\}_2]^{2+}$ and $[\{\text{CuL}(\text{H}_2\text{O})_2\}_2\text{ox}]^{2+}$ (L = phenantroline, 2,2'-bipyridine) to lead to hybrids with different dimensionalities such as discrete molecular POMs, monodimensional chain-like coordination polymers, or bidimensional coordination networks. In addition, the effect of the counterions of the acetate buffer used as solvent on the final arrangement of the hybrid compounds was also investigated. Later on, the assembly of Cu^{2+} -based complexes bearing aromatic and chelating N-donor ligands (e.g. 2,2'-bipyridine, 1,10-phenanthroline and 2,9-dimethyl-1,10-phenanthroline) with plenary Keggin-type tungstogermanates and -silicates was evaluated under hydrothermal conditions.¹²²

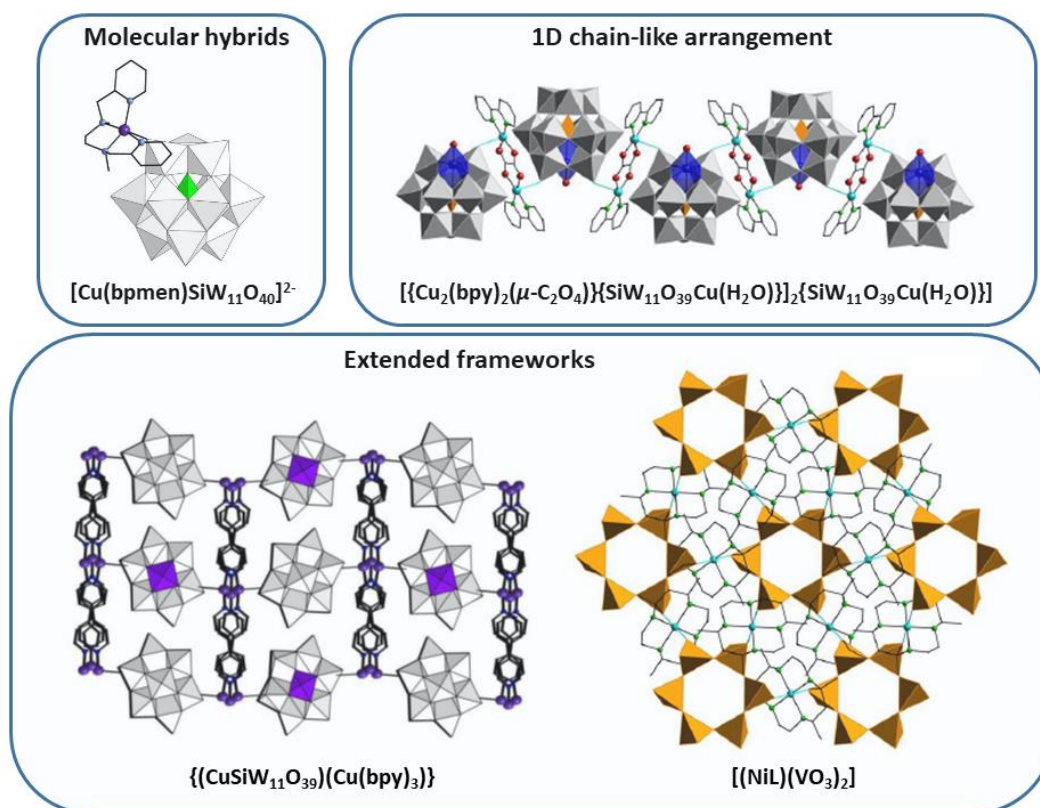


Figure 1.14. Representative examples of hybrid compounds of different dimensionalities, with transition metal complexes grafted to POM surfaces.

Some of our more recent examples of POMs with grafted $\{\text{Cu}(\text{cyclam})\}$ (cyclam = 1,4,8,11-tetraazacyclotetradecane) complexes showed interesting thermostructural behaviors, displaying the ability to undergo single-crystal-to-single-crystal transformations under thermal stimuli.¹²³ In the case of extended framework, the anhydrous and porous networks displayed interesting gas sorption and catalytic properties.¹²⁴

1.5. POROUS POM-METALORGANIC HYBRID FRAMEWORKS

In recent years, POM-based porous crystalline solids have attracted a lot of attention due to the possibility of combining their intrinsic multifunctionality (e.g. catalytic activity, magnetism or luminescence) with the properties of extended open networks with a large internal surface area, such as a high density of active catalytic centers or the selective capacity of adsorption/separation of gases and water sorption.¹²⁵ In fact, the development of porous materials with high internal surface areas represents an alternative viable solution to current global issues such as atmospheric pollution¹²⁶ and scarcity of freshwater.¹²⁷ In fact, water vapor capturing from air not only addresses the global water shortage crisis, but provides also opportunities to fabricate practical devices for water purification,¹²⁸ dehumidification,¹²⁹ or indoor humidity control.¹³⁰ In this sense, Metal-Organic Frameworks (MOFs) are highly promising materials for gas sorption and separation

CHAPTER 1

processes,¹³¹ because their modular constitution allows the fine-tuning of pore size and nature. However, water sorption could be challenging due to the limited hydrolytic stability displayed by some classical MOFs.¹³² Incorporation of rigid, inorganic building-blocks that expose electronegative atoms toward the framework pores such as POM frameworks, might improve the stability of the system and enhance its selectivity towards polar adsorbates like water.¹³³

Insoluble ionic crystals, in which discrete metal-organic macro-cations bearing carboxylate ligands are combined with Keggin-type heteropolyanions $[XW_{12}O_{40}]^{n-}$ ($X = Co^{II}, B^{III}, Si^{IV}, P^V$),¹³⁴ have exhibited selective water sorption properties,¹³⁵ or photocatalytic activity¹³⁶ because the non-efficient packing of such macro-ionic entities renders to the structure a meaningful amount of porosity available for guest molecules.¹³⁷ The wide catalog of such ionic porous compounds prepared by Mizuno et al. in which both the size of the voids and the interactions that take place within them can be finely tuned, give rise to materials with improved and controlled selectivity towards adsorbates of a very different nature (Figure 1.15).¹³⁸ Initial work on the system $[SiW_{12}O_{40}]^{4-}$ and bulky $[M^{III}_3O(OOCR)_6(L)_3]$ macrocations ($M^{III} = Cr, L = H_2O, R = H$) showed selective adsorption of short-chain ($<C_3$) aliphatic alcohols and nitriles based on their size, as well as catalytic activity in selective oxidation of alcohols.¹³⁹ The substitution of the heteroatom ($X = Co^{II}, B^{III}, Si^{IV}, P^V$) and subsequent change in the overall charge of the polyanion differentiates polar molecules of diverse nature (esters, nitriles, alcohols, water) in such a way that the adsorption of smaller molecules is favored in systems in which the POM shows a lower negative charge.¹⁴⁰ In addition, the introduction of aliphatic or halogen groups in the system $R = C_2H_5, Cl, Br$, have resulted in materials capable of showing hydrophobic and hydrophilic channels at the same time for the efficient separation of gases in an ethylene/ethane mixture.¹⁴¹ Finally, the replacement of the water molecules present in the macrocation by monodentate organic ligands $L = pyridine, 4\text{-ethylpyridine}$ favors the affinity of the network towards CO_2 , so it could be used in industrial gas purification processes such as the production of acetylene.¹⁴²

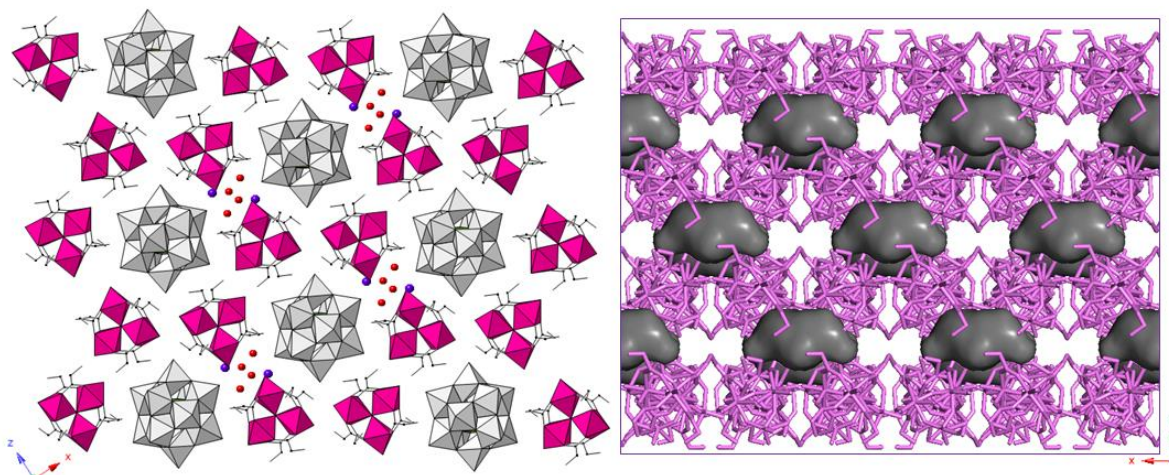


Figure 1.15. Crystal packing of the $\text{Na}_2[\text{Cr}_3\text{O}(\text{OOCC}_2\text{H}_5)_6(\text{H}_2\text{O})_3]_2[\alpha\text{-SiW}_{12}\text{O}_{40}]$ porous ionic crystal. Color code: Cr, pink polyhedra; Na, purple; O, red.

Beyond ionic crystals, different strategies have been followed to build POM-based covalent porous solids.¹⁴³ These include the connection of clusters directly by means of metallic centers to give rise to purely inorganic porous structures with high thermal stability¹⁴⁴ or the preparation of extended hybrid networks analogous to the popular MOFs, but using derivatives of POMs as nodes or linkers. The first synthetic approach lacks predictability, whereas the second involves complicated stepwise preparation processes, because it implies the organic derivatization of POM units so that they can connect metal nodes or generate metal-polysubstituted POMs that can be linked by bridging organic ligands.¹⁴⁵ An alternative route consists in the self-assembly of POMs through metallic linkers belonging to coordination complexes with peripheral organic ligands.¹⁴⁶ In this context, it is worth highlighting the work carried out in our research group on open structures based on POMs and Cu^{II} coordination complexes of N4-tetradentate macrocyclic ligands.

1.5.1 Complexes of macrocyclic polyamines: cyclam and DMC

Transition metal complexes of naturally occurring macrocyclic ligands such as porphyrin, peptides or polyamines, have long been studied due to their biological properties.¹⁴⁷ From the beginning, macrocyclic polyamines were discovered to possess some common properties such as the high affinity for metal complexation. This *chelation effect* leads to an increased stability of the final metalorganic complexes. Moreover, the stability of the metal-complex increases upon cyclization if compared to that of acyclic tetramine ligands, which is known as *macrocyclic effect*.¹⁴⁸ The cyclic tetradentate cyclam (1,4,8,11-tetraazacyclotetradecane) ligand has been one of the most studied macrocyclic polyamines due to its flexibility and ability to coordinate to a variety of transition metal ions. The cyclam molecule was first synthesized by Van Alphen in 1937, through the reaction of 1,3-dibromopropane and ethylenediamine.¹⁴⁹ Metalorganic complexes of most

transitions metals can be found on the Cambridge Structural Database, CSD¹⁵⁰ (i.e. V, Cr, Mn, Fe, Co, Ni, Cu and Zn of the first row transition metals; Tc, Ru, Rh, Pd, Ag and Cd 4d-metals, and; Re, Os, Pt, Au and Hg 5d-metal ions). From this long list, 3d-metal ions have been the most studied, specially Ni^{II} and Cu^{II}, which have shown biomedical activity, as well as the ability to act as catalyst in the photoreduction of CO₂. This activity was first reported in 1980 by Fisher and Eisenberg,¹⁵¹ although Sauvage and coworkers demonstrated that the Ni^{II}-containing complex was unique in its efficiency and selectivity for CO₂ reduction in aqueous solutions with minimal production of H₂.¹⁵²

Upon metal coordination, there are five possible configurations of metal cyclam complexes, which depend on the ligand conformation and, specially, on the spatial arrangement of the NH protons. In this way, RSRS, RSRR, SSRR, RSSR or RRRR, designated as *trans-I* to *trans-V* isomers, respectively, can be found for cyclam depending on the NH bonds, which can lie either above or below the mean MN₄ plane (Figure 1.16).¹⁵³ The energies of different configurations have been calculated based on molecular models and using molecular mechanics, semi-empirical methods and density functional theory.¹⁵⁴ Bosnich and coworkers¹⁵⁵ calculated the semiquantitative estimates of the energies of these five cyclam isomers, which indicates that the *trans-III* configuration constituted the most stable isomer for a {Ni(cyclam)}²⁺ complex with ideal octahedral coordination geometry.¹⁵⁶ Molecular calculations also demonstrated that the *trans-I* form is more stable than *trans-II* when the metal coordination sphere changes from octahedral to square-planar, square-pyramidal or trigonal-bipyramidal. A similar result was obtained for Cu^{II} complexes with a cyclam backbone.¹⁵⁷

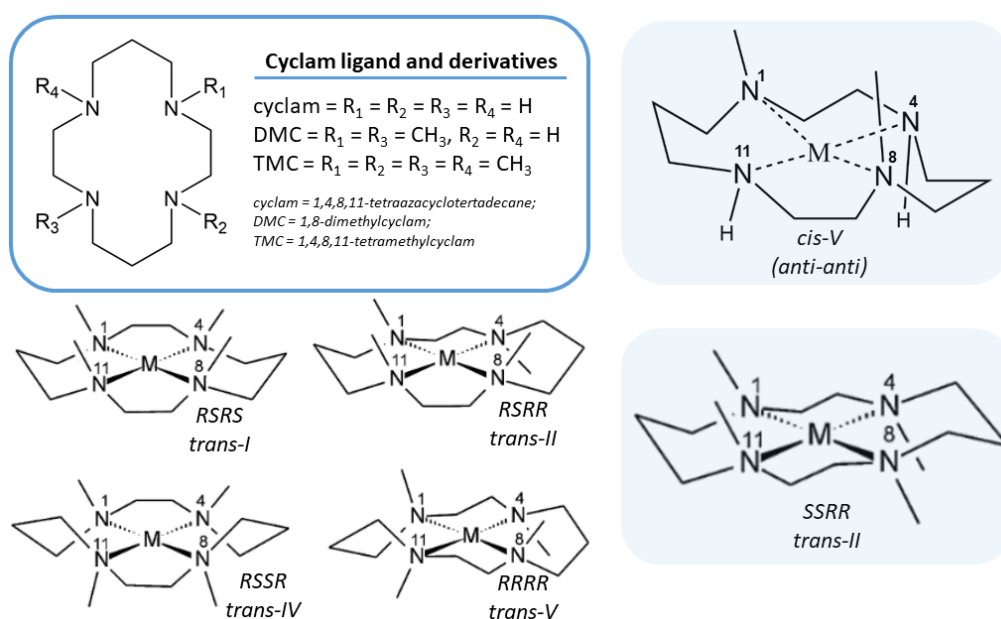


Figure 1.16. Chemical structure of cyclam ligand and its methylated derivatives together with the five different *trans* configurations that the cyclam ligand can adopt. The most common *trans-III* configuration for cyclam and *cis-V* exhibited by various DMC ligands, are highlighted in blue.

Alkylation of N atoms leads to a number of cyclam derivatives. The simplest products are the DMC (dimethylcyclam = 1,8-dimethyl-1,4,8,11-tetraazacyclotetradecane) and TMC (tetramethylcyclam = 1,4,8,11-tetramethyl-1,4,8,11-tetraazacyclotetradecane) molecules (Figure 1.16). Generally, the complexing ability of alkylated ligands is lower than that of cyclam. This fact can be explained taking into account the steric hindrance that results from the incorporation of additional methyl groups into the cyclic tetraamine. Although metal complexation and stability of TMC complexes have been long studied,¹⁵⁸ only six 3d-metal-containing DMC complexes can be found in the CSD for metals like Zn, Cu, Cr and Fe. Contrary to the cyclam ligand in which the number of metalorganic complexes based on Ni^{II} and Cu^{II} stand out with respect to the rest of the transition metals, no Ni^{II}-containing complex with DMC ligand is found in the CSD database. On the contrary, complexes with Cr^{III}, Cu^{II} and Zn^{II} are found in literature, which exhibit a *cis*-folded conformation instead of the most common *trans-III* configuration found for cyclam-based complexes.¹⁵⁹ Surprisingly, only {Cu^{II}(DMC)} units in which the Cu^{II} center shows an octahedral geometry, is found to exhibit a *trans-III* configuration, whereas the remaining complexes show the *cis-V* (*anti-anti*) conformation more commonly (Figure 1.16).¹⁶⁰

The fact that the equatorial positions on coordination sphere of the transition metals are blocked by the cyclam ligand (or derivatives), and only the axial positions remain accessible for coordination, makes these transition metal of macrocyclic polyamines complexes excellent candidates for the construction of POM-based high-dimensional hybrid frameworks. This fact is especially relevant for Cu^{II} complexes showing axially elongated coordination geometries. In addition, the large negative charge of POMs requires a high number of M^{II}-containing metalorganic moieties to achieve electroneutrality. In this way, the number of grafting sites for each POM cluster increases, raising the possibility of generating extended covalent networks. Moreover, the tendency of these ligands to establish N–H···O and C–H···O type contacts above and below the MN₄ plane, also contributes to the overall stability of the resulting hybrid framework. The transition metal on the metalorganic building block can adopt up to three different coordination geometries (Figure 1.17): (a) octahedral MN₄O₂ geometry, when the metal center is coordinated to either O atoms from the POM surface or solvent (usually water) molecules. The complexes can play a bridging role when the two axial positions are occupied by O atoms from adjacent clusters; (b) square-pyramidal MN₄O geometry, when the metal is coordinated only to one O_{POM} atom (antenna complex) or water molecule (counterion), and; (c) square-planar MN₄ geometry when the metal center acts as counterion, although occasionally they can reinforce the hybrid framework through N–H···O and C–H···O contacts.

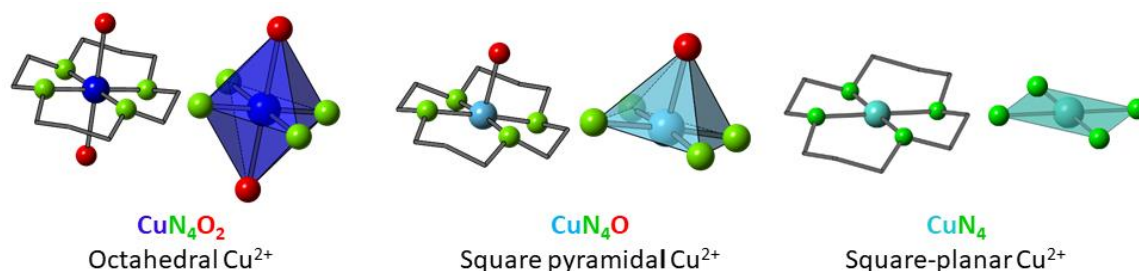


Figure 1.17. Polyhedral and ball&stick representation of the different coordination geometries showed by *trans-III* $\{\text{M}(\text{cyclam})\}^{2+}$ building blocks.

Despite all these advantages and the high number of available $\{\text{TM}(\text{cyclam})\}$ complexes, the coordination of these type of complexes to POM clusters was not reported until 2015 by our group. The pH-dependent assembly of $\{\text{Cu}(\text{cyclam})\}^{2+}$ moieties with isopolyoxovanadates resulted in extended open networks with ability to undergo thermally-triggered single-crystal-to-single-crystal (SCSC) transformations. Basic pH conditions resulted in the $[\{\text{Cu}(\text{cyclam})\}(\text{VO}_3)_2] \cdot 5\text{H}_2\text{O}$ three-dimensional open framework, which loses its porosity upon thermal evacuation of guest solvent molecules.¹⁶¹ Conversely, the $[\text{Cu}(\text{cyclam})][\{\text{Cu}(\text{cyclam})\}_2(\text{V}_{10}\text{O}_{28})] \cdot 10\text{H}_2\text{O}$ supramolecular hybrid framework with permanent porosity was isolated at slightly acidic pH. The network remained unaltered upon dehydration in such a way that it showed the ability to selectively adsorb gaseous CO_2 over N_2 , as well as catalytic activity for the selective oxidation of adamantane (Figure 1.18).^{124a} These studies were later extended to isopolyoxotungstates (and more recently to heteropolyoxotungstates),^{124b} which led to the hybrid compound $[\{\text{Cu}(\text{cyclam})\}_3(\text{W}_7\text{O}_{24})] \cdot 15.5\text{H}_2\text{O}$. This compound exhibited a three-dimensional covalent structure built of heptatungstate clusters linked through metalorganic complexes in an open framework structure with interesting thermostructural behavior. The dynamic architecture undergoes two sequential SCSC transformations upon thermal evacuation of water molecules to result in the partially dehydrated $[\{\text{Cu}(\text{cyclam})\}_3(\text{W}_7\text{O}_{24})] \cdot 12\text{H}_2\text{O}$ and anhydrous $[\text{Cu}(\text{cyclam})]_{0.5}[\{\text{Cu}(\text{cyclam})\}_{2.5}(\text{W}_7\text{O}_{24})]$ phases. The permanent microporosity of the anhydrous phase allowed the adsorption of both gaseous N_2 and CO_2 .^{124b} Some other research groups also reported hybrid compounds based on different $\{\text{M}(\text{cyclam})\}^{2+}$ /POM combination, including Ni^{II} complexes and vanadates,¹⁶² and $\text{M} = \text{Fe}^{\text{II}}$, Ni^{II} , Cu^{II} and Hg^{II} moieties and polyoxoniobates.¹⁶³

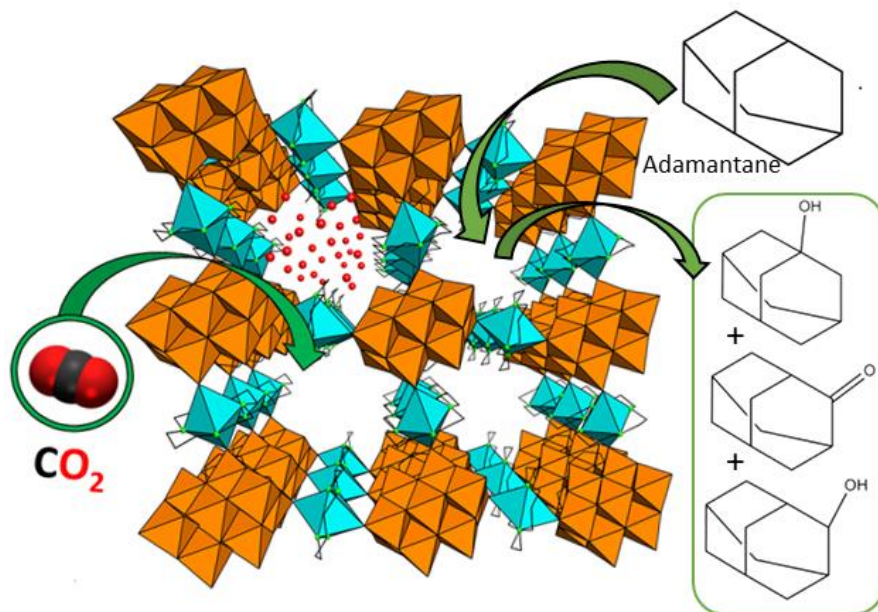


Figure 1.18. The $[\text{Cu}(\text{cyclam})][\{\text{Cu}(\text{cyclam})\}_2(\text{V}_{10}\text{O}_{28})] \cdot 10\text{H}_2\text{O}$ porous hybrid framework exhibits catalytic and gas sorption properties.

1.5.2. Single-Crystal-to-Single-Crystal transformations

Solid-state reactions and transformations promoted by external stimuli are a field of great interest due to the possibility of obtaining compounds with characteristics, compositions and structures different from those synthesized using conventional techniques. More specifically, the structural changes arising from the application of external stimuli may modify properties of the parent structure (e.g. magnetic, optical, or adsorptive) and lead to applications in sensing, selective storage and molecular switches, among others.¹⁶⁴

Among these solid-state transformations, those in which crystalline order and crystal integrity are maintained stand out, which are commonly called single-crystal-to-single-crystal phase transitions, abbreviated as SCSC. This type of transformations constitutes an increasing field in the world of crystallography as it is a powerful tool to characterize the structural response mechanism of crystalline entities that result from the application of a given stimulus (pressure, heat, light...), providing information on the variation in the position of atoms and molecules during it and, additionally, the correlation between the altered property and the crystalline structure.¹⁶⁵ Regarding the structural behavior presented by the compounds, three types of transitions are differentiated; polymorphic, dynamic and robust transitions. Polymorphism is the ability of solid bodies to change their crystalline structure without changing their chemical composition; thus, it is usually the result of a change in symmetry. On the other two cases, whereas dynamic SCSC transitions are based on the formation or breaking of covalent bonds that generate changes in the

CHAPTER 1

physical properties of the compound (color, magnetic properties, luminescence or porosity, among others), robust transformations are characterized by the maintenance of the fundamental crystalline structure, except for small variations such as the insertion or evacuation of solvent molecules or changes in the oxidation state of the constituent atoms.

In recent years, SCSC transformations have been widely studied in systems of metal-organic nature such as MOFs (Metal-Organic Frameworks), among which a large number of examples can be found. The weak strength of the links of these systems implies that, on many occasions, they are not capable of resisting these phase transitions and the structures collapse after the application of the stimulus. This problem can be overcome by the introduction of anions that provide greater rigidity to the overall system, such as POMs. Nevertheless, POM-based compounds able to undergo SCSC transformations are still much less common. Among these examples, SCSC transformation activated by light, redox processes or due to the action of a different chemical species should be mentioned.¹⁶⁶ Some examples include the $(\text{TBA})_4[\text{SiV}_2\text{W}_{10}\text{O}_{39}] \cdot 2\text{DCE}$ (TBA = tetrabutylammonium, DCE = 1,2-dichloroethane),¹⁶⁷ which transforms its linear (μ -oxo)-divanadium(V) core into a bis(μ -hydroxo)-divanadium moiety when exposed to H_2O vapors; change on the dimensionality through a cationic exchange and incorporation of transition-metal cations to lead to $[\text{M}_2(\text{H}_2\text{O})_6][\text{Mn}_4(\text{H}_2\text{O})_{16}][\text{WZnMn}_2(\text{H}_2\text{O})_2(\text{ZnW}_9\text{O}_{34})_2] \cdot 10\text{H}_2\text{O}$ ($\text{M} = \text{Co}, \text{Cu}$);¹⁶⁸ photopolymerization of discrete clusters into a $[\text{Gd}(\text{NMP})_6(\text{PW}_{12}\text{O}_{40})]_{\infty}$ 1-dimensional polymer chains after exposure to sunlight,¹⁶⁹ or redox-triggered SCSC transformations of the $[\text{H}_m\text{M}_{12}\text{X}_7\text{W}_{72}\text{O}_{268}]^{n-}$ ($\text{M} = \text{Mn}^{\text{III}}, \text{Co}^{\text{II}}$; $\text{X} = \text{Si}, \text{Ge}$) family with the selective reduction of M^{III} to Mn^{II} and oxidation from Co^{II} to Co^{III} .¹⁷⁰ Nevertheless, to our knowledge, the largest change in volume on a SCSC transformation reported to date corresponds to the fully-inorganic $\text{Li}_9\text{K}_7\text{WCo}_{10}[\text{H}_2\text{P}_8\text{W}_{48}\text{O}_{186}]$ salt (from 2170 \AA^3 to 1720 \AA^3), reported by Cronin's group.¹⁷¹ This fully-inorganic compound is formed by $[\text{P}_8\text{W}_{48}\text{O}_{184}]^{40-}$ moieties that are connected to each other by cobalt(II) linkers. The resulting flexible compound is dynamically switchable between eight crystalline states by applying different thermal and chemical (exposure to NH_3) stimuli.

However, thermally triggered SCSC transformations are the most common by far.¹⁷² These include examples in which the change in temperature directly generates modifications in the unit cell parameters of a given compound, or when the exposure of single-crystals to an external thermal stimuli implies the loss of solvent molecules and hence, it promotes the solid-phase transition. The first example of the latter type of transitions dates from 2005, when Mizuno's group¹³⁵ characterized the reversible and thermally dependent evacuation of the hydration molecules on the robust microporous $\text{Cs}_5[\text{Cr}_3\text{O}(\text{OOCH})_6(\text{H}_2\text{O})_3][\text{CoW}_{12}\text{O}_{40}] \cdot 7.5\text{H}_2\text{O}$ ionic crystal, giving rise to the trihemihydrate compound $\text{Cs}_5[\text{Cr}_3\text{O}(\text{OOCH})_6(\text{H}_2\text{O})_3][\text{CoW}_{12}\text{O}_{40}] \cdot 3.5\text{H}_2\text{O}$. Since then, several microporous

inorganic-metalorganic hybrid materials based on trinuclear $[M^{III}_3O(OOCR)_6(L)_3]^+$ macrocations have demonstrated the ability to undergo SCSC transformations.^{137,138,140,142}

Similarly, hybrid frameworks based on transition metal complexes of N-donor tetradentate ligands that are coordinated to POM surfaces can also undergo SCSC transformations triggered by the evacuation of guest solvent molecules, which could involve the rupture and formation of new covalent bonds (Table 1.1). First examples of this type are found on compounds $[Cu(bpmen)(H_2O)][SiW_{12}O_{40}\{Cu(bpmen)\}]$ and $[Cu(bpmen)(H_2O)]-[GeW_{12}O_{40}\{Cu(bpmen)\}]\cdot 3.5H_2O$ (bpmen = N,N'-dimethyl-N,N'-bis-(pyridin-2-ylmethyl)-1,2-diaminoethane).¹⁷³ Under applied thermal stimuli the water molecule completing the coordination sphere of the $\{Cu(bpmen)\}^{2+}$ moiety that acts as counterion is lost, with the subsequent coordination of the complex cation to the surface O atoms from the POM, which leads to $[XW_{12}O_{40}\{Cu(bpmen)\}_2]$ (X = Si; Ge) type molecular entities. Examples of Keggin-type heteroPOMs in combination with $\{Cu(cyclam)\}^{2+}$ complexes include hybrids like $[Cu(cyclam)(H_2O)][\{Cu(cyclam)\}_2SiW_{11}O_{39}Cu(H_2O)]\cdot 5H_2O$ ^{123d} and $[Cu(cyclam)]_2\cdot[\{Cu(cyclam)\}_4\{\alpha-GeW_{11}O_{39}\}Ln(H_2O)(OAc)]_2\cdot 18H_2O$ (Ln = La to Lu).¹⁷⁴ In regard to the first example, the thermal evacuation of guest solvent molecules and the rotation of the Keggin anion also involves the grafting of the $\{Cu(cyclam)\}^{2+}$ moiety acting as counterion to the POM surface, leading to the surface-decorated, molecular hybrid $[\{Cu(cyclam)\}_3SiW_{11}O_{39}Cu]$. The second family of compounds undergo two sequential SCSC transformations involving the grafting and release of different $\{Cu(cyclam)\}^{2+}$ moieties from the Keggin surface. It should be highlighted that the nature of the Ln governs the kinetics of the reversibility from anhydrous phase to the parent system, being faster for structures containing larger Ln^{3+} ions. Finally, it is worth mentioning the hybrid compound $[Cu(cyclam)(H_2O)_2]_{0.5}\cdot[\{Cu(cyclam)\}_{1.5}\{B-H_2As_2Mo_6O_{26}(H_2O)\}]\cdot 9H_2O$,¹⁷⁵ which represents one of the scarce examples of POM-based systems that simultaneously displays crystal dynamics induced by the evacuation of solvent molecules and exhibits permanent microporosity, which renders the anhydrous phase with selective gas sorption properties. Although this compound can undergo up to two thermally triggered phase transitions, it does not preserve its single-crystalline nature upon heating. In contrast, when solvent molecules are released under vacuum, the anhydrous phase $[\{Cu(cyclam)\}_2(A-H_2As_2Mo_6O_{26})]$ is isolated through SCSC transformations. This fact reveals the key importance of the dehydration mechanism. Phase transition not only provoke changes in the dimensionality of the parent lattice, but it also leads to important modifications within the inorganic cluster skeleton in such a way that an unprecedented solid-state B to A isomerization of the polyoxoanion is observed (Figure 1.19).

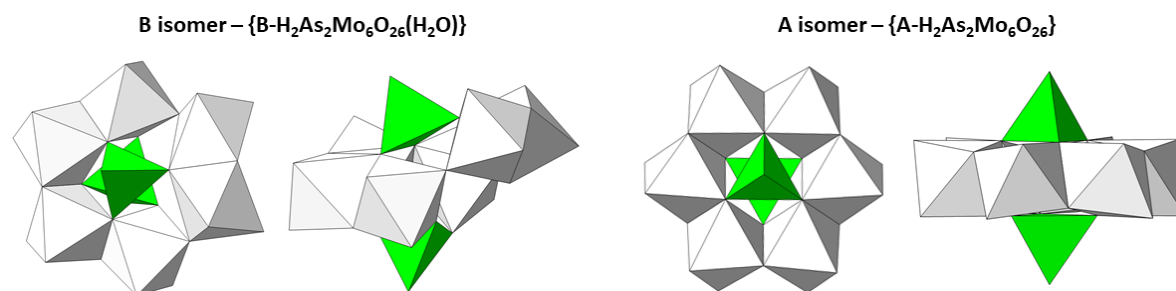


Figure 1.19. Comparison between the molecular structures of the {B-H₂As₂Mo₆O₂₆(H₂O)}

Table 1.1. Summary of POM-based hybrid frameworks with N4-tetradentate organic ligands able to exhibit single-crystal-to-single-crystal transformations.

Initial – Final compounds	Structural changes	Ref.
[Cu(bpmen)(H ₂ O)][SiW ₁₂ O ₄₀ {Cu(bpmen)}] [SiW ₁₂ O ₄₀ {Cu(bpmen)}] ₂	Coordination of complex cations to the POM surface	[173a]
[Cu(bpmen)(H ₂ O)][GeW ₁₂ O ₄₀ {Cu(bpmen)}]·3.5H ₂ O [GeW ₁₂ O ₄₀ {Cu(bpmen)}] ₂	Coordination of complex cations to the POM surface	[173b]
[SiW ₁₂ O ₄₀ {Cu(bpmpn)(H ₂ O)}] ₂ ·3H ₂ O [SiW ₁₂ O ₄₀ {Cu(bpmpn)}] ₂ ·3H ₂ O	Modifications on the coordination geometries of Cu ^{II} centers from octahedral to square-pyramid	[173a]
[GeW ₁₂ O ₄₀ {Cu(bpmpn)(H ₂ O)}] ₂ ·3H ₂ O [GeW ₁₂ O ₄₀ {Cu(bpmpn)}] ₂ ·3H ₂ O	Modifications on the coordination geometries of Cu ^{II} centers from octahedral to square-pyramid	[173b]
[Cu(cyclam)][{Cu(cyclam)} ₂ (V ₁₀ O ₂₈)]·10H ₂ O [Cu(cyclam)][{Cu(cyclam)} ₂ (V ₁₀ O ₂₈)]	Retention of the robust supramolecular framework with accessible empty channels	[124a]
[{Cu(cyclam)} ₃ (W ₇ O ₂₄)]·15.5H ₂ O [{Cu(cyclam)} ₃ (W ₇ O ₂₄)]·12H ₂ O [{Cu(cyclam)} ₃ (W ₇ O ₂₄)]	Modifications in the Cu ^{II} coordination geometries with retention of the porosity of the parent framework	[124b]
{Cu(cyclam)(VO ₃) ₂ }·5H ₂ O [{Cu(cyclam)(VO ₃) ₂ }]·3H ₂ O [{Cu(cyclam)(VO ₃) ₂ }]·1.3H ₂ O [{Cu(cyclam)(VO ₃) ₂ }]	Modifications in the Cu–O bond lengths and progressive contraction of the parent microporous architecture	[161]
[Cu(cyclam)] ₂ {Cu(cyclam)} ₄ {(α-GeW ₁₁ O ₃₉)Ln(H ₂ O)(OAc)} ₂ ·18H ₂ O (Ln = La–Lu) [{Cu(cyclam)} ₆ {(α-GeW ₁₁ O ₃₉)Ln(H ₂ O)(OAc)} ₂]·4H ₂ O (Ln = Eu or Er) [Cu(cyclam)] _{0.5} {[Cu(cyclam)] _{5.5} {(α-GeW ₁₁ O ₃₉)Ln(OAc)} ₂ } (Ln = Ce or Eu)	Changes on the Cu ^{II} coordination geometries and coordination and release of complex cations to the POM surface	[174]
[Cu(cyclam)] ₂ [Mo ₈ O ₂₆]·1.5H ₂ O [Cu(cyclam)] ₂ [Mo ₈ O ₂₆]	Retention of the robust covalent framework with accessible empty micropores	[176]
[Cu(cyclam)(H ₂ O)][{Cu(cyclam)} ₂ SiW ₁₁ O ₃₉ Cu(H ₂ O)]·5H ₂ O [{Cu(cyclam)} ₃ SiW ₁₁ O ₃₉ Cu]	Grafting of complex cations to the POM surface	[123d]

1.6. AIM OF THE WORK

The work described in this dissertation fits within one of the research lines of *Departamento de Química Orgánica e Inorgánica* from the *Facultad de Ciencia y Tecnología* at the *Universidad del País Vasco (UPV/EHU)*. The research group has widely explored the reactivity between POM clusters and transition-metal complexes of polydentate-macrocyclic ligands with the aim of preparing hybrid materials with novel structural motifs and properties. Attracted by the varied topologies and inherent properties exhibited by POMs (redox, luminescent, magnetic, catalytic...), this research consists in the synthesis, structural characterization and the analysis of the most interesting properties displayed by either extended or molecular organic-inorganic hybrid compounds formed by the combination of POM units with 3d- or 4f-metal complexes bearing multidentate ligands.

Based on the two main synthetic approaches mentioned above for the synthesis of POM hybrids comprising 3d- or 4f-metal complexes, **the aim of this work is, i) to evaluate the capacity of polyoxomolybdates in combination with transition-metal complexes of macrocyclic tetraaza ligands to generate extended hybrid frameworks; and ii) to prepare hybrid molecular clusters by the organic derivatization of lanthanide-substituted POMs.** In the first case, the resulting compounds could exhibit permanent porosity associated with interesting functionalities such as gas or water sorption properties, as well as the ability to undergo structural transitions upon thermal evacuation of guest solvent molecules. The most appropriate systems could also exhibit the ability to undergo SCSC transformations triggered by a given external stimuli, in such a way that it allows to monitor the location of each specific atom throughout the structural transition. In the second case, systems may display interesting magnetic and luminescent properties.

This work has been divided into well-differentiated sections. The systematic study on the pH-dependent reactivity between isopolyoxomolybdates and $\{\text{Cu}(\text{cyclam})\}^{2+}$ (cyclam = 1,4,8,11-tetraazacyclotetradecane) metalorganic building blocks are described in **Chapters 2 and 3**. The coordination of metal-complexes to the POM surface resulted in up to four different extended structures based on hepta- and octamolybdate anions. The compounds isolated have been characterized by elemental and thermal analyses, infrared spectroscopy and powder- and single-crystal X-ray diffraction. Two of these compounds exhibit an interesting thermostructural behavior, because they undergo thermally triggered structural transitions that lead to porous structures with the potential to absorb small gas molecules. More interestingly, the hybrid framework described in **Chapter 3** contains octamolybdate-anions and it is able to undergo SCSC transformations promoted by the thermal evacuation of guest solvent molecules, leading to new crystalline phases. Phase transitions do not only imply remarkable modifications in the crystal packing, but also the isomerization of octamolybdate anions through metal migrations. Furthermore, the reversibility of such

CHAPTER 1

SCSC transformations is also studied in depth. Results from water vapor sorption analyses are also evaluated together with extended studies on the absorption capacity and selectivity of the different anhydrous phases towards small gas molecules. Conversely, compounds described in **Chapter 4** exhibit hybrid structures formed by Anderson-Evans type $[H_6CrMo_6O_{24}]^{3-}$ anions and the $\{Cu(DMC)\}^{2+}$ complexes (DMC = dimethylcyclam) with dimensionalities that go from surface decorated molecular species to extended, three dimensional hybrid frameworks, as a result of the presence/absence of diverse alkali metal cations in the reaction media. These hybrids have also been characterized by elemental and thermal analyses, infrared spectroscopy and powder- and single-crystal X-ray diffraction. Structures showing a thermal stability range in TGA analyses were also analyzed by variable-temperature PXRD experiments, which result in potentially interesting thermally-induced solid-phase transitions.

The second part of this research work (**Chapter 5**) is focused on the preparation of molecular compounds by the simultaneous coordination of lacunary POM anions and organic Mannich-base ligands to mid-to-late trivalent lanthanide ions. All the then isostructural compounds have been characterized by elemental and thermal analyses, infrared spectroscopy and powder- and single-crystal X-ray diffraction. Photoluminescent and magnetic properties of these compounds is also studied in depth, in such a way that solid-state, i) low temperature photophysical properties have been analyzed for compounds emitting in the visible and near infrared region; and ii) magnetization and phase- and out-of-phase magnetic susceptibility studies at different temperatures and frequencies, together with electron paramagnetic resonance (EPR) experiments has allowed the description of the slow relaxation of magnetization displayed by some derivatives and the determination of energy level diagrams for the different analogues. Solution stability of the molecular hybrid POMs in different media is assessed by ESI-MS experiments and 1H -NMR spectroscopy.

In conclusion, Table 1.2 shows the three multidentate ligands employed along this work, whereas Table 1.3 compiles all the 26 compounds reported within this dissertation.

Table 1.2. Representation of the three multidentate ligands that have been employed during this work.

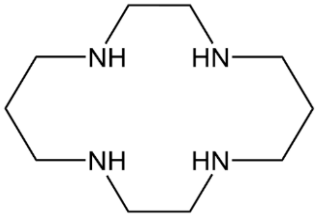
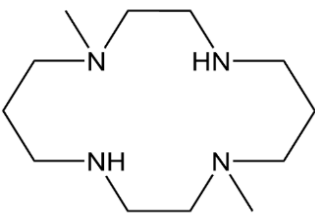
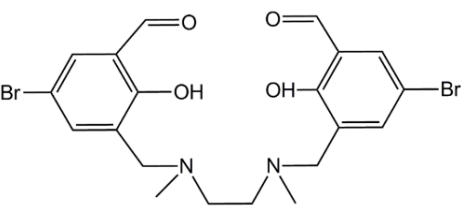
Chapters 2 and 3	Chapter 4	Chapter 5
		
<p><i>Cyclam</i> = $C_{10}N_4H_{24}$ 1,4,8,11-tetraazacyclotetradecane</p>	<p><i>DMC</i> = $C_{12}N_4H_{28}$ 1,8-dimethyl-1,4,8,11-tetraazacyclotetradecane</p>	<p><i>H₂L</i> = $C_{20}H_{22}Br_2N_2O_4$ <i>N,N'</i>-dimethyl-<i>N,N'</i>-bis(2-hydroxy-3-formyl-5-bromobenzyl)ethylene-diamine</p>

Table 1.3. Summary of all hybrid structures prepared and characterized within this work.

	Code	Compounds	
Chapter 2	1-Mo7	$\{[\text{Cu}(\text{cyclam})]_3(\text{Mo}_7\text{O}_{24})\} \cdot 15.5\text{H}_2\text{O}$	
	1B-Mo7	$(\text{NH}_4)\{[\text{Cu}(\text{cyclam})]_{2.5}(\text{Mo}_7\text{O}_{24})\} \cdot 5.5\text{H}_2\text{O}$	
	MoCu	$[\text{Cu}(\text{cyclam})][\text{MoO}_4] \cdot 4\text{H}_2\text{O}$	
Chapter 3	1-Mo8	$\{[\text{Cu}(\text{cyclam})]_3(\kappa\text{-Mo}_8\text{O}_{27})\} \cdot 14\text{H}_2\text{O}$	
	2-Mo8	$[\text{Cu}(\text{cyclam})][\{[\text{Cu}(\text{cyclam})]_2(\lambda\text{-Mo}_8\text{O}_{27})\}]$	
	3-Mo8	$\{[\text{Cu}(\text{cyclam})]_3(\mu\text{-Mo}_8\text{O}_{27})\}$	
	4-Mo8	$\{[\text{Cu}(\text{cyclam})]_3(\gamma\text{-Mo}_8\text{O}_{26}(\text{OH})_2)\} \cdot 11\text{H}_2\text{O}$	
	5-Mo8	$\{[\text{Cu}(\text{cyclam})]_3(\kappa\text{-Mo}_8\text{O}_{27})\} \cdot 13\text{H}_2\text{O}$	
	6-Mo8	$\{[\text{Cu}(\text{cyclam})]_3(\gamma\text{-Mo}_8\text{O}_{26}(\text{OH})_2)\}$	
Chapter 4	1-CuMo8	$\{[\text{Cu}(\text{DMC})]_3\{\text{H}_4\text{CuMo}_6(\text{MoO}_4)_2\text{O}_{22}\}\} \cdot 13\text{H}_2\text{O}$	
	1-CrMo6	$[\text{Cu}(\text{DMC})][\{[\text{Cu}(\text{DMC})]_{0.5}\{\text{H}_6\text{CrMo}_6\text{O}_{24}\}\} \cdot 11\text{H}_2\text{O}$	
	1Na-CrMo6	$\text{Na}\{[\text{Cu}(\text{DMC})]\{\text{H}_6\text{CrMo}_6\text{O}_{24}\}\} \cdot 8\text{H}_2\text{O}$	
	1Na2-CrMo6	$\text{Na}_2\{[\text{Cu}(\text{DMC})]_{0.5}\{\text{H}_6\text{CrMo}_6\text{O}_{24}\}\} \cdot 11.5\text{H}_2\text{O}$	
	1NO3-CrMo6	$\{[\text{Cu}(\text{DMC})]_2\{\text{H}_6\text{CrMo}_6\text{O}_{24}\}\}\text{NO}_3 \cdot 5\text{H}_2\text{O}$	
	1Cl-CrMo6	$\{[\text{Cu}(\text{DMC})]_2\{\text{H}_6\text{CrMo}_6\text{O}_{24}\}\}\text{Cl} \cdot 4.5\text{H}_2\text{O}$	
	CrMo6	$\text{K}_3[\text{H}_6\text{CrMo}_6\text{O}_{24}] \cdot 6\text{H}_2\text{O}$	
Chapter 5	1-Sm	$\text{K}_5[\text{Sm}(\text{H}_2\text{L})(\alpha\text{-SiW}_{11}\text{O}_{39})] \cdot 14\text{H}_2\text{O}$	
	1-Eu	$\text{K}_5[\text{Eu}(\text{H}_2\text{L})(\alpha\text{-SiW}_{11}\text{O}_{39})] \cdot 14\text{H}_2\text{O}$	
	1-Gd	$\text{K}_5[\text{Gd}(\text{H}_2\text{L})(\alpha\text{-SiW}_{11}\text{O}_{39})] \cdot 14\text{H}_2\text{O}$	
	1-Tb	$\text{K}_5[\text{Tb}(\text{H}_2\text{L})(\alpha\text{-SiW}_{11}\text{O}_{39})] \cdot 14\text{H}_2\text{O}$	
	1-Dy	$\text{K}_5[\text{Dy}(\text{H}_2\text{L})(\alpha\text{-SiW}_{11}\text{O}_{39})] \cdot 14\text{H}_2\text{O}$	
	1-Ho	$\text{K}_5[\text{Ho}(\text{H}_2\text{L})(\alpha\text{-SiW}_{11}\text{O}_{39})] \cdot 14\text{H}_2\text{O}$	
	1-Er	$\text{K}_5[\text{Er}(\text{H}_2\text{L})(\alpha\text{-SiW}_{11}\text{O}_{39})] \cdot 14\text{H}_2\text{O}$	
	1-Tm	$\text{K}_5[\text{Tm}(\text{H}_2\text{L})(\alpha\text{-SiW}_{11}\text{O}_{39})] \cdot 14\text{H}_2\text{O}$	
	1-Yb	$\text{K}_5[\text{Yb}(\text{H}_2\text{L})(\alpha\text{-SiW}_{11}\text{O}_{39})] \cdot 14\text{H}_2\text{O}$	
	1-Lu	$\text{K}_5[\text{Lu}(\text{H}_2\text{L})(\alpha\text{-SiW}_{11}\text{O}_{39})] \cdot 14\text{H}_2\text{O}$	

1.7. REFERENCES

- [1] (a) Pope, M. T. *Heteropoly and Isopoly Oxometalates*; Springer-Verlag: Berlin, Germany, **1983**. (b) Pope, M. T. *Comprehensive Coordination Chemistry*; Wilkinson, G.; Gillard, R. D.; McCloerty, J. A., Eds.; Pergamon Press: New York, USA, **1987**, pp. 1023-1058. (c) Pope, M. T. *Encyclopedia of Inorganic Chemistry*; King, R. B., Eds.; John Wiley & Sons: Chichester, UK, **1994**, 3361-3371. (d) *Polyoxometalate Chemistry from Topology via Self-Assembly to Applications*; Pope, M. T., Müller, A., Eds.; Kluwer: Dordrecht, The Netherlands, **2001**.
- [2] (a) Neumann, R.; Dahan, M. A Ruthenium-Substituted Polyoxometalate as an Inorganic Dioxygenase for Activation of Molecular Oxygen. *Nature* **1997**, *388*, 353-355. (b) Misono, M. Catalysis of Heteropoly Compounds, In *Heterogeneous Catalysis of Mixed Oxides*; Elsevier Ltd.: Oxford, UK, **2013**. (c) Wang, S. S.; Yang, G.-Y. Recent Advances in Polyoxometalate-Catalyzed Reactions. *Chem. Rev.* **2015**, *115*, 4893-4962.
- [3] (a) Clemente-Juan, J. M.; Coronado, E. Magnetic clusters from polyoxometalate complexes. *Coord. Chem. Rev.* **1999**, *193-195*, 361-394. (b) Kortz, U.; Müller, A.; van Slageren, J.; Schnack, J.; Dalal, N. S.; Dressel, M. Polyoxometalates: Fascinating Structures, Unique Magnetic Properties. *Coord. Chem. Rev.* **2009**, *253*, 2315-2327. (c) Clemente-Juan, J. M.; Coronado, E.; Gaita-Ariño, A. Magnetic Polyoxometalates: From Molecular Magnetism to Molecular Spintronics and Quantum Computing. *Chem. Soc. Rev.* **2012**, *41*, 7464-7478.
- [4] (a) Song, Y.-F.; Tsunashima, R. Recent Advances on Polyoxometalate-Based Molecular and Composite Materials. *Chem. Soc. Rev.* **2012**, *41*, 7384-7402. (b) Ammam, M. Polyoxometalates: Formation, Structures, Principal Properties, Main Deposition Methods and Application in sensing. *J. Mater. Chem. A* **2013**, *1*, 6291-6312. (c) Gao, Y.; Choudhari, M.; Such, G. K.; Ritchie, C. Polyoxometalates as Chemically and Structurally Versatile Components in Self-Assembled Materials. *Chem. Sci.* **2022**, *13*, 2510-2527.
- [5] (a) Rhule, J. T.; Hill, C. L.; Judd, D. A. Polyoxometalates in Medicine, *Chem. Rev.* **1998**, *98*, 327-357. (b) Bijelic, A.; Aureliano, M.; Rompel, A. The Antibacterial Activity of Polyoxometalates: Structures, Antibiotic Effects and Future Perspectives, *Chem. Commun.* **2018**, *54*, 1153-1169. (c) Aureliano, M. The Future is Bright for Polyoxometalates. *BioChem* **2022**, *2*, 8-26.
- [6] Berzelius, J. J. Beitrag zur Näheren Kenntniss des Molybdäns. *Poggend. Ann. Phys. Chem.* **1826**, *6*, 369-392.
- [7] (a) De Luyart, F.; De Luyart, J. J. *Extractos de las Juntas Generales celebradas por la R.S.B.A.P.* **1783**, 46. (b) Román, P. *Los hermanos Delhuyar, la Bascongada y el Wolframio* R.S.B.A.P., Bilbao, **2000**. (c) Goya, P.; Martín, N.; Román, P. W for Tungsten and Wolfram. *Nature Chemistry* **2011**, *3*, 336.
- [8] Keggin, J. F. Structure of the Molecule 12-Phosphotungstic Acid. *Nature* **1933**, *131*, 908-909.
- [9] (a) *Polyoxometalate Chemistry for Nano-Composite Design*; Yamase, T., Pope, M. T., Eds.; Kluwer: Dordrecht, The Netherlands, **2002**. (b) *Polyoxometalate Molecular Science*; Borrás-Almenar, J. J., Coronado, E., Müller, A., Pope, M. T., Eds.; Kluwer: Dordrecht, The Netherlands, **2003**. (c) *Complexity in Chemistry and Beyond: Interplay Theory and Experiments*; Hill, C. L., Musaev, D. G., Eds.; Springer: Dordrecht, The Netherlands, **2012**. (d) *Polyoxometalate Chemistry: Some Recent Trends*; Sécheresse, F., Ed.; World Scientific: Singapore, **2013**. (e) *Polyoxometalate-Based Assemblies and Functional Materials*, Song, Y.-F. Eds.; Springer, New York, USA, **2018**. (f) *Polyoxometalates: Advances, Properties and Applications*, Ruiz Rubio, L.; Vilas Vilela, J. L.; Artetxe, B.; Gutiérrez-Zorrilla, J. M., Eds.; Jenny Stanford Publishing, New York, USA, **2022**.
- [10] (a) Hill, C. L. Ed. Polyoxometalates-Multicomponent Molecular Vehicles to Probe Fundamental Issues and Practical Problems. *Chem. Rev.* **1998**, *98*, issue 1. (b) Kortz, U., Ed. Polyoxometalates. *Eur. J. Inorg. Chem.* **2009**, issue 34. (c) De-Liang, L.; Cronin, L., Eds. *Dalton Trans.* **2012**, *41*, issue 33. (d) Cronin, L.; Müller, A., Eds. *Chem. Soc. Rev.* **2012**, *41*, issue 22. (e) Kortz, U.; Liu, T., Eds. *Eur. J. Inorg. Chem.* **2013**, special issue 10-11. (f) Galán-Mascarós, J. R.; Kortz, U. Eds. *Acta Crystallogr.* **2018**, *C74*, special issue 11. (g) Gumerova, N. I.; Rompel, A. Synthesis, Structures and Applications of Electron-Rich Polyoxometalates. *Nat. Rev. Chem.* **2018**, *2*, 1-20.

- [11] (a) Graeber, E. J.; Morosin, B. The Molecular Configuration of the Decaniobate ion ($\text{Nb}_{17}\text{O}_{28}^{6-}$). *Acta Crystallogr.* **1977**, *B33*, 2137–2143. (b) Nyman, M. Polyoxoniobate Chemistry in the 21st Century. *Dalton Trans.* **2011**, *40*, 8049–8059. (c) Matsumoto, M.; Ozawa, Y.; Yagasaki, A.; Zhe, Y. Decatantalate-The Last Member of the Group 5 Decametallate Family. *Inorg. Chem.* **2013**, *52*, 7825–7827.
- [12] Izarova, N. V.; Pope, M. T.; Kortz, U. Noble Metals in Polyoxometalates. *Angew. Chem., Int. Ed.* **2012**, *51*, 9492–9510.
- [13] (a) Nyman, M.; Burns, P. C. A Comprehensive Comparison of Transition-Metal and Actinyl Polyoxometalates. *Chem. Soc. Rev.* **2012**, *41*, 7354–7367. (b) Qiu, J.; Burns, P. C. Clusters of Actinides with Oxide, Peroxide, or Hydroxide Bridges. *Chem. Rev.* **2013**, *113*, 1097–1120.
- [14] (a) Müller, A.; Krickemeyer, E.; Meyer, J.; Bögge, H.; Peters, F.; Plass, W.; Diemann, E.; Dillinger, S.; Nonnenbruch, F.; Randerath, M.; Menke, C. $[\text{Mo}_{154}(\text{NO})_{14}\text{O}_{420}(\text{OH})_{28}(\text{H}_2\text{O})_{70}]^{(25 \pm 5)-}$: A Water-Soluble Big Wheel with More than 700 Atoms and a Relative Molecular Mass of About 24000. *Angew. Chem. Int. Ed. Eng.* **1995**, *34*, 2122–2124. (b) Müller, A.; Sarkar, S.; Shah, S. Q. N.; Bögge, H.; Schmidtman, M.; Sarkar, S.; Kögerler, P.; Hauptfleisch, B.; Traitwein, A. X.; Schünemann, V. Archimedean Synthesis and Magic Numbers: "Sizing" Giant Molybdenum-Oxide-Based Molecular Spheres of the Keplerate Type. *Angew. Chem. Int. Ed.* **1999**, *38*, 3238–3241. (c) Müller, A.; Beckmann, E.; Bögge, H.; Schmidtman, M.; Dress, A. Inorganic Chemistry Goes Protein Size: A Mo_{368} Nano-Hedgehog Initiating Nanochemistry by Symmetry Breaking. *Angew. Chem. Int. Ed.* **2002**, *41*, 1162–1167.
- [15] Lipscomb, W. N. Paratungstate Ion. *Inorg. Chem.* **1965**, *4*, 132–134.
- [16] (a) López, X.; Carbó, J. J.; Bo, C.; Poblet, J. M. Structure, Properties and Reactivity of Polyoxometalates: A Theoretical Perspective. *Chem. Soc. Rev.* **2012**, *41*, 7537–7571. (b) Müller, A.; Gouzerh, P. From Linking of Metal-Oxide Building Blocks in a Dynamic Library to Giant Clusters with Unique Properties and Towards Adaptive Chemistry. *Chem. Soc. Rev.* **2012**, *41*, 7431–7463.
- [17] (a) Fuchs, J.; Hartl, H.; Schiller, W.; Gerlach, U. Die Kristallstruktur des Tributylammoniumdekawolframats $[(\text{C}_4\text{H}_9)_2\text{NH}]_4\text{W}_{10}\text{O}_{32}$. *Acta Crystallogr.* **1976**, *B32*, 740–749. (b) Bharadwaj, P. K.; Ohashi, Y.; Sasada, Y.; Sasaki, Y.; Yamase, T. Structure of Octakis(methylammonium) Decamolybdate(8-) Dihydrate. *Acta Crystallogr.* **1986**, *C42*, 545–547. (c) Wéry, A. S. J.; Gutiérrez-Zorrilla, J. M.; Luque, A.; Román, P.; Martínez-Ripoll, M. Influence of Protonation on Crystal Packing and Thermal Behaviour of Tert-Butylammonium Decavanadates. *Polyhedron* **1996**, *15*, 4555–4564.
- [18] (a) Fuchs, V. J.; Hartl, H.; Schiller, W.; Gerlach, U. Die Kristallstruktur des Tributylammoniumdekawolframats $[(\text{C}_4\text{H}_9)_3\text{NH}]_4\text{W}_{10}\text{O}_{32}$. *Acta Cryst.* **1976**, *B32*, 740–749. (b) Fuchs, J.; Freiwald, W.; Hartl, H. Neubestimmung der Kristallstruktur von Tetrabutylammonium hexawolfram. *Acta Crystallogr. Sec. B* **1978**, *34*, 1764–1770. (c) Rheingold, A. L.; White, C. B.; Haggerty, B. S.; Maatta, E. A. Bis(tetrabutylammonium) Nonadecaohexamolybdenum(VI): A Second Polymorph. *Acta Crystallogr.* **1993**, *C49*, 756–758. (d) Gutiérrez-Zorrilla, J. M.; Yamase, T.; Sugeta, M. Tetrakis(isopropylammonium) β -octamolybdate(VI). *Acta Crystallogr.* **1994**, *C50*, 196–198. (e) Román, P.; Wéry, A. S. J.; Luque, A.; Gutiérrez-Zorrilla, J. M. Hexakis(tert-butylammonium) heptamolybdate(VI)-water (1/7). *Acta Crystallogr.* **1994**, *C50*, 1031–1034.
- [19] Lindqvist, I. On the Structure of the Paratungstate Ion. *Acta Cryst.* **1952**, *5*, 667–670.
- [20] (a) Román, P.; Wéry, A. S. J.; Luque, A.; Gutiérrez-Zorrilla, J. M. Observation of a Novel Cyclic Tetrametavanadate Anion Isolated from Aqueous Solution. *Inorg. Chem.* **1993**, *32*, 775–776. (b) Wéry, A. S. J.; Gutiérrez-Zorrilla, J. M.; Luque, A.; Ugalde, M.; Román, P. Phase Transition in Metavanadates. Polymerization of Tetrakis(tert-Butylammonium)-cyclo-Tetrametavanadate. *Chem. Mater* **1996**, *8*, 408–413.
- [21] Kozhevnikov, I. V. Catalysis by Polyoxometalates, volume 2. John Wiley & Sons Inc., New York, USA, **2002**.
- [22] Maestre, J. M.; Lopez, X.; Bo, C.; Poblet, J.-M.; Casañ-Pastor, N. Electronic and Magnetic Properties of a α -Keggin Anions: A DFT Study of $[\text{XM}_{12}\text{O}_{40}]^{n-}$, ($\text{M} = \text{W}, \text{Mo}$; $\text{X} = \text{Al}^{\text{III}}, \text{Si}^{\text{IV}}, \text{P}^{\text{V}}, \text{Fe}^{\text{III}}, \text{Co}^{\text{I}}, \text{Co}^{\text{II}}$) and $[\text{SiM}_{11}\text{VO}_{40}]^{m-}$ ($\text{M} = \text{Mo}$ and W). *J. Am. Chem. Soc.* **2001**, *123*, 3749–3758.

CHAPTER 1

- [23] Wang, H.; Hamanaka, S.; Nishimoto, Y.; Irle, S.; Yokoyama, T.; Yoshikawa, H.; Awaga, K. In Operando X-ray Absorption Fine Structure Studies of Polyoxometalate Molecular Cluster Batteries: Polyoxometalates as Electron Sponges. *J. Am. Chem. Soc.* **2012**, *134*, 4918–4924.
- [24] Nyman, M.; Bonhomme, F.; Alam, T. M.; Parise, J. B.; Vaughan, G. M. B. [SiNb₁₂O₄₀]¹⁶⁻ and [GeNb₁₂O₄₀]¹⁶⁻: Highly Charged Keggin Ions with Sticky Surfaces. *Angew. Chem. Int. Ed.* **2004**, *43*, 2787–2792.
- [25] Selling, A.; Andersson, I.; Pettersson, L.; Schramm, C. M.; Downey, S. L.; Grate, J. H. Multicomponent Polyanions. 47: The Aqueous Vanadophosphate System. *Inorg. Chem.* **1994**, *33*, 3141–3150.
- [26] Tézé, A.; Hervé, G. Inorganic Syntheses 27, eds. Finke, R. G. and Lyon, D. K., Chapter 16. α -, β - and γ -Dodecatungstosilicic acids: isomers and related lacunary compounds, John Wiley & Sons, New York, **1990**, 85–96.
- [27] Casey, W. H. Large Aqueous Aluminum Hydroxide Molecules. *Chem. Rev.* **2006**, *106*, 1–16.
- [28] Sartzi, H.; Miras, H. N.; Vilà-Nadal, L.; Long, D.-L.; Cronin, L. Trapping the δ Isomer of the Polyoxometalate-Based Keggin Cluster with a Tripodal Ligand. *Angew. Chem. Int. Ed.* **2015**, *54*, 15488–15492.
- [29] Mialane, P.; Dolbecq, A.; Lisnard, L.; Mallard, A.; Marrot, J.; Sécheresse, F. [ϵ -PMo₁₂O₃₆(OH)₄{La(H₂O)₄}]⁵⁺: The First ϵ -PMo₁₂O₄₀ Keggin Ion and Its Association with the Two-Electron-Reduced α -PMo₁₂O₄₀ Isomer. *Angew. Chem. Int. Ed.* **2002**, *41*, 2398–2401.
- [30] Tézé, A.; Canny, J.; Gurban, L.; Thouvenot, R.; Hervé, G. Synthesis, Structural Characterization, and Oxidation-Reduction Behavior of the γ -Isomer of the Dodecatungstosilicate Anion. *Inorg. Chem.* **1996**, *35*, 1001-1005.
- [31] Bösing, M.; Loose, I.; Pohlmann, H.; Krebs, B. New Strategies for the Generation of Large Heteropolymetalate Clusters: The β -B-SbW₉ Fragment as a Multifunctional Unit. *Chem. Eur. J.* **1997**, *3*, 1232–1237.
- [32] Dawson, B. The Structure of the 9(18)-Heteropoly Anion in Potassium 9(18)-Tungstophosphate, K₆(P₂W₁₈O₆₂)·14H₂O. *Acta Crystallogr.* **1953**, *6*, 113–126.
- [33] (a) Contant, R.; Thouvenot, R. A Reinvestigation of Isomerism in the Dawson Structure: Syntheses and ¹⁸³W NMR Structural Characterization of Three New Polyoxotungstates [X₂W₁₈O₆₂]⁶⁻ (X=P^V, As^V). *Inorg. Chim. Acta* **1993**, *212*, 41–50. (b) Vilà-Nadal, L.; Mitchell, S. G.; Long, D.-L.; Rodríguez-Forteza, A.; López, X.; Poblet, J. M.; Cronin, L. Exploring the Rotational Isomerism in Non-Classical Wells-Dawson Anions {W₁₈X}: A Combined Theoretical and Mass Spectrometry Study. *Dalton Trans.* **2012**, *41*, 2264-2271.
- [34] Zhang, Z.; Li, Y.; Wang, Y.; Qi, Y.; Wang, E. Extended Organic-Inorganic Hybrids Based on Dawson and Double-Dawson-Type Polyoxometalates. *Inorg. Chem.* **2008**, *47*, 7615-7622.
- [35] (a) Contant, R.; Ciabrini, J. P. Stereospecific Preparations of New n-molybdo-(18-n)-tungsto-2-phosphates and Related “Defect” Compounds (n = 2, 4 or 5). *J. Inorg. Nucl. Chem.* **1991**, *43*, 1525–1528. (b) López, X.; Bo, C.; Poblet, J.-M. Relative Stability in α - and β -Wells-Dawson Heteropolyanions: A DFT Study of {P₂M₁₈O₆₂}ⁿ⁻ (M = W and Mo) and [P₂W₁₅V₃O₆₂]ⁿ⁻. *Inorg. Chem.* **2002**, *42*, 2634-2638.
- [36] Contant, R.; Tézé, A. A New Crown Heteropolyanion K₂₈Li₅H₇P₈W₄₈O₁₈₄·92H₂O: Synthesis, Structure, and Properties. *Inorg. Chem.* **1985**, *24*, 4610–4614.
- [37] Alizadeh, M. H.; Harmalkar, S. P.; Jeannin, Y.; Martin-Frere, J.; Pope, M. T. A Heteropolyanion with Fivefold Molecular Symmetry that Contains a Nonlabile Encapsulated Sodium Ion. The Structure and Chemistry of [NaP₅W₃₀O₁₁₀]¹⁴⁻. *J. Am. Chem. Soc.* **1985**, *107*, 2662–2669.
- [38] (a) Veríssimo, M. I. S.; Evtuguin, D. V.; Gomes, M. T. S. R. Polyoxometalate Functionalized Sensors: A Review. *Front. Chem.* **2022**, *10*, 840657. (b) Granadeiro, C. M.; de Castro, B.; Balula, S. S.; Cunha-Silva, L. Lanthanopolyoxometalates: From the Structure of Polyanions to the Design of Functional Materials. *Polyhedron* **2013**, *52*, 10-24.

- [39] (a) Reinoso, S. Heterometallic 3d-4f Polyoxometalates: Still and Incipient Field. *Dalton Trans.* **2011**, *40*, 6610-6615. (b) Das, V.; Kaushik, R.; Hussain, F. Heterometallic 3d-4f Polyoxometalates: An Emerging Field with Structural Diversity to Multiple Applications. *Coord. Chem. Rev.* **2020**, *413*, 213271.
- [40] (a) Al-Oweini, R.; Bassil, B. S.; Friedl, J.; Kottisch, V.; Ibrahim, M.; Asano, M.; Keita, B.; Novitchi, G.; Lan, Y.; Powell, A.; Stimming, U.; Kortz, U. Synthesis and Characterization of Multinuclear Manganese-Containing Tungstosilicates. *Inorg. Chem.* **2014**, *53*, 5663-5673. (b) Li, N.; Zhang, S.; Zhao, J.; Pan, Q.; Xing, B.; Li, J.; Jiang, S.; Qu, W. Synthesis of Two Monomeric Tri-Substituted γ^* -Dawson-Type Polyoxotungstates. *Eur. J. Inorg. Chem.* **2020**, 690-694.
- [41] (a) Weakley, T. J. R.; Finke, R. G. Single-Crystal X-Ray Structures of the Polyoxotungstate Salts $K_{8.3}Na_{1.7}[Cu_4(H_2O)_2(PW_9O_{34})_2] \cdot 24H_2O$ and $Na_{14}Cu[Cu_4(H_2O)_2(P_2W_{15}O_{56})_2] \cdot 53H_2O$. *Inorg. Chem.* **1990**, *29*, 1235-1241. (b) Mbomekalle, I. M.; Mialane, P.; Dolbecq, A.; Marrot, J.; Sécheresse, F.; Berthet, P.; Keita, B.; Nadjo, L. Rational Synthesis, Structure, Magnetism and Electrochemistry of Mixed Iron-Nickel-Containing Wells-Dawson-Fragment-Based Sandwich-Type Polyoxometalates. *Eur. J. Inorg. Chem.* **2009**, 5194-5204. (c) Yin, Q.; Tan, J. M.; Besson, C.; Geletti, Y. V.; Musaev, D. G.; Kuznetsov, A. E.; Luo, Z.; Hardcastle, K. I.; Hill, C. L. A Fast Soluble Carbon-Free Molecular Water Oxidation Catalyst Based on Abundant Metals. *Science* **2010**, *328*, 342-345.
- [42] (a) Knoth, W. H.; Domaille, P. J.; Harlow, R. L. Heteropolyanions of the Types $M_3(W_9PO_{34})_2^{12-}$ and $MM'M''(W_9PO_{34})_2^{12-}$: Novel Coordination of Nitrate and Nitrite. *Inorg. Chem.* **1986**, *25*, 1577-1584. (b) Okun, N. M.; Anderson, T. M.; Hill, C. L. $[(Fe^{III}(OH)_2)_3(A-\alpha-PW_9O_{34})_2]^{9-}$ on Cationic Silica Nanoparticles, a New Type of Material and Efficient Heterogeneous Catalyst for Aerobic Oxidations. *J. Am. Chem. Soc.* **2003**, *125*, 3194-3195. (c) Guo, J.; Zhang, D.; Chen, L.; Song, Y.; Zhu, D.; Xu, Y. Syntheses, structures and magnetic properties of two unprecedented hybrid compounds constructed from open Wells-Dawson anions and high-nuclear transition metal clusters. *Dalton Trans.* **2013**, *42*, 8454-8459.
- [43] Robert, F.; Leyrie, M.; Hervé, G. Structure of Potassium Diaquatricuprooctadecatungstodiarsonate(III)(12-) Undecahydrate. *Acta Crystallogr.* **1982**, *B38*, 358-362. (b) Kortz, U.; Al-Kassem, N.; Savelieff, M. G.; Al Kadi, N. A.; Sadakane, M. Synthesis and Characterization of Copper-, Zinc-, Manganese-, and Cobalt-Substituted Dimeric Heteropolyanions, $[(\alpha-XW_9O_{33})_2M_3(H_2O)_3]^{n-}$ ($n = 12, X = As^{III}, Sb^{III}, M = Cu^{2+}, Zn^{2+}; n = 10, X = Se^{IV}, Te^{IV}, M = Cu^{2+}$) and $[(\alpha-AsW_9O_{33})_2WO(H_2O)M_2(H_2O)_2]^{10-}$ ($M=Zn^{2+}, Mn^{2+}, Co^{2+}$). *Inorg. Chem.* **2001**, *40*, 4742-4749.
- [44] (a) Loose, I.; Droste, E.; Bösing, M.; Pohlmann, H.; Dickman, M. H.; Rosu, C.; Pope, T.; Krebs, B. Heteropolymetalate Clusters of the Subvalent Main Group Elements Bi^{III} and Sb^{III}. *Inorg. Chem.* **1999**, *38*, 2688-2694. (b) Zhang, F.-Q.; Guan, W.; Yan, L.-K.; Zhang, Y.-T.; Xu, M.-T.; Hayfron-Benjamin, E.; Su, Z.-M. On the Origin of the Relative Stability of Well-Dawson Isomers: A DFT Study of $r-, \beta-, \gamma-, r^*-, \beta^*-,$ and $\gamma^*-[(PO_4)_2W_{18}O_{54}]^{6-}$ Anions. *Inorg. Chem.* **2011**, *50*, 4967-4977.
- [45] (a) Fang, X.; Kögerler, P.; Furukawa, Y.; Speldrich, M.; Luban, M. Molecular Growth of a Core-Shell Polyoxometalate. *Angew. Chem. Int. Ed.* **2011**, *50*, 5212-5216. (b) Oms, O.; Dolbecq, A.; Mialane, P. Diversity in Structures and Properties of 3d-Incorporating Polyoxotungstates. *Chem. Soc. Rev.* **2012**, *41*, 7497-7536. (c) Liu, J.-C.; Zhao, J.-W.; Streb, C.; Song, Y.-F. Recent Advances on High-Nuclear Polyoxometalate Clusters. *Coord. Chem. Rev.* **2022**, *471*, 214734.
- [46] Boskovic, C. Rare Earth Polyoxometalates. *Acc. Chem. Res.* **2017**, *50*, 2205-2214.
- [47] Peacock, R. D.; Weakley, T. J. R. Heteropolytungstate Complexes of the Lanthanide Elements. Part I. Preparation and Reactions. *J. Chem. Soc. A*, **1971**, 1836-1839.
- [48] Li, H.; Yang, W.; Wang, X.; Chen, L.; Ma, J.; Zheng, L.; Zhao, J. Self-Assembly of a Family of Isopolytungstates Induced by the Synergistic Effect of the Nature of Lanthanoids and the pH Variation in the Reaction Process: Syntheses, Structures, and Properties. *Cryst. Growth Des.* **2016**, *16*, 108-120.
- [49] Iijima, J.; Ishikawa, E.; Nakamura, Y.; Naruke, H. Synthesis and Structural Investigation of Sandwich Polyoxotungstates Containing Cerium (III/IV) and Mono-Lacunary Keggin Tungstophosphate Units. *Inorg. Chim. Acta* **2010**, *363*, 1500-1506.
- [50] Bassil, B. S.; Dickman, M. H.; von der Kammer, B.; Kortz, U. The Monolanthanide-Containing Silicotungstates $[Ln(\beta_2-SiW_{11}O_{39})_2]^{13-}$ ($Ln = La, Ce, Sm, Eu, Gd, Tb, Yb, Lu$): A Synthetic and Structural Investigation. *Inorg. Chem.* **2007**, *46*, 2452-2458.

CHAPTER 1

- [51] Luo, Q.; Howell, R. C.; Dankova, M.; Bartis, J.; Williams, C. W.; DeW. Horrocks, W. Jr.; Young, V. G. Jr.; Rheingold, A. L.; Francesconi, L. C.; Antonio, M. R. Coordination of Rare-Earth Elements in Complexes with Monovacant Wells–Dawson Polyoxoanions. *Inorg. Chem.* **2001**, *40*, 1894–1901.
- [52] Sadakane, M.; Dickman, M. H.; Pope, M. T. Controlled Assembly of Polyoxometalate Chains from Lacunary Building Blocks and Lanthanide-Cation Linkers. *Angew. Chem. Int. Ed.* **2000**, *39*, 2914–2916.
- [53] (a) Artetxe, B.; Reinoso, S.; San Felices, L.; Lezama, L.; Gutiérrez-Zorrilla, J. M.; García, J. A.; Galán-Mascarós, J. R.; Haider, A.; Kortz U.; Vicent, C. Cation-Directed Dimeric versus Tetrameric Assemblies of Lanthanide-Stabilized Dilacunary Keggin Tungstogermanates. *Chem. Eur. J.* **2014**, *20*, 12144–12156. (b) Fang, X.; Anderson, T. M.; Benelli, C.; Hill, C. L. Polyoxometalate-Supported Y[–] and Yb^{III}–Hydroxo/Oxo Clusters from Carbonate-Assisted Hydrolysis. *Chem. Eur. J.* **2005**, *11*, 712–718.
- [54] Tourné, C. M.; Tourné, G. F.; Zonnevillje, F. Chiral Polytungstometalates [WM₃(H₂O)₂(XW₉O₃₄)₂]^{12–} (X = M = Zn or Co^{II}) and their M-Substituted Derivatives. Syntheses, Chemical, Structural and Spectroscopic Study of some D,L Sodium and Potassium Salts. *J. Chem. Soc. Dalton Trans.* **1991**, 143–155.
- [55] Ma, P.; Wan, R.; Wang, Y.; Hu, F.; Zhang, D.; Niu, J.; Wang, J. Coordination-Driven Self-Assembly of a 2D Graphite-Like Framework Constructed from High-Nuclear Ce₁₀ Cluster Encapsulated Polyoxotungstates. *Inorg. Chem.* **2016**, *55*, 918–924.
- [56] Howell, R. C.; Perez, F. G.; Jain, S.; DeW. Horrocks, W. Jr.; Rheingold, A. L.; Francesconi, L. C. A New Type of Heteropolyoxometalates formed from Lacunary Polyoxotungstate Ions and Europium or Yttrium Cations. *Angew. Chem. Int. Ed.* **2001**, *40*, 4031–4034.
- [57] Fukaya, K.; Yamase, T. Alkali-Metal-Controlled Self-Assembly of Crown-Shaped Ring Complexes of Lanthanide/[α -AsW₉O₃₃]^{9–}: [K $\left\{Eu(H_2O)_2(\alpha\text{-AsW}_9\text{O}_{33})\right\}_6$]^{35–} and [Cs $\left\{Eu(H_2O)_2(\alpha\text{-AsW}_9\text{O}_{33})\right\}_4$]^{23–}. *Angew. Chem. Int. Ed.* **2003**, *42*, 654–658.
- [58] Liu, J. C.; Han, Q.; Chen, L.-J.; Zhao, J.-W.; Streb, C.; Song, Y.-F. Aggregation of Giant Cerium–Bismuth Tungstate Clusters into a 3D Porous Framework with High Proton Conductivity. *Angew. Chem. Int. Ed.* **2018**, *57*, 8416–8420.
- [59] Fang, X.; Kögerler, P.; Furukawa, Y.; Speldrich, M.; Luban, M. Molecular Growth of a Core–Shell Polyoxometalate. *Angew. Chem. Int. Ed.* **2011**, *50*, 5212–5216.
- [60] Wassermann, K.; Dickman, M. H.; Pope, M. T. Self-Assembly of Supramolecular Polyoxometalates: The Compact, Water-Soluble Heteropolytungstate Anion [As₁₂^{III}Ce₁₆^{III}(H₂O)₃₆W₁₄₈O₅₂₄]^{76–}. *Angew. Chem. Int. Ed.* **1997**, *36*, 1445–1448.
- [61] Bassil, B. S.; Dickman, M. H.; Römer, I.; von der Kammer, B.; Kortz, U. The Tungstogermanate [Ce₂₀Ge₁₀W₁₀₀O₃₇₆(OH)₄(H₂O)₃₀]^{56–}: A Polyoxometalate Containing 20 Cerium(III) Atoms. *Angew. Chem. Int. Ed.* **2007**, *46*, 6192–6195.
- [62] Hussain, F.; Conrad, F.; Patzke, G. R. A Gadolinium-Bridged Polytungstoarsenate(III) Nanocluster: [Gd₈As₁₂W₁₂₄O₄₃₂(H₂O)₂₂]^{60–}. *Angew. Chem. Int. Ed.* **2009**, *48*, 9088–9091.
- [63] Reinoso, S.; Giménez-Marqués, M.; Galán-Mascarós, J. R.; Vitoria, P.; Gutiérrez-Zorrilla, J. M. Giant Crown-Shaped Polytungstate Formed by Self-Assembly of Ce^{III}-Stabilized Dilacunary Keggin Fragments. *Angew. Chem. Int. Ed.* **2010**, *49*, 8384–9091.
- [64] Li, Z.; Lv, Z.-H.; Sun, Y.-Q.; Li, X.-X.; Zheng, S.-T. Giant Ln₃₀-Cluster-Embedded Polyoxotungstate Nanoclusters with Exceptional Proton-Conducting and Luminescent Properties. *CCS Chem.* **2022**, *4*, 2938–2945.
- [65] (a) Artetxe, B.; Reinoso, S.; San Felices, L.; Gutiérrez-Zorrilla, J. M.; García, J. A.; Haso, F.; Liu, T.; Vicent, C. Crown-Shaped Tungstogermanates as Solvent-Controlled Dual Systems in the Formation of Vesicle-Like Assemblies. *Chem. Eur. J.* **2015**, *21*, 7736–7745. (b) Wang, K.-Y.; Bassil, B. S.; Lin, Z.; Römer, I.; Vanhaecht, S.; Parac-Vogt, T. N.; Sáenz de Pipaón, C.; Galán-Mascarós, J. R.; Fan, L.; Cao, J.; Kortz, U. Ln₁₂-Containing 60-Tungstogermanates: Synthesis, Structure, Luminescence, and Magnetic Studies. *Chem. Eur. J.* **2015**, *21*, 18168–18176.

- [66] Niu, J.; Wang, K.; Chen, H.; Zhao, J.; Ma, P.; Wang, J.; Li, M.; Bai, Y.; Dang, D. Assembly Chemistry between Lanthanide Cations and Monovacant Keggin Polyoxotungstates: Two Types of Lanthanide Substituted Phosphotungstates $[(\alpha\text{-PW}_{11}\text{O}_{39}\text{H})\text{Ln}(\text{H}_2\text{O})_3]^{6-}$ and $[(\alpha\text{-PW}_{11}\text{O}_{39})\text{Ln}(\text{H}_2\text{O})(\eta^2, \mu\text{-}1, 1)\text{-CH}_3\text{COO}]_2^{10-}$. *Cryst. Growth Des.* **2009**, *9*, 4362-4372.
- [67] Mialane, P.; Lisnard, L.; Mallard, A.; Marrot, J.; Antic-Fidancev, E.; Aschehoug, P.; Vivien, D.; Sécheresse, F. Solid-State and Solution Studies of $\{\text{Ln}_n(\text{SiW}_{11}\text{O}_{39})\}$ Polyoxoanions: An Example of Building Block Condensation Dependent on the Nature of the rare Earth. *Inorg. Chem.* **2003**, *42*, 2102-2108.
- [68] (a) Trautwein, G.; El Bakkali, B.; Alcañiz-Monge, J.; Artetxe, B.; Reinoso, S.; Gutiérrez-Zorrilla, J. M. Dimeric Assemblies of Lanthanide-Stabilised Dilacunary Keggin Tungstogermanates: A New Class of Catalysts for the Selective Oxidation of Aniline. *J. Catal.* **2015**, *331*, 110-117. (b) Li, S.; Zhou, Y.; Peng, Q.; Wang, R.; Feng, X.; Liu, S.; Ma, X.; Ma, N.; Zhang, J.; Chang, Y.; Zheng, Z.; Chen, X. Controllable Synthesis and Catalytic Performance of Nanocrystals of Rare-Earth-Polyoxometalates. *Inorg. Chem.* **2018**, *57*, 6624-6631.
- [69] (a) Boglio, C.; Lemiere, G.; Hasenknopf, B.; Thorimbert, S.; Lacôte, E.; Malacria, M. Lanthanide Complexes of the Monovacant Dawson Polyoxotungstate $[\alpha_1\text{-P}_2\text{W}_{17}\text{O}_{61}]^{10-}$ as Selective and Recoverable Lewis Acid Catalysts. *Angew. Chem., Int. Ed.* **2006**, *45*, 3324-3327. (b) Dupre, N.; Rémy, P.; Micoine, K.; Boglio, C.; Thorimbert, S.; Lacôte, E.; Hasenknopf, B.; Malacria, M. Chemoselective Catalysis with Organosoluble Lewis Acidic Polyoxotungstate. *Chem. Eur. J.* **2010**, *16*, 7256-7264. (c) Moll, H. E.; Nohra, B.; Mialane, P.; Marrot, J.; Dupré, N.; Riffade, B.; Malacria, M.; Thorimbert, S.; Hasenknopf, B.; Lacôte, E.; Aparicio, P. A.; Lopez, X.; Poblet, J. M.; Dolbecq, A. Lanthanide Polyoxocationic Complexes: Experimental and Theoretical Stability Studies and Lewis Acid Catalysis. *Chem. Eur. J.* **2011**, *17*, 14129-14138. (d) Suzuki, K.; Sugawa, M.; Kikukawa, Y.; Kamata, K.; Yamaguchi, K.; Mizuno, N. Strategic Design and Refinement of Lewis Acid-Base Catalysis by Rare-Earth-Metal-Containing Polyoxometalates. *Inorg. Chem.* **2012**, *51*, 6953-6961. (e) Li, S.; Zhou, Y.; Peng, Q.; Wang, R.; Feng, X.; Liu, S.; Ma, X.; Ma, N.; Zhang, J.; Chang, Y.; Zheng, Z.; Chen, X. Controllable Synthesis and Catalytic Performance of Nanocrystals of Rare-Earth-Polyoxometalates. *Inorg. Chem.* **2018**, *57*, 6624-6631.
- [70] Yang, G.-P.; Shang, S.-X.; Yu, B.; Hu, C.-H. Ce(III)-Containing Tungstotellurate(VI) with a Sandwich Structure: An Efficient Lewis Acid-Base Catalyst for the Condensation Cyclization of 1,3-Diketones with Hydrazines/Hydrazides or Diamines. *Inorg. Chem. Front.* **2018**, *5*, 2472-2477.
- [71] (a) Stroobants, K.; Moelants, E.; Ly, H. G. T.; Proost, P.; Bartik, K.; Parac-Vogt, T. N. Polyoxometalates as a Novel Class of Artificial Proteases: Selective Hydrolysis of Lysozyme under Physiological pH and Temperature Promoted by a Cerium(IV) Keggin-Type Polyoxometalate. *Chem. Eur. J.* **2013**, *19*, 2848-2858. (b) Tanuhadi, E.; Al-Sayed, E.; Roller, A.; Čipčić-Paljetak, H.; Verbanac, D.; Rompel, A. Synthesis, Characterization, and Phosphoesterase Activity of a Series of 4f- and 4d-Sandwich-Type Germanotungstates $[(n\text{-C}_4\text{H}_9)_4\text{N}]_{l/m}\text{H}_2[(\text{M}(\text{H}_2\text{O})_3)(\gamma\text{-GeW}_{10}\text{O}_{35})_2]$ (M = Ce^{III}, Nd^{III}, Gd^{III}, Er^{III}, I = 7; Zr^{IV}, m = 6). *Inorg. Chem.* **2020**, *59*, 14078-14084.
- [72] (a) Clemente-Juan, J. M.; Coronado, E.; Gaita-Ariño, A. Magnetic Polyoxometalates: From Molecular Magnetism to Molecular Spintronics and Quantum Computing. *Chem. Soc. Rev.* **2012**, *41*, 7464-7478. (b) S. Gao (Eds), *Molecular Nanomagnets and Related Phenomena*, Springer-Verlag, Berlin-Heidelberg, **2015**.
- [73] Cardona-Serra, S.; Clemente-Juan, J. M.; Coronado, E.; Gaita-Ariño, A.; Camón, A.; Evangelisti, M.; Luis, F.; Martínez-Pérez, M. J.; Sesé, J. Lanthanoid Single-Ion Magnets Based on Polyoxometalates with a 5-fold Symmetry: The Series $[\text{LnP}_5\text{W}_{30}\text{O}_{110}]^{12-}$ (Ln³⁺ = Tb, Dy, Ho, Er, Tm, and Yb). *J. Am. Chem. Soc.* **2012**, *134*, 14982-14990.
- [74] (a) AlDamen, M. A.; Clemente-Juan, J. M.; Coronado, E.; Martí-Gastaldo, C.; Gaita-Ariño, A. Mononuclear Lanthanide Single-Molecule Magnets Based on Polyoxometalates. *J. Am. Chem. Soc.* **2008**, *130*, 8874-8875. (b) AlDamen, M. A.; Cardona-Serra, S.; Clemente-Juan, J. M.; Coronado, E.; Gaita-Ariño, A.; Martí-Gastaldo, C.; Luis, F.; Montero, O. Mononuclear Lanthanide Single Molecule Magnets Based on the Polyoxometalates $[\text{Ln}(\text{W}_5\text{O}_{18})_2]^{9-}$ and $[\text{Ln}(\beta_2\text{-SiW}_{11}\text{O}_{39})_2]^{13-}$ (Ln^{III} = Tb, Dy, Ho, Er, Tm, and Yb). *Inorg. Chem.* **2009**, *48*, 3467-3479. (c) Mougharbel, A. S.; Bhattacharya, S.; Bassil, B. S.; Rubab, A.; van Leusen, J.; Kögerler, P.; Wojciechowski, J.; Kortz, U. Lanthanide-Containing 22-Tungsto-2-germanates $[\text{Ln}(\text{GeW}_{11}\text{O}_{39})_2]^{13-}$: Synthesis, Structure and Magnetic Properties. *Inorg. Chem.* **2020**, *59*, 4340-4348.

CHAPTER 1

- [75] (a) Bartolomé, J.; Luis, J.; Fernández, J. F. Eds., *Molecular Magnets, Physics and Applications*, Springer-Verlag, Berlin-Heidelberg, **2014**. (b) Shiddiq, M.; Komijani, D.; Duan, Y.; Gaita-Ariño, A.; Coronado, E.; Hill, S. Enhancing Coherence in Molecular Spin Qubits via Atomic Clock Transitions. *Nature* **2016**, *531*, 348–351. (c) Suzuki, K.; Sato, R.; Mizuno, N. Reversible Switching of Single Molecule Magnet Behaviors by Transformation of Dinuclear Dysprosium Cores in Polyoxometalates. *Chem. Sci.* **2013**, *4*, 596–600.
- [76] Zabala-Lekuona, A.; Seco, J. M.; Colacio, E. Single-Molecule Magnets: From Mn₁₂-ac to Dysprosium Metallocenes, a Travel in Time. *Coord. Chem. Rev.* **2021**, *441*, 213984.
- [77] Abragam, A.; Bleaney, B. Eds. *Electron Paramagnetic Resonance of Transition Ions*, Clarendon Press: Oxford, UK, **1970**.
- [78] Armelao, L.; Quici, S.; Barigelletti, F.; Accorsi, G.; Bottaro, G.; Cavazzini, M.; Tondello, E. Design of Luminescent Lanthanide Complexes: From Molecules to Highly Efficient Photo-Emitting Materials. *Coord. Chem. Rev.* **2010**, *254*, 487–505.
- [79] Yamase, T. Chapter 243 Luminescence of Polyoxometallolanthanoates and Photochemical Nano-Ring Formation. In *Handbook on the Physics and Chemistry of Rare Earths*; Gschneidner, K. A., Bünzli, J.-C. G., Pecharsky, V. K., Eds.; Elsevier: Amsterdam, **2009**; pp 297–356.
- [80] Bünzli, J.-C. G. Lanthanide Luminescence for Biomedical analyses and Imaging. *Chem. Rev.* **2010**, *110*, 2729–2755.
- [81] (a) Vicinelli, V.; Ceroni, P.; Maestri, M.; Balzani, V.; Gorka, M.; Vögtle, F. Luminescent Lanthanide Ions Hosted in a Fluorescent Polylysine Dendrimer. Antenna-Like Sensitization of Visible and Near-Infrared Emission. *J. Am. Chem. Soc.* **2002**, *124*, 6461–6468. (b) Døssing, A. Luminescence from Lanthanide(3+) Ions in Solution. *Eur. J. Inorg. Chem.* **2005**, 1425–1434. (c) Bünzli, J.-C. G.; Piguet, C. Taking Advantage of Luminescent Lanthanide Ions. *Chem. Soc. Rev.* **2005**, *34*, 1048–1077.
- [82] Sugeta, M.; Yamase, T. Crystal Structure and Luminescence Site of Na₉[EuW₁₀O₃₆]·32H₂O. *Bull. Chem. Soc. Jpn.* **1993**, *66*, 444–449.
- [83] (a) Li, H.; Qi, W.; Li, W.; Sun, H.; Bu, W.; Wu, L. A Highly Transparent and Luminescent Hybrid Based on the Copolymerization of Surfactant-Encapsulated Polyoxometalate and Methyl Methacrylate. *Adv. Mater.* **2005**, *17*, 2688–2692. (b) Liang, L.; Sun, N.; Yu, Y.; Ren, S.; Wu, A.; Zheng, L. Photoluminescent Polymer Hydrogels with Stimuli-Responsiveness Constructed from Eu-Containing Polyoxometalate and Imidazolium Zwitterions. *Soft Matter* **2020**, *16*, 2311–2320.
- [84] (a) Li, H.; Qi, W.; Li, W.; Sun, H.; Bu, W.; Wu, L. A Highly Transparent and Luminescent Hybrid Based on the Copolymerization of Surfactant-Encapsulated Polyoxometalate and Methyl Methacrylate. *Adv. Mater.* **2005**, *17*, 2688–2692. (b) Granadeiro, C. M.; Ferreira, R. A. S.; Soares-Santor, P. C. R.; Carlos, L. D.; Trindade, T.; Nogueira, H. I. S. Lanthanopolyoxotungstates in Silica Nanoparticles: Multi-Wavelength Photoluminescent Core/Shell Materials. *J. Mater. Chem.* **2010**, *20*, 3313–3318. (c) Fujita, Y.; Ishihara, N.; Fuyaka, K.; Srafa, A.; Naruke, H. Fabrication of Lanthanide Decatungstate [Ln^{III/IV}(W₅O₁₈)₂]^{8-/9-} (Ln = Ce^{IV/III}, Eu^{III}, and Er^{III}) Thin Films Using Spin-Coating from Aqueous Solutions. *J. Alloys Compd.* **2012**, *519*, 136–139. (d) Pinto, R. J. B.; Granadeiro, C. M.; Freire, C. S. R.; Silvestre, A. J. D.; Neto, C. P.; Ferreira, R. A. S.; Carlos, L. D.; Cavaleiro, A. M. V.; Trindade, T.; Nogueira, H. I. S. Luminescent Transparent Composite Films Based on Lanthanopolyoxometalates and Filmogenic Polysaccharides. *Eur. J. Inorg. Chem.* **2013**, 1890–1896. (e) Song, C.-Y.; Chai, D.-F.; Zhang, R.-R.; Liu, H.; Qiu, Y.-F.; Guo, H.-D.; Gao, G.-G. A Silver-Alkynyl Cluster Encapsulating a Fluorescent Polyoxometalate Core: Enhanced Emission and Fluorescence Modulation. *Dalton Trans.* **2015**, *44*, 3997–4002. (f) Zhang, J.; Shi, N.; Zhang, J.; Guan, Y.; Qiao, W.; Wan, X. Light Triggered Co-Assembly of Photocleavable Copolymers and Polyoxometalates with Enhanced Photoluminescence. *Macromol. Rapid Commun.* **2017**, *38*, 1600550.
- [85] Izzet, G.; Volatron, F.; Proust, A. Tailor-made Covalent Organic-Inorganic Polyoxometalate Hybrids: Versatile Platforms for the Elaboration of Functional Molecular Architectures. *Chem. Rec.* **2017**, *17*, 250–266.
- [86] Anyushin, A.; Kondinski, A.; Parac-Vogt, T. N. Hybrid Polyoxometalates as Post-Functionalization Platforms: From Fundamentals to Emerging Applications. *Chem. Soc. Rev.* **2020**, *49*, 382–432.

- [87] Dolbecq, A.; Dumas, E.; Mayer, C. R.; Mialane, P. Hybrid Organic–Inorganic Polyoxometalate Compounds: From Structural Diversity to Applications. *Chem. Rev.*, **2010**, *110*, 6009–6048.
- [88] Izzet, G.; Abécassis, B.; Brouri, D.; Piot, M.; Matt, B.; Serapin, S. A.; Bo, C.; Proust, A. Hierarchical Self-Assembly of Polyoxometalate-Based Hybrids Driven by Metal Coordination and Electrostatic Interactions: From Discrete Supramolecular Species to Dense Monodisperse Nanoparticles. *J. Am. Chem. Soc.* **2016**, *138*, 5093–5099.
- [89] Zhang, T.; Mazaud, L.; Chamoreau, L.-M.; Paris, C.; Proust, A.; Guillemot, G. Unveiling the Active Surface Sites in Heterogeneous Titanium-Based Silicalite Epoxidation Catalysts: Input of Silanol-Functionalized Polyoxotungstates as Soluble Analogues. *ACS Catal.* **2018**, *8*, 2330–2342.
- [90] Lombana, A.; Rinfray, C.; Volatron, F.; Izzet, G.; Battaglini, N.; Alves, S.; Decorse, P.; Lang, P.; Proust, A. Surface Organization of Polyoxometalate Hybrids Steered by a 2D Supramolecular PTCDI/Melamine Network. *J. Phys. Chem. C* **2016**, *120*, 2837–2845.
- [91] Villanneau, R.; Marzouk, A.; Wang, Y.; Djamaa, A. B.; Laugel, G.; Proust, A.; Launay, F. Covalent Grafting of Organic–Inorganic Polyoxometalates Hybrids onto Mesoporous SBA-15: A Key Step for New Anchored Homogeneous Catalysts. *Inorg. Chem.* **2013**, *52*, 2958–2965. (b) Hampson, E.; Cameron, J. M.; Amin, S.; Kyo, J.; Watts, J. A.; Oshio, H.; Newton, G. N. Asymmetric Hybrid Polyoxometalates: A Platform for Multifunctional Redox-Active Nanomaterials. *Angew. Chem. Int. Ed.* **2019**, *58*, 18281–18285.
- [92] Hussain, F.; Kortz, U.; Reicke, M. The Ball-Shaped Heteropolytungstates $[\{\text{Sn}(\text{CH}_3)_2(\text{H}_2\text{O})\}_{24}\{\text{Sn}(\text{CH}_3)_2\}_{12}(\text{A-XW}_9\text{O}_{34})_{12}]^{36-}$. *Angew. Chem. Int. Ed.* **2005**, *44*, 3773–3777.
- [93] Ma, T.; Yang, P.; Dammann, I.; Lin, Z.; Mougharbel, A. S.; Li, M.-X.; Adăscăliței, F.; Mitea, R.; Silvestru, C.; Thorstenson, C.; Ullrich, M. S.; Cseh, K.; Jakupec, M. A.; Keppler, B. K.; Donalizio, M.; Caalli, R.; Lembo, D.; Kortz, U. Tetra-(p-tolyl)antimony(III)-Containing Heteropolytungstates, $[\{(p\text{-tolyl})\text{Sb}^{\text{III}}\}_4(\text{A-}\alpha\text{-XW}_9\text{O}_{34})_2]^{n-}$ (X = P, As, or Ge): Synthesis, Structure, and Study of Antibacterial and Antitumor Activity. *Inorg. Chem.* **2020**, *59*, 2978–2987.
- [94] (a) Marcano, D. E. S.; Moussawi, M. A.; Anyushin, A. V.; Lentink, S.; Meervelt, L. V.; Ivanović-Burmazović, I.; Parac-Vogt, T. N. Versatile Post-Functionalization Strategy for the Formation of Modular Organic–Inorganic Polyoxometalate Hybrids. *Chem. Sci.* **2022**, *13*, 2891–2899. (b) Blazevic, A.; Rompel, A. The Anderson–Evans Polyoxometalate: From Inorganic Building Blocks via Hybrid Organic–Inorganic Structures to Tomorrows “Bio-POM”. *Coord. Chem. Rev.* **2016**, *307*, 42–64.
- [95] Hasenknopf, B.; Delmont, R.; Herson, P.; Gouzerh, P. Anderson-Type Heteropolymolybdates Containing Tris(alkoxo) Ligands: Synthesis and Structural Characterization. *Eur. J. Inorg. Chem.* **2002**, 1081–1087.
- [96] Zhang, J.; Huang, Y.; Hao, J.; Wei, Y. β - $\{\text{Cr}[\text{RC}(\text{CH}_2\text{O})_3]_2\text{Mo}_6\text{O}_{18}\}^{3-}$: The First Organically-Functionalized β Isomer of Anderson-Type Polyoxometalates. *Inorg. Chem. Front.* **2017**, *4*, 1215–1218.
- [97] Gumerova, N. I.; Fraile, T. C.; Roller, A.; Giester, G.; Pascual-Borràs, M.; Ohlin, C. A.; Rompel, A. Direct Single- and Double-Side Triol-Functionalization of the Mixed Type Anderson Polyoxotungstate $[\text{Cr}(\text{OH})_3\text{W}_6\text{O}_{21}]^{6-}$. *Inorg. Chem.* **2019**, *58*, 106–113.
- [98] (a) Song, Y.-F.; Long, D.-L.; Kelly, S. E.; Cronin, L. Sorting the Assemblies of Unsymmetrically Covalently Functionalized Mn-Anderson Polyoxometalate Clusters with Mass Spectrometry. *Inorg. Chem.* **2008**, *47*, 9137–9139. (b) Rosnes, M. H.; Musumeci, C.; Pradeep, C. P.; Mathieson, J. S.; Long, D.-L.; Song, Y.-F.; Pignataro, B.; Cogdell, R.; Cronin, L. Assembly of Modular Asymmetric Organic–Inorganic Polyoxometalate Hybrids into Anisotropic Nanostructures. *J. Am. Chem. Soc.* **2010**, *132*, 15490–15492. (c) Wu, P.; Yin, P.; Zhang, J.; Hao, J.; Xiao, Z.; Wei, Y. Single-Side Organically Functionalized Anderson-Type Polyoxometalates. *Chem. Eur. J.* **2011**, *17*, 12002–12005. (d) Oms, O.; Hakouk, K.; Dessap, R.; Deniard, P.; Jobic, S.; Dolbecq, A.; Palacin, T.; Nadjo, L.; Keita, B.; Marrot, J.; Mialane, P. Photo- and Electrochromic Properties of Covalently Connected Symmetrical and Unsymmetrical Spiropyran–Polyoxometalate Dyads. *Chem. Commun.* **2012**, *48*, 12103–12105. (e) Zhang, J.; Liu, Z.; Huang, Y.; Zhang, J.; Hao, J.; Wei, Y. Unprecedented χ Isomers of Single-Side

CHAPTER 1

Triofunctionalized Anderson Polyoxometalates and Their Proton-Controlled Isomer Transformation. *Chem. Commun.* **2015**, 51, 9097-9100.

[99] Pradeep, C. P.; Long, D.-L.; Newton, G. N.; Song, Y.-F.; Cronin, L. Supramolecular Metal Oxides: Programmed Hierarchical Assembly of a Protein-Sized 21 kDa $[(C_{16}H_{36}N)_{19}\{H_2NC(CH_2O)_3P_2V_3W_{15}O_{59}\}_4]^{5-}$ Polyoxometalate Assembly. *Angew. Chem. Int. Ed.* **2008**, 47, 4388-4391.

[100] (a) Pradeep, C. P.; Misrahi, M. F.; Li, F.-Y.; Zhang, J.; Xu, L.; Long, D.-L.; Liu, T.; Cronin, L. Synthesis of Modular "Inorganic-Organic-Inorganic" Polyoxometalates and Their Assembly into Vesicles. *Angew. Chem. Int. Ed.* **2009**, 48, 8309-8313. (b) Han, Y.; Xiao, Y.; Zhang, Z.; Liu, B.; Zheng, P.; He, S.; Wang, W. Synthesis of Polyoxometalate-Polymer Hybrid Polymers and Their Hybrid Vesicular Assembly. *Macromolecules* **2009**, 42, 6543-6548.

[101] Lachkar, D.; Vilona, D.; Dumont, E.; Lelli, M.; Lacôte, E. Grafting of Secondary Diolamides onto $[P_2W_{15}V_3O_{62}]^{9-}$ Generates Hybrid Heteropoly Acids. *Angew. Chem. Int. Ed.* **2016**, 55, 5961-5965.

[102] Zhu, Y.; Huang, Y.; Li, Q.; Zang, D.; Gu, J.; Tang, Y.; Wei, Y. Polyoxometalate-Based Photoactive Hybrid: Uncover the First Crystal Structure of Covalently Linked Hexavanadate-Porphyrin Molecule. *Inorg. Chem.* **2020**, 59, 2575-2583.

[103] Müller, A.; Meyer, J.; Mögge, H.; Stammer, A.; Botar, A. Z. Cis-/Trans-Isomerie bei Bis-(trisalkoxy)-hexavanadaten: $cis-Na_2[V_6^{IV}O_7(OH)_6\{(OCH_2)_3CCH_2OH\}_2] \cdot 8H_2O$, $cis-(CN_3H_6)_3[V^{IV}V_5VO_{13}\{(OCH_2)_3CCH_2OH\}_2] \cdot 4,5H_2O$ und $trans-(CN_3H_6)_2[V_6^{IV}O_{13}\{(OCH_2)_3CCH_2OH\}_2] \cdot H_2O$. *Anorg. Allg. Chem.* **1995**, 621, 1818-1831.

[104] Du, Y.; Rheingold, A. L.; Maatta, E. A. A Polyoxometalate Incorporating an Organoimido Ligand: Preparation and Structure of $[Mo_5O_{18}(MoNC_6H_4CH_3)]^{2-}$. *J. Am. Chem. Soc.* **1992**, 114, 345-346.

[105] Zhang, J.; Hao, J.; Wei, Y.; Xia, F.; Yin, P.; Wang, L. Nanoscale Chiral Rod-like Molecular Triads Assembled from Achiral Polyoxometalates. *J. Am. Chem. Soc.* **2010**, 132, 14-15.

[106] Wei, Y.; Xu, B.; Barnes, C. L.; Peng, Z. An Efficient and Convenient Reaction Protocol to Organoimido Derivatives of Polyoxometalates. *J. Am. Chem. Soc.* **2001**, 123, 4083-4084.

[107] Zhang, J., Xiao, F., Hao, J. and Wei, Y. The Chemistry of Organoimido Derivatives of Polyoxometalates. *Dalton Trans.* **2012**, 41, 3599-3615.

[108] Kwen, H.; Young, V. G.; Maatta, E. A. A Diazoalkane Derivative of a Polyoxometalate: Preparation and Structure of $[Mo_6O_{18}(NNC(C_6H_4OCH_3)CH_3)]^{2-}$. *Angew. Chem. Int. Ed.* **1999**, 38, 1145-1146.

[109] (a) Liu, H.; Gómez-García, C. J.; Peng, J.; Sha, J.; Li, Y.; Yan, Y. 3D-Transition Metal Substituted Keggin Polyoxotungstate With an Antenna Molecule: Synthesis, Structure and Characterization. *Dalton Trans.*, **2008**, 6211-6218. (b) Liu, H.; Gómez-García, C. J.; Peng, J.; Sha, J.; Wang, L.; Yan, Y. A Co-Monosubstituted Keggin Polyoxometalate With an Antenna Ligand and Three Cobalt(II) Chains as Counterion. *Inorganica. Chim. Acta* **2009**, 362, 1957-1962.

[110] (a) Baker, L. C. W.; Figgis, J. S. New Fundamental Type of Inorganic Complex: Hybrid Between Heteropoly and Conventional Coordination Complexes. Possibilities for Geometrical Isomerisms in 11-, 12-, 17-, and 18-Heteropoly Derivatives, *J. Am. Chem. Soc.* **1970**, 92, 3794-3797. (b) Liu, H.; Gómez-García, C. J.; Peng, J.; Sha, J.; Li, Y.; Yan, Y. 3D-Transition Metal Mono-Substituted Keggin Polyoxotungstate with an Antenna Molecule: Synthesis, Structure and Characterization. *Dalton Trans.* **2008**, 6211-6218. (c) Liu, H.; Gómez-García, C. J.; Peng, J.; Sha, J.; Wang, L.; Yan, Y. A Co-Monosubstituted Keggin Polyoxometalate with an Antenna Ligand and Three Cobalt(II) Chains as Counterion. *Inorganica Chim. Acta* **2009**, 362, 1957-1962.

[111] Artetxe, B.; Reinoso, S.; San Felices, L.; Vitoria, P.; Pache, A.; Martín-Caballero, J.; Gutiérrez-Zorrilla, J. M. Functionalization of Krebs-Type Polyoxometalates with N,O Chelating Ligands: A Systematic Study. *Inorg. Chem.* **2015**, 54, 241-252.

[112] (a) Belai, N.; Pope, M. T. Chelated Heteroatoms in Polyoxometalates and the Topological Equivalence of $\{Co^{III}(en)\}$ to Type II *cis*-Dioxometal Centers. Synthesis and Structure of $\{[Co(en)(\mu-OH)_2Co(en)]\{PW_{10}O_{37}Co(en)\}_2\}^{8-}$ and

[K $\left\{Co(en)WO_4\right\}\{WO(H_2O)\}\{PW_9O_{34}\}_2\right]^{12-}$. *Chem. Commun.* **2005**, 5760-5762. (b) Belai, N.; Kapoor, P. N.; Dickman, M. H.; Butcher, R. J.; Pope, M. T. Fusion of Coordination- and Polyoxometalate Chemistry – Chelated Cobalt(III) Centers as Structural Components of Polyoxomolybdates – $\left\{Co(en)\right\}_4Mo_{10}O_{38}\left]4-\right.$ and Macrocyclic $\left\{Co^II(H_2O)_2\right\}\{Co(en)\}_8\{Mo_{20}O_{76}\}^{6-}$. *Eur. J. Inorg. Chem.* **2009**, 5215-5218.

[113] (a) Hasenknopf, B.; Micoine, K.; Lacôte, E.; Thorimbert, S.; Malacria, M.; Thouvenot, R. Chirality in Polyoxometalate Chemistry. *Eur. J. Inorg. Chem.* **2008**, 5001-5013. (b) Du, D.-Y.; Yan, L.-K.; Su, Z.-M.; Li, S.-L.; Lan, Y.-Q.; Wang, E.-B. Chiral Polyoxometalate-Based Materials: From Design Syntheses to Functional Applications. *Coord. Chem. Rev.* **2013**, 257, 702-717. (c) Zhu, Z.; Wei, M.; Li, B.; Wu, L. Constructing Chiral Polyoxometalate Assemblies via Supramolecular Approaches. *Dalton Trans.* **2021**, 50, 5080-5098.

[114] (a) Fang, X.; Anderson, T. M.; Hill, C. L. Enantiomerically Pure Polytungstates: Chirality Transfer through Zirconium Coordination Centers to Nanosized Inorganic Clusters. *Angew. Chem. Int. Ed.* **2005**, 44, 3540-3544. (b) Fang, X.; Anderson, T. M.; Hou, Y.; Hill, C. L. Stereoisomerism in Polyoxometalates: Structural and Spectroscopic Studies of Bis(malate)-Functionalized Cluster Systems. *Chem. Commun.* **2005**, 5044-5046.

[115] (a) Rousseau, G.; Oms, O.; Dolbecq, A.; Marrot, J.; Mialane, P. Route for the Elaboration of Functionalized Hybrid 3d-Substituted Trivacant Keggin Anions. *Inorg. Chem.* **2011**, 50, 7376-7378. (b) Rousseau, G.; Rivière, E.; Dolbecq, A.; Marrot, J.; Oms, O.; Mialane, P. Monomeric, Dimeric Helical, and 1D Nickel Polyoxotungstates Structured by Carboxylate Derivatives. *Eur. J. Inorg. Chem.* **2013**, 1793-1798.

[116] Zheng, S.-T.; Zhang, J.; Yang, G.-Y. Designed Synthesis of POM–Organic Frameworks from $\{Ni_6PW_9\}$ Building Blocks under Hydrothermal Conditions. *Angew. Chem. Int. Ed.*, **2008**, 47, 3909–3913.

[117] (a) Errington, R. J.; Petkar, S. S.; Middleton, P. S.; McFarlane, W.; Clegg, W.; Coxall, R. A.; Harrington, R. W. Synthesis and Reactivity of the Methoxozirconium Pentatungstate ($^nBu_4N\right)_6\left\{\left[\mu-MeO\right]ZrW_5O_{18}\right\}_2$: Insights into Proton-Transfer Reactions, Solution Dynamics, and Assembly of $\{ZrW_5O_{18}\}^{2-}$ Building Blocks. *J. Am. Chem. Soc.* **2007**, 129, 12181-12196. (b) Errington, R. J.; Petkar, S. S.; Middleton, P. S.; McFarlane, W.; Clegg, W.; Coxall, R. A.; Harrington, R. W. Non-Aqueous Synthetic Methodology for TiW_5 Polyoxometalates: Protonolysis of $\left\{MeO\right\}TiW_5O_{18}\}^{3-}$ with Alcohols, Water and Phenols. *Dalton Trans.* **2007**, 5211-5222. (c) Bakri, R.; Booth, A.; Harle, G.; Middleton, P. S.; Wills, C.; Clegg, W.; Harrington, R. W.; Errington, R. J. Rational Addition of Capping Groups to the Phosphomolybdate Keggin Anion $\left[PMo_{12}O_{40}\right]^{3-}$ by Mild, Non-Aqueous Reductive Aggregation. *Chem. Commun.* **2012**, 48, 2779-2781. (d) Hirano, T.; Uehara, K.; Uchida, S.; Hibino, M.; Kamata, K.; Mizuno, N. Synthesis and Structural Characterization of Inorganic–Organic Inorganic Hybrids of Dipalladium-Substituted γ -Keggin Silicodecatungstates. *Inorg. Chem.* **2013**, 52, 2662-2670.

[118] (a) Godin, B.; Chen, Y.-G.; Vaissermann, J.; Ruhlmann, L.; Verdager, M.; Gouzerh, P. Coordination Chemistry of the Hexavacant Tungstophosphate $\left[H_2P_2W_{12}O_{48}\right]^{12-}$ with Fe^{III} Ions: Towards Original Structures of Increasing Size and Complexity. *Angew. Chem. Int. Ed.* **2005**, 44, 3072-3075. (b) Pichon, C.; Mialane, P.; Dolbecq, A.; Marrot, J.; Rivière, E.; Bassil, B. S.; Kortz, U.; Keita, B.; Nadjo, L.; Sécheresse, F. Octa- and Nonanuclear Nickel(II) Polyoxometalate Clusters: Synthesis and Electrochemical and Magnetic Characterizations. *Inorg. Chem.* **2008**, 47, 11120-11128. (c) Ritchie, C.; Moore, E. G.; Speldrich, M.; Kögerler, P.; Boskovic, C. Terbium Polyoxometalate Organic Complexes: Correlation of Structure with Luminescence Properties. *Angew. Chem. Int. Ed.* **2010**, 49, 7702–7705.

[119] Dolbecq, A.; Mialane, P.; Lisnard, L.; Marrot, J.; Sécheresse, F. Hybrid Organic-Inorganic 1D and 2D Frameworks with ϵ -Keggin Polyoxomolybdates as Building Blocks. *Chem. Eur. J.* **2003**, 9, 2914–2920.

[120] (a) He, W.-W.; Li, S.-L.; Zang, H.-Y.; Yang, G.-S.; Zhang, S.-R.; Su, Z.-M.; Lan, Y.-Q. Entangled Structures in Polyoxometalate-Based Coordination Polymers. *Coord. Chem. Rev.* **2014**, 279, 141-160. (b) Wang, X.; Tian, A.; Wang, X. Architectural Chemistry of Polyoxometalate-Based Coordination Frameworks Constructed from Flexible N-donor Ligands. *RSC Adv.* **2015**, 5, 41155-41168. (c) Li, D.; Ma, O.; Niu, J.; Wang, J. Recent Advances in Transition-Metal-Containing Keggin-Type Polyoxometalate-Based Coordination Polymers. *Coord. Chem. Rev.* **2019**, 392, 49-80.

[121] (a) Warren, C. J.; Haushalter, R. C.; Rose, D. J.; Zubieta, J. Three-Dimensional Organic/Inorganic Composite Materials: Hydrothermal Synthesis and Structural Characterization of the Open-Framework Oxovanadium Borophosphate $[\text{H}_3\text{NCH}_2\text{CH}_2\text{NH}_3]_2[(\text{VO})_5(\text{H}_2\text{O})\{\text{O}_3\text{POB}(\text{O})_2\text{OPO}_3\}_2]\cdot 1.5\text{H}_2\text{O}$. *Chem. Mater.* **1997**, *9*, 2694-2696. (b) Zapf, P.; Haushalter, R. C.; Zubieta, J. Hydrothermal Synthesis and Structural Characterization of a Series of One-Dimensional Organic/Inorganic Hybrid Materials of the $[(\text{MoO}_3)_n(2,2'\text{-bipy})_m]$ Family: $[\text{MoO}_3(2,2'\text{-bipy})]$, $[\text{Mo}_2\text{O}_6(2,2'\text{-bipy})]$, and $[\text{Mo}_3\text{O}_9(2,2'\text{-bipy})_2]$. *Chem. Mater.* **1997**, *9*, 2019-2024. (c) Hagrman, D.; Zubieta, C.; Rose, D. J.; Zubieta, J.; Haushalter, R. C. Composite Solids Constructed From One-Dimensional Coordination Polymer Matrices and Molybdenum Oxide Subunits: Polyoxomolybdate Clusters within $[\{\text{Cu}(4,4'\text{-bpy})\}_4\text{Mo}_8\text{O}_{26}]$ and $[\{\text{Ni}(\text{H}_2\text{O})_2(4,4'\text{-bpy})_2\}_2\text{Mo}_8\text{O}_{26}]$ and One-Dimensional Oxide Chains in $[\{\text{Cu}(4,4'\text{-bpy})\}_4\text{Mo}_{15}\text{O}_{47}]\cdot 8\text{H}_2\text{O}$. *Angew. Chem. Int. Ed. Engl.* **1997**, *36*, 873-876. (d) Hagrman, P. L.; Hagrman, D.; Zubieta, J. Organic-Inorganic Hybrid Materials: From "Simple" Coordination Polymers to Organodiamine-Templated Molybdenum Oxides. *Angew. Chem. Int. Ed.* **1999**, *38*, 2638-2684.

[122] (a) Reinoso, S.; Vitoria, P.; San Felices, L.; Lezama, L.; Gutiérrez-Zorrilla, J. M. Organic-Inorganic Hybrids Based on Novel Bimolecular $[\text{Si}_2\text{W}_{22}\text{Cu}_2\text{O}_{78}(\text{H}_2\text{O})]^{12-}$ Polyoxometalates and the Polynuclear Complex Cations $[\text{Cu}(\text{ac})(\text{phen})(\text{H}_2\text{O})]_n^{n+}$ ($n=2, 3$). *Chem. Eur. J.* **2005**, *11*, 1538-1548. (b) Reinoso, S.; Vitoria, P.; Gutiérrez-Zorrilla, J. M.; Lezama, L.; San Felices, L.; Beitia, J. I. Inorganic-Metalorganic Hybrids Based on Copper(II)-Monosubstituted Keggin Polyanions and Dinuclear Copper(II)-Oxalate Complexes. Synthesis, X-ray Structural Characterization, and Magnetic Properties. *Inorg. Chem.* **2005**, *44*, 9731-9742. (c) Reinoso, S.; Vitoria, P.; San Felices, L.; Lezama, L.; Gutiérrez-Zorrilla, J. M. Analysis of Weak Interactions in the Crystal Packing of Inorganic Metalorganic Hybrids Based on Keggin Polyoxometalates and Dinuclear Copper(II)-Acetate Complexes. *Inorg. Chem.* **2006**, *45*, 108-118. (d) Reinoso, S.; Vitoria, P.; Gutiérrez-Zorrilla, J.-M.; Lezama, L.; Madariaga, J. M.; San Felices, L.; Iturrospe, A. Coexistence of Five Different Copper(II)-Phenanthroline Species in the Crystal Packing of Inorganic-Metalorganic Hybrids Based on Keggin Polyoxometalates and Copper(II)-Phenanthroline-Oxalate Complexes. *Inorg. Chem.* **2007**, *46*, 4010-4021. (e) Reinoso, S.; Vitoria, P.; San Felices, L.; Montero, A.; Lezama, L.; Gutiérrez-Zorrilla, J. M. Tetrahydroxy-p-benzoquinone as a Source of Polydentate O-Donor Ligands. Synthesis, Crystal Structure, and Magnetic Properties of the $[\text{Cu}(\text{bpy})(\text{dhmal})]_2$ Dimer and the Two-Dimensional $[\{\text{SiW}_{12}\text{O}_{40}\}\{\text{Cu}_2(\text{bpy})_2(\text{H}_2\text{O})(\text{ox})\}_2]\cdot 16\text{H}_2\text{O}$ Inorganic-Metalorganic Hybrid. *Inorg. Chem.* **2007**, *46*, 1237-1249.

[123] (a) San Felices, L.; Vitoria, P.; Gutiérrez-Zorrilla, J. M.; Lezama, L.; Reinoso, S. Hybrid Inorganic-Metalorganic Compounds Containing Copper(II)-Monosubstituted Keggin Polyanions and Polymeric Copper(I) Complexes. *Inorg. Chem.* **2006**, *45*, 7748-7757. (b) Iturrospe, A.; Artetxe, B.; Reinoso, S.; San Felices, L.; Vitoria, P.; Lezama, L.; Gutiérrez-Zorrilla, J. M. Copper(II) Complexes of Tetradentate Pyridyl Ligands Supported on Keggin Polyoxometalates: Single-Crystal to Single-Crystal Transformations Promoted by Reversible Dehydration Processes. *Inorg. Chem.* **2013**, *52*, 3084-3093. (c) Iturrospe, A.; San Felices, L.; Reinoso, S.; Artetxe, B.; Lezama, L.; Gutiérrez-Zorrilla, J. M. Reversible Dehydration in Polyoxometalate-Based Hybrid Compounds: A Study of Single-Crystal to Single-Crystal Transformations in Keggin-Type Germanotungstates Decorated with Copper(II) Complexes of Tetradentate N-Donor Ligands. *Cryst. Growth Des.* **2014**, *14*, 2318-2328. (d) Fernández-Navarro, L.; Iturrospe, A.; Reinoso, S.; Artetxe, B.; Ruiz-Bilbao, E.; San Felices, L.; Gutiérrez-Zorrilla, J. M. Thermally Induced Structural Transitions between Single-Crystalline States in the First Hybrid Compound Combining Keggin-Type Clusters with Metal-Cyclam Complexes: From Two-Dimensional Covalent Assemblies to Discrete Molecular Species. *Cryst. Growth Des.* **2020**, *20*, 3499-3509.

[124] (a) Martín-Caballero, J.; Wéry, A. S. J.; Reinoso, S.; Artetxe, B.; San Felices, L.; El Bakkali, B.; Trautwein, G.; Alcañiz-Monge, J.; Vilas, J. L.; Gutiérrez-Zorrilla, J. M. A Robust Open Framework Formed by Decavanadate Clusters and Copper(II) Complexes of Macrocyclic Polyamines: Permanent Microporosity and Catalytic Oxidation of Cycloalkanes. *Inorg. Chem.* **2016**, *55*, 4970-4979. (b) Martín-Caballero, J.; Artetxe, B.; Reinoso, S.; San Felices, L.; Castillo, O.; Beobide, G.; Vilas, J. L.; Gutiérrez-Zorrilla, J. M. Thermally-Triggered Crystal Dynamics and Permanent Porosity in the First Heptatungstate-Metalorganic Three-Dimensional Hybrid Framework. *Chem. Eur. J.* **2017**, *23*, 14962-14974.

[125] (a) Miras, H. N.; Vilà-Nadal, L.; Cronin, L. Polyoxometalate Based Open-Frameworks (POM-OFs). *Chem. Soc. Rev.* **2014**, *43*, 5679-5699. (b) Du, D.-Y.; Qin, J.-S.; Li, S.-L.; Su, Z.-M.; Lan, Y.-Q. Recent Advances in Porous Polyoxometalate-Based Metal-Organic Framework Materials. *Chem. Soc. Rev.* **2014**, *43*, 4615-4632.

- [126] Metal-Organic Frameworks (MOFs) for Environmental Applications; Ghosh, S. K., Ed.; Elsevier: Amsterdam, The Netherlands, **2019**.
- [127] Canivet, J.; Fateeva, A.; Guo, Y.; Coasne, B.; Farrusseng, D. Water Adsorption in MOFs: Fundamentals and Applications. *Chem. Soc. Rev.* **2014**, *43*, 5594-5617.
- [128] Xu, W.; Yaghi, O. M. Metal–Organic Frameworks for Water Harvesting from Air, Anywhere, Anytime. *ACS Cent. Sci.* **2020**, *6*, 1348-1354.
- [129] Cui, S.; Qin, M.; Marandi, A.; Steggles, V.; Wang, S.; Feng, X.; Nouar, F.; Serre, C. Metal-Organic Frameworks as Advanced Moisture Sorbents for Energy-Efficient High Temperature Cooling. *Sci. Rep.* **2018**, *8*, 15284.
- [130] AbdulHalim, R. G.; Bhatt, P. M.; Belmabkhout, Y.; Shkurenko, A.; Adil, K.; Barbour, L. J.; Eddaoudi, M. A Fine-Tuned Metal–Organic Framework for Autonomous Indoor Moisture Control. *J. Am. Chem. Soc.* **2017**, *139*, 10715-10722.
- [131] (a) He, T.; Kong, X.-J.; Bian, Z.-X.; Zhang, Y.-Z.; Si, G.-R.; Xie, L.-H.; Wu, X.-Q.; Huang, H.; Chang, Z.; Bu, X.-H.; Zaworotko, M. J.; Nie, Z.-R.; Li, J.-R. Trace Removal of Benzene Vapour Using Double-Walled Metal–Dipyrzolate Frameworks. *Nat. Mater.* **2022**, *21*, 689-695. (b) Li, J.-R.; Kuppler, R. J.; Zhou, H.-C. Selective Gas Adsorption and Separation in Metal–Organic Frameworks. *Chem. Soc. Rev.* **2009**, *38*, 1477-1504.
- [132] (a) Férey, G.; Mellot-Draznieks, C.; Serre, C.; Millange, F.; Dutour, J.; Surblé, S.; Margiolaki, I. A Chromium Terephthalate-Based Solid with Unusually Large Pore Volumes and Surface Area. *Science* **2005**, *309*, 2040-2042. (b) Chui, S. S.-Y.; Lo, S. M.-F.; Charmant, J. P. H.; Orpen, A. G.; Williams, I. D. A Chemically Functionalizable Nanoporous Material $[\text{Cu}_3(\text{TMA})_2(\text{H}_2\text{O})_3]_n$. *Science* **1999**, *283*, 1148-1150.
- [133] Scott, H. S.; Shivanna, M.; Bajpai, A.; Madden, D. G.; Chen, K.-J.; Pham, T.; Forrest, K. A.; Hogan, A.; Space, B.; Perry, J. J.; Zaworotko, M. J. Highly Selective Separation of C_2H_2 from CO_2 by a New Dichromate-Based Hybrid Ultramicroporous Material. *ACS Appl. Mater. Interfaces* **2017**, *9*, 33395–33400.
- [134] Shimoyama, Y.; Uchida, S. Structure-function Relationships of Porous Ionic Crystals (PICs) Based on Polyoxometalate Anions and Oxo-centered Trinuclear Metal Carboxylates as Counter Cations. *Chem. Lett.* **2021**, *50*, 21-30.
- [135] Uchida, S.; Mizuno, N. Zeotype Ionic Crystal of $\text{Cs}_5[\text{Cr}_3\text{O}(\text{OOCH})_6(\text{H}_2\text{O})_3][\alpha\text{-CoW}_{12}\text{O}_{40}]\cdot 7.5\text{H}_2\text{O}$ with Shape-Selective Adsorption of Water. *J. Am. Chem. Soc.* **2004**, *126*, 1602–1603.
- [136] Napal, J.; Artetxe, B.; Beobide, G.; Castillo, O.; Luque, A.; Pascual-Colino, J.; Pérez-Yáñez, S.; Perfecto-Irigaray, M. Merging the Chemistry of Metal–Organic and Polyoxometalate Clusters to Form Enhanced Photocatalytic Materials. *Inorg. Chem. Front.* **2022**, *9*, 935-940.
- [137] (a) Kawamoto, R.; Uchida, S.; Mizuno, N. Amphiphilic Guest Sorption of $\text{K}_2[\text{Cr}_3\text{O}(\text{OOCCH}_2\text{H}_5)_6(\text{H}_2\text{O})_3]_2[\alpha\text{-SiW}_{12}\text{O}_{40}]$ Ionic Crystal. *J. Am. Chem. Soc.* **2005**, *127*, 10560-10567. (b) Uchida, S.; Mizuno, N. Design and Syntheses of Nano-Structured Ionic Crystals with Selective Sorption Properties. *Coord. Chem. Rev.* **2007**, *251*, 2537-2546.
- [138] Lesbani, A.; Kawamoto, R.; Uchida, S.; Mizuno, N. Control of Structures and Sorption Properties of Ionic Crystals of $\text{A}_2[\text{Cr}_3\text{O}(\text{OOCCH}_2\text{H}_5)_6(\text{H}_2\text{O})_3]_2[\alpha\text{-SiW}_{12}\text{O}_{40}]$ (A = Na, K, Rb, NH_4 , Cs, TMA). *Inorg. Chem.* **2008**, *47*, 3349-3357.
- [139] (a) Uchida, S.; Hashimoto, M.; Mizuno, N. A Breathing Ionic Crystal Displaying Selective Binding of Small Alcohols and Nitriles: $\text{K}_3[\text{Cr}_3\text{O}(\text{OOCH})_6(\text{H}_2\text{O})_3][\alpha\text{-SiW}_{12}\text{O}_{40}]\cdot 16\text{H}_2\text{O}$. *Angew. Chem. Int. Ed.* **2002**, *41*, 2814-2817. (b) Uchida, S.; Mizuno, N. Unique Guest-Inclusion Properties of a Breathing Ionic Crystal of $\text{K}_3[\text{Cr}_3\text{O}(\text{OOCH})_6(\text{H}_2\text{O})_3][\alpha\text{-SiW}_{12}\text{O}_{40}]\cdot 16\text{H}_2\text{O}$. *Chem. Eur. J.* **2003**, *9*, 5850-5857.
- [140] Uchida, S.; Kawamoto, R.; Mizuno, N. Recognition of Small Polar Molecules with an Ionic Crystal of α -Keggin-Type Polyoxometalate with a Macroanion. *Inorg. Chem.* **2006**, *45*, 5136-5144.
- [141] (a) Jiang, C.; Lesbani, A.; Kawamoto, R.; Uchida, S.; Mizuno, N. Channel-Selective Independent Sorption and Collection of Hydrophilic and Hydrophobic Molecules by $\text{Cs}_2[\text{Cr}_3\text{O}(\text{OOCCH}_2\text{H}_5)_6(\text{H}_2\text{O})_3]_2[\alpha\text{-SiW}_{12}\text{O}_{40}]$ Ionic Crystal. *J. Am. Chem. Soc.* **2006**, *128*, 14240-14241. (b) Uchida, S.; Kawamoto, R.; Tagami, H.; Nakagawa, Y.; Mizuno, N. Highly Selective

Sorption of Small Unsaturated Hydrocarbons by Nonporous Flexible Framework with Silver Ion. *J. Am. Chem. Soc.* **2008**, *130*, 12370-12376. (c) Uchida, S.; Eguchi, R.; Nakamura, S.; Ogasawara, Y.; Kurosawa, N.; Mizuno, N. Selective Sorption of Olefins by Halogen-Substituted Macroocation-Polyoxometalate Porous Ionic Crystals. *Chem. Mater.* **2012**, *24*, 325-330.

[142] (a) Tagami, H.; Uchida, S.; Mizuno, N. Size-Selective Sorption of Small Organic Molecules in One-Dimensional Channels of an Ionic Crystalline Organic-Inorganic Hybrid Compound Stabilized by π - π Interactions. *Angew. Chem., Int. Ed.* **2009**, *58*, 6160-6164. (b) Eguchi, R.; Uchida, S.; Mizuno, N. Inverse and High CO₂/C₂H₂ Sorption Selectivity in Flexible Organic-Inorganic Ionic Crystals. *Angew. Chem., Int. Ed.* **2012**, *51*, 1635-1639.

[143] Wang, Y.; Ye, L.; Wang, T.-G.; Cui, X.-B.; Shi, S.-Y.; Wang, G.-W.; Xu, J.-Q. Hydrothermal Syntheses and Characterizations of Two Novel Frameworks Constructed from Polyoxometalates, Metals and Organic Units. *Dalton Trans.* **2010**, *39*, 1916-1919.

[144] (a) Liu, D.; Lu, Y.; Tan, H.-Q.; Chen, W.-L.; Zhang, Z.-M.; Li, Y.-G.; Wang, E.-B. Polyoxometalate-Based Purely Inorganic Porous Frameworks with Selective Adsorption and Oxidative Catalysis Functionalities. *Chem. Commun.* **2013**, *49*, 3673-3675. (b) Zhang, Z.; Sadakane, M.; Murayama, T.; Izumi, S.; Yasuda, N.; Sakaguchi, N.; Ueda, W. Tetrahedral Connection of ϵ -Keggin-type Polyoxometalates To Form an All-Inorganic Octahedral Molecular Sieve with an Intrinsic 3D Pore System. *Inorg. Chem.* **2014**, *53*, 903-911. (c) Zhang, Z.; Sadakane, M.; Noro, S.; Murayama, T.; Kamachi, T.; Yoshizawa, K.; Ueda, W. Selective Carbon Dioxide Adsorption of ϵ -Keggin-Type Zincomolybdate-Based Purely Inorganic 3D Frameworks. *J. Mater. Chem. A* **2015**, *3*, 746-755.

[145] (a) Han, J. W.; Hill, C. L. A Coordination Network That Catalyses O₂-Based Oxidations. *J. Am. Chem. Soc.* **2007**, *129*, 15094-15095. (b) Zheng, S.-T.; Zhang, J.; Yang, G.-Y. Designed Synthesis of POM-Organic Frameworks from {Ni₆PW₉} Building Blocks under Hydrothermal Conditions. *Angew. Chem., Int. Ed.* **2008**, *47*, 3909-3913. (c) Nohra, B.; El Moll, H.; Rodriguez Albelo, M.; Mialane, P.; Marrot, J.; Mellot-Draznieks, C.; O'Keeffe, M.; Biboum, R. N.; Lemaire, J.; Keita, B.; Nadjio, L.; Dolbecq, A. Polyoxometalate-Based Metal Organic Frameworks (POMOFs): Structural Trends, Energetics, and High Electrocatalytic Efficiency for Hydrogen Evolution Reaction. *J. Am. Chem. Soc.* **2011**, *133*, 13363-13374. (d) Qin, J.-S.; Du, D.-Y.; Guan, W.; Bo, X.-J.; Li, Y.-F.; Guo, L.-P.; Su, Z.-M.; Wang, Y.-Y.; Lan, Y.-Q.; Zhou, H.-C. Ultrastable Polymolybdate-Based Metal-Organic Frameworks as Highly Active Electrocatalysts for Hydrogen Generation from Water. *J. Am. Chem. Soc.* **2015**, *137*, 7169-7177.

[146] Dolbecq, A.; Dumas, E.; Mayer, C. R.; Mialane, P. Hybrid Organic-Inorganic Polyoxometalate Compounds: From Structural Diversity to Applications. *Chem. Rev.* **2010**, *110*, 6009-6048.

[147] (a) Kimura, E.; Dalimunte, C. A.; Yamashita, A.; Machida, R. A Proton-Driven Copper(II) Ion Pump with a Macrocyclic Dioxotetra-amine. A New Type of Carrier for Solvent Extraction of Copper. *J. Chem. Soc., Chem. Commun.* **1985**, 1041-1043. (b) Volkert, W. A.; Hoffman, T. J. Therapeutic Radiopharmaceuticals. *Chem. Rev.* **1999**, *99*, 2269-2292.

[148] (a) Christensen, J. J.; Eatough, D. J.; Izatt, R. M. The Synthesis and I₂ binding of Synthetic Multidentate Macrocyclic Compounds. *Chem. Rev.* **1974**, *74*, 351-384. (b) Kimura, E. Macrocyclic Polyamines with Intelligent Functions. *Tetrahedron* **1992**, *48*, 6175-6217. (c) Cabbiness, D. K.; Margerum, D. W. Macrocyclic Effect on the Stability of Copper(II) Tetramine Complexes. *J. Am. Chem. Soc.* **1969**, 6540-6541.

[149] Van Alphen, J. Aliphatic Polyamines VI. *Rec. Trav. Chim.* **1937**, *56*, 1343.

[150] Groom, C. R.; Bruno, I. J.; Lightfoot, M. P.; Ward, S. C. The Cambridge Structural Database. *Acta Crystallogr.* **2016**, *B72*, 171-179.

[151] Fisher, B. J.; Eisenberg, R. Electrocatalytic Reduction of Carbon Dioxide by Using Macrocycles of Nickel and Cobalt. *J. Am. Chem. Soc.* **1980**, *102*, 7361-7363.

[152] (a) Beley, M.; Collin, J. P.; Ruppert, R.; Sauvage, J. P. Electrocatalytic Reduction of CO₂ by Ni Cyclam²⁺ in Water: Study of the Factors Affecting the Efficiency and the Selectivity of the Process. *J. Am. Chem. Soc.* **1986**, *108*, 7461-7467. (b) Froehlich, J. D.; Kubiak, C. P. Homogeneous CO₂ Reduction by Ni(cyclam) at a Grassy Carbon Electrode. *Inorg. Chem.* **2012**, *51*, 3932-3934. (c) Murase, M.; Kitahara, G.; Suzuki, T. M.; Ohta, R. Efficient Catalytic Electrode for CO₂ Reduction Realized

by Physisorbing Ni(cyclam) Molecules with Hydrophobicity Based on Hansen's Theory. *ACS Appl. Mater. Interfaces* **2016**, *8*, 24315-24318.

[153] Barefield, E. K. Coordination Chemistry of N-tetraalkylated Cyclam Ligands—A Status Report. *Coord. Chem. Rev.* **2010**, 1607-1627.

[154] Whimp, P. O.; Bailey, M. F.; Curtis, N. F. Some Cyclic Tetra-amines and their Metal-ion Complexes. Part VI. The Crystal Structure of Acetato-*C-rac*-(5,7,7,12,14,14-hexamethyl-1,4,8,11-tetra-azacyclotetradecane)nickel(II) Perchlorate. *J. Chem. Soc. A* **1970**, 1956-1963.

[155] Bosnich, B.; Poon, C. K.; Tobe, M. L. Complexes of Cobalt(III) with a Cyclic Tetradentate Secondary Amine. *Inorg. Chem.*, **1965**, *4*, 1102-1108.

[156] (a) Connolly, P. J.; Billo, E. J. ¹H-NMR Evidence for the R,S,R,S Isomer of the (1,4,8,11-Tetraazacyclotetradecane)Nickel(II) Ion. *Inorg. Chem.* **1987**, *26*, 3224-3226. (b) Donnelly, M. A.; Zimmer, M. Structural Analysis of All the Nickel 14-Membered Tetraaza Macrocyces in the Cambridge Structural Database. *Inorg. Chem.* **1999**, *38*, 1650-1658.

[157] Bakaj, M.; Zimmer, M. Conformational Analysis of Copper(II) 1,4,8,11-Tetraazacyclotetradecane Macrocylic Systems. *J. Mol. Struct.* **1999**, *508*, 59-72.

[158] (a) Barefield, E. K.; Wagner, F. Metal Complexes of 1,4,8,11-Tetramethyl-1,4,8,11-tetraazacyclotetradecane, *N*-Tetramethylcyclam. *Inorg. Chem.* **1973**, *12*, 2435-2439. (b) Zhou, A.; Prakash, J.; Rohde, G. T.; Klein, J. E. M. N.; Kleespies, S. T.; Draksharapu, A.; Fan, R.; Guo, Y.; Cramer, C. J.; Que, L. The Two Faces of Tetramethylcyclam in Iron Chemistry: Distinct Fe-O-M Complexes Derived from [Fe^{IV}(O_{anti/syn})(TMC)]²⁺ Isomers. *Inorg. Chem.* **2017**, *56*, 518-527. (c) Banziger, S. D.; Ren, T. Syntheses, Structures and Bonding of 3d Metal Alkynyl Complexes of Cyclam and its Derivatives. *J. Organomet. Chem.* **2019**, *885*, 39-48.

[159] (a) Hubin, T. J.; Alcock, N. W.; Morton, M. D.; Busch, D. H. Synthesis, Structure, and Stability in Acid of Copper(II) and Zinc(II) Complexes of Cross-Bridged Tetraazamacrocycles. *Inorg. Chem. Acta* **2003**, *348*, 33-40. (b) DeRosa, F.; Bu, X.; Ford, P. C. Synthesis and Photophysical Properties of New Chromium(III) Complexes of *N*-Derivatized 1,4,8,11-Tetraazacyclotetradecane Ligands *cis*-[Cr(1,8-R₂cyclam)Cl₂]Cl, Where R Is a Pendant Chromophore. Exclusive Formation of the *cis* Isomer. *Inorg. Chem.* **2003**, *42*, 4171-4178. (c) Brewer, S. M.; Wilson, K. R.; Jones, D. G.; Reinheimer, E. W.; Archibald, S. J.; Prior, T. J.; Ayala, M. A.; Foster, A. L.; Hubin, T. J. Green, K. N. Increase of Direct C-C Coupling Reaction Yield by Identifying Structural and Electronic Properties of High-Spin Iron Tetraazamacrocyclic Complexes. *Inorg. Chem.* **2018**, *57*, 8890-8902. (d) Kin, G.; Lelong, E.; Kang, J.; Suh, J.-M.; Le Bris, N.; Bernard, H.; Kim, D.; Tripier, R.; Lim, M. H. Reactivities of cyclam derivatives with metal-amyloid-β. *Inorg. Chem. Front.* **2020**, *7*, 4222-4238.

[160] (a) Kim, S.; Minier, M. A.; Loas, A.; Becker, S.; Wang, F.; Lippard, S. J. Achieving Reversible Sensing of Nitroxyl by Tuning the Ligand Environment of Azamacrocyclic Copper(II) Complexes. *J. Am. Chem. Soc.* **2016**, *138*, 1804-1807. (b) Kim, G.; Lelong, E.; Kang, J.; Suh, J.-M.; Le Bris, N.; Bernard, H.; Kim, D.; Tripier, R.; Lim, M. H. Reactivities of Cyclam Derivatives with Metal-Amyloid-β. *Inorg. Chem. Front.* **2020**, *7*, 4222-4238.

[161] Martín-Caballero, J.; Wéry, A. S. J.; Artetxe, B.; Reinoso, S.; San Felices, L.; Vilas, J. L.; Gutiérrez-Zorrilla, J. M. Sequential Single-Crystal-to-Single-Crystal Transformations Promoted by Gradual Thermal Dehydration in a Porous Metavanadate Hybrid. *CrystEngComm* **2015**, *17*, 8915-8925.

[162] (a) Ou, G.-C.; Yuan, X.-Y.; Li, Z.-Z.; Li, W.-Y.; Zeng, F.; Deng, J.-H.; Zhong, D.-C. Vanadium Polyoxoanions within Coordination Polymers Based on a Macrocylic Nickel Complex: Structural Diversities and Single-Crystal to Single-Crystal Transformation. *Eur. J. Inorg. Chem.* **2016**, 3500-3505. (b) Ou, G.-C.; Liao, Y.; Xiang, Y.-F.; Yuan, X.-Y.; Li, Z.-Z. Syntheses and Structures of Three Hybrid Materials Using Vanadium Polyoxoanions and Macrocylic Copper Complex as Building Blocks. *Chin. J. Struct. Chem.* **2017**, *36*, 135-142.

[163] (a) Dopta, J.; Krause, D.-C.; Näther, C.; Bensch, W. Controlling Fast Nucleation and Crystallization of Two New Polyoxoniobates. *Cryst. Growth Des.* **2018**, *18*, 4130-4139. (b) Müscher-Polzin, P.; Näther, C.; Bensch, W. A hexaniobate

expanded by six [Hg(cyclam)]²⁺ complexes via Hg–O bonds yields a positively charged polyoxoniobate cluster. *Z. Naturforsch* **2019**, *75*, 171. (c) Müscher-Polzin, P.; Näther, C.; Bensch, W. Capturing the Heptaniobate {Nb₇O₂₂}⁹⁻ Anion by Covalent Bond Formation: Synthesis, Crystal Structure, and Selected Properties of {[Fe(cyclam)]₃Nb₇O₂₂}·≈19 H₂O. *Z. Anorg. Allg. Chem.* **2020**, *646*, 193–198. (d) Müscher-Polzin, P.; Näther, C.; Bensch, W. Hexaniobate Anions Connected by [Ni(cyclam)]²⁺ Complexes Yield Two Interpenetrating Three-Dimensional Networks. *Z. Naturforsch* **2020**, *75*, 43.

[164] Chaudhary, A.; Mohammad, A.; Mobin, S. M. Recent Advances in Single-Crystal-to-Single-Crystal Transformation at the Discrete Molecular Level. *Crystal Growth & Design* **2017**, *17*, 2893–2910.

[165] (a) Zhang, Y. J.; Liu, T.; Kanegawa, S.; Sato, O. Reversible Single-Crystal-to-Single-Crystal Transformation from Achiral Antiferromagnetic Hexanuclear to a Chiral Ferrimagnetic Double Zigzag Chain. *J. Am. Chem. Soc.* **2009**, *131*, 7942–7943. (b) Coronado, E.; Mínguez Espallargas, G. Dynamic Magnetic MOFs. *Chem. Soc. Rev.* **2013**, *42*, 1525–1539.

[166] Reinoso, S.; Artetxe, B.; San Felices, L.; Gutiérrez-Zorrilla, J. M. Single-Crystal-to-Single-Crystal Transformations in Stimuli-Responsive Compounds Based on Polyoxometalate Clusters. In *Polyoxometalates: Properties, Structure and Synthesis*; Roberts, A. P., Ed.; Nova Science Publishers: Hauppauge, NY, **2016**; pp 143–212.

[167] Uehara, K.; Mizuno, N. Heterolytic Dissociation of Water Demonstrated by Crystal-to-Crystal Core Interconversion from (μ-Oxo)Divanadium to Bis(μ-Hydroxo)Divanadium Substituted Polyoxometalates. *J. Am. Chem. Soc.* **2011**, *133*, 1622–1625.

[168] Shi, L.-X.; Zhao, W.-F.; Xu, X.; Tang, J.; Wu, C.-D. From 1D to 3D Single-Crystal-to-Single-Crystal Structural Transformations Based on Linear Polyanion [Mn₄(H₂O)₁₈WZnMn₂(H₂O)₂{ZnW₉O₃₄}]⁴⁻. *Inorg. Chem.* **2011**, *50*, 12387–12389.

[169] Zhang, L.-Z.; Gu, W.; Liu, X.; Dong, Z.; Li, B. Solid-State Photopolymerization of a Photochromic Hybrid Based on Keggin Tungstophosphates. *CrystEngComm* **2008**, *10*, 652–654.

[170] (a) Ritchie, C.; Streb, C.; Thiel, J.; Mitchell, S. G.; Miras, H. N.; Long, D.-L.; Boyd, T.; Peacock, R. D.; McGlone, T.; Cronin, L. Reversible Redox Reactions in an Extended Polyoxometalate Framework Solid. *Angew. Chem. Int. Ed.* **2008**, *47*, 6881–6884. (b) Thiel, J.; Ritchie, C.; Streb, C.; Long, D.-L.; Cronin, L. Heteroatom-Controlled Kinetics of Switchable Polyoxometalate Frameworks. *J. Am. Chem. Soc.* **2009**, *131*, 4180–4181. (c) Thiel, J.; Ritchie, C.; Miras, H. N.; Streb, C.; Mitchell, S. G.; Boyd, T.; Corella Ochoa, M. N.; Rosnes, M. H.; Mclver, J.; Long, D.-L.; Cronin, L. Modular Inorganic Polyoxometalate Frameworks Showing Emergent Properties: Redox Alloys. *Angew. Chem Int. Ed.* **2010**, *49*, 6984–6988.

[171] Zhan, C.; Cameron, J. M.; Gabb, D.; Boyd, T.; Winter, R. S.; Vilà-Nadal, L.; Mitchell, S. G.; Glatzel, S.; Breternitz, J.; Gregory, D. H.; Long, D.-L.; Macdonell, A.; Cronin, L. A Metamorphic Inorganic Framework That Can Be Switched between Eight Single-Crystalline States. *Nat. Commun.* **2017**, *8*, 14185.

[172] Reinoso, S.; Artetxe, B.; Gutiérrez-Zorrilla, J. M. Single-Crystal-to-Single-Crystal Transformations Triggered by Dehydration in Polyoxometalate-Based Compounds. *Acta Cryst.* **2018**, *C74*, 1222–1242.

[173] (a) Iturraspe, A.; Artetxe, B.; Reinoso, S.; San Felices, L.; Vitoria, P.; Lezama, L.; Gutiérrez-Zorrilla, J. M. Copper(II) Complexes of Tetradentate Pyridyl Ligands Supported on Keggin Polyoxometalates: Single-Crystal to Single-Crystal Transformations Promoted by Reversible Dehydration Processes. *Inorg. Chem.* **2013**, *52*, 3084–3093. (b) Iturraspe, A.; San Felices, L.; Reinoso, S.; Artetxe, B.; Lezama, L.; Gutiérrez-Zorrilla, J. M. Reversible Dehydration in Polyoxometalate-Based Hybrid Compounds: A Study of Single-Crystal to Single-Crystal Transformations in Keggin-Type Germanotungstates Decorated with Copper(II) Complexes of Tetradentate N-Donor Ligands. *Cryst. Growth Des.* **2014**, *14*, 2318–2328.

[174] Martín-Caballero, J.; Artetxe, B.; Reinoso, S.; San Felices, L.; Vitoria, P.; Larrañaga, A.; Vilas, J. L.; Gutiérrez-Zorrilla, J. M. Thermostructural Behavior in a Series of Lanthanide-Containing Polyoxotungstate Hybrids with Copper(II) Complexes of the Tetraazamacrocyclic Cyclam: A Single-Crystal-to-Single-Crystal Transformation Study. *Inorg. Chem.* **2019**, *58*, 4365–4375.

[175] Dissem, N.; Artetxe, B.; San Felices, L.; Beobide, G.; Castillo, O.; Ruiz-Bilbao, E.; Lezama, L.; Vivanco, M. dM.; Haddad, A.; Gutiérrez-Zorrilla, J. M. Single-Crystal-to-Single-Crystal Cluster Transformation in a Microporous Molybdoarsenate(V)-Metalorganic Framework. *Inorg. Chem.* **2021**, *60*, 14913-14923.

[176] Dissem, N.; Artetxe, B.; San Felices, L.; Lezama, L.; Haddad, A.; Gutiérrez-Zorrilla, J. M. A Robust Framework Based on Polymeric Octamolybdate Anions and Copper(II) Complexes of Tetradentate N-donor Ligands. *Crystals* **2018**, *8*, 20.

Thermostructural Studies in Heptamolybdate-Metalorganic Hybrid Frameworks

- 2.1. Introduction
- 2.2. Experimental section
- 2.3. Results and discussion
- 2.4. Conclusions
- 2.5. References

ABSTRACT: The influence of the pH on the aqueous reaction between in situ prepared $\{\text{Cu}(\text{cyclam})\}^{2+}$ complexes and commercial ammonium heptamolybdate in a stoichiometric 3:1 ratio is studied in depth. When the synthesis takes place at basic pH (above 10), $[\text{Cu}(\text{cyclam})][\text{MoO}_4]\cdot 4\text{H}_2\text{O}$ (**MoCu**) chains are obtained, which are formed by tetrahedral oxoanions connected through octahedral metalorganic complexes. Similar synthetic conditions can also lead to other oxoanion/metal-complex analogues $[\text{M}(\text{cyclam})][\text{XO}_4]\cdot n\text{H}_2\text{O}$ ($X = \text{Cr}, \text{V}, \text{Mo}, \text{W}$; $M = \text{Co}, \text{Ni}, \text{Cu}, \text{Zn}$) as described in Appendix 1. In contrast, acidic pH conditions facilitate further condensation and hence, the robust framework $[\text{Cu}(\text{cyclam})]_2[\gamma\text{-Mo}_8\text{O}_{26}]\cdot 1.5\text{H}_2\text{O}$ is isolated, which is constituted by $[\text{Mo}_8\text{O}_{26}]^{4-}$ chains linked to each other through the coordination spheres of $\{\text{Cu}(\text{cyclam})\}^{2+}$ complexes. Slow evaporation of the final solutions for the reactions carried out at neutral to moderately basic conditions (pH values in the 6–9 range) initially afford $[\{\text{Cu}(\text{cyclam})\}_3(\kappa\text{-Mo}_8\text{O}_{27})]\cdot 14\text{H}_2\text{O}$ (**1-Mo8**), the rich thermostructural behavior of which, together with its interesting sorption properties, deserve a separate chapter (see Chapter 3). If **1-Mo8** is removed from the reaction media, further evaporation of the final solution yields the 3D covalent framework $[\{\text{Cu}(\text{cyclam})\}_3(\text{Mo}_7\text{O}_{24})]\cdot 15.5\text{H}_2\text{O}$ (**1-Mo7**) as a pure crystalline phase, whereas a second compound co-crystallizes at pH values between 6 and 8, namely, $(\text{NH}_4)[\{\text{Cu}(\text{cyclam})\}_{2.5}(\text{Mo}_7\text{O}_{24})]\cdot 5.5\text{H}_2\text{O}$ (**1B-Mo7**). Crystal structures of **1-Mo7** and **1B-Mo7** have been elucidated by single-crystal X-ray diffraction. Both phases cannot be visually distinguished under an optical microscope and thus, this chapter only describes the full characterization of **1-Mo7**. This hybrid framework undergoes two solid-phase transformations upon thermal evacuation of guest solvent molecules to lead to two new partially dehydrated and anhydrous phases, namely **2-Mo7** and **3-Mo7**, respectively.

2.1. INTRODUCTION

The chemistry of polyoxomolybdates is centered in the existence of a large diversity of species that are formed in aqueous solution, as a result of the presence of a number of simultaneous equilibria.¹ The complex speciation of isoPOMOs has been widely studied even though their low kinetic stability prevents them from displaying well-defined pH-dependent stability ranges. In fact, structures exhibiting reduced molybdenum centers usually consist in large species different from those of the parent fully-oxidized clusters. In this sense, in basic aqueous solutions of Mo(VI) only the molybdate $[\text{MoO}_4]^{2-}$ ion is stable. When the pH of a molybdate solution is acidified, the acidic condensation of these tetrahedral anions leads to the heptamolybdate (or paramolybdate-A) $[\text{Mo}_7\text{O}_{24}]^{6-}$ cluster. It is worth mentioning that the paramolybdate anion is the first stable form of isoPOMO obtained in acidified molybdate solutions, therefore, this anion has been widely studied and obtained in a variety of conditions, synthetic procedures and concentrations.² Further acidification leads to the formation of the well-known β -octamolybdate $[\text{Mo}_8\text{O}_{26}]^{4-}$ anion at a pH value near 4, which is formed by eight edge-sharing octahedra. In aqueous solution, this isomer is in equilibria with the α - $\{\text{Mo}_8\text{O}_{26}\}$ form, which is precipitated using organic cations. The α -isomer consists on a six member ring of octahedral $\{\text{MoO}_6\}$ units that is bicapped by two $\{\text{MO}_4\}$ tetrahedra. These two co-existing clusters are the most important and common ones that can be isolated from aqueous solution from the nine different isomers found for $\{\text{Mo}_8\text{O}_{26}\}$. Moreover, these two $\{\text{Mo}_8\text{O}_{26}\}$ anions can isomerize easily in acetonitrile solutions.³ Larger aggregates are formed at pH below 2, which is the case of the $[\text{Mo}_{36}\text{O}_{112}(\text{H}_2\text{O})_{18}]^{8-}$ anion.⁴ This cluster is the predominant species in very acidic aqueous media, and represents the largest polyoxomolybdate assembled under non-reducing conditions. In this type of large clusters, some Mo centers exhibit the $\{(\text{Mo})\text{Mo}_5\}$ -type unit in which the central atom occupies a seven-coordinated $\{\text{MoO}_7\}$ pentagonal bipyramid that shares edges with the surrounding five $\{\text{Mo}_6\}$ octahedra.

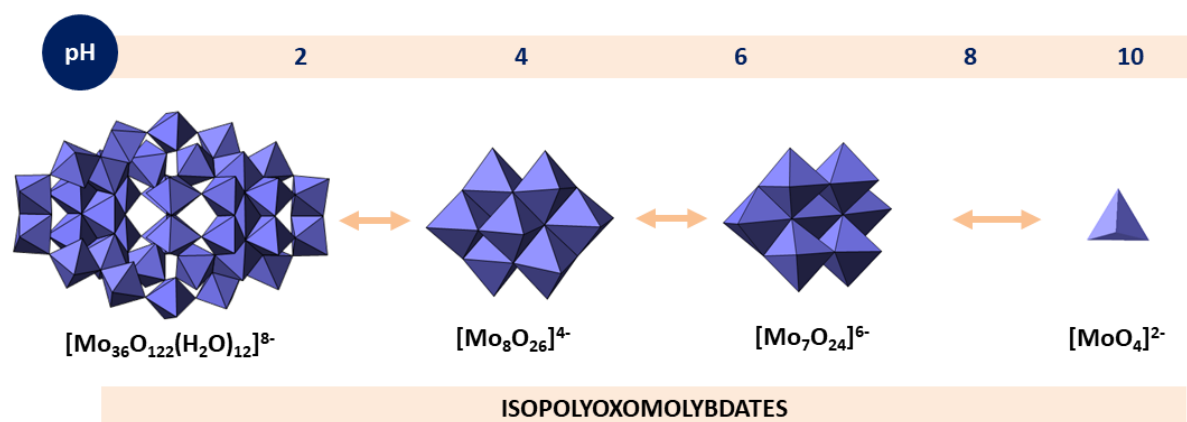


Figure 2.1. Illustration of the predominant isoPOMO structures in aqueous solution as a function of the pH.

Partial reduction of acidified molybdate solutions allows the generation of even larger assemblies. This type of large and complex molecular systems are built *via* stepwise self-assembly processes. Structures exhibiting reduced molybdenum centers usually consist in large species different from those of the parent fully-oxidized cluster which exhibit $\{(Mo)Mo_5\}$ -type building blocks. Such considerable structural and chemical diversity arises from the combination of favorable kinetics, thermodynamics and structural factors, which makes the so-called Molybdenum “Blue” and “Brown” giant cluster families unique within the field of inorganic chemistry.⁵ Mo-blues are defined by the fact that they contain mixed-valence Mo^V/Mo^{VI} *addenda* metals and have delocalized electrons capable of charge transfer from Mo^V to Mo^{VI} facilitated by the π -orbitals of the bridging oxo-ligands. This electronic interaction is responsible for their characteristic intense blue color and accounts for their reversible redox nature. In contrast, Mo-browns are further reduced polyanions and have electrons localized between reduced Mo^V centers as Mo–Mo bonds, which contributes to the brown color of these clusters, and makes them less sensitive to redox processes than their blue counterparts.⁶ Müller’s group have extensively studied and synthesized numerous of giant species which architectures and sizes range between wheel-shaped $\{Mo_{154}\} = [Mo_{154}O_{462}H_{14}(H_2O)_{70}]^{14-}$ anion,⁷ “big wheels” or Keplerates (big balls), such as $\{Mo_{132}\} = Mo^{VI}_{72}Mo^V_{60}O_{372}(CH_3COO)_{30}(H_2O)_{72}]^{42-}$ cluster,⁸ and the $\{Mo_{368}\}$ “hedgehog” or “blue lemon” structure $[H_{16}Mo_{368}O_{1032}(H_2O)_{240}(SO_4)_{48}]^{48-}$ which still represents the largest (c.a. 5 nm) POM obtained to date.⁹ The possible characterization of all these species revealed the structural flexibility of molybdenum in aqueous equilibria against tungstate analogues.

2.1.1. Heptamolybdate-metalorganic hybrids

Heptamolybdate $[Mo_7O_{24}]^{6-}$ is the predominant species in slightly acidic aqueous solutions of molybdate. The structure of the $[Mo_7O_{24}]^{6-}$ anion was described for the first time by Lindqvist,¹⁰ and then, its solution behavior fully characterized by other authors.¹¹ This anion is described as a seven edge-sharing $\{MO_6\}$ octahedral units exhibiting a C_{2v} symmetry, in which all *addenda* metals are linked to two terminal oxygens, except for the central octahedra, which is located in the core of the cluster. Among all the reported structures based on this fragment, most of them consist on salts with both inorganic and organic counterions, in which alkyl ammonium cations stand out.¹² Organic-inorganic hybrids based on polyoxomolybdates of organoammonium cations have been reported as potential photochromic materials when exposed under UV light.¹³ This process provokes a reduction in the oxidation state of some Mo metals leading to the formation of mixed valence $M^{VI}M^V$ compounds that exhibit a different color than the fully-oxidized molecule. In addition, several studies have also proved the capacity of heptamolybdate salts to act as active catalyst in several reactions as the epoxidation of styrenes with H_2O_2 ,¹⁴ oxidation of

sulfides to sulfones,¹⁵ or hydrolysis of phosphoesters.¹⁶ It should be also highlighted the anticancer activity exhibited by the isopropyl ammonium salts and derived photolytes. In this sense, Yamase and co-workers described the antitumoral activity of this salt and its mechanism of action¹⁷ and, subsequent studies have observed a significant activity in the suppression of tumors from different types of cancer and cell lines.¹⁸ Besides isolated $\{\text{Mo}_7\text{O}_{24}\}$ salts, the coordination of transition metals and/or rare earth elements to the O atoms of their surface has led to extended purely inorganic structures,¹⁹ with interesting applications in materials science, such as the luminescent properties exhibited by some lanthanide derivatives.²⁰

Among the versatile catalogue of hybrid structures based on transition metal complexes and polyoxomolybdates,²¹ examples containing paramolybdate anions are quite scarce in the CSD database.²² The vast majority of this type of systems are based on molecular compounds in which the transition metal complex acts as counterion. This is the case of the salts, namely $[\text{Co}(\text{en})_3]_2[\text{Mo}_7\text{O}_{24}] \cdot 8\text{H}_2\text{O}$,²³ $(\text{H}_3\text{O})[\text{Co}(\text{en})_3]_2[\text{Mo}_7\text{O}_{24}]\text{Cl} \cdot 9\text{H}_2\text{O}$ ²⁴ and $[\text{Co}^{\text{III}}(\text{C}_2\text{O}_4)(\text{NH}_3)_4]_3[(\text{NH}_3)_4\text{Co}^{\text{III}}(\mu\text{-C}_2\text{O}_4)\text{Co}^{\text{II}}(\text{H}_2\text{O})_4][\text{Mo}_7\text{O}_{24}] \cdot 9\text{H}_2\text{O}$.²⁵ Other examples include systems formed by inorganic chains of paramolybdate anions linked by Na^+ or NH_4^+ cations, further connected through intermolecular interactions established between metalorganic units and POM anions (Figure 2.2). This usually leads to supramolecular networks as exemplified by $[\text{Co}(\text{en})_3]_2[\text{NaMo}_7\text{O}_{24}]\text{Cl} \cdot 9\text{H}_2\text{O}$,²⁵ $\text{Na}_2[\text{M}(\text{Bis-tris})\text{-(H}_2\text{O)}]_2[\text{Mo}_7\text{O}_{24}] \cdot 10\text{H}_2\text{O}$ [$\text{M} = \text{Cu; Ni; Co; Zn; Bis-tris} = 2,2\text{-Bis}(\text{hydroxymethyl})\text{-}2,2',2''\text{-nitrilotriethanol}$], and $(\text{NH}_4)_2[\text{M}(\text{Bis-tris})\text{(H}_2\text{O)}]_2[\text{Mo}_7\text{O}_{24}] \cdot 6\text{H}_2\text{O}$ ($\text{M} = \text{Zn; Cu}$) salts.²⁶

To our knowledge, there is only one compound reported in literature with a transition metal complex covalently linked to the surface of a paramolybdate cluster, namely $[\text{3-ampH}]_4\{[\text{M}(\text{3-ampy})(\text{H}_2\text{O})_4]\text{Mo}_7\text{O}_{24}\} \cdot 4\text{H}_2\text{O}$ ($\text{M} = \text{Co, Zn; ampy} = \text{aminopyridine}$). In this case, each metalorganic complex is just bonded to one cluster, whereas hybrid $\{[\text{M}(\text{3-ampy})(\text{H}_2\text{O})_4]\text{Mo}_7\text{O}_{24}\}$ units are linked through H-bonding interactions established between the coordination water molecules from the complex and the surface O atoms from heptamolybdate anions. This supramolecular arrangement results in a porous three-dimensional supramolecular network (Figure 2.2).²⁷

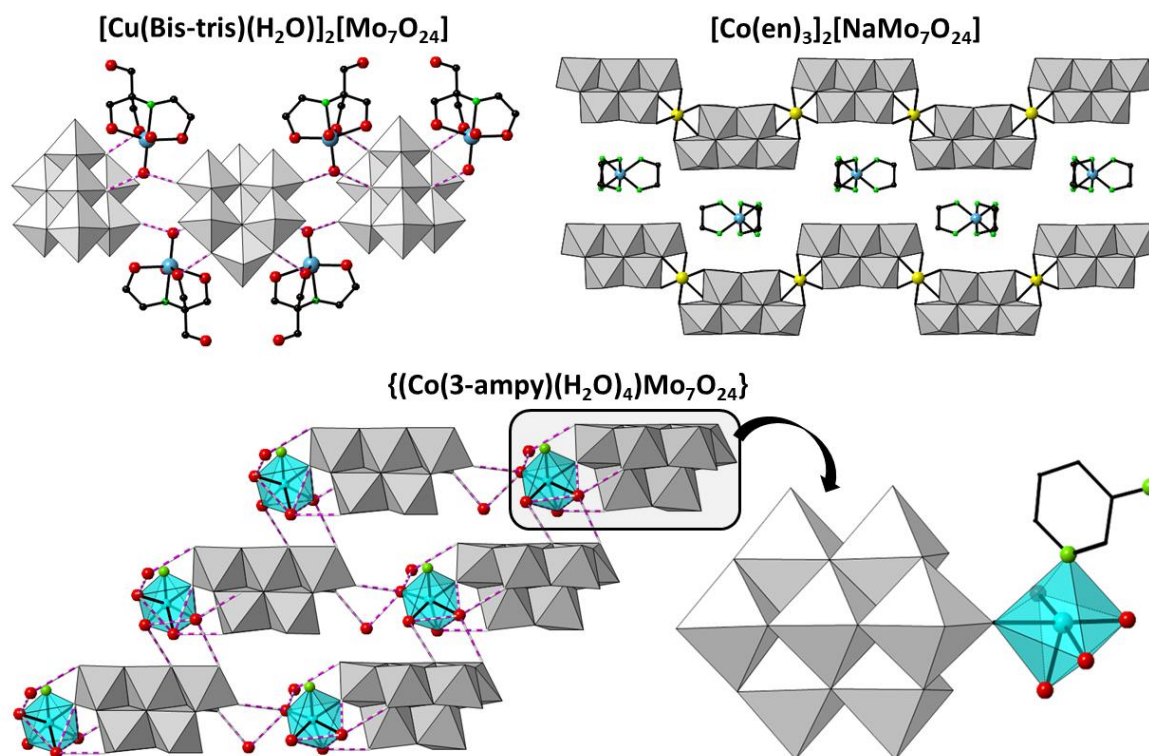


Figure 2.2. Crystal structures of some $\{\text{Mo}_7\text{O}_{24}\}$ -metalorganic hybrids found in the literature. Organic ligands: Bis-tris = 2,2-Bis(hydroxymethyl)-2,2',2''-nitrioltriethanol; ampy = aminopyridine. Color code: MoO_6 , grey octahedra; transition metal coordination polyhedra, blue; Na, yellow; C, black; N, green; O, red. The $\text{O}-\text{H}\cdots\text{O}$ hydrogen bonds are depicted as dashed purple lines.

Encouraged by the interesting thermostructural behavior exhibited by the porous frameworks constructed by isopolyoxovanadates and -tungstates with the $\{\text{Cu}(\text{cyclam})\}^{2+}$ complex, we decided to extend these studies to molybdates. Regarding vanadates, $[\text{Cu}(\text{cyclam})][\{\text{Cu}(\text{cyclam})\}_2(\text{V}_{10}\text{O}_{28})]\cdot 10\text{H}_2\text{O}$ supramolecular material²⁸ shows the ability to undergo two single-crystal-to-single-crystal transformations after the gradual loss of hydration water molecules under thermal stimulus in which the anhydrous phase turned out to be the first decavanadate-based microporous hybrid able to adsorb both N_2 and CO_2 gases. In a similar way, the covalent $[\{\text{Cu}(\text{cyclam})\}_3(\text{W}_7\text{O}_{24})]\cdot 15.5\text{H}_2\text{O}$ network²⁹ also undergoes thermally-triggered SCSC transformations to lead to a microporous anhydrous phase able to adsorb selectively CO_2 over N_2 .

On the basis of the above, we investigated the reactivity in aqueous media between a commercial heptamolybdate salt towards the $\{\text{Cu}(\text{cyclam})\}^{2+}$ metalorganic complex at different pH conditions. In this present chapter, a total six different hybrid compounds are obtained from the aqueous reactions involving the $\{\text{Mo}_7\text{O}_{24}\}/\{\text{Cu}(\text{cyclam})\}^{2+}$ system at different pH values. These are $[\text{Cu}(\text{cyclam})][\text{MoO}_4]\cdot 4\text{H}_2\text{O}$ (**MoCu**); $[\{\text{Cu}(\text{cyclam})\}_3(\text{Mo}_7\text{O}_{24})]\cdot 15.5\text{H}_2\text{O}$ (**1-Mo7**); $(\text{NH}_4)[\{\text{Cu}(\text{cyclam})\}_{2.5}(\text{Mo}_7\text{O}_{24})]\cdot 5.5\text{H}_2\text{O}$ (**1B-Mo7**); $[\{\text{Cu}(\text{cyclam})\}_3(\kappa\text{-Mo}_8\text{O}_{27})]\cdot 14\text{H}_2\text{O}$ (**1-Mo8**); $[\text{Cu}(\text{cyclam})]_2[\gamma\text{-Mo}_8\text{O}_{26}]\cdot 1.5\text{H}_2\text{O}$,³⁰ and; $[\text{C}_{10}\text{N}_4\text{H}_{28}][\text{CuCl}_4]\text{Cl}_2$.³¹ Hybrid compounds were chemically and structurally characterized by

elemental analyses, infrared spectroscopy (FTIR) and thermogravimetric analyses (TGA), and the structure determined by single-crystal X-ray diffraction (scXRD) measurements. Their thermostructural behavior and the ability to undergo SCSC transformation have also been studied by variable temperature analyses. Due to the interesting thermostructural behavior and sorption properties of **1-Mo8**, its discussion deserves a separate chapter (see chapter 3). Compound **MoCu** was also isolated as crystalline product in the course of these systematic studies, but its full characterization together with those of the related analogues using different combinations of group V and VI and first row transition metals are given in the Appendix 1.

2.2. EXPERIMENTAL SECTION

2.2.1. Synthesis

All the starting materials were purchased on commercial sources without further purification.

$[\{Cu(cyclam)\}_3(Mo_7O_{24})] \cdot 15.5H_2O$ (**1-Mo7**). To a hot solution of $Cu(OAc)_2$ (54 mg, 0.3 mmol) and cyclam ligand (60 mg, 0.3 mmol) in water (15 mL), the same volume of an aqueous solution of $(NH_4)_6(Mo_7O_{24}) \cdot 4H_2O$ (0.1 mmol, 124 mg) was added dropwise. The pH of the resulting solution was adjusted to 8 with 1M NaOH, and then, the mixture was kept at 90°C for 90 min. After cooling down to room temperature, the solution was filtered and left evaporate in an open container. Purple crystals of **1-Mo7** are obtained after 2 weeks. Yield: 29 mg, 14% based on Mo. Elem. Anal. Calcd. (%) for $C_{30}H_{103}Cu_3Mo_7N_{12}O_{39.5}$: C, 16.95%; H, 4.89%; N, 7.90%. Found: C, 17.08%; 4.85%; 7.93%. IR: ν (cm^{-1}) 3228 (vs), 3163 (vs), 2936 (s), 2864 (s), 1474 (w), 1454 (w), 1441 (w), 1429 (w), 1385 (w), 1358 (w), 1312 (w), 1292 (w), 1254 (w), 1235 (w), 1105 (m), 1074 (m), 1063 (m), 1017 (m), 1009 (m), 963 (s) 883 (vs), 843 (s), 812 (w), 652 (m), 577 (m), 486 (w), 434 (m).

$(NH_4)[\{Cu(cyclam)\}_{2.5}(Mo_7O_{24})] \cdot 5.5H_2O$ (**1B-Mo7**). If the pH of the mixture is adjusted to 6.5 purple single crystals of **1B-Mo7** appear together with those of **1-Mo7** after 3 weeks.

2.2.2. Single-crystal X-ray crystallography

Crystallographic data for **1-Mo7** and **1B-Mo7** isopolyoxomolybdate hybrids are summarized in Table 2.1.

Table 2.1. Crystallographic data for compounds **1-Mo7** and **2-Mo7**.

	1-Mo7	1B-Mo7
empirical formula	C ₃₀ H ₁₀₃ Cu ₃ Mo ₇ N ₁₂ O _{39.5}	C ₂₅ H ₇₉ Cu _{2.5} Mo ₇ N ₁₁ O _{29.5}
fw (g mol⁻¹)	2126.44	1836.42
crystal system	Triclinic	Triclinic
space group (number)	<i>P</i> -1 (2)	<i>P</i> -1 (2)
<i>a</i> (Å)	11.6000(3)	14.3356(10)
<i>b</i> (Å)	15.7298(5)	15.4231(9)
<i>c</i> (Å)	20.9536(6)	16.8501(11)
α (°)	83.508(2)	100.190(5)
β (°)	74.598(2)	103.392(6)
γ (°)	74.353(2)	115.826(6)
<i>V</i> (Å³)	3545.87(18)	3093.7(4)
<i>Z</i>	2	2
<i>T</i> (K)	100.03(11)	150.00(10)
ρ_{calcd} (g cm⁻³)	1.992	1.971
μ (mm⁻¹)	2.170	2.292
reflins collected	25001	21141
unique reflins (<i>R</i>_{int})	13996 (0.017)	11874 (0.063)
observed reflins [<i>I</i> > 2σ(<i>I</i>)]	12816	7691
Parameters (restraints)	907 (0)	728 (72)
<i>R</i>(<i>F</i>)^a [<i>I</i> > 2σ(<i>I</i>)]	0.028	0.075
<i>wR</i>(<i>F</i>²)^b [all data]	0.065	0.241
GoF	1.025	1.032

$$^a R(F) = \frac{\sum ||F_o - F_c||}{\sum |F_o|};$$

$$^b wR(F^2) = \frac{\sum [w(F_o^2 - F_c^2)^2]}{\sum [w(F_o^2)^2]}^{1/2}$$

Thermal vibrations of atoms were treated anisotropically for all the non-hydrogen atoms, except for the hydration water molecules in **1B-Mo7**. Hydrogen atoms of the organic cyclam ligands and those belonging to hydration water molecules in **1-Mo7**, were placed in calculated positions and refined using standard SHEXL parameters. Some of the anisotropic thermal ellipsoids from the cyclam ligands in **1B-Mo7** were normalized using ISOR-type restrains from SHELXL. Compounds **1-Mo7** and **1B-Mo7** display a significant disorder in their lattice water molecules. 18 and 8 suitable positions for hydrations water molecules were located in the Fourier maps of **1-Mo7** and **1B-Mo7**, respectively and their occupancy was initially refined without restriction. These were rounded to the first decimal figure in the last refinement cycle to result in a total number of 15.5 and 5.5 water molecules of hydration per heptamolybdate fragment, respectively.

2.3. RESULTS AND DISCUSSION

2.3.1. Synthetic considerations

Encouraged by the low number of hybrid architectures based on heptamolybdate anions, and in the course of our systematic studies on the assembly of isopolyoxovanadates and tungstates with $\{\text{Cu}(\text{cyclam})\}^{2+}$,²⁹⁻³² for which strong pH dependences of the resulting hybrid frameworks was found, we decided to evaluate this effect on the aqueous synthetic system formed by a combination of commercial ammonium heptamolybdate and the in-situ prepared $\{\text{Cu}(\text{cyclam})\}^{2+}$ complex in a stoichiometric 1:3 ratio. It is well known that the $[\text{Mo}_7\text{O}_{24}]^{6-}$ anion is predominant in slightly acidic aqueous solutions of molybdates,³³ however, the presence of additional chemical species in the solution might change this equilibrium.

Acidic conditions yielded a pink precipitate that did not dissolve even if the reaction was heated to 100 °C for 1h. The amount of this precipitate increases as the pH value decreases from 6 to 2. This solid was later identified on the basis of FTIR spectroscopy and PXRD analyses (Figure 2.3) as the robust framework $[\text{Cu}(\text{cyclam})]_2[\gamma\text{-Mo}_8\text{O}_{26}]\cdot 1.5\text{H}_2\text{O}$ previously reported in our research group.³⁰ This compound is constituted by $\{\gamma\text{-Mo}_8\text{O}_{26}\}_n$ chains which are linked to each other through the coordination spheres of $\{\text{Cu}(\text{cyclam})\}^{2+}$ complexes leading to a three-dimensional open network. This structural assembly generates voids that can be described as a succession of cavities communicated through narrow bottlenecks. The robust open framework remained virtually unaltered upon thermal evacuation of guest solvent molecules at 130 °C, resulting in an anhydrous phase with potentially accessible voids as demonstrated by scXRD measurements (Figure 2.4).

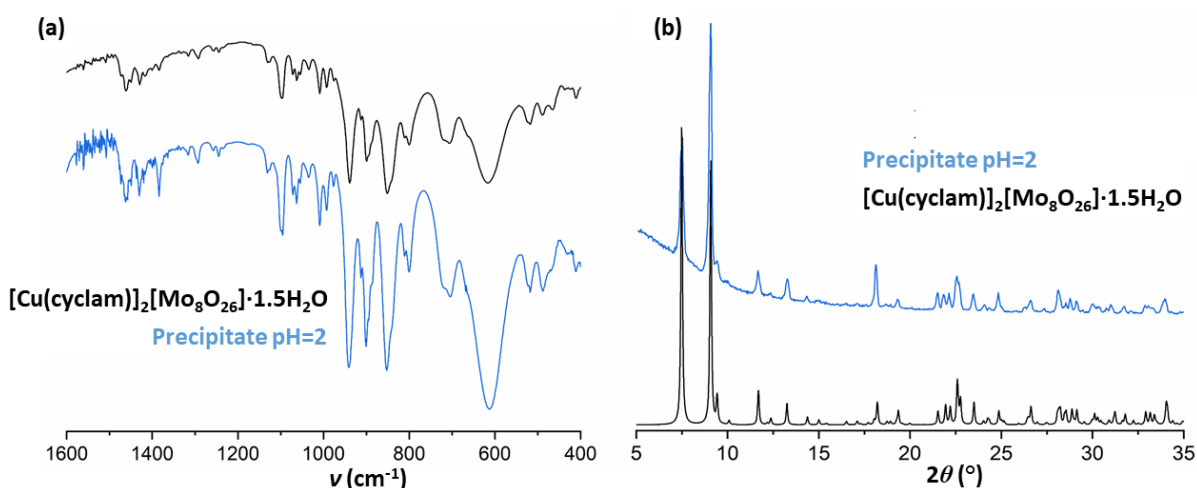


Figure 2.3. Comparison of the (a) FTIR spectra of the polycrystalline powder obtained at pH=2 and that of $[\text{Cu}(\text{cyclam})]_2[\gamma\text{-Mo}_8\text{O}_{26}]\cdot 1.5\text{H}_2\text{O}$ prepared *ex profeso* for comparative purposes; (b) PXRD patterns of this precipitate and that calculated from scXRD data for $[\text{Cu}(\text{cyclam})]_2[\gamma\text{-Mo}_8\text{O}_{26}]\cdot 1.5\text{H}_2\text{O}$.

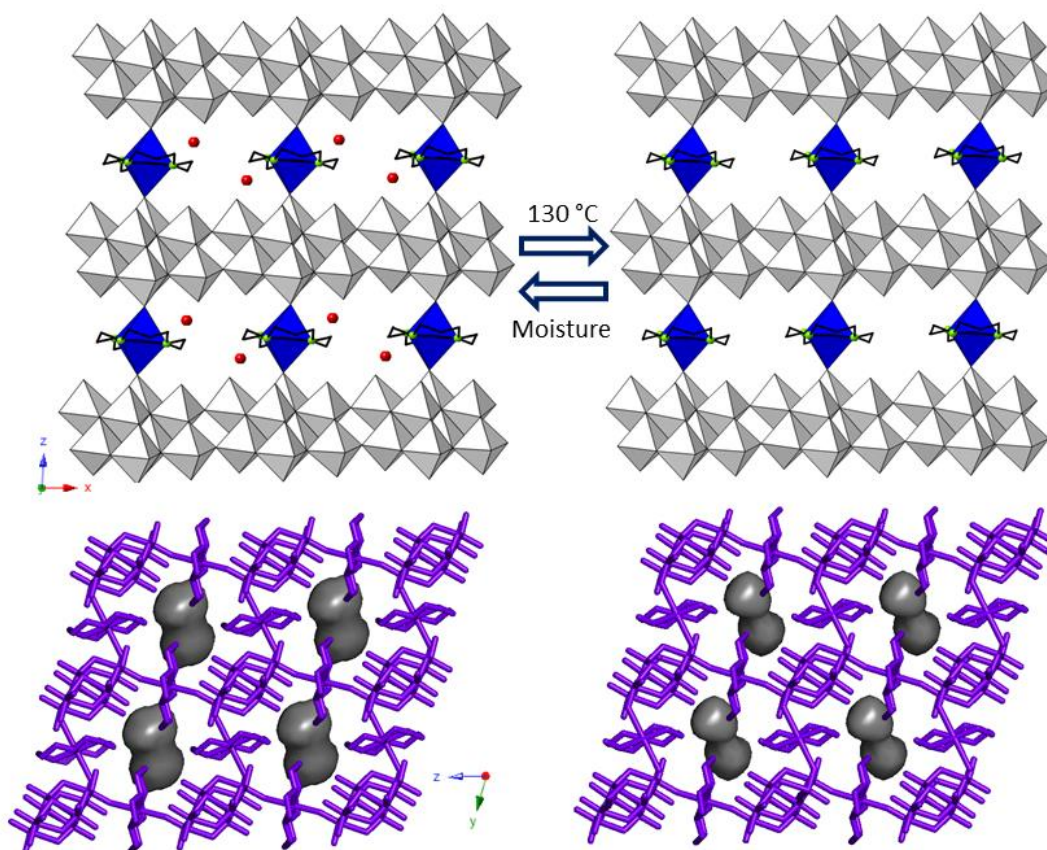


Figure 2.4. Comparison between the crystal packings view along the crystallographic y axis and solvent accessible volumes viewed along the a axis for $\{[\text{Cu}(\text{cyclam})]_2[\gamma\text{-Mo}_8\text{O}_{26}]\cdot 1.5 \text{H}_2\text{O}\}$ and its anhydrous $\{[\text{Cu}(\text{cyclam})]_2[\gamma\text{-Mo}_8\text{O}_{26}]\}$ form. Hydrogen atoms are omitted for clarity.

When the reaction medium was adjusted to values below pH 2 with aqueous HCl, green crystals were obtained from the evaporation of the final solution after filtering out the initial pink precipitate. FTIR analyses suggested the absence of any POM anion in this compound because no band of strong intensity can be observed in the inorganic region of the spectrum below 1000 cm^{-1} . In contrast, the organic region above 1000 cm^{-1} is dominated by signals of medium-weak intensity associated with C–N, C–C, C–H bonds that confirm the presence of the cyclam ligand. Single-crystal³⁴ and powder XRD analyzes coincide well with those already reported for the $[\text{C}_{10}\text{N}_4\text{H}_{28}][\text{CuCl}_4]\text{Cl}_2$ complex (Figure 2.5), in which one tetrahedral $[\text{CuCl}_4]^{2-}$ complex and two Cl^- anions act as counterions of a tetra-protonated cyclam ligand.³¹

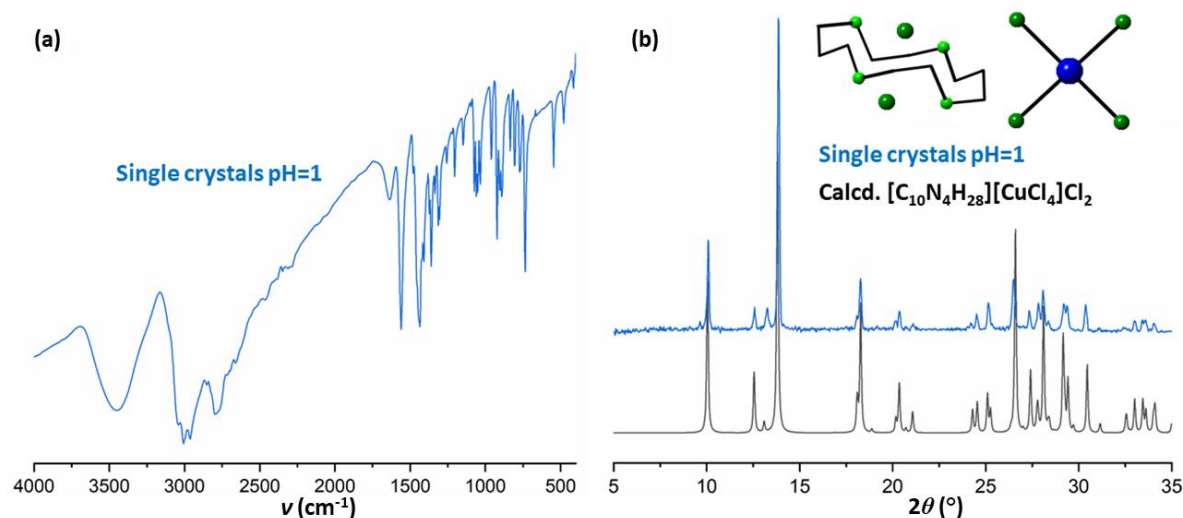


Figure 2.5. (a) FTIR spectrum of the crystals obtained at pH = 1 and, (b) PXRD pattern of these crystals compared with that calculated from scXRD data for [C₁₀N₄H₂₈][CuCl₄]Cl₂, together with its ball & stick representation.

On the contrary, when the pH was basified above 6 the initial pink powder was slowly dissolved to result in a clear solution. At very alkaline conditions (above pH 9), [MoO₄]²⁻ oxoanions are the main species in solution and thus, crystals of [Cu(cyclam)][MoO₄]²⁻·3H₂O (**MoCu**) (see A1.4 in Appendix 1) are isolated. Conversely, slow evaporation of the solutions from reactions carried out at neutral to moderately basic conditions (pH values in the 6–9 range) initially afforded a purple polycrystalline powder that was later identified as [Cu(cyclam)]₃(κ-Mo₈O₂₇)·14H₂O (**1-Mo8**) in a very low yield (< 1%). The rich thermostructural behavior of **1-Mo8** together with its interesting sorption properties are described in-depth in **Chapter 3**. After the removal of this solid by filtration, the solution was transferred to a small container and kept at room temperature. Purple single crystals of **1-Mo7** appeared after a total of 2 weeks of evaporation of the solution at pH = 8.0. FTIR studies on **1-Mo7** (Figure 2.6) clearly showed the hybrid nature of the compound because i) the organic region above 1000 cm⁻¹ display signals associated with the cyclam ligand, whereas those of the inorganic region fit well with those found in the spectrum of the ammonium heptamolybdate precursor, which indicates the presence of a [Mo₇O₂₄]⁶⁻ heptamolybdate cluster (Mo₇). Specifically, the characteristic peaks for Mo₇ anions at 963, 883 and 843 cm⁻¹ have been assigned to $\nu_{\text{as}}(\text{Mo}-\text{O}_t)$, $\nu(\text{Mo}-\text{O}_b)$ and $\nu_s(\text{Mo}-\text{O}_b-\text{Mo})$ vibrational bands, respectively (O_t: *terminal oxygen* atoms; O_b: *bridging oxygen* atoms). Bands at 577, and 486 cm⁻¹ have been attributed to $\delta(\text{Mo}-\text{O}_b-\text{Mo})$ vibrational modes.³⁵

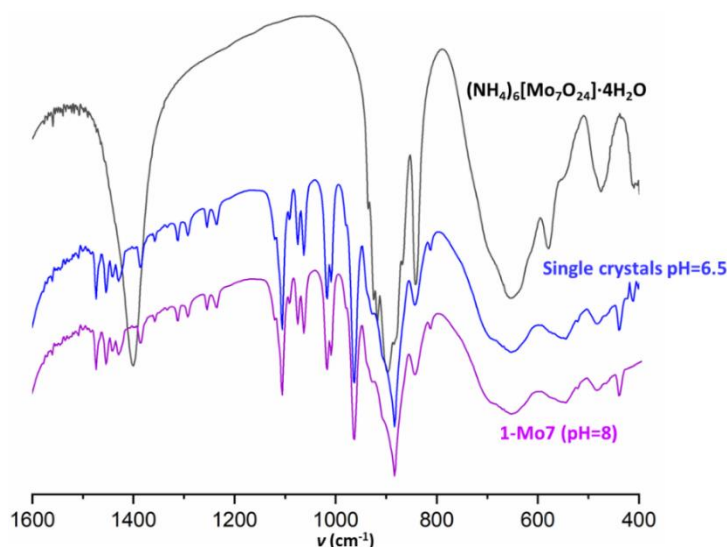


Figure 2.6. Expanded region of the FTIR spectrum of $(\text{NH}_4)_6[\text{Mo}_7\text{O}_{24}]\cdot 4\text{H}_2\text{O}$ precursor compared with those registered for single crystals obtained for reactions at pH=6.5 and pH=8 (**1-Mo7**).

Crystals isolated from reactions at lower pH (6 to 7.5) yielded purple crystals, which looked visually identical to those of **1-Mo7** and displayed a similar FTIR spectrum (Figure 2.5). Nevertheless, comparison of the PXRD pattern recorded for these crystals with that of **1-Mo7** exhibited three additional maxima at $2\theta = 6.8, 7.7$ and 9.6° that might be originating from a new crystalline phase (Figure 2.7). This secondary compound was later identified as **1B-Mo7** based on scXRD studies. Unfortunately, manual separation of these two phases under optical microscope was impossible because they showed the same color and shape. Alternative separation methods were tested (separation by density while suspended in a liquid phase, recrystallization in different solvents...) but with no success. Therefore, only compound **1-Mo7** was isolated as a pure crystalline phase (at pH =8) and this allowed its further characterization.

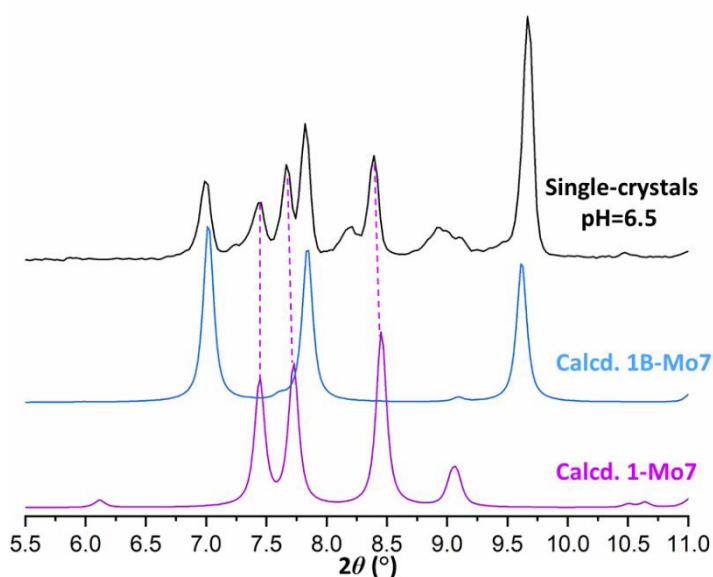


Figure 2.7. PXRD pattern of single-crystals obtained at pH = 6.5 in comparison to those calculated from scXRD data for **1-Mo7** and **1B-Mo7**.

It should be mentioned that **1-Mo7** can alternatively be prepared starting from the $[\text{Cu}(\text{cyclam})]_2[\text{Mo}_8\text{O}_{26}] \cdot 1.5\text{H}_2\text{O}$ precipitate, which dissolves at basic pH (above 11) at 90 °C. The pH of the resulting purple solution is re-adjusted to pH = 8 with aqueous 1M HCl and the mixture is left to evaporate. Crystals of **1-Mo7** can be obtained in ca. 3 weeks, but in a very low yield (< 3%). In conclusion, all the compounds synthesized from the $\{\text{Mo}_7\text{O}_{24}\}/\{\text{Cu}(\text{cyclam})\}$ system are summarized in Figure 2.8.

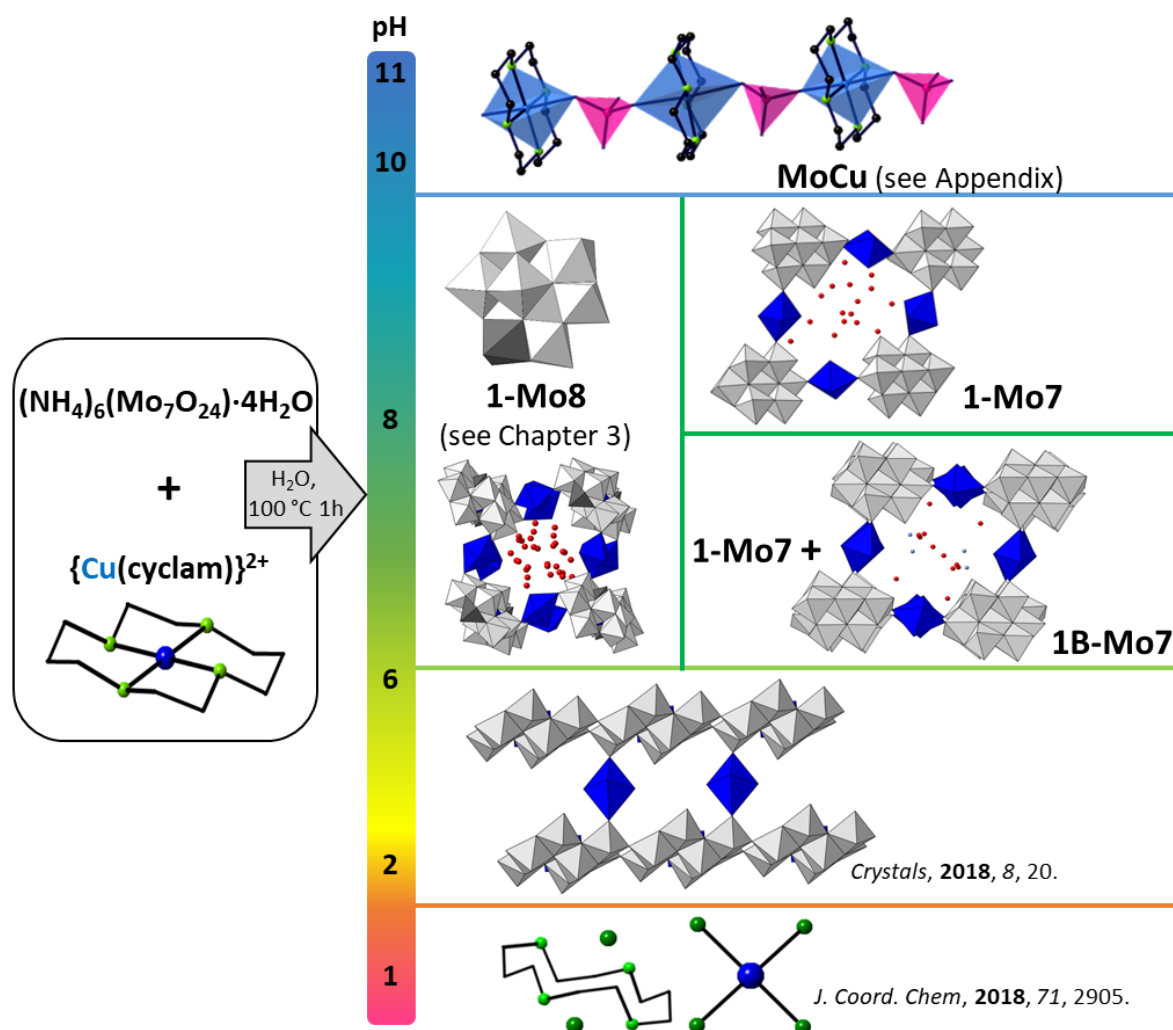


Figure 2.8. Influence of the pH in the $\{\text{Mo}_7\text{O}_{24}\}/\{\text{Cu}(\text{cyclam})\}$ synthetic system. Color code: Cl, dark green; Cu, dark blue; $\{\text{MoO}_4\}$ tetrahedra, pink; N from cyclam ligand, light green; N from NH_4^+ cations, light blue spheres.

2.3.2. Thermostructural behavior of 1-Mo7

Thermal stability of **1-Mo7** was firstly investigated by thermogravimetric and differential thermal (TGA/DTA) analysis. The TGA curve in Figure 2.9a shows a thermal decomposition that proceeds *via* two mass loss steps. The first stage occurs from room temperature to ca. 120 °C, and it is associated to the endothermic loss of the 15.5 H_2O molecules of hydration (m% calcd. 13.1%; found 12.8%). The dehydration is followed by a

thermal stability range that extends up to ca. 220 °C. Above this temperature, the anhydrous phase undergoes a decomposition process through two overlapping mass losses associated with the combustion of the organic ligands and breakdown of the POM framework. The overall mass loss for this second stage is in good agreement with that calculated for three cyclam ligands per heptamolybdate anion (m% calcd. 28.2%; found 27.9%). The final residue is obtained at temperatures above 510 °C (m% calcd. 58.6%; found 59.3%).

Taking into account the thermal stability range found in the TGA curve of **1-Mo7**, and encouraged by the interesting thermostructural behavior showed by related $\{\text{Cu}(\text{cyclam})\}^{2+}$ / POM systems,³⁶ we studied whether **1-Mo7** was able to exhibit a similar behavior. With this aim, variable-temperature PXRD patterns were collected from room temperature to 610 °C every 20 °C. The room temperature pattern of **1-Mo7** (Figure 2.9) displays three characteristic high intensity maxima at $2\theta = 7.3, 7.7$ and 8.3° , together with two additional signals with lower intensity at 6.0 and 9.0° . This pattern resembles that reported for the $\{\{\text{Cu}(\text{cyclam})\}_3(\text{W}_7\text{O}_{24})\}\cdot 15.5\text{H}_2\text{O}$ hybrid previously reported in our group,²⁹ which indicates that the structures of both compounds could be strongly related. Figure 2.9d shows that **1-Mo7** transforms into a new partially hydrated phase (**2-Mo7**) at 50 °C, as demonstrated by the notable modifications in the positions of the most intense diffraction maxima at low 2θ region. Upon heating, the maxima at 7.3 and 7.7° get 0.1° closer to each other, that located at 8.3° is shifted to 8.8° , and a new maximum is clearly formed at 6.9° . The diffraction pattern of **2-Mo7** was compared to that calculated from scXRD data for the partially hydrated compound $\{\{\text{Cu}(\text{cyclam})\}_3(\text{W}_7\text{O}_{24})\}\cdot 12\text{H}_2\text{O}$ obtained from the partial dehydration of the parent hydrated phase at 50 °C. Even if the maxima at $2\theta = 6.8, 7.4$ and 8.8° coincide well in both patterns, that of **2-Mo7** exhibits an extra maximum at $2\theta = 7.6^\circ$. This implies that the two partially hydrated phases may not be isostructural.

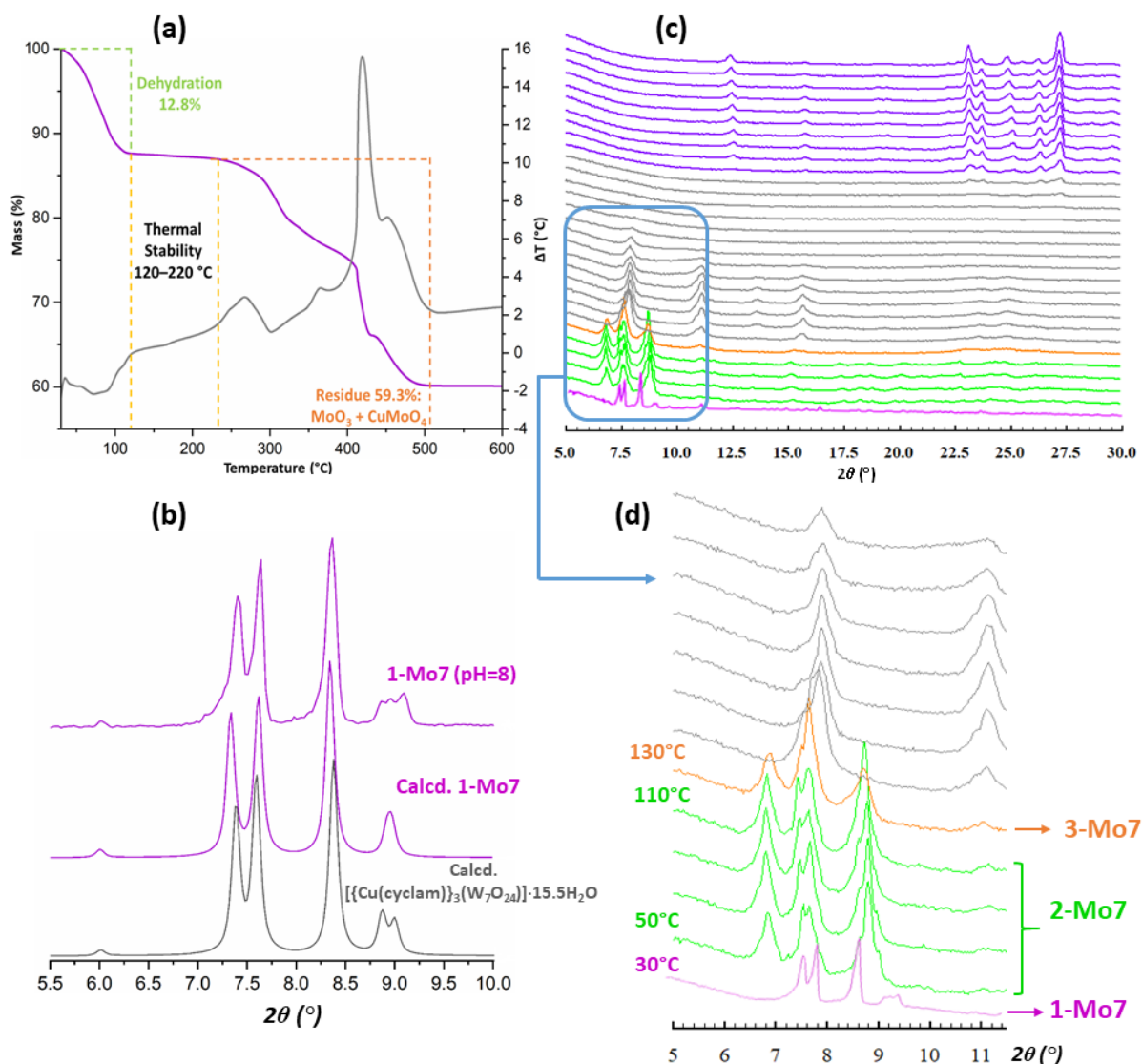


Figure 2.9. Thermostructural studies for **1-Mo7** hybrid; (a) TGA/DTA curve, (b) comparison between calculated PXRD pattern for $[\{\text{Cu}(\text{cyclam})\}_3(\text{W}_7\text{O}_{24})] \cdot 15.5\text{H}_2\text{O}$,²⁹ **1-CuW7** and the experimental pattern of **1-Mo7** at pH = 8. (c) Variable-temperature PXRD studies from 30 to 610 °C and (d) detail of the most characteristic maxima in the $2\theta = 5$ to 11° range.

Compound **2-Mo7** is stable up to 110 °C. Above this temperature, the disappearance of the maximum at $2\theta = 7.4^\circ$ indicates that it transforms into a second thermal derivative (**3-Mo7**). The pattern of **3-Mo7** is similar to that calculated from scXRD data for the anhydrous phase prepared from the aforementioned tungsten-analogue at 110 °C (Figure 2.10b). However, in contrast to that observed for anhydrous phase of the tungsten analogue which proves to be stable up to 230 °C, **3-Mo7** decomposes and gradually loses its crystallinity at temperatures higher than 130 °C, as observed by the progressive loss of intensity and widening of the diffraction maxima upon heating until complete amorphization at 290 °C. Diffraction maxima belonging to the final residue of the thermal decomposition start to appear above *ca.* 430 °C and they allow its identification as a mixture of orthorhombic *Pbnm* MoO_3 (PDF: 01-076-1003)³⁷ and triclinic *P*-1 CuMoO_4 (PDF:

01-073-0488)³⁸ phases in an approximate 4:3 ratio (Figure 2.11). This is in good agreement with the observed mass percentage values from the thermogravimetric analyses (calcd. 58.6%; found 59.3%).

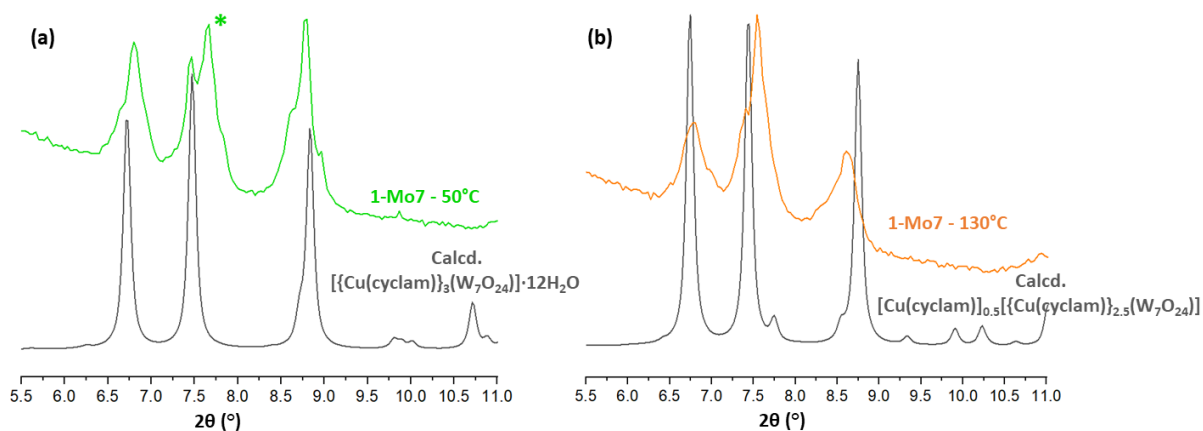


Figure 2.10. Comparison between the; (a) calculated pattern of $[\text{Cu}(\text{cyclam})]_3(\text{W}_7\text{O}_{24}) \cdot 12\text{H}_2\text{O}$ and the **2-Mo7** compound obtained at 50 °C, and; (b) calculated pattern of $[\text{Cu}(\text{cyclam})]_{0.5}[\text{Cu}(\text{cyclam})]_{2.5}(\text{W}_7\text{O}_{24})$ and the **3-Mo7** compound obtained at 130 °C. Extra maximum at $2\theta = 7.6^\circ$ for **2-Mo7** is highlighted (*).

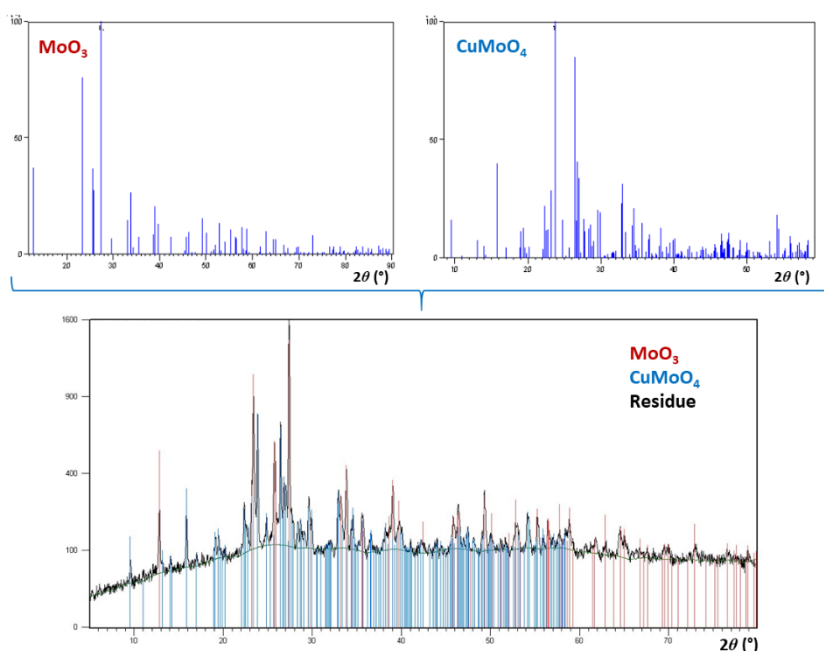


Figure 2.11. Identification by PXR D analyses of the final residue from the thermal decomposition of **1-Mo7** into MoO_3 and CuMoO_4 .

2.3.3. Crystal structure of 1-Mo7 and SCSC transformations

Single-crystal X-ray diffraction analyses showed that **1-Mo7** compound crystallizes in the triclinic $P-1$ space group. The asymmetric unit consists one $\{\text{Mo}_7\text{O}_{24}\}$ heptamolybdate fragment, five $\{\text{Cu}(\text{cyclam})\}^{2+}$ complexes divided in four centrosymmetric complexes (Cu1A, Cu1C, Cu1D and Cu1E) and one Cu1B located in a general position, and 15.5 hydration water molecules disordered in 18 positions. The heptamolybdate anion shows a typical A-

paramolybdate structure described by a six $\{\text{MoO}_6\}$ member ring in which each octahedra are linked by edge-sharing. The empty space displayed in the center of the ring comprises the seventh $\{\text{MoO}_6\}$ unit connected through edge-sharing (Figure 2.12).³⁹ This last central unit gives to the heptatungstate cluster its characteristic V-shape that differentiates this anion from other planar clusters with the same POM arrangement, such as Anderson-Evans anion. All the Mo atoms are bounded to two terminal oxygens except for the central Mo7 octahedron. In this way, the oxygens can be organized in four categories: O_t (terminal oxygen atoms); $\mu^2\text{-O}$ (oxygen atoms bridging two *addenda* metals); $\mu^3\text{-O}$ (oxygen atoms bridging two *addenda* metals), and; $\mu^4\text{-O}$ (oxygen atoms bridging two *addenda* metals). Mo–O bond lengths are comparable to those reported on literature, and fall in the 1.714–2.370 Å range.⁴⁰

Regarding $\{\text{Cu}(\text{cyclam})\}$ complexes, all the Cu^{II} centers display a CuN_4O_2 octahedral coordination geometry with the N atoms of the cyclam ligands in equatorial positions and terminal O atoms from different POM units occupying axial positions. In this way, these moieties act as bridging blocks between heptamolybdate anion, exhibiting a *trans-III* configuration in all the cases. As seen from the Cu–O bond lengths on Table 2.2, Jahn-Teller distortion is present for all the Cu^{II} centers of **1-Mo7**.

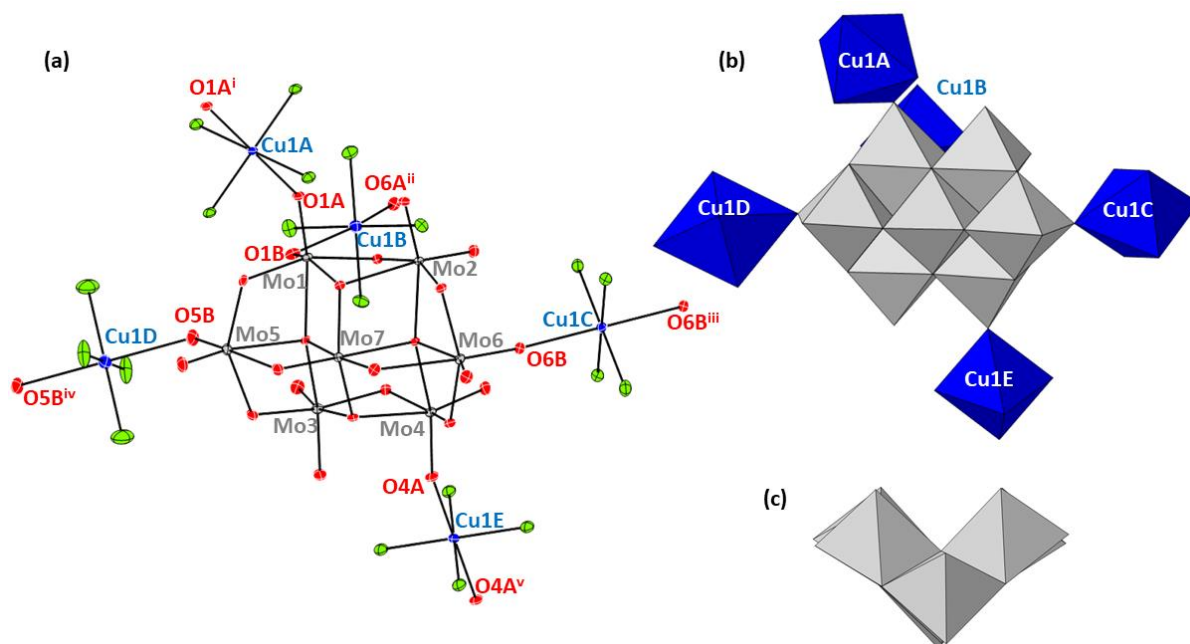


Figure 2.12. (a) ORTEP representation of **1-Mo7**, showing 50% probability ellipsoids, together with the atoms labelling scheme (carbon atoms, hydrogen atoms and water hydration molecules have been omitted for clarity). Color code: Mo, light grey; Cu, blue; O, red; N, green. Symmetry codes: i) $-x, 1-y, 2-z$; ii) $1+x, y, z$; iii) $-x, 1-y, 1-z$; iv) $-x, 2-y, 2-z$; v) $-x, 2-y, 1-z$; (b) polyhedral representation of the hybrid POM, and; (c) side view of the heptamolybdate cluster.

The heptamolybdate anion shows a well-known structure described by a six $\{\text{MoO}_6\}$ member ring linked to each other and to a seventh central octahedron through edge-

sharing (Figure 2.12).⁴¹ This last central unit confers the cluster with its characteristic bent, V-shape (C_{2v}) and differentiates the anion from other clusters with 7 edge-sharing $\{MO_6\}$ units, such as planar $\{M'M_6O_{24}\}$ Anderson-Evans anions (D_{3d}). All the Mo atoms are bounded to two terminal O atoms except for the central $\{MoO_6\}$ octahedron. In this way, O atoms can be organized in four categories: O_t (terminal oxygen atoms); μ^2-O (oxygen atoms bridging two *addenda* metals); μ^3-O (oxygen atoms bridging three *addenda* metals), and; μ^4-O (oxygen atoms bridging four *addenda* metals). Mo–O bond lengths are comparable to those reported on literature, and fall in the 1.714(2)–2.370(2) Å range.⁴²

Regarding $\{Cu(cyclam)\}^{2+}$ complexes, all the Cu^{II} centers display an axially elongated octahedral CuN_4O_2 coordination geometry with the N atoms of the cyclam ligands in equatorial positions and terminal O atoms from different POM units occupying axial positions. In this way, these moieties act as bridging units between heptamolybdate anion, and exhibit a *trans-III* configuration, in which the N–H bonds of the two pairs of propylene-bridged N atoms point to opposite directions. This configuration has been shown by DFT-calculations to be the most favorable for octahedral coordination geometries out of the five different geometrical isomers that the transition–metal complexes of the cyclam ligand can adopt depending on the ligand conformation.⁴³ As seen from the Cu–O bond lengths on Table 2.2, Jahn-Teller distortion is operative in all the Cu^{II} centers.

Table 2.2. Cu–N bond lengths and Cu–O distances present in the $\{Cu(cyclam)\}$ complexes of **1-Mo7**.

Cu1A		Cu1C	
Cu1A–O1A	2.503(2)	Cu1C–O6B	2.343(2)
Cu1A–O1A ⁱ	2.503(2)	Cu1C–O6B ⁱⁱⁱ	2.343(2)
Cu1A–N1A	2.026(2)	Cu1C–N1C	2.036(2)
Cu1A–N4A	2.004(2)	Cu1C–N4C	2.018(2)
Cu1A–N1A ⁱ	2.026(2)	Cu1C–N1C ⁱⁱⁱ	2.036(2)
Cu1A–N4A ⁱ	2.004(2)	Cu1C–N4C ⁱⁱⁱ	2.018(2)
Cu1B		Cu1D	
Cu1B–O1B	2.668(2)	Cu1D–O5B	2.487(2)
Cu1B–O6A ⁱⁱ	2.610(2)	Cu1D–O5B ^{iv}	2.487(2)
Cu1B–N1B	2.003(3)	Cu1D–N1D	2.001(3)
Cu1B–N4B	2.020(3)	Cu1D–N4D	2.026(3)
Cu1B–N8B	2.008(2)	Cu1D–N1D ^{iv}	2.001(3)
Cu1B–N11B	2.011(3)	Cu1D–N4C ^{iv}	2.026(3)
Cu1E			
	Cu1E–O4A		2.570(2)
	Cu1E–O4A ^v		2.570(2)
	Cu1E–N1E		2.014(3)
	Cu1E–N4E		2.002(2)
	Cu1E–N1E ^v		2.014(2)
	Cu1E–N4E ^v		2.002(2)

Symmetry codes: **1-Mo7**: i) -x, 1-y, 2-z; ii) 1+x, y, z; iii) -x, 1-y, 1-z; iv) -x, 2-y, 2-z; v) -x, 2-y, 1-z.

The crystals packing of **1-Mo7** consists in a 3D covalent open-framework constructed by $\{\text{Mo}_7\text{O}_{24}\}/\{\text{Cu}(\text{cyclam})\}$ hybrid layers on the yz plane, that are further connected through additional metalorganic moieties along the x -axis, generating voids in which the water molecules of hydration are hosted (Figure 2.13). Within the same layer, each heptamolybdate anion is linked to four neighboring clusters through four $\{\text{Cu}^{\text{II}}(\text{cyclam})\}^{2+}$ complexes (Cu1A, Cu1C, Cu1D and Cu1E). This arrangement generates water-filled rhombic-like voids with a cross section of $9.1 \times 10.1 \text{ \AA}^2$ (interatomic distances between opposite N atoms in the void; that is N1A...N4E and N1C...N1D). It should also be mentioned that the cleft of $\{\text{Mo}_7\text{O}_{24}\}$ anions from the same hybrid layer point alternatively at either above or below the mean plane of the layer (Figure 2.13b). These hybrid layers are further connected through additional $\{\text{Cu}(\text{cyclam})\}^{2+}$ metalorganic moieties (Cu1B) along the x -axis, in such a way that each polyanion shows a total number of 6 complexes coordinated to its surface. Beyond the iso-reticular tungsten-containing analogue mentioned above,²⁹ **1-Mo7** represents the first hybrid structure based on $\{\text{Mo}_7\text{O}_{24}\}$ anions reported to date that forms an extended covalent framework and only the second example of a hybrid with transition metal complexes coordinated to the surface of such POM besides the $[\text{3-ampH}]_4\{\text{M}(\text{3-ampy})(\text{H}_2\text{O})_4\}\text{Mo}_7\text{O}_{24}\cdot 4\text{H}_2\text{O}$ (3-ampy = aminopyridine)⁴⁴ The stacking of the hybrid grids is such that the rhombic voids result superimposed on each other generating channels where all the water molecules of hydration are hosted. These channels are interconnected along the $[100]$ direction to result in a two-dimensional system of cavities as depicted in the surface representation of the solvent accessible voids (Figure 2.14). The total solvent accessible volume accounts for 1051 \AA^3 , which corresponds to the 30% of the total cell volume of **1-Mo7**, as calculated by PLATON software.⁴⁵ Additional C–H...O and N–H...O interactions established between the cyclam ligand and the O atoms from the POM anions contribute to the overall stability of the crystal packing (Table 2.3).

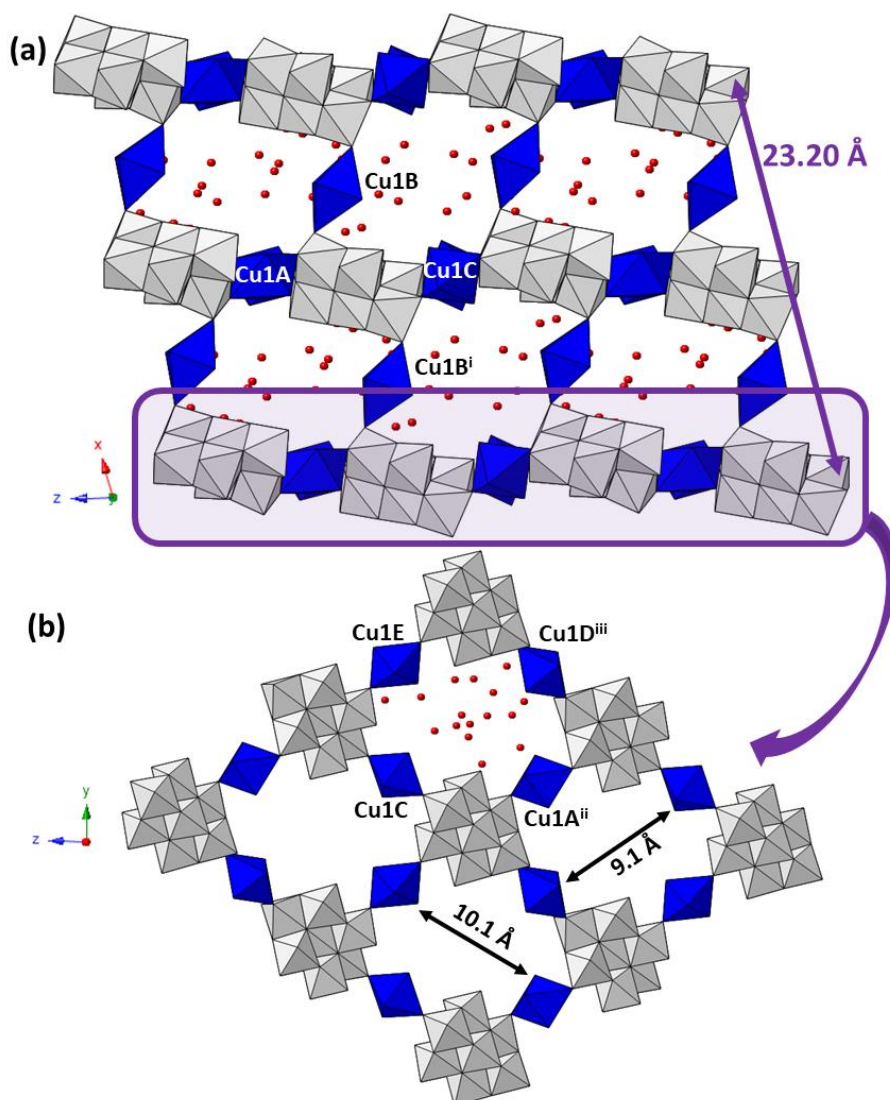


Figure 2.13. (a) View of the crystal packing of **1-Mo7** along the [010] direction showing Mo1...Mo1 distances and; (b) polyhedral representation of the hybrid layer in the yz plane, with approximate dimensions of the voids. Cyclam ligand and hydration water molecules of some channels have been omitted for clarity. Color code: Mo polyhedra, grey; Cu polyhedra, blue; O, red balls. Symmetry codes: i) $-1+x, y, z$; ii) $-x, 1-y, 1-z$; iii) $-x, 2-y, 1-z$.

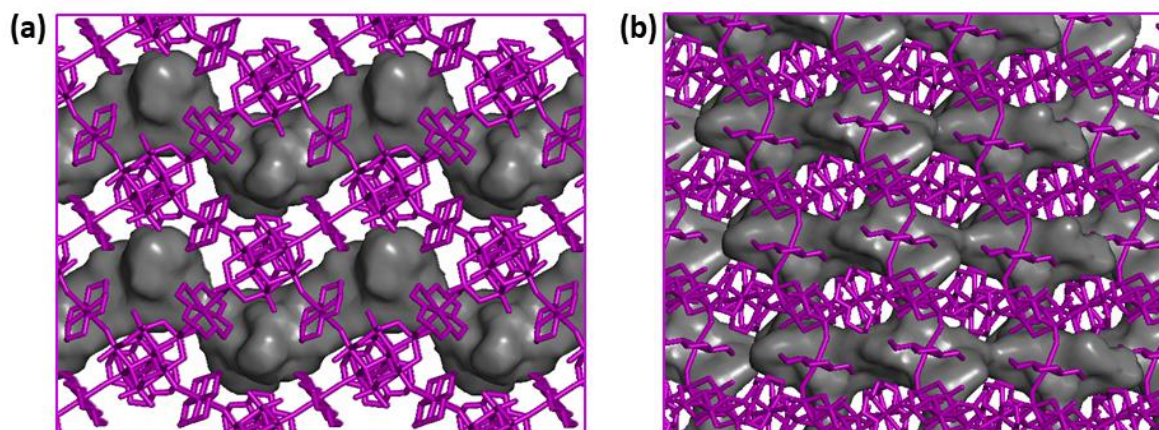


Figure 2.14. Surface representation of the total accessible volume in **1-Mo7** forming channels connected bidimensionally along the crystallographic (a) x axis and (b) y axis.

Table 2.3. N–H⋯O and C–H⋯O interactions in **1-Mo7**.

Donor–H⋯Acceptor	D⋯A (Å)	Donor–H⋯Acceptor	D⋯A (Å)
N1A–H1A⋯O2A	3.102(3)	C14B–H14A⋯O1B	2.992(4)
N4A–H4A⋯O15 ⁱ	2.770(3)	N1C–H1C⋯O4B ⁱⁱⁱ	3.115(3)
C3A–H3AB⋯O2A	3.096(4)	N4C–H4C⋯O2B	2.835(3)
N1B–H1B⋯O7B ⁱⁱ	2.729(3)	N1D–H1D⋯O5A ^{iv}	2.904(4)
N4B–H4B⋯O3B	3.161(3)	N4D–H4D⋯O14W	3.175(5)
N8B–H8B⋯O12	2.800(3)	C7D–H7DB⋯O5B	3.188(5)
N11B–H11B⋯O7W ⁱⁱ	2.923(4)	N1E–H1E⋯O11W ^v	3.070(4)
C6B–H6BB⋯O34	3.401(4)	N4E–H4E⋯O3A	2.816(3)
C12B–H12A⋯O1W	3.408(12)	C5E–H5EA⋯O4B ^v	3.294(4)

Symmetry codes: **1-Mo7**: i) -x, 1-y, 2-z; ii) 1+x, y, z; iii) -x, 1-y, 1-z; iv) -x, 2-y, 2-z; v) -x, 2-y, 1-z.

SCSC transformations

Encouraged by the results from variable-temperature PXRD analyses, we tested whether these structural transformation could be followed by scXRD. Thus, single crystals of **1-Mo7** were heated in an oven at 50 °C for 1h and immediately afterwards, covered with Paratone oil and mounted on the diffractometer. Unfortunately, the scXRD analyses only allowed us to determine the unit cell parameters of **2-Mo7** (Table 2.4), which revealed that its crystal structure could be strongly related with that of the tungstate analogue, $[\{\text{Cu}(\text{cyclam})\}_3(\text{W}_7\text{O}_{24})] \cdot 12\text{H}_2\text{O}$.²⁹ Although different crystal batches were tested, the quality of the PXRD diffraction data was not good enough to allow the structural solution. Similar studies were attempted on crystals of **1-Mo7** heated in an oven at 130 °C or kept under vacuum for 1h, but with no success. In the same way, crystals of the anhydrous **3-Mo7** also cracked in both cases.

Table 2.4. Crystallographic data for compounds **2-Mo7** and $[\{\text{Cu}(\text{cyclam})\}_3(\text{W}_7\text{O}_{24})] \cdot 12\text{H}_2\text{O}$.

	2-Mo7	$[\{\text{Cu}(\text{cyclam})\}_3(\text{W}_7\text{O}_{24})] \cdot 12\text{H}_2\text{O}$
crystal system	Triclinic	Triclinic
space group (number)	<i>P</i> -1 (2)	<i>P</i> -1 (2)
<i>a</i> (Å)	16.378(3)	16.0175(2)
<i>b</i> (Å)	19.741(3)	20.1960(3)
<i>c</i> (Å)	20.310(4)	20.5149(3)
α (°)	91.403(17)	89.9080(10)
β (°)	90.930(19)	96.2760(10)
γ (°)	97.467(16)	84.7810(10)
<i>V</i> (Å ³)	6508(2)	6568.79(16)

These studies together with variable-temperature PXRD experiments indicate that thermal derivatives could be analogous to those reported in the literature for the tungstate analogue; these are $[\{\text{Cu}(\text{cyclam})\}_3(\text{Mo}_7\text{O}_{24})] \cdot 12\text{H}_2\text{O}$ (**2-Mo7**) and $[\text{Cu}(\text{cyclam})]_{0.5}[\{\text{Cu}(\text{cyclam})\}_{2.5}(\text{Mo}_7\text{O}_{24})]$ (**3-Mo7**). In contrast, crystals of **1-Mo7** do not

retain their integrity upon heating and thus, these transitions cannot be followed by scXRD. Despite the difficulties for the structural characterization of thermally related phases **2-Mo7** and **3-Mo7**, the faster redox processes of Mo in comparison to W could make the anhydrous and potentially porous **3-Mo7** suitable for being used as active material in heterogeneous catalysis or in electrochemical energy storage systems.

2.3.4. Crystal structure of **1B-Mo7**

Although attempts to isolate a pure crystalline sample of **1B-Mo7** were not successful, its structure was elucidated by scXRD experiments. Compound **1B-Mo7** crystallizes in the triclinic *P*-1 space group and the asymmetric unit contains one heptamolybdate anion, 5 halves of centrosymmetric $\{\text{Cu}(\text{cyclam})\}^{2+}$ fragments accounting for a total number of 2.5 metalorganic complexes, 5.5 lattice hydration molecules disordered over 8 crystallographic sites and one NH_4^+ cation disordered over two positions. The ammonium counterion balances the charges between the $[\text{Mo}_7\text{O}_{24}]^{6-}$ inorganic anion and the 2.5 $\{\text{Cu}(\text{cyclam})\}^{2+}$ metalorganic moieties, which leads to a final formula of $(\text{NH}_4)[\{\text{Cu}(\text{cyclam})\}_{2.5}(\text{Mo}_7\text{O}_{24})] \cdot 5.5\text{H}_2\text{O}$ (Figure 2.15). As in **1-Mo7**, the $\{\text{Mo}_7\text{O}_{24}\}$ unit presents the well-known structure of the paramolybdate anion. Regarding the metalorganic fragments, all the cyclam ligands exhibit a *trans-III* configuration, and the Cu^{II} centers an axially elongated octahedral CuN_4O_2 geometry. This Jahn-Teller distortion is specially remarkable for the Cu1B-O1B bond length, which shows values close to that of semi-coordination (above 2.7 Å) (Table 2.5).

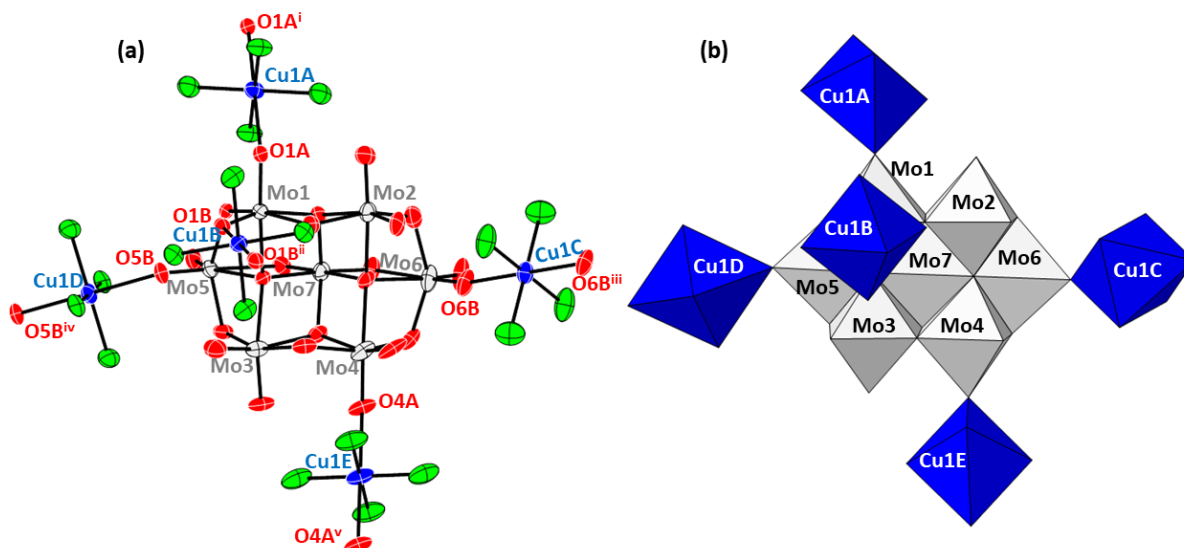


Figure 2.15. (a) ORTEP representation of **1B-Mo7**, showing 50% probability ellipsoids, together with the atoms labelling scheme, together with (b) polyhedral representation of the hybrid POM. Carbon atoms, hydrogen atoms and water hydration molecules have been omitted for clarity. Symmetry codes: i) $-x, -y, -z$; ii) $1-x, 1-y, 1-z$; iii) $-x, -y, -z$; iv) $1-x, 2-y, 1-z$; v) $1-x, 1-y, -z$.

Table 2.5. Cu–N bond lengths and Cu–O distances present in the {Cu(cyclam)} complexes of **1B-Mo7**.

Cu1A		Cu1C	
Cu1A–O1A	2.571(9)	Cu1C–O6B	2.376(9)
Cu1A–O1A ⁱ	2.571(9)	Cu1C–O6B ⁱⁱⁱ	2.376(9)
Cu1A–N1A	2.006(11)	Cu1C–N1C	1.992(11)
Cu1A–N4A	2.016(11)	Cu1C–N4C	2.019(16)
Cu1A–N1A ⁱ	2.006(11)	Cu1C–N1C ⁱⁱⁱ	1.992(11)
Cu1A–N4A ⁱ	2.016(11)	Cu1C–N4C ⁱⁱⁱ	2.019(16)
Cu1B		Cu1D	
Cu1B–O1B	2.710(9)	Cu1D–O5B	2.430(7)
Cu1B–O1B ⁱⁱ	2.710(9)	Cu1D–O5B ^{iv}	2.430(7)
Cu1B–N1B	2.012(9)	Cu1D–N21D	2.02(2)
Cu1B–N4B	2.029(11)	Cu1D–N24D	1.98(2)
Cu1B–N1B ⁱⁱ	2.012(9)	Cu1D–N21D ^{iv}	2.02(2)
Cu1B–N4B ⁱⁱ	2.029(11)	Cu1D–N24D ^{iv}	1.98(2)
		Cu1D–N31D	2.04(3)
		Cu1D–N34D	1.97(5)
		Cu1D–N31D ^{iv}	2.04(3)
		Cu1D–N34D ^{iv}	1.97(5)
Cu1E			
	Cu1E–O4A	2.490(12)	
	Cu1E–O4A ^v	2.490(12)	
	Cu1E–N1E	1.998(13)	
	Cu1E–N4E	1.988(14)	
	Cu1E–N1E ^v	1.998(13)	
	Cu1E–N4E ^v	1.988(14)	

Symmetry codes: **1B-Mo7**: i) -x, -y, -z; ii) 1-x, 1-y, 1-z; iii) -x, -y, -z; iv) 1-x, 2-y, 1-z; v) 1-x, 1-y, -z.

The crystal packing of **1B-Mo7** is based on {Mo₇O₂₄}/{Cu(cyclam)}²⁺ hybrid layers parallel to the (1-11) plane, which are constituted by heptamolybdate units connected through four octahedral {Cu(cyclam)}²⁺ metalorganic moieties (Cu1A, Cu1C, Cu1D and Cu1E). This arrangement is similar to that observed for **1-Mo7**, and once again the cleft of {Mo₇O₂₄} anions from the same sheets point alternatively at either above or below the mean plane of the layer (Figure 2.16). In comparison to **1-Mo7**, half of the bridging complexes in the interlammellar space are missing, in such a way that each POM anion is only linked to 5 neighbors. The bridging Cu1B complex binds one hybrid layer to the sheets located above and below alternately by its coordination to the surface of contiguous heptamolybdate units. The N–H⋯O and C–H⋯O type interactions established between cyclam ligands and POM O atoms also contribute to reinforce the overall crystal packing (Figure 2.17 and Table 2.6). The stacking of these hybrid grids along the [101] direction generates a 3D porous network with voids exhibiting a cross section of 8.6 x 9.9 Å² (N4C⋯N21D and N1A⋯N4E distances), in which the water molecules of hydration and ammonium counterions are hosted (Figure 2.17).

Table 2.6. N–H...O and C–H...O interactions in **1B-Mo7**.

Donor–H...Acceptor	D...A (Å)	Donor–H...Acceptor	D...A (Å)
N1A–H1A...O2A	2.997(16)	C7B–H7BB...O1B ⁱⁱ	3.151(15)
N4A–H4A...O15	2.887(17)	N1C–H1C...O2B ⁱⁱⁱ	2.900(14)
C2A–H2AB...O15 ⁱ	3.225(18)	N4C–H4C...O6B	3.035(19)
C6A–H6AB...O127	3.39(2)	N1E–H1E...O4B	3.24(2)
N1B–H1B...O12	2.730(14)	N4E–H4E...O3A	2.94(2)
N4B–H4B...O3B ⁱⁱ	3.243(15)	C3E–H3EAB...O4B ^{iv}	3.16(2)
C5B–H5BB...O1B	3.260(16)	C5E–H5EA...O5W ^v	3.37(3)
C6B–H6BA...O34	3.350(17)		

Symmetry codes: **1B-Mo7**: i) $-x, 1-y, 1-z$; ii) $1-x, 1-y, 1-z$; iii) $-x, -y, -z$; iv) $1-x, 1-y, -z$; v) $1+x, 1+y, z$.

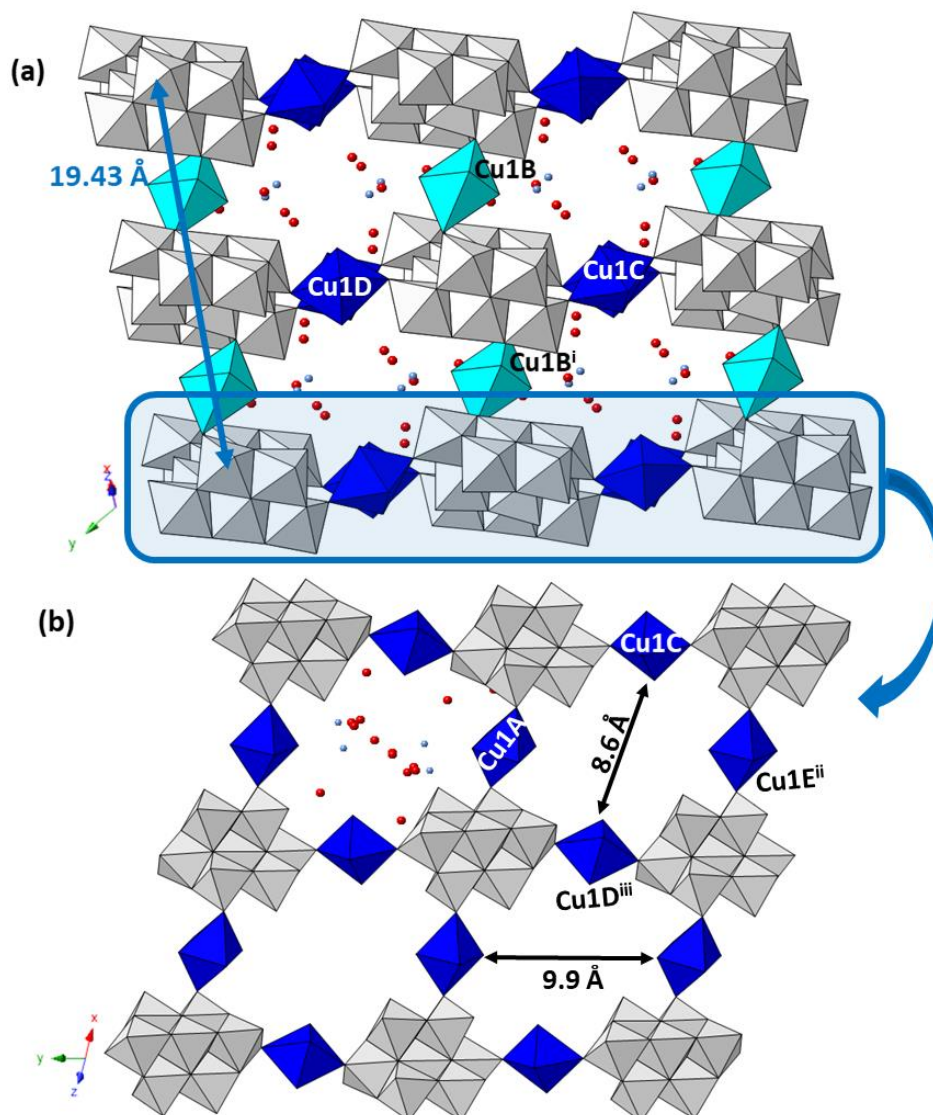


Figure 2.16. (a) View of the crystal packing of **1B-Mo7** along the [10-1] direction showing Mo1...Mo1 distances, and; (b) polyhedral representation of the hybrid layer in the (1-11) plane, with approximate dimensions of the voids. Cyclam ligand and hydration water molecules of some channels have been omitted for clarity. Color code: Mo polyhedra, grey; Cu polyhedra of the same layer, dark blue; Cu polyhedra linking the layers (Cu1B), light blue; O, red; N, blue. Symmetry codes: i) $1-x, 1-y, -z$; ii) $-x, -y, -z$; iii) $-x, 1-y, 1-z$.

The solvent accessible void in **1B-Mo7** accounts for 843 Å³, which corresponds to the 27% of the total cell volume, as calculated by PLATON software. Although the total accessible volume in **1B-Mo7** is similar to that in **1-Mo7**, the lack of one half of the metalorganic moieties joining the contiguous hybrid layers considerably reduces the interlammellar distance in 4 Å (Mo1...Mo1 = 23.20 Å in **1-Mo7** vs. Mo1...Mo1 = 19.43 Å in **1B-Mo7**). This contraction decreases the connectivity of the voids in **1B-Mo7**, and, hence, they only show a monodimensional character with channels running along the [101] direction (Figure 2.18).

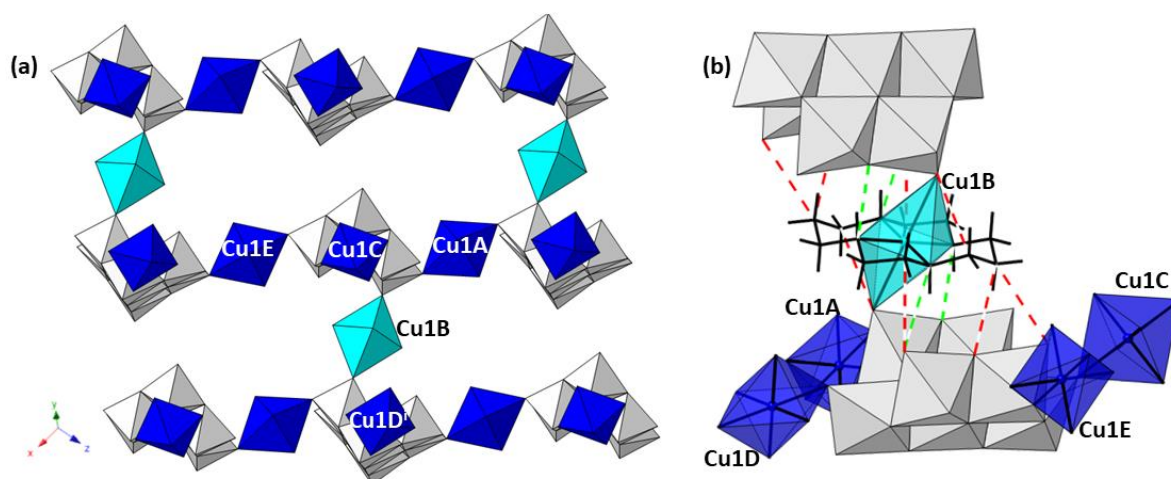


Figure 2.17. (a) View of the crystal packing of **1B-Mo7** along the [121] direction showing the alternating union to the upper and lower layer, and; (b) detail of the connectivity between hybrid layers. N-H...O and C-H...O interactions are depicted as dashed green and red lines, respectively.

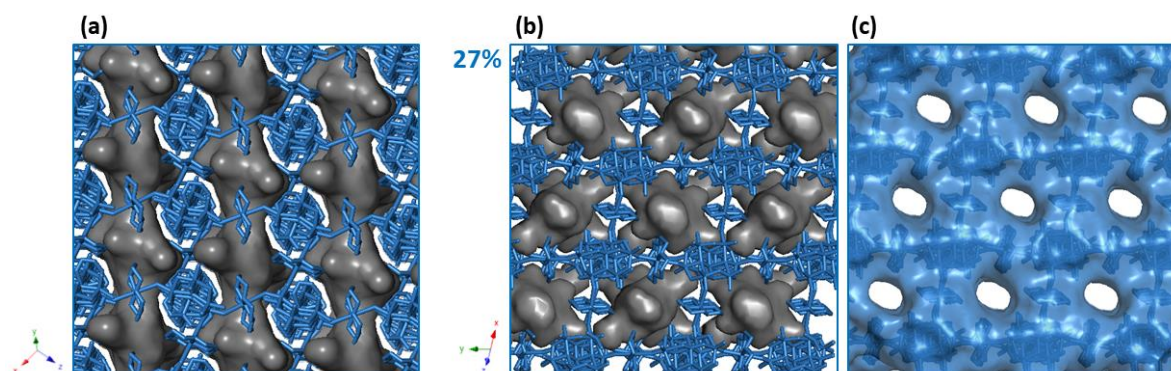


Figure 2.18. (a) (b) Representation of the total accessible volume in **1B-Mo7** with 1D channels growing along [101] direction and; (c) the porous framework showing the empty channels.

2.4. CONCLUSIONS

This chapter nicely illustrates the pH-dependent aqueous equilibria of isopolyoxomolybdates. Up to 5 different compounds can be isolated from the reaction between a commercial heptamolybdate salt and *in-situ* prepared $\{\text{Cu}(\text{cyclam})\}^{2+}$ complexes in water under mild bench conditions, which is strongly influenced by the pH of the media. As expected, the nuclearity of the final oxoanion increases when going to acidic pH values: compound $[\text{Cu}(\text{cyclam})][\text{MoO}_4]\cdot 4\text{H}_2\text{O}$ (**MoCu**) formed by chains constituted by tetrahedral oxoanions connected through octahedral metalorganic complexes is isolated above $\text{pH} > 10$, whereas acidic $\text{pH} < 6$ conditions led the 3D robust framework $[\text{Cu}(\text{cyclam})]_2[\gamma\text{-Mo}_8\text{O}_{26}]\cdot 1.5\text{H}_2\text{O}$, which is constituted by $[\text{Mo}_8\text{O}_{26}]_n^{4n-}$ chains linked to each other through the coordination spheres of $\{\text{Cu}(\text{cyclam})\}^{2+}$ complexes.

In contrast, reactions carried out at neutral to moderately basic conditions (pH values in the 6–9 range) initially afford $[\{\text{Cu}(\text{cyclam})\}_3(\kappa\text{-Mo}_8\text{O}_{27})]\cdot 14\text{H}_2\text{O}$ (**1-Mo8**) (see chapter 3). If **1-Mo8** is removed from the reaction media, further evaporation of the final solution yields the 3D covalent framework $[\{\text{Cu}(\text{cyclam})\}_3(\text{Mo}_7\text{O}_{24})]\cdot 15.5\text{H}_2\text{O}$ (**1-Mo7**) as a pure crystalline phase, whereas a second compound co-crystallizes at pH values between 6 and 8, namely, $(\text{NH}_4)[\{\text{Cu}(\text{cyclam})\}_{2.5}(\text{Mo}_7\text{O}_{24})]\cdot 5.5\text{H}_2\text{O}$ (**1B-Mo7**). Compound **1-Mo7** is isostructural with $[\{\text{Cu}(\text{cyclam})\}_3(\text{W}_7\text{O}_{24})]\cdot 15.5\text{H}_2\text{O}$,²⁹ but represents i) the first example of polyoxometalate–metalorganic extended framework based on $\{\text{Mo}_7\text{O}_{24}\}$ anions and ii) the second structure reported to date, in which a transition metal complex is coordinated to the surface of the heptamolybdate cluster. The structure of **1-Mo7** consists in a stacking of heptamolybdate– $\{\text{Cu}(\text{cyclam})\}^{2+}$ grids with rhombic voids superimposed on each other to generate a two-dimensional system of interconnected channels where the water molecules of hydration are hosted. Studies on the thermostructural behavior of **1-Mo7** revealed two thermally triggered solid-phase transitions which led to two new phases at 50 °C (**2-Mo7**) and 130 °C (**3-Mo7**). Although crystals cracked upon heating avoiding the phase transformation to be followed by scXRD, cell unit parameters of **2-Mo7** were determined. These studies together with variable-temperature PXRD experiments indicate that thermal derivatives could be analogous to those reported in the literature for the tungstate analogue; these are $[\{\text{Cu}(\text{cyclam})\}_3(\text{Mo}_7\text{O}_{24})]\cdot 12\text{H}_2\text{O}$ (**2-Mo7**) and $[\text{Cu}(\text{cyclam})]_{0.5}[\{\text{Cu}(\text{cyclam})\}_{2.5}(\text{Mo}_7\text{O}_{24})]$ (**3-Mo7**). The faster redox processes of Mo in comparison to W could make the anhydrous and potentially porous **3-Mo7** suitable for being used as active material in heterogeneous catalysis or in electrochemical energy storage systems. Crystals of **1-Mo7** and **1B-Mo7** cannot be visually distinguished under an optical microscope, which prevented the full characterization of the latter compound. Thus, only the crystal structure was elucidated by scXRD, which reveals a similar crystal packing showed by **1-Mo7**, but for the one half of the bridging metalorganic complexes in the

interlamellar space, which are missing. Ammonium cations located in the channels compensate the lack of positive charges. This new arrangement make hybrid layers to be closer to each other than in the case of **1-Mo7** and thus, **1B-Mo7** only exhibits monodimensional accessible voids.

2.5. REFERENCES

- [1] (a) Simon, K. Y.; Gulari, E. Spectroscopic and Scattering Investigation of Isopoly-molybdate and Tungstate Solutions. *Polyhedron*, **1984**, *3*, 1001-1011. (b) Maksimovskaya, R. I.; Maksimov, G. M. ^{95}Mo and ^{17}O NMR Studies of Aqueous Molybdate Solutions, *Inorg. Chem.*, **2007**, *46*, 3688–3695. (c) Gumerova, N. I.; Rompel, A. Polyoxometalates in solution: speciation under spotlight. *Chem. Soc. Rev.*, **2020**, *49*, 7568-7601.
- [2] (a) Pavani, K.; Ramanan, A. Influence of 2-Aminopyridine on the Formation of Molybdates under Hydrothermal Conditions. *Eur. J. Inorg. Chem.*, **2005**, 3080-3087. (b) Coué, V.; Dessapt, R.; Bujoli-Doeuff, M.; Evain, M.; Jobic, S. Synthesis, Characterization, and Photochromic Properties of Hybrid Organic-Inorganic Materials Based on Molybdate, DABCO, and Piperazine. *Inorg. Chem.*, **2007**, *46*, 28224-2835. (c) Wang, S.-M.; Chen, W.-L.; Wang, E.-B.; Li, Y.-G.; Feng, X.-J.; Liu, L. Three New Polyoxometalate-Based Hybrids Prepared from Choline Chloride/Urea Deep Eutectic Mixture at Room Temperature. *Inorg. Chem. Commun.*, **2010**, *13*, 972-975. (d) Wutkowski, A.; Srinivasan, B. R.; Naik, A. R.; Schütt, C.; Näther, C.; Bensch, W. Synthesis, Structure, and Photochemistry of an Organic Heptamolybdate-Monomolybdate. *Eur. J. Inorg. Chem.*, **2011**, 2254-2263.
- [3] (a) Bridgeman, A. M. The Electronic Structure and Stability of the Isomers of Octamolybdate. *J. Phys. Chem. A*, **2002**, *106*, 12151-12160. (b) Allis, D. G.; Burkholder, E.; Zubieta, J. A new octamolybdate: observation of the θ -isomer in $[\text{Fe}(\text{tpyprz})_2][\text{Mo}_8\text{O}_{26}]\cdot 3.7\text{H}_2\text{O}$ (tpyprz = tetra-2-pyridylpyrazine). *Polyhedron*, **2004**, *23*, 1145-1152. (c) Yue, Z.-C.; Du, H.-J.; Niu, Y.-Y.; Jin, G.-X. An unprecedented ι -type octamolybdate: $[\text{Tb}_{12}][(\beta\text{-Mo}_8\text{O}_{26})_{0.5}(\iota\text{-Mo}_8\text{O}_{26})]$ directed by a new tricationic template. *CrystEngComm*, **2013**, *15*, 9844-9848.
- [4] (a) Paulat-Böschen, I. X-Ray Crystallographic Determination of the Structure of the Isopolyanion $[\text{Mo}_{36}\text{O}_{112}(\text{H}_2\text{O})_{16}]^{8-}$ in the Compound $\text{K}_8[\text{Mo}_{36}\text{O}_{112}(\text{H}_2\text{O})_{16}]\cdot 36\text{H}_2\text{O}$. *J. Chem. Soc. Chem. Commun.*, **1979**, 780-782. (b) Krebs, B.; Stiller, S.; Tytko, K. H.; Mehmke, J. Structure and bonding in the high molecular weight isopolymolybdate ion, $[\text{Mo}_{36}\text{O}_{112}(\text{H}_2\text{O})_{16}]^{8-}$. The crystal structure of $\text{Na}_8[\text{Mo}_{36}\text{O}_{112}(\text{H}_2\text{O})_{16}]\cdot 58\text{H}_2\text{O}$. *Eur. J. Solid State Inorg. Chem.*, **1991**, *28*, 883–903.
- [5] Müller, A.; Gouzerh, P. From Linking of Metal-Oxide Building Blocks in a Dynamic Library to Giant Clusters with Unique Properties and Towards Adaptive Chemistry. *Chem. Soc. Rev.*, **2012**, *41*, 7431–7463.
- [6] Piepgrass, K.; Pope, M. T. Heteropoly “Browns” as Class I Mixed Valence (W(IV,VI)) Complexes. Tungsten-183 NMR of W(IV) Trimers. *J. Am. Chem. Soc.*, **1987**, *109*, 1586-1587.
- [7] Müller, A.; Krickemeyer, E.; Meyer, J.; Bögge, H.; Peters, F.; Plass, W.; Diemann, E.; Dillinger, S.; Nonnenbruch, F.; Randerath, M.; Menke, C. $[\text{Mo}_{154}(\text{NO})_{14}\text{O}_{420}(\text{OH})_{28}(\text{H}_2\text{O})_{70}]^{(25 \pm 5)-}$: a water-soluble big wheel with more than 700 atoms and a relative molecular mass of about 24000. *Angew. Chem. Int. Ed. Engl.*, **1995**, *34*, 2122–2124.
- [8] (a) Müller, A.; Sarkar, S.; Shah, S. Q. N.; Bögge, H.; Schmidtman, M.; Sarkar, S.; Kögerler, P.; Hauptfleisch, B.; Traitwein, A. X.; Schünemann, V. Archimedean Synthesis and Magic Numbers: “Sizing” Giant Molybdenum-Oxide-Based Molecular Spheres of the Keplerate Type. *Angew. Chem. Int. Ed.*, **1999**, *38*, 3238–3241. (b) Schäffer, C.; Todea, A. M.; Gouzerh, P.; Müller, A. Spontaneous self-Assembly of a Giant Spherical Metal-Oxide Keplerate: Addition of one Building Block Induces “Immediate” Formation of the Complementary one From a Constitutional Dynamic Library. *Chem. Commun.*, **2012**, *48*, 350-352.
- [9] Müller, A.; Beckmann, E.; Bögge, H.; Schmidtman, M.; Dress, A. Inorganic Chemistry Goes Protein Size: A Mo368 Nano-Hedgehog Initiating Nanochemistry by Symmetry Breaking. *Angew. Chem. Int. Ed.*, **2002**, *41*, 1162–1167.

- [10] (a) Lindqvist, I. A crystal structure investigation of the paramolybdate ion. *Arkiv. Kemi.*, **1950**, *2*, 325–341. (b) Lindqvist, I. The Structure of the Paramolybdate Ion. *Acta. Cryst.*, **1950**, *3*, 159-160.
- [11] (a) Maksimovskaya, R. I.; Maksimov, G. M. ^{95}Mo and ^{17}O NMR Studies of Aqueous Molybdate Solutions. *Inorg. Chem.*, **2007**, *46*, 3688-3695. (b) Howarth, O. W.; Kelly, P.; Petterson, L. Aqueous Isopolymolybdates(VI): An Oxygen-17 and Molybdenum-95 Nuclear Magnetic Resonance Study. *J. Chem. Soc., Dalton Trans.*, **1990**, 84-94.
- [12] (a) Kortz, U.; Pope, M. T. $\text{Cs}_6[\text{Mo}_7\text{O}_{24}]\cdot 7\text{H}_2\text{O}$. *Acta. Cryst.*, **1995**, *C51*, 1717-1719. (b) Shima, E. Structure of the Mo_{10}Ti Ion in a Crystal of Ammonium Heptamolybdate Tetrahydrate. *Nature*, **1967**, *214*, 170-171. (c) Gatehouse, B. M.; Leverett, P. The Crystal Structure of Potassium Heptamolybdate Tetrahydrate, $\text{K}_6\text{Mo}_7\text{O}_{24}\cdot 4\text{H}_2\text{O}$. *Chem. Commun.*, **1968**, 901-902. (d) Evans, H. T.; Gatehouse, B. M.; Leverett, P. Crystal Structure of the Heptamolybdate(VI) (Paramolybdate) Ion, $[\text{Mo}_7\text{O}_{24}]^{6-}$, in the Ammonium and Potassium Tetrahydrate Salts. *J. Chem. Soc., Dalton Trans.*, **1975**, 505-514. (e) Wutkowski, A.; Srinivasan, B. R.; Naik, A. R.; Schütt, C.; Näther, C.; Bensch, W. Synthesis, Structure, and Photochemistry of an Organic Heptamolybdate-Monomolybdate. *Eur. J. Inorg. Chem.*, **2011**, 2254-2263. (f) Khandolkar, S. S.; Näther, C.; Bensch, W.; Srinivasan, B. R. Syntheses and Structures of Two New Lithium-Heptamolybdates. *J. Coord. Chem.*, **2016**, *69*, 1166-1178. (g) Khandolkar, S. S.; Naik, A. R.; Näther, C.; Bensch, W.; Srinivasan, B. R. Synthesis, Crystal Structure and Photochemistry of Hexakis(butan-1-aminium) Heptamolybdate(VI) Tetrahydrate. *J. Chem. Sci.*, **2016**, *128*, 1737-1744.
- [13] (a) He, T.; Yao, J. Photochromism in Composite and Hybrid Materials Based on Transition-Metal Oxides and Polyoxometalates. *Prog. Mater. Sci.*, **2006**, *51*, 810-879. (b) Coué, V.; Dessapt, R.; Bujoli-Doeuff, M.; Evain, M.; Jobic, S. Synthesis, Characterization, and Photochromic Properties of Hybrid Organic-Inorganic Materials Based on Molybdate, DABCO, and Piperazine. *Inorg. Chem.*, **2007**, *46*, 2824-2835.
- [14] Inoue, M.; Nakayama, E.; Nakamura, Y.; Rengakuji, S.; Nishibe, K. Effect of Anions on the Epoxidation of Styrenes with H_2O_2 in the Presence of ammonium Heptamolybdate(VI)-Diocetyl tin Oxide Catalyst. *Bull. Chem. Soc. Jpn.*, **1991**, *64*, 3442-3444.
- [15] (a) Jeyakumar, K.; Chakravarthy, R. D., Chand D. K. Simple and efficient method for the oxidation of sulfides to sulfones using hydrogen peroxide and a Mo(VI) based catalyst. *Catalysis Communications*, **2009**, *10*, 1948-1451. (b) Porter, A. G.; Hu, H.; Liu, X.; Raghavan, A.; Adhikari, S.; Hall, D. R.; Thomson, D. J.; Liu, B.; Xia, Y.; Ren, T. Heptamolybdate: A Highly Active Sulfide Oxygenation Catalyst. *Dalton Trans.*, **2018**, *47*, 11882-11887. (c) Chang, Y.; Yu, W.-D.; Li, B.; Chen, Z.-F.; Yan, J. Discovery of a New Family of Polyoxometalate-Based Hybrids with Improved Catalytic Performances for Selective Sulfoxidation: The Synergy between Classic Heptamolybdate Anions and Complex Cations. *Inorg. Chem.*, **2019**, *58*, 14876-14884.
- [16] Absillis, G.; Cartuyvels, E.; Deun, R. V.; Parac-Vogt, T. Hydrolytic Cleavage of an RNA-Model Phosphodiester Catalyzed by a Highly Negatively Charged Polyoxomolybdate $[\text{Mo}_7\text{O}_{24}]^{6-}$ Cluster. *J. Am. Chem. Soc.*, **2008**, *130*, 17400-17408.
- [17] Yamase, T. Polyoxometalates for Molecular Devices: Antitumor Activity and Luminescence. *Mol. Eng.*, **1993**, *3*, 241-262.
- [18] (a) Mitsui, A.; Ogata, A.; Yanagie, H.; Kasano, H.; Hisa, T.; Yamase, T.; Eriguchi, M. Antitumor Activity of Polyoxomolybdate, $[\text{NH}_3\text{Pr}']_6[\text{Mo}_7\text{O}_{24}]\cdot 3\text{H}_2\text{O}$, Against Human Gastric Cancer Model. *Biomedicine & Pharmacotherapy*, **2006**, *60*, 353-358. (b) Yanagie, H.; Ogata, A.; Mitsui, S.; Hisa, T.; Yamase, T.; Eriguchi, M. Anticancer Activity of Polyoxomolybdate. *Biomedicine & Pharmacotherapy*, **2006**, *60*, 349-352. (c) Guo, R.; Cheng, Y.; Ding, D.; Li, X.; Zhang, L.; Jiang, X.; Liu, B. Synthesis and Antitumor Activity of Gelatin/Polyoxometalate Hybrid Nanoparticles. *Macromol. Biosci.*, **2011**, *11*, 839-847.
- [19] (a) Li, T.; Lü, J.; Gao, S.; Cao, R. A new heptamolybdate-based supramolecular compound with an alternating organic and inorganic layer structure: Synthesis, crystal structure and properties of $(\text{Hapy})_4[\text{Co}(\text{H}_2\text{O})_5\text{Mo}_7\text{O}_{24}]\cdot 9\text{H}_2\text{O}$. *Inorg. Chem. Commun.*, **2007**, *10*, 1342-1346. (b) Damjanović, V.; Kuzman, D.; Vrdoljak, V.; Muratović, S.; Žilić, D.; Stilić, V.; Cindrić, M. Hydrothermal Reactions of $[\text{Co}^{\text{III}}(\text{C}_2\text{O}_4)(\text{NH}_3)_4]^+$ and Polyoxomolybdates: Depolymerization of Polyoxomolybdates and In Situ Reduction of Cobalt. *Cryst. Growth Des.*, **2019**, *19*, 6763-6773. (c) Wu, S.-T.; Deng, B.-B.; Jiang, X.; Li, R.; Guo, J.; Lai, F.;

Huang, X.-H.; Huang, C.-C. Step-by-Step Assembly of 4d-4f-3d Complex Based on Heptamolybdate Anion. *J. Solid State Chem.*, **2012**, *196*, 451-457. (d) Wu, S.-T.; Lu, S.-M.; Tang, H.-L.; Deng, B.-B.; Huang, X.-H.; Huang, C.-C. Synthesis, Crystal Structure and Characterization of 3d-4d-4f Heterometallic Clusters Based on Super Tetrahedron Anions. *J. Clust. Sci.*, **2014**, *25*, 1413-1424.

[20] (a) Naruke, H.; Ozeki, T.; Yamase, T. Structure of Photoluminescent Polyoxomolybdoeuropate $(\text{NH}_4)_{12}\text{H}_2[\text{Eu}_4(\text{MoO}_4)(\text{H}_2\text{O})_{16}(\text{Mo}_7\text{O}_{24})_4]\cdot 13\text{H}_2\text{O}$. *Acta Cryst.*, **1991**, *C47*, 489-492. (b) Kaczmarek, A. M.; Liu, J.; Laforce, B.; Vincze, L.; Van Hecke, K.; Van Deun, R. Cryogenic Luminescent Thermometers Based on Multinuclear $\text{Eu}^{3+}/\text{Tb}^{3+}$ Mixed Lanthanide Polyoxometalates. *Dalton Trans.*, **2017**, *46*, 5781-5785.

[21] (a) Mialane, P.; Dolbecq, A.; Sécheresse, F. Functionalization of Polyoxometalates by Carboxylato and Azido Ligands: Macromolecular Complexes and Extended Compounds. *Chem. Commun.* **2006**, 3477-3485. (b) Onet, C. I.; Zhang, L.; Clérac, R.; Jean-Denis, J. B.; Feeney, M.; McCabe, T.; Schmitt, W. Self-Assembly of Hybrid Organic-Inorganic Polyoxomolybdates: Solid-State Structures and Investigation of Formation and Core Rearrangements in Solution. *Inorg. Chem.* **2011**, *50*, 604-613. (c) Pardiwala, A.; Kumar, S.; Jangir, R. Insights into Organic-Inorganic Hybrid Molecular Materials: Organoimido Functionalized Polyoxomolybdates. *Dalton Trans.* **2022**, *51*, 4945-4975.

[22] Groom, C. R.; Bruno, I. J.; Lightfoot, M. P.; Ward, S. C. The Cambridge Structural Database. *Acta Crystallogr.* **2016**, *B72*, 171-179.

[23] Kuzman, D.; Damjanović, V.; Vrdoljak, V.; Stilinović, V.; Cindrić, M. Directing Role of the Synthetic Route on the Self-Assembly Process of MoO_4^{2-} Units to $\text{Mo}_7\text{O}_{24}^{2-}$ or $\text{Mo}_{22}\text{O}_{74}^{16-}$ Ions. *Inorganica Chim. Acta*, **2020**, *510*, 119765.

[24] Damjanović, V.; Pisk, J.; Kuzman, D.; Agustin, D.; Vrdoljak, V.; Stilinović, V.; Cindrić, M. The Synthesis, Structure and Catalytic Properties of the $[\text{Mo}_7\text{O}_{24}(\mu\text{-Mo}_8\text{O}_{26})\text{Mo}_7\text{O}_{24}]^{16-}$ Anion Formed via Two Intermediate Heptamolybdates $[\text{Co}(\text{en})_3]_2[\text{NaMo}_7\text{O}_{24}]\text{Cl}\cdot n\text{H}_2\text{O}$ and $(\text{H}_3\text{O})[\text{Co}(\text{en})_3]_2[\text{Mo}_7\text{O}_{24}]\text{Cl}\cdot 9\text{H}_2\text{O}$. *Dalton Trans.*, **2019**, *48*, 9974-9983.

[25] Damjanović, V.; Kuzman, D.; Vrdoljak, V.; Muraatović, S.; Žilić, D.; Stilinović, V.; Cindrić, M. Hydrothermal Reactions of $[\text{Co}^{\text{III}}(\text{C}_2\text{O}_4)(\text{NH}_3)_4]^+$ and Polyoxomolybdates: Depolymerization of Polyoxomolybdates and in Situ Reduction of Cobalt. *Cryst. Growth Des.*, **2019**, *19*, 6763-6773.

[26] Zhang, Y.; Yu, W.-D.; Li, B.; Chen, Z.-F.; Yan, J. Discovery of a New Family of Polyoxometalate-Based Hybrids with Improved Catalytic Performances for Selective Sulfoxidation: The Synergy between Classic Heptamolybdate Anions and Complex Cations. *Inorg. Chem.*, **2019**, *58*, 14876-14884.

[27] Arumuganathan, T.; Srinivasa Rao, A.; Das, K. Polyoxometalate Supported Transition Metal Complexes: Synthesis, Crystal Structures, and Supramolecular Chemistry. *Cryst. Growth Des.* **2010**, *10*, 4272-4284.

²⁸ Martín-Caballero, J.; Wéry, A. S. J.; Reinoso, S.; Artetxe, B.; San Felices, L.; El Bakkali, B.; Trautwein, G.; Alcañiz-Monge, J.; Vilas, J. L.; Gutiérrez-Zorrilla, J. M. A Robust Open Framework Formed by Decavanadate Clusters and Copper(II) Complexes of Macrocyclic Polyamines: Permanent Microporosity and Catalytic Oxidation of Cycloalkanes. *Inorg. Chem.*, **2016**, *55*, 4970-4979.

[29] Martín-Caballero, J.; Artetxe, B.; Reinoso, S.; San Felices, L.; Castillo, O.; Beobide, G.; Vilas, J. L.; Gutiérrez-Zorrilla, J. M. Thermally-Triggered Crystal Dynamics and Permanent Porosity in the First Heptamolybdate-Metalorganic Three-Dimensional Hybrid Framework. *Chem. Eur. J.*, **2017**, *23*, 14962-14974.

[30] Dissem, N.; Artetxe, B.; San Felices, L.; Lezama, L.; Haddad, A.; Gutiérrez-Zorrilla, J. M. A Robust Framework Based on Polymeric Octamolybdate Anions and Copper(II) Complexes of Tetradentate N-Donor Ligands. *Crystals*, **2018**, *8*, 20.

[31] Shamir, D.; Meyerstein, D.; Zilbermann, I.; Burg, A.; Albo, Y.; Shames, A. I.; Vainer, R.; Borojovich, E. J. C.; Yardeni, G.; Kornweitz, H.; Maimon, E. Copper(II) Catalyses the Reduction of Perchlorate by Both Formaldehyde and by Dihydrogen in Aqueous Solutions. *J. Coord. Chem.*, **2018**, *71*, 2905-2912.

- [32] (a) Martín-Caballero, J.; San José Wéry, A.; Artetxe, B.; Reinoso, S.; San Felices, L.; Vilas, J. L.; Gutiérrez-Zorrilla, J. M. Sequential Single-Crystal-to-Single-Crystal Transformations Promoted by Gradual Thermal Dehydration in a Porous Metavanadate Hybrid. *CrystEngComm*, **2015**, *17*, 8915-8925.
- [33] Gumerova, N. I.; Rompel, A. Polyoxometalates in Solution: Speciation Under Spotlight. *Chem. Soc. Rev.*, **2020**, *49*, 7568-7601.
- [34] Crystal data: [C₁₀N₄H₂₈][CuCl₄]Cl₂ (**1-Cu**): C₁₀H₂₈Cl₆CuN₄; fw=480.60 g mol⁻¹; triclinic, *P*-1 (2) space group; *a*=7.1270(7); *b*=7.3332(8); *c*=9.6410(9) Å; α =73.773(9); β =71.307(9); γ =85.468(8) °; *V*=458.25(8) Å³; *Z*=1; ρ_{calcd} =1.742 g cm⁻³; μ =2.064 mm⁻¹; 2941 reflections collected; 1838 unique (*R*_{int}= 0.019); 1649 observed (*I* > 2 σ (*I*)), 113 parameters, *R*(*F*)= 0.029 (*I* > 2 σ (*I*)), *wR*(*F*₂)= 0.070 (all data), *GoF*=1.058.
- [35] (a) Baran, E. J. Structural Data and Vibrational Spectra of the Copper(II) Complex of L-Selenomethionine, *Z. Naturforsch.*, **2005**, *60b*, 663-666. (b) Nakamoto, K. Chapter 1: Applications in Coordination Chemistry, in *Infrared and Raman Spectra of Inorganic and Coordination Compounds: Part B: Applications in Coordination, Organometallic, and Bioinorganic Chemistry*; John Wiley & Sons, New York, USA, **2008**. (c) Yan, G.; Wang, X.; Ma, Y.; Cheng, X.; Wang, Y.; Li, Y. A new paratungstate-A-based organiceinorganic hybrid compound: Synthesis, structure and photocatalytic property of [Co(en)₃]₂[H₂W₇O₂₄]·8H₂O. *Solid State Sci.*, **2013**, *17*, 146-150.
- [36] (a) Reinoso, S.; Artetxe, B.; Gutiérrez-Zorrilla, J. M. Single-Crystal-to-Single-Crystal Transformations Triggered by Dehydration in Polyoxometalate-Based Compounds. *Acta Cryst.* **2018**, *C74*, 1222-1242. (b) Dissem, N.; Artetxe, B.; San Felices, L.; Beobide, G.; Castillo, O.; Ruiz-Bilbao, E.; Lezama, L.; Vivanco, M. dM.; Haddad, A.; Gutiérrez-Zorrilla, J. M. Single-Crystal-to-Single-Crystal Cluster Transformation in a Microporous Molybdoarsenate(V)-Metalorganic Framework. *Inorg. Chem.* **2021**, *60*, 14913-14923.
- [37] Kihlberg, L. The Crystal Structure of Mo₁₈O₅₂ and the Existence of Homologous Series of Structures Based on MoO₃. *Ark. Kemi* **1963**, *21*, 443-460.
- [38] Abrahams, S. C.; Bernstein, J. L.; Jamieson, P. B. Crystal Structure of the Transition-Metal Molybdates and Tungstates IV. Paramagnetic CuMoO₄. *J. Chem. Phys.* **1968**, *48*, 2619-2629.
- [39] Lindqvist, I. The structure of the Paramolybdate Ion. *Acta Cryst.*, **1950**, *3*, 159-160.
- [40] Román, P.; Gutiérrez-Zorrilla, J. M.; Luque, A. Crystal Structure and Spectroscopic Study of Polymolybdates. The Crystal Structure and Bonding of Hexakis(*n*-pentylammonium)heptamolybdate(VI) Trihydrate. *J. Crystallogr. Spectrosc. Res.*, **1998**, *18*, 117-131.
- [41] Lindqvist, I. The structure of the Paramolybdate Ion. *Acta Cryst.*, **1950**, *3*, 159-160.
- [42] Román, P.; Gutiérrez-Zorrilla, J. M.; Luque, A. Crystal Structure and Spectroscopic Study of Polymolybdates. The Crystal Structure and Bonding of Hexakis(*n*-pentylammonium)heptamolybdate(VI) Trihydrate. *J. Crystallogr. Spectrosc. Res.*, **1998**, *18*, 117-131.
- [43] Barefield, E. K. Coordination Chemistry of N-tetraalkylated Cyclam Ligands—A Status Report. *Coord. Chem. Rev.* **2010**, 1607-1627.
- [44] Arumuganathan, T.; Srinivasa Rao, A.; Das, K. Polyoxometalate Supported Transition Metal Complexes: Synthesis, Crystal Structures, and Supramolecular Chemistry. *Cryst. Growth Des.*, **2010**, *10*, 4272-4284.
- [45] Spek, L. A. Structure Validation in Chemical Crystallography. *Acta Crystallogr. Sect. D: Biol. Crystallogr.* **2009**, *D65*, 148-155.

Sequential Single-Crystal-to-Single-Crystal Isomerizations of Octamolybdate Anions within a Microporous Hybrid Framework with Selective Sorption Properties

- 3.1. Introduction
- 3.2. Experimental section
- 3.3. Results and discussion
- 3.4. Water vapor sorption properties
- 3.5. Gas sorption measurements
- 3.6. Conclusions
- 3.7. References

ABSTRACT: The hybrid compound $[\{\text{Cu}(\text{cyclam})\}_3(\kappa\text{-Mo}_8\text{O}_{27})]\cdot 14\text{H}_2\text{O}$ (**1-Mo8**) (cyclam = 1,4,8,11-tetraazacyclotetradecane) is built of an unprecedented octamolybdate cluster linked through metalorganic complexes in a 3-dimensional covalent open framework intersected with a 3D system of interconnected water-filled channels. Compound **1-Mo8** undergoes two sequential single-crystal-to-single-crystal (SCSC) transformations upon thermal evacuation of water molecules to lead to two different anhydrous phases at 36 °C and 120 °C; these are $[\text{Cu}(\text{cyclam})][\{\text{Cu}(\text{cyclam})\}_2(\lambda\text{-Mo}_8\text{O}_{27})]$ (**2-Mo8**) and $[\{\text{Cu}(\text{cyclam})\}_3(\mu\text{-Mo}_8\text{O}_{27})]$ (**3-Mo8**), respectively. Phase transitions do not only imply remarkable modifications in the Cu–O bonding scheme affecting the framework dimensionality, but also the isomerization of octamolybdate anions through metal migration. Reversible hydration of **3-Mo8** upon air exposure involves condensation of one additional water molecule to the cluster, and hence, the well-known $[\gamma\text{-Mo}_8\text{O}_{26}(\text{OH})_2]^{6-}$ anion can be found in $[\{\text{Cu}(\text{cyclam})\}_3\{\gamma\text{-Mo}_8\text{O}_{26}(\text{OH})_2\}]\cdot 11\text{H}_2\text{O}$ (**4-Mo8**), which dehydrates below 120 °C without any apparent significant change in its unit cell parameters to lead to the third anhydrous phase **6-Mo8**. In contrast, **2-Mo8** rapidly hydrates to form $[\{\text{Cu}(\text{cyclam})\}_3(\kappa\text{-Mo}_8\text{O}_{27})]\cdot 13\text{H}_2\text{O}$ (**5-Mo8**), which displays unit cell parameters similar to those in **2-Mo8**, but with the same octamolybdate cluster as that in **1-Mo8**. It is worth highlighting that i) the system is able to undergo four sequential SCSC transformations; ii) three of the octamolybdate clusters have never been observed before; and iii) up to three different microporous phases with accessible voids can be isolated from the parent compound. These accessible voids have proved to adsorb C1 and C2 gases at high temperatures (273 and 298 K), as well as to be able to selectively adsorb C₂H₆ over C₂H₄. Results from water vapor sorption analyses are in good agreement with structural transitions and show high cyclability, as well as, some of the highest uptake values reported to date for POM-based systems. The isotherms display an abrupt adsorption capacity at 20-30% relative humidity level that could be potentially desirable for humidity control devices in confined spaces.

3.1. INTRODUCTION

As already reviewed, the most common polyoxomolybdate (POMo) clusters isolated from aqueous solutions are the $\{\text{Mo}_7\text{O}_{24}\}^{6-}$ anion previously studied in Chapter 2, and the β -form of the octamolybdate $[\text{Mo}_8\text{O}_{26}]^{4-}$ cluster. Since Schwing-Weill and Arnaud-Neu reported the first evidence of octamolybdate anion in 1970,¹ the number of $\{\text{Mo}_8\text{O}_{26}\}$ isomers has grown up to nine different clusters reported in literature; α , β , γ , δ , ε , ζ , η , θ and ι - $\{\text{Mo}_8\text{O}_{26}\}$.² The β -form has been the most studied one due to its stability in aqueous solution, and is the only isomer presenting an octahedral coordination in all the *addenda* atoms forming a compact structure with a C_{2h} symmetry in which the eight $\{\text{MoO}_6\}$ units are linked by edge-sharing. In aqueous solutions, this isomer is in equilibria with the α -form, which consists on a six member ring of octahedral $\{\text{MoO}_6\}$ units bicapped in opposite faces by two $\{\text{Mo}_4\}$ tetrahedra with a D_{3d} symmetry. These two co-existing clusters are the most important and common ones that can be isolated from aqueous solution. The interconversion between these two cluster revealed a third isomer (γ) as an intermediate between α and β -forms, which consists on a six edge-sharing MO_6 octahedra and two square pyramids on the sides.³ Despite the vast variety of structural isomers reported to date for $[\text{Mo}_8\text{O}_{26}]^{4-}$ octamolybdate anions, only the γ form has been observed stabilized either by protonation, leading to the oxygen-rich $[\text{Mo}_8\text{O}_{26}(\text{OH})_2]^{6-}$ anion,⁴ or by polymerization,⁵ resulting in $\{\text{Mo}_8\text{O}_{27}\}_n$ and $\{\text{Mo}_8\text{O}_{26}\}_n$ chain-like assemblies depending on the number of corners shared to polymerize. However, this isomer has not been able to be isolated from aqueous solution.

The remaining isomers can be individually isolated in solid state only as hybrid compounds by coordination of the cluster to metalorganic moieties. In fact, Zubietta and co-workers were able to synthesize all the isomers under hydrothermal conditions and the presence of a transition metal containing metalorganic complex. The δ -isomer is constituted by four MO_6 octahedra and four MO_4 tetrahedra in an arrangement similar to that found in the α -isomer, except that the six-member ring is formed by four MO_6 octahedra linked by corner-sharing to two MO_4 square pyramids. The open structure of the ε - $\{\text{Mo}_8\text{O}_{26}\}$ consists of two $\{\text{Mo}_3\text{O}_{11}\}$ square pyramid arrangement linked by edge-sharing through two MO_6 octahedra. The next isomer, known as ζ - $\{\text{Mo}_8\text{O}_{26}\}$, contains two pairs of octahedra $\{\text{Mo}_2\text{O}_{10}\}$ units and two pairs of $\{\text{Mo}_2\text{O}_8\}$ square pyramid units, all of them linked by edge-sharing. The last four clusters (γ , δ , ε , ζ) exhibit a C_i symmetry in solid state. The next η - $\{\text{Mo}_8\text{O}_{26}\}$ cluster shows an arrangement similar to that of α -form, but in this case, the six-member ring of octahedral MO_6 units is capped on either faces by corner-sharing by MoO_5 square pyramids instead of two tetrahedra. In addition, the θ -isomer is the only one exhibiting three different molybdenum polyhedra. This cluster consists on a ring of four MoO_6 octahedra and two MoO_5 square pyramids bicapped by tetrahedral MoO_4 units

linked by corner-sharing. Recently, the last isomer known as ι - $\{\text{Mo}_8\text{O}_{26}\}$ has been reported. This cluster is better described as a six-member ring formed by five $\{\text{MoO}_6\}$ units and one $\{\text{MoO}_4\}$ tetrahedra, which is further capped via corner-sharing on either sides of the plane by two additional $\{\text{MoO}_4\}$ subunits. Figure 3.1 and Table 3.1 compiles all the isomers together with the three unprecedented clusters synthesized in this work by stabilization with metalorganic $\{\text{Cu}(\text{cyclam})\}$ complexes. These three new octamolybdate clusters will be described in detail along this chapter.

Table 3.1. List of the polyhedral components of the octamolybdate isomers reported to date.

Isomer	Polyhedra	Oxo-group types	Ref.
α - $\text{Mo}_8\text{O}_{26}^{4-}$	6 octahedra, 2 tetrahedra	14t, $6\mu^2$, $6\mu^3$	[6]
β - $\text{Mo}_8\text{O}_{26}^{4-}$	8 octahedra	14t, $6\mu^2$, $4\mu^3$, $2\mu^5$	[6]
γ - $\text{Mo}_8\text{O}_{26}^{4-}$	6 octahedra, 2 square pyramids (Type A)	14t, $10\mu^2$, $2\mu^3$	[6]
γ - $\text{Mo}_8\text{O}_{26}(\text{OH})_2^{6-}$	8 octahedra	16t, $10\mu^2$, $2\mu^3$	[7]
δ - $\text{Mo}_8\text{O}_{26}^{4-}$	4 octahedra, 4 tetrahedra	14t, $10\mu^2$, $2\mu^3$	[6]
ε - $\text{Mo}_8\text{O}_{26}^{4-}$	6 square pyramids, 2 octahedra	16t, $4\mu^2$, $6\mu^3$	[6]
ζ - $\text{Mo}_8\text{O}_{26}^{4-}$	4 octahedra, 4 square pyramids	14t, $6\mu^2$, $6\mu^3$	[6]
η - $\text{Mo}_8\text{O}_{26}^{4-}$	6 octahedra, 2 square pyramids (Type B)	14t, $4\mu^2$, $8\mu^3$	[8]
θ - $\text{Mo}_8\text{O}_{26}^{4-}$	4 octahedra, 2 square pyramids, 2 tetrahedra	14t, $8\mu^2$, $4\mu^3$	[8]
ι - $\text{Mo}_8\text{O}_{26}^{4-}$	5 octahedra, 3 tetrahedra	14t, $8\mu^2$, $4\mu^3$	[9]
κ - $\text{Mo}_8\text{O}_{27}^{6-}$	7 octahedra, 1 square pyramid	14t, $9\mu^2$, $1\mu^3$, $3\mu^4$	This work
λ - $\text{Mo}_8\text{O}_{27}^{6-}$	7 octahedra, 1 tetrahedra	14t, $9\mu^2$, $2\mu^3$, $2\mu^4$	This work
μ - $\text{Mo}_8\text{O}_{27}^{6-}$	7 octahedra, 1 tetrahedra	15t, $8\mu^2$, $2\mu^3$, $2\mu^4$	This work

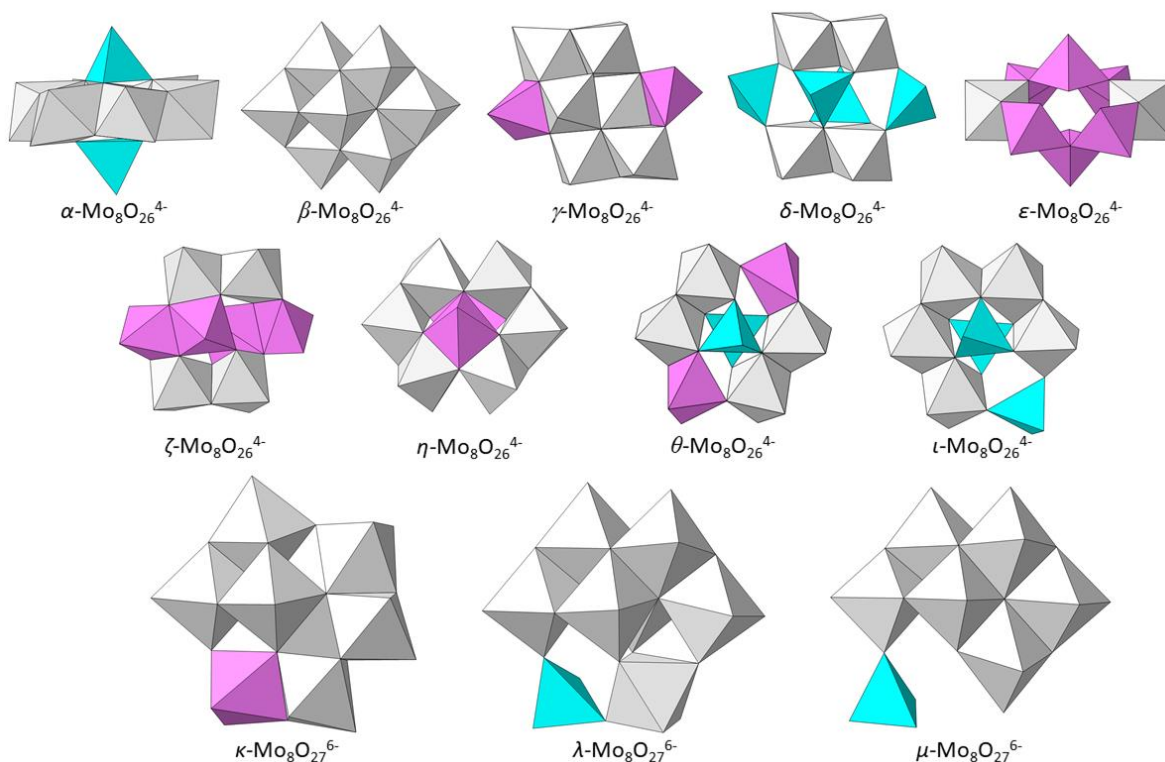


Figure 3.1. Polyhedral representation of the octamolybdate isomers reported to date.

3.1.1. Octamolybdate-based hybrid compounds

From the analysis of octamolybdate cluster containing hybrids on the Cambridge Structural Database (CSD),¹⁰ a total of 723 hits revealed the great attention that $\{\text{Mo}_8\text{O}_{26}\}$ anions have attracted in comparison to the small amount of hybrids found for heptamolybdate-based hybrid structures. From the long list of extended structures based on octamolybdate units and transition metal metalorganic complexes, more than the 72% of structures contain the β - $\{\text{Mo}_8\text{O}_{26}\}$ form. Reaction of β -isomer with transition metal containing complexes of N-donor ligands has led to structures with different dimensionalities that ranges from molecular 0D hybrids, to extended structures formed by hybrid chains, layers of 3D networks (Figure 3.2).¹¹ The covalent coordination of metalorganic complexes to octamolybdate anions has enhanced the potential application of this hybrids in fields such as electrocatalysis for water oxidation¹² or reduction of nitrile,¹³ or photocatalytic activities.¹⁴ Molecular hybrids containing 4f-metals have also been briefly studied.¹⁵ Similar results can be found for α - and γ -isomers which stand for around the 20% of the total octamolybdate-containing organic-inorganic hybrids.¹⁶ It should be mentioned that some of these structures contain both isomers at the same time.¹⁷

Regarding the remaining isomers, less than 10% of hybrid structures found in literature are based on δ , ϵ , ζ , η and θ isomers. For example, the $\{[\text{Cu}_4(\text{dmatrix})_6]\{\delta\text{-Mo}_8\text{O}_{26}\}\}$ ($\text{dmatrix} = 3,5\text{-dimethyl-4-amino-1,2,4-triazole}$)¹⁸ represents the first hybrid structure assembled by $\{\delta\text{-Mo}_8\text{O}_{26}\}$ units. On the contrary, the first hybrid containing the ϵ -isomer was reported in 1997 as the $\{[\text{Ni}(\text{H}_2\text{O})_2(4,4'\text{-bpy})_2]_2\{\epsilon\text{-Mo}_8\text{O}_{26}\}\}$ ($\text{bpy} = \text{bipyridyl}$)¹⁹ as a polymeric scaffold formed by anionic $\{\text{Ni}(\text{H}_2\text{O})_2(4,4'\text{-bpy})_2\}$ cations which are covalently linked by octamolybdate units to form a 3D covalent framework. It should be highlighted the pioneering work carried out by Zubietta and co-workers in the study of such structures. In a similar way, the ζ -isomer is found in the $\{[\text{Cu}_2(\text{tpyrpyz})]_2\{\zeta\text{-Mo}_8\text{O}_{26}\}\cdot 7\text{H}_2\text{O}$ ($\text{tpyrpyz} = \text{tetra-2-pyridylpyrazine}$)²⁰ hybrid as $\zeta\text{-Mo}_8\text{O}_{26}$ units covalently link $\{\text{Cu}_2(\text{tpyrpyz})\}_n$ -chains leading to a tridimensional network. Only one organic-inorganic hybrid has been reported for $\eta\text{-Mo}_8\text{O}_{26}$ which consist in monodimensional chains constructed by the assembly of discrete η -octamolybdate clusters through $\{\text{Cu}(t\text{-Bu}_2\text{bpy})_2\}$ units ($t\text{-Bu}_2\text{bpy} = 4,4'\text{-di-tert-butyl-2,2'-bipyridine}$).²¹ The bidimensional arrangement between θ -octamolybdate and $\{\text{Cu}(\text{L})\}$ ($\text{L} = 3\text{-}((1\text{H-imidazol-1-yl)methyl)pyridine}$) complexes,²² and the interpenetrated $[\text{Cu}^{\text{II}}(\text{bth})_2(\theta\text{-Mo}_8\text{O}_{26})_{0.5}]\cdot \text{H}_2\text{O}$ ($\text{bth} = 1,6\text{-bis}(1,2,4\text{-triazol-1-yl})\text{hexane}$) 3D network²³ represents the only two examples of hybrid structures containing the θ -isomer. In contrast, no hybrid structures have been reported yet constructed by the $\iota\text{-Mo}_8\text{O}_{26}$ isomer.

It should be mentioned that all the previous examples consist on octamolybdate anion covalently linked exclusively to N-donor ligands, mainly, organoimine-, triazol- and

pyridine-derivatives. Nevertheless, only few examples of hybrids containing N,O-donor or O-donor ligands have been found in literature.²⁴

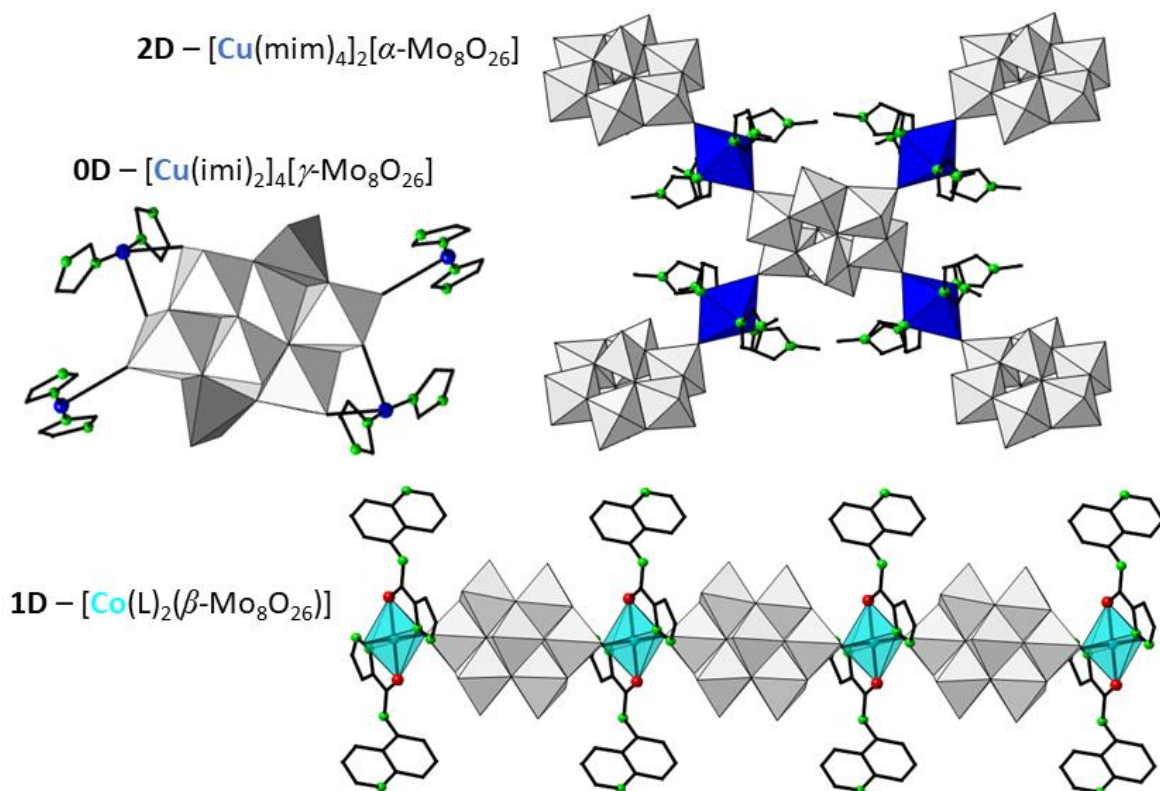


Figure 3.2. Some examples of {Mo₈O₂₆}-isomer-containing hybrids. L = N-(quinolin-5-yl)-1H-pyrazole-3-carboxamide}; mim = 1-methylimidazole; imi = imidazole.

3.2. EXPERIMENTAL SECTION

3.2.1. Synthesis

General synthetic procedure

$[{\text{Cu}}(\text{cyclam})]_3(\kappa\text{-Mo}_8\text{O}_{27}) \cdot 14\text{H}_2\text{O}$ (**1-Mo8**). The pH of a mixture of (NH₄)₆[Mo₇O₂₄]·4H₂O (0.124 g, 0.1 mmol), Cu(OAc)₂ (0.054 g, 0.3 mmol) and cyclam (0.060 g, 0.3 mmol) in water (25 mL) was adjusted to a value of 6.5 with aqueous 1M NaOH. The solution was then stirred for 1h at room temperature, transferred into a Teflon-lined autoclave, and kept at 140 °C for 72 h in an oven. After slowly cooling to room temperature for 48 h, purple prismatic single crystals of **1-Mo8** were isolated by filtration and washed with water. Yield: 7 mg, 4% based on Mo. Elem. Anal. Calcd. (%) for C₃₀H₁₀₀Cu₃N₁₂Mo₇O₄₁: C, 16.05%; H, 4.46%; N, 7.49%. Found: C, 15.49%; H, 4.58%; N, 7.00%. IR (cm⁻¹): 3229 (w), 3165 (w), 2934 (w), 2864 (w), 1474 (w), 1453 (w), 1443 (w), 1437 (w), 1430 (w), 1387 (w), 1383 (w), 1312 (w), 1292 (w), 1255 (w), 1235 (w), 1105 (m), 1075 (m), 1063 (m), 1017 (m),

CHAPTER 3

1009 (m), 963 (s), 936 (m), 926 (m), 917 (m), 897 (vs), 883 (vs), 842 (s), 638 (m), 578 (w), 473 (w), 439 (w), 409 (w).

To obtain bulk polycrystalline samples, a solution of $\text{Cu}(\text{OAc})_2$ (0.054 g, 0.3 mmol) and cyclam (0.060 g, 0.3 mmol) in water (15 mL) was added dropwise to an aqueous solution (15 mL) of $(\text{NH}_4)_6[\text{Mo}_7\text{O}_{24}]\cdot 4\text{H}_2\text{O}$ (0.124 g, 0.1 mmol). After adjusting the pH to 6.5, the mixture was heated at 100 °C for 1 h. The resulting purple solution was filtered and 1,4-dioxane (1 mL) was added. Compound **1-Mo8** was isolated upon room-temperature evaporation for 4 days and identified as a pure crystalline phase by PXRD (Figure 3.3). Yield: 30 mg, 15% based on Mo.

$[\text{Cu}(\text{cyclam})][\{\text{Cu}(\text{cyclam})\}_2(\lambda\text{-Mo}_8\text{O}_{27})]$ (**2-Mo8**); $[\{\text{Cu}(\text{cyclam})\}_3(\mu\text{-Mo}_8\text{O}_{27})]$ (**3-Mo8**); $[\{\text{Cu}(\text{cyclam})\}_3\{\gamma\text{-Mo}_8\text{O}_{26}(\text{OH})_2\}]\cdot 11\text{H}_2\text{O}$ (**4-Mo8**) and; $[\{\text{Cu}(\text{cyclam})\}_3(\kappa\text{-Mo}_8\text{O}_{27})]\cdot 13\text{H}_2\text{O}$ (**5-Mo8**). The anhydrous phases **2-Mo8** and **3-Mo8** were obtained by heating a sample of **1-Mo8** in an oven for 1 h at 50 °C or 120 °C, respectively. The hydrated phase **4-Mo8** was isolated by exposing crystals of **3-Mo8** to air for 9 days, whereas **5-Mo8** is rapidly obtained in ca. 1 h from **2-Mo8** under similar conditions.

3.2.2. Single-crystal X-ray crystallography

Crystallographic data for compounds **1-Mo8–5-Mo8** are given in Table 3.2. Intensity data were collected on an Agilent Technologies Supernova diffractometer equipped with monochromated Mo $K\alpha$ radiation ($\lambda = 0.71073 \text{ \AA}$) and an Eos CCD detector for all phases but **5-Mo8**. For the latter, the data collection was carried out under monochromated Cu $K\alpha$ radiation ($\lambda = 1.54184 \text{ \AA}$) and Atlas CCD detector. Data collection temperatures for hydrated phases were 100 K (**1-Mo8** and **5-Mo8**) and 150 K (**4-Mo8**). Measurements for the anhydrous **2-Mo8** were performed at 293 K, whereas for **3-Mo8**, single-crystals were first heated to 393 K, and then quenched to 100 K to perform the full data acquisition.

Thermal vibrations for all of the atoms except oxygen atoms belonging to water molecules were treated anisotropically in **1-Mo8**, **2-Mo8** and **3-Mo8** whereas anisotropic treatment had to be restricted to heavy atoms (Mo and Cu) and POM oxygen atoms only in **4-Mo8** and **5-Mo8**. Hydrogen atoms of organic ligands were placed in calculated positions using standard SHELXL parameters. Some of the thermal ellipsoids from the lighter atoms (C and N) were restrained using ISOR- and SIMU-type commands from SHELXL, whereas C–C and C–N bond lengths were normalized using SADI and DFIX. Different crystallographic positions suitable for water molecules of hydration were located in the Fourier maps of **1-Mo8**, **4-Mo8** and **5-Mo8**, their occupancies being initially refined without restrictions to be fixed to the first decimal in the last refinement cycle. This resulted in a total number of 14 water molecules delocalized over 20 sites for **1-Mo8**, 6 over 9 sites for **4-Mo8** (the

asymmetric unit displays one half of the formula), and 13 over 16 sites for **5-Mo8**. The anhydrous structures show large accessible voids, which account for 24 and 23 % of the unit cell volume for **2-Mo8** and **3-Mo8**, respectively. According to PLATON, the location and volume of these voids are as follows: one void at $x,y,z = 0, 0, 0$ in **2-Mo8**, accounting for 824 Å³; two voids at $x,y,z = 0, 1/4, 2/3$ and $0, 3/4, 1/3$ in **3-Mo8**, which account for 784 and 775 Å³, respectively.

Table 3.2. Crystallographic data for **1-Mo8**, **2-Mo8**, **3-Mo8**, **4-Mo8** and **5-Mo8**.

	1-Mo8	2-Mo8	3-Mo8	4-Mo8	5-Mo8
empirical formula	C ₃₀ H ₁₀₀ Cu ₃ Mo ₈ N ₁₂ O ₄₁	C ₃₀ H ₇₂ Cu ₃ Mo ₈ N ₁₂ O ₂₇	C ₃₀ H ₇₂ Cu ₃ Mo ₈ N ₁₂ O ₂₇	C ₃₀ H ₉₆ Cu ₃ Mo ₈ N ₁₂ O ₃₉	C ₃₀ H ₉₈ Cu ₃ Mo ₈ N ₁₂ O ₄₀
fw (g mol⁻¹)	2243.35	1991.13	1991.13	2207.32	2225.34
crystal system	Monoclinic	Triclinic	Monoclinic	Triclinic	Triclinic
Space group (number)	<i>P</i> 2 ₁ / <i>n</i> (14)	<i>P</i> -1 (2)	<i>P</i> 2 ₁ / <i>n</i> (14)	<i>P</i> -1 (2)	<i>P</i> -1 (2)
<i>a</i> (Å)	17.0889(4)	12.4703(5)	17.3830(7)	12.465(2)	12.2304(5)
<i>b</i> (Å)	17.6476(4)	16.1004(6)	18.1282(9)	12.722(2)	17.1665(6)
<i>c</i> (Å)	25.4652(6)	17.4477(7)	22.8519(12)	12.7592(13)	17.5702(7)
α (deg)	90	87.866(3)	90	104.113(11)	87.179(3)
β (deg)	98.496(2)	88.813(3)	109.520(6)	95.540(11)	87.928(3)
γ (deg)	90	76.859(3)	90	107.474(15)	83.282(3)
<i>V</i> (Å³)	7595.5(3)	3408.7(2)	6787.3(6)	1839.9(5)	3657.4(2)
<i>Z</i>	4	2	4	1	2
ρ_{calcd} (g cm⁻³)	1.962	1.940	1.949	1.992	2.021
μ (mm⁻¹)	2.186	2.408	2.419	2.253	12.589
reflins collected	56439	27996	53807	11585	25344
unique reflns (<i>R</i>_{int})	15720 (0.065)	14107 (0.056)	13706 (0.114)	7050 (0.069)	13033 (0.041)
observed reflns [<i>I</i> > 2σ(<i>I</i>)]	11755	10156	9271	4979	11265
Params (restrains)	861 (144)	727 (30)	724 (0)	308 (58)	791 (114)
<i>R</i>(<i>F</i>)^a [<i>I</i> > 2σ(<i>I</i>)]	0.061	0.068	0.090	0.196	0.115
<i>wR</i>(<i>F</i>²)^b (all data)	1.168	0.193	0.227	0.523	0.300
GoF	1.066	1.064	1.162	1.156	1.123

3.2.3. Gas sorption and dynamic vapor sorption (DVS) experiments

The samples were first thermally activated at 50 °C (**2-Mo8**) and 120 °C (**3-Mo8**), and then, degassed under vacuum and at the same temperature for 4 h prior to gas sorption experiments. The PXRD analyses of the degasified samples demonstrated that the structures of the anhydrous phases retain crystallinity and remain unmodified after being exposed to vacuum conditions. Nitrogen isotherms were recorded at 77 K whereas carbon dioxide isotherms were acquired at 195 K. The specific surface areas were calculated from

the N₂ adsorption branch using the Brunauer-Emmet-Teller (BET) method²⁵ and considering the consistency criteria for microporous materials.

Dynamic water vapor sorption studies were conducted using a DVS Endeavor Surface Measurement System device, which gravimetrically measures the uptake and loss of vapor. Samples of **1-Mo8** were thermally activated at 50 (**2-Mo8**) and 120 °C (**3-Mo8**) for 1 h before performing the sorption experiments from 0 to 95% Relative Humidity (RH) in 5% incremental RH steps. The sequential steps were controlled with an equilibrium criterion of $dm/dt = 0.05 \text{ \% min}^{-1}$. The temperature was maintained constant at 298 K by enclosing the system in a temperature-controlled incubator, and pure water was used as adsorbate. After reaching a RH level of 95%, this parameter was then decreased in a similar manner to achieve a full adsorption/desorption cycle. Two complete adsorption/desorption cycles were run for **2-Mo8**, and three for **3-Mo8**. Kinetics were monitored under a constant air flow of 30 % and 60% RH, whereas 100 adsorption/desorption cycles of 15 min were used for stability studies under a constant airflow of 60 % RH.

3.3. RESULTS AND DISCUSSION

3.3.1. Synthetic considerations

In the course of our systematic studies on the assembly of isopolyoxomolybdates with $\{\text{Cu}(\text{cyclam})\}^{2+}$, strong pH dependences of the resulting hybrid frameworks were found (Chapter 2). Conditions close to neutrality (pH = 6.9 to 8.5) in the aqueous system formed by a combination of commercial ammonium heptamolybdate and the in-situ prepared $\{\text{Cu}(\text{cyclam})\}^{2+}$ complex in a stoichiometric 1:3 ratio yielded to a purple crystalline powder in yields lower than 1% after slow evaporation of the final solution at room temperature for two weeks. The FTIR spectrum of **1-Mo8** revealed a collection of bands ascribed to the $\{\text{Cu}(\text{cyclam})\}^{2+}$ complex²⁶ in the organic region of the spectrum above 1100 cm⁻¹ and characteristic signals of the inorganic building-block below this wavenumber, which considerably differ from those of the heptamolybdate and the $\beta\text{-Mo}_8$ species well-known to predominate in solution at these conditions, thereby suggesting the presence of a novel polyoxomolybdate (Figure 3.3). In order to decrease the solubility, 1,4-dioxane was added in the last step to the reaction carried out at pH = 6.5. This synthetic modification did not change the nature of the final product according to FTIR and PXRD analyses (Figure 3.3), but shortened the crystallization time to 3 days and substantially increased the reaction yield to ca. 15 %.

However, the above crystals were not suitable in size for their structural characterization via single-crystal X-ray diffraction (sc-XRD), and hence, hydrothermal methods were selected as an alternative route to improve the crystallization process. The solution at pH 6.5 was stirred for 1 h at room temperature, transferred into a Teflon-lined autoclave, and kept at 140 °C for 72 h in an oven. Fortunately, the harsh conditions of this synthetic method allowed us to isolate purple prismatic crystals of **1-Mo8** suitable for sc-XRD analyses, the FTIR spectrum and PXRD pattern of which fits well with those obtained for the polycrystalline samples described above (Figure 3.3).

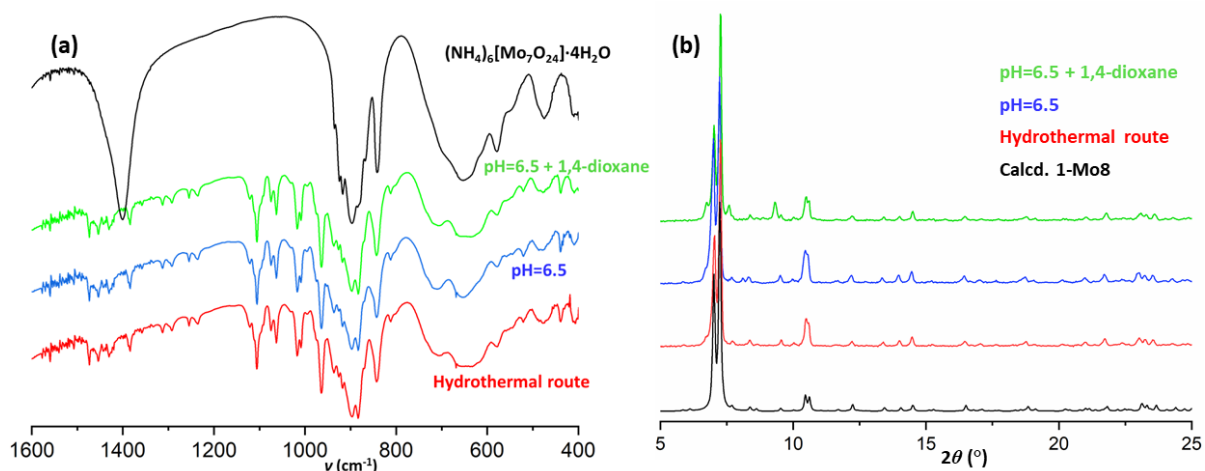


Figure 3.3. Comparison between (a) the FTIR spectrum and (b) PXRD pattern of the ammonium heptamolybdate precursor (black) and those registered for **1-Mo8** i) synthesized under mild bench conditions, followed by the addition of 1,4-dioxane as precipitating agent (green), ii) without the addition of 1,4-dioxane (blue); and, iii) single-crystals obtained by the hydrothermal route (red).

3.3.2. Thermostructural behavior

Thermal stability of **1-Mo8** was first investigated by a combination of thermogravimetric/ differential thermal analyses (TGA/DTA) and variable temperature PXRD. The TGA curve evidences that the thermal decomposition of **1-Mo8** occurs via three well-defined stages (Figure 3.5a). The first thermal event goes from room temperature to ca. 100 °C and corresponds to the endothermic loss of 14 H₂O molecules per Mo₈ unit (m%, calcd. 88.8 %; found 88.5 %). The resulting anhydrous form displays a significant thermal stability range that extends up to ca. 230 °C, which is followed by a second mass loss associated with the combustion of the organic ligands and the breakdown of the POM framework (calcd. 26.7 %; found 26.3 %). PXRD analyses (Figure 3.4) proved that the final residue at 540 °C corresponds to a mixture of orthorhombic *Pbnm* MoO₃ (PDF: 01-076-1003) and triclinic *P-1* CuMoO₄ (PDF: 01-073-0488) in an approximate 5:3 ratio, in good agreement with the observed mass percentage values (calcd. for Cu₃Mo₈O₂₇ 62.0 %; found 62.2 %).

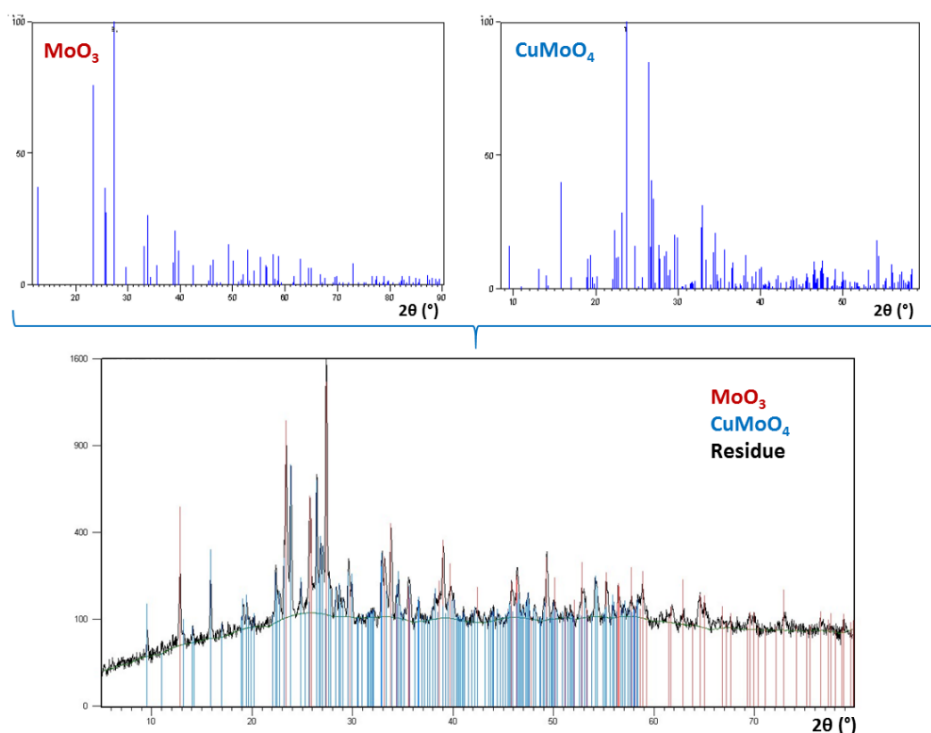


Figure 3.4. Identification by PXRD analyses of the final residue from the thermal decomposition of **1-Mo8** into MoO_3 and CuMoO_4 .

To explore the thermostructural behavior of framework **1-Mo8** (i.e. whether it shows crystallinity retention over amorphization with increasing temperature, and in the former case, whether it displays framework dynamism vs robustness) variable temperature PXRD patterns were recorded from room temperature to 600 °C every 20 °C (Figure 3.5b). Results showed that our hybrid is able to retain crystallinity throughout the whole dehydration process and beyond up to 230 °C, in line with the thermal stability range found in the TGA curve. Upon heating, compound **1-Mo8** rapidly transforms into a new crystalline phase (**2-Mo8**) as indicated by major modifications in both positions and relative intensities of the main diffraction maxima. In particular, the two intense maxima at $2\theta = 7.1$ and 7.4° positions split into three different signals located at 7.3 , 7.5 , and 7.7° for **2-Mo8** (Figure 3.5c). It is also worth mentioning the fact that the maxima at 10.5° vanish upon structural transition and new signals can be observed at $2\theta = 11.3$, 22.5 , and 23.2° . Considering that this transformation takes place at values close to room temperature, additional PXRD patterns were collected from 30 to 46 °C every 2 °C to explore this phase transition in depth (Figure 3.5d). These experiments revealed that **2-Mo8** is already fully formed at 36 °C, and according to the TGA curve from **1-Mo8**, could be thought to correspond to a partially dehydrated phase. However, no mass loss associated with the release of water molecules was observed in the thermogravimetric analyses carried out for a crystalline sample of **1-Mo8** previously kept in an oven at 40 °C for 1 h to ensure its full conversion into **2-Mo8**. This fact confirms i) the slow kinetics governing the removal of guest solvent molecules

from **1-Mo8**, and ii) the anhydrous nature of **2-Mo8**. Compound **2-Mo8** keeps stable until 110 °C, but undergoes an additional transition above this temperature, transforming in turn into a high-temperature second anhydrous phase (**3-Mo8**), as indicated by the emergence of a new pair of most intense maxima at 7.4 and 7.8° with an approximate 3:1 intensity ratio.

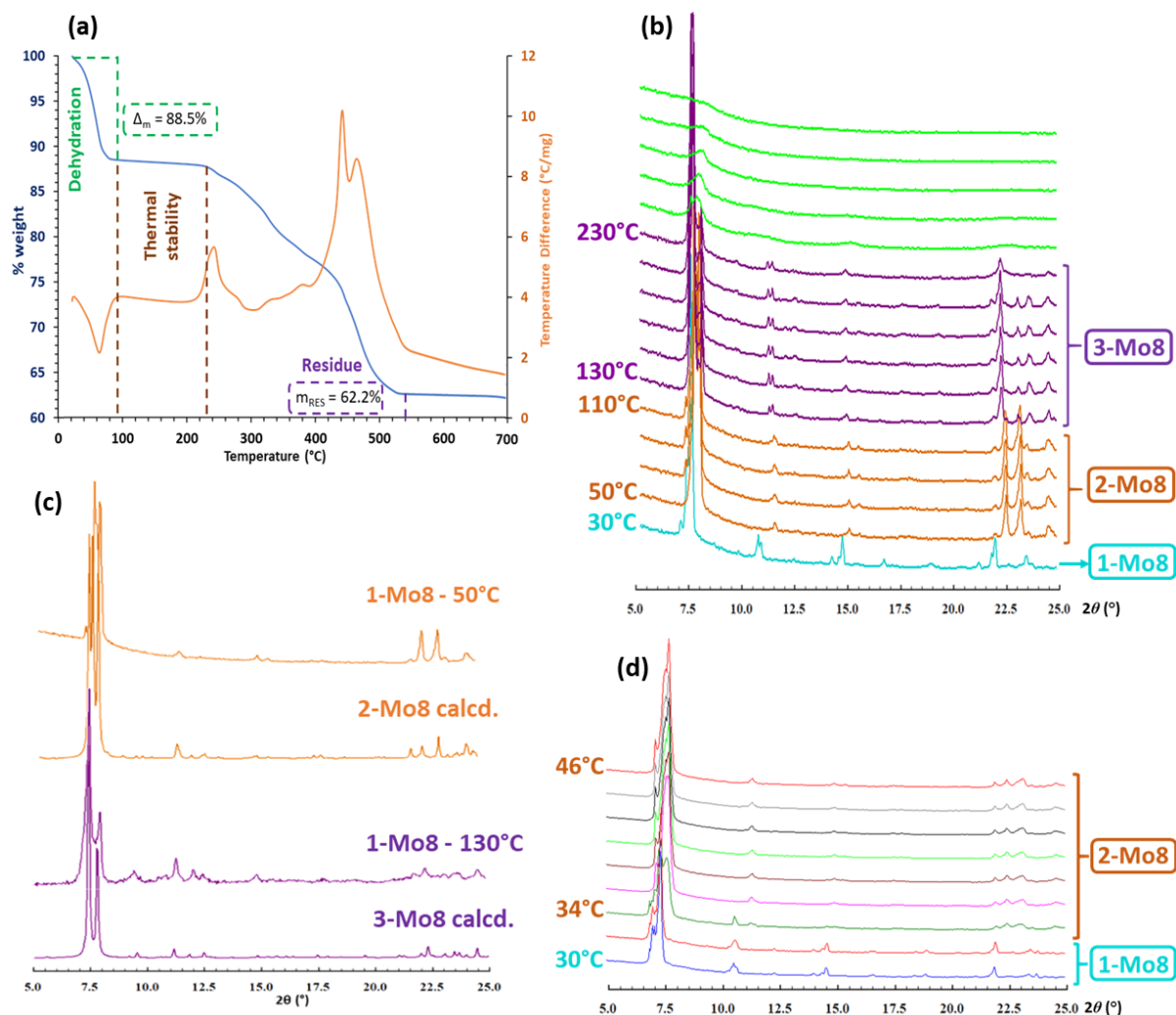


Figure 3.5. (a) TGA/DTA experiments; (b) variable-temperature powder X-ray diffraction patterns of **1-Mo8** in the 30–320 °C range, and; (c) comparison between the experimental patterns for **2-Mo8** and **3-Mo8** and those simulated from sc-XRD data.

3.3.3. Crystal structure of 1-Mo8

Compound **1-Mo8** crystallizes in the monoclinic space group $P2_1/n$ with an asymmetric unit containing one $[\kappa\text{-Mo}_8\text{O}_{27}]$ -octamolybdate anion ($\kappa\text{-Mo8}$), a total of three $\{\text{Cu}(\text{cyclam})\}^{2+}$ complexes, of which two (Cu1A and Cu1B) located in general positions and another two on centers of symmetry (Cu1C and Cu2C), and 14 water molecules of hydration disordered over 20 crystallographic sites (Figure 3.6). The $\kappa\text{-Mo8}$ anion is unprecedented, thereby enlarging the current catalog of octamolybdate clusters in the

CHAPTER 3

literature (Table 3.1). It can be best described as one $\{\text{Mo}_4\text{O}_{16}\}$ tetramer and one $\{\text{Mo}_3\text{O}_{13}\}$ trimer fused together by sharing one face and one corner between MoO_6 octahedra. The eighth Mo-metal center exhibits square pyramidal geometry and being connected to the tetramer by edge-sharing and to the trimer by sharing two corners (Figure 3.6b). It is worth remarking that face-sharing octahedra have never been observed in any of the octamolybdate species reported to date, which to our knowledge comprise up to nine different structural isomers for the $[\text{Mo}_8\text{O}_{26}]^{4-}$ anion, namely $\alpha, \beta, \gamma, \delta, \epsilon, \zeta, \eta, \theta$ and ι ,⁶⁻⁹ and a single isomeric form (γ) for the oxygen-rich $\{\text{Mo}_8\text{O}_{28}\}^{6-}$ counterpart. Despite the huge variety of MoO_x units ($x = 4-6$) and polyhedral connectivity shown in Table 3.1 for octamolybdate isomers, the face-sharing feature of $\kappa\text{-Mo8}$ remarks on its structural novelty.

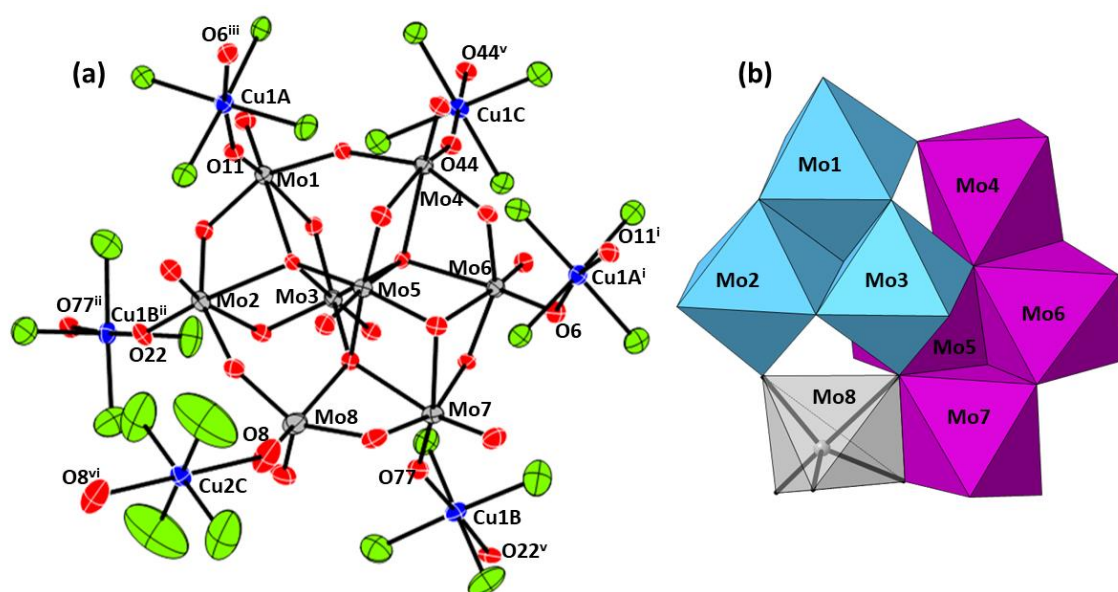


Figure 3.6. (a) ORTEP representation of **1-Mo8**, showing 50% probability ellipsoids, together with the atom labelling scheme. The C and H atoms, as well as water molecules of hydration have been omitted for clarity. Color code: Mo, light grey; Cu, blue; O, red; N, green. Symmetry codes: i) $1/2-x, 1/2+y, 3/2-z$; ii) $3/2-x, -1/2+y, 3/2-z$; iii) $1/2-x, -1/2+y, 3/2-z$; iv) $1-x, 1-y, 2-z$; v) $3/2-x, 1/2+y, 3/2-z$; vi) $1-x, 1-y, 1-z$. (b) Polyhedral representation of the $\kappa\text{-Mo8}$ anion in **1-Mo8**, together with the atom labelling scheme. The $\{\text{Mo}_4\text{O}_{16}\}$ tetramer and $\{\text{Mo}_3\text{O}_{13}\}$ trimer are highlighted in pink and light blue, respectively, whereas the pentacoordinated center is represented in ball & stick in a translucent grey polyhedra.

All Cu^{II} centers from $\{\text{Cu}(\text{cyclam})\}^{2+}$ complexes display octahedral CuN_4O_2 coordination geometry with the N atoms of the cyclam ligands in equatorial positions and terminal O_{POM} atoms occupying both axial positions. Significant Jahn-Teller distortions are present in all complexes, the longest $\text{Cu1A}-\text{O}_{\text{POM}}$ bond length of $2.876(5)$ Å being close to that of semi-coordination (Table A3.1 in Appendix 3). The crystal packing of **1-Mo8** (Figure 3.7) consists of a 3-dimensional covalent open-framework in which hybrid layers of $\kappa\text{-Mo8}$ clusters linked to four neighbors through four bridging complexes (Cu1A, Cu1B, Cu1C and Cu2C) can be identified in the crystallographic (1-10) plane (Figure 3.7b). This pattern

results in rhombic-like grids with two types of voids arranged alternately along the crystallographic z axis and with adjacent κ -**Mo8** anions pointing their $\{\text{MoO}_5\}$ unit at opposite sides of the layer midplane. Such grids are further connected through coordination of two additional octahedral complexes (Cu1A^i and Cu1B^{ii} , see Figure 3.7 for the symmetry codes) to result in a 3-dimensional covalent architecture in which multiple $\text{C-H}\cdots\text{O}_{\text{POM}}$ and $\text{N-H}\cdots\text{O}_{\text{POM}}$ contacts established between cyclam ligands and POM surfaces play a relevant reinforcing role (Table A3.2 in Appendix 3).

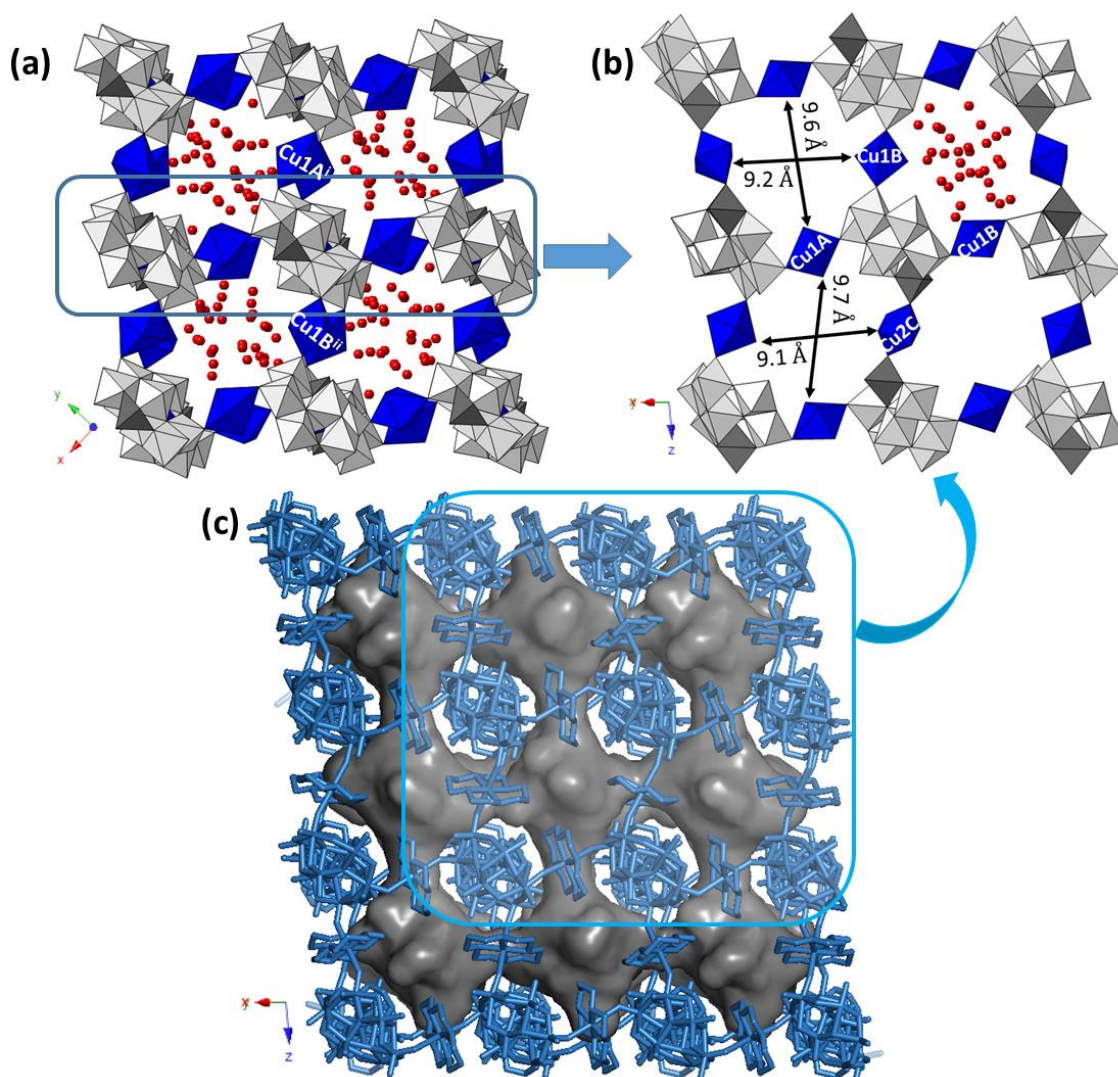


Figure 3.7. (a) Packing of κ -**Mo8** along the crystallographic z axis with the $\{\text{MoO}_5\}$ polyhedra of κ -**Mo8** highlighted in dark gray, the $\{\text{CuN}_4\text{O}_2\}$ octahedra of the complexes in blue and O_w atoms depicted as red spheres. The C, and H atoms are omitted for clarity. Symmetry codes, i) $1/2-x, -1/2+y, 3/2-z$; ii) $3/2-x, 1/2+y, 3/2-z$. (b) Projection of a hybrid layer in κ -**Mo8** parallel to the (1-10) plane. (c) Surface representation of the water-filled, interconnected channels in the crystal packing of κ -**Mo8** in the [1-10] direction.

This open-framework architecture exhibits a 3-dimensional system of intersected, water-filled channels made of globular wide cavities located at the space between 8 neighboring clusters and connected through narrow necks defined by 4 neighboring complexes. These channels run along the crystallographic [001], [1-10] and [110] directions, their necks show cross-sections of *ca.* 9.7 × 9.1 and 9.6 × 9.2 Å (interatomic distances between opposite N atoms of the grid voids), and their total solvent accessible volume accounts for 32 % of the unit cell volume as calculated by PLATON (Figure 3.7c).²⁷

3.3.4. SCSC transformations upon heating: isomerization of octamolybdate anions

To determine the structural changes that the aforementioned thermally-triggered transitions imply, scXRD experiments were conducted on crystals of **1-Mo8** heated for 1h at 50 and 120 °C in an oven to ensure full transformation into the anhydrous **2-Mo8** and **3-Mo8** phases, respectively. Crystals were mounted on the diffractometer previously set at such temperatures, unit cell parameters were registered to confirm the transformation and to check for any potential cracking or twinning, and samples were afterwards quenched down to 100 K to get diffraction data sets of the best possible quality.

Removal of water molecules at 50 °C provokes a decrease of the total unit cell volume to less than one half in comparison to **1-Mo8**, which is associated to the reduction of the total symmetry to the triclinic *P*-1 space group. Unit cell parameters of **2-Mo8** are similar to those of the parent hydrated phase except for the *a* dimension which is one half of *c* dimension in **1-Mo8**. Now the asymmetric unit contains one [λ -Mo₈O₂₇]⁶⁻·(**λ-Mo8**) cluster and a total of three {Cu(cyclam)}²⁺ moieties; one of them located in a general position (Cu1C) and four halves of centrosymmetric complexes (Cu1A, Cu2A, Cu1B, Cu2B) (Figure 3.8).

Table 3.3. Mo...Mo distances (Å) in **1-Mo8**, **2-Mo8**, **3-Mo8**, **4-Mo8**, and **5-Mo8**.

	1-Mo8	2-Mo8	3-Mo8	4-Mo8	
Mo1...Mo5	3.949	3.204	3.192		
Mo2...Mo5	3.943	4.054	4.266		
Mo3...Mo4	4.023	3.242	3.217		
Mo3...Mo5	3.085	3.381	3.453		
Mo3...Mo6	3.919	4.027	4.402		
Mo7...Mo3	3.975	3.787	3.228		
Mo7...Mo5	3.433	3.648	3.388		
Mo7...Mo6	3.258	3.717	3.291		
Mo8...Mo2	3.666	3.685	3.658	3.317	Mo4...Mo2
Mo8...Mo3	3.994	4.466	4.724	3.401	Mo4...Mo3
Mo8...Mo5	3.450	4.016	4.972	5.733	Mo4...Mo1
Mo8...Mo7	3.209	3.418	4.397	3.869	Mo4...Mo1'

The octamolybdate cluster undergoes a κ to λ isomerization upon structural transition. This isomerization implies rupture of the face-sharing connection between $\{\text{Mo}_4\text{O}_{16}\}$ and $\{\text{Mo}_3\text{O}_{13}\}$ fragments observed in the κ -form and formation of the edge-sharing $\{\text{Mo}_6\text{O}_{22}\}$ moiety exhibited by the new λ -type anion, which is similar to the cap displayed by the well-known $[\beta\text{-Mo}_8\text{O}_{26}]^{8-}$ anion (Figure 3.8). This process involves the rupture of two Mo– $\mu^3\text{O}$ bonds and consequent modifications, as follows: i) the seventh $\{\text{MoO}_6\}$ octahedron goes from exclusively sharing edges in the κ -form to exclusively sharing corners in the λ isomer, and ii) the eighth metal-oxo unit decreases its coordination number from five to four (tetrahedral geometry) and is linked to each of the fragments above by sharing one corner. These rearrangement involves solid-state migration of some metal centers within the cluster skeleton (Table 3.3).

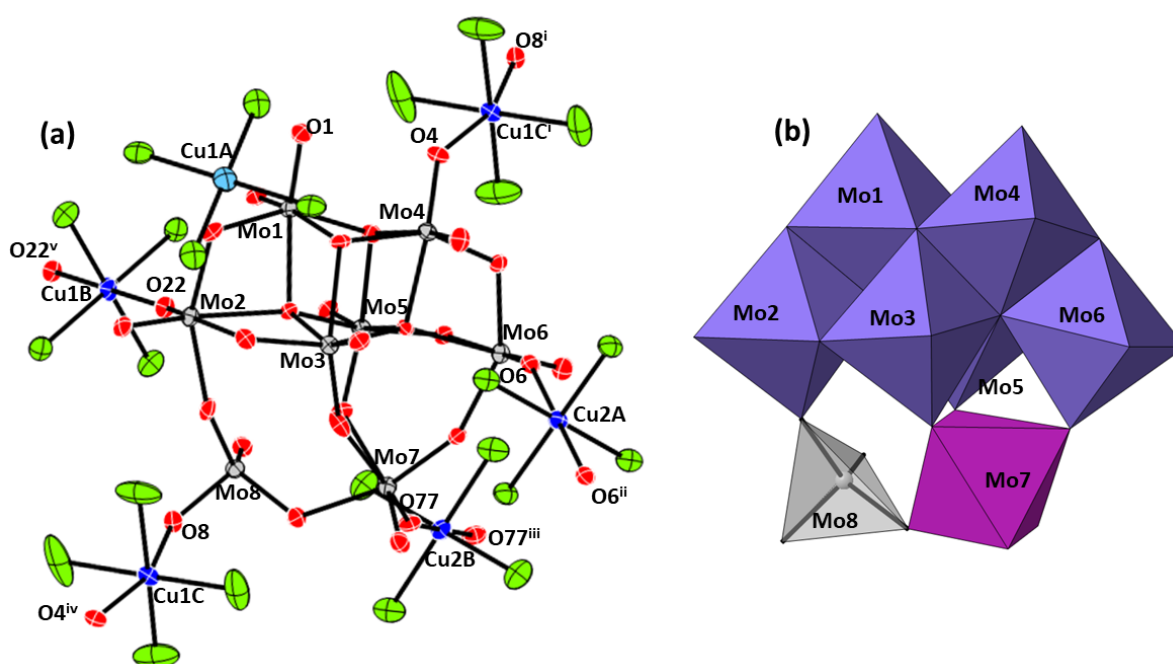


Figure 3.8. (a) ORTEP representation of **2-Mo8**, showing 50% probability ellipsoids, together with the atom labelling scheme. The C, and H atoms, as well as water molecules of hydration have been omitted for clarity. Color code: octahedral Cu, blue, square planar Cu, light blue. Symmetry codes: i) $-1+x, y, z$; ii) $1-x, -y, -z$; iii) $1-x, 1-y, -z$; iv) $1+x, y, z$; v) $1-x, 1-y, 1-z$. (b) Polyhedral representation of the λ -**Mo8** anion in **2-Mo8**, together with the atom labelling scheme. Color code: $\{\text{Mo}_6\text{O}_{22}\}$ hexamer, lilac; additional $\{\text{MoO}_6\}$, pink; tetracoordinated $\{\text{MoO}_4\}$, grey polyhedra.

With regard to the crystal packing of **2-Mo8**, hybrid layers in the (01-1) plane are analogous to those described for **1-Mo8** with each λ -**Mo8** unit linked to four neighboring clusters through four bridging metal complexes to result in a rhombic-like grid. However, two distinct cavities very distinct in size can be defined in **2-Mo8**: those delimited by Cu1B and Cu1C complexes, which are comparable in size to the voids in **1** ($9.2 \times 9.4 \text{ \AA}$), and those delimited by Cu2A and Cu1C complexes with much smaller dimensions of $7.5 \times 8.6 \text{ \AA}$ (Figure 3.9). The connection between these sheets is also different in comparison to **1-Mo8**,

because only one half of the $\{\text{Cu}(\text{cyclam})\}^{2+}$ complexes located in the intralamellar space retain their axially elongated octahedral geometry (Cu2B), whereas the other half becomes square planar (Figures 3.10 and 3.11). The latter Cu1A complexes lose their character as covalent linkers [$\text{Cu1A}\cdots\text{OPOM}$: $3.446(7)\text{\AA}$], but still play a significant role in stabilizing the stacking of hybrid grids by establishing massive hydrogen bonding with tetrameric faces of $\lambda\text{-Mo8}$ clusters from adjacent sheets (Figure 3.10 and Table A3.2 in Appendix 3). The connection between interlamellar cavities located at the space among clusters is disrupted through the necks involving Cu1A and Cu2A fragments; hence, the 3-dimensional solvent-accessible network found in **1-Mo8** is dismantled in **2-Mo8**. Those cavities nevertheless remain connected through strings of alternate wider and narrower necks arranged along the crystallographic y axis in zig-zagging mode, giving rise to a porous system of parallel individual channels that diagonally intersect the stacking of hybrid layers (Figure S14). These pores are obviously empty in **2-Mo8** and correspond to 24 % of the unit cell volume according to PLATON (Figure 3.9c).

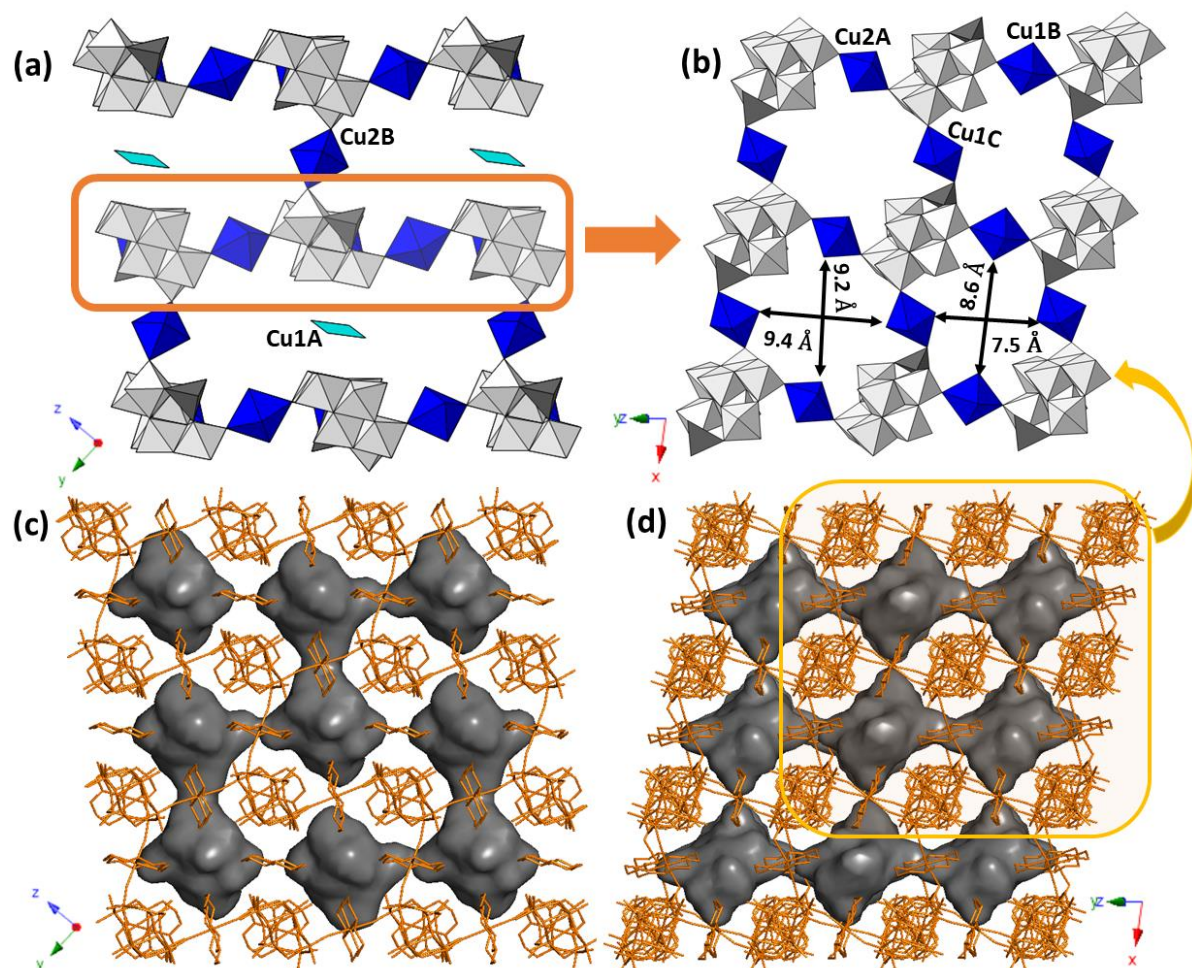


Figure 3.9. (a) View of the crystal packing of **2-Mo8** along the crystallographic x axis. (b) Projection of hybrid layers in **2-Mo8** parallel to the (01-1) plane. Surface representation of interconnected solvent accessible channels in the (c) x axis, and (d) [01-1] direction.

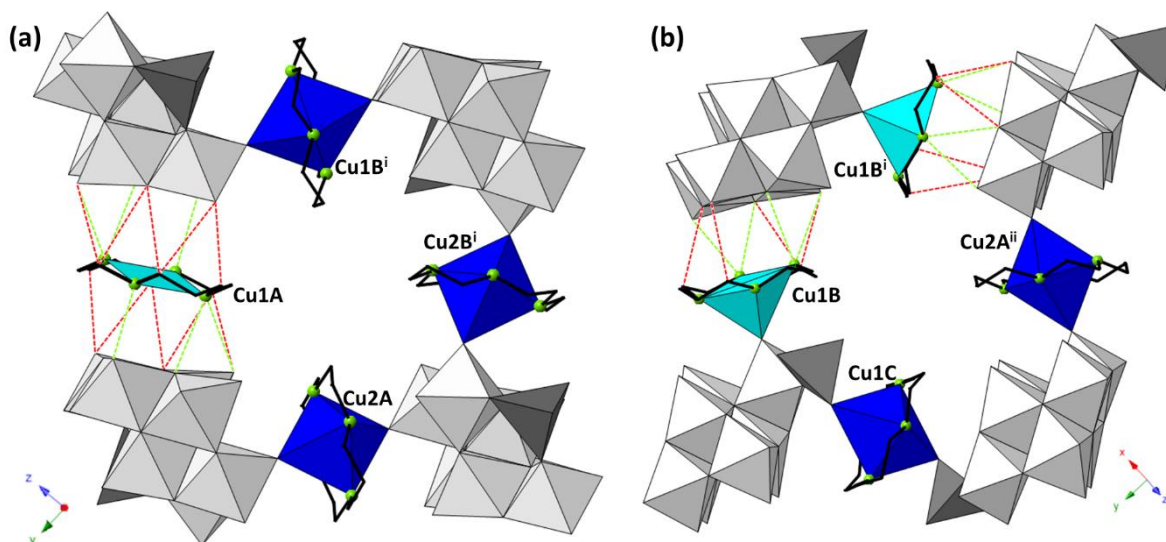


Figure 3.10. (a) Connectivity between contiguous layers in **2-Mo8** via C–H···O and N–H···O type contacts established between interlamellar {Cu(cyclam)}²⁺ complexes and tetrameric faces of the Mo8 fragments. (b) Intralamellar contacts in **3-Mo8**. N–H···O_{POM} and C–H···O_{POM} contacts are depicted as dashed red and green lines, respectively. Symmetry codes: (a) i) $x, -1+y, z$; (b) i) $\frac{1}{2}-x, -\frac{1}{2}+y, \frac{1}{2}-z$; ii) $1-x, 1-y, -z$.

1-Mo8	2-Mo8	3-Mo8	4-Mo8	5-Mo8
Cu1A ¹⁻⁶	Cu1A ¹⁻¹ (sq pl) Cu2A ⁶⁻⁶	Cu1A ¹⁻⁷ Cu2A ⁶⁻⁶	Cu1A ¹⁻¹	Cu1A ¹⁻¹
Cu1B ²⁻⁷	Cu1B ²⁻² Cu2B ⁷⁻⁷	Cu1B ²⁻⁴ (sq pyr)	Cu1B ²⁻²	Cu1B ²⁻⁶ Cu2B ⁷⁻⁷
Cu1C ⁴⁻⁴ Cu2C ⁸⁻⁸	Cu1C ⁴⁻⁸	Cu1C ⁸⁻⁸	Cu1C ⁴⁻⁴	Cu1C ⁴⁻⁴ Cu2C ⁸⁻⁸

CuN₄O₂
Octahedral Cu²⁺

CuN₄O
Square pyramidal
(sq pyr) Cu²⁺

CuN₄
Square planar
(sq pl) Cu²⁺

Figure 3.11. Coordination geometries and equivalences of the {Cu(cyclam)}²⁺ complexes found in compounds **1-Mo8**, **2-Mo8**, **3-Mo8**, **4-Mo8** and **5-Mo8**, indicating linkage sites to Mo8 anions as superscript. Color code: Cu, blue spheres; O, red spheres; N, green spheres; C, black sticks.

When crystals are heated at higher temperatures, a second anhydrous phase (**3-Mo8**) is obtained, which crystallizes in the same monoclinic group as **1-Mo8** with similar unit cell dimensions, but a different β angle. The a and b dimensions are lengthened in ca. 0.5 Å when going from **1-Mo8** to **3-Mo8**, whereas c is shortened as much as 2.5 Å. The

asymmetric unit in **3-Mo8** (Figure 3.12) contains one $[\mu\text{-Mo}_8\text{O}_{27}]^{6-}$ ($\mu\text{-Mo8}$) cluster and a total of four $\{\text{Cu}(\text{cyclam})\}^{2+}$ moieties; two of them located in a general position (Cu1A and Cu1B) and two halves of centrosymmetric complexes (Cu2A, Cu1C). Phase transition involves further isomerization of the Mo_8 cluster to the μ isomer (Figure 3.12b), which exhibits the $\{\text{Mo}_7\text{O}_{24}\}$ fragment of the $[\beta\text{-Mo}_8\text{O}_{26}]^{8-}$ anion, with a highly distorted $\{\text{MoO}_6\}$ unit originating from that which only exhibited corner sharing linkage in the λ isomer. The eighth tetrahedral $\{\text{MoO}_4\}$ unit shares a single O atom with the former fragment. It is worth highlighting that the three isomers reported in this work have never been observed before and hence, this fact suggests that solid-state transformations can afford POM anions, different from those obtained by conventional synthetic routes in solution.

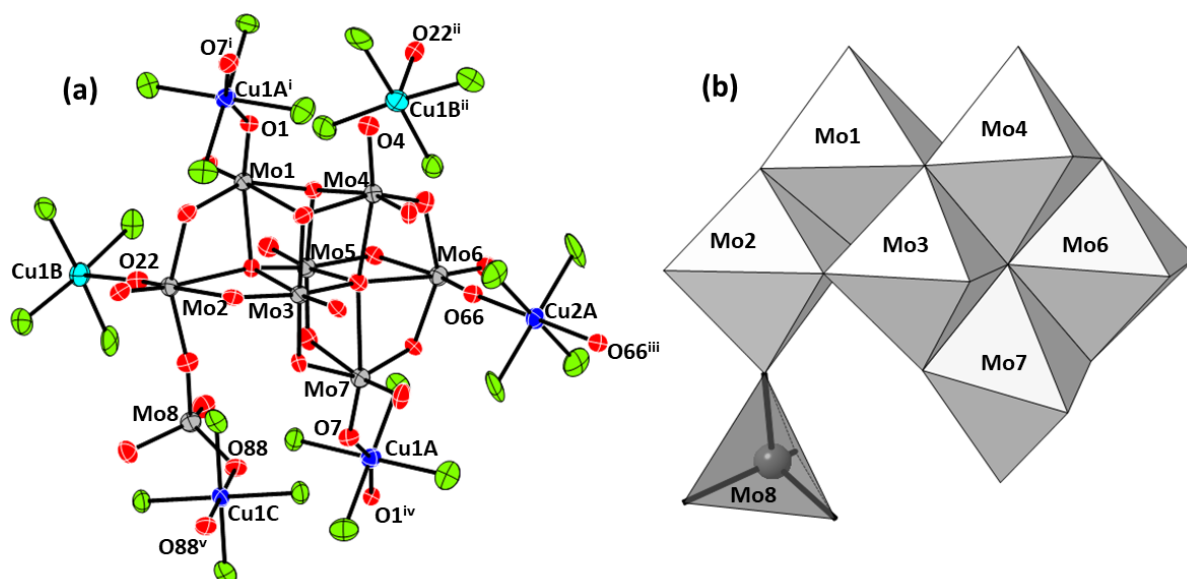


Figure 3.12. (a) ORTEP representation of **3-Mo8**, showing 50% probability ellipsoids, together with the atom labelling scheme. The C, and H atoms have been omitted for clarity. Symmetry codes: i) $-1+x, y, z$; ii) $1-x, -y, -z$; iii) $1-x, 1-y, -z$; iv) $1+x, y, z$; v) $1-x, 1-y, 1-z$. (b) Polyhedral representation of the $\mu\text{-Mo}_8$ anion in **3-Mo8**, together with the atom labelling scheme. The tetracoordinated center is highlighted in dark grey.

In comparison to **1-Mo8** and **2-Mo8**, the covalent 3-dimensional framework in **3-Mo8** is broken, because the intralamellar moiety Cu1B becomes pentacoordinated as a result of a Cu–O bond cleavage. This complex loses its character as covalent linker and becomes a surface appended unit. Conversely, complexes Cu2A and Cu1C retain their bridging role in such a way that each $\mu\text{-Mo}_8$ anion gets covalently connected to two neighbors (Figure 3.13). Nevertheless, surface appended complexes still play an important role stabilizing the hybrid layer by establishing a massive hydrogen bonding network with the tetrameric faces of $\mu\text{-Mo}_8$ fragments (Figure 3.10 and Table A3.2 in Appendix 3). The stacking of these supramolecular arrangements along the $[101]$ direction is facilitated by bridging and octahedral Cu1A complexes located in the interlamellar space (Figure 3.13). The supramolecular network exhibits a priori accessible channels along the $[101]$ direction with

an approximate cross-section of $8.6 \times 8.4 \text{ \AA}$. These voids account for 1561 \AA^3 per unit cell, that is, 23% of the total cell volume, as calculated by PLATON.

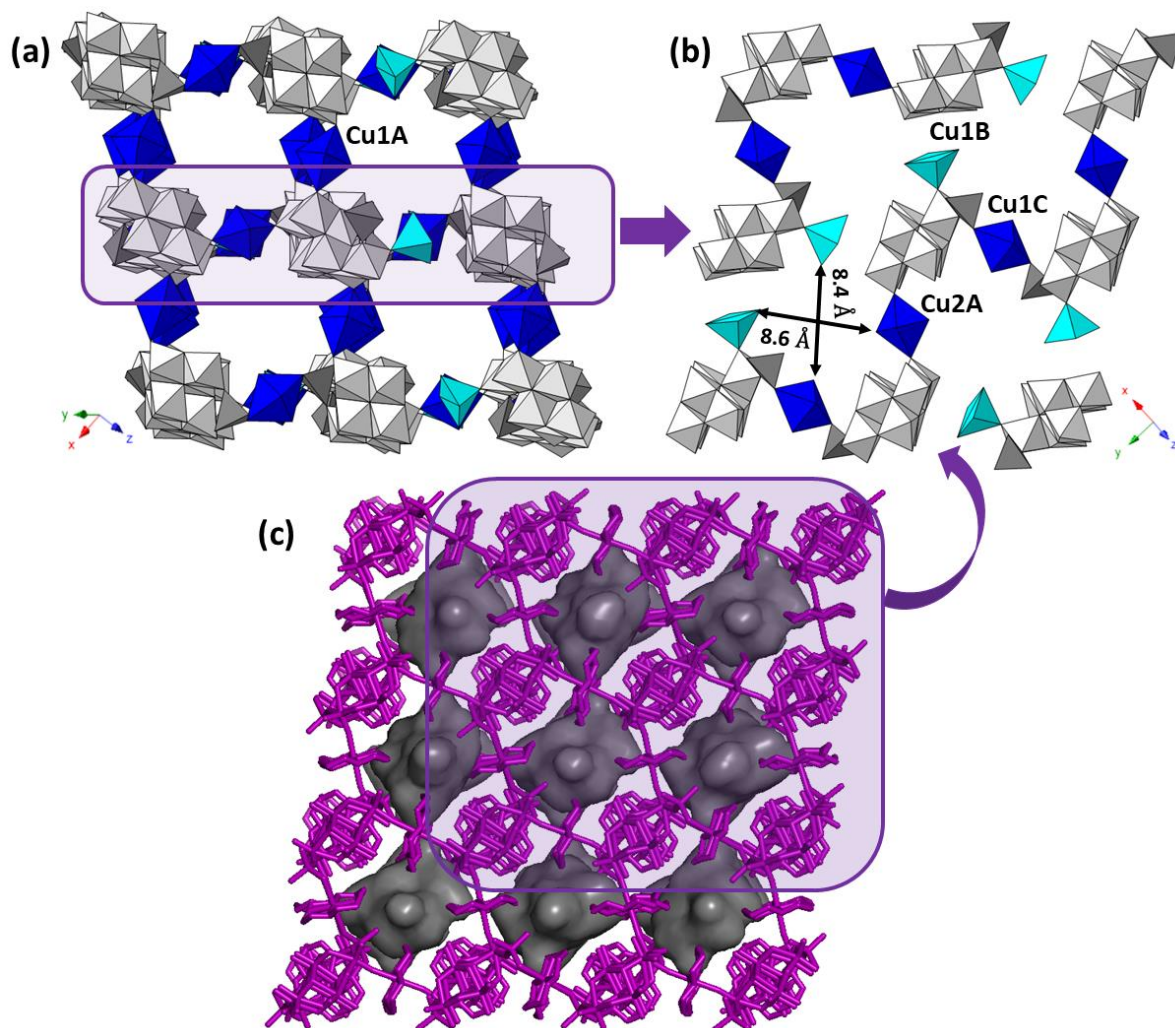


Figure 3.13. (a) Crystal packing of **3-Mo8** viewed along the $[-121]$ direction. (b) Projection of supramolecular hybrid layer in **3-Mo8** parallel to the (101) plane. Square pyramidal $\{\text{Cu}(\text{cyclam})\}^{2+}$ complexes are highlighted in light blue. c) Surface representation of isolated voids in the $[101]$ direction.

3.3.5. Reversibility of the SCSC transformations

In order to study the reversibility of the thermally-triggered structural transformations, crystalline samples of anhydrous **2-Mo8** and **3-Mo8** were exposed to open atmosphere and monitored by a combination of TGA and PXRD analyses. When it comes to **3-Mo8**, thermal analyses recorded after 1, 3, and 7 days of air exposure revealed that the anhydrous phase captures a significant amount of water for one week. Mass losses account for approx. 10, 11 and 12 (%m, calcd. 9.8, found 9.6) water molecules, respectively. After this period, no additional water molecules were adsorbed and hydration/dehydration processes proved to be fully reversible (Figures 3.14). These results are in line with those from PXRD studies which indicates that a new crystalline phase (**4-Mo8**) different from the parent hydrated phase **1-Mo8** starts forming upon hydration, but it is not fully formed until

CHAPTER 3

the seventh day (Figure 3.15a). In an attempt to favor a faster transformation, additional studies (Figure 3.15b) showed that **3-Mo8** could hydrate in 24 hours, if crystals are placed in a humid atmosphere (see Appendix A2).

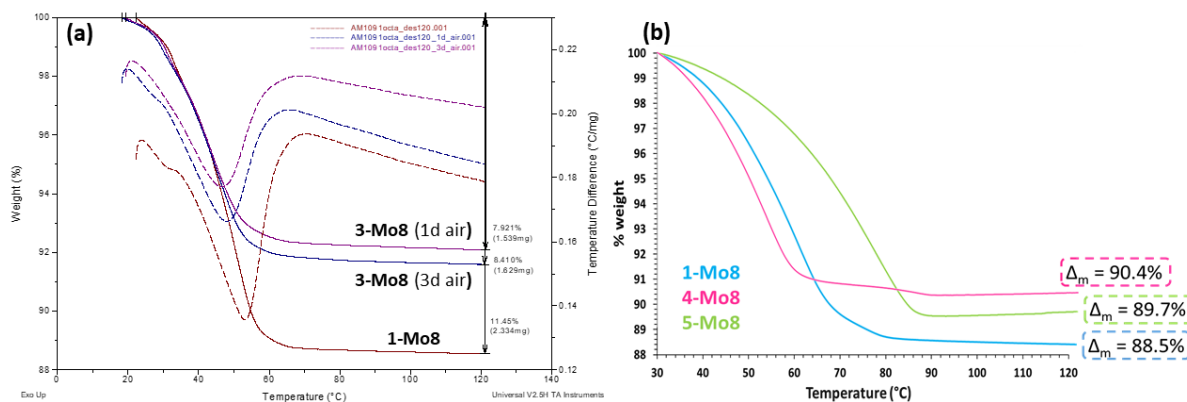


Figure 3.14. (a) TGA curves for dehydration steps in **1-Mo8**, and samples of **3-Mo8** hydrated in air for 1 and 3 days. (b) TGA curves for the dehydration steps in **1-Mo8**, **4-Mo8** and **5-Mo8**.

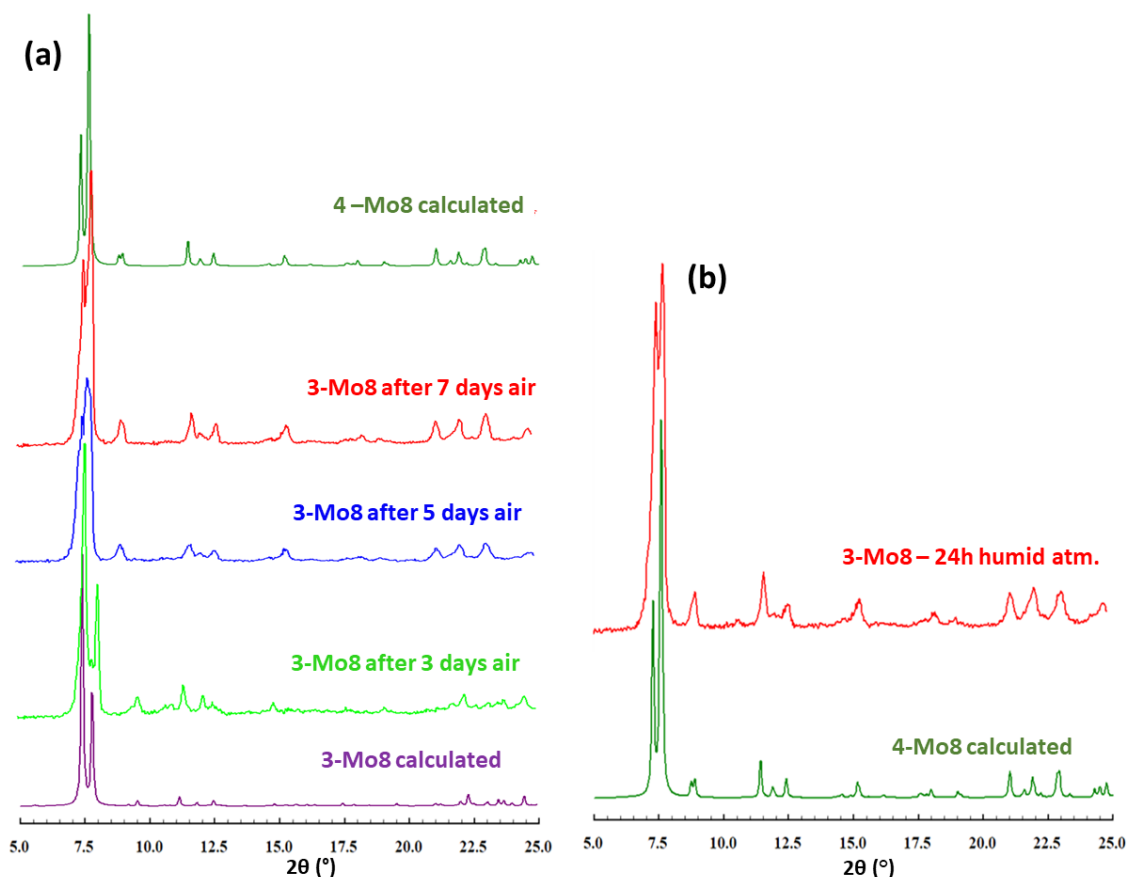


Figure 3.15. (a) PXRD patterns of **3-Mo8** exposed to open atmosphere for 3, 5 and 7 days compared with calculated patterns from scXRD data for **3-Mo8** and **4-Mo8**. (b) PXRD pattern of **3-Mo8** exposed to a humid atmosphere for 24h compared with the calculated pattern from scXRD data for **4-Mo8**.

Taking into account the interesting crystal dynamics displayed by this system, we tested whether the structure of **4-Mo8** could be elucidated by scXRD analyses. Fortunately, the full data acquisition on a single-crystal of **3-Mo8** hydrated in air for 7 week was suitable enough to allow its structural resolution. Compound $[\{\text{Cu}(\text{cyclam})\}_3\{\gamma\text{-Mo}_8\text{O}_{26}(\text{OH})_2\}]\cdot 11\text{H}_2\text{O}$ (**4-Mo8**) crystallizes in the triclinic $P-1$ space group and its asymmetric unit contains one-half of the $\{\gamma\text{-Mo}_8\text{O}_{26}(\text{OH})_2\}^{6-}$ polyanion, three halves of crystallographically independent, $\{\text{Cu}(\text{cyclam})\}^{2+}$ moieties and a total of 5.5 water molecules disordered over 9 sites (Figure 3.16).

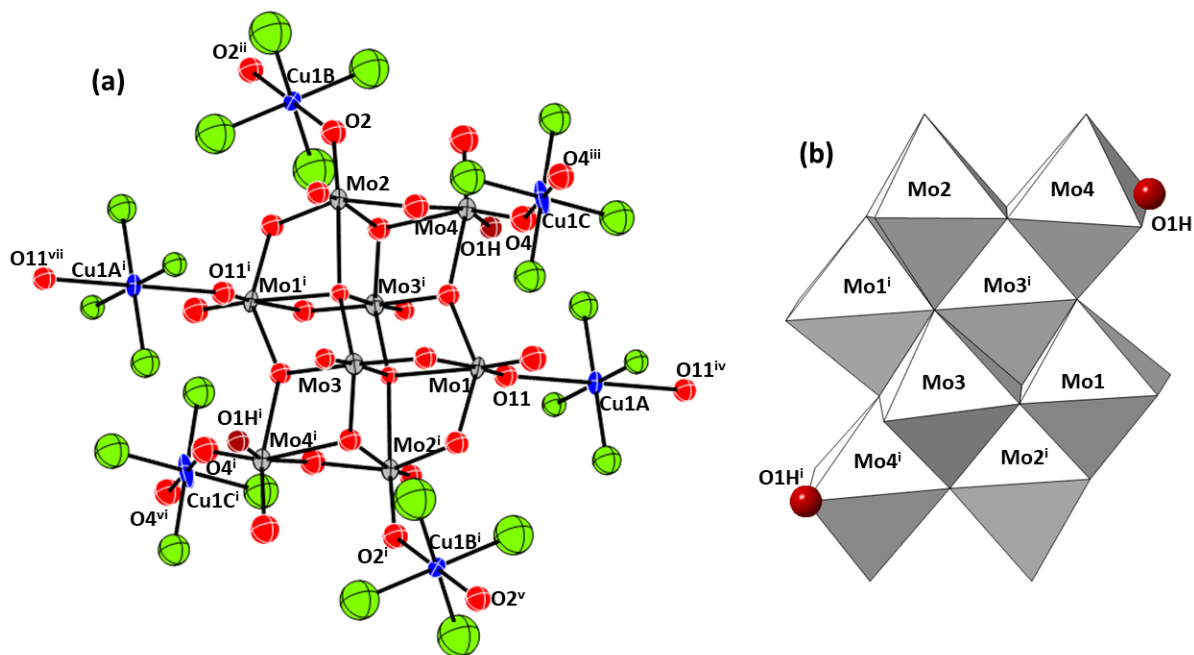


Figure 3.16. (a) ORTEP representation of **4-Mo8**, showing 50% probability ellipsoids, together with the atom labelling scheme. The C, and H atoms, as well as water molecules of hydration have been omitted for clarity. Symmetry codes: i) $-x, 1-y, 2-z$; ii) $-x, 1-y, 1-z$; iii) $1-x, 1-y, 2-z$; iv) $-x, -y, 2-z$; v) $x, y, 1+z$; vi) $-1+x, y, z$; vii) $x, 1+y, z$. (b) Polyhedral representation of the $[\gamma\text{-Mo}_8\text{O}_{26}(\text{OH})_2]^{6-}$ anion in **4-Mo8**, together with the atom labelling scheme. The protonated O atoms from the POM anion are depicted as dark red balls.

The octamolybdate anion in **4-Mo8** is the well-known $[\gamma\text{-Mo}_8\text{O}_{26}(\text{OH})_2]^{6-}$ isomer formed by two $\{\text{Mo}_4\text{O}_{15}(\text{OH})\}$ tetramers that share three edges.²¹ This implies that one water molecule is condensed to the inorganic POM skeleton along the hydration process. Protonation sites have been unequivocally assigned on the basis of Bond Valence Sum (BVS) calculations,²⁸ which afforded BVS values of 0.80 for hydroxide groups (Table 3.4). The isomerization of the Mo_8 anion to a more condensed form suggests that the thermodynamically favored species is obtained after all the dehydration-hydration processes, whereas all the previous isomers in **1-Mo8**, **2-Mo8** and **3-Mo8** can only be obtained because of the stabilization arising from the presence of a massive network of hydrogen bonding established between cyclam ligands and surface O atoms from the POM.

In fact, these weak but cooperative forces could be considered the key factor to allow such consecutive SCSC transformations.

Table 3.4. BVS calculation values for the O atoms from Mo8 anions in 4-Mo8.

O _t (terminal oxygen)	BVS	O _b (bridging oxygen)	BVS
O1	1.75	O12	1.86
O11	1.90	O13	1.85
O2	1.57	O123	1.96
O22	1.97	O134	2.06
O3	1.63	O24	1.82
O4	2.02	O234	1.76
O44	1.64		
O1H	0.80		

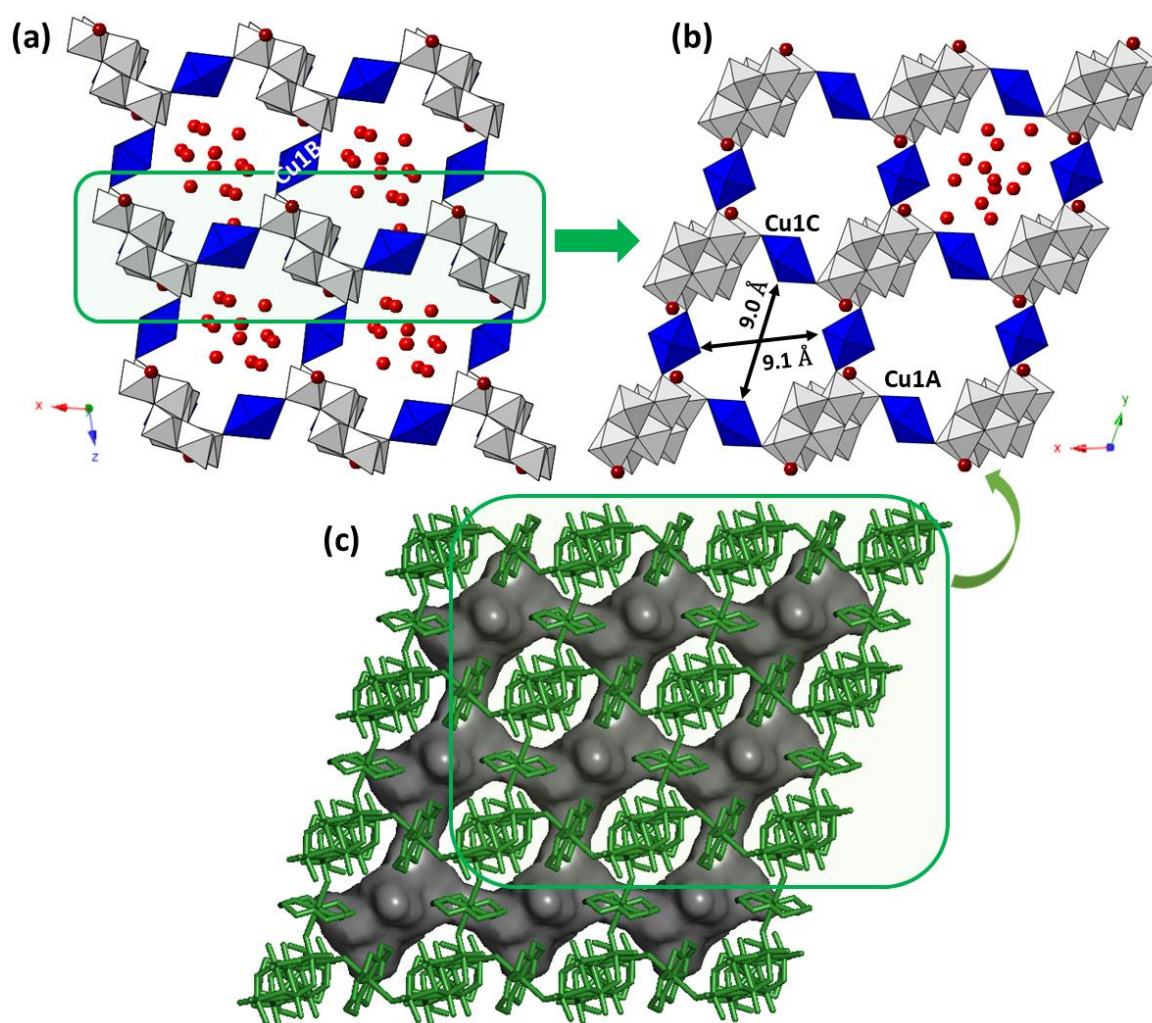


Figure 3.17. (a) Crystal packing of 4-Mo8 viewed along the crystallographic y axis. (b) Projection of the hybrid layer in the (001) plane, highlighting the structural voids in which hydration water molecules are hosted. (c) Surface representation of interconnected channels along the crystallographic z axis.

In the case of **2-Mo8**, complete hydration is achieved in 24 h of air exposure (Figure 3.14 and 3.18a) and both the number calculated water molecules from TGA profiles and the PXRD pattern does not match with any of the previously characterized crystalline phases. That means that the transition from **1-Mo8** to **2-Mo8** is irreversible. In fact, variable temperature PXRD patterns recorded every 2 °C for the cooling process of **2-Mo8** from 46 °C to 30 °C showed that a new phase (**5-Mo8**) starts forming at room temperature in the experimental time-scale (Figure 3.18b). This transition from **2-Mo8** to **5-Mo8** is fully reversible as indicated by PXRD analyses carried out for **5-Mo8** when heating from 30 to 100 °C every 5 °C (Figure 3.18c).

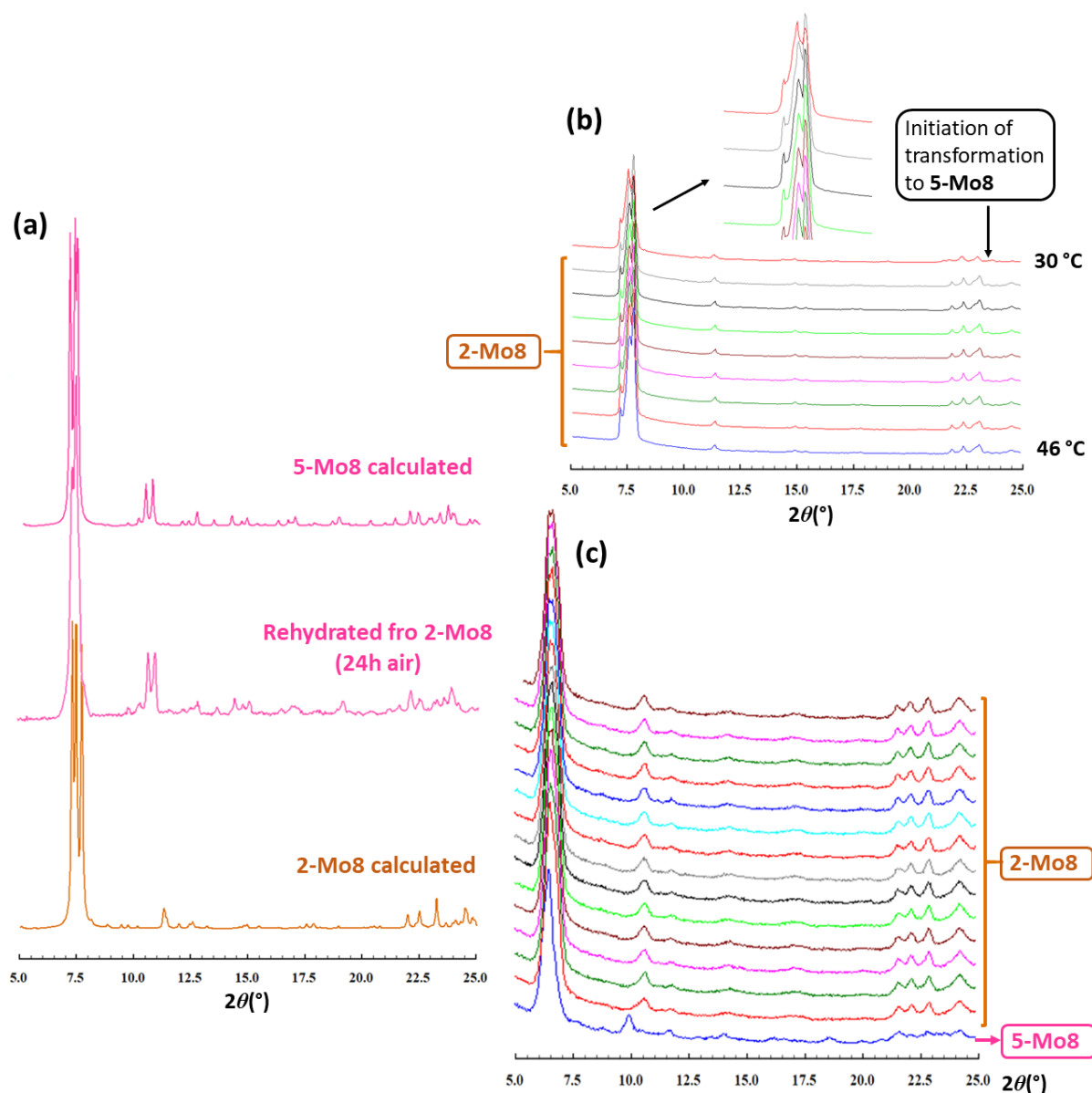


Figure 3.18. (a) PXRD pattern of **2-Mo8** exposed to open atmosphere for 24 h, compared with those calculated from scXRD data for **2-Mo8** and **5-Mo8**. (b) Variable-temperature PXRD patterns for **2-Mo8** when cooling from 46 °C to 30 °C every 2 °C. (c) Variable-temperature PXRD analyses for **5-Mo8** in the 30-100 °C range every 5 °C.

Single crystals of **2-Mo8** were exposed to open atmosphere for 24 h to ensure its full hydration, mounted on the diffractometer and quenched to 100 K to perform the full data acquisition for **5-Mo8**. Compound $[\{\text{Cu}(\text{cyclam})\}_3(\kappa\text{-Mo}_8\text{O}_{27})]\cdot 13\text{H}_2\text{O}$ (**5-Mo8**) crystallizes in the triclinic *P*-1 space group with an asymmetric unit containing one $\kappa\text{-Mo}_8$ anion, a total of three $\{\text{Cu}(\text{cyclam})\}^{2+}$ complexes; one of the located in a general position (Cu1B) and four halves of centrosymmetric moieties (Cu1A, Cu2B, Cu1C and Cu2C), and 13 hydration water molecules disordered in 16 crystallographic sites (Figure 3.19). It is worth highlighting that **5-Mo8** exhibits the same $\kappa\text{-Mo}_8$ isomer found in **1-Mo8**, but displays the same space group and similar unit cell parameters to those in **2-Mo8**. Therefore, **5-Mo8** might be considered a transient state between **1-Mo8** and **2-Mo8**.

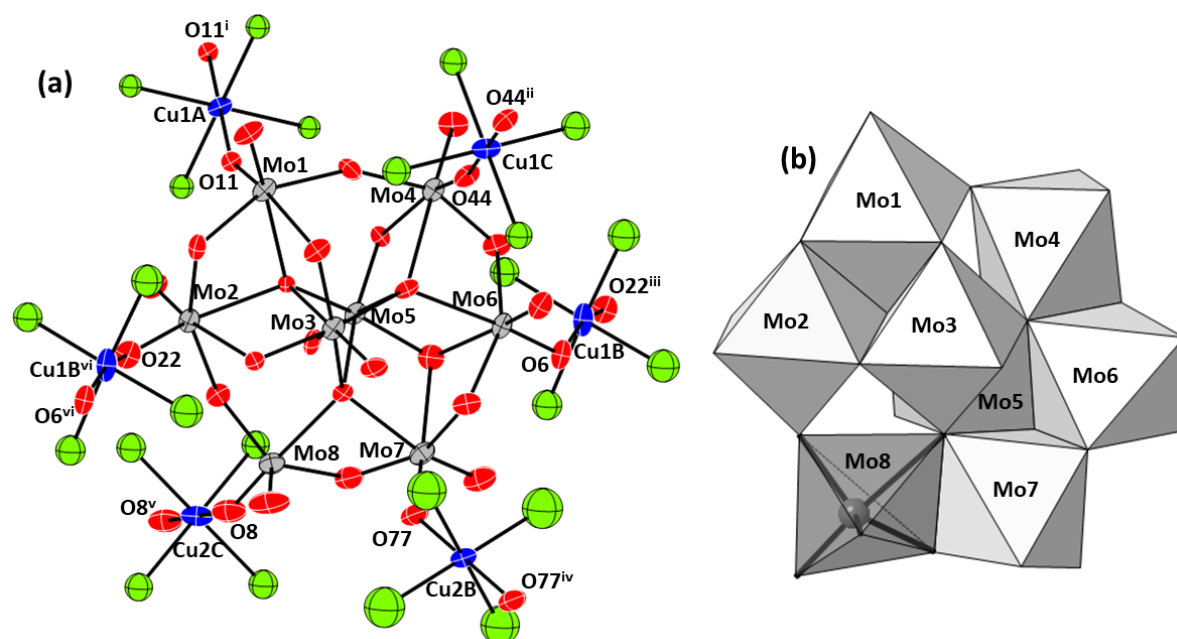


Figure 3.19. (a) ORTEP representation of **5-Mo8**, showing 50% probability ellipsoids, together with the atom labelling scheme. The C, and H atoms, as well as water molecules of hydration have been omitted for clarity. Symmetry codes: i) $2-x, 1-y, 1-z$; ii) $2-x, -y, 1-z$; iii) $-1+x, y, z$; iv) $2-x, -y, 2-z$; v) $2-x, 1-y, 2-z$; vi) $1+x, y, z$. (b) Polyhedral representation of the $\kappa\text{-Mo}_8$ anion in **1-Mo8**, together with the atom labelling scheme. The pentacoordinated center is highlighted in dark grey.

Regarding the crystal packing, the arrangement of hybrid POM/metal-organic layers in **5-Mo8** is virtually identical to that of **2-Mo8**, with each Mo_8 unit linked to four neighboring clusters through four bridging metal complexes (Figure 3.20). The cavities delimited by the grid are larger than those found in **2-Mo8** (9.1×8.7 and 9.6×9.4 Å) probably due to the breathing effect provided by the incorporation of water molecules of hydration. In contrast to that observed in **2-Mo8**, the stacking of hybrid sheets takes place through the coordination axially elongated complexes in octahedral geometry and no additional coordination modes are found within the structure (Figure 3.20b). The resulting framework displays interconnected channels running along $[011]$ and $[100]$ directions,

whereas the connection along the [0-11] direction is alternately prevented by narrower necks. These voids occupy 1063 \AA^3 per unit cells, which accounts for 29% of the total cell volume as calculated by PLATON and host all the water molecules of hydration.

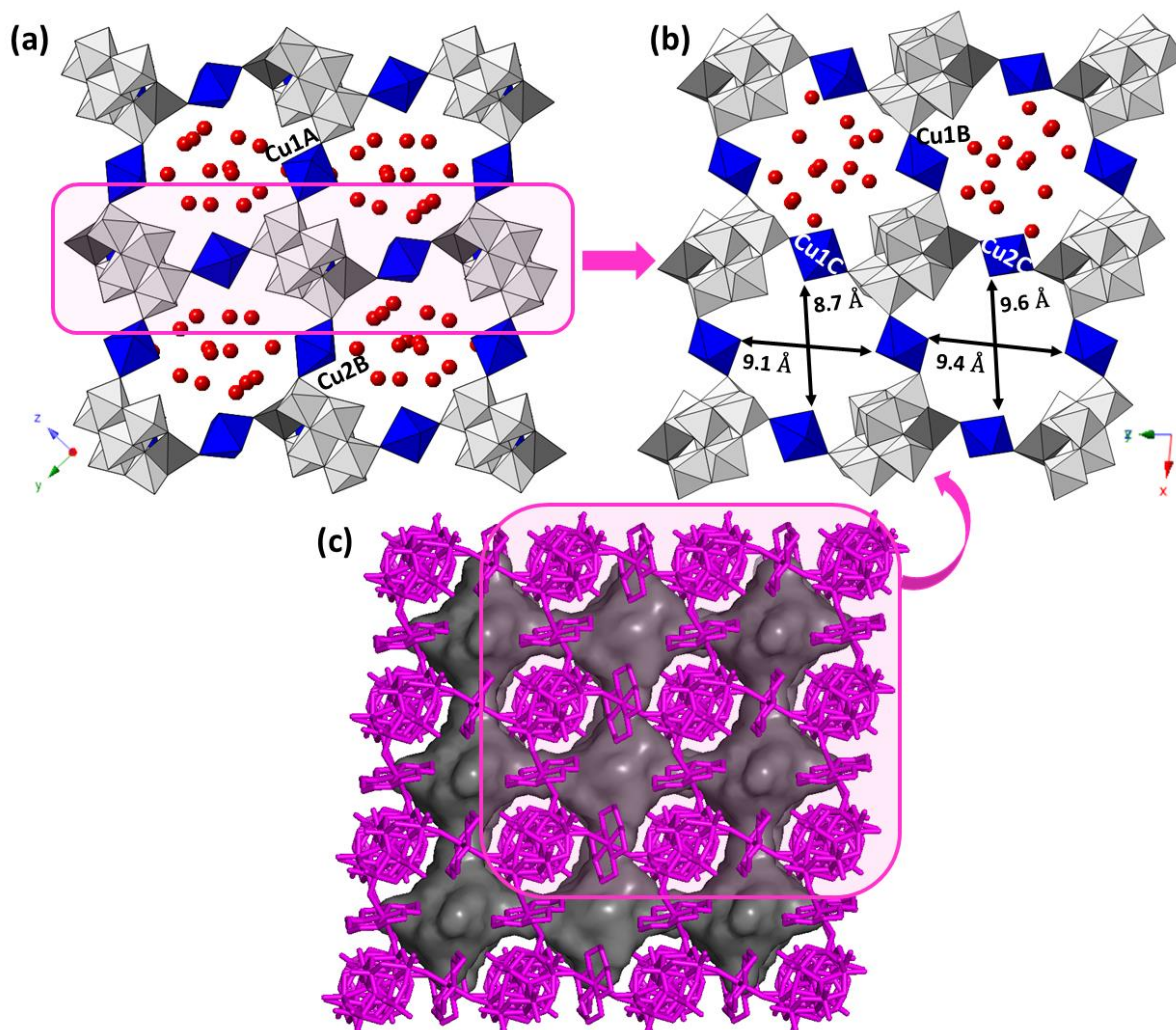


Figure 3.20. (a) View of the crystal packing of **5-Mo8** along the crystallographic x axis. (b) Projection of the hybrid layer in the $(01-1)$ plane, highlighting the structural voids in which hydration water molecules are hosted. (c) Surface representation of interconnected voids in the $[01-1]$ direction.

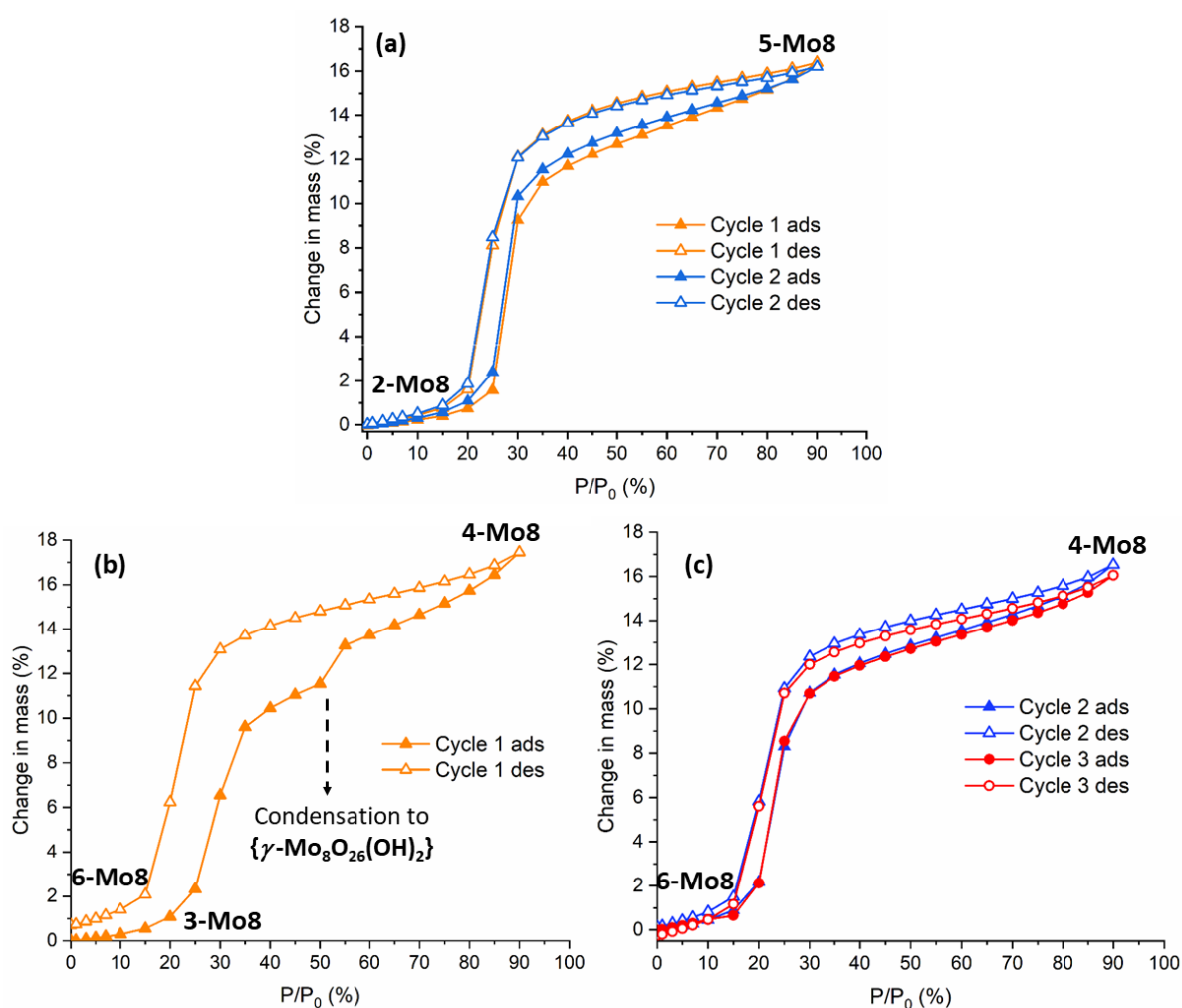
3.4. WATER VAPOR SORPTION PROPERTIES

The reversible nature of the transitions from **2-Mo8** to **5-Mo8** and from **3-Mo8** to **4-Mo8** established by TGA and XRD experiments motivated us to study the water-vapor sorption capacity of our thermally-activated microporous materials. Thus, dynamic vapor sorption (DVS) experiments were conducted at 298 K from vacuum to 90% relative humidity (RH) for both anhydrous phases. In the case of **2-Mo8**, the adsorption isotherm indicates that pores remain virtually empty up to almost 20 % of RH. After this point, a sudden increase of the water uptake occurs with a steep adsorption that reaches ca. 70 % of the total adsorption capacity at 35% RH. The maximum uptake at 90% RH implies an increase of 16.4 % of the total mass with respect to that of the original anhydrous phase. Small differences between the calculated mass for the 13 H₂O molecules in the resulting hydrated phase **5-Mo8** and the values found experimentally (Table 3.5) could arise from the surface condensation that can take place near the pores.² These values result in a maximum working capacity of 220 cm³·g⁻¹ for **2-Mo8**, which is one of the highest values observed to date for POM-based water sorbents (Table 3.6). The desorption process is almost superimposable to the adsorption, which suggests the total reversibility of the process. In order to confirm its cyclability, a second isotherm was measured under the same conditions and the working capacity remained virtually identical (218 cm³ g⁻¹, 16.2 % change in mass at 90 % RH) (Figure 3.21a). PXRD experiments on **2-Mo8** proved that the active material keeps stable and retains its crystallinity after the adsorption/desorption processes (Figure 3.22a).

When it comes to **3-Mo8**, the anhydrous phase does not adsorb any significant amount of water below 15 % RH. From this point, fast water uptake is observed up to 35 % RH, after which the adsorption process slows down. This slower step extends up to 50 % RH and accounts for the mass of a single H₂O molecule. Thus, this fact could originate from the structural transition from **3-Mo8** to **4-Mo8** associated with the incorporation of one water molecule to the POM skeleton and subsequent structural rearrangement from $[\mu\text{-Mo}_8\text{O}_{27}]^{6-}$ to $[\gamma\text{-Mo}_8\text{O}_{26}(\text{OH})_2]^{6-}$ (Figure 3.21b). After reaching a maximum working capacity of 234 cm³ g⁻¹ (17.4 % change in mass) at 90 % RH, the desorption process suggests that the $[\gamma\text{-Mo}_8\text{O}_{26}(\text{OH})_2]^{6-}$ anion remains stable upon dehydration because one water molecule is retained in the active material.

Table 3.5. DVS data for compounds **2-Mo8** and **3-Mo8**.

		Calc. Mass change (%)	Expected H ₂ O	Exp. Mass change (%)	Found H ₂ O
2-Mo8	Cycle 1	11.7	13	16.4	18
	Cycle 2	11.7	13	16.2	18
3-Mo8	Cycle 1	10.9	12	17.4	19
4-Mo8	Cycle 2	9.9	11	16.5	18
	Cycle 3	9.9	11	16.1	18

Figure 3.21. DVS isotherms from 0% to 90% relative humidity at 298 K for (a) **2-Mo8** (2 cycles), and **3-Mo8**, (b) first cycle leading to the phase **6-Mo8**, and (c) second and third cycles.

CHAPTER 3

Table 3.6. POM-based compounds with water sorption capacity.

Compounds	Adsorption capacity (cm ³ g ⁻¹)	REF
2-Mo8	217	
3-Mo8	222	Chapter 3
6-Mo8	215	
[Cu(en) ₂] ₆ {[Cu(en) ₂] ₆ [[Cu ₂ (trz) ₂ (en) ₂] ₆ [H ₁₀ Nb ₆₈ O ₁₈₈]]}	224	
K ₄ @[Cu ₂₉ (OH) ₇ (H ₂ O) ₂ (en) ₈ (trz) ₂₁][Nb ₂₄ O ₆₇ (OH) ₂ (H ₂ O) ₃] ₄ *	193	[29]
[Cu(en) ₂] ₆ @[Cu ₂ (en) ₂ (trz) ₂] ₆ (Nb ₆₈ O ₁₈₈)	188	
{[Cu(en) ₂] ₆ @[Cu ₂ (en) ₂ (trz) ₂] ₆ (Nb ₆₈ O ₁₈₈)}	219	[30]
[Cu(en) ₂ (H ₂ O)] ₂ {[Cu(en)] ₄ [Cu(en) ₂] ₅ [[Cu(en) ₂ KNb ₂₄ O ₇₂ H ₁₀] ₂ }	204	[31]
[Zn ₁₂ (trz) ₂₀][SiW ₁₂ O ₄₀]	150	[32]
Cu ₆ (trz) ₁₀ (H ₂ O) ₄ [H ₂ SiW ₁₂ O ₄₀]	118	[33]
K ₃ [Cr ₃ O(OOCH) ₆ (H ₂ O) ₃][α-SiW ₁₂ O ₄₀]	115	
Rb ₄ [Cr ₃ O(OOCH) ₆ (H ₂ O) ₃][α-BW ₁₂ O ₄₀]	57	[34]
Cs ₅ [Cr ₃ O(OOCH) ₆ (H ₂ O) ₃][α-CoW ₁₂ O ₄₀]	32	
[Cr ₃ O(OOCCH=CH ₂) ₆ (H ₂ O) ₃] ₃ [α-PW ₁₂ O ₄₀]	70.7	[35]
(NH ₄) ₇ [Cr ₃ O(OOCH) ₆ (H ₂ O) ₃] ₂ [α-P ₂ W ₁₅ V ₃ O ₆₂]	87	
(NH ₄) ₅ [Cr ₃ O(OOCH) ₆ (H ₂ O) ₃] ₂ [α ₂ -P ₂ W ₁₇ VO ₆₂]	69	[36]
(NH ₄) ₄ [Cr ₃ O(OOCH) ₆ (H ₂ O) ₃] ₂ [α-P ₂ W ₁₈ O ₆₂]	65	
[Cu ₄ (dpdo) ₁₂][H(H ₂ O) ₂₇ (CH ₃ CN) ₁₂][PW ₁₂ O ₄₀] ₃	65.1	[37]
H ₁₄ [Na ₆ (H ₂ O) ₁₂] ₄ [K ₄₂ Ge ₈ W ₇₂ O ₂₇₂ (H ₂ O) ₆₀]	52	[38]
[Cu ₃ (L) ₂ (H ₂ O) ₄][Cu(dmf) ₄ (SiW ₁₂ O ₄₀)]	51.7	[39]
Li ₂ [Cr ₃ O(OOCH) ₆ (etpy) ₃] ₂ [α-SiW ₁₂ O ₄₀]	66.3	
Na ₂ [Cr ₃ O(OOCH) ₆ (etpy) ₃] ₂ [α-SiW ₁₂ O ₄₀]	60.3	
(etpyH ⁺) ₂ [Cr ₃ O(OOCH) ₆ (etpy) ₂ (H ₂ O) ₂] ₂ [α-SiW ₁₂ O ₄₀]	44	
K ₂ [Cr ₃ O(OOCH) ₆ (etpy) _{2.5} (H ₂ O) _{0.5}] ₂ [α-SiW ₁₂ O ₄₀]	38.9	[40]
(NH ₄) ₂ [Cr ₃ O(OOCH) ₆ (etpy) ₃] ₂ [α-SiW ₁₂ O ₄₀]	38.5	
K ₂ [Cr ₃ O(OOCH) ₆ (etpy) ₃] ₂ [α-SiW ₁₂ O ₄₀]	38.1	
Cs ₂ [Cr ₃ O(OOCH) ₆ (etpy) ₃] ₂ [α-SiW ₁₂ O ₄₀]	34	
K ₂ [Cr ₃ O(OOCH) ₆ (mepy) ₃] ₂ [α-PMo ₁₂ O ₄₀]	47	
Rb ₂ [Cr ₃ O(OOCH) ₆ (mepy) ₃] ₂ [α-PMo ₁₂ O ₄₀]	43	
Na ₂ [Cr ₃ O(OOCH) ₆ (mepy) ₃] ₂ [α-PMo ₁₂ O ₄₀]	40	
Cs ₂ [Cr ₃ O(OOCH) ₆ (mepy) ₃] ₂ [α-PMo ₁₂ O ₄₀]	38	[41]
K[Cr ₃ O(OOCH) ₆ (mepy) ₃] ₂ [α-PMo ₁₂ O ₄₀]	30	
(mepyH)[Cr ₃ O(OOCH) ₆ (mepy) ₃] ₂ [α-PMo ₁₂ O ₄₀]	17	
Cs ₄ [PW ₁₁ O ₃₉ (Sn-n-C ₄ H ₉)]	67	
Cs ₄ [SiW ₁₂ O ₄₀]	50.4	[42]
Cs ₄ [PW ₁₁ O ₃₉ (Sn-OH)]	32	
H[Ni(HbpdC)(H ₂ O) ₂] ₂ [PW ₁₂ O ₄₀]	31	[43]
[Co ^{II} (pn) ₃] ₄ [PNb ₁₂ O ₄₀ (V ^{IV} O) ₆][OH] ₅	19.7	[44]
(DODA) ₂₃ [Mo ₁₅₄ O ₄₆₂ H ₅]	20	[45]
K _{1.5} [Cr ₃ O(OOCH) ₆ (C ₅ H ₅ N) ₃] ₂ [Cr ₃ O(OOCH) ₆ (C ₅ H ₅ N)(CH ₃ OH) ₂] _{0.5} [α-SiW ₁₂ O ₄₀]	0.04	[46]
K ₂ [Cr ₃ O(OOCH) ₆ (mepy) ₃] ₂ [α-SiW ₁₂ O ₄₀]	0.025	[47]
Cs ₂ [Cr ₃ O(OOCC ₂ H ₅) ₆ (H ₂ O) ₃] ₂ [α-SiW ₁₂ O ₄₀]	0.022	[48]
Cs ₃ H _{0.3} [SiW ₁₂ O ₄₀] _{0.83}	0.02	[49]
K ₂ [Cr ₃ O(OOCH) ₆ (H ₂ O) ₃] ₂ [α-SiW ₁₂ O ₄₀]	0.02	[50]
K ₂ [Cr ₃ O(OOCC ₂ H ₅) ₆ (H ₂ O) ₃] ₂ [α-SiW ₁₂ O ₄₀]	0.018	
Rb ₂ [Cr ₃ O(OOCC ₂ H ₅) ₆ (H ₂ O) ₃] ₂ [α-SiW ₁₂ O ₄₀]	0.018	[34a]
(NH ₄) ₂ [Cr ₃ O(OOCC ₂ H ₅) ₆ (H ₂ O) ₃] ₂ [α-SiW ₁₂ O ₄₀]	0.018	

*en=ethanediamine; Htrz=1,2,4-triazole; dpdo=4,4'-bipyridine, *N,N'*-dioxide; etpy=4-ethylpyridine; mepy=methylpyridine; H₂bpdC=2,2'-bipyridyl-3,3'-dicarboxylic acid; pn=1,2-diaminopropane; DODA=dimethyldioctadecylammonium.

PXRD analyses (Figure 3.22b) confirmed that **4-Mo8** does not revert back to **3-Mo8** under vacuum and indicate that a third anhydrous phase (**6-Mo8**) could be generated as a result. The reversibility of the water uptake between phases **4-Mo8** and **6-Mo8** was confirmed because both curves were virtually identical and they showed a maximum working capacity of $216 \text{ cm}^3 \text{ g}^{-1}$ at 90 % RH (16.5 % change in mass). This presence of **6-Mo8** was corroborated through variable-temperature PXRD analyses (Figure 3.23) on **4-Mo8**, which showed an intermediate phase in the transition from **4-Mo8** to **3-Mo8**. The new phase is stable at temperatures below $120 \text{ }^\circ\text{C}$ and the XRD pattern of which fits well to that observed for a sample of **4-Mo8** treated under vacuum. Further studies show that this phase is also obtained by exposure **4-Mo8** under vacuum (Figure XX). Unfortunately, we were not able to collect any sc-XRD data set of good quality for the structural resolution of the intermediate phase **6-Mo8** despite testing several different crystal batches. Nevertheless, the cell parameters of **6-Mo8** are similar to those of **4-Mo8**, which could indicate that this new phase is similar to **4-Mo8** but without hydration water molecules (Table 3.7).

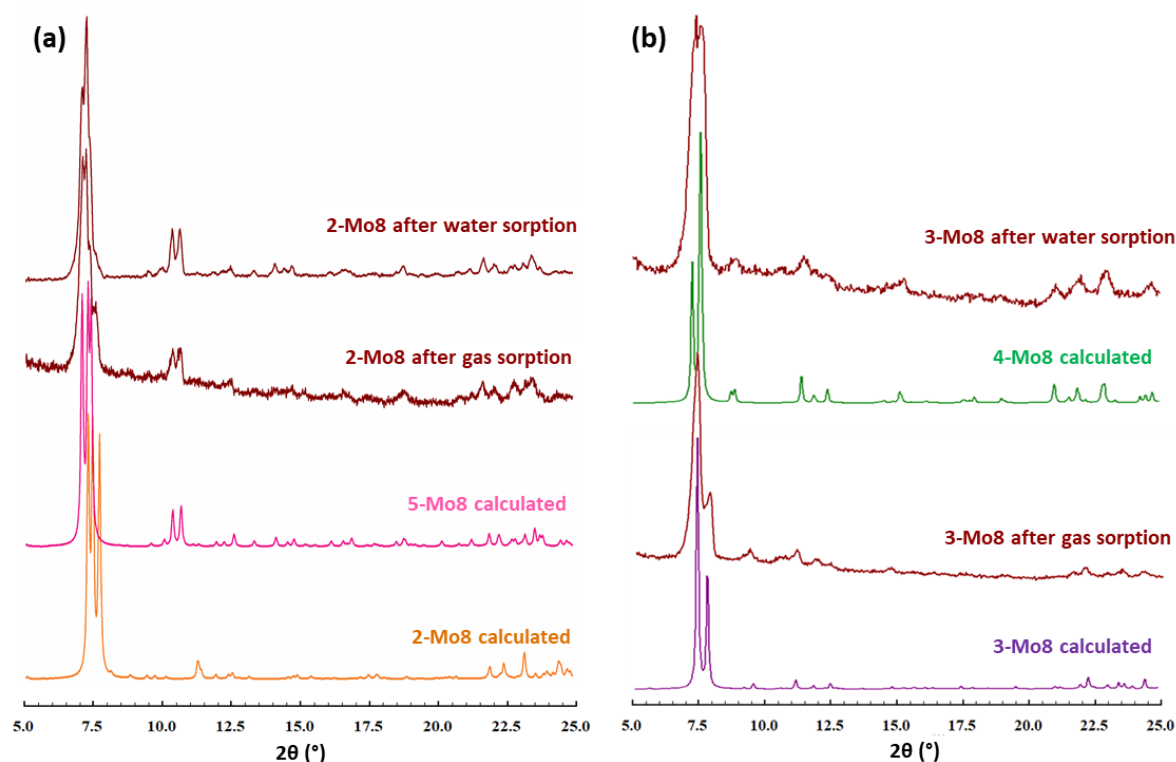


Figure 3.22. PXRD patterns of (a) **2-Mo8** and (b) **3-Mo8** after gas and water sorption measurements together with those calculated from sc-XRD data for (a) **2-Mo8**, **5-Mo8**, (b) **3-Mo8** and **4-Mo8**.

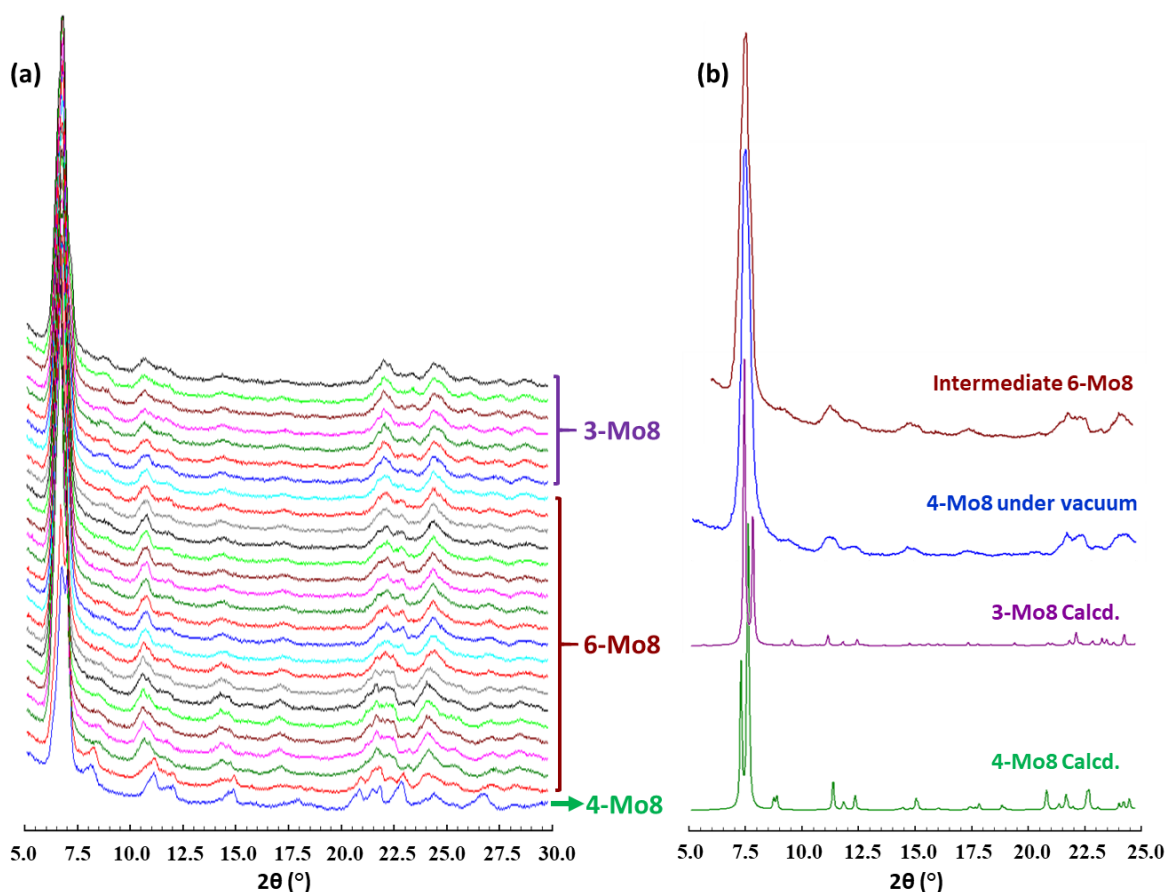


Figure 3.23. (a) Variable-temperature PXRD pattern of **4-Mo8** in the 30-160 °C range every 5 °C. (b) Comparison of PXRD patterns of **4-Mo8** under vacuum with that of **4-Mo8** heated at 50 °C (intermediate **6-Mo8**) and those calculated from sc-XRD data for **3-Mo8** and **4-Mo8**.

Besides the total capacity, the reversibility of the system (cyclability) and sorption kinetics are also important factors that should be taken into consideration for industrial applications. Considering that i) the steep uptake takes place at 20-35 % RH range in all cases, and ii) the 80 % of the total capacity is reached at 60% RH (standard working conditions for some common commercial desiccants),⁵¹ the kinetics of these two processes were studied at a constant vapor flow rate of 30 and 60 % RH, respectively. Lower vapor flow (0-30-0 % RH) makes the water uptake to take as long as 100 min to be completed (Figure 3.24), whereas both adsorption and desorption processes are achieved in less than 15 minutes at a RH swing of 0-60-0 % for both phases at room temperature.

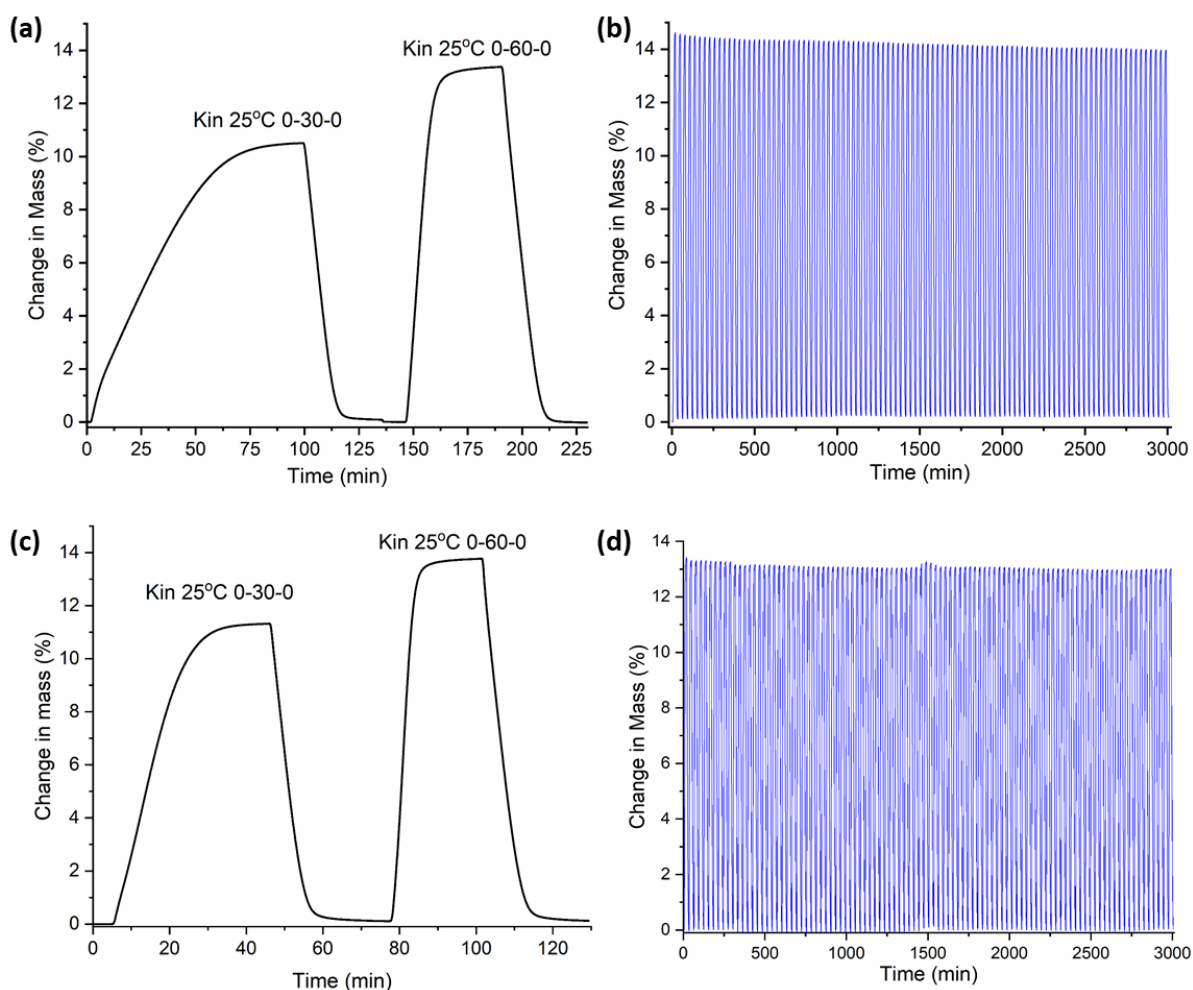


Figure 3.24. Kinetic measurement of the adsorption-desorption process of (a) **2-Mo8** and (b) **3-Mo8** at two different relative humidity swings: 0-30-0% RH and 0-60-0% RH, and water sorption cycling test on (c) **2-Mo8** and (d) **3-Mo8**. Each cycle is measured in 30 minutes (15 min for adsorption and 15 min for the desorption process) at 298 K, with a 0-60-0% relative humidity swing.

The durability and recyclability of the adsorbents were evaluated by multiple (100 cycles) water adsorption-desorption experiments at 298 K and a constant vapor flow rate of 0-60-0 % RH. As shown in Figure 3.24, the regeneration of the materials is completed after 100 cycles only by humidity swing. Plots show an average water uptake of 14 % and 13 % for **2-Mo8** and **6-Mo8**, respectively, values that are very close to those observed in the initial isotherms. Materials with this type of fast, reversible behavior are ideal for their application in heat bombs or air conditioners.⁵² Moreover, the fast kinetics and reproducibility in the adsorption-desorption process make these materials suitable for dehumidification in highly humid areas or water harvesting and purification in confined spaces.⁵³

3.5. GAS SORPTION MEASUREMENTS

Taking into account that **1-Mo8** is able to retain microporosity upon thermal evacuation of guest water molecules, and considering that pore necks are *a priori* wide enough to enable the percolation of small adsorbents, we decided to evaluate the gas sorption properties of the two different anhydrous phases in this work. Thus, preliminary N₂ and CO₂ sorption experiments were carried out at 77 and 195 K, respectively on crystalline samples of **1-Mo8** thermally activated at 50 and 120 °C under vacuum to ensure its full conversion into **2-Mo8** and **3-Mo8**, respectively.

The N₂ adsorption curves for **2-Mo8** and **3-Mo8** are displayed in Figure 3.25 and correspond to type I isotherms typical of microporous materials. In both cases, micropores are filled rapidly at low relative pressures ($P/P_0 < 0.1$) to achieve a saturation level that extends up to $P/P_0 = 1$. The maximum gas uptake for **2-Mo8** and **3-Mo8** reaches the values of 72 and 76 cm³ (STP) g⁻¹, respectively, which account for 6.4 and 6.8 adsorbed N₂ molecules per Mo₈ unit. The adsorption processes were observed to be completely reversible, and hence, all the gas molecules are desorbed at $P/P_0 = 0$. Fitting of both adsorption branches to the Brunauer-Emmett-Teller (BET) model³⁵ affords similar values of BET surfaces areas for **2-Mo8** (302 m² g⁻¹) and **3-Mo8** (298 m² g⁻¹). Although these values are much lower than those found in POM-loaded MOFs, which can exhibit surface areas of hundreds or thousands m² g⁻¹,⁵⁴ our results are comparable to those displayed by some other POM-metal organic frameworks, such as [Cu(cyclam)][Cu(cyclam)]₂(V₁₀O₂₈) (205 m² g⁻¹),^{14a} or (TBA)₂[Cu(BBTZ)₂(α-Mo₈O₂₆)] (773 m² g⁻¹; BBTZ = 1,4-bis(1,2,4-triazol-1-ylmethyl)-benzene).⁵⁵

In regard to the CO₂ uptake isotherms (orange), saturation is only achieved at much higher relative pressures ($P/P_0 = 1$). This effect can be ascribed to the stronger interaction of a polarizable molecule such as CO₂ with the O-enriched pore walls of the hybrid host materials. The adsorption processes were also observed to be fully reversible and the maximum uptakes were also found to reach very similar values for **2-Mo8** and **3-Mo8** (66 and 64 cm³ (STP) g⁻¹), accounting for 5.9 and 5.7 adsorbed CO₂ molecules per Mo₈ unit. In contrast to what we previously observed in related POM/Cu(cyclam) porous frameworks, in which N₂ adsorption was negligible^{14b} or the maximum uptake accounted only for the 30% of the simulated value,^{14a} both N₂ and CO₂ seem to be efficiently adsorbed in **2-Mo8** and **3-Mo8**. Similar studies for **6-Mo8** will be carried out in a near future.

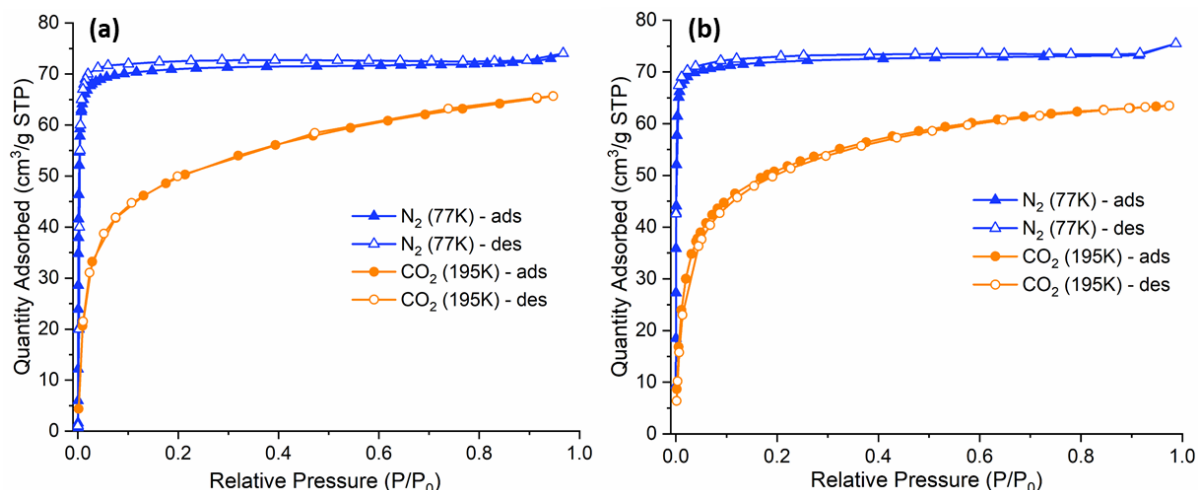


Figure 3.25. Experimental N₂ (blue) and CO₂ (orange) adsorption/desorption isotherms for (a) **2-Mo8** and (b) **3-Mo8**. Filled and empty markers correspond to the adsorption and desorption branches, respectively.

The similar adsorption capacity of **2-Mo8** and **3-Mo8** for both N₂ and CO₂ is a result of empty channels with similar shape and cross sections, which are larger than the size of these two gases. Pore size distribution was calculated for **3-Mo8** by Horvath-Kawazoe (HK) Pore Plots (Appendix A2.X),⁵⁶ as a representation of both samples, which shows cavities wide enough to host these two gases (diameter CO₂ = 3.3 Å; N₂ = 3.64 Å), as well as for larger molecules such as CH₄ (d = 3.8 Å) C₂H₂ (d = 3.3 Å), C₂H₄ (d = 3.9 Å) and C₂H₆ (d = 3.99 Å) (Figure 3.26).

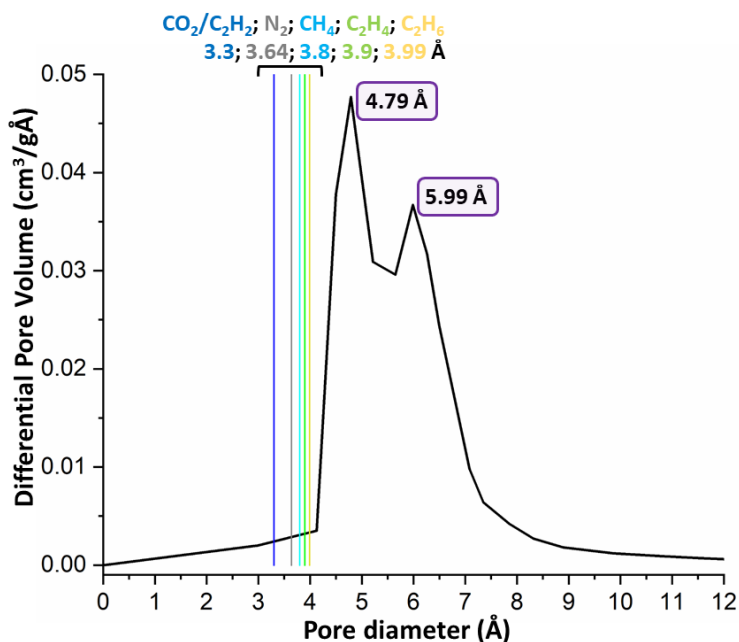


Figure 3.26. Calculated pore size distribution for **3-Mo8**. The kinetic diameters of different gases are indicated with lines as CO₂ and C₂H₂, dark blue; N₂, grey; CH₄, light blue; C₂H₄, green; C₂H₆, yellow.

3.5.1. Multi-component adsorption selectivity

Preliminary studies encouraged us to carry out additional experiments at different temperatures to get a better understanding of the adsorptive properties of the anhydrous phases, and furthermore, to test their performance in purification or selective capture of gas mixtures consisting of small molecules. To examine the adsorption behavior of **2-Mo** and **3-Mo** in gas mixtures, multi-component isotherms and selectivity values were calculated using the ideal adsorbed solution theory (IAST).⁵⁷ Before IAST analyses, single-component isotherms of N₂, CO₂, CH₄, C₂H₂, C₂H₄ and C₂H₆ were acquired for **3-Mo8** at high temperatures (273 and 298 K). All the different isotherms and maximum uptake values for each gas are compiled in Figure 3.27 and Table 3.7, respectively. Experimental measurements revealed that the highest uptake values were displayed by C₂H₂ regardless the temperature of the experiment. Similar uptake values were obtained for both C₂H₄ and C₂H₆, which is higher than that registered for CO₂ at 298K. This trend is inverted at 273K, in such a way that CO₂ is better adsorbed than the two C₂ molecules. Much lower adsorption capacity was observed for CH₄ despite its smaller kinetic diameter in comparison to those of C₂H₄ and C₂H₆. Conversely, as previously observed for some other POM-based systems,⁵⁸ no significant amount of N₂ was adsorbed (maximum uptake value of 1.9 cm³g⁻¹ at 298 K) in **3-Mo8**. This behavior has been classically assigned to i) the low temperature in which N₂ isotherms are collected (77 K), which hinders the diffusion of the molecular probe through narrow pore necks as a result of its lower kinetic energy, ii) the larger kinetic diameter of N₂ in comparison to other sorbates like CO₂, and iii) the low polarizability of the molecule, which prevents its interaction with oxygen-rich pore-walls in the framework. Selective sorption of CO₂ over N₂ at 273 K has already been observed for some POM-based materials.^{14a} None of the first two reasons could apply in this case.

Table 3.7. Gas sorption uptakes (cm³g⁻¹) of **3-Mo8** for different gases at 273 and 298 K.

T	N ₂	CO ₂	CH ₄	C ₂ H ₂	C ₂ H ₄	C ₂ H ₆
273 K	–	22.4	8.0	33.3	22.0	22.0
298 K	1.9	13.9	4.8	27.7	17.7	17.7

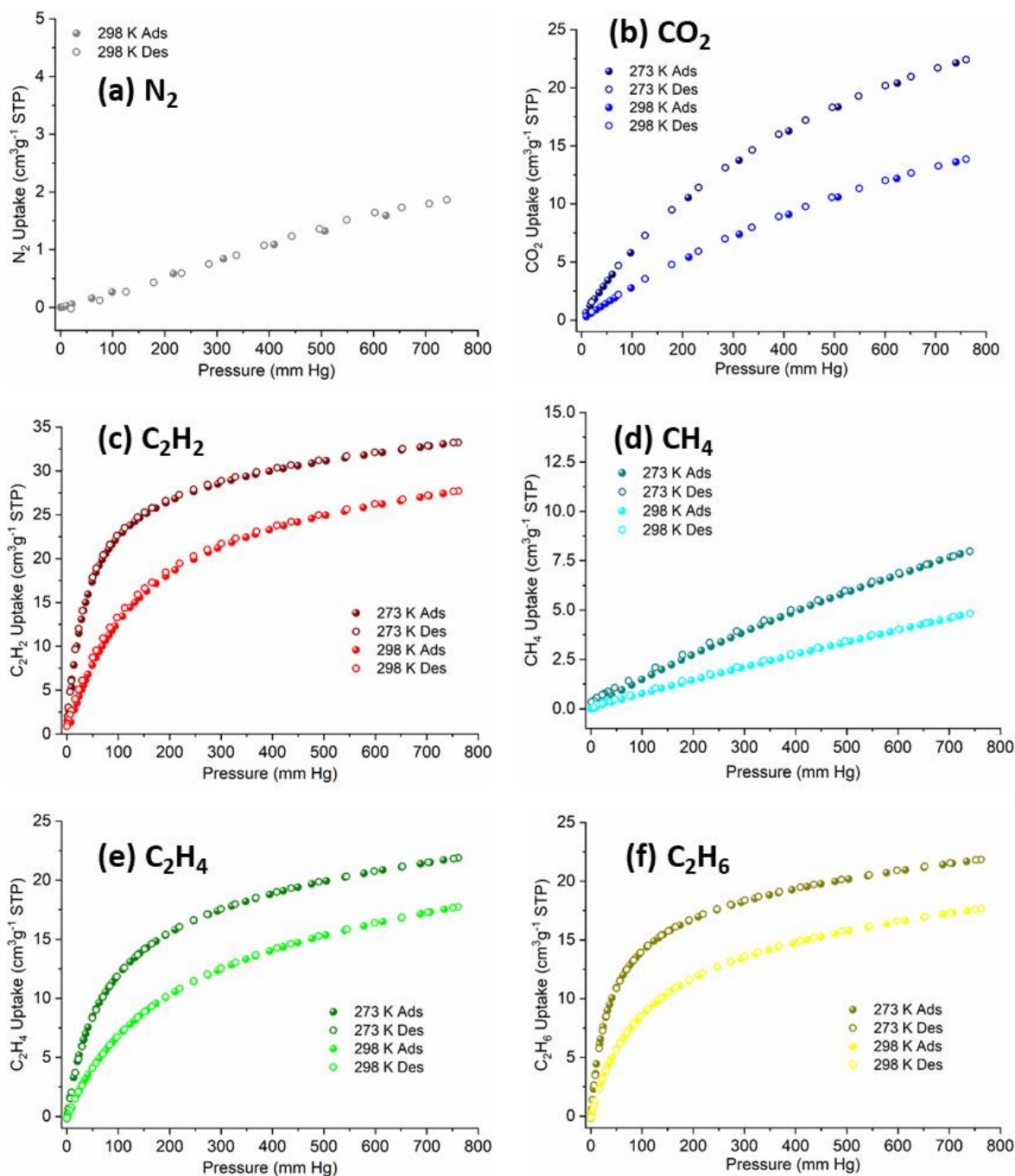


Figure 3.27. Experimental gas adsorption isotherms of **3-Mo8** at 273 and 298 K for (a) N₂, (b) CO₂, (c) CH₄, (d) C₂H₂, (e) C₂H₄, and (f) C₂H₆. Filled and empty markers correspond to the adsorption and desorption branches, respectively.

To get further understanding of the affinities of gas adsorption processes and envisage the selective adsorption properties, isosteric heats (Q_{st}) were estimated for C1 and C2 gases (Figure 3.28 and Table 3.8). The Q_{st} values were calculated from the adsorption isotherms at 273 and 298 K by using virial-type expressions (See Section A2.5 in Appendix 2). As observed in isosteric heat plots, the Q_{st} value decreases as the pressure goes up in all cases except for CO₂. The favorable adsorbate-adsorbate interactions within the channels

CHAPTER 3

of **3-Mo8** at higher loadings could originate the increase of the Q_{st} value as the loading increases. Average Q_{st} values result in the following affinity trend $C_2H_2 > C_2H_6 > C_2H_4 > CO_2 > CH_4$, which is in line with the uptakes values observed at 298K.

Table 3.8. Q_{st} values ($KJ \cdot mol^{-1}$) of **3-Mo8** towards different gases.

	CO ₂	CH ₄	C ₂ H ₂	C ₂ H ₄	C ₂ H ₆
Q_{st} (0 uptake)	24	23	34	27.5	31
Q_{st} (final uptake)	24	17.5	31	24	30

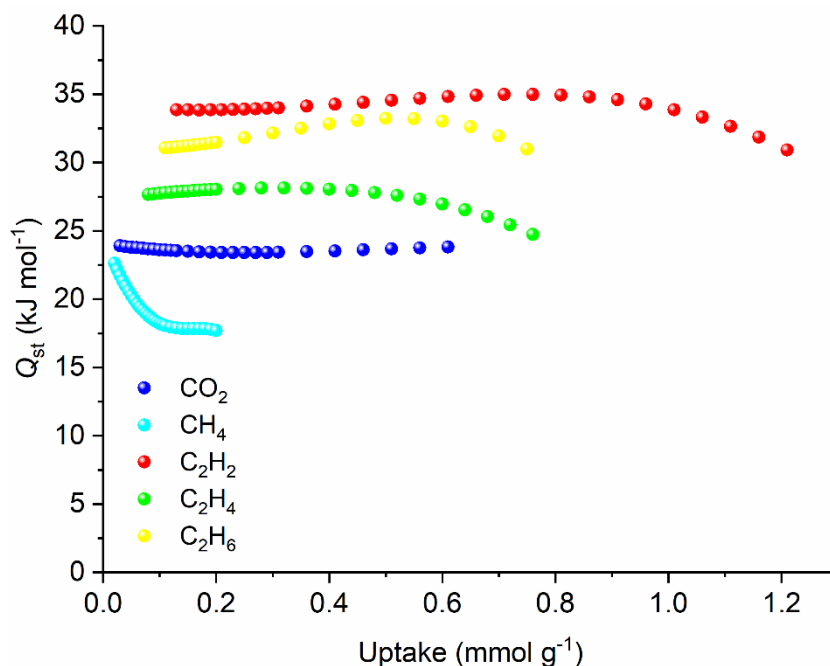


Figure 3.28. Isothermic heat plots of **3-Mo8** towards different gases.

Moving a step forward, the selective adsorption from different gas mixtures was studied for **3-Mo8** (Figure 3.29), starting from the smallest molecules (CO₂, N₂ and CH₄) (See Section A2.5 in Appendix 2). First, a high selectivity for CO₂ over N₂ (S_{CO_2/N_2}) is observed in a mixture of 1:1 ratio, with a S_{CO_2/N_2} values of 10.5 at low pressures, which goes up to 12.5 as the pressure increases. This behavior can be easily explained by the aforementioned low uptake of N₂ at 298 K (Figure 3.27). A similar behavior was displayed by mixtures showing a lower CO₂ concentration (CO₂:N₂ 15:85), in which the highest S_{CO_2/N_2} values were found to be 11.0 at $P = 1$. However, although **3-Mo8** does really exhibit some significant adsorption selectivity of CO₂ towards N₂, this value is much lower than other reported POM-based compounds such as $\{XMo_6O_{18}[CH_3C(CH_2O)_3]_2\}$ ($X = Fe, Co, Ni, Cu$ and Zn), which exhibits selectivity values for separation of CO₂/N₂ gas mixtures in a 15:85 ratio between 28 and 225 at 1atm.⁵⁹

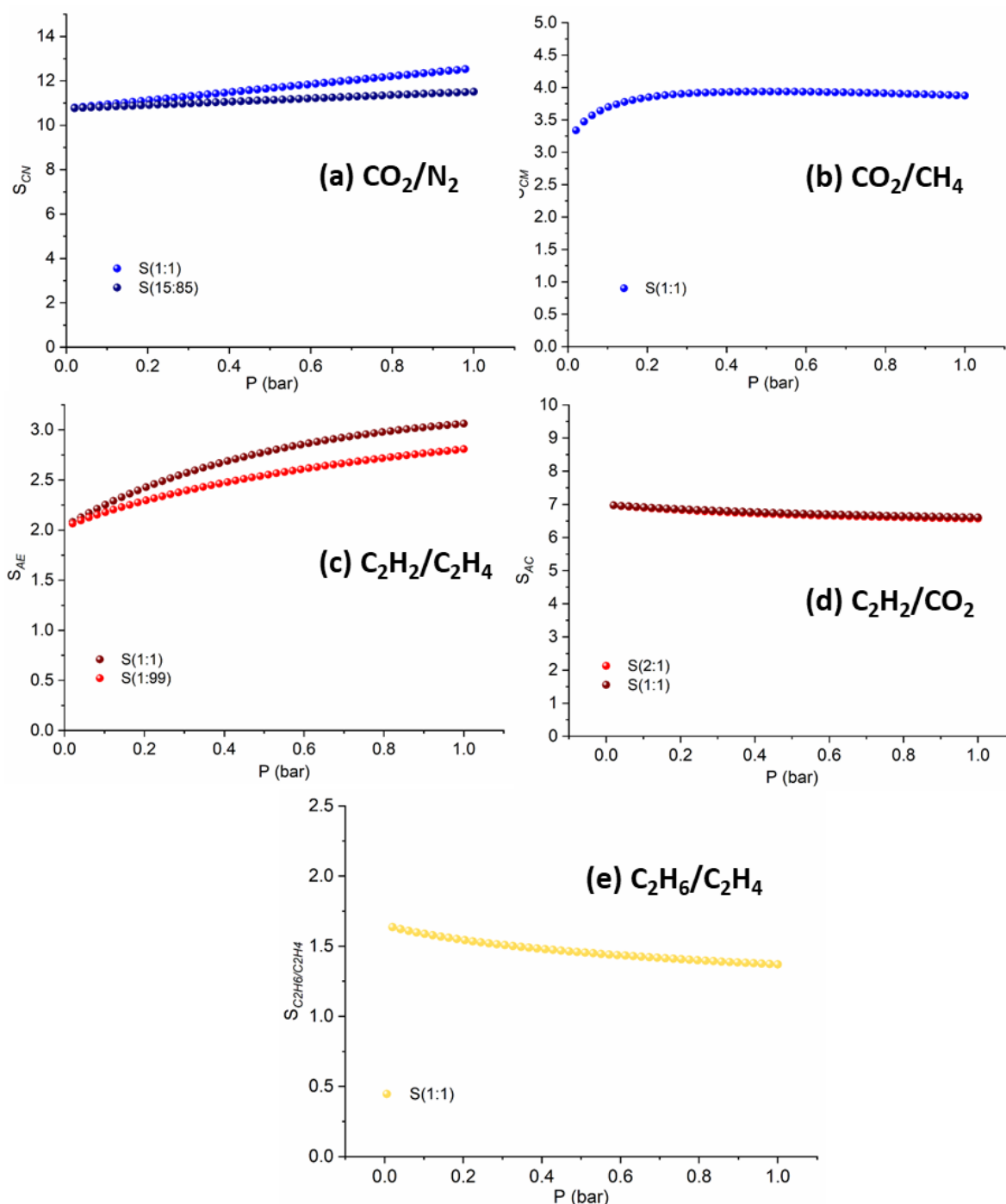


Figure 3.29. Sorption selectivity of different C1 and C2 gas mixtures on **3-Mo8** predicted by IAST calculation; (a) CO_2/N_2 ; (b) CO_2/CH_4 ; (c) $\text{C}_2\text{H}_2/\text{C}_2\text{H}_4$; (d) $\text{C}_2\text{H}_2/\text{C}_2\text{H}_4$, and; (e) $\text{C}_2\text{H}_6/\text{C}_2\text{H}_4$.

On the contrary, **3-Mo8** is not that selective for $\text{CO}_2 / \text{CH}_4$ mixtures. The highest $S_{\text{CO}_2/\text{CH}_4}$ value in a 1:1 gas mixture is of 3.7 at $P = 1$. Taking into account the adsorption data found at high temperatures for these two gases, a higher affinity for CO_2 would be expected. Nevertheless, the IAST data is in good agreement with those values obtained from Q_{st} studies, in which both CO_2 and CH_4 show similar affinity values for empty voids in **3-Mo8**. Generally, the amount of CO_2 adsorbed is significantly higher than that for CH_4 due to the quadrupole moment showed by the CO_2 if compared to CH_4 . Therefore the

CHAPTER 3

selectivity value found for **3-Mo8** differs from those reported in literature,⁶⁰ even for POM-based ionic crystals such as $K_2[Cr_3O(OOCH)_6(4\text{-etpy})_3]_2[\alpha\text{-SiW}_{12}O_{40}] \cdot 2H_2O$ (etpy = ethylpyridine) ($S_{CO_2/CH_4} = 27$)⁶¹ or $\{CoMo_6O_{18}[CH_3C(CH_2O)_3]_2\}$ (S_{CO_2/CH_4} values up to 1720).⁵⁹ All in all, we can suggest that **3-Mo8** could be able to selectively adsorb C1 gases from a ternary mixture containing CO_2 , N_2 and CH_4 .

Regarding C2 gases, separation of C_2H_2 and CO_2 is very challenging as both gases present the same kinetic diameter (3.3 Å).⁶² For **3a**, $S_{C_2H_2/CO_2}$ is maintained almost stable in all the pressure range, with a value of 6.5 at standard conditions. Although this value is not as high as that displayed by some MOFs with this capacity, in which selectivity values higher than 35 have been reported,⁶³ this is the highest selectivity found for any POM-based material towards acetylene to our knowledge, above the $S_{C_2H_2/CO_2} = 4.8$ value calculated for the ionic crystal $K_2[Cr_3O(OOCH)_6(4\text{-ethylpyridine})_3]_2[\alpha\text{-SiW}_{12}O_{40}]$ at 278 K.⁶⁴ In the case of acetylene/ethylene (1:1) mixtures, selectivity values are still lower. Selective adsorption of acetylene yields $S_{C_2H_2/C_2H_4}$ values of 2.0 at low pressures, which increases up to 3.0 at standard conditions. Furthermore, this selectivity is retained for gas mixtures with a lower concentration of acetylene (C_2H_2/C_2H_4 1:99), which highlights the selectivity of **3-Mo8** for acetylene uptake.

Finally, the lowest selectivity value was found for the C_2H_6/C_2H_4 (1:1) mixture ($S_{C_2H_6/C_2H_4} = 1.4$). This value could be expected taking into account the single-component adsorption capacities for both gases at 273 and 298 K, as well as the similar Q_{st} value displayed by both gases. Nevertheless, it is worth mentioning that for most of the materials reported in literature,⁶⁵ the selectivity trend is the opposite, as ethylene is much better adsorbed than ethane. In fact, development of ethane-selective adsorbents is highly desirable in C_2H_4/C_2H_6 separation processes because current methods usually require higher costs and many steps. Therefore, despite the low selectivity values found for **3-Mo8**, this material presents an unusual selectivity of acetylene over ethane, with values comparable to those exhibited by the scarce adsorbents with this capacity reported in the literature.⁶⁶

Similar experiments were carried out for **2-Mo8**. However, adsorption curves at 273 and 298 K revealed a similar gas sorption capacity as in **3-Mo8**; therefore, no selectivity tested were studied (Figure 3.30 and Table 3.9).

Table 3.9. Gas sorption uptakes (cm^3g^{-1}) of **2-Mo8** for different gases at 273 and 298 K.

T	N_2	CO_2	CH_4	C_2H_2	C_2H_4	C_2H_6
273 K	–	23.9	9.2	36.2	25.6	26.6
298 K	3.05	13.3	5.3	31.3	20.5	21.4

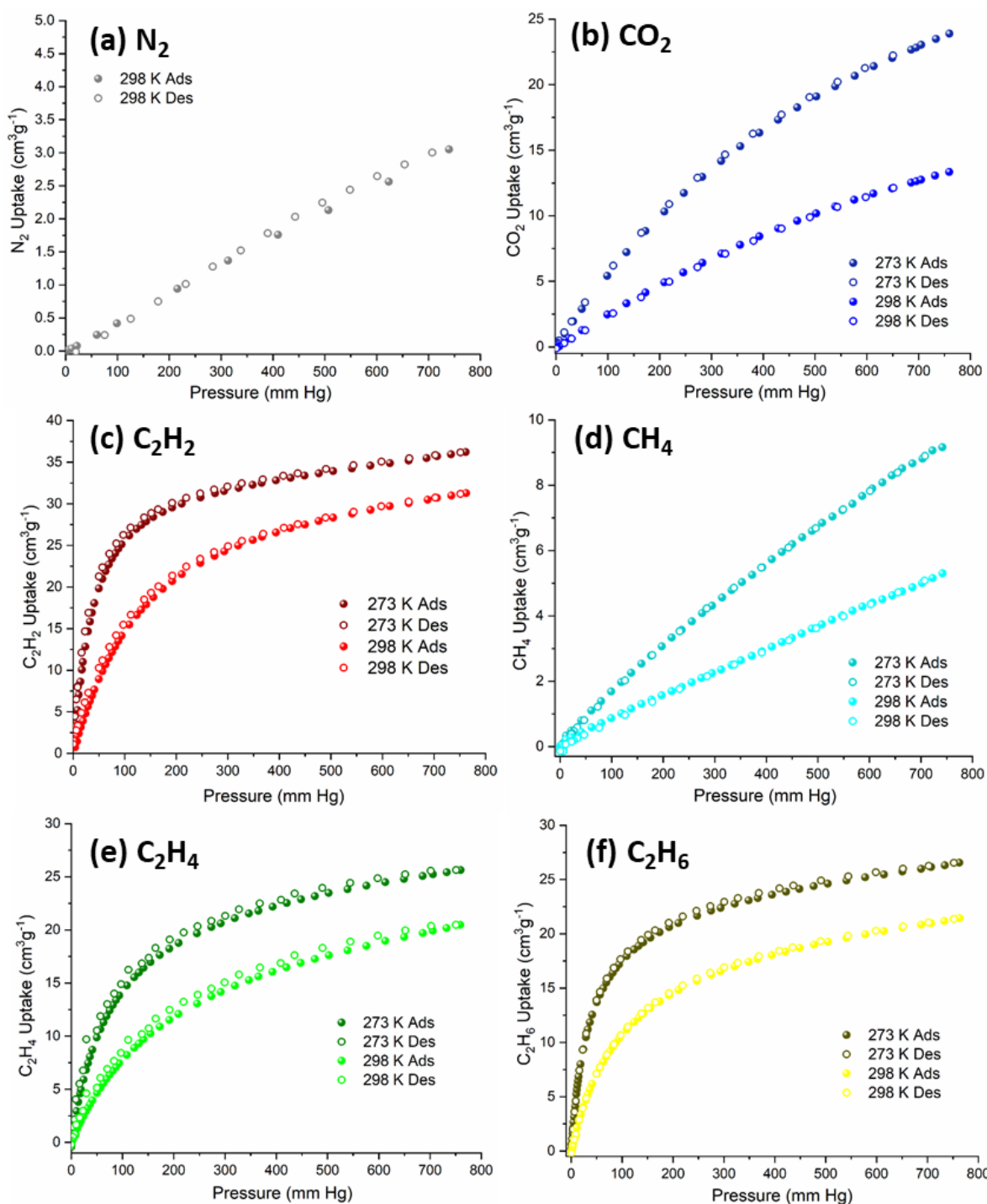


Figure 3.30. Experimental gas adsorption isotherms of **2-Mo8** at 273 and 298 K for (a) N₂, (b) CO₂, (c) CH₄, (d) C₂H₂, (e) C₂H₄, and (f) C₂H₆. Filled and empty markers correspond to the adsorption and desorption branches, respectively.

3.6. CONCLUSIONS

The POM/metalorganic covalent framework $[\{\text{Cu}(\text{cyclam})\}_3(\kappa\text{-Mo}_8\text{O}_{27})]\cdot 14\text{H}_2\text{O}$ (**1-Mo8**) constituted by octamolybdate anions (Mo_8) linked by the coordination of octahedral $\{\text{Cu}(\text{cyclam})\}^{2+}$ complexes, undergoes up to four consecutive thermally-triggered SCSC transformations. The removal of guest water molecules at different temperatures results in two different anhydrous phases, namely, $[\text{Cu}(\text{cyclam})][\{\text{Cu}(\text{cyclam})\}_2(\lambda\text{-Mo}_8\text{O}_{27})]$ (**2-Mo8**), and $[\{\text{Cu}(\text{cyclam})\}_3(\mu\text{-Mo}_8\text{O}_{27})]$ (**3-Mo8**), which implies the solid state isomerization of Mo_8 clusters through migration of some of the metal centers. It is worth highlighting that all the three isomers are totally unprecedented. This suggests that solid-state transformations could afford novel POM clusters that have not been isolated before by classical synthetic methods in solution. Structural transitions also involve the rearrangement of Cu-O_{POM} bonding scheme, which provoke changes in the coordination geometries of the metal complexes. One additional water molecule is condensed to the Mo_8 cluster when **3-Mo8** is exposed to open atmosphere and affords the framework $[\{\text{Cu}(\text{cyclam})\}_3\{\gamma\text{-Mo}_8\text{O}_{26}(\text{OH})_2\}]\cdot 11\text{H}_2\text{O}$ (**4-Mo8**), which dehydrates below 120 °C without any apparent major structural change to lead to a third anhydrous phase **6-Mo8**. In contrast, **2-Mo8** rapidly hydrates to form $[\{\text{Cu}(\text{cyclam})\}_3(\kappa\text{-Mo}_8\text{O}_{27})]\cdot 13\text{H}_2\text{O}$ (**5-Mo8**), which displays similar unit cell parameters to those in **2-Mo8**, but with the same Mo_8 cluster as that in **1-Mo8**.

Up to three different anhydrous phases (**2-Mo8**, **3-Mo8** and **6-Mo8**) with accessible micropores can be isolated from **1-Mo8**, which showed one of the highest water sorption capacity reported for any POM-based compound. These results together with their great cyclability after 100 adsorption/desorption cycles as well as their high adsorption capacity at low relative humidity environments (20-30% RH), endows the system with interesting properties for their use as humidity control devices. Beyond the preliminary characterization of the gas sorption behavior to determine the textural properties of **2-Mo8** and **3-Mo8**, further studies on the adsorption selectivity of **3-Mo8** have been carried out. Especially, this compound is able to adsorb C_2H_2 over C_2H_4 even in gas mixtures with very low concentration of acetylene. Moreover, **3-Mo8** has demonstrated the ability to adsorb C_2H_6 selectively over C_2H_4 , which is not a common behavior among the most usual materials with gas sorption ability. This feature gives **3-Mo8** the potential as molecular separator with interesting sensing ability.

3.7. REFERENCES

- [1] Schwing-Weill, M. J.; Arnaud-Neu, F. Etude des Molybdates de Certaines Pipéridine Substituées à Propriétés Photochromes. *Bull. Soc. Chim. Fr.*, **1970**, 60-68.
- [2] (a) Bridgeman, A. M. The Electronic Structure and Stability of the Isomers of Octamolybdate. *J. Phys. Chem. A*, **2002**, *106*, 12151-12160. (b) Allis, D. G.; Burkholder, E.; Zubieta, J. A new octamolybdate: observation of the θ -isomer in $[\text{Fe}(\text{tpyprz})_2]_2[\text{Mo}_8\text{O}_{26}]\cdot 3.7\text{H}_2\text{O}$ (tpyprz = tetra-2-pyridylpyrazine). *Polyhedron*, **2004**, *23*, 1145-1152. (c) Yue, Z.-C.; Du, H.-J.; Niu, Y.-Y.; Jin, G.-X. An unprecedented ι -type octamolybdate: $[\text{TbI}_2][(\beta\text{-Mo}_8\text{O}_{26})_{0.5}(\iota\text{-Mo}_8\text{O}_{26})]$ directed by a new tricationic template. *CrystEngComm*, **2013**, *15*, 9844-9848.
- [3] Kemperer, W. G.; Shum, W. Synthesis and Interconversion of the Isomeric α - and β -molybdate ($\text{Mo}_8\text{O}_{26}^{4-}$) ion. *J. Am. Chem. Soc.*, **1976**, *98*, 8291-8293.
- [4] Isobe, M.; Marumo, F.; Yamase, T.; Ikawa, T. The Crystal Structure of Hexakis(isopropylammonium) Dihydrogenoctamolybdate(6-) Dihydrate, $(\text{C}_3\text{H}_{10}\text{N}_6)_6[\text{H}_2\text{Mo}_8\text{O}_{28}]\cdot 2\text{H}_2\text{O}$. *Acta Crystallogr., Sect. B: Struct. Crystallogr. Cryst. Chem.* **1978**, *34*, 2728-2731.
- [5] Dissem, N.; Artetxe, B.; San Felices, L.; Lezama, L.; Haddad, A.; Gutiérrez-Zorrilla, J. M. A Robust Framework Based on Polymeric Octamolybdate Anions and Copper(II) Complexes of Tetradentate N-donor Ligands. *Crystals* **2018**, *8*, 20-34.
- [6] Bridgeman, A. J. The Electronic Structure and Stability of the Isomers of Octamolybdate. *J. Phys. Chem. A* **2002**, *106*, 12151-12160.
- [7] Isobe, M.; Marumo, F.; Yamase, T.; Ikawa, T. The Crystal Structure of Hexakis(isopropylammonium) Dihydrogenoctamolybdate(6-) Dihydrate, $(\text{C}_3\text{H}_{10}\text{N}_6)_6[\text{H}_2\text{Mo}_8\text{O}_{28}]\cdot 2\text{H}_2\text{O}$. *Acta Crystallogr., Sect. B: Struct. Crystallogr. Cryst. Chem.* **1978**, *34*, 2728-2731.
- [8] Allis, D. G.; Burkholder, E.; Zubieta, J. A New Octamolybdate: Observation of the θ -isomer in $[\text{Fe}(\text{tpyprz})_2]_2[\text{Mo}_8\text{O}_{26}]\cdot 3.7\text{H}_2\text{O}$ (tpyprz = tetra-2-pyridylpyrazine), *Polyhedron* **2004**, *23*, 1145-1152.
- [9] Yue, Z.-C.; Du, H.-J.; Niu, Y.-Y.; Jin, G.-X. An Unprecedented ι -type Octamolybdate: $[\text{TbI}_2][(\beta\text{-Mo}_8\text{O}_{26})_{0.5}(\iota\text{-Mo}_8\text{O}_{26})]$ Directed by a New Tricationic Template. *CrystEngComm* **2013**, *15*, 9844-9848.
- [10] Groom, C. R.; Bruno, I. J.; Lightfoot, M. P.; Ward, S. C. The Cambridge Structural Database. *Acta Crystallogr.* **2016**, *B72*, 171-179.
- [11] (a) Rarig, R. S.; Zubieta, J. Influences of Secondary Metal-Ligand Subunits on Molybdenum Oxide Structures: The Hydrothermal Syntheses and Structures of $[\text{M}(\text{tpytrz})_2\text{Mo}_4\text{O}_{13}]$ ($\text{M} = \text{Fe}, \text{Co}, \text{Ni}, \text{Zn}$; tpytrz = tripyridyltriazine), $[\text{Ni}(\text{tpytrz})\text{Mo}_2\text{O}_7]$ and $[\text{Zn}_2(\text{tpytrz})\text{Mo}_2\text{O}_8]$. *J. Chem. Soc., Dalton Trans.* **2001**, 3446-3452. (b) Meng, J.-X.; Lu, Y.; Li, Y.-G.; Fu, H.; Wang, E.-B. Base-Directed Self-Assembly of Octamolybdate-Based Frameworks Decorated by Flexible N-Containing Ligands. *Cryst. Growth & Des.* **2009**, *9*, 4116-4126. (c) Dong, B.-X.; Xu, Q. Investigation of Flexible Organic Ligands in the Molybdate System: Delicate Influence of a Peripheral Cluster Environment on the Isopolymolybdate Frameworks. *Inorg. Chem.* **2009**, *48*, 5861-5873. (d) Zhang, C.-J.; Pang, H.-J.; Tang, Q.; Wang, H.-Y.; Chen, Y.-G. Three 3D Hybrid Networks Based on Octamolybdates and Different $\text{Cu}^{\text{I}}/\text{Cu}^{\text{II}}$ -Bis(triazole) Motifs. *J. Solid State Chem.* **2010**, *183*, 2945-2959. (e) Tian, A.-X.; Liu, J.-N.; Ji, X.-B.; Liu, G.-Y.; Li, T.-T.; Tian, Y.; Ni, H.-P.; Liu, G.-C.; Ying, J. Tuning Dimensionality of Octamolybdate Structures Through Selecting Different Ligands. *J. Mol. Struct.* **2018**, *1155*, 371-379. (f) Guo, H.; Gong, C.; Zeng, X.; Xu, H.; Zeng, Q.; Zhang, J.; Zhong, Z.; Xie, J. Isopolymolybdate-Based Inorganic-Organic Hybrid Compounds Constructed by Multidentate N-Donor Ligands: Syntheses, Structures and Properties. *Dalton Trans.* **2019**, *48*, 5541-5550.
- [12] Tian, A.-X.; Fu, Y.-B.; Cui, H.-T.; Ying, J.; Yang, M.-L.; Yang, Y.; Wang, X.-L. A Series of Metal-Organic Loops Templated by $[\text{SiMo}_{12}\text{O}_{40}]^{4-}$ and $[\beta\text{-Mo}_8\text{O}_{26}]^{4-}$ Anions Using Double Chelating Ligands: Amperometric Sensing and Selective Photocatalytic Properties. *New J. Chem.* **2019**, *43*, 9980-9988.

- [13] Zheng, Y.; Zhou, W.; Liu, X.; Yuan, G.; Peng, J. Experimental and Theoretical Study of Bifunctional Electro-Catalysts Constructed from Different Polyoxometalates and Ag-bimpy Segments. *Electrochim. Acta* **2021**, *391*, 138930.
- [14] (a) Kan, W.-Q.; Wen, S.-Z.; He, Y.-C. Two Octamolybdate-Based Coordination Polymers With High Photocatalytic Activities Under Visible Light Irradiation. *Inorg. Chem. Commun.* **2017**, *86*, 90-93. (b) Kumar, N. T.; Bhoi, U.; Naulakha, P.; Das, S. K. A Polyoxometalate Supported Copper Dimeric Complex: Synthesis, Structure and Electrocatalysis. *Inorganica Chim. Acta* **2020**, *506*, 119554.
- [15] (a) Wu, C.-D.; Lu, C.-Z.; Lin, X.; Zhuang, H.-H.; Huang, J.-S. Two New β -Octamolybdate Supported Rare Earth Metal Complexes: $[\text{NH}_4]_2\{[\text{Gd}(\text{DMF})_7]_2(\beta\text{-Mo}_8\text{O}_{26})\}[\beta\text{-Mo}_8\text{O}_{26}]$ and $[\text{NH}_4][\text{La}(\text{DMF})_7(\beta\text{-Mo}_8\text{O}_{26})]$. *Inorg. Chim. Commun.* **2002**, *5*, 664-666. (b) Chen, L.-J.; Lu, C.-Z.; Zhang, Q.-Z.; Chen, S.-M. Poly[μ_2 -hexacosaoxooctamolybdate)sodium]]. *Acta Cryst.* **2005**, *C61*, 269-271.
- [16] (a) Rarig, R. S.; Zubieta, J. Octamolybdate Subunits as Building Blocks in the Hydrothermal Synthesis of Organically Templated Mixed Metal Oxides: The Synthesis and X-ray Characterization of $[\text{Cu}_2\text{Mo}_4\text{O}_{13}(3,3'\text{-bipy})_2]\cdot\text{H}_2\text{O}$, $[\text{CuMo}_4\text{O}_{13}(\text{Hdipyreth})]$, and $[\text{Cu}(\text{dpp})]_2[\text{Cu}_2(\alpha\text{-Mo}_8\text{O}_{26})(\text{dpp})_2]\cdot 2\text{H}_2\text{O}$ (3,3'-bipy = 3,3'-bipyridine; dipyreth = 1,2-bis(2-pyridyl)ethylene; dpp = 4,4'-trimethylenedipyridine). *Polyhedron*, **2003**, *22*, 177-188. (b) Burkholder, E.; Zubieta, J. Two-Dimensional Oxides Constructed from Octamolybdate Clusters and Mn^+ /Tetrapyridylpyrazine Subunits (M = Co, Ni: n = 2; M = Cu: n = 1). *Inorganica Chim. Acta* **2005**, *358*, 116-122. (c) Alam, N.; Feldman, C. $[\text{Cu}(\text{mim})_4]_2[\alpha\text{-Mo}_8\text{O}_{26}]$ – A Layer-type Octamolybdate Framework. *Solid State Sci.* **2010**, *12*, 471-475. (d) Fu, H.; Qin, C.; Lu, Y.; Zhang, Z.-M.; Li, Y.-G.; Su, Z.-M.; Li, W.-L.; Wang, E.-B. An Ionothermal Synthetic Approach to Porous Polyoxometalate-Based Metal–Organic Frameworks. *Angew. Chem. Int. Ed.* **2012**, *51*, 7985–7989.
- [17] (a) Hagrman, D.; Sangregorio, C.; O'Connor, C. J.; Zubieta, J. Solid State Coordination Chemistry: Two-Dimensional Oxides Constructed from Polyoxomolybdate Clusters and Copper–Organoamine Subunits. *J. Chem. Soc., Dalton Trans.*, **1998**, 3707–3709. (b) Springsteen, C. H.; Johnston, L. L.; LaDuca, R. L. Synthesis and Structure of a Bimetallic Hybrid Inorganic/Organic Layered Coordination Polymer With an Octamolybdate Cluster Variant Trapped Between the α and β Isomeric Forms. *Solid State Sci.* **2007**, *9*, 804-811. (c) Lan, Y.-Q.; Li, S.-L.; Wang, X.-L.; Shao, K.-Z.; Su, Z.-M.; Wang, E.-B. Supramolecular Isomerism with Polythreaded Topology Based on $[\text{Mo}_8\text{O}_{26}]^{4-}$ Isomers. *Inorg. Chem.* **2008**, *47*, 529-534.
- [18] Zhai, Q.; Lu, C.; Zhang, Q.; Wu, X.; Xu, X.; Chen, S.; Chen, L. Influence of Substituents on the Structures of Hybrid Complexes Constructed from Tetranuclear Copper(I) 1,2,4-Triazolates Clusters and Octamolybdates. *Inorganica Chim. Acta* **2006**, *359*, 3875-3887.
- [19] Hagrman, D.; Zubieta, C.; Rose, D. J.; Zubieta, J.; Haushalter, R. C. Composite Solids Constructed From One-Dimensional Coordination Polymer Matrices and Molybdenum Oxide Subunits: Polyoxomolybdate Clusters within $\{[\text{Cu}(4,4'\text{-bpy})]_4\text{Mo}_8\text{O}_{26}\}$ and $\{[\text{Ni}(\text{H}_2\text{O})_2(4,4'\text{-bpy})_2]_2\text{Mo}_8\text{O}_{26}\}$ and One-Dimensional Oxide Chains in $\{[\text{Cu}(4,4'\text{-bpy})]_4\text{Mo}_{15}\text{O}_{47}\}\cdot 8\text{H}_2\text{O}$. *Angew. Chem. Int. Ed. Engl.* **1997**, *36*, 873-876.
- [20] Allis, D. G.; Rarig, R. S.; Burkholder, E.; Zubieta, J. A Three-Dimensional Bimetallic Oxide Constructed from Octamolybdate Clusters and Copper–Ligand Cation Polymer Subunits. A Comment on the Stability of the Octamolybdate Isomers. *J. Mol. Struct.* **2004**, *688*, 11-31.
- [21] Rarig, R. S.; Bewley, L.; Burkholder, E.; Zubieta, J. Organic-Inorganic Hybrid Materials of the Copper Molybdate Family. Syntheses and Structures of $[\text{Cu}(\text{tpa})\text{Mo}_2\text{O}_7]$, $[\text{Cu}(\text{Me}_2\text{bpy})\text{Mo}_2\text{O}_7]$ and $[\text{Cu}(t\text{-Bu}_2\text{bpy})\text{Mo}_4\text{O}_{13}]$ (tpa = tri-2-pyridylamine, Me_2bpy = 5,5'-dimethyl-2,2'-bipyridine, $t\text{-Bu}_2\text{bpy}$ = 4,4'-di-tert-butyl-2,2'-bipyridine). *Indian J. Chem.* **2003**, *42A*, 2235-2243.
- [22] Zang, H.-Y.; Lan, Y.-Q.; Yang, G.-S.; Wang, X.-L.; Shao, K.-Z.; Xu, G.-J.; Su, Z.-M. Construction and Property Investigation of Transition-Metal Complexes Modified Octamolybdate Hybrid Materials Based on V-Shaped Organic Ligands. *CrystEngComm* **2010**, *12*, 434-445.
- [23] Du, X.-D.; Li, C.-H.; Zhang, Y.; Liu, S.; Ma, Y.; You, X.-Z. Coordination Polymers Based on the Octamolybdate and Flexible Bis(triazole) Ligands with Different Spacer Lengths. *CrystEngComm* **2011**, *13*, 2350-2357.

- [24] (a) Li, Y.; Wang, Y.; Li, Y.; Wang, E. A New Supramolecular Compound Based on Mn^{III}-Schiff-Base and β -Octamolybdate. *Inorg. Chem. Commun.* **2009**, *12*, 112-115. (b) Gao, Q.; Xu, L.; Hu, D.; Li, D.; Yang, J. 3D Organic-Inorganic Hybrid Framework Built Upon $[\beta\text{-Mo}_8\text{O}_{26}]^{4-}$ Units and Polymeric Copper(II) Complexes with Magnetic Properties and Electrocatalytic Activities for H₂O₂ Reduction. *Inorg. Chem. Commun.* **2019**, *104*, 160-164. (c) Wang, X.-L.; Cui, Z.-W.; Lin, H.-Y.; Chang, Z.-H. The Rational Design of Four Multifunctional Octamolybdate-Based Complexes for Detecting Different Ions and Removing Organic Dyes from Aqueous Solution. *CrystEngComm* **2021**, *23*, 2113-2121. (d) Wang, X.; Li, L.; Wang, X.; Zhang, Y. Various Amide-Derived Ligands Induced Five Octamolybdate-Based Metal-Organic Complexes: Synthesis, Structure, Electrochemical Sensing and Photocatalytic Properties. *CrystEngComm* **2021**, *23*, 5176-5183.
- [25] Rouquerol, J.; Llewellyn, P.; Rouquerol, F. Is the BET equation applicable to microporous adsorbents? *Stud. Surf. Sci. Catal.* **2007**, *160*, 49-56.
- [26] Bosnich, B.; Poom, C. K.; Tobe, M. L. Complexes of Cobalt(III) with a Cyclic Tetradentate Secondary Amine. *Inorg. Chem.* **1965**, *4*, 1102-1108.
- [27] Spek, A. L. Structure Validation in Chemical Crystallography. *Acta Crystallogr., Sect. D: Biol. Crystallogr.* **2009**, *65*, 148-155.
- [28] Brown, I. D.; Wu, K. K. Empirical Parameters for Calculating Cation-Oxygen Bond Valences. *Acta Crystallogr., Sect. B: Struct. Crystallogr. Cryst. Chem.* **1976**, *B32*, 1957-1959.
- [29] Zhu, Z.-K.; Lin, Y.-Y.; Yu, H.; Li, X.-X.; Zheng, S.-T. Inorganic–Organic Hybrid Polyoxoniobates: Polyoxoniobate Metal Complex Cage and Cage Framework. *Angew. Chem.*, **2019**, *131*, 17020–17024.
- [30] Zhu, Z.-K.; Lin, Y.-Y.; Lin, L.-D.; Li, X.-X.; Sun, Y.-Q.; Zheng, S.-T. A Rare 3D Porous Inorganic–Organic Hybrid Polyoxometalate Framework Based on a Cubic Polyoxoniobate-Cupric-Complex Cage with a High Water Vapor Adsorption Capacity. *Inorg. Chem.*, **2020**, *59*, 11925–11929.
- [31] Zhu, Z.-K.; Lin, L.-D.; Zhang, J.; Li, X.-X.; Sun, Y.-Q.; Zheng, S.-T. A Rare 4-Connected Neb-Type 3D Chiral Polyoxometalate Framework Based on {KNb₂₄O₇₂} Clusters. *Inorg. Chem. Front.*, **2020**, *7*, 3919-3924.
- [32] Zhou, E.-L.; Qin, C.; Wang, X.-L.; Shao, K.-Z.; Su, Z.-M. Steam-Assisted Synthesis of an Extra-Stable Polyoxometalate-Encapsulating Metal Azolate Framework: Applications in Reagent Purification and Proton Conduction. *Chem. Eur. J.*, **2015**, *21*, 13058-13064.
- [33] Zhou, E.-L.; Qin, C.; Huang, P.; Wang, X.-L.; Chen, W.-C.; Shao, K.-Z.; Su, Z.-M. A Stable Polyoxometalate-Pillared Metal-Organic Framework for Proton-Conducting and Colorimetric Biosensing. *Chem. Eur. J.*, **2015**, *21*, 11894-11898.
- [34] (a) Uchida, S.; Kawamoto, R.; Mizuno, N. Recognition of Small Polar Molecules with an Ionic Crystal of α -Keggin-Type Polyoxometalate with a Macroocation. *Inorg. Chem.*, **2006**, *45*, 5136-5144. (b) Uchida, S.; Mizuno, N. Zeotype Ionic Crystal of Cs₅[Cr₃O(OOCH)₆(H₂O)₃][α -CoW₁₂O₄₀] \cdot 7.5H₂O with Shape-Selective Adsorption of Water. *J. Am. Chem. Soc.*, **2004**, *126*, 1602-1603. (c) Uchida, S.; Mizuno, N. Unique Guest-Inclusion Properties of a Breathing Ionic Crystal of K₃[Cr₃O(OOCH)₆(H₂O)₃][α -SiW₁₂O₄₀] \cdot 16H₂O. *Chem. Eur. J.*, **2003**, *9*, 5850-5857.
- [35] Kawahara, R.; Uchida, S.; Mizuno, N. Concerted Functions of Anions and Cations in a Molecular Ionic Crystal with Stable Three-Dimensional Micropores. *Inorg. Chem.*, **2014**, *53*, 3655-3661.
- [36] Uchida, S.; Kawamoto, T.; Akatsuka, T.; Hikichi, S.; Mizuno, N. Structures and Sorption Properties of Ionic Crystals of Macroocation-Dawson-Type Polyoxometalates with Different Charges. *Chem. Mater.*, **2005**, *17*, 1367-1375.
- [37] Wei, M.; Chen, L.; Duan, X. A Porous Cu(II)-MOF Containing [PW₁₂O₄₀]³⁻ and a Large Protonated Water Cluster: Synthesis, Structure, and Proton Conductivity. *Journal of Coordination Chemistry*, **2014**, *67*, 2809-2819.
- [38] Li, Z.; Lin, L.-D.; Yu, H.; Li, X.-X.; Zheng, S.-T. All-Inorganic Ionic Porous Material Based on Giant Spherical Polyoxometalates Containing Core-Shell K₆@K₃₆-Water Cage. *Angew. Chem. Int. Ed.*, **2018**, *57*, 15777–15781.

- [39] Wei, M.-L.; Sun, J.-J.; Duan, X.-Y. A Complex Based on a Cu^{II}-Schiff-Base Complex and POM-MOF Chain: Synthesis, Structure and Proton Conductivity. *Eur. J. Inorg. Chem.*, **2014**, 345–351.
- [40] (a) Uchida, S.; Takahashi, E.; Mizuno, N. Porous Ionic Crystals Modified by Post-Synthesis of K₂[Cr₃O(OOCH)₆(etpy)₃]₂[α-SiW₁₂O₄₀]·8H₂O through Single-Crystal-to-Single-Crystal Transformation. *Inorg. Chem.*, **2013**, 53, 9320–9326. (b) Uchida, S.; Hosono, R.; Eguchi, R.; Kawahara, R.; Osuga, R.; Kondo, J. N.; Hibino, M.; Mizuno, N. Proton Conduction in Alkali Metal Ion-Exchanged Porous Ionic Crystals. *Phys. Chem. Chem. Phys.*, **2017**, 19, 29077–29083. (c) Miyazawa, S.; Hosono, R.; Osuga, R.; Kondo, J. N.; Uchida, S. Effect of the Ammonium Ion on Proton Conduction in Porous Ionic Crystals Based on Keggin-Type Silicododecatungstate. *Acta Cryst.*, **2018**, C74, 1289–1294.
- [41] Kawahara, R.; Uchida, S.; Mizuno, N. Redox-Induced Reversible Uptake-Release of Cations in Porous Ionic Crystals based on Polyoxometalate: Cooperative Migration of Electrons with Alkali Metal Ions. *Chem. Mater.*, **2015**, 27, 2092–2099.
- [42] Miura, Y.; Imai, H.; Yokoi, T.; Tatsumi, T.; Kamiya, Y. Microporous Cesium Salts of Tetravalent Keggin-Type Polyoxotungstates Cs₄[SiW₁₂O₄₀], Cs₄[PW₁₁O₃₉(Sn-n-C₄H₉)], and Cs₄[PW₁₁O₃₉(Sn-OH)] and their Adsorption Properties. *Microporous Mesoporous Mater.*, **2013**, 174, 34–43.
- [43] Wei, M.; Wang, X.; Sun, J.; Duan, X. A 3D POM-MOF Composite Based on Ni(II) Ion and 2,2'-Bipyridyl-3,3'-Dicarboxylic Acid: Crystal Structure and Proton Conductivity. *Journal of Solid State Chemistry*, **2013**, 202, 200–206.
- [44] Hu, J.; Xu, Y.; Zhang, D.; Chen, B.; Lin, Z.; Hu, C. A Highly Symmetric Ionic Crystal Constructed by Polyoxoniobates and Cobalt Complexes for Preferential Water Uptake over Alcohols. *Inorg. Chem.*, **2017**, 56, 10844–10847.
- [45] Noro, S.-I.; Tsunashima, R.; Kamiya, Y.; Uemura, K.; Kita, H.; Cronin, L.; Akutagawa, T.; Nakamura, T. Adsorption and Catalytic Properties of the Inner Nanospace of a Gigantic Ring-Shaped Polyoxometalate Cluster. *Angew. Chem. Int. Ed.*, **2009**, 48, 8703–8706.
- [46] Tagami, H.; Uchida, S.; Mizuno, N. Size-Selective Sorption of Small Organic Molecules in One-Dimensional Channels of an Ionic Crystalline Organic-Inorganic Hybrid Compound Stabilized by π–π Interactions. *Angew. Chem. Int. Ed.*, **2009**, 48, 6160–6164.
- [47] Uchida, S.; Eguchi, R.; Mizuno, N. Zeotype Organic-Inorganic Ionic Crystals: Facile Cations Exchange and Controllable Sorption Properties. *Angew. Chem. Int. Ed.*, **2010**, 49, 9930–9934.
- [48] (a) Jiang, C.; Lesbani, A.; Kawamoto, R.; Uchida, S.; Mizuno, N. Channel-Selective Independent Sorption and Collection of Hydrophilic and Hydrophobic Molecules by Cs₂[Cr₃O(OOCC₂H₅)₆(H₂O)₃]₂[α-SiW₁₂O₄₀] Ionic Crystals. *J. Am. Chem. Soc.*, **2006**, 128, 14240–14241. (b) Lesbani, A.; Kawamoto, R.; Uchida, S.; Mizuno, N. Control of Structures and Sorption Properties of Ionic Crystals of A₂[Cr₃O(OOCC₂H₅)₆(H₂O)₃]₂[α-SiW₁₂O₄₀] (A = Na, K, Rb, NH₄, Cs, TMA). *Inorg. Chem.*, **2008**, 47, 3349–3357.
- [49] Ogasawara, Y.; Uchida, S.; Maruichi, T.; Ishikawa, R.; Shibata, N.; Ikuhara, Y.; Mizuno, N. Cubic Cesium Hydrogen Silicododecatungstate with Anisotropic Morphology and Polyoxometalate Vacancies Exhibiting Selective Water Sorption and Cation-Exchange Properties. *Chem. Mater.*, **2013**, 25, 905–911.
- [50] Kawamoto, R.; Uchida, S.; Mizuno, N. Amphiphilic Guest Sorption of K₂[Cr₃O(OOCH)₆(H₂O)₃]₂[α-SiW₁₂O₄₀] Ionic Crystals. *J. Am. Chem. Soc.*, **2005**, 127, 10560–10567.
- [51] Seo, Y.-K.; Yoon, J. W.; Lee, J. S.; Hwang, Y. K.; Jun, C.-H.; Chang, J.-S.; Wuttke, S.; Bazin, P.; Vimont, A.; Daturi, M.; Bourrelly, S.; Llewellyn, P. L.; Horcajada, P.; Serre, C.; Férey, G. Energy-Efficient Dehumidification over Hierarchically Porous Metal–Organic Frameworks as Advanced Water Adsorbents. *Adv. Mater.* **2012**, 24, 806–810.
- [52] Chen, L.; He, C. Experimental Investigation of the Dehumidification Performance of a Metal-Organic Framework MIL-101(Cr)/Ceramic Fibre Paper for Use as a Desiccant Wheel. *Microporous and Mesoporous Mater.* **2020**, 305, 110378–110386.

- [53] Zu, K.; Qin, M.; Cui, S. Progress and Potential of Metal-Organic Frameworks (MOFs) as Novel Desiccants for Built Environment Control: A Review. *Renewable Sustainable Energy Rev.* **2020**, *133*, 110246. (b) Furukawa, H.; Gándara, F.; Zhang, Y.-B.; Jiang, J.; Queen, W. L.; Hudson, M. R.; Yaghi, O. M. Water Adsorption in Porous Metal-Organic Frameworks and Related Materials. *J. Am. Chem. Soc.* **2014**, *136*, 4369-4381.
- [54] (a) Miras, H. N.; Vilà-Nadal, L.; Cronin, L. Polyoxometalate based open-frameworks (POMOFs). *Chem. Soc. Rev.* **2014**, *43*, 5679-5699. (b) Buru, C. T.; Li, P.; Mahdi, B. L.; Dohnalkova, A.; Platero-Prats, A. E.; Browning, N. D.; Chapman, K. W.; Hupp, J. T.; Farha, O. K. Adsorption of a Catalytically Accessible Polyoxometalate in a Mesoporous Channel-type Metal-Organic Framework. *Chem. Mater.* **2017**, *29*, 5174-5181.
- [55] Fu, H.; Qin, C.; Lu, Y.; Zhang, Z.-M.; Li, Y.-G.; Su, Z.-M.; Li, W.-L.; Wang, E.-B. An Ionothermal Synthetic Approach to Porous Polyoxometalate-Based Metal-Organic Frameworks. *Angew. Chem. Int. Ed.* **2012**, *51*, 7985-7989.
- [56] Horvath, G.; Kawazoe, K. Method for the Calculation of Effective Pore Size Distribution in Molecular Sieve Carbon," *J. Chem. Eng. Jpn.* **1983**, *16*, 470-475.
- [57] (a) Myers, A.L.; and Prausnitz, J.M. Thermodynamics of mixed-gas adsorption. *AIChE J* **1965**, *11*, 121-127. (b) Fraux, G.; Boutin, A.; Fuchs, A. H.; Coudert, F.-X. On the use of the IAST method for gas separation studies in porous materials with gate-opening behavior. *Adsorption* **2018**, *24*, 233-241.
- [58] Kawahara, R.; Uchida, S.; Mizuno, N. Concerted Functions of Anions and Cations in a Molecular Ionic Crystal with Stable Three-Dimensional Micropores. *Inorg. Chem.* **2014**, *53*, 3655-3661.
- [59] Duan, F.; Liu, X.; Qu, D.; Li, B.; Wu, L. Polyoxometalate-Based Ionic Frameworks for Highly Selective CO₂ Capture and Separation. *CCS Chem.* **2020**, *2*, 2676-2687.
- [60] (a) Gao, X.; Zou, X.; Ma, H.; Meng, S.; Zhu, G. Highly Selective and Permeable Porous Organic Framework Membrane for CO₂ Capture. *Adv. Mater.* **2014**, *26*, 3644-3648. (b) Qian, J.; Li, Q.; Liang, L.; Li, T.-T.; Hu, Y.; Huang, S. A microporous MOF with open metal sites and Lewis basic sites for selective CO₂ capture. *Dalton. Trans.* **2017**, *46*, 14102-14106.
- [61] Eguchi, R.; Uchida, S.; Mizuno, N. Highly Selective Sorption and Separation of CO₂ from a Gas Mixture of CO₂ and CH₄ at Room Temperature by a Zeolitic Organic-Inorganic Ionic Crystal and Investigation of the Interaction with CO₂. *J. Phys. Chem. C* **2012**, *116*, 16105-16110.
- [62] (a) Gao, J.; Qian, X.; Lin, R.-B.; Krishna, R.; Wu, H.; Zhou, W.; Chen, B. Mixed Metal-Organic Framework with Multiple Binding Sites for Efficient C₂H₂/CO₂ Separation. *Angew. Chem., Int. Ed.* **2020**, *59*, 4396-4400. (b) Forrest, K. A.; Pham, T.; Chen, K.-J.; Jiang, X.; Madden, D. G.; Franz, D. M.; Hogan, A.; Zaworotko, M. J.; Space, B. Tuning the Selectivity Between C₂H₂ and CO₂ in Molecular Porous Materials. *Langmuir* **2021**, *37*, 13838-13845.
- [63] (a) Chen, K.-J.; Scott, H. S.; Madden, D. G.; Pham, T.; Kumar, A.; Bajpai, A.; Lusi, M.; Forrest, K. A.; Space, B.; Perry IV, J. J.; Zaworotko, M. J. Benchmark C₂H₂/CO₂ and CO₂/C₂H₂ Separation by Two Closely Related Hybrid Ultramicroporous Materials. *Chem* **2016**, *1*, 753-765. (b) Fu, X.-P.; Wang, Y.-L.; Liu, Q.-Y. Metal-organic frameworks for C₂H₂/CO₂ Separation. *Dalton Trans.* **2020**, *49*, 16598-16607. (c) Zhang, L.; Jian, K.; Yang, L.; Li, L.; Hu, E.; Y.; Shao, K.; Xing, H.; Cui, Y.; Yang, Y.; Li, B.; Chen, B.; Qian, G. Benchmark C₂H₂/CO₂ Separation in an Ultra-Microporous Metal-Organic Framework via Copper(I)-Alkynyl Chemistry. *Angew. Chem.* **2021**, *133*, 16131-16138.
- [64] Eguchi, R.; Uchida, S.; Mizuno, N. Inverse and High CO₂/C₂H₂ Sorption Selectivity in Flexible Organic-Inorganic Ionic Crystals. *Angew. Chem. Int. Ed.* **2012**, *51*, 1635-1639.
- [65] (a) Bloch, E. D.; Queen, W.; L.; Krishna, R.; Zadrozny, J. M.; Brown, C. M.; Long, J. R. Hydrocarbon Separation in a Metal-Organic Framework with Open Iron(II) Coordination Sites. *Science*, **2012**, *355*, 1606-1610. (b) Aguado, S.; Bergeret, G.; Daniel, C.; Farrusseng, D. Absolute Molecular Sieve Separation of Ethylene/Ethane Mixtures with Silver Zeolite A. *J. Am. Chem. Soc.* **2012**, *134*, 14635-14637. (c) Bereciartua, P. J.; Cantín, Á.; Corma, A.; Jordá, J. L.; Palomino, M.; Rey, F.; Valencia, S.; Corcoran, E. W.; Kortunov, P.; Ravikovitch, P. I.; Burton, A.; Yoon, C.; Wang, Y.; Paur, C.; Guzman, J.; Bishop, A. R.; Casty, G. L. Control of Zeolite Framework Flexibility and Pore Topology for Separation of Ethane and Ethylene. *Science*,

2017, 358, 1068-1071. (d) Cui, E.-G.; Hu, T.-L.; Bu, X.-H. Metal-Organic Framework Materials for the separation and Purification of Light Hydrocarbons. *Adv. Mater.* **2020**, 32, 1806445.

[66] (a) Li, L.; Lin, R.-B.; Krishna, R.; Li, H.; Xiang, S.; Wu, H.; Li, J.; Zhou, W.; Chen, B. Ethane/Ethylene Separation in a Metal-Organic Framework with Iron-Peroxo Sites. *Science* **2018**, 362, 443-446. (b) Lin, R.-B.; Wu, H.; Li, L.; Tang, X.-L.; Li, Z.; Gao, J.; Cui, H.; Zhou, W.; Chen, B. Boosting Ethane/Ethylene Separation within Isoreticular Ultramicroporous Metal-Organic Frameworks. *J. Am. Chem. Soc.* **2018**, 140, 12940-12946. (c) Zhang, X.; Li, L.; Wang, J.-X.; Wen, H.-M.; Krishna, R.; Wu, H.; Zhou, W.; Chen, Z.-N.; Li, B.; Qian, G.; Chen, B. Selective Ethane/Ethylene Separation in a Robust Microporous Hydrogen-bonded Organic Framework. *J. Am. Chem. Soc.* **2020**, 142, 633-640.

Structural Diversity in POM-Metalorganic Hybrids Containing Anderson-Evans Anions

4.1. Introduction

4.2. Experimental section

4.3. Results and discussion

4.4. Conclusions

4.5. References

ABSTRACT: The reaction between $(\text{NH}_4)_6\text{Mo}_7\text{O}_{24}\cdot 4\text{H}_2\text{O}$ salt and the $\{\text{Cu}(\text{DMC})\}^{2+}$ (DMC = 1,8-dimethyl-1,4,8,11-tetraazacyclotetradecane) complex is studied under mild aqueous conditions. The parent polyanion undergoes a full rearrangement to lead to an unprecedented $[\text{H}_4\text{CuMo}_6(\text{MoO}_3)_2\text{O}_{24}]^{6-}$ anion formed by a classical Anderson-Evans scaffold with two $\{\text{MoO}_3\}$ tetrahedra condensed to its surface and stabilized by the H-bonding interactions established with protonated faces of the Anderson-Evans surface. The final compound $[\{\text{Cu}(\text{DMC})\}_3\{\text{H}_4\text{CuMo}_6(\text{MoO}_3)_2\text{O}_{24}\}]\cdot 13\text{H}_2\text{O}$ (**1-CuMo8**) exhibits a porous three-dimensional hybrid framework structure. Following this results, the second part of this chapter analyses the $\{\text{H}_6\text{CrMo}_6\text{O}_{24}\}^{3-}/\{\text{Cu}(\text{DMC})\}^{2+}$ synthetic system in different aqueous media. When the synthesis is carried out in pure water, the mono-dimensional $[\text{Cu}(\text{DMC})(\text{H}_2\text{O})][\{\text{Cu}(\text{DMC})\}_{0.5}\{\text{H}_6\text{CrMo}_6\text{O}_{24}\}]\cdot 10\text{H}_2\text{O}$ (**1-CrMo6**) hybrid is formed in a very low yield. On the contrary, reactions in high ionic strength aqueous 1M NaCl media leads to the assembly of two different two-dimensional compounds: $\text{Na}[\{\text{Cu}(\text{DMC})\}\{\text{H}_6\text{CrMo}_6\text{O}_{24}\}]\cdot 8\text{H}_2\text{O}$ (**1Na-CrMo6**) and $\text{Na}_2[\{\text{Cu}(\text{DMC})\}_{0.5}\{\text{H}_6\text{CrMo}_6\text{O}_{24}\}]\cdot 11.5\text{H}_2\text{O}$ (**1Na2-CrMo6**). It is worth noting that compound **1Na-CrMo6** exhibits two sequential thermally triggered structural transitions that have been assessed by powder X-ray diffraction. When the reaction is carried out in aqueous 1M NaNO_3 or 1M LiCl solutions, two different two-dimensional hybrids are obtained, which are constituted by hybrid POM-metalorganic layers with hydration water molecules and counterions occupying interlamellar spaces. These are, the $[\{\text{Cu}(\text{DMC})\}_2\{\text{H}_6\text{CrMo}_6\text{O}_{24}\}]\text{NO}_3\cdot 5\text{H}_2\text{O}$ (**1NO3-CrMo6**) and $[\{\text{Cu}(\text{DMC})\}_2\{\text{H}_6\text{CrMo}_6\text{O}_{24}\}]\text{Cl}\cdot 5\text{H}_2\text{O}$ (**1Cl-CrMo6**), respectively. Apparently, anhydrous phases for both cases are thermally stable up to ca 200 °C with no major modifications in their diffraction pattern, which could indicate a robust thermostructural behavior. This fact could generate activated structures with empty channels available for the adsorption of chemical species. It is worth highlighting that the most common cis-V configuration of the DMC ligand has only been observed for the square-pyramidal, charge compensating $[\text{Cu}(\text{DMC})(\text{H}_2\text{O})]^{2+}$ unit in **1-CrMo6**, whereas all the remaining octahedral $\{\text{Cu}(\text{DMC})\}^{2+}$ complexes display a trans-III configuration. Finally, the fully inorganic salt $\text{K}_3[\text{H}_6\text{CrMo}_6\text{O}_{24}]\cdot 6\text{H}_2\text{O}$ (**CrMo6**) crystallizes from the reaction at aqueous 1M KCl.

4.1. INTRODUCTION

Beyond the Keggin-type anion described in the *General Introduction*, there are some other archetypical POMs that have been extensively studied within the last few years. This is the case of the Anderson-Evans polyanion with the general formula $[\text{XM}_6\text{O}_{24}]^{n-}$.¹ The crystal structure of the $[\alpha\text{-Te}^{\text{VI}}\text{Mo}_6\text{O}_{24}]^{6-}$ anion was first proposed by Anderson back in 1937² and ten years later confirmed by Evans making use of X-ray diffraction experiments.³ This cluster can be best described as a ring of six edge-sharing octahedra encapsulating a central $\{\text{XO}_6\}$ heteroatom in an ideal D_{3d} symmetry. The most common α -isomer exhibits a planar geometry, whereas the “bent” β -isomer with an ideal C_{2v} symmetry has only been isolated for some specific heteroatom/addenda metal combinations.⁴ The β -isomer is structurally similar to the heptametalate clusters, but with a heteroatom in its central position. It is worth highlighting the great compositional variability that this cluster can show, because both Mo and W can act as *addenda* metals, whereas many of the first-row transition metals and p-block elements in their highest oxidation states can play the role of heteroatoms. This diversity is specially rich in the case of heteropolyoxomolybdates ($\text{M} = \text{Mo}$, $\text{X} = \text{first row transition metals, Rh}^{\text{III}}, \text{Pd}^{\text{IV}}, \text{Pt}^{\text{IV}}, \text{Al}^{\text{III}}, \text{Ga}^{\text{III}}, \text{Sb}^{\text{V}}, \text{Te}^{\text{VI}}, \text{I}^{\text{VII}}$; and $\text{M} = \text{W}$, $\text{X} = \text{Mn}^{\text{II}}, \text{Mn}^{\text{IV}}, \text{Ni}^{\text{II}}, \text{Ir}^{\text{IV}}, \text{Pt}^{\text{IV}}, \text{Sb}^{\text{V}}, \text{Te}^{\text{VI}}$).⁵

Three different types of oxygen atoms can be found in the Anderson-Evans cluster: six triple-bridged O atoms ($\mu_3\text{-O}$) each of them connecting the central heteroatom to two *addenda* atoms from the six-member ring, six double-bridged $\mu_2\text{-O}$ atoms linking two *addenda* atoms, and twelve terminal O atoms (O_t), two per *addenda* metal center. Traditionally, Anderson-Evans type POMs can be classified into two groups: i) the non-protonated A-type with central heteroatoms in high oxidation states that show the general formula $[\text{X}^{n+}\text{M}_6\text{O}_{24}]^{(12-n)-}$; and, ii) protonated B-type with heteroatoms in low oxidation states and the general formula $[\text{H}_6\text{X}^{n+}\text{M}_6\text{O}_{24}]^{(6-n)-}$. Central $\mu_3\text{-O}$ atoms show a basic character, and they can be easily protonated (Figure 4.1). This protonation is a key factor to allow condensation reactions with trisalkoxo ligands leading to the organic functionalization of the inorganic cluster, as detailed in the *General Introduction*. These features together with its small size, planar shape, presence of heavy atoms and solution stability make Anderson–Evans polyoxotungstates ideal additives for protein crystallography.⁶ Different related structural examples include i) those in which the central heteroatom is replaced by one $\{\text{XO}_4\}$ tetrahedral unit ($\text{X} = \text{V, As, Te}$) on each side of the planar ring (Figure 4.1c),⁷ and ii) the Evans-Showell-type $[\text{Co}_2\text{Mo}_{10}\text{O}_{34}(\text{OH})_4]^{6-}$ heteropolyanion formed by the perpendicular interpenetration of two Anderson-Evans clusters (Figure 4.1d).⁸

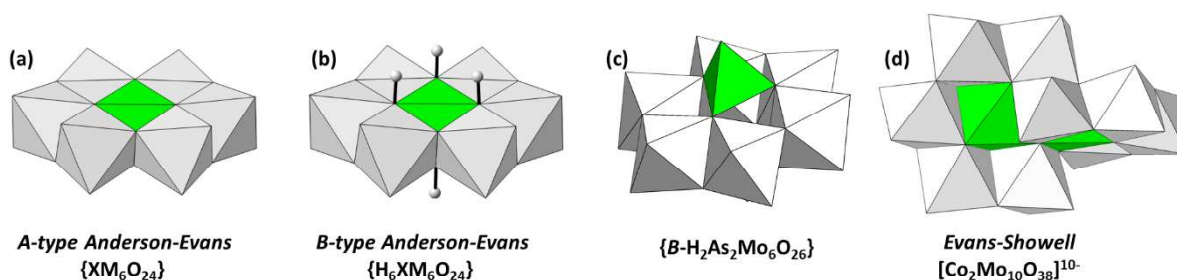


Figure 4.1. Polyhedral representation of (a) A- and (b) B-type Anderson-Evans clusters together with (c) those in which the central heteroatom is replaced by one tetrahedral unit, and (d) Evans-Showell related structural.

4.1.1. Hybrid POM-metalorganic compounds based on Anderson-Evans anion.

The planar structure of the Anderson-Evans polyanions together with the fact that each *addenda* atoms has two accessible terminal oxygen atoms facilitates the coordination of transition metal complexes to its surface (Figure 4.2). In this sense, several hybrids have been prepared in the last decades by combining Anderson-Evans polyoxomolybdates⁹ or tungstates¹⁰ together with 3d-metal complexes of monodentate N-donor ligands (e.g. pyridine, imidazole, pyrazine, triazine, tetraazol...). Whereas the variability in heteroatom position is considerable in the case of molybdates ($X =$ mainly first row transition metals), this is limited to $X = Te^{VI}$ and Pt^{IV} for tungstates. However, the number of reported hybrid structures with high dimensionality are comparatively scarce,¹¹ and most of them display Anderson-Evans-type heteropolyoxomolybdates with trivalent metal centers in heteroatomic position ($X = Al^{III}$, Cr^{III}). In the case of $\{CrMo_6O_{24}\}$,¹² the vast majority of extended hybrid structures has been constructed by using Cu^{II} complexes of N-donor, or N,O-/N,N'-chelating ligands such as pyridine,¹³ phenantroline,¹⁴ pyrazine¹⁵, nicotine¹⁶ or aminoacids (e.g. alanine,¹⁷ glycine,¹⁸ and histidine¹⁹). Wang's group followed hydrothermal routes to prepare mono- and three-dimensional systems based on POM anions linked through complexes bearing triazole²⁰ and, 4-dpye ligands (4-dpye = N,N'-bis(4-pyridinecarboxamide)-1,2-ethane),²¹ respectively, with interesting catalytic activity towards the photooxidation of dyes. Besides, they studied the assembly of copper(II)/3-bpye complexes (3-bpye = 1,4-bis(3-pyridinecarboxamido)benzene) with $\{CrMo_6O_{24}\}$ anions, which lead to hybrid 2D or 3D structures depending on the pH of the reaction medium.²² In addition, Wu and co-workers observed the occurrence of a SMM behavior by grafting the "non-magnetic" $\{[Mn(salen)(H_2O)]_2\}(ClO_4)_2 \cdot H_2O$ complex [salen = N,N'-ethylene-bis(salicylimine)] at the surface of a $\{CrMo_6O_{24}\}$ cluster, which allows the magnetic isolation of $\{Mn^{III}_2\}$ units by reducing considerably the inter-molecular interactions between metalorganic complexes.²³ Some other authors have opted for studying the photocatalytic properties of hybrid containing complexes such as $\{Mn(salen)(H_2O)_2\}$,²⁴ $\{Cu_2L(H_2O)_4\}$ ($L =$ N,N'-bis(4-pyridinecarboxamide)-piperazine),²⁵ $\{M(H_2O)DABT\}$ ($M = Co^{II}$, Zn^{II} ; DABT = 3,3'-

diamino-5,5'-bis(1*H*-1,2,4-triazole))²⁶ or those bearing pyridinecarboxamide derivatives²⁷ for the photodegradation of dyes under UV irradiation or the photoreduction of CO₂ to CO.

Conversely, no extended structure has been reported in literature for the {CrMo₆O₂₄} building block, with the exception of the extended systems constituted by Anderson-Evans anions bicapped in opposite faces by {As₃O₆} trimeric units. Structures exhibiting the [As₆CuMo₆O₃₀]⁴⁻ polyanion include the two-dimensional networks in [Cu(en)₂]₂[CuMo₆O₁₉(As₃O₃)₂] (en = ethylenediamine),²⁸ and [{Cu(imi)₄]₃·{As₆CuMo₆O₃₀}]₂·6H₂O.²⁹

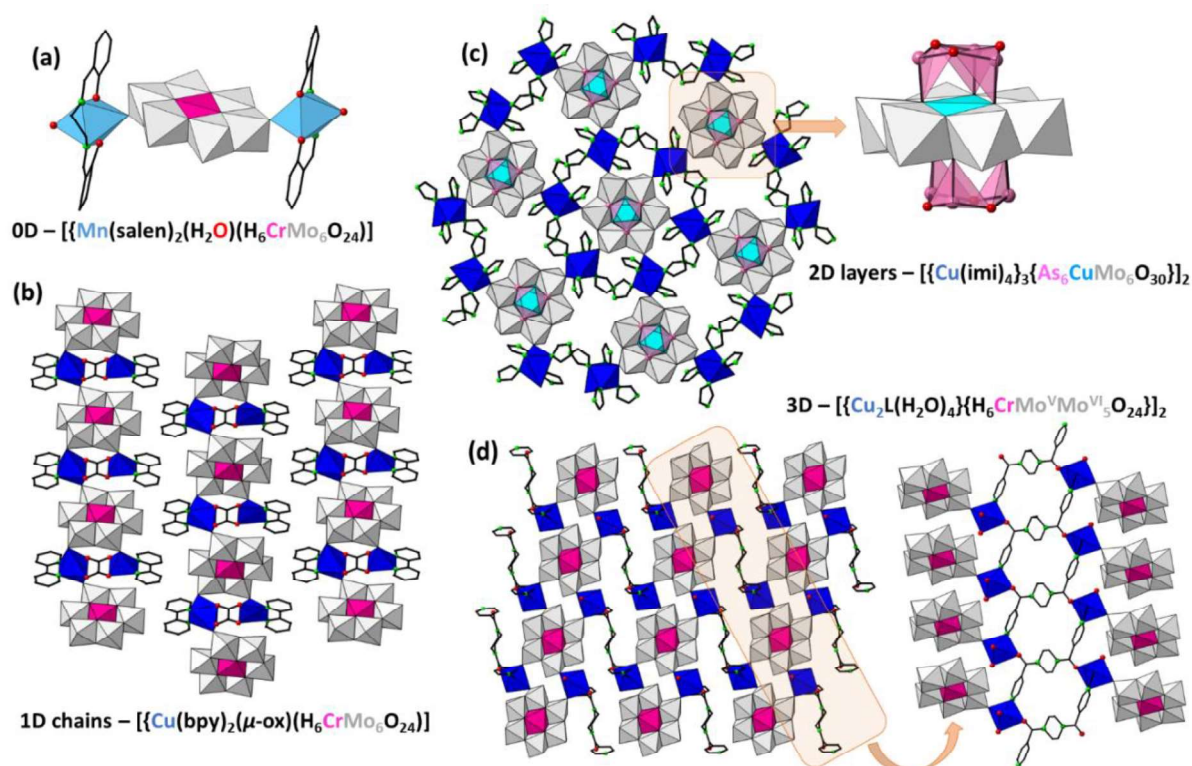


Figure 4.2. Polyhedral representation of some Anderson-Evans/metalorganic hybrids with different dimensionalities. Abbreviations: Salen = N,N'-ethylene-bis(salicylimine); bpy = 2,2'-bipyridine; imi = imidazole; L = N,N'-bis(4-pyridinecarboxamide)-piperazine.

In the course of our systematic studies with 3d-metal-containing complexes of the N4-tetradentate macrocyclic cyclam (cyclam = 1,4,8,11-tetraazacyclotetradecane) ligand, our research group investigated the reaction between the [H₆CrMo₆O₂₄]⁶⁻ Anderson-Evans anions and {M^{II}(cyclam)} (M^{II} = Ni^{II}, Cu^{II}, Zn^{II}) complexes.³⁰ The covalent attachment results in three different compounds, namely, [Ni(cyclam)]₂·[Ni(cyclam)](H₆CrMo₆O₂₄)₂·18H₂O, [H₂(cyclam)]_{1.3}[Zn(cyclam)]_{0.3}·[Zn(cyclam)]_{1.4}(H₆CrMo₆O₂₄)₂·18H₂O and [Cu(cyclam)]₃·(H₆CrMo₆O₂₄)₂·18H₂O, each one exhibiting a distinct dimensionality to lead to 0D, 1D and 2D structures, respectively. (Figure 4.3). In order to continue with this research, the combination of Anderson-Evans building blocks towards copper(II)-complexes bearing similar macrocyclic ligands is studied in this section, together with the effect of the reaction media in the final

assembly of the two building blocks. The potentially interesting thermostructural behavior of these systems is also evaluated within this chapter.

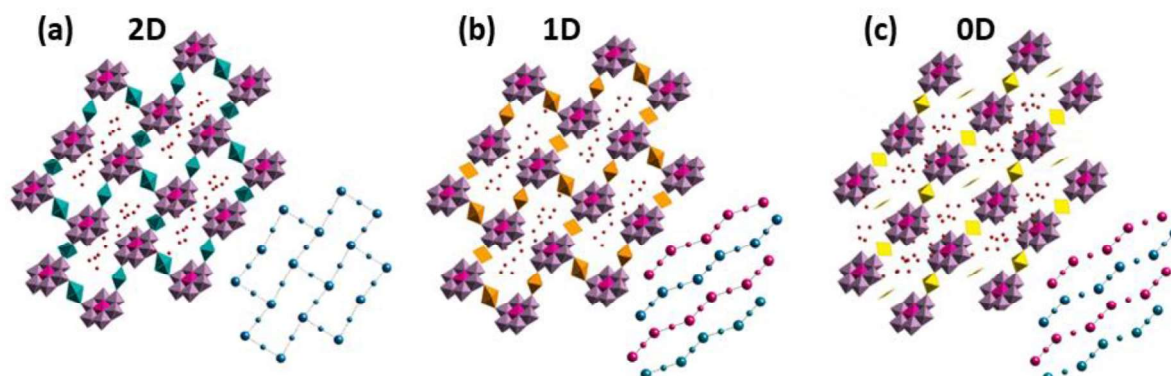


Figure 4.3. Comparison of the three different dimensionalities observed in the Anderson/{M^{II}(cyclam)} systems: (a) M = Cu^{II}; (b) M = Zn^{II} and; (c) M = Ni^{II}.

4.2. EXPERIMENTAL SECTION

4.2.1. Synthesis

The sodium chromiumhexamolybdate salt precursor, Na₃[H₆CrMo₆O₂₄] \cdot 8H₂O, was synthesized according to literature methods and identified by FTIR spectroscopy and PXRD analyses.³¹ All other reagents, including the 1,8-dimethyl-1,4,8,11-tetraazacyclotetradecane (DMC) ligand were purchased from commercial sources.

General synthetic procedure

[{Cu(DMC)}₃{H₄CuMo₆(MoO₃)₂O₂₄}] \cdot 13H₂O (**1-CuMo8**). To a solution of (NH₄)₆(Mo₇O₂₄) \cdot 4H₂O (0.124 g, 0.1 mmol) in water (15 mL), the same volume of an aqueous solution of Cu(OAc)₂ (0.054 g, 0.3 mmol) and DMC ligand (0.069 g, 0.3 mmol) was added dropwise. The pH of the resulting solution was 6.3-6.6. The mixture was stirred at room temperature for 90 min, then filtered and left to evaporate in an open container. Purple prismatic crystals of **1-CuMo8** were obtained after 3 weeks. Yield: < 1%.

[Cu(DMC)][{Cu(DMC)}_{0.5}{H₆CrMo₆O₂₄}] \cdot 11H₂O (**1-CrMo6**). To a solution of Na₃[H₆CrMo₆O₂₄] \cdot 8H₂O (0.123 g, 0.1 mmol) in water (15 mL), the same volume of an aqueous solution of Cu(OAc)₂ (0.036 g, 0.2 mmol) and DMC ligand (0.046 g, 0.2 mmol) was added dropwise. The mixture was stirred at room temperature for 90 min, then filtered and left to evaporate in an open container. Purple prismatic crystals of **1-CrMo6** were obtained after 3 weeks. Yield: < 1%.

$Na\{[Cu(DMC)]_2[H_6CrMo_6O_{24}]\} \cdot 8H_2O$ (**1Na-CrMo6**) and $Na_2\{[Cu(DMC)]_{0.5}[H_6CrMo_6O_{24}]\} \cdot 11.5H_2O$ (**1-Na2-CrMo6**). The synthetic procedure is similar to that of **1-CrMo6** except for the use of aqueous 1M NaCl reaction medium and the use of $CuCl_2 \cdot 2H_2O$ (0.034 g, 0.2 mmol) as copper(II) source. Purple prismatic crystals of **1Na-CrMo6** were obtained after 1 week. After filtering out crystals of **1Na-CrMo6**, purple single-crystals of **1Na2-CrMo6** are obtained in another week. **1Na-CrMo6**: Yield: 24 mg, 16% based on Mo. Elem. Anal. Calcd. (%) for $C_{12}H_{50}CuCrMo_6N_4NaO_{32}$: C, 9.76%; H, 3.41%; N, 3.79%. Found: C, 9.81%; H, 3.45%; N, 3.82%. IR: ν (cm^{-1}) 3460 (s), 3342 (s), 3204 (s), 1622 (m), 1463 (m), 1454 (m), 1409 (m), 1388 (w), 1324 (w), 1303 (w), 1257 (w), 1249 (w), 1206 (w), 1151 (w), 1100 (w), 1074 (w), 1023 (w), 940 (vs), 916 (vs), 901 (vs), 854 (w), 763 (m), 647 (s), 568 (m), 475 (w), 454 (w), 419 (m). **1Na2-CrMo6**: Yield: 17 mg, 12% based on Mo. Elem. Anal. Calcd. (%) for $C_6H_{43}Cu_{0.5}CrMo_6N_2Na_2O_{35.5}$: C, 5.09%; H, 3.06%; N, 1.98%. Found: C, 5.12%; H, 3.15%; N, 2.03%. IR: ν (cm^{-1}) 3523 (s), 3392 (s), 3198 (s), 1631 (m), 1460 (w), 1441 (w), 1423 (w), 1391 (w), 1326 (w), 1302 (w), 1250 (w), 1239 (w), 1208 (w), 1152 (w), 1102 (m), 1075 (m), 1023 (m), 952 (vs), 919 (vs), 897 (vs), 849 (w), 814 (w), 763 (w), 646 (s), 564 (m), 531 (m), 417 (m).

$\{[Cu(DMC)]_2[H_6CrMo_6O_{24}]\}NO_3 \cdot 5H_2O$ (**1NO3-CrMo6**). The synthetic procedure is similar to that of **1-CrMo6** except for the use of aqueous 1M $NaNO_3$ reaction medium and the use of $Cu(NO_3)_2 \cdot 3H_2O$ (0.034 g, 0.2 mmol) (0.048 g, 0.2 mmol) as copper(II) source. Purple prismatic crystals of **1NO3-CrMo6** were obtained after 10 days. Yield: 37 mg, 21% based on Mo. Elem. Anal. Calcd. (%) for $C_{24}H_{72}Cu_2CrMo_6N_9O_{32}$: C, 16.44%; H, 4.14%; N, 7.19%. Found: C, 16.39%; H, 4.21%; N, 7.03%. IR: ν (cm^{-1}) 3410 (s), 3206 (s), 2933 (m), 2887 (m), 1638 (m), 1473 (m), 1426 (m), 1389 (vs), 1351 (s), 1299 (w), 1249 (w), 1241 (w), 1212 (w), 1174 (w), 1153 (w), 1101 (m), 1074 (m), 1022 (m), 966 (w), 940 (vs), 908 (vs), 895 (vs), 854 (w), 837 (w), 762 (w), 748 (w), 646 (s), 575 (m), 525 (w), 497 (w), 474 (w), 458 (w), 421 (w), 400 (m).

$\{[Cu(DMC)]_2[H_6CrMo_6O_{24}]\}Cl \cdot 5H_2O$ (**1Cl-CrMo6**). The synthetic procedure is similar to that of **1-CrMo6** except for the use of aqueous 1M LiCl reaction medium and the use of $CuCl_2 \cdot 2H_2O$ (0.034 g, 0.2 mmol) as copper(II) source. Purple prismatic crystals of **1Cl-CrMo6** were obtained after 2 weeks. Yield: 21 mg, 12% based on Mo. Elem. Anal. Calcd. (%) for $C_{24}H_{71}ClCu_2CrMo_6N_8O_{28.5}$: C, 16.78%; H, 4.17%; N, 6.52%. Found: C, 16.74%; H, 4.28%; N, 6.47%. IR: ν (cm^{-1}) 3410 (s), 3192 (s); 2923 (s); 2877 (s); 1681 (m); 1459 (m); 1443 (m), 1424 (m), 1392 (w), 1324 (w), 1301 (w), 1249 (w), 1238 (w), 1209 (w), 1153 (w), 1102 (m), 1072 (m), 1024 (m), 967 (w), 941 (vs), 906 (vs), 897 (vs), 852 (w), 761 (w), 646 (s), 574 (w), 539 (w), 498 (w), 445 (w), 402 (m).

4.2.2. Single-Crystal X-ray Crystallography

Crystallographic data for **1-CuMo8**, **1-CrMo6**, **1Na-CrMo6**, **1Na2-CrMo6**, **1NO3-CrMo6** and **1Cl-CrMo6** are compiled in Table 4.1.

Table 4.1. Crystallographic data for **1-CuMo8**, **1-CrMo6**, **1Na-CrMo6**, **1Na2-CrMo6**, **1NO3-CrMo6** and **1Cl-CrMo6**.

	1-CuMo8	1-CrMo6	1Na-CrMo6
empirical formula	C ₃₆ H ₁₁₄ Cu ₄ Mo ₈ N ₁₂ O ₄₃	C ₁₈ H ₇₀ CrCu _{1.5} Mo ₆ O ₃₅	C ₁₂ H ₅₀ CrCuMo ₆ N ₄ NaO ₃₂
fw (g mol ⁻¹)	2425.07	1653.75	1476.73
crystal system	Triclinic	Triclinic	Triclinic
Space group (number)	<i>P</i> -1 (2)	<i>P</i> -1 (2)	<i>P</i> -1 (2)
<i>a</i> (Å)	13.3544(5)	13.9996(3)	8.5407(4)
<i>b</i> (Å)	13.6088(6)	14.9585(4)	11.4159(3)
<i>c</i> (Å)	14.4136(6)	15.0409(3)	11.5870(3)
α (deg)	108.092(4)	61.200(3)	71.478(3)
β (deg)	105.471(4)	77.582(2)	83.784(3)
γ (deg)	99.932(3)	64.166(3)	68.887(4)
<i>V</i> (Å ³)	2304.69(17)	2484.26(13)	999.28(7)
<i>Z</i>	1	2	1
ρ_{calcd} (g cm ⁻³)	1.747	2.211	2.454
μ (mm ⁻¹)	2.032	2.404	2.718
reflns collected	24082	29785	11445
unique reflns (<i>R</i> _{int})	9045 (0.066)	9735 (0.035)	4125 (0.041)
observed reflns [<i>I</i> > 2 σ (<i>I</i>)]	6434	8366	3507
Params (restraints)	455 (54)	616 (0)	281 (1)
<i>R</i> (<i>F</i>) ^a [<i>I</i> > 2 σ (<i>I</i>)]	0.084	0.040	0.049
<i>wR</i> (<i>F</i> ²) ^b (all data)	0.274	0.119	0.137
GoF	1.067	1.090	1.030

Thermal vibration of atoms were treated anisotropically for all the non-hydrogen compounds, except for the hydration water molecules in **1-CuMo8** and **1Cl-CrMo6** and the C atoms from the DMC ligand in **1NO3-CrMo6** due to the structural disorder displayed by organic ligand. Hydrogen atoms of the organic DMC ligand, as well as those belonging to the hydration water molecules in **1Na2-CrMo6** were placed in calculated positions and refined using standard SHEXL parameters. Some of the anisotropic thermal ellipsoids from the DMC ligand in **1-CuMo8** were normalized using ISOR-type restraints from SHELXL. In a similar way, the protonated oxygen atoms from the Anderson-Evans-type clusters in **1Na-CrMo6** and **1Na2-CrMo6** and some atoms from the DMC ligands in **1-CrMo6**, **1NO3-CrMo6** and **1-CuMo6** were normalized using DFIX and DANG type restraints. All the samples except **1-CrMo6** and **1Na-CrMo6**, display a significant disorder in their lattice water molecules, and different crystallographic positions suitable for hydration molecules were located in their Fourier maps. Their occupancies were initially refined without restrictions and then fixed to the first

decimal in the last refinement cycle. This resulted in a total number of 6.5 water molecules delocalized over 10 sites for **1-CuMo8** (the asymmetric unit displays one half of the formula), 11.5 over 12 sites for **1Na2-CrMo6**, 1.25 over 3 positions for **1NO3-CrMo6** (the asymmetric unit displays one quarter of the formula) and 5 over 8 sites for **1Cl-CrMo6**.

Table 4.1. (continuation). Crystallographic data for **1-CuMo8**, **1-CrMo6**, **1Na-CrMo6**, **1Na2-CrMo6**, **1NO3-CrMo6** and **1Cl-CrMo6**.

	1Na2-CrMo6	1NO3-CrMo6	1Cl-CrMo6
empirical formula	C ₆ H ₄₃ CrCu _{0.5} Mo ₆ N ₂ Na ₂ O _{35.5}	C ₂₄ H ₇₂ CrCu ₂ Mo ₆ N ₉ O ₃₂	C ₂₄ H ₇₂ ClCrCu ₂ Mo ₆ N ₈ O ₂₉
fw (g mol⁻¹)	1416.81	1753.62	1727.06
crystal system	Triclinic	Monoclinic	Triclinic
Space group (number)	<i>P</i> -1 (2)	<i>I</i> / <i>m</i> (12)	<i>P</i> -1 (2)
<i>a</i> (Å)	11.1588(5)	8.7882(3)	8.55507(15)
<i>b</i> (Å)	12.4998(6)	18.2158(5)	13.1413(2)
<i>c</i> (Å)	15.4064(7)	17.5379(5)	25.8854(4)
<i>α</i> (deg)	67.635(5)	90	77.4180(13)
<i>β</i> (deg)	86.320(4)	102.116(3)	81.1696(14)
<i>γ</i> (deg)	73.671(4)	90	74.5690(15)
<i>V</i> (Å³)	1904.91(17)	2744.99(14)	2723.73(8)
<i>Z</i>	2	2	2
ρ_{calcd} (g cm⁻³)	2.470	2.122	2.095
μ (mm⁻¹)	2.592	2.366	2.425
reflns collected	22500	16765	35464
unique reflns (<i>R</i>_{int})	7476 (0.064)	3549 (0.036)	12993 (0.036)
observed reflns [<i>I</i> > 2σ(<i>I</i>)]	5853	3083	10205
Params (restraints)	512 (6)	218 (4)	509 (0)
<i>R</i>(<i>F</i>)^a [<i>I</i> > 2σ(<i>I</i>)]	0.076	0.042	0.057
<i>wR</i>(<i>F</i>²)^b (all data)	0.223	0.107	0.164
GoF	1.046	1.029	1.064

4.3. RESULTS AND DISCUSSION

4.3.1. Synthetic considerations

As described in Chapters 2 and 3, the reaction between a heptamolybdate source and {Cu(cyclam)}²⁺ complexes can lead to covalent networks with interesting thermostructural properties capable to exhibit SCSC transformations as well as water and gas sorption properties. Thus, we decided to assess the effect of slight modifications of the organic ligand on the final assemblies and evaluate whether hybrid systems could exhibit similar rich thermostructural behavior. Taking this into account, the reaction between (NH₄)₆Mo₇O₂₄·4H₂O salt towards {Cu(DMC)}²⁺ (DMC = 1,8-dimethyl 1,4,8,11-tetraazacyclotetradecane) complex in a POM:complex 1:3 ratio was studied in aqueous media and at a pH close to neutrality (pH = 6.0), as these stoichiometric conditions proved to

be successful for building such extended hybrid architectures. After several weeks of evaporation of the final solution at room temperature, purple single-crystals of **1-CuMo8** were formed in a very low yield (< 1%). Due to the low amount of available sample, only scXRD analyses were conducted (see Section 4.3.3), which revealed the full rearrangement of the initial $[\text{Mo}_7\text{O}_{24}]^{6-}$ precursor to lead to an unprecedented $[\text{H}_4\text{CuMo}_6\text{O}_{24}(\text{MoO}_3)_2]^{3-}$ assembly formed by an $\{\text{H}_4\text{CuMo}_6\text{O}_{24}\}$ Anderson-Evans-anion with two additional $\{\text{MoO}_4\}$ tetrahedral units condensed to two of its $\mu_3\text{-O}$ atoms from opposite faces.

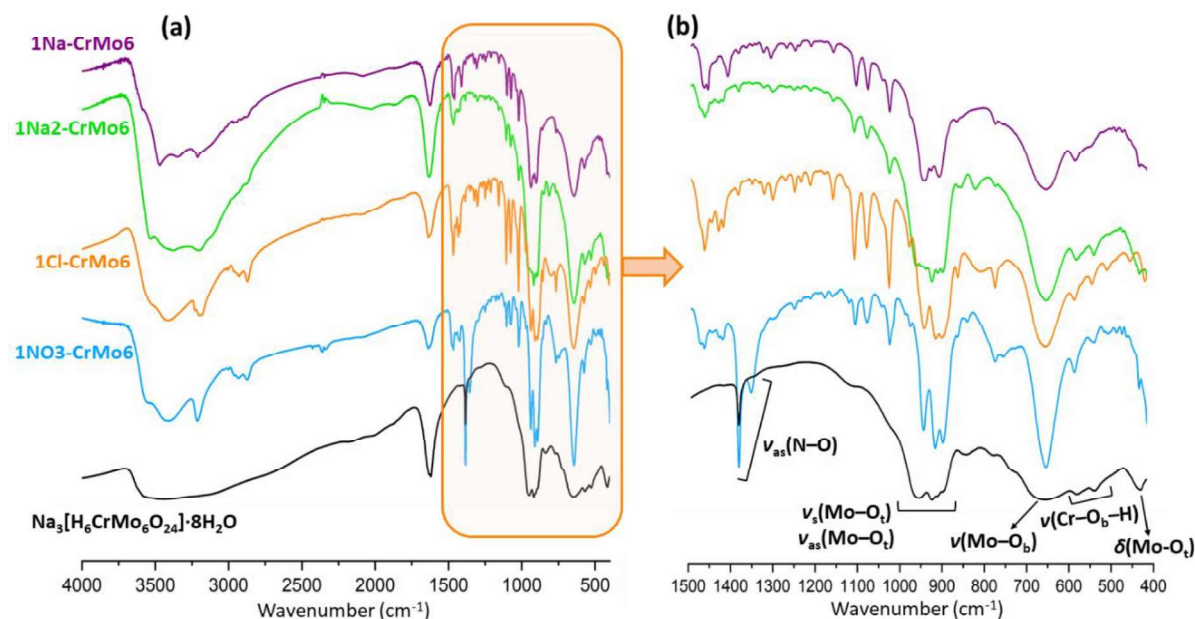


Figure 4.4. (a) Full FTIR spectra of **1Na-CrMo6**, **1Na2-CrMo6**, **1Cl-CrMo6** and **1NO3-CrMo6** compared to that of the $\text{Na}_3[\text{H}_6\text{CrMo}_6\text{O}_{24}] \cdot 8\text{H}_2\text{O}$ precursor with (b) detail of the inorganic region in the 1500-400 cm^{-1} range.

In view of these results, we extended our studies to the combination of the well-known $[\text{H}_6\text{CrMo}_6\text{O}_{24}]^{6-}$ polyanion and $\{\text{Cu}(\text{DMC})\}^{2+}$ complexes. First, the synthesis was carried out under aforementioned conditions for the synthesis of **1-CuMo8**. Unfortunately, again only a few single-crystals (yield < 1%) were obtained, which prevented us from fully characterizing the sample and hence, only scXRD analyses were performed on crystals of **1-CrMo6** (see Section 4.3.4). The use of different copper(II) salts (i.e. chloride and acetate) and POM: complex ratio (1:2) was evaluated, but results from scXRD analyses indicated no effect neither in the nature of the resulting compound nor in the reaction yield. In contrast, heating the reaction to 90 °C yielded a powdered sample in a similar poor yield.

Taking into account that higher ionic strength could favor the crystallization process and hence, the reaction yield,³² together with the success mentioned in the introduction in the reactions between the same Anderson-Evans anion and $\{\text{M}(\text{cyclam})\}^{2+}$ complexes,³² we carried out the reaction of **1-CrMo8**, but using aqueous 1M NaCl instead of pure water. Crystals of **1Na-CrMo6** appeared after one week of slow evaporation of the final solution in a moderate yield, the FTIR spectrum of which identified them as POM-metalorganic hybrids.

Comparison of the FTIR spectrum with that of the POM precursor is depicted in Figure 4.4. Close inspection to the spectra reveals two well-differentiated regions: the inorganic POM region below 1000 cm^{-1} and the metalorganic region above this wavenumber. Strong bands corresponding to the symmetric and asymmetric $\nu(\text{Mo-O}_t)$ vibrations in the $837\text{--}967\text{ cm}^{-1}$ range, as well as the $\nu(\text{Mo-O}_b)$ vibration at ca. 645 cm^{-1} can be easily found in both spectra with no significant changes upon the combination with the metalorganic complexes. The signals corresponding to $\nu(\text{Cr-O}_c\text{-H})$ vibration in the $575\text{--}540\text{ cm}^{-1}$ area remained almost invariable in all the hybrids. However, the bands arising from $\delta(\text{Mo-O}_t)$ bending at low wavenumbers (below 450 cm^{-1}) are hardly appreciated. Concerning the metalorganic region, the bands associated to the stretching of the -N-H and -C-H bonds of the organic ligands ($3200\text{--}2870\text{ cm}^{-1}$) are shadowed by the broad band arising from the -O-H stretching which belongs to water molecules of hydration. The remaining signals that correspond to the DMC ligand are found in the $1470\text{--}1000\text{ cm}^{-1}$ region. After filtering out crystals of **1Na-CrMo6** from their mother liquors, a new batch crystalized after another week. Although the FTIR spectrum of **1Na2-CrMo6** looked virtual identical to that of **1Na-CrMo6** (Figure 4.5), crystal were different in its size and shape, in such a way that they could be distinguished visually. In fact, they PXRD patterns considerably differ as observed in Figure 4.5, as evidenced in the intense maxima present in **1Na-CrMo6** at $2\theta = 11.1, 11.4$ and 13.6° , whereas in **1Na2-CrMo6** the main maxima appear at $2\theta = 8.0, 8.2$ and 12.4° . However, the homogeneity of the **1Na2-CrMo6** crystalline phase was assessed by the perfect match (Figure 4.5) between its experimental PXRD pattern and that simulated from scXRD data (see Section 4.3.6).

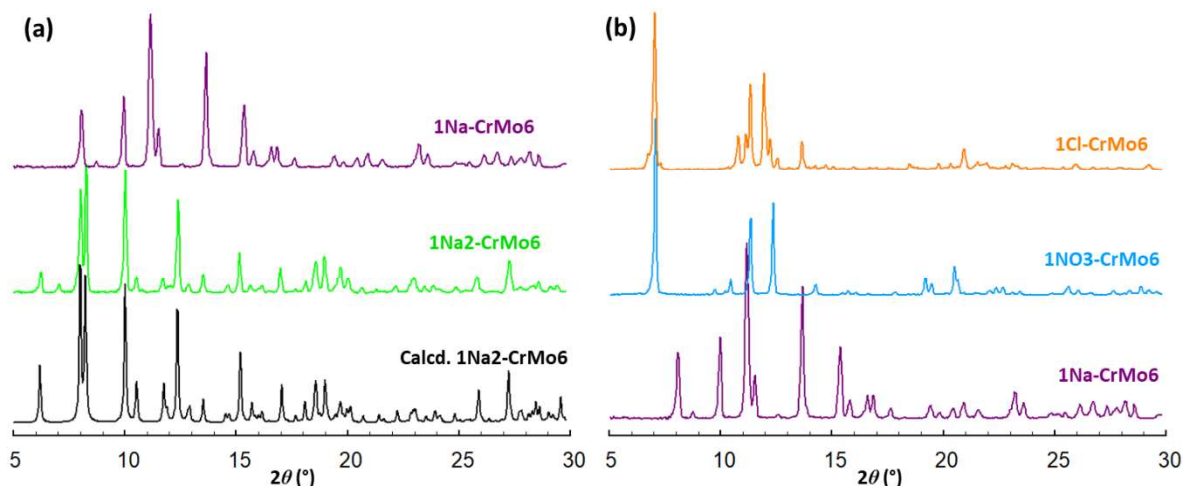


Figure 4.5. (a) PXRD pattern collected for **1Na2-CrMo6** sample compared to that calculated from scXRD data.

Encouraged by these results, the effect of changing the reaction media was evaluated by modifying either the alkaline metal cation or the anion (Figure 4.5), because previous works has highlighted the strong influence of the presence of distinct alkaline metal cations on the final assembly of POMs and metalorganic units.³³ The FTIR spectra of crystals isolated from

reactions carried out in aqueous 1M NaNO₃ (**1NO3-CrMo6**), and LiCl (**1Cl-CrMo6**) solutions are virtually identical to those synthesized in NaCl (aq), except for the two intense bands at 1389 and 1351 cm⁻¹ that corresponds to the asymmetric $\nu(\text{N-O})$ stretching from the NO₃⁻ anion in the former case, but their PXRD patterns are considerably different. In contrast, aqueous 1M KCl solution decreases the solubility of the synthetic system and after filtering the initial precipitate from the reaction, a few light-purple single-crystals of small size are obtained together with white precipitate after the slow evaporation of the final solution. These crystals were later identified as the potassium salt of the Anderson-Evans anion, namely K₃[H₆CrMo₆O₂₄]·6H₂O (**CrMo6**).³⁴ The PXRD analyses revealed that **CrMo6** crystallizes together with KCl (white precipitate) as indicated in Figure 4.6. All the synthesized compounds are further summarized in Figure 4.7.

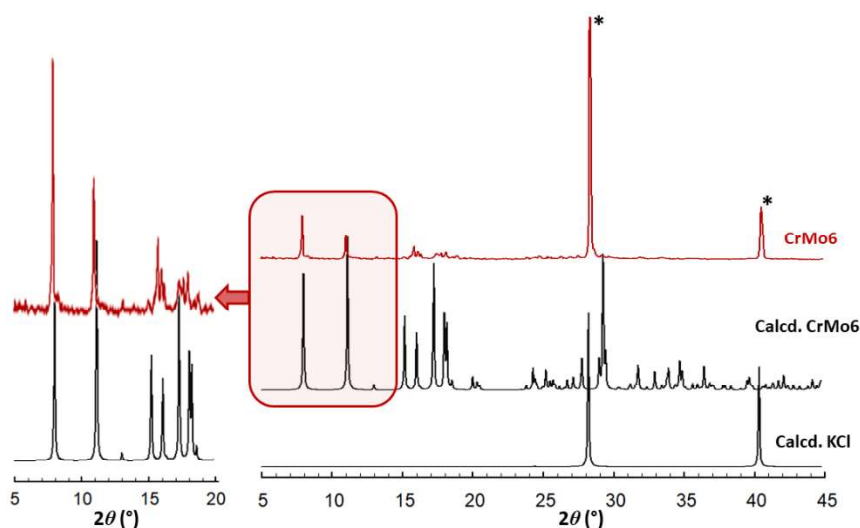


Figure 4.6. Experimental PXRD pattern of **CrMo6** compared to that calculated from sc-XRD data and that of KCl registered for comparative purposes. Maxima in the experimental pattern of **CrMo6** coming from KCl impurities are highlighted with a star.

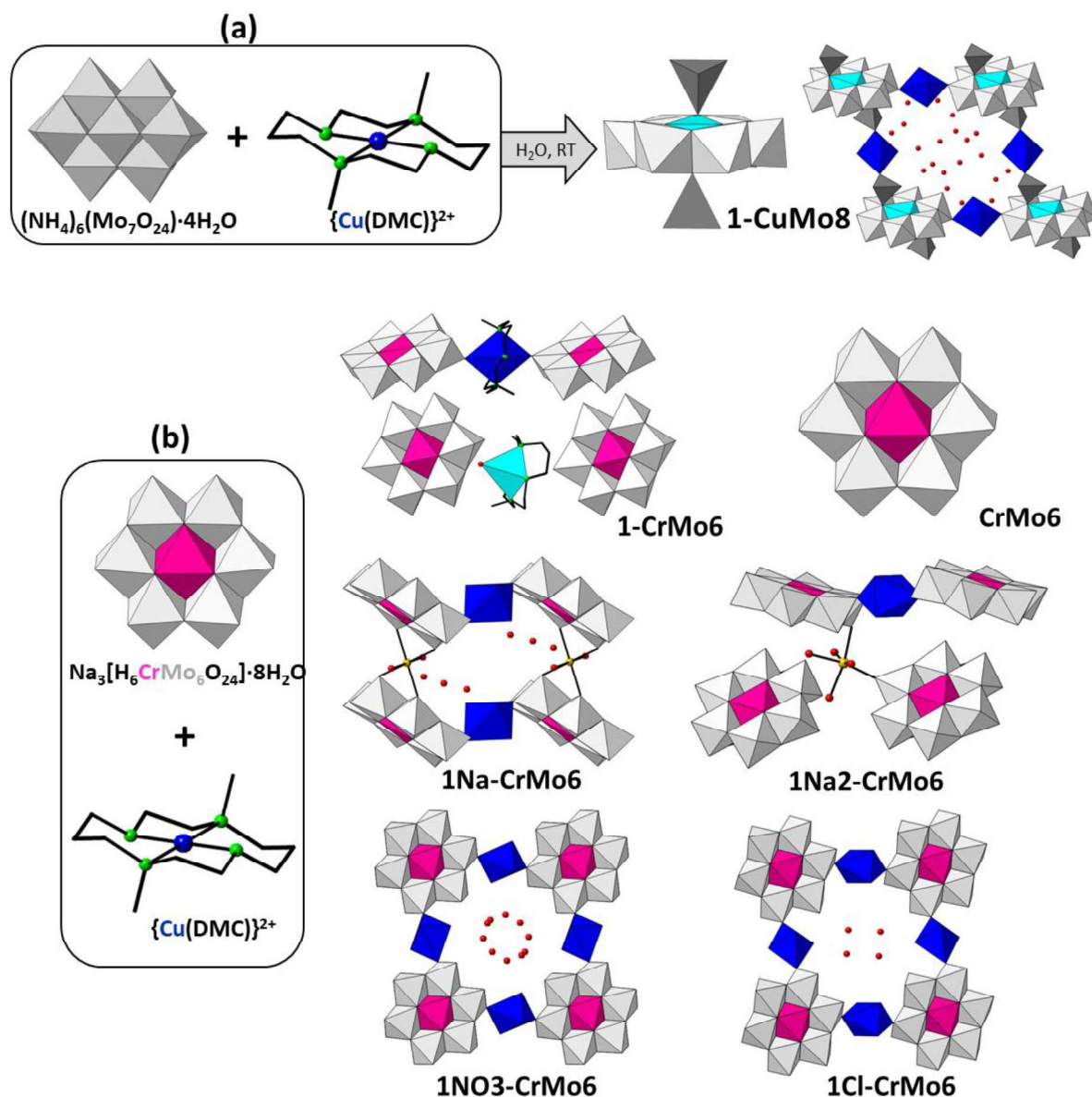


Figure 4.7. Overview of all the compounds presented in this chapter from the reactions between, (a) an heptamolybdate salt and $\{\text{Cu}(\text{DMC})\}^{2+}$ in water and (b) an hexamolybdatechromate salt and $\{\text{Cu}(\text{DMC})\}^{2+}$ in different aqueous media. Color code: $\{\text{MoO}_6\}$, light grey; $\{\text{MoO}_4\}$, dark grey; Cu_{POM} , light blue; Cu, blue; O, red; (b) influence of the ionic strength on the $\{\text{CrMo}_6\}/\{\text{Cu}(\text{DMC})\}$ system. Color code: octahedral Cu, dark blue; square pyramidal Cu, light blue; Cr, pink; K, purple; N, light green; Na, yellow.

4.3.2. Thermostructural behavior

The thermal behavior of the four compounds fully characterized in this chapter was initially analyzed by TGA/DTA analyses (Figure 4.8). All the TGA curves showed a thermal stability range, except for that of **1Na2-CrMo6**, which exhibits a first complex dehydration stage that goes from room temperature to *ca.* 150 °C and accounts for 11.5 H₂O molecules (calcd. 14.6%, found 14.8% mass loss). The second step shows different overlapped thermal events and correspond to the combustion of the organic DMC ligand and the breakdown of the POM anion, with an overall mass loss accounting for one half of DMC ligand and 3 water

molecules (calcd. 11.9%, found 12.3%). The final residue is obtained at temperatures above 430 °C (calcd. for $\text{CrCu}_{0.5}\text{Mo}_6\text{Na}_2\text{O}_{21}$ 73.5%, found 72.9%).

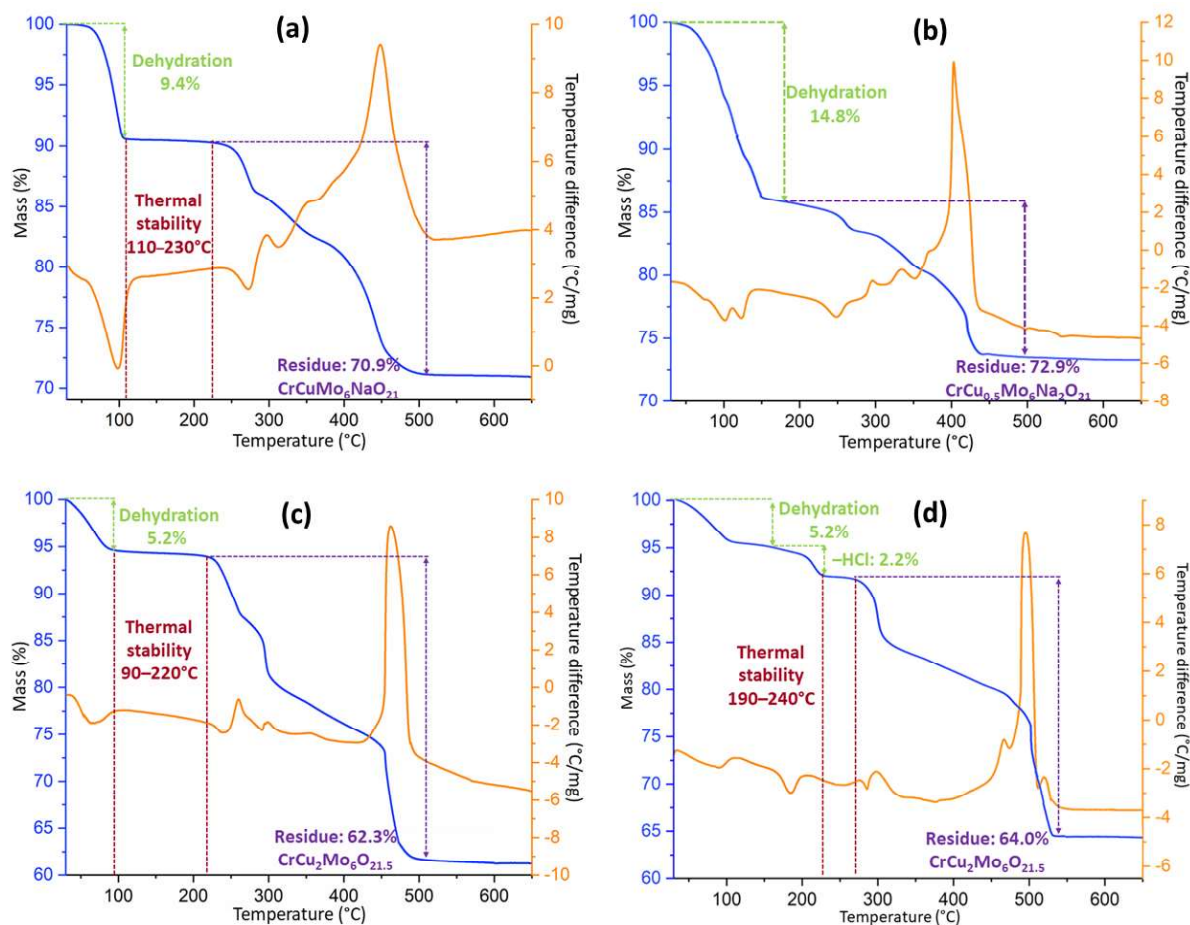


Figure 4.8. TGA/DTA curves for (a) **1Na-CrMo6**, (b) **1Na2-CrMo6**, (c) **1NO3-CrMo6** and (d) **1Cl-CrMo6**.

When it comes to **1Na-CrMo6**, and **1NO3-CrMo6**, their TGA curves show a similar shape, which start with an endothermic dehydration step that extends from room temperature up to *ca.* 100 °C and the mass loss accounts for 8 and 5 H_2O molecules of hydration, respectively (calcd. 9.7%, found 9.4% for **1Na-CrMo6**; calcd. 5.1%, found 5.2% for **1NO3-CrMo6**). Then, both compounds exhibit a thermal stability range up to 220–230 °C, which suggests the presence of a thermally stable anhydrous phase. The anhydrous phase undergoes further decomposition through the overlapping mass loss steps associated to the breakdown of the POM anion and the loss of one DMC molecule for **1Na-CrMo6** and one HNO_3 and two DMC molecules for **1NO3-CrMo6**. The final residue is obtained at temperatures above 500 °C and coincides well with the expected general formula $\text{CrCuMo}_6\text{NaO}_{21}$ for **1Na-CrMo6** (calcd. 71.1%, found 70.9%), and $\text{CrCu}_2\text{Mo}_6\text{O}_{21.5}$ for **1NO3-CrMo6** (calcd. 62.6%, found 62.3%).

The TGA curve of **1Cl-CrMo6** displays two consecutive endothermic mass losses below 190 °C, that could well be ascribed to the evacuation of 5 H₂O molecules (calcd. 5.2%, found 5.2%) and one HCl molecule (calcd. 2.1%, found 2.2%), respectively. Afterwards, a short thermal stability range is found from 190 °C to 240 °C, which is followed by a third mass loss stage associated to the removal of two DMC ligands and the breakdown of the POM cluster with an overall mass loss of 28.6% (calcd. 29.0%). The final residue is obtained at temperatures above 530 °C (calcd. for CrCu₂Mo₆O_{21.5} 63.7%, found 64.0%).

To determine whether these compounds are able to maintain their crystallinity at high temperatures and study any structural change that they can undergo upon heating, variable-temperature PXRD studies between 30 and 610 °C were performed for the three compounds exhibiting a thermal stability range on TGA experiments, which suggests the presence of a thermally stably anhydrous phase. Important modifications are observed in the position and intensity of the most intense diffraction maxima from the PXRD patterns of **1Na-CrMo6** upon heating (Figure 4.9). The room temperature phase correspond to a homogenous crystalline phase as corroborated by the comparison of its diffraction pattern with that calculated from scXRD data, and it stable up to 50 °C.

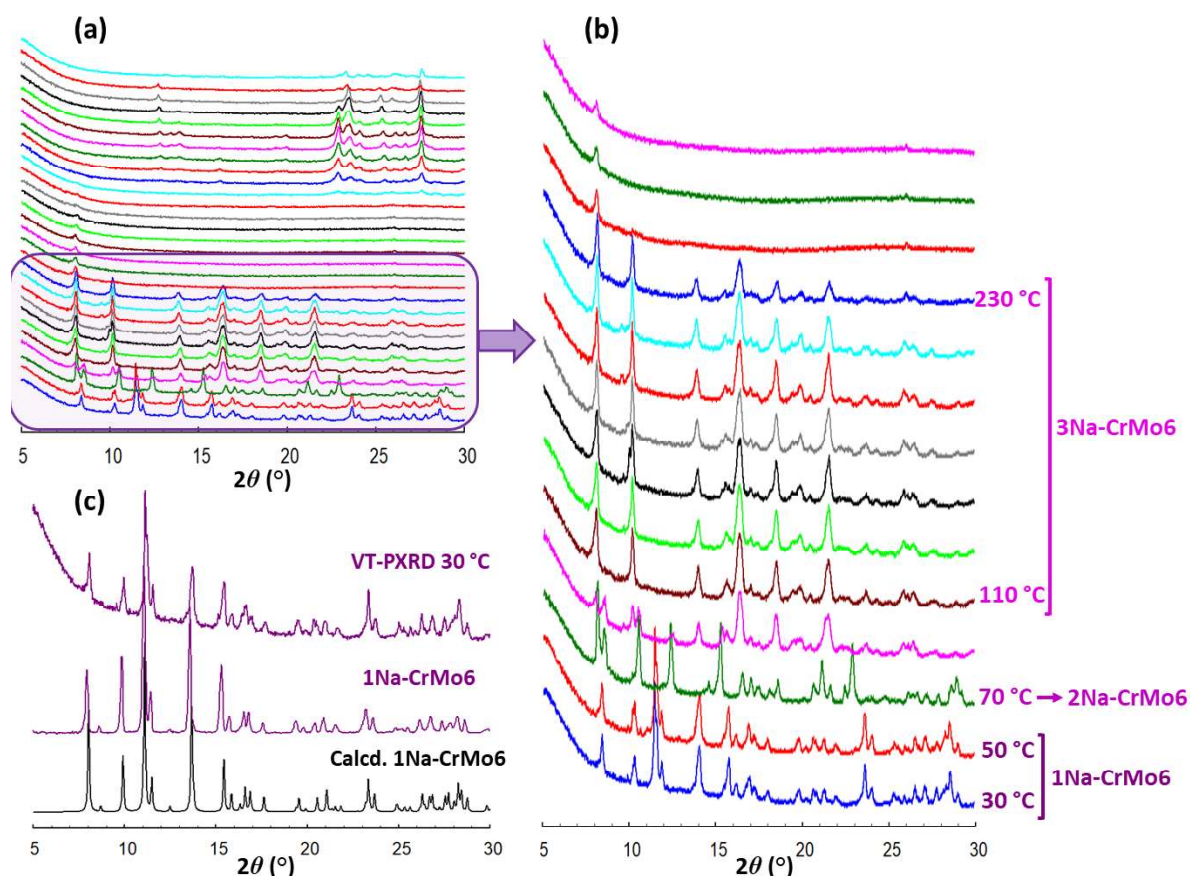


Figure 4.9. (a) Variable-temperature PXRD patterns of **1Na-CrMo6** collected from 30 to 610 °C with (b) detail of the solid-phase transformations occurring from 30 to 230 °C. (c) Comparison between the pattern collected at 30 °C in the VT-PXRD measurement, experimental **1Na-CrMo6** pattern and that calculated from sc-XRD data.

At 70 °C the parent compound undergoes an structural transition to lead to **2Na-CrMo6**, as observed by the vanishing of the maxima at low 2θ angles (more specifically, those at 11.4, 11.9, and 15.9°) and the formation of new peaks at 12.4 and 15.2°. Furthermore, maxima at 8.3° splits into two different signals appearing at 8.1 and 8.5°, whereas that at 10.2° is shifted to 10.5° upon structural transformation. A second transition is completed at temperatures above 110 °C to lead to **3Na-CrMo6**, with new peaks at $2\theta = 10.1, 13.9, 16.3$ and 18.5°. This third phase is thermally stable up to 230 °C, which is in concordance with the thermal stability range found in TGA experiments. Above this temperature, the anhydrous phase **3Na-CrMo6** becomes amorphous until the final residue is formed at 420 °C (Figure 4.9).

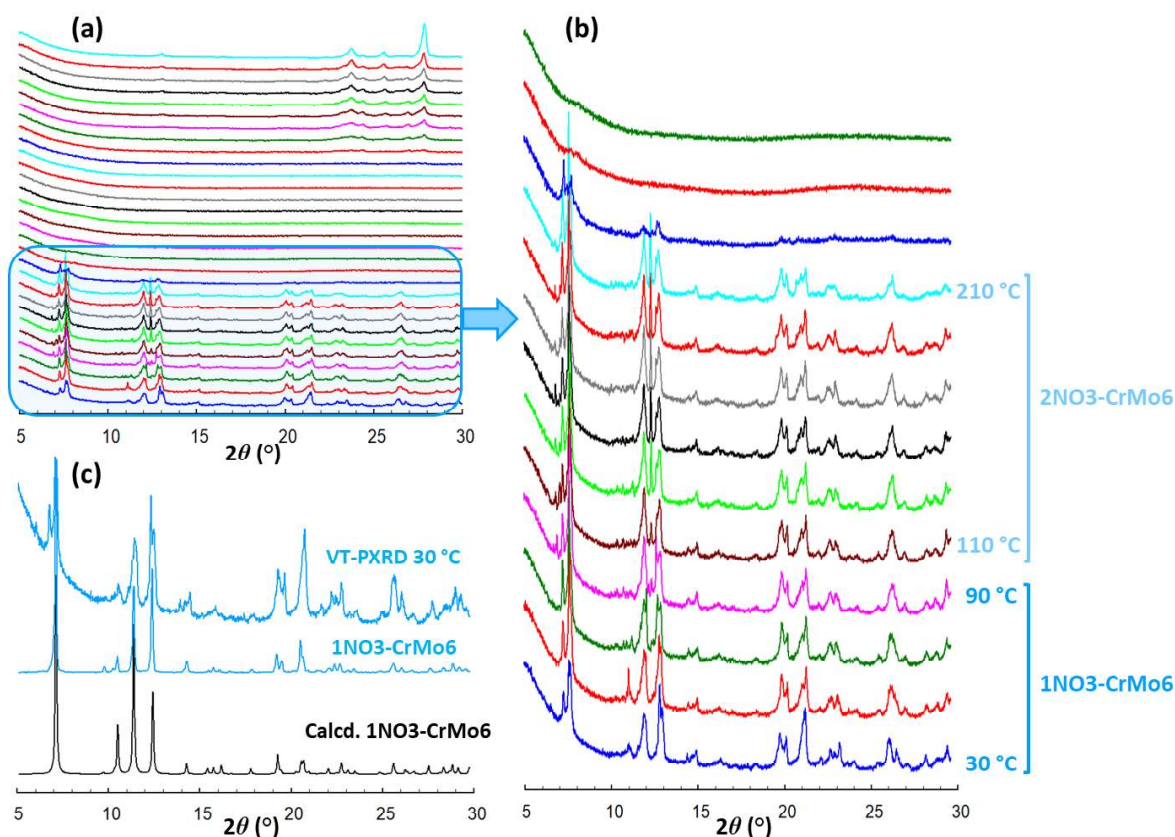


Figure 4.10. (a) Variable-temperature PXRD patterns of **1NO3-CrMo6** collected from 30 to 610 °C with (b) detail of the solid-phase transformations occurring from 30 to 210 °C. (c) Comparison between the pattern collected at 30 °C in the VT-PXRD measurement, experimental **1NO3-CrMo6** pattern and the one calculated from sc-XRD data.

As observed in Figure 4.10 and 4.11, **1NO3-CrMo6** and **1Cl-CrMo6** retain their crystallinity up to 210 °C and 190°C, respectively, in good agreement with TGA results. However, unlike the previous compound, no major modification in neither the positions nor the intensities of the diffraction maxima is observed upon heating, which could indicate that the crystal packing of the parent compounds remain virtually unaltered upon thermal evacuation of guest solvent molecules. In the case of **1NO3-CrMo6**, two additional maxima

of low intensity are formed at $2\theta = 6.9$ and 12.5° upon total dehydration above 110°C , which could indicate small modifications in the structure of the anhydrous compound (**2NO3-CrMo6**) in comparison to that of the totally hydrated phase. Anhydrous phases in **1NO3-CrMo6** and **1Cl-CrMo6** becomes amorphous until the formation of the final residues is completed at 470 and 510°C , respectively, in good agreement with TGA results.

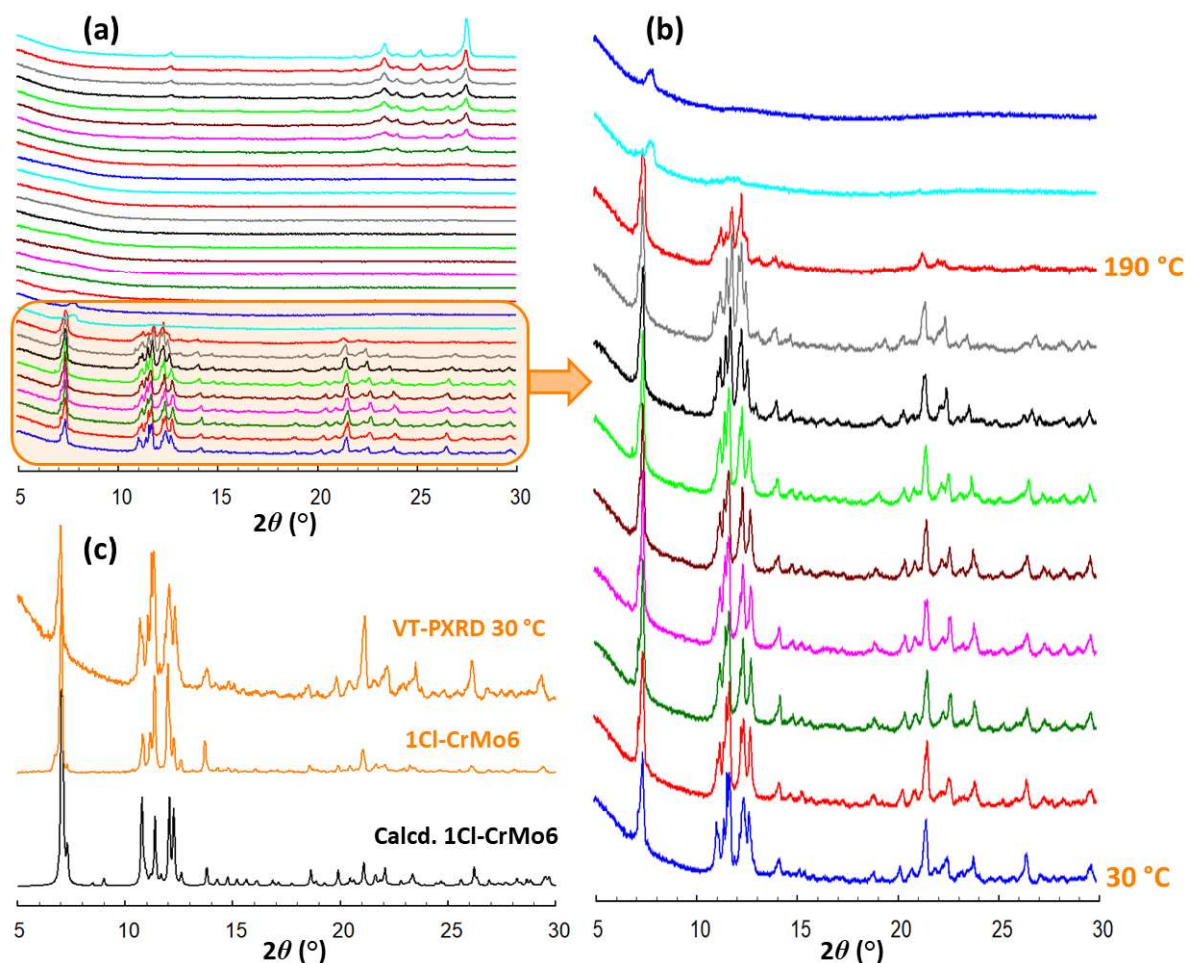


Figure 4.11. (a) Variable-temperature PXRD patterns of **1Cl-CrMo6** collected from 30 to 610°C with (b) detail of the stability of **1Cl-CrMo6** occurring from 30 to 230°C . (c) Comparison between the pattern collected at 30°C in the VT-PXRD measurement, experimental **1Cl-CrMo6** pattern and the one calculated from scXRD data.

4.3.3. Crystal structure of **1-CuMo8**

Compound **1-CuMo8** crystallizes in the triclinic $P-1$ space group and its asymmetric unit contains one half of the $[\text{H}_4\text{CuMo}_6(\text{MoO}_3)_2\text{O}_{24}]^{6-}$ anion, three halves of $\{\text{Cu}(\text{DMC})\}^{2+}$ metalorganic moieties and a total number of 13 hydration water molecules per POM cluster disordered over 10 crystallographic sites (Figure 4.12). The structure of the unprecedented $[\text{H}_4\text{CuMo}_6(\text{MoO}_3)_2\text{O}_{24}]^{6-}$ anion can be best described as the well-known $[\text{H}_{6-x}\text{CuMo}_6\text{O}_{24}]^{(4+x)-}$ Anderson-Evans archetype³⁵ with two additional $\{\text{MoO}_4\}$ tetrahedral units condensed to μ_3 -O atoms from opposite faces. This arrangement is stabilized by the O–H \cdots O type

intramolecular hydrogen bonds established between the protonated μ_3 -O atoms and $\{\text{MoO}_4\}$ units (Figure 4.12 and Table 4.4). These findings prove that basic O atoms from the Anderson-Evans scaffold are available not only for the substitution with trisalkoxo-type moieties, but also for the condensation of additional addenda metal centers. In fact, the linkage of additional addenda metal centers to the Anderson-Evans platform via formation of M–O–M (M = Mo, W) bonds have rarely been observed in the literature.³⁶ The Mo–O bond lengths within $\{\text{MoO}_4\}$ tetrahedra (Table 4.2), together with bond-valence sum calculations, confirm that these groups are not protonated, and hence, the four remaining μ^3 -O atoms surrounding the heteroatom must be to obey the electroneutrality rule.

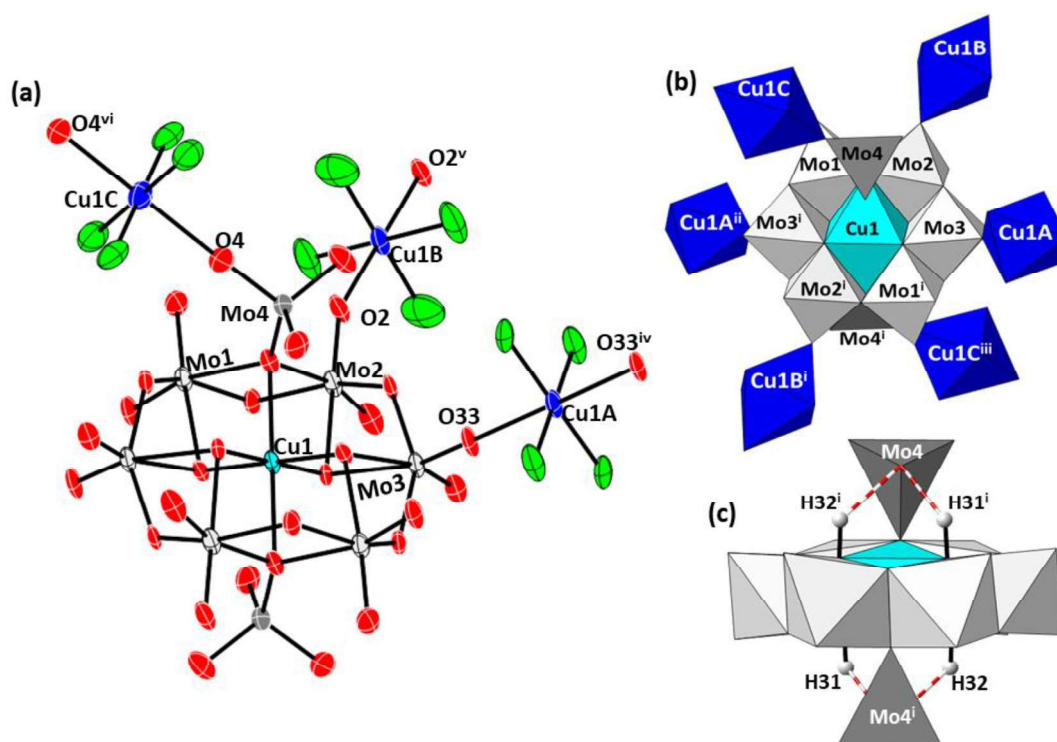


Figure 4.12. (a) Polyhedral view of the $[\text{H}_4\text{CuMo}_6(\text{MoO}_3)_2\text{O}_{24}]^{6-}$ anion with the intramolecular O–H \cdots O bonds marked in dashed red lines. (b) polyhedral representation of the connectivity in **1-CuMo8**, and (c) ORTEP representation of **1-CuMo8** asymmetric unit showing 50% probability thermal ellipsoids, together with the atom labelling scheme. The C and H atoms, as well as the water hydration molecules have been omitted for clarity. Color code: $\{\text{MoO}_4\}$, dark grey; CuPOM , light blue. Symmetry codes: i) $-x, 2-y, -z$; ii) $-1+x, y, z$; iii) $x, -1+y, z$; iv) $1-x, 2-y, -z$; v) $-x, 2-y, -1-z$; vi) $-x, 3-y, -z$.

Table 4.2. Mo–O bond lengths (\AA) for the terminal O atoms from the $[\text{H}_4\text{CuMo}_6(\text{MoO}_3)_2\text{O}_{24}]^{6-}$ anion in **1-CrMo8**.

Mo–O	Bond length (\AA)	Mo–O	Bond length (\AA)
Mo1–O1	1.729(8)	Mo4–O4	1.723(9)
Mo1–O11	1.716(7)	Mo4–O44	1.764(8)
Mo2–O2	1.717(8)	Mo4–O444	1.715(10)
Mo2–O22	1.725(8)		
Mo3–O3	1.712(7)		
Mo3–O33	1.707(7)		

Three crystallographically independent and centrosymmetric $\{\text{Cu}(\text{DMC})\}^{2+}$ complexes are found in **1-CuMo8**, all of them showing the DMC ligand in a *trans-III* configuration which is the most usual configuration for $\{\text{Cu}(\text{cyclam})\}^{2+}$ complexes, but not that common for $\{\text{Cu}(\text{DMC})\}^{2+}$ according to reported works.³⁷ All the Cu^{II} centers display octahedral CuN_4O_2 coordination geometry with the N atoms from the DMC ligands occupying equatorial positions, while the axial coordination sites remain accesible for connecting contiguous POM units through coordination to terminal O_{POM} atoms. No significant Jahn-Teller distortion is observed for Cu^{II} centers, with the longest bond length being of 2.483(7) Å (Table 4.3) despite the steric hindrance generated by methyl groups, which is comparatively shorter than those displayed by $\{\text{Cu}(\text{cyclam})\}^{2+}$ units in compounds reported in Chapters 2 and 3.

Table 4.3. Cu–N and Cu– O_{POM} bond lengths for $\{\text{Cu}(\text{DMC})\}^{2+}$ complexes in **1-CuMo8**.

Cu1A		Cu1B		Cu1C	
Cu1A–N1A	2.070(11)	Cu1B–N1B	2.052(13)	Cu1C–N1C	2.033(9)
Cu1A–N4A	1.980(10)	Cu1B–N4B	1.994(14)	Cu1C–N4C	2.041(11)
Cu1A–N1A ⁱ	2.070(11)	Cu1B–N1B ⁱⁱ	2.052(13)	Cu1C–N1C ⁱⁱⁱ	2.033(9)
Cu1A–N4A ⁱ	1.980(10)	Cu1B–N4B ⁱⁱ	1.994(14)	Cu1C–N4C ⁱⁱⁱ	2.041(11)
Cu1A–O33	2.397(7)	Cu1B–O2	2.483(7)	Cu1C–O4	2.428(9)
Cu1A–O33 ⁱ	2.397(7)	Cu1B–O2 ⁱⁱ	2.483(7)	Cu1C–O4 ⁱⁱⁱ	2.428(9)

Symmetry codes: i) 1-x, 2-y, -z; ii) -x, 2-y, -1-z; iii) -x, 3-y, -z.

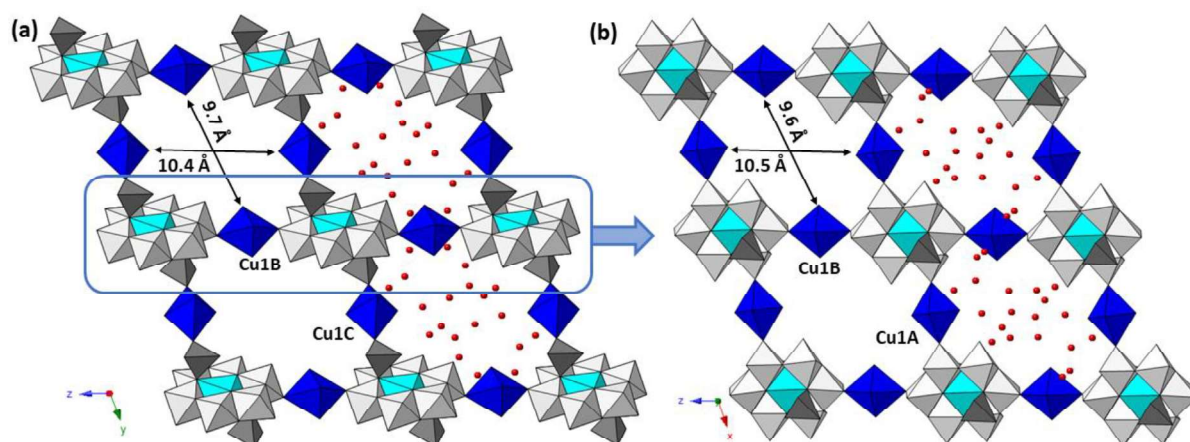


Figure 4.13. (a) View of the crystal packing of **1-CuMo8** along the crystallographic *x* axis and (b) projection of a hybrid layer parallel to the (010) plane. The C and H atoms are omitted for clarity.

The crystal packing of **1-CuMo8** can be viewed as a 3-dimensional covalent open-framework displaying an interconnected network of channels, where the hydration water molecules are hosted (Figure 4.13). This structure is formed by hybrid $\{\text{H}_4\text{CuMo}_6(\text{MoO}_3)_2\}/\{\text{Cu}(\text{DMC})\}$ layers in the *xz* plane, in which each polyanion is linked to four neighbouring clusters through $\{\text{Cu}(\text{DMC})\}^{2+}$ bridging complexes (Cu1A and Cu1B), resulting water-filled rhombic-like voids (average cross-sections of *ca.* 10.5 × 9.6 Å considering the interatomic distances between opposite N atoms of the grid voids). These layers are covalently connected to each other along the crystallographic *y* axis through the octahedral

Cu1C complex coordinated to the $\{\text{MoO}_4\}$ tetrahedral unit from the POM anion. The $\text{N-H}\cdots\text{O}_{\text{POM}}$ and $\text{C-H}\cdots\text{O}_{\text{POM}}$ interactions established between the metalorganic complexes and the O atoms from the POM anion contribute to the overall stability of **1-CuMo8** (Table 4.4). The stacking of hybrid grids generates a three-dimensional system of interconnected channels constituted by wider voids connected through narrower necks running along the three crystallographic (x , y and z) axes. The total solvent accessible volume of accounts for the 37% (848 \AA^3) of the unit cell volume as calculated by PLATON (Figure 4.14).³⁸

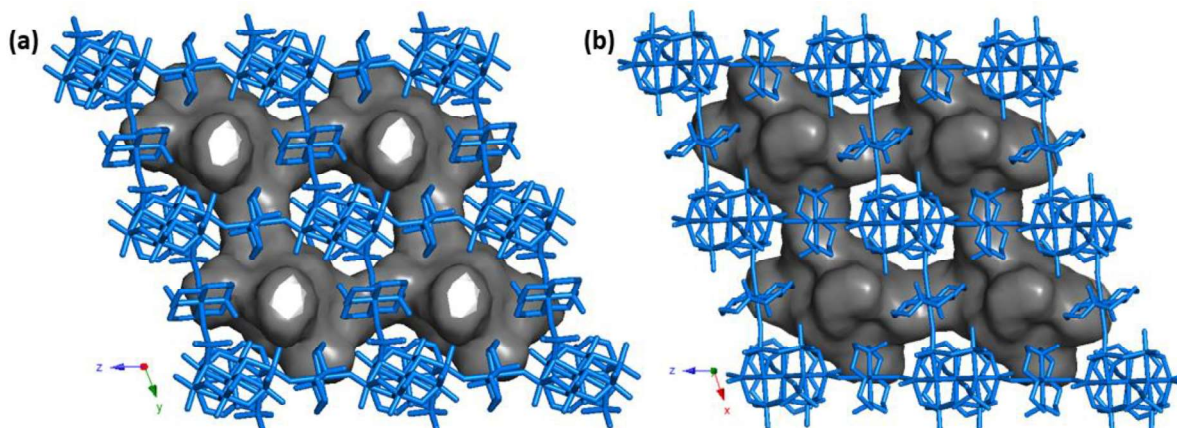


Figure 4.14. View of the surface representation of water-filled interconnected channels in **1-CuMo8** along the crystallographic (a) x and (b) y axes.

Table 4.4. $\text{N-H}\cdots\text{O}$, $\text{C-H}\cdots\text{O}$ and $\text{O-H}\cdots\text{O}$ type interactions in **1-CuMo8**. Intramolecular $\text{O-H}\cdots\text{O}$ hydrogen-bonds occurring within the polyanion are highlighted in bold.

Donor-H \cdots Acceptor	D \cdots A (\AA)	Donor-H \cdots Acceptor	D \cdots A (\AA)
O31-H31\cdotsO44ⁱ (Intra)	2.807(11)	C6C-H6CB \cdots O3 ⁱⁱⁱ	3.448(18)
O32-H32\cdotsO44ⁱ (Intra)	2.963(11)	C7A-H7AB \cdots O3 ^{iv}	3.428(17)
N4B-H4B \cdots O22 ⁱⁱ	3.122(15)	C7A-H7AB \cdots O33 ^{iv}	3.099(18)
N4A-H4A \cdots O11 ⁱ	2.895(13)	C7C-H7CB \cdots O4	3.128(16)
N32-H32 \cdots O44 ⁱ	2.963(11)	C7B-H7BB \cdots O2 ⁱⁱ	3.14(2)
C2C-H2CB \cdots O1	3.263(17)	C8B-H8BB \cdots O444	3.459(19)

Symmetry codes: i) $-x, 2-y, -z$; ii) $-x, 2-y, -1-z$; iii) $x, 1+y, z$; iv) $1-x, 2-y, -z$.

4.3.4. Crystal structure of 1-CrMo6

Compound **1-CrMo6** crystallizes in the triclinic $P-1$ space group and its asymmetric unit contains two halves of the $[\text{H}_6\text{CrMo}_6\text{O}_{24}]^{3-}$ Anderson-Evans cluster, one $\{\text{Cu}(\text{DMC})(\text{H}_2\text{O})\}^{2+}$ metalorganic moiety in general position (Cu1A) and one $\{\text{Cu}(\text{DMC})\}^{2+}$ complex located in a symmetry center (Cu1B), together with 11 hydration water molecules (Figure 4.15). Charge balance considerations indicate that the POM anions must be hexa-protonated. The six protonation sites in the Anderson-Evans cluster are located in the $\mu^3\text{-O}$ atoms surrounding the central $\{\text{CrO}_6\}$ heteroatom. Residual electron density peaks in Fourier maps suggest the approximate location for these H-atoms.

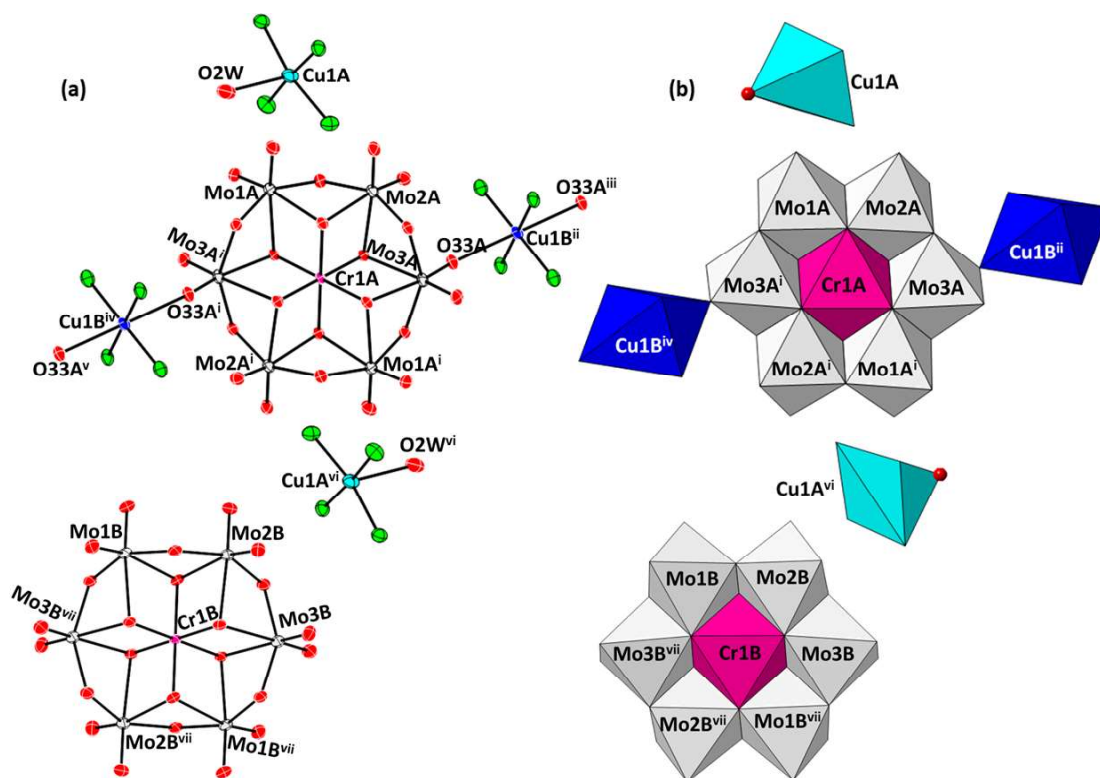


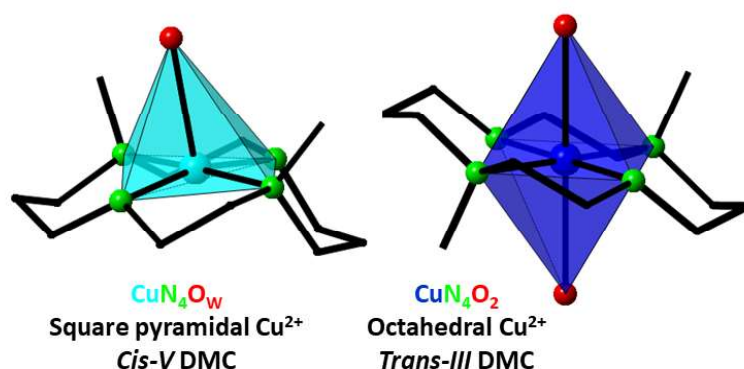
Figure 4.15. (a) ORTEP representation of 1-CrMo_6 showing 50% probability thermal ellipsoids, together with the atom labelling scheme. (b) Polyhedral representation of 1-CrMo_6 . The C and H atoms, as well as the water hydration molecules have been omitted for clarity. Color code: Cr, pink; octahedral CuN_4O_w , light blue. Symmetry codes: i) $-1-x, 2-y, -1-z$; ii) $x, 1+y, 1+z$; iii) $-x, 2-y, -1-z$; iv) $-1-x, 1-y, -z$; v) $-1+x, y, z$; vi) $-1-x, 2-y, -1-z$; vii) $-1-x, 2-y, -z$.

There are two types of metalorganic complexes in the crystal structure of 1-CrMo_6 . The $[\text{Cu}(\text{DMC})(\text{H}_2\text{O})]^{2+}$ (Cu1A) moiety acts as a charge compensating unit and exhibits a CuN_4O chromophore with an tetragonally elongated square-based pyramidal geometry, in which the four N atoms of the ligand form the basal plane and the apical position is occupied by one coordination water molecule [Cu–O bond length, $2.633(6)\text{\AA}$]. In contrast, the $\{\text{Cu}(\text{DMC})\}^{2+}$ complex (Cu1B) bridges contiguous Anderson-Evans units through coordination to their surface O atoms. The Cu atom in Cu1B shows an axially elongated CuN_4O_2 octahedral geometry with four N atoms in the equatorial plane and two terminal O_{POM} atoms in axial positions. Bond lengths in Table 4.5 are consistent with those shown in the few $\{\text{Cu}(\text{DMC})\}^{2+}$ complexes reported to date.^{37a} The more flexible coordination geometry of Cu1A allows the bending of the ligand, in such a way that it shows the more common *cis-V* configuration (Figure 4.16). Conversely, the ligand from the octahedral Cu1B unit displays a *trans-III* configuration.

Table 4.5. Cu–N bond lengths and Cu–O_{POM} distances present in the {Cu(DMC)}²⁺ complexes of **1-CrMo6**.

Cu1A		Cu1B	
Cu1A–N1A	2.083(6)	Cu1B–N1B	2.066(5)
Cu1A–N4A	2.006(6)	Cu1B–N4B	2.013(5)
Cu1A–N8A	2.071(6)	Cu1B–N1B ⁱ	2.066(5)
Cu1A–N11A	2.014(6)	Cu1B–N4B ⁱ	2.013(5)
Cu1A–O2W	2.633(6)	Cu1B–O33	2.511(5)
		Cu1B–O33 ⁱⁱ	2.511(5)

Symmetry codes: i) $-x, -y, 1-z$; ii) $x, -1+y, 1+z$.

**Figure 4.16.** Polyhedral representation of the different coordination geometries and ligand configurations showed by {Cu(DMC)}²⁺ building blocks in **1-CrMo6**.

Two crystallographically independent Anderson-Evans anions are also found in **1-CrMo6**, one of which is decorated by two octahedral Cu1B complexes in opposite positions and hence, it connects adjacent POMs forming hybrid chains running along the crystallographic x axis. As depicted in Figure 4.17, the non-decorated Anderson-Evans anion is located between these covalent chains, forming supramolecular layers parallel to the xz plane through the hydrogen-bonding network established between protonated faces from Anderson-Evans units. Even though the protonated faces from the POM clusters are displaced 45.7° from the ideal parallel arrangement, they can act as both donors and acceptors of H-bonds, which facilitates the stacking. One hydration water molecule (O11W) located in an intralamellar position reinforces the formation of these supramolecular layers (Figure 4.17b). These sheets are further linked to each other through O–H \cdots O, N–H \cdots O and C–H \cdots O type interactions (Table 4.6), which involve the Cu1A moiety located in the intralamellar space and O_{POM} atoms.

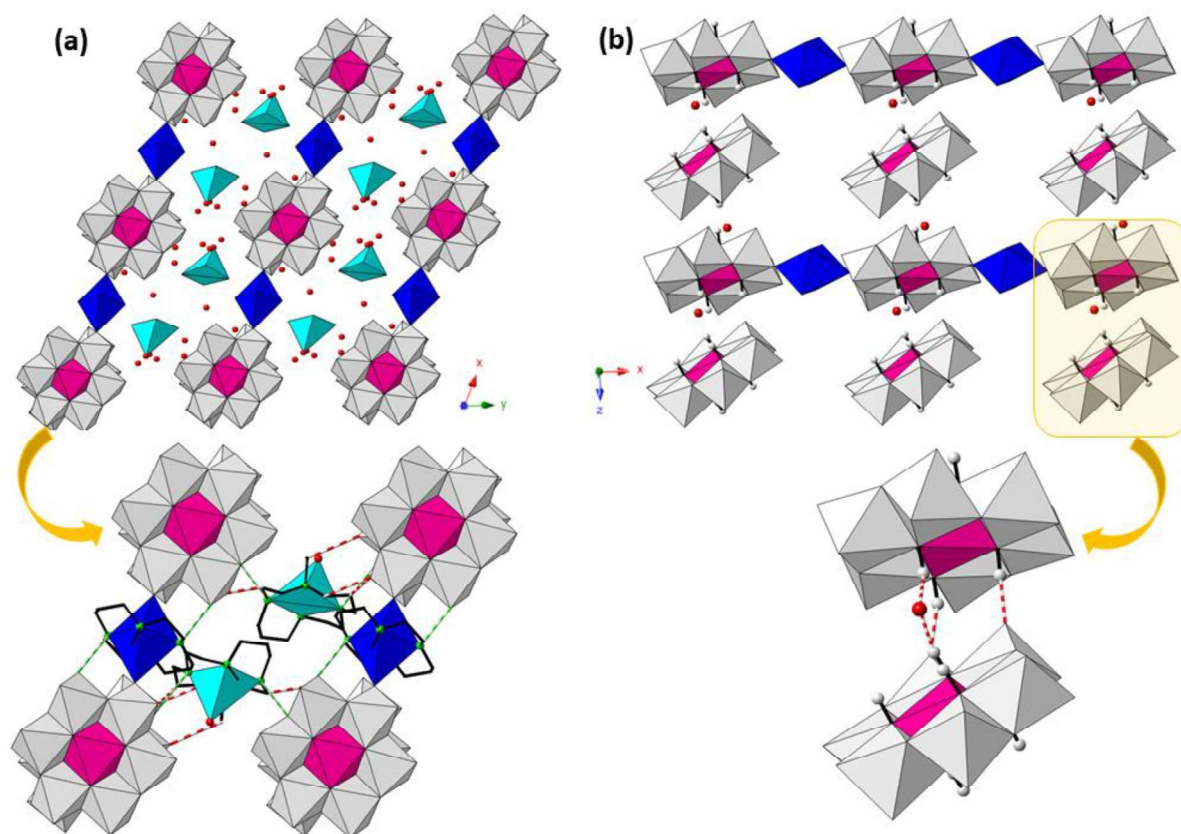


Figure 4.17. (a) Crystal packing of **1-CrMo6** along the crystallographic *z* axis and (b) view of the hybrid layers in the *xz* plane, both with detail of the H-bond interactions that help to the overall crystal packing.

Table 4.6. O–H...O, N–H...O and C–H...O interactions in **1-CrMo6**.

Donor–H...Acceptor	D...A (Å)	Donor–H...Acceptor	D...A (Å)
O21A–H21A...O11W ⁱ	2.720(6)	C10A–H10B...O22B	3.417(10)
O21B–H21B...O11W ⁱⁱ	2.649(6)	C12A–H12A...O6W	3.280(9)
O31A–H31A...O10W ⁱⁱⁱ	2.788(6)	C12A–H12B...O22A	3.163(8)
O31B–H31B...O10W ^{iv}	2.770(7)	C7B–H7AB...O33A ^{iv}	3.093(8)
O32A–H32A...O2B	2.697(6)	C15A–H15B...O2W	3.253(8)
O32B–H32B...O8W ^{iv}	2.670(6)	C16A–H16A...O11B ^{vi}	3.423(10)
N4A–H4A...O3B ^v	3.023(8)	C6A–H6AA...O3A	3.065(8)
N4B–H4B...O22A ^{iv}	2.940(8)		
N11A–H11A...O2	2.902(7)		

Symmetry codes: i) $-1-x, 2-y, -1-z$; ii) $-1+x, 1+y, z$; iii) $x, -1+y, z$; iv) $-x, 1-y, -z$; v) $-x, 1-y, -1-z$; vi) $-1-x, 1-y, -z$.

4.3.5. Crystal structure of **1Na-CrMo6**

Compound **1Na-CrMo6** crystallizes in the triclinic *P*-1 space group and its asymmetric unit contains one half of the $[\text{H}_6\text{CrMo}_6\text{O}_{24}]^{3-}$ Anderson-Evans-type anion, one centrosymmetric $\{\text{Cu}(\text{DMC})\}^{2+}$ metalorganic moiety, one sodium cation and a total of 8 hydration water molecules per POM cluster (Figure 4.18). As in the case of **1-CrMo6**, the Anderson-Evans anion is hexa-protonated in the $\mu^3\text{-O}$ atoms, in good agreement with elemental and thermal analyses, as well as, charge balancing considerations.

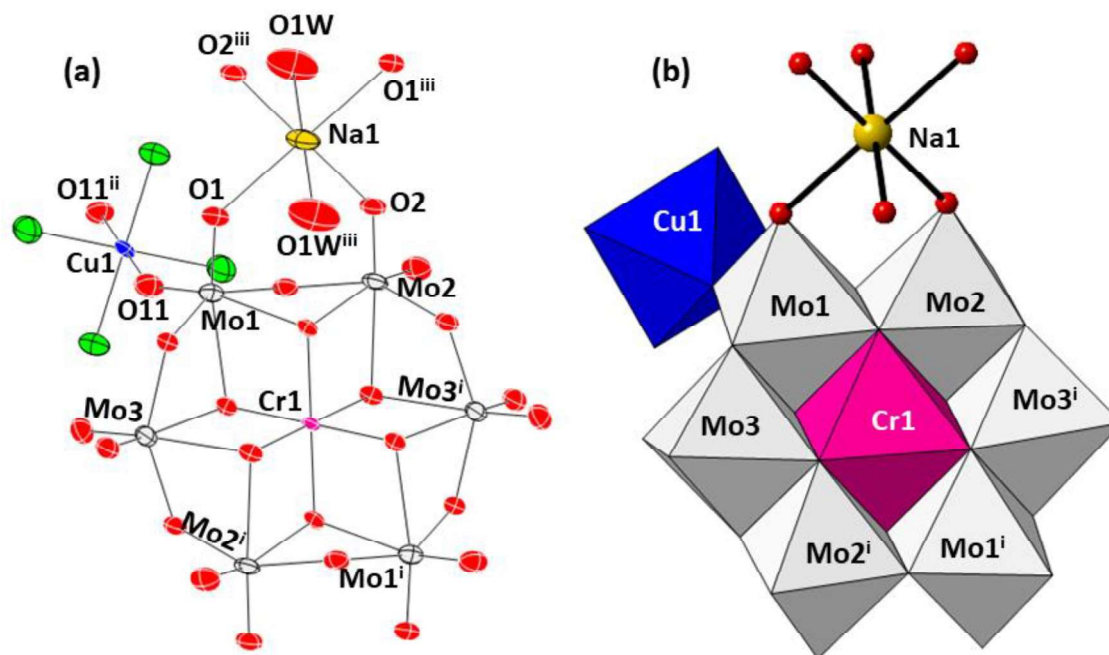


Figure 4.18. (a) ORTEP representation of 1Na-CrMo_6 showing 50% probability thermal ellipsoids, together with the atom labelling scheme. (b) polyhedral representation of 1Na-CrMo_6 . The C and H atoms, as well as the water hydration molecules not coordinated to the Na center have been omitted for clarity. Color code: Na, yellow. Symmetry codes: i) $1-x, -y, 2-z$; ii) $1-x, 1-y, 1-z$; iii) $-x, 1-y, 2-z$.

The two main building-blocks in the structure of 1Na-CrMo_6 are the well-known $[\text{H}_6\text{CrMo}_6\text{O}_{24}]^{3-}$ anion and the $\{\text{Cu}(\text{DMC})\}^{2+}$ complex, with an octahedral Cu^{II} center showing N atoms from the ligand in equatorial positions [$\text{Cu1-N1} = 2.054(6)\text{\AA}$ and $\text{Cu1-N4} = 2.013(6)\text{\AA}$] and a significant Jahn-Teller distortion with axial sites occupied by O_{POM} atoms from contiguous POM units [$\text{Cu1-O11} = 2.699(5)\text{\AA}$]. The DMC ligand exhibits a *trans-III* configuration, which according to the structures reported in this work it is the most common form for octahedral bridging complexes with bulky groups occupying axial positions. The crystal packing of 1Na-CrMo_6 can be best described as POM-metalorganic hybrid chains running along the $[01-1]$ direction. These hybrid chains are linked to each other by a sodium cation directly coordinated to terminal O atoms from the POM surface and with the O1W water molecule completing the coordination sphere. Furthermore, protonated faces of the polyanion reinforce this bidimensional arrangement by establishing $\text{O}_w\text{-H}\cdots\text{O}_{\text{POM}}$ hydrogen-bonding interactions with hydration and coordination water molecules. As depicted in Figure 4.19, the stacking of inorganic layers parallel to the xz plane takes place through an extensive network of $\text{O}_w\text{-H}\cdots\text{O}_{\text{POM}}$, and $\text{C-H}\cdots\text{O}_{\text{POM}}$ type contacts involving organic ligands, hydration water molecules in the intralamellar space and POM surface O atoms (Table 4.7). This overall packing displays small structural voids accounting for the 9% (93\AA^3) of the unit cell volume, as calculated by PLATON. However, surface representation of accessible voids could not be represented by PyMol using the standard molecular probe provided by the software.³⁹

According to the variable-temperature PXRD analyses described in the previous section, **1Na-CrMo6** undergoes two sequential thermally-triggered structural transitions upon heating. Total dehydration of **1Na-CrMo6** could a priori imply that the two coordination water molecules from sodium cations are removed and hence, it would promote the collapse of the crystal architecture. However, the stability of the new crystalline phase formed upon total dehydration must involve either a) a sodium cation with a unusually low coordination number or ii) the completion of the coordination sphere of the sodium cation with O_{POM} atoms from contiguous layers. These facts will be assessed in the near future by means of scXRD studies at high temperature.

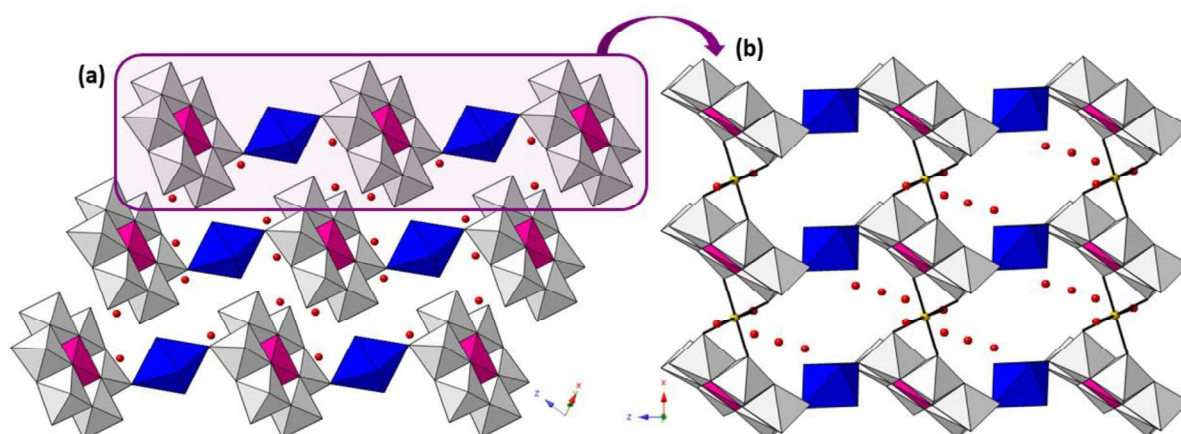


Figure 4.19. (a) View of the crystal packing of **1Na-CrMo6** along the [1-10]; (b) projection of the hybrid layer parallel to the xz plane.

Table 4.7. O–H...O and C–H...O interactions in **1Na-CrMo6**.

Donor–H...Acceptor	D...A (Å)	Donor–H...Acceptor	D...A (Å)
O1W–H1WB...O22 ⁱ	2.794(10)	C2–H2A...O12	3.311(9)
O3W–H3WA...O33 ⁱⁱ	2.842(7)	C3–H3B...O2 ⁱ	3.308(9)
O3W–H3WB...O23 ⁱⁱⁱ	2.735(7)	C7–H7B...O11	3.286(9)
O4W–H4WA...O3 ^{iv}	2.789(8)	C8–H8A...O33 ^v	3.309(11)
O21–H21...O4W ⁱⁱⁱ	2.946(7)		
O31–H31...O4W	2.717(8)		
O32–H32...O2W ⁱⁱⁱ	2.714(9)		

Symmetry codes: i) 1-x, 1-y, 2-z; ii) 1-x, -y, 1-z; iii) 1-x, -y, 2-z; iv) 1+x, y, z; v) 1-x, 1-y, 1-z.

4.3.6. Crystal structure of **1Na2-CrMo6**

Compound **1Na2-CrMo6** crystallizes in the triclinic *P*-1 space group and its asymmetric unit contains two halves of the $[\text{H}_6\text{CrMo}_6\text{O}_{24}]^{3-}$ Anderson-Evans-type cluster, one half of the centrosymmetric $\{\text{Cu}(\text{DMC})\}^{2+}$ complex, two sodium cations and a total of 11.5 hydration water molecules (Figure 4.20). The Anderson-Evans anion is hexa-protonated in the $\mu_3\text{-O}$

atoms, in good agreement with elemental and thermal analyses, as well as, charge balancing considerations.

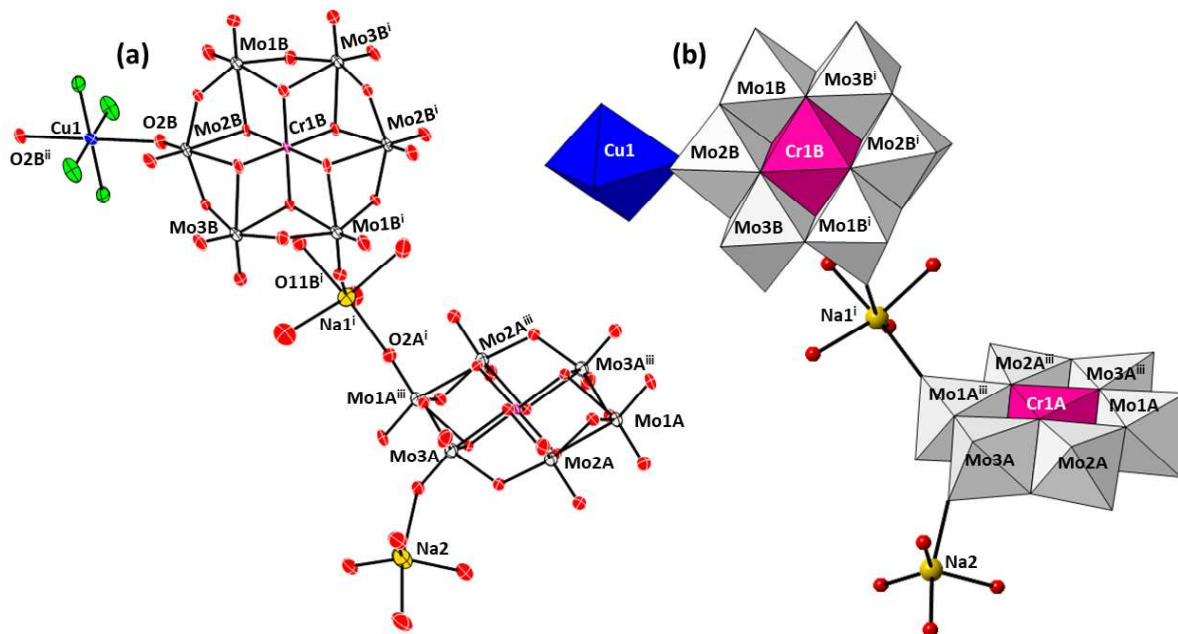


Figure 4.20. (a) ORTEP representation of $1\text{Na}_2\text{-CrMo}_6$ showing 50% probability thermal ellipsoids, together with the atom labelling scheme. (b) Polyhedral representation of $1\text{Na}_2\text{-CrMo}_6$. The C and H atoms have been omitted for clarity. Symmetry codes: i) $-x, -y, -1-z$; ii) $-1-x, 1-y, -1-z$; iii) $-x, 1-y, -z$.

The axially elongated, octahedral $\{\text{Cu}(\text{DMC})\}^{2+}$ complex shows i) the CuN_4O_2 chromophore with equatorial positions occupied by the ligand N atoms [Cu–N bond lengths of 2.028(10) and 2.003(12) Å] and O_{POM} atoms in axial sites [Cu–O2B = 2.555(9) Å] and ii) the DMC ligand in *trans III* configuration. As in the case of 1-CrMo_6 , two crystallographically independent Anderson-Evans anions are found in $1\text{Na}_2\text{-CrMo}_6$, one of which is decorated by two octahedral complexes in opposite positions and hence, it connects adjacent POMs forming hybrid chains running along the $[1-10]$ direction. As depicted in Figure 4.21, the non-decorated Anderson-Evans anion is located between these covalent chains, and connected to hybrid chains through the coordination of the Na1 cation together with the hydrogen-bonding network established between protonated faces from the two different Anderson-Evans units. Even though the protonated faces from the POM clusters are displaced 41.0° from the ideal parallel arrangement, they can act as both donors and acceptors of H-bonds (Table 4.8). This arrangement generates layers parallel to the (211) plane (Figure 4.21), the stacking of which is facilitated by the network of $\text{O-H}\cdots\text{O}$ and $\text{C-H}\cdots\text{O}$ type contacts established between coordination water molecules of the second crystallographically independent sodium cation coordinated to the surface of the nude Anderson-Evans anion, organic ligands and O_{POM} atoms.

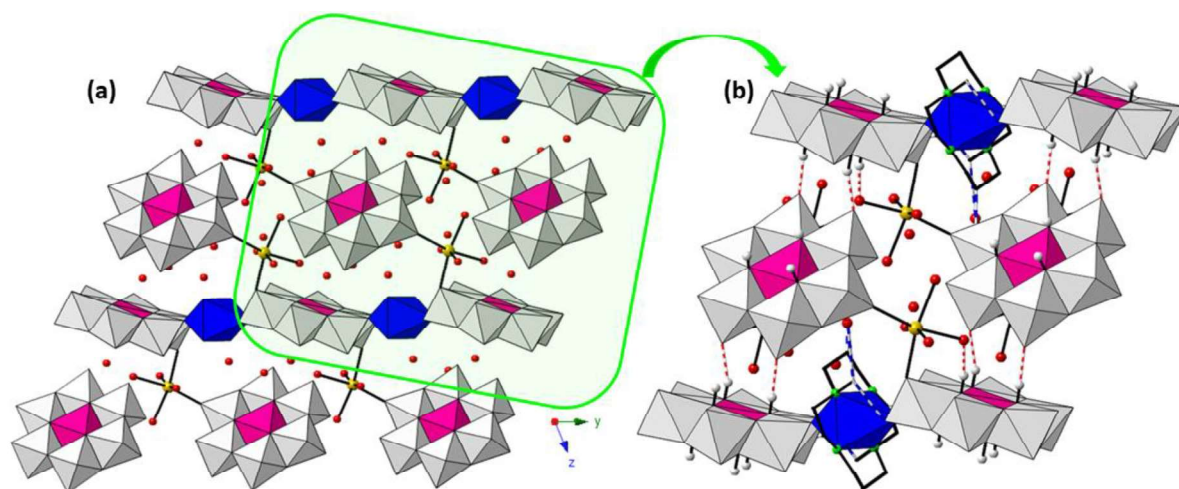


Figure 4.21. (a) Projection of a layer in **1Na2-CrMo6** parallel to the yz plane, and (b) detail of the as $O-H\cdots O$ and $C-H\cdots O$ interactions bridging the hybrid chains.

Table 4.8. $O-H\cdots O$ and $C-H\cdots O$ interactions in **1Na2-CrMo6**.

Donor-H...Acceptor	D...A (Å)	Donor-H...Acceptor	D...A (Å)
O21A-H21A...O9W ⁱ	2.636(11)	C3-H3A...O33B	3.393(19)
O21B-H21B...O3A ⁱⁱ	2.687(9)	C6-H6A...O22A	3.282(17)
O31A-H31A...O32A	2.921(10)	C8-H8A...O1B ^v	3.450(17)
O31A-H31A...O10W ⁱ	2.671(11)	C8-H8C...O9W ⁱⁱⁱ	3.360(17)
O31B-H31B...O4W	2.729(9)		
O32A-H32A...O7W ⁱⁱⁱ	2.727(11)		
O32B-H32B...O11A ^{iv}	2.710(9)		

Symmetry codes: i) $-x, 1-y, -z$; ii) $-x, 1-y, -1-z$; iii) $1-x, 1-y, -z$; iv) $-x, -y, -z$; v) $1+x, y, z$.

4.3.7. Crystal structure of **1NO3-CrMo6**

The **1NO3-CrMo6** compound is the only one crystallizing in a non-triclinic space group. In fact, **1NO3-CrMo6** crystallizes in the monoclinic $I2/m$ space group and its asymmetric unit contains $1/3$ of a $[H_6CrMo_6O_{24}]^{3-}$ Anderson-Evans-type cluster, one half of a $\{Cu(DMC)\}^{2+}$ complex disordered over two crystallographic sites showing equivalent occupancies, one half of a nitrate anion as well as 5 H_2O molecules of hydration. The Anderson-Evans anion is hexa-protonated in the μ_3-O atoms, in good agreement with elemental and thermal analyses, as well as, charge balancing considerations.

The axially elongated octahedral $\{Cu(DMC)\}^{2+}$ complex in **1NO3-CrMo6** shows i) the CuN_4O_2 chromophore with equatorial positions occupied by the ligand N atoms and O_{POM} atoms in axial sites (Table 4.9) and ii) the DMC ligand in *trans III*. Regarding the crystal packing, each Anderson-Evans anion is connected to four neighboring clusters through $\{Cu(DMC)\}^{2+}$ bridging units to form hybrid layers parallel to the yz plane. The $C-H\cdots O_{POM}$ and $N-H\cdots O_{POM}$ type contacts established between the DMC ligand and O_{POM} atoms reinforce this

arrangement, which generates square-like voids with an approximate cross-section of 11.2 x 11.2 Å (interatomic distances between opposite N atoms of the grid voids). Hybrid layers are stacked through trifurcated H-bonding interactions established between the nitrate anions in interlamellar position and protonated O_{POM} atoms (Figure 4.22 and Table 4.10). This stacking generates water-filled channels running along the crystallographic x axis, in which all the hydration water molecules are hosted (Figure 4.22c). The total solvent accessible volume in **1NO3-CrMo6** accounts for the 14% (360 Å³) of the unit cell volume as calculated by PLATON.

Table 4.9. Cu–N and Cu–O_{POM} bond lengths (Å) for {Cu(DMC)}²⁺ complexes in **1NO3-CrMo6**.

Cu1A		Cu1B	
Cu1–*N1A	2.040(12)	Cu1–*N1B	2.030(12)
Cu1–*N4A	2.016(14)	Cu1–*N4B	1.946(15)
Cu1–*N1A ⁱ	2.040(12)	Cu1–*N1B ⁱ	2.030(12)
Cu1A–*N4A ⁱ	2.016(14)	Cu1A–*N4B ⁱ	1.946(15)
Cu1–O11	2.487(3)		
Cu1A–O11 ⁱ	2.487(3)		

Symmetry codes: i) ½-x, ½-y, 1/-z.

According to the variable-temperature PXRD analyses described in the previous section, **1NO3-CrMo6** is able to undergo structural transformations under thermal-stimuli. Total dehydration of **1NO3-CrMo6** could lead to a water-free structure with monodimensional channels accessible for sorption studies. The structure of this new possible anhydrous compound will be assessed in the near future by means of scXRD studies at high temperature.

Table 4.10. Distances (Å) for O_{POM}–H···O_N, N–H···O and C–H···O interactions in **1NO3-CrMo6**.

Donor–H···Acceptor	D···A (Å)	Donor–H···Acceptor	D···A (Å)
O4–H4···O2N ⁱ	2.956(12)	C7A–H7AB···O11	3.17(3)
O21–H21···O3N	2.701(12)	C6B–H6BA···O1W	3.28(4)
O21–H21···O2N ⁱⁱ	2.805(10)	C2B–H2BA···O12 ⁱⁱⁱ	3.28(2)
N4A–H4A···O2	3.175(17)	C2B–H2BB···O11 ^{iv}	3.18(2)
N4B–H4B···O2	3.041(16)	C2A–H2AB···O11	3.140(18)
C8–H8BC···O3N ⁱⁱ	2.93(3)	C8B–H8BA···O11	2.98(3)
C8A–H8AC···O1 ⁱⁱⁱ	3.277(19)		

Symmetry codes: i) 1+x, y, z; ii) -x, y, z; iii) -1+x, y, z; iv) ½-x, ½-y, ½-z.

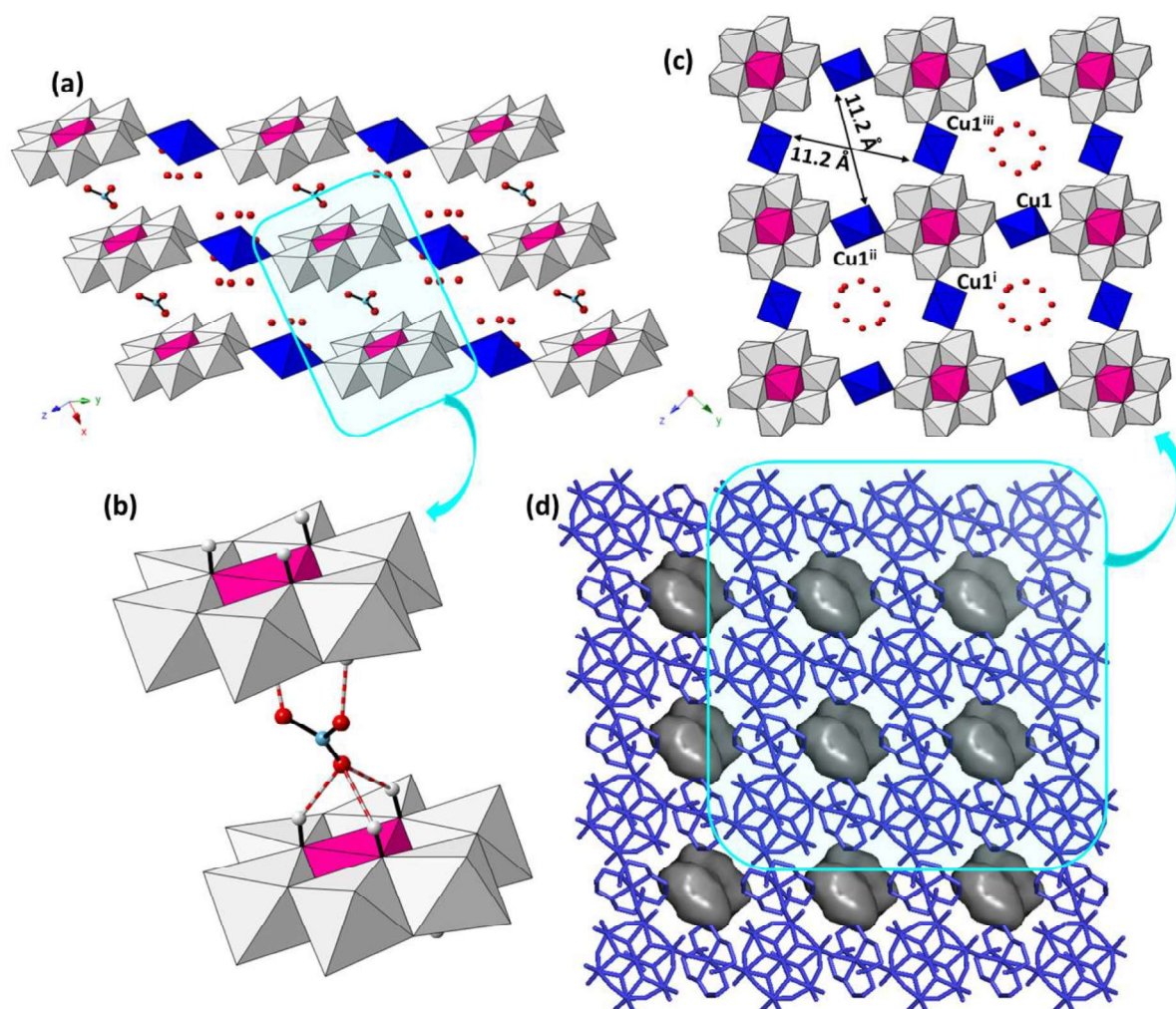


Figure 4.22. (a) View of the crystal packing of **1NO3-CrMo6** along the crystallographic x axis (b) detail of interactions for the stacking of layers. (c) Projection of the hybrid layers parallel to the yz plane and (d) surface representation of the water-filled channels. The C and H atoms are omitted for clarity Color code: N from the nitrate, light blue. Symmetry codes: i) $1-x, y, -z$; ii) $1-x, -y, -z$; iii) $x, -y, z$.

4.3.8. Crystal structure of **1Cl-CrMo6**

Compound **1Cl-CrMo6** crystallizes in the triclinic $P-1$ space group and its asymmetric unit contains one $[\text{H}_6\text{CrMo}_6\text{O}_{24}]^{3-}$ Anderson-Evans anion, and $\{\text{Cu}(\text{DMC})\}^{2+}$ metalorganic moieties divided into: one Cu1A located in a general position and two centrosymmetric complexes (Cu1B and Cu1C); together with 5 hydration water molecules disordered over 8 crystallographic positions (Figure 4.23). The Anderson-Evans anion is hexa-protonated in the $\mu_3\text{-O}$ atoms, in good agreement with elemental and thermal analyses, as well as, charge balancing considerations.

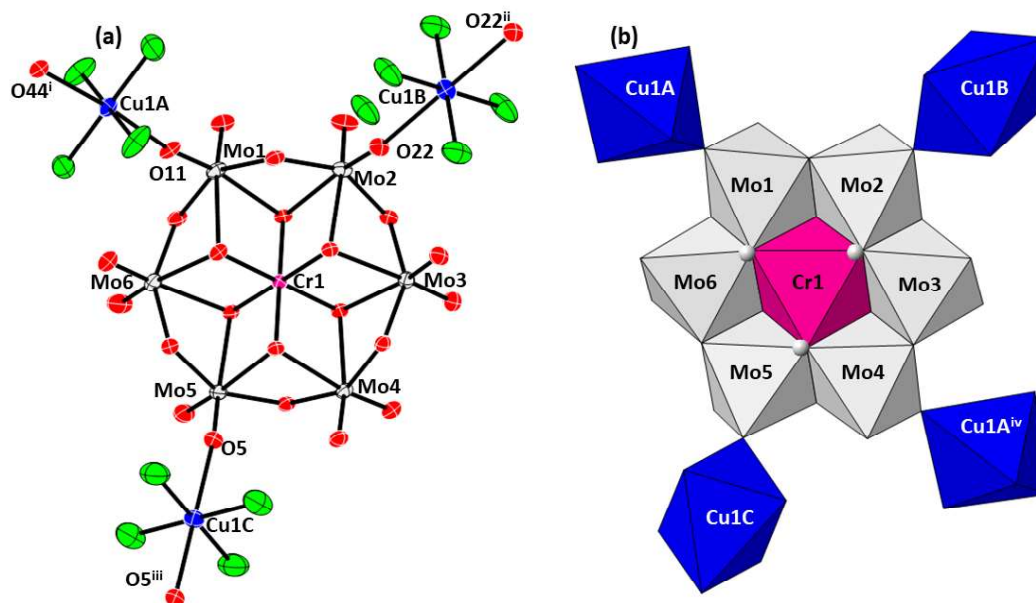


Figure 4.23. (a) ORTEP representation of **1Cl-CrMo6** showing 50% probability thermal ellipsoids, together with the atom labelling scheme. (b) polyhedral representation of **1Cl-CrMo6**. The C and H atoms, as well as the water hydration molecules have been omitted for clarity. Symmetry codes: i) $1+x, -1+y, z$; ii) $1-x, 1-y, 1-z$; iii) $-x, 1-y, 2-z$; iv) $-1+x, 1+y, z$

All the three DMC complexes in **1Cl-CrMo6** show axially elongated octahedral geometries with equatorial positions occupied by the ligand N atoms and O_{POM} atoms in axial sites (Table 4.11), as well as, DMC ligands in trans III configuration.

Table 4.11. Cu–N and Cu– O_{POM} bond lengths for {Cu(DMC)} complexes in **1Cl-CrMo6**.

Cu1A		Cu1B		Cu1C	
Cu1A–N1A	2.061(7)	Cu1B–N1B	2.048(8)	Cu1C–N1C	2.060(9)
Cu1A–N4A	1.992(8)	Cu1B–N4B	1.995(8)	Cu1C–N4C	2.002(8)
Cu1A–N8A	2.057(7)	Cu1B–N1B ⁱⁱ	2.048(8)	Cu1C–N1C ⁱⁱⁱ	2.060(9)
Cu1A–N11A	1.980(8)	Cu1B–N4B ⁱⁱ	1.995(8)	Cu1C–N4C ⁱⁱⁱ	2.002(8)
Cu1A–O11	2.398(5)	Cu1B–O22	2.499(4)	Cu1C–O5	2.446(5)
Cu1A–O44 ⁱ	2.489(4)	Cu1B–O22 ⁱⁱ	2.499(4)	Cu1C–O4 ⁱⁱⁱ	2.446(5)

Symmetry codes: i) $1+x, -1+y, z$; ii) $1-x, 1-y, 1-z$; iii) $-x, 1-y, 2-z$.

The crystal packing of **1Cl-CrMo6** resembles to that of **1NO3-CrMo6**, but for the interlamellar nitrate anions, which are replaced by chloride ions. In this sense, this structure is formed by hybrid POM-metalorganic layers parallel to the yz plane, in which each POM cluster is covalently bonded to four neighboring clusters through $\{\text{Cu(DMC)}\}^{2+}$ bridging complexes. In this case, these layers are corrugated with a $\text{Cr}\cdots\text{Cr}\cdots\text{Cr}$ corrugation angle of 137° , as depicted in Figure 4.24. Hybrid grids show two different types of voids with cross-sections of 9.9×10.9 and 10.0×10.3 Å (interatomic distances between opposite N atoms of the grid voids). The stacking of these layers through $O_{\text{W}}\text{--H}\cdots O_{\text{POM}}$ and $O_{\text{POM}}\text{--H}\cdots \text{Cl}$

interactions established between the protonated μ^3 -O oxygen atoms from the POM cluster and the Cl^- ions located in the intralamellar space and enclosed by two polyanions (Figure 4.24a), generates water filled channels running in the [100] direction. The total solvent accessible volume accounts for the 9% (265 \AA^3) and 6% (169 \AA^3) of the unit cell volume for each type of void, as calculated by PLATON (Figure 4.24c). Apart from the O–H...Cl interactions, C–H...O and N–H...O hydrogen-bonds between the metalorganic $\{\text{Cu}(\text{DMC})\}^{2+}$ complexes and the oxygen atoms from the inorganic clusters and water molecules contribute to the overall stability of **1Cl-CrMo6** (Table 4.12).

Table 4.12. O–H...Cl, O–H...O_w, N–H...O and C–H...O interactions in **1Cl-CrMo6**.

Donor–H...Acceptor	D...A (Å)	Donor–H...Acceptor	D...A (Å)
O21–H21...Cl1	3.282(5)	C2A–H2AA...O34 ^{iv}	3.379(15)
O32–H32...Cl1 ⁱ	3.466(5)	C7A–H7AA...O6 ⁱ	3.373(16)
O43–H43...Cl1	3.222(5)	C7A–H7AB...O44 ⁱⁱⁱ	3.201(15)
O65–H65...Cl1	3.126(5)	C9A–H9AB...O1 ⁱ	3.363(16)
O54–H54...O6W	2.692(12)	C2C–H2CA...O6W ⁱⁱ	3.186(16)
O54–H54...O7W	2.764(13)	C2C–H2CB...O55 ^v	3.324(15)
O61–H61...O7W	2.694(13)	C14A–H14B...O33 ^{iv}	3.436(15)
O61–H61...O8W	3.044(18)	C7C–H7CB...O5	3.165(13)
N4A–H4A...O66	2.984(10)	C2B–H2BB...O2 ^{vi}	3.230(13)
N4B–H4B...O33	3.334(9)	C7B–H7BA...O22 ^{vii}	3.140(13)
N4C–H4C...O4 ⁱⁱ	3.225(9)	C8B–H8BC...O33	3.408(9)
N11A–H11A...O3 ⁱⁱⁱ	2.963(9)		

Symmetry codes: i) 1+x, y, z; ii) -x, 1-y, 2-z; iii) 1+x, -1+y, z; iv) x, -1+y, z; v) -1-x, 1-y, 2-z; vi) -x, 1-y, 1-z; vii) 1-x, 1-y, 1-z.

According to variable temperature PXRD analyses, anhydrous phases from compounds are stable up to ca 200 °C with no major modifications in their diffraction patterns, which could indicate a robust thermostructural behavior. This fact could allow the isolation activated structures with empty channels available for the adsorption for chemical species.

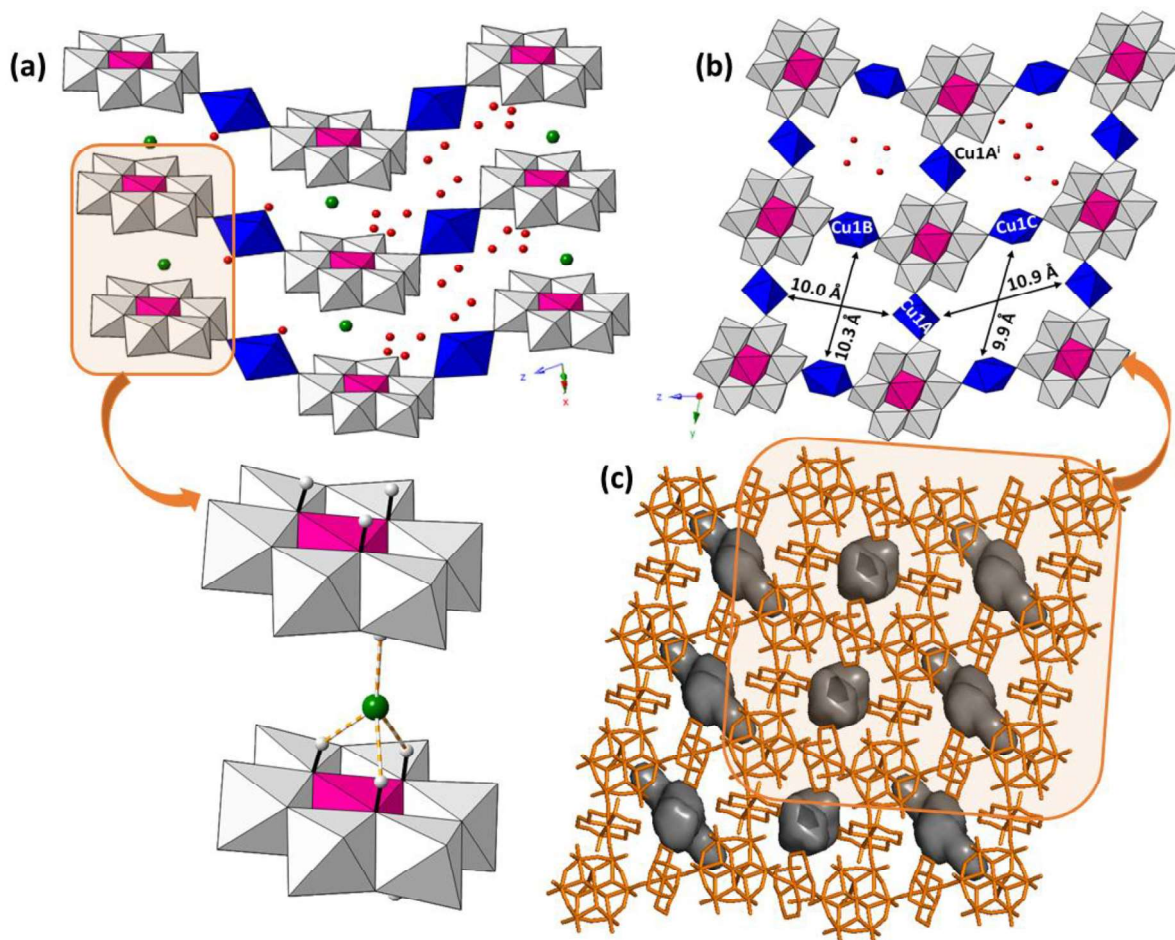


Figure 4.24. (a) View of the crystal packing in **1Cl-CrMo6** in the $[1-10]$ direction with detail of the O–H···Cl Interactions occurring between the layers; (b) projection of a hybrid layer parallel to the yz plane and (c) surface representation of the water-filled interconnected channels showed by **1Cl-CrMo6** along the crystallographic x axis. The C and H atoms are omitted for clarity. Color code: Cl ions, dark green. Symmetry codes: i) $-1+x, 1+y, z$.

4.4. CONCLUSIONS

In this chapter, two different heteropolyoxomolybdate clusters containing structures have been obtained in presence of $\{\text{Cu}(\text{DMC})\}^{2+}$ complexes. In the first reaction, a new $\{\text{H}_4\text{CuMo}_6(\text{MoO}_3)_2\text{O}_{24}\}$ polyanion is obtained starting from a solution of $\{\text{Mo}_7\text{O}_{24}\}$ precursor and the Cu^{II} -containing N4-tetradentate metalorganic complex. This unprecedented cluster is described as a well-known Anderson-Evans cluster with copper(II) as heteroatom, which is bicapped in opposite faces by two $\{\text{MoO}_4\}$ tetrahedra linked by corner-sharing. The presence of these two $\{\text{MoO}_4\}$ units generates a covalent 3D architecture with $\{[\text{Cu}(\text{DMC})]_3\{\text{H}_4\text{CuMo}_6(\text{MoO}_3)_2\text{O}_{24}\}\cdot 13\text{H}_2\text{O}$ (**1-CuMo8**) formula, that exhibits channels interconnected in the three crystallographic axis, in which the hydration water molecules are hosted.

The remaining structures described within this chapter are based on the system formed by reacting a chromium(III) containing Anderson-Evans POM and $\{\text{Cu}(\text{DMC})\}^{2+}$ metalorganic complexes in solvents with different ionic strength. First, from aqueous solution, a bidimensional structure is obtained in which the $\{\text{CrMo}_6\}/\{\text{Cu}(\text{DMC})\}$ hybrid layers are bonded by H-bond interactions that include an additional Cu^{II} complexes acting as counterions, to lead to the final $[\text{Cu}(\text{DMC})(\text{H}_2\text{O})][\{\text{Cu}(\text{DMC})\}_{0.5}\{\text{H}_6\text{CrMo}_6\text{O}_{24}\}]\cdot 10\text{H}_2\text{O}$ (**1-CrMo6**) obtained in a very low yield. Higher synthetic yields are achieved when the reaction is carried out in solution media with higher ionic strength like NaCl. In this case, two compounds are obtained: $\text{Na}[\{\text{Cu}(\text{DMC})\}\{\text{H}_6\text{CrMo}_6\text{O}_{24}\}]\cdot 8\text{H}_2\text{O}$ (**1Na-CrMo6**) formed by monodimensional chains linked to each other by Na^+ cations to form 2D layers, and $\text{Na}_2[\{\text{Cu}(\text{DMC})\}_{0.5}\{\text{H}_6\text{CrMo}_6\text{O}_{24}\}]\cdot 11.5\text{H}_2\text{O}$ (**1Na2-CrMo6**) in which similar hybrid layers are covalently linked to each other through additional Na^+ cations. However, when the synthesis is carried out in solvent media with a different source of monovalent sodium cations such as NaNO_3 , the porous $[\{\text{Cu}(\text{DMC})\}_2\{\text{H}_6\text{CrMo}_6\text{O}_{24}\}]\text{NO}_3\cdot 5\text{H}_2\text{O}$ (**1NO3-CrMo6**) compound is obtained. Moreover, in solvents with less ionic strength such as LiCl the $[\{\text{Cu}(\text{DMC})\}_2\{\text{H}_6\text{CrMo}_6\text{O}_{24}\}]\text{Cl}\cdot 5\text{H}_2\text{O}$ (**1Cl-CrMo6**) structure is obtained exhibiting a crystal packing similar to that of **1NO3-CrMo6** but with the interlamellar nitrate anion replaced by chloride ions. On the contrary, same reaction carried out in a solution of KCl only leads to the potassium salt of the Anderson-Evans anion, $\text{K}_3[\text{H}_6\text{CrMo}_6\text{O}_{24}]\cdot 6\text{H}_2\text{O}$ (**CrMo6**). All these compounds exhibit the B-type Anderson-Evans type anion hexaprotonated in the $\mu_3\text{-O}$ oxygen atoms. Furthermore, it is observed that DMC ligands exhibit a *trans-III* configuration when the Cu^{II} center on the $\{\text{Cu}(\text{DMC})\}$ unit exhibits an octahedral coordination geometry, whereas in square pyramidal $\{\text{Cu}(\text{DMC})\}$ metalorganic moieties, the organic gains space for bending in the *cis-V* conformation, as seen in **1-CrMo6**.

Finally, variable-temperature PXRD experiments on **1Na-CrMo6**, **1NO3-CrMo6** and **1Cl-CrMo6** shows the ability of these compounds to maintain crystallinity up to temperatures between 190 and 230 °C. For the first two hybrids, thermally-induced changes in the diffraction patterns revealed that **1Na-CrMo6** and **1NO3-CrMo6** could undergo solid-phase transformations under thermally stimuli which could lead to the formations of new anhydrous structures different from the stable one at room temperature. Moreover, **1Cl-CrMo6** also shows ability to maintain crystallinity up to 190 °C but with no visual changes in the diffraction pattern, which could indicate that the structure remains virtually unaltered upon thermal evacuation of guest solvent molecules.

4.5. REFERENCES

- [1] Wu, P.; Wang, Y.; Huang, B.; Xiao, Z. Anderson-Type Polyoxometalates: From Structures to Functions. *Nanoscale*, **2021**, *13*, 7119-7133.
- [2] Anderson, J. S. Constitution of the Poly-acids. *Nature*, **1937**, *140*, 850.
- [3] Evans, H. T. Jr. The Crystal Structures of Ammonium and Potassium Molybdo-tellurates. *J. Am. Chem. Soc.*, **1948**, *70*, 1291-1292.
- [4] Lee, U.; Sasaki, Y. Isomerism of the hexamolybdo-platinate(IV) polyanion. crystal structures of $K_{3.5}[\alpha\text{-H}_{4.5}\text{PtMo}_6\text{O}_{24}] \cdot 3\text{H}_2\text{O}$ and $(\text{NH}_4)_4[\beta\text{-H}_4\text{PtMo}_6\text{O}_{24}] \cdot 1.5\text{H}_2\text{O}$. *Chem. Lett.*, **1984**, *13*, 1297-1300.
- [5] Blazevic, A.; Rompel, A. The Anderson-Evans Polyoxometalate: From Inorganic Building Blocks via Hybrid Organic-Inorganic Structures to Tomorrows "Bio-POM". *Coord. Chem. Rev.*, **2016**, *307*, 42-64.
- [6] (a) Bijelic, A.; Rompel, A. The Use of Polyoxometalates in Protein Crystallography – An Attempt to Widen a well-Known Bottleneck. *Coord. Chem Rev.* **2015**, *299*, 22-38. (b) Bijelic, A.; Rompel, A. Ten Good Reasons for the Use of the Tellurium-Centered Anderson–Evans Polyoxotungstate in Protein Crystallography. *Accounts Chem. Res.*, **2017**, *50*, 1441-1448.
- [7] Vidyavathy, B.; Vidyasagar, K. Low-Temperature Syntheses and Characterization of Novel Layered Tellurites, $\text{A}_2\text{Mo}_3\text{TeO}_{12}$ (A = NH_4 , Cs), and "Zero-Dimensional" Tellurites, $\text{A}_4\text{Mo}_6\text{Te}_2\text{O}_{24} \cdot 6\text{H}_2\text{O}$ (A = Rb, K). *Inorg. Chem.*, **1998**, *37*, 4764-4774.
- [8] Evans, H. T.; Showell, J. S. Molecular Structure of the Decamolybdodicobaltate(III) Ion. *J. Am. Chem. Soc.*, **1969**, *91*, 6881-6882.
- [9] Wang, X.; Sun, J.; Lin, H.; Chang, Z.; Tian, A.; Liu, G.; Wang, X. Novel Anderson-type $[\text{TeMo}_6\text{O}_{24}]^{6-}$ -Based Metal–Organic Complexes Tuned by Different Species and Their Coordination Modes: Assembly, Various Architectures and Properties. *Dalton Trans.* **2016**, *45*, 2709-2719.
- [10] (a) Lee, U.; Jang, S.-J.; Joo, H.-C.; Park, K.-M. Anhydrous Octaguanidinium Hexatungstoptatinate(IV). *Acta Cryst.* **2003**, *E59*, m116-m118. (b) Mo, S.; Ju, Z.; Xu, Z.; Wu, J.; Yao, K. Anderson-Evans Type Tungstotellurate with Metal-Organic Complex Moieties: Preparation, Structure and Properties of $\text{Na}_2[\text{Co}(\text{C}_{12}\text{H}_8\text{N}_2)_3]_2[\text{TeW}_6\text{O}_{24}] \cdot 25 \cdot 16\text{H}_2\text{O}$. *Synth. React. Inorg. M.* **2006**, *36*, 687-692. (c) Xu, Z.-H.; Xi, P.-X.; Chen, F.-J.; Zeng, Z.-Z. Synthesis and Characterization of a Novel Anderson-Type Tungstotellurate Decorated by Transition Metal Complexes: $[\text{Na}(\text{H}_2\text{O})_3]_2\{\{\text{Cu}(2,2'\text{-bipy})_2\}_2(\text{TeW}_6\text{O}_{24})\} \cdot 4\text{H}_2\text{O}$. *Transition Met. Chem.* **2008**, *33*, 237-241.
- [11] (a) Cao, R.-G.; Liu, S.-X.; Xie, L.; Pan, Y.; Cao, J.; Ren, Y.; Xu, L. Organic–Inorganic Hybrids Constructed of Anderson-Type Polyoxoanions and Oxalato-Bridged Dinuclear Copper Complexes. *Inorg. Chem.* **2007**, *46*, 3541-3547. (b) Cao, R.-G.; Liu, S.-X.; Liu, Y.; Tang, Q.; Wang, L.; Xie, L.-H.; Su, Z.-M. Organic-Inorganic Hybrids Constructed by Anderson-Type Polyoxoanions and Copper Coordination Complexes. *J. Solid State Chem.* **2009**, *182*, 49-54. (c) Xu, Z.-H.; Li, X.-F.; Zhang, X.-W. A Novel Water Cluster Held Up by a Tungstotellurate of the $[\text{Ni}(2,2'\text{-bipy})_3]^{2+}$ Cations: Synthesis and Characterization of $[\text{Ni}(2,2'\text{-bipy})_3]_2[\text{H}_2(\text{TeW}_6\text{O}_{24})] \cdot 28\text{H}_2\text{O}$. *Synth. React. Inorg. M.* **2012**, *42*, 140-144.
- [12] (a) Singh, M.; Lofland, S. E.; Ramanijachary, K. V.; Ramanan, A. Crystallization of Anderson–Evans Type Chromium Molybdate Solids Incorporated with a Metal Pyrazine Complex or Coordination Polymer. *Cryst. Growth Des.* **2010**, *10*, 5105-5112. (b) An, H.; Liu, X.; Chen, H.; Han, Z.; Zhang, H.; Chen, Z. Assembling Anderson-Type Polyoxometalates with Manganese(II) in the Presence of Piridylacrylic Acidligands: A 2D Layer and Two Polymorphs. *CrystEngComm* **2011**, *13*, 5384-5393. (c) Zhang, Y.-C.; Chen, Y.-Z.; Chang, Z.-H.; Liu, Q.-Q.; Wang, X.-L. Metal-Directed Two New Anderson-Type Polyoxometalate-Based Metal–Organic Complexes with Different Electrocatalytic Sensing Performance. *Polyhedron*, **2022**, *221*, 115874.
- [13] (a) Shivaiah, V.; Nagaraju, M.; Das, S. K. Formation of a spiral-Shaped Inorganic–Organic Hybrid Chain $[\text{Cu}^{\text{II}}(2,2'\text{-bipy})(\text{H}_2\text{O})_2\text{Al}(\text{OH})_6\text{Mo}_6\text{O}_{18}]_n^{n-}$: Influence of Intra- and Interchain Supramolecular Interactions. *Inorg. Chem.* **2003**, *42*, 6604-6606. (b) Li, J.-H.; Wang, X.-L.; Song, G.; Lin, H.-Y.; Wang, X.; Liu, G.-C. Various Anderson-Type Polyoxometalate-Based Metal-

Organic Complexes Induced by Diverse Solvents: Assembly, Structures and Selective Adsorption for Organic Dyes. *Dalton Trans.*, **2020**, *49*, 1265-1275.

[14] (a) Shivaiah, V.; Das, S. K. Polyoxometalate-Supported Transition Metal Complexes and Their Charge Complementarity: Synthesis and Characterization of $[M(OH)_6Mo_6O_{18}\{Cu(Phen)(H_2O)_2\}_2][M(OH)_6Mo_6O_{18}\{Cu(Phen)(H_2O)Cl\}_2]\cdot 5H_2O$ ($M = Al^{3+}$, Cr^{3+}) *Inorg. Chem.* **2005**, *44*, 8846-8854. (b) Ma, H.-Y.; Wu, L.-Z.; Pang, H.-J.; Meng, X.; Peng, J. Hydrothermal Synthesis of two Anderson POM-Supported Transition Metal Organic-Inorganic Compounds. *J. Molec. Struct.* **2010**, *967*, 15-19.

[15] Li, S.; Ma, P.; Wang, J.; Guo, Y.; Niu, H.; Zhao, J.; Niu, J. A 3D Organic-Inorganic Network Constructed From an Anderson-Type Polyoxometalate Anion, a Copper Complex and a Tetrameric $[Na_4(H_2O)_{14}]^{4+}$ Cluster. *CrystEngComm* **2010**, *12*, 1718-1721.

[16] Chen, H.; An, H.; Liu, X.; Wang, H.; Chen, Z.; Zhang, H.; Hu, Y. A Host-Guest Hybrid Framework with Anderson Anions as Template: Synthesis, Crystal Structure and Photocatalytic Properties. *Inorg. Chem. Commun.* **2012**, *21*, 65-68.

[17] An, H.; Xu, T.; Wang, E.; Meng, C. A Pillar-Layered Three-Dimensional Open Framework Constructed from Polyoxometalate-Supported Metal Coordination Complex Layers and Bi-Supporting Polyoxometalate Clusters. *Inorg. Chem. Commun.* **2007**, *10*, 1453-1456.

[18] (a) Wang, Y.; Xiao, D.; Qi, Y.; Wang, E.; Liu, J. Synthesis and Characterization of Two Extended High-dimensional Architectures Formed by Transition Metal-Glycine Complexes. *J. Clust. Sci.* **2008**, *19*, 367-378. (b) Dutta, D.; Jana, A. D.; Debnath, M.; Bhaumik, A.; Marek, J.; Ali, M. Robust 1D Open Rack-Like Architecture in Coordination Polymers of Anderson POMs $\{[Na_4(H_2O)_{14}\{Cu(gly)\}_2][TeMo_6O_{24}]\}$ and $\{[Cu(en)_2]_3\{TeW_6O_{24}\}\}$: Synthesis, Characterization and Heterogeneous Catalytic Epoxidation of Olefines. *Dalton Trans.* **2010**, *39*, 11551-11559.

[19] Zhang, P.-P.; Peng, J.; Tian, A.-X.; Sha, J.-Q.; Pang, H.-J.; Chen, Y.; Zhu, M.; Wang, Y.-H. A Series of Compounds Based on the Anderson-Type Polyoxoanions and Cu-Amino Acid Complexes. *J. Molec. Struct.* **2009**, *931*, 50-54.

[20] Wang, X.-L.; Gong, C.-H.; Zhang, J.-W.; Liu, G.-C.; Kan, X.-M.; Xu, N. Polyoxometalate-Directed Assembly of Various Multinuclear Metal-Organic Complexes with 4-Amino-1,2,4-triazole and Selective Photocatalysis for Organic Dye Degradation. *CrystEngComm* **2015**, *17*, 4179-4189.

[21] Wang, X.; Sun, J.; Lin, H.; Chang, Z.; Liu, G.; Wang, X. pH-Tuned Diverse Structures and Properties: Two Anderson-Type Polyoxometalate-Based Metal-Organic Complexes for Selective Photocatalysis and Adsorption of Organic Dyes. *RSC Adv.* **2016**, *6*, 110583-110591.

[22] Wang, X.-L.; Xu, N.; Zhao, X.-Z.; Zhang, J.-W.; Gong, C.-H.; Li, T.-J. Polyoxometalate-Directed Assembly and Various Structures of Inorganic-Organic Hybrid Compounds Based on a Semi-Rigid Bis-pyridyl-bis-amide. *CrystEngComm*, **2015**, *17*, 7038-7047.

[23] Wu, Q.; Li, Y.-G.; Wang, Y.-H.; Clérac, R.; Lu, Y.; Wang, E.-B. Polyoxometalate-Based $\{Mn^{II}_2\}$ -Schiff Base Composite Materials Exhibiting Single-Molecule Magnet Behaviour. *Chem. Commun.* **2009**, *38*, 2488-2498.

[24] Wu, Q.; Chen, W.-L.; Liu, D.; Liang, C.; Li, Y.-G.; Lin, S.-Q.; Wang, E. New Class of Organic-Inorganic Hybrid Aggregates Based on Polyoxometalates and Metal-Schiff-base. *Dalton Trans.* **2011**, *40*, 56-61.

[25] Wang, X.; Zhang, Z.; Lin, H.; Tian, A.; Liu, G.; Zhang, J. Assembly and Photocatalysis of Two Novel 3D Anderson-Type Polyoxometalate-Based Metal-Organic Frameworks Constructed from Isomeric Bis(pyridylformyl)piperazine Ligands. *Dalton Trans.* **2014**, *43*, 12272-12278

[26] Yang, J.-B.; Pan, J.-H.; Zhu, Y.-H.; Wang, J.-L.; Mei, H.; Xu, Y. Two 1D Anderson-Type Polyoxometalate-Based Metal-Organic Complexes as Bifunctional Heterogeneous Catalysts for CO_2 Photoreduction and Sulfur Oxidation. *Inorg. Chem.* **2022**, *61*, 11775-11786.

[27] Wang, X.-L.; Sun, J.; Lin, H.; Chang, Z.; Bai, X.; Wang, X. Assembly, Structures, Electrocatalytic and Photocatalytic Properties of a Series of Anderson-Type Polyoxometalate-Based Metal-Organic Complexes Based on Flexible Pyridyl-Amine Ligands. *Polyhedron*, **2017**, *124*, 30-40.

- [28] Wu, Q.; Han, Q.; Chen, L.; Ma, P.; Niu, J. Synthesis and Structural Characterization of a New Two-dimensional Organic-Inorganic Hybrid Molybdoarsenate: $[\text{Cu}(\text{en})_2]_2[(\text{CuO}_6)\text{Mo}_6\text{O}_{18}(\text{As}_3\text{O}_3)_2]$. *Z. Naturforsch.* **2010**, *65b*, 163-167.
- [29] Li, L.; Liu, B.; Xue, G.; Hu, H.; Fu, F.; Wang, J. Three Hybrid Organic-Inorganic Assemblies Based on Different Arsenatomolybdates and Cu^{II} -Organic Units. *Cryst. Growth Des.* **2009**, *12*, 5209-5212.
- [30] Martín-Caballero, J. *Hybrid Polyoxometalates: Synthesis, Crystal Structures, Thermostructural Behavior and Anchoring to Tailored Polymeric Surfaces*. Ph.D. UPV/EHU, Leioa, **2017**.
- [31] Perloff, A. The Crystal Structure of Sodium Hexamolybdochromate(III) Octahydrate, $\text{Na}_3(\text{CrMo}_6\text{O}_{24}\text{H}_6)\cdot 8\text{H}_2\text{O}$. *Inorg. Chem.* **1970**, *9*, 2228-2239.
- [32] (a) Veen, S. J.; Kegel, W. K. Structural Instability of Shell-Like Assemblies of a Keplerate-Type Polyoxometalate Induced by Ionic Strength. *J. Phys. Chem. B* **2009**, *113*, 15137-15140. (b) Hutin, M.; Long, D.-L.; Cronin, L. Controlling the Molecular Assembly of Polyoxometalates from the Nano to the Micron Scale: Molecules to Materials. *Isr. J. Chem.* **2011**, *51*, 205-214. (c) Cai, J.; Ye, R.; Liu, X.; Guo, L.; Qiao, X. Ionic Strength Effect on Regulating the Synthetic Assembly of Polyoxometalate Clusters with Slow Magnetic Relaxation Behavior. *Dalton Trans.* **2020**, *49*, 16954-16961.
- [33] (a) Reinoso, S.; Vitoria, P.; Gutiérrez-Zorrilla, J. M.; Lezama, L.; San Felices, L.; Beitia, J. I. Inorganic-Metalorganic Hybrids Based on Copper(II)-Monosubstituted Keggin Polyanions and Dinuclear Copper(II)-Oxalate Complexes. Synthesis, X-ray Structural Characterization, and Magnetic Properties. *Inorg. Chem.* **2005**, *44*, 9731-9742. (b) Misra, A.; Kozma, K.; Streb, C.; Nyman, M. Beyond Charge Balance: Counter-Cations in Polyoxometalate Chemistry. *Angew. Chem. Int. Ed.* **2020**, *59*, 596-612.
- [34] Crystal data: $\text{K}_3[\text{H}_6\text{CrMo}_6\text{O}_{24}]\cdot 6\text{H}_2\text{O}$ (**1K-CrMo6**); $\text{CrH}_{18}\text{K}_3\text{Mo}_6\text{O}_{30}$: fw=1258.72 g mol⁻¹; monoclinic $P2_1/c$ (14) space group; $a=11.1284(3)$; $b=10.8084(3)$; $c=11.7450(3)$ Å; $\alpha=90$; $\beta=98.936(3)$; $\gamma=90^\circ$; $V=1395.54(7)$ Å³; $Z=2$; $\rho_{\text{calcd}}=2.995$ g cm⁻³; $\mu=3.602$ mm⁻¹; 14772 reflections collected; 3503 unique ($R_{\text{int}}=0.040$); 2945 observed ($I > 2\sigma(I)$); 91 parameters; $R(F)=0.047$ ($I > 2\sigma(I)$), $wR(F^2)=0.117$ (all data), $\text{GoF}=1.064$.
- [35] Ito, F.; Ozeki, T.; Ichida, H.; Miyamae, H.; Sasaki, Y. Structure of Tetraammonium Hexahydrogenhexamolybdocuprate(II) Tetrahydrate. *Acta Crystallogr.* **1989**, *C45*, 946-947.
- [36] Artetxe, B.; Reinoso, S.; San Felices, L.; Lezama, L.; Gutiérrez-Zorrilla, J. M.; Vicent, C.; Haso, F.; Liu, T. New Perspectives for Old Clusters: Anderson-Evans Anions as Building Blocks of Large Polyoxometalate Frameworks in a Series of Heterometallic 3d-4 f Species. *Chem. Eur. J.* **2016**, *22*, 4616-4625.
- [37] (a) Kim, S.; Minier, M. A.; Loas, A.; Becker, S.; Wang, F.; Lippard, S. J. Achieving Reversible Sensing of Nitroxyl by Tuning the Ligand Environment of Azamacrocyclic Copper(II) Complexes. *J. Am. Chem. Soc.* **2016**, *138*, 1804-1807. (b) Kin, G.; Lelong, E.; Kang, J.; Suh, J.-M.; Le Bris, N.; Bernard, H.; Kim, D.; Tripier, R.; Lim, M. H. Reactivities of cyclam derivatives with metal-amyloid- β . *Inorg. Chem. Front.* **2020**, *7*, 4222-4238.
- [38] Spek, A. L. Structure Validation in Chemical Crystallography. *Acta Crystallogr., Sect. D: Biol. Crystallogr.* **2009**, *65*, 148-155.
- [39] DeLano, W. L. The PyMOL Molecular Graphics System; DeLano Scientific: San Carlos, CA, **2002**.

Mononuclear Lanthanide-Containing Polyoxometalates with Compartmental Organic Ligands

- 5.1. Introduction
- 5.2. Experimental section
- 5.3. Results and discussion
- 5.4. Conclusions
- 5.5. References

ABSTRACT: In this final chapter, the study of the simultaneous coordination of organic and inorganic ligands to lanthanide(III) ions is investigated because both multidentate organic ligands and POM clusters separately have demonstrated the ability to sensitize lanthanide luminescent emission as well as to influence in the magnetic behavior of 4f centers. Reaction of *N,N'*-dimethyl-*N,N'*-bis(2-hydroxy-3-formyl-5-bromobenzyl)-ethylene-diamine (*H₂L*) organic ligand and monolacunary Keggin type $[\alpha\text{-SiW}_{11}\text{O}_{39}]^{8-}$ anion with different mid-to-late lanthanide salts have resulted in ten isostructural hybrids with the general formula $K_5[\text{Ln}^{\text{III}}(\text{H}_2\text{L})(\alpha\text{-SiW}_{11}\text{O}_{39})]\cdot 14\text{H}_2\text{O}$ ($\text{Ln}^{\text{III}} = \text{Sm}$ to Lu , **1-Ln**). These molecular sandwich-type complexes are formed by a central Ln^{III} ion in a biaugmented trigonal prismatic geometry, which occupies the external O_4 site of the organic ligand and the vacant site of the lacunary POM unit. The empty N_2O_2 coordination site of the organic ligand allows its unprecedented folding which displays a relative perpendicular arrangement of aromatic groups. Weak $\text{Br}\cdots\text{Br}$ and $\pi\text{-}\pi$ interactions established between adjacent molecular units govern the crystal packing, which results in the formation of assemblies containing six hybrid species assembled in a chair-like conformation. **1-Gd** and **1-Yb** display slow relaxation of the magnetization after the application of an external magnetic field with maxima in the out-of-phase magnetic susceptibility plots below $\sim 5\text{-}6$ K, which is ascribed to the presence of various relaxation mechanisms. Moreover, photoluminescent emission is sensitized for **1-Sm** and **1-Eu** in the visible region and **1-Er** and **1-Yb** in the NIR. In contrast, the quenching of metal-centered luminescence in the **1-Tb** derivative has been attributed to the out-of-pocket coordination mode to the lanthanide center of the POM fragment. It is demonstrated that the **1-Yb** represents the first lanthanide-containing POM reported to date behaving as a dual magneto-luminescent material. Solution stability of the hybrid molecular species is also confirmed by ESI-mass spectrometry experiments and $^1\text{H-NMR}$ studies for the diamagnetic **1-Lu**.

5.1. INTRODUCTION

Lanthanide-containing POMs could be considered as ideal precursors for direct organic derivatization because they usually show several water molecules coordinated to accessible 4f-metal centers. Except for Peacock-Weakley type clusters, lanthanide centers incorporated to POM clusters usually show several accessible coordination positions. However, direct organic ligand replacement on those 4f-metal centers can be more challenging than a priori expected. The oxo-phylic nature of lanthanide centers makes carboxylic acids suitable ligands for such functionalization, but the negative charge of both lanthanide-containing POMs and carboxylate groups, as well as the steric hindrance that a given POM could produce, are the main difficulties for the reaction to take place. These drawbacks have been overcome by using small ligands in a large excess, chelating ligands or even positively charged POMs.

Figure 5.1 displays some representative examples of organically derivatized lanthanide-containing POMs. Incorporation of organic ligands such as acetates or tartaric acid into monomeric $\{\text{Ln}(\text{POM})\}$ species have resulted in dimeric $[\{\text{Ln}(\text{OAc})(\text{H}_2\text{O})(\text{POM})\}_2]^{n-}$ hybrids constituted by monolacunary α -Keggin,¹ or α_2 -Wells-Dawson fragments.² Similar structures have been assembled with the N,O-chelating picolinic acid,³ with the difference that in this case four ligands can participate as linkers between the two POM units, instead of two ligands as in the previous cases. Furthermore, late-lanthanide monosubstituted Wells-Dawson or Keggin anions presenting acetate bridging ligands allow the synthesis of oligomeric POMs.⁴ Similar reaction results in hybrid $[\text{Yb}_2(\text{H}_2\text{O})_2(\text{ox})\{\alpha\text{-(1,11)-PW}_{10}\text{O}_{38}\}]_n^{3-}$ chains when Yb^{III} is used as lanthanide source. Boskovic and co-workers succeeded in preparing organically functionalized Tb or Eu derivatives of the $[\text{As}_2\text{W}_{19}\text{O}_{67}(\text{H}_2\text{O})]^{14-}$ lacunary polyanion with picolinic acid, which show interesting photoluminescent properties.⁵ Starting from the trilacunary $[\text{A-}\alpha\text{-AsW}_9\text{O}_{34}]^{9-}$ anion, Ln^{III} disubstituted Keggin clusters linked to carboxylic ligands (citrate, malate or tartaric acid) have proved to form monomeric,⁶ dimeric,⁷ or tetrameric⁸ organic-inorganic hybrids. Similarly, Sb-containing trilacunary A- α -Keggin anion together with picolinic acid also results in the sandwich-type $[\text{Ln}_2(\text{H}_2\text{O})_4\{\text{WO}_2(\text{pic})\}_2(\text{SbW}_8\text{O}_{30})_2]^{10-}$ hybrids.⁹ More examples include hexanuclear species, in which the monocarboxylic formate ligands stabilize Ce^{III} coordination spheres that link trilacunary $\{\text{AsW}_9\text{O}_{33}\}$ anions.¹⁰

In contrast, mixed-valence polyoxomolybdates have been used as building block for the design of extended hybrid organic-inorganic frameworks, as in the case of the $[\{\epsilon\text{-PMo}^{\text{V}}_8\text{Mo}^{\text{VI}}_4\text{O}_{36}(\text{OH})_4\}\{\text{La}(\text{H}_2\text{O})_4\}]^{5+}$ cation containing an ϵ -Keggin type core capped with four lanthanum ions (Figure 5.1f).¹¹ The lability of the terminal water molecules on the 4f-metal center allows the reaction of the precursor with bidentate bridging ligands leading to one-, two- or three-dimensional arrangements in the solid state. For constructing such type

of arrangements, polycarboxylic ligands like glutarate, squarate and di-, tri- or tetra-substituted benzenecarboxylates have been used.¹² The cationic nature of the cluster makes the functionalization easier in such a way that it takes place even at room temperature under mild conditions.

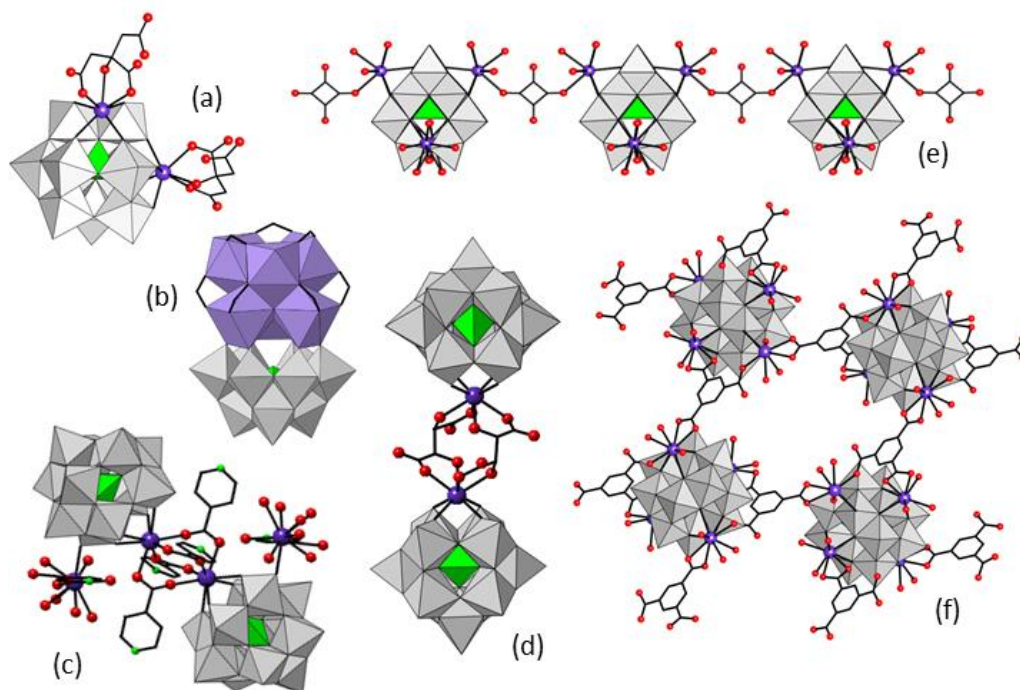


Figure 5.1. Representative examples of organically derivatized lanthanide-containing POMs: Monomeric (a) $[\text{Dy}_2\{\text{COH}(\text{COO})(\text{CH}_2\text{COO})_2\}_2(\text{AsW}_{10}\text{O}_{38})]^{11-}$ and (b) $[\text{Ce}_6(\text{As}^{\text{III}}\text{W}_9\text{O}_{33})(\text{HCOO})_9]^{6-}$. Dimeric (c) $[(\text{H}_2\text{O})_7(4\text{-Hpic})\text{Ln}][(\text{Hpic})_2\text{LnPW}_{11}\text{O}_{39}]$ ($\text{Ln} = \text{La}, \text{Ce}$) and (d) $[\text{Ln}(\text{C}_4\text{H}_2\text{O}_6)(\alpha\text{-PW}_{11}\text{O}_{39})]_2$ ($\text{Ln} = \text{Dy}, \text{Ho}, \text{Er}, \text{Yb}$). (e) Chains of $[\{\epsilon\text{-PMo}_{12}\text{O}_{39}(\text{OH})\}]\text{La}_4(\text{H}_2\text{O})_{22}(\text{C}_4\text{O}_4)$. (f) Three-dimensional network in $[\{\epsilon\text{-PMo}_{12}\text{O}_{35}(\text{OH})_5\}]\text{La}_4(\text{H}_2\text{O})_{10}(\text{C}_9\text{H}_3\text{O}_6)_2$.

Despite the interesting optical and magnetic properties that the resulting complexes may exhibit, the coordination of multidentate aromatic ligands to mononuclear lanthanide-substituted POM species has been comparatively less studied (Figure 5.2). In fact, compounds $[n\text{-NBu}_4]_3[\text{LnH}(\text{PW}_{11}\text{O}_{39})(\text{phen})_2]\cdot\text{H}_2\text{O}$ ($\text{Ln} = \text{Dy}, \text{Er}$; phen = phenanthroline) were reported very recently as the first examples on the literature of mononuclear hybrid organic-inorganic complexes with SMM behavior.¹³ In a similar way, the recently reported $(\text{N}(\text{nBu})_4)_4\text{H}_2[\text{Ln}^{\text{III}}\text{Pc}(\text{PW}_{11}\text{O}_{39})]$ ($\text{Ln}^{\text{III}} = \text{Dy}, \text{Tb}$; Pc = phthalocianine) specie constituted the first 4f-functionalized polyanion coordinated to a N-chelating cyclic ligand, in which the Dy derivative exhibit slow relaxation of magnetization.¹⁴ The incorporation of organic ligands to the system has proven to be a suitable approach to dramatically lower magnetic relaxation times in comparison to the purely inorganic analogues. Moreover, efficient sensitization of 4f metal containing POMs has also been achieved by the simultaneous coordination of aromatic antenna ligands (e.g. benzoate, phenanthroline) to the emitting centers.¹⁵ Furthermore, the incorporation of organic ligands into lanthanide-functionalized POMs have recently proved to be helpful as a catalyst in hydrogen evolution reactions

(HER).¹⁶ This is the example of the $K_6Ln[(pdc)_2Ln(H_2O)_2SiW_{11}O_{39}]$ ($Ln = La, Pr, Dy$; $pdc = 3,4$ -pyridinedicarboxylate) mononuclear compound, in which the organic pdc ligands stabilize the lanthanide ions for their employment in catalysis.

Among the tens if not hundreds of examples reported for lanthanide-based complexes showing aromatic multidentate ligands,¹⁷ compartmental, aminophenol Mannich- or Schiff-base derivatives represent great potential.¹⁸ Reaction between secondary amines, paraformaldehyde and phenol moieties can easily afford multidentate O- and N-donor ligands with two different potential coordination sites. For example, the N,N' -dimethyl- N,N' -bis(2-hydroxy-3-formyl-5-bromobenzyl)ethylene-diamine (H_2L) displays an outer O_4 site which can easily accommodate large oxophilic 4f metals and the inner N_2O_2 pocket, which is available for the coordination of smaller 3d metal centers (Figure 5.2b). In some cases, heterometallic 3d-4f complexes¹⁹ have been identified as a convenient way to improve the SMM properties of a given complex, because i) the use of diamagnetic 3d metal ions can attenuate the intermolecular magnetic interactions responsible for quantum tunneling of magnetization (QTM) and consequently, the loss of magnetization, and ii) strong magnetic exchange interactions can fully or partially quench QTM. When it comes to lanthanide-containing POMs with compartmental organic ligands, the $[CuTbL_{Schiff}(H_2O)_3Cl_2]Cl$ complex ($L_{Schiff} = N,N'$ -bis(3-methoxysalicylidene)ethylenediamine) in combination with an Anderson-Evans anion constitutes the unique example of such type. Coordination of the metal complex to the oxygen-rich surface of the POM anion induced SMM behavior in a precursor that did not exhibit slow relaxation of the magnetization by itself.²⁰

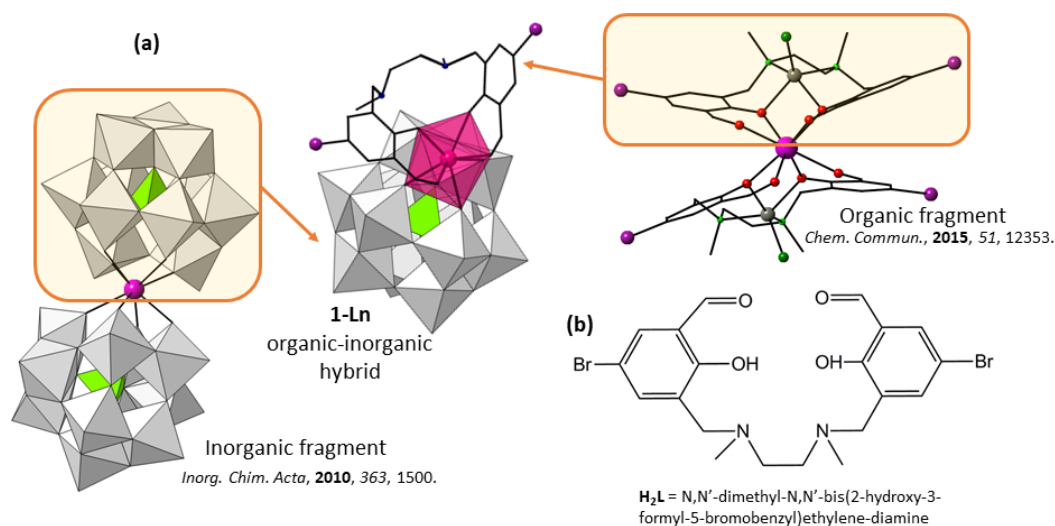


Figure 5.2. (a) Schematic representation of a lanthanide-containing $\{Ln(\alpha-XW_{11}O_{39})\}$ Peacock-Weakley-type POM structure, the trinuclear sandwich-type $[ZnCl(\mu-L)Dy(\mu-L)ClZn]$ complex, and the schematic representation of the combination of both organic and inorganic counterparts in order to generate a sandwich-type organic-inorganic hybrid containing a central lanthanide ion. (b) Schematic representation of the H_2L ligand. Color codes: Br, purple; Cl, dark green; Ln ion, pink; Zn, grey.

Encouraged by all the above, we studied the simultaneous coordination to a lanthanide center of i) the monolacunary Keggin-type $[\alpha\text{-SiW}_{11}\text{O}_{39}]^{8-}$ anion and ii) H_2L ligand, which showed to be suitable to induce bright luminescence and SMM behavior in previous works (Figure 5.2a).^{19b} This chapter describes the synthesis, structure and solution stability of a series of ten hybrid anions formed by mid-to-late lanthanide-containing Keggin-type polyoxotungstates and the compartmental organic ligand H_2L , namely $\text{K}_5[\text{Ln}(\text{H}_2\text{L})(\alpha\text{-SiW}_{11}\text{O}_{39})]\cdot\approx 14\text{H}_2\text{O}$ (**1-Ln**, Ln = Sm to Lu). A complete solid state photophysical analysis have shown the efficient emission of different **1-Ln** derivatives in the visible and NIR region, whereas magnetic studies have revealed field induced SMM-behavior for **1-Gd** and **1-Yb** analogues under the presence of an external field. Moreover, solution stability of the hybrid POMs in aqueous solution is confirmed by proton nuclear magnetic resonance ($^1\text{H-NMR}$) spectroscopy as well as electrospray ionization Mass Spectrometry (ESI-MS).

5.2. EXPERIMENTAL SECTION

5.2.1. Synthesis

Preparation of starting materials

The monolacunary Keggin-type $\text{K}_8[\alpha\text{-SiW}_{11}\text{O}_{39}]\cdot 13\text{H}_2\text{O}$ ²¹ precursor and the *N,N'*-dimethyl-*N,N'*-bis(2-hydroxy-3-formyl-5-bromobenzyl)ethylene-diamine (H_2L)²² ligand were synthesized according to reported procedures, and identified by FT-IR spectroscopy and $^1\text{H-NMR}$, respectively (See Figures A4.1 and A4.2 in Appendix 4). All other chemicals were purchased from commercial sources and used without further purification.

$\text{K}_8[\alpha\text{-SiW}_{11}\text{O}_{39}]\cdot 13\text{H}_2\text{O}$: To a hot solution of $\text{Na}_2\text{WO}_4\cdot 2\text{H}_2\text{O}$ (91 g, 0.275 mol) dissolved in water (150 mL) aqueous 4M HCl (82.5 mL) was added dropwise. Over this mixture, Na_2SiO_3 (5.5 g, 25 mmol) dissolved in water (50 mL) and 4M HCl (25 mL) were added to maintain the pH in the 5-6 range and then, the solution was kept under reflux for 1h. After cooling down to room temperature, the solution was filtered and the product precipitated with 75 g of KCl. The resulting white powder was filtered under vacuum, and washed twice with a 1M KCl solution (25 mL). Yield: 69 g, 85% based on W. IR (cm^{-1}): 1626 (s), 995 (w), 960 (w), 887 (m), 794 (m), 725 (m), 505 (w).

***N,N'*-dimethyl-*N,N'*-bis(2-hydroxy-3-formyl-5-bromobenzyl)ethylene-diamine (H_2L)**: *N,N'*-Dimethylethylenediamine (1.1 g, 12.5 mmol), 5-bromosalicylaldehyde (5.0 g, 25 mmol), and paraformaldehyde (1.0 g, 33.5 mmol) were dissolved in ethanol (75 mL) and the mixture was refluxed for 1 week. The resulting white precipitate is separated from the solution by vacuum filtration, and washed twice with ethanol. Yield: 3.6 g, 55%. $^1\text{H-NMR}$ (δ , ppm in

CDCl₃): 2.30 (s, 6H, N-CH₃), 2.70 (s, 4H, -CH₂CH₂-), 3.68 (s, 4H, Ar-CH₂-N), 7.71 (s, 2H, aromatic), 7.72 (s, 2H, aromatic), 10.18 (s, 2H, -CHO).

General synthetic procedure

A mixture of the H₂L ligand (0.1 mmol, 0.051 g) and the corresponding lanthanide salt (0.1 mmol) in 5 mL of MeOH was added dropwise to a solution of K₈[α-SiW₁₁O₃₉]·13H₂O Keggin precursor (0.322 g, 0.1 mmol) in 25 mL of 0.5 M aqueous KAc/HAc buffer (pH = 4.6) at 90 °C. The resulting solution was heated for 30 min, filtered, and then left to evaporate at room temperature in an open container. Powders that precipitate over the first 12 h were filtered off, and yellow single crystals of K₅[Ln^{III}(H₂L)(α-SiW₁₁O₃₉)]·14H₂O (**1-Ln**, Ln^{III} = Sm to Lu; H₂L = C₂₀H₂₂Br₂N₂O₄) were obtained from the resulting clear solutions in less than 1 week.

K₅[Sm(C₂₀H₂₂Br₂N₂O₄)(α-SiW₁₁O₃₉)]·14H₂O (1-Sm). Sm(NO₃)₃·6H₂O (0.044 g) was used as the 4f metal source. Yield: 19 mg, 5% based on W. IR (cm⁻¹): 1625 (vs), 1544 (s), 1443 (m), 1419 (w), 1380 (w), 1204 (w), 1162 (w), 1001 (m), 941 (s), 885 (vs), 766 (w), 748 (w) 790 (m), 701 (m), 507 (w). Elem. Anal. Calcd. (%) for C₂₀H₅₀Br₂K₅N₂O₅₇SiSmW₁₁: C, 6.34%; H, 1.33%; K, 5.53%; N, 0.74%; Si, 0.80%; Sm, 4.25%. Found: C, 6.03%; H, 1.68%; K, 5.57%; N, 0.79%; Si, 0.77%; Sm, 4.20%.

K₅[Eu(C₂₀H₂₂Br₂N₂O₄)(α-SiW₁₁O₃₉)]·14H₂O (1-Eu). EuCl₃·6H₂O (0.026 g) was used as the 4f metal source. Yield: 16 mg, 4% based on W. IR (cm⁻¹): 1624 (vs), 1540 (s), 1441 (m), 1422 (w), 1381 (w), 1207 (w), 1163 (w), 1003 (m), 940 (s), 885 (vs), 767 (w), 748 (w) 792 (m), 702 (m), 506 (w). Elem. Anal. Calcd. (%) for C₂₀H₅₀Br₂EuK₅N₂O₅₇SiW₁₁: C, 6.34%; H, 1.33%; Eu, 4.30%; K, 5.53%; N, 0.74%; Si, 0.79%. Found: C, 6.11%; H, 1.57%; Eu, 4.17%; K, 5.62%; N, 0.62%; Si, 0.75%.

K₅[Gd(C₂₀H₂₂Br₂N₂O₄)(α-SiW₁₁O₃₉)]·14H₂O (1-Gd). Gd(NO₃)₃·6H₂O (0.045 g) was used as the 4f metal source. Yield: 21 mg, 6% based on W. IR (cm⁻¹): 1627 (vs), 1545 (s), 1444 (m), 1423 (w), 1384 (w), 1209 (w), 1165 (w), 1007 (m), 940 (s), 884 (vs), 769 (w), 746 (w), 795 (m), 702 (m), 505 (w). Elem. Anal. Calcd. (%) for C₂₀H₅₀Br₂GdK₅N₂O₅₇SiW₁₁: C, 6.33%; H, 1.33%; Gd, 4.44%; K, 5.52%; N, 0.74%; Si, 0.79%. Found: C, 6.18%; H, 1.71%; Gd, 4.36%; K, 5.48, N, 0.79%; Si, 0.76%.

K₅[Tb(C₂₀H₂₂Br₂N₂O₄)(α-SiW₁₁O₃₉)]·14H₂O (1-Tb). Tb(NO₃)₃·5H₂O (0.044 g) was used as the 4f metal source. Yield: 17 mg, 4% based on W. IR (cm⁻¹): 1622 (vs), 1541 (s), 1437 (m), 1421 (w), 1383 (w), 1206 (w), 1159 (w), 1002 (m), 944 (s), 880 (vs), 768 (w), 749 (w), 789 (m), 702 (m), 503 (w). Elem. Anal. Calcd. (%) for C₂₀H₅₀Br₂K₅N₂O₅₇SiTbW₁₁: C, 6.33%; H, 1.33%; K, 5.52%; N, 0.74%; Si, 0.79%; Tb, 4.49%. Found: C, 6.20%; H, 1.64%; K, 5.55%; N, 0.81%; Si, 0.80%; Tb, 4.43%.

$K_5[\text{Dy}(\text{C}_{20}\text{H}_{22}\text{Br}_2\text{N}_2\text{O}_4)(\alpha\text{-SiW}_{11}\text{O}_{39})]\cdot 14\text{H}_2\text{O}$ (1-Dy). Dy(NO₃)₃·6H₂O (0.045 g) was used as the 4f metal source. Yield: 21 mg, 6% based on W. IR (cm⁻¹): 1621 (vs), 1546 (s), 1441 (m), 1420 (w), 1378 (w), 1201 (w), 1162 (w), 1003 (m), 940 (s), 883 (vs), 766 (w), 747 (w), 792 (m), 702 (m), 501 (w). Elem. Anal. Calcd. (%) for C₂₀H₅₀Br₂DyK₅N₂O₅₇SiW₁₁: C, 6.32%; H, 1.33%; Dy, 4.50%; K, 5.51%; N, 0.74%; Si, 0.79%. Found: C, 6.12%; H, 1.58%; Dy, 4.36%; K, 5.49, N, 0.76%; Si, 0.77%.

$K_5[\text{Ho}(\text{C}_{20}\text{H}_{22}\text{Br}_2\text{N}_2\text{O}_4)(\alpha\text{-SiW}_{11}\text{O}_{39})]\cdot 14\text{H}_2\text{O}$ (1-Ho). Ho(NO₃)₃·5H₂O (0.044 g) was used as the 4f metal source. Yield: 22 mg, 6% based on W. IR (cm⁻¹): 1623 (vs), 1547 (s), 1444 (m), 1419 (w), 1381 (w), 1208 (w), 1162 (w), 1001 (m), 940 (s), 885 (vs), 768 (w), 748 (w), 790 (m), 702 (m), 505 (w). Elem. Anal. Calcd. (%) for C₂₀H₅₀Br₂HoK₅N₂O₅₇SiW₁₁: C, 6.32%; H, 1.33%; Ho, 4.65%; K, 5.51%; N, 0.74%; Si, 0.79%. Found: C, 6.18%; H, 1.67%; Ho, 4.71%; K, 5.69%; N, 0.74%; Si, 0.78%.

$K_5[\text{Er}(\text{C}_{20}\text{H}_{22}\text{Br}_2\text{N}_2\text{O}_4)(\alpha\text{-SiW}_{11}\text{O}_{39})]\cdot 14\text{H}_2\text{O}$ (1-Er). Er(NO₃)₃·5H₂O (0.044 g) was used as the 4f metal source. Yield: 14 mg, 4% based on W. IR (cm⁻¹): 1623 (vs), 1544 (s), 1443 (m), 1421 (w), 1381 (w), 1207 (w), 1162 (w), 1001 (m), 940 (s), 885 (vs), 769 (w), 747 (w), 790 (m), 702 (m), 505 (w). Elem. Anal. Calcd. (%) for C₂₀H₅₀Br₂ErK₅N₂O₅₇SiW₁₁: C, 6.32%; H, 1.32%; Er, 4.71%; K, 5.51%; N, 0.74%; Si, 0.79%. Found: C, 6.38%; H, 1.89%; Er, 4.60%; K, 5.59%; N, 0.84%; Si, 0.72%.

$K_5[\text{Tm}(\text{C}_{20}\text{H}_{22}\text{Br}_2\text{N}_2\text{O}_4)(\alpha\text{-SiW}_{11}\text{O}_{39})]\cdot 14\text{H}_2\text{O}$ (1-Tm). Tm(NO₃)₃·5H₂O (0.045 g) was used as the 4f metal source. Yield: 19 mg, 5% based on W. IR (cm⁻¹): 1623 (vs), 1544 (s), 1444 (m), 1419 (w), 1381 (w), 1207 (w), 1162 (w), 1001 (m), 942 (s), 885 (vs), 767 (w), 750 (w), 790 (m), 702 (m), 505 (w). Elem. Anal. Calcd. (%) for C₂₀H₅₀Br₂K₅N₂O₅₇SiTmW₁₁: C, 6.31%; H, 1.32%; K, 5.50%; N, 0.74%; Si, 0.79%; Tm, 4.75%. Found: C, 6.22%; H, 1.34%; K, 5.53%; N, 0.68%; Si, 0.80%; Tm, 4.72%.

$K_5[\text{Yb}(\text{C}_{20}\text{H}_{22}\text{Br}_2\text{N}_2\text{O}_4)(\alpha\text{-SiW}_{11}\text{O}_{39})]\cdot 14\text{H}_2\text{O}$ (1-Yb). Yb(NO₃)₃·5H₂O (0.045 g) was used as the 4f metal source. Yield: 18 mg, 5% based on W. IR (cm⁻¹): 1623 (vs), 1547 (s), 1444 (m), 1420 (w), 1381 (w), 1207 (w), 1162 (w), 1003 (m), 940 (s), 885 (vs), 766 (w), 747 (w), 790 (m), 702 (m), 505 (w). Elem. Anal. Calcd. (%) for C₂₀H₅₀Br₂K₅N₂O₅₇SiW₁₁Yb: C, 6.31%; H, 1.32%; K, 5.50%; N, 0.74%; Si, 0.79%; Yb, 4.86%. Found: C, 6.28%; H, 1.52%; K, 5.61%; N, 0.67%; Si, 0.83%; Yb, 4.94%.

$K_5[\text{Lu}(\text{C}_{20}\text{H}_{22}\text{Br}_2\text{N}_2\text{O}_4)(\alpha\text{-SiW}_{11}\text{O}_{39})]\cdot 14\text{H}_2\text{O}$ (1-Lu). Lu(NO₃)₃·5H₂O (0.046 g) was used as the 4f metal source. Yield: 20 mg, 5% based on W. IR (cm⁻¹): 1623 (vs), 1546 (s), 1444 (m), 1419 (w), 1381 (w), 1205 (w), 1162 (w), 1001 (m), 940 (s), 885 (vs), 765 (w), 748 (w), 790 (m), 702 (m), 505 (w). Elem. Anal. Calcd. (%) for C₂₀H₅₀Br₂K₅LuN₂O₅₇SiW₁₁: C, 6.30%; H, 1.32%; K, 5.49%; Lu, 4.92%; N, 0.74%; Si, 0.79%. Found: C, 6.34%; H, 1.47%; K, 5.59%; Lu, 4.89%; N, 0.75%; Si, 0.77%.

5.2.2. Thermal analyses

Thermogravimetric analyses (TGA) (Table 5.1 and Figure A4.3 in the Appendix 4) were performed over solid crystalline samples, which were filtered from mother solution and left to dry overnight. All compounds **1-Ln** show similar TGA curves. First, a dehydration process is observed as a continuous mass loss. This step extends from room temperature up to ca. 120 °C and accounts for 5.9% (**1-Sm** and **1-Ho**) to 7.2% (**1-Lu**) of the initial mass, involving the release of 14 hydration water molecules per formula of **1-Ln**. Combustion of the ligand together with POM decomposition take place in a second thermal event, which leads to the final residues in the 650–750 °C temperature range. Two main phases were identified in the residues by powder X-ray diffraction, which correspond to hexagonal $K_{0.33}WO_{3.16}$ (PDF: 00–020–0940)²³ and analogues of the monoclinic C2/c $KLn(WO_4)_2$ (Ln = Sm to Lu; PDF for Ln = Dy: 00–023–0479)²⁴ (Figure A4.4 in the Appendix 4).

Table 5.1. Thermal data for compounds **1-Ln**.

	Dehydration (Δm , %)		Decomposition (°C)	Residue (m , %)	
	Δm_{calc} for 14H ₂ O	Δm_{exp}	T_d	Calc. for $K_5LnO_{39}SiW_{11}$	Exp.
1-Sm	6.7	5.9	665	79.8	79.7
1-Eu	6.7	6.7	740	79.8	79.3
1-Gd	6.7	7.0	690	79.8	79.0
1-Tb	6.6	6.7	750	79.8	79.3
1-Dy	6.6	6.9	705	79.8	78.9
1-Ho	6.6	5.9	670	79.8	79.9
1-Er	6.6	6.0	655	79.8	79.6
1-Tm	6.6	7.1	720	79.9	79.2
1-Yb	6.6	7.0	720	79.9	79.5
1-Lu	6.6	7.2	680	79.9	79.0

5.2.3. Single-crystal X-ray crystallography

Crystallographic data for compounds **1-Ln** (Ln = Sm to Lu) are summarized in Table 5.2. Thermal vibrations for heavy atoms (W, Ln, Br, K and Si) were treated anisotropically. Hydrogen atoms from the organic H₂L ligand were placed in calculated positions and refined using SHELXL parameters. In **1-Tm**, some of the anisotropic thermal ellipsoids from potassium and silicon atoms were normalized using ISOR-type restraints from SHELXL. All compounds display significant disorder between potassium counterions and lattice water molecules, which prevents us from modeling all the cation/solvent network. For the isostructural **1-Ln** compounds, between 11 and 17 sites with appropriate geometries for potassium cations were located in Fourier maps. These occupancies were initially refined without restrictions and fixed to the first decimal in the last cycle, which result in a total number of 9.0 (**1-Eu**) to 12.3 (**1-Tb**) potassium atoms per each asymmetric unit containing three hybrid polyanions.

Analogously, only 27 to 36 lattice water molecules were determined in the crystal structures of **1-Ln**. Large solvent accessible voids accounting for 17 to 25% of the unit cell volume can be found in the final structural solutions due to the severe structural disorder. According to PLATON, the largest voids are located at i) $x,y,z = 0, 0, 0$ and occupy a volume of 3130 (**1-Sm**), 3028 (**1-Dy**), 2207 (**1-Ho**), 3277 (**1-Er**), 2432 (**1-Tm**) and 2737 Å³ (**1-Yb**); ii) $x,y,z = 0, 0.5, 0$ and occupy a volume of 3423 (**1-Gd**) and 2293 Å³ (**1-Lu**); iii) $x,y,z = 0, 0.5, 0.5$ and occupy a volume of 3335 Å³ (**1-Eu**); and iv) $x,y,z = 0, 1, 0.5$ and occupy a volume of 2814 Å³ (**1-Tb**).

Table 5.2. Crystallographic data for compounds **1-Ln** (Ln = Sm to Lu).

	1-Sm	1-Eu	1-Gd	1-Tb	1-Dy
empirical formula	C ₂₀ H ₅₀ Br ₂ K ₅ N ₂ O ₅₇ SiSmW ₁₁	C ₂₀ H ₅₀ Br ₂ EuK ₅ N ₂ O ₅₇ SiW ₁₁	C ₂₀ H ₅₀ Br ₂ GdK ₅ N ₂ O ₅₇ SiW ₁₁	C ₂₀ H ₅₀ Br ₂ K ₅ N ₂ O ₅₇ SiTbW ₁₁	C ₂₀ H ₅₀ Br ₂ DyK ₅ N ₂ O ₅₇ SiW ₁₁
fw (g mol⁻¹)	3786.73	3788.34	3793.63	3795.3	3798.88
crystal system	Triclinic	Triclinic	Triclinic	Triclinic	Triclinic
space group (number)	<i>P</i> -1 (2)	<i>P</i> -1 (2)	<i>P</i> -1 (2)	<i>P</i> -1 (2)	<i>P</i> -1 (2)
<i>a</i> (Å)	21.8698(5)	21.7085(3)	21.9076(3)	21.8324(2)	21.8829(3)
<i>b</i> (Å)	24.7133(7)	24.6560(4)	24.7469(5)	24.6742(4)	24.7289(7)
<i>c</i> (Å)	28.4487(5)	28.2290(4)	28.4996(5)	28.2891(5)	28.3578(6)
α (°)	113.136(2)	113.8651(14)	113.1773(17)	112.7352(15)	112.833(2)
β (°)	95.4719(18)	95.3806(12)	95.4645(13)	95.2612(11)	95.4831(15)
γ (°)	103.874(2)	103.7301(13)	103.8326(14)	104.1432(11)	104.0587(19)
<i>V</i> (Å³)	13413.7(5)	13112.8(3)	13478.1(4)	13330.7(3)	13406.7(5)
<i>Z</i>	6	6	6	6	6
ρ_{calcd} (g cm⁻³)	2.813	2.878	2.804	2.837	2.823
μ (mm⁻¹)	15.956	35.113	33.938	33.400	16.143
reflins collected	103153	98099	103890	98895	92085
unique reflins (<i>R</i>_{int})	48790 (0.099)	49575 (0.090)	50920 (0.077)	50232 (0.057)	51216 (0.052)
observed reflins [<i>I</i> > 2σ(<i>I</i>)]	27923	37493	39632	39221	33784
Parameters (restraints)	1503 (0)	1444 (0)	1478 (6)	1538 (6)	1508 (6)
<i>R</i>(<i>F</i>)^a [<i>I</i> > 2σ(<i>I</i>)]	0.091	0.100	0.081	0.060	0.074
<i>wR</i>(<i>F</i>²)^b [all data]	0.274	0.279	0.226	0.171	0.191
GoF	1.047	1.037	1.051	1.034	1.057

^a $R(F) = \sum ||F_o - F_c|| / \sum |F_o|$;

^b $wR(F^2) = \{ \sum [w(F_o^2 - F_c^2)^2] / \sum [w(F_o^2)^2] \}^{1/2}$

Elemental and thermal analyses were essential to unequivocally determine the presence of 15 K ions and 42 hydration water molecules that is 5 potassium and 14 water molecules per formulae. The remaining cations and solvent molecules could well be located in these structural voids. It is worth noting that the presence of methanol solvent molecules was dismissed on the basis of elemental analyses. Furthermore, all the structures show large maxima of residual electron density, which are located close to the W atoms according to the final difference density map. Large residual maxima in the final Fourier map is a common fact found in the refinement of polyoxotungstate structures due to the high absorption of heavy atoms such as W.

Table 5.2 (continuation). Crystallographic data for compounds **1-Ln** (Ln = Sm to Lu).

	1-Ho	1-Er	1-Tm	1-Yb	1-Lu
empirical formula	C ₂₀ H ₅₀ Br ₂ HoK ₅ N ₂ O ₅₇ SiW ₁₁	C ₂₀ H ₅₀ Br ₂ ErK ₅ N ₂ O ₅₇ SiW ₁₁	C ₂₀ H ₅₀ Br ₂ K ₅ N ₂ O ₅₇ SiTmW ₁₁	C ₂₀ H ₅₀ Br ₂ K ₅ N ₂ O ₅₇ SiW ₁₁ Yb	C ₂₀ H ₅₀ Br ₂ K ₅ LuN ₂ O ₅₇ SiW ₁₁
fw (g mol⁻¹)	3801.31	3803.64	3805.31	3809.42	3811.35
crystal system	Triclinic	Triclinic	Triclinic	Triclinic	Triclinic
space group	<i>P</i> -1 (2)	<i>P</i> -1 (2)	<i>P</i> -1 (2)	<i>P</i> -1 (2)	<i>P</i> -1 (2)
<i>a</i> (Å)	21.8093(5)	21.8169(4)	21.6072(5)	21.8183(5)	21.7850(6)
<i>b</i> (Å)	24.6894(4)	24.6880(6)	24.5873(7)	24.6679(5)	24.6164(7)
<i>c</i> (Å)	28.3007(5)	28.3880(8)	28.1327(6)	28.2720(8)	28.1935(7)
α (°)	113.5373(18)	113.204(3)	113.784(3)	113.330(2)	113.292(3)
β (°)	95.5146(17)	95.439(2)	95.1376(19)	95.463(2)	95.557(2)
γ (°)	104.1725(18)	103.9133(19)	103.855(2)	104.2692(19)	104.228(2)
<i>V</i> (Å³)	13219.6(4)	13329.7(6)	12984.0(5)	13219.5(5)	13137.5(6)
<i>Z</i>	6	6	6	6	6
ρ_{calcd} (g cm⁻³)	2.865	2.843	2.920	2.871	2.890
μ (mm⁻¹)	16.422	16.340	16.831	16.585	16.748
collected reflns	99941	102581	88278	91644	92261
unique reflns (<i>R</i>_{int})	50681 (0.070)	51191 (0.098)	49686 (0.065)	50619 (0.058)	50321 (0.071)
observed reflns [<i>I</i> > 2σ(<i>I</i>)]	36150	28546	29139	32826	31503
Parameters (restraints)	1557 (0)	1489 (18)	1523 (18)	1514 (12)	1543 (6)
<i>R</i>(<i>F</i>)^a [<i>I</i> > 2σ(<i>I</i>)]	0.066	0.097	0.082	0.063	0.064
<i>wR</i>(<i>F</i>²)^b [all data]	0.186	0.277	0.229	0.175	0.178
GoF	1.047	1.063	1.044	1.038	1.055

^a $R(F) = \sum ||F_o - F_c| / \sum |F_o|$;

^b $wR(F^2) = \{ \sum [w(F_o^2 - F_c^2)^2] / \sum [w(F_o^2)^2] \}^{1/2}$

5.3. RESULTS AND DISCUSSION

5.3.1. Synthetic considerations

Reactivity of 4f metal ions in the simultaneous presence of both lacunary POMs and multidentate aromatic ligands under mild bench conditions was systematically studied in this chapter. The monolacunary $[\alpha\text{-SiW}_{11}\text{O}_{39}]^{8-}$ Keggin-type anion was selected as inorganic ligand, whereas the Mannich base *N,N'*-dimethyl-*N,N'*-bis(2-hydroxy-3-formyl-5-bromobenzyl)ethylene-diamine (H_2L) was chosen as organic molecule. This compartmental ligand displays an outer O_4 site, which can easily accommodate large oxophilic 4f metals and the inner N_2O_2 pocket, which is potentially available for the coordination of smaller 3d metal centers (Figure 5.2b)

Encouraged by the SMM behavior exhibited by both the Peacock-Weakley type $[\text{Dy}(\beta_2\text{-SiW}_{11}\text{O}_{39})_2]^{13-}$ anion²⁵ and the heterometallic $[\text{Zn}(\mu\text{-L})(\mu\text{-OAc})\text{Dy}(\text{NO}_3)_2]$ complex^{19b} based on the H_2L ligand, the reactivity of Dy^{III} salt was first explored for the $\text{Ln}^{\text{III}}/\text{H}_2\text{L}/\text{POM}$ synthetic system. Due to the low solubility of the organic ligand in water, a mixture of $\text{Dy}(\text{NO}_3)_3$ and H_2L dissolved in methanol was reacted with a hot solution of $\text{K}_8[\text{SiW}_{11}\text{O}_{39}] \cdot 13\text{H}_2\text{O}$ in aqueous 1M NaOAc buffer (1:1:1 molar ratio). Taking into account the role that alkaline cations played as crystallizing species in some previous works on lanthanide-containing POMs,²⁶ aqueous 1M CsCl was also tested as structural directing agent. The addition of Cs^+ cations led to the formation of yellow single crystals (**2-Dy**) that were initially characterized by FT-IR spectroscopy. Vibrational bands originating from both the H_2L and POM precursors can be observed in its IR spectrum, which establishes the hybrid nature of the compound. Weak- to medium-intensity peaks in the 1100–1800 cm^{-1} range confirm the presence of the organic H_2L ligand, whereas bands belonging to the POM framework can be observed in the inorganic region below 1000 cm^{-1} (Figure 5.3). The POM domain strongly resembles that of the precursor with small variations which consist of red shifts of 10 and 25 cm^{-1} of signals associated with $\nu_{\text{as}}(\text{W}-\text{O}_a-\text{W})$ and $\nu_{\text{as}}(\text{W}-\text{O}_t)$ modes at ca. 705 and 950 cm^{-1} , respectively. These facts indicate that FT-IR spectroscopy represents a straightforward tool to confirm the functionalization of the parent cluster. Single-crystal X-ray diffraction experiments on **2-Dy** revealed the presence of hybrid $[\text{Dy}(\text{H}_2\text{L})(\alpha\text{-SiW}_{11}\text{O}_{39})]^{5-}$ anions.²⁷ Unfortunately, the severe disorder in the cation/solvent network as a result of the simultaneous presence of (a) Na^+ coming from the buffer, (b) K^+ from the lacunary POM precursor, and (c) Cs^+ from the crystallizing agent, did not allow us to crystallographically determine the exact amount of each species. We tried to ascertain this issue by performing ICP-MS analyses on different crystal batches, but the low reproducibility of results precluded us from reporting this compound as a pure phase.

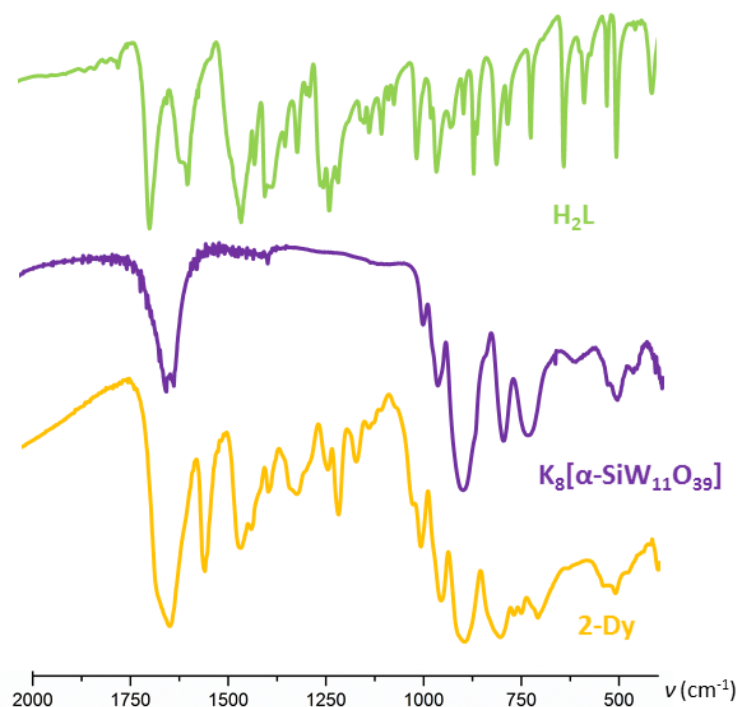


Figure 5.3. FT-IR spectra of compound **2-Dy** in comparison to the starting materials (H_2L ligand, and the $\text{K}_8[\alpha\text{-SiW}_{11}\text{O}_{39}]$ POM precursor).

To avoid the presence of so many different alkaline cations, similar reaction conditions were selected but using aqueous 1 M KOAc buffer instead. In this case, the solubility of the synthetic system drastically decreases in such a way that a significant amount of yellow precipitate is created and a colorless solution is obtained after filtering out this solid. These drawbacks were overcome by reducing the concentration of the buffer to 0.5 M. Although some yellow solid is still formed in the reaction, slow evaporation of the final solution at room temperature affords crystals of **1-Dy**. The FT-IR spectra recorded for crystals of **1-Dy** and yellow precipitates are virtually identical to that registered for the **2-Dy** phase (Figure 5.4). In contrast, the low reaction yield obtained for crystals of **1-Dy** encouraged us to make use of powder X-ray diffraction (PXRD) experiments to determine whether both powdered and crystalline samples correspond to the same phase.

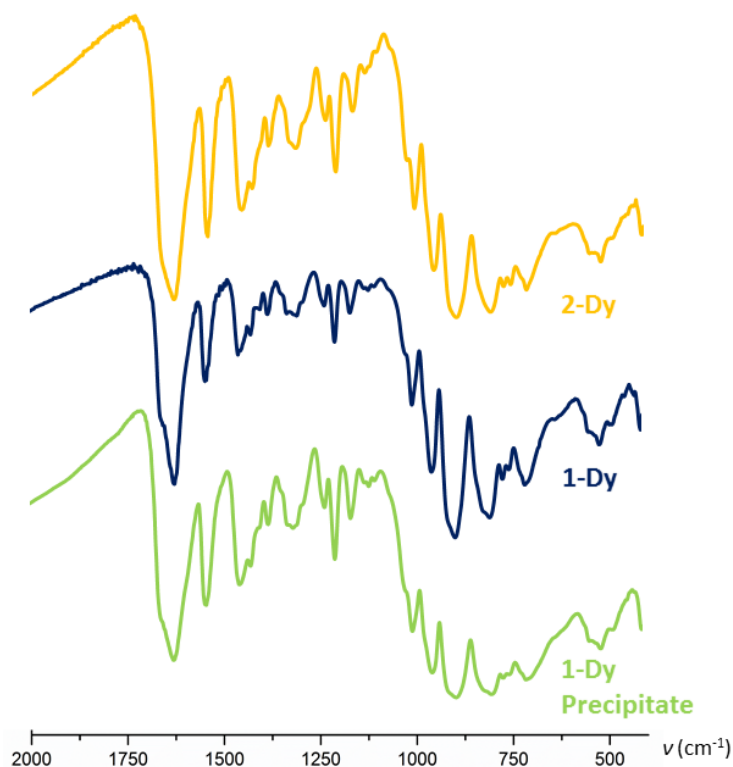


Figure 5.4. FT-IR spectra of **1-Dy** and the yellow precipitate formed in its synthesis compared with **2-Dy**.

The experimental pattern collected for freshly filtered crystals of **1-Dy** compares well with the pattern-matching procedure carried out with single-crystal X-ray diffraction data, which suggests that samples are constituted by a single crystalline phase. Unfortunately, yellow precipitates display diffraction patterns with only a couple of poorly resolved maxima, which evidence the nearly amorphous nature of the solid (Figure 5.5). Although efficient functionalization can be easily inferred from FT-IR spectroscopy (Figure 5.4), this fact did not allow us to confirm that both samples present the same crystal structure; thus, only crystals of **1-Dy** were employed in further studies. Additional experiments also revealed that the change of the Dy^{III} salt (chloride or nitrate) does not affect into the final product or reaction yield.

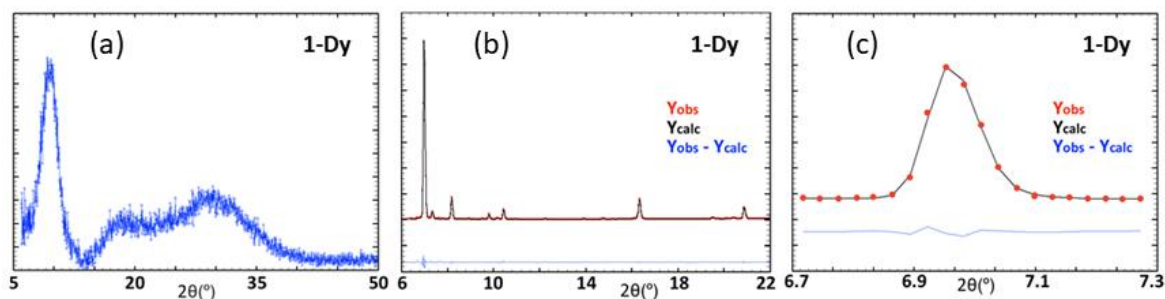


Figure 5.5. (a) Experimental powder X-ray diffraction pattern of the precipitate formed in the reaction of **1-Dy**; (b) powder XRD pattern matching between the experimental pattern of **1-Dy** and cell parameters determined by single-crystal X-ray diffraction analyses, together with (c) the detail of the most intense diffraction maxima.

Synthetic studies were later extended to the remaining lanthanide(III) ions (Figure 5.6). It is well-known that lanthanide-containing POM assemblies are highly dependent on the size of the 4f metal. Frequently, architectures obtained for early lanthanides considerably differ from those comprising smaller 4f metals.²⁶ In this case, FT-IR spectroscopy (Figure A4.5 in the Appendix 4) confirms that the use of early lanthanides (La to Nd) yields Peacock-Weakley-type $[\text{Ln}^{\text{III}}(\text{SiW}_{11}\text{O}_{39})_2]^{13-}$ anions²⁸ constituted by two Keggin-type monolacunary units encapsulating one 4f metal ion. On the contrary, the use of mid-to-late lanthanides affords the isostructural compounds **1-Ln** ($\text{Ln}^{\text{III}} = \text{Sm}$ to Lu) (Figures A4.6 and A4.7 in the Appendix 4).

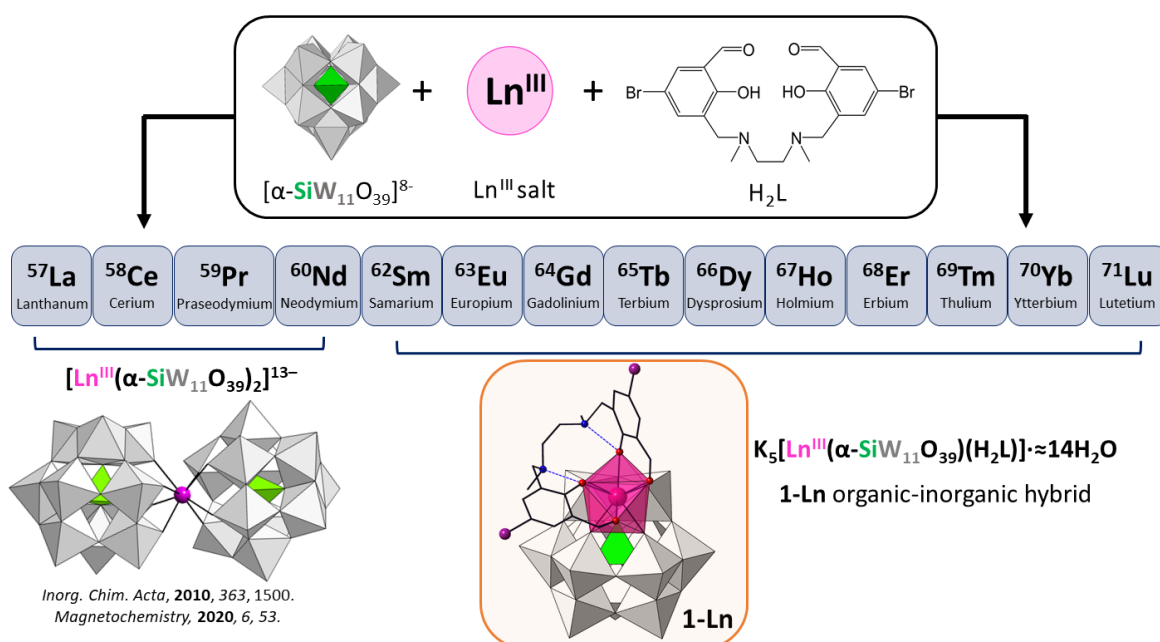


Figure 5.6. Schematic representation of the Peacock-Weakley-type compounds found with lanthanide ions of big size (La to Nd), and the **1-Ln** compounds found from the remaining lanthanide series (Sm to Lu), together with the corresponding FT-IR spectra to see the difference in the bands between the 1100–1800 cm^{-1} range, which correspond to the organic H_2L ligand.

5.3.2. Single-crystal X-ray diffraction

All **1-Ln** compounds are isostructural and crystallize in the triclinic $P\bar{1}$ space group containing three crystallographic independent $[\text{Ln}(\text{H}_2\text{L})(\alpha\text{-SiW}_{11}\text{O}_{39})]^{5-}$ ($\{\text{Ln}\}$) molecular clusters ($Z = 6$) asymmetric unit. Hybrid species are constituted by a trivalent Ln^{III} cation coordinated by four oxygen atoms that belong to two aldehyde (O_a) and two phenoxy (O_p) groups from the H_2L ligand and the four oxygen atoms delimiting the vacant site of the monolacunary $[\alpha\text{-SiW}_{11}\text{O}_{39}]^{8-}$ Keggin-type fragment (O_{POM}). The organic ligand adopts a tetradentate- O_4 mode, and leaves the inner N_2O_2 coordination site available for the potential incorporation of additional metal cations (Figure 5.2). Coordination of phenoxy oxygen atoms to the lanthanide center promotes the migration of protons to amine groups, and the resulting zwitterionic form is stabilized by a pair of intramolecular $\text{N}\cdots\text{O}$ type

hydrogen bonds established between protonated amine groups and deprotonated phenolate oxygen atoms (Table 5.3). Although related mono-lanthanide complexes of aminophenolic Mannich-base compartmental ligands are scarcely found in literature,²⁹ they show a similar zwitterionic arrangement.

Table 5.3. Donor...acceptor distances (Å) for intramolecular N–H...O type hydrogen bonds in **1-Ln**.

Donor...Acceptor (Å)	1-Sm	1-Eu	1-Gd	1-Tb	1-Dy	1-Ho	1-Er	1-Tm	1-Yb	1-Lu
N1A...O2LA	2.67(3)	2.71(3)	2.69(2)	2.712(17)	2.65(3)	2.67(2)	2.76(3)	2.68(3)	2.69(2)	2.70(2)
N2A...O3LA	2.68(3)	2.68(3)	2.69(2)	2.676(18)	2.71(3)	2.70(2)	2.67(3)	2.70(3)	2.67(2)	2.70(2)
N1B...O2LB	2.70(4)	2.69(3)	2.69(2)	2.692(18)	2.71(3)	2.72(2)	2.67(3)	2.72(3)	2.71(2)	2.69(3)
N2B...O3LB	2.71(3)	2.73(3)	2.69(2)	2.684(19)	2.70(3)	2.67(2)	2.69(3)	2.69(3)	2.70(2)	2.68(2)
N1C...O2LC	2.66(3)	2.76(3)	2.70(2)	2.695(19)	2.71(3)	2.71(2)	2.67(3)	2.70(3)	2.73(2)	2.65(2)
N2C...O3LC	2.67(3)	2.69(3)	2.71(2)	2.670(17)	2.67(2)	2.65(2)	2.71(4)	2.70(3)	2.66(2)	2.70(2)

Close inspection to the Cambridge Structural Database (CSD)³⁰ reveals that the coordination mode makes the H₂L adopt an unusual conformation in comparison with the metalorganic complexes reported to date and it confirms that compounds **1-Ln** represent the first examples of mononuclear lanthanide complexes with this specific ligand. Geometrical parameters of 59 crystallographically independent ligands belonging to 42 structures have been determined (Table A4.1 in the Appendix 4). These can be classified into three groups: i) heterometallic dinuclear Ln-M^{II} complexes (M^{II} = Cu, Zn); ii) heterometallic dinuclear Ln-M^{II} complexes (M^{II} = Co, Ni); and iii) sandwich-type M^{II}-Ln-M^{II} species (M^{II} = Cu, Zn) with more than one H₂L ligand (Figure 5.7).^{19b, 31}

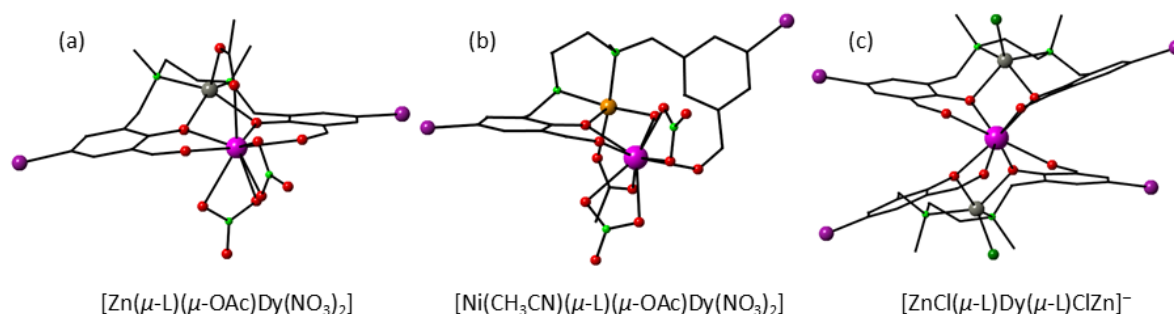


Figure 5.7. Examples of the three different groups of lanthanide(III) complexes bearing the H₂L ligand found in the CSD database; heterometallic dinuclear Ln-M^{II} complexes (a) M^{II} = Cu, Zn; (b) M^{II} = Co, Ni, and; (c) sandwich-type M^{II}-Ln-M^{II} species (M^{II} = Cu, Zn). Color code: Br, purple; Cl, dark green; Ln, pink; N, green; Ni, orange; O, red; Zn, grey.

The scatter plot of intramolecular centroid...centroid distance between the aromatic rings from the same ligand versus the angle between the planes which contain those rings (Figure 5.8) allows these three groups to be easily distinguished. Dihedral angles in the

155–173° range are found for the heterometallic complexes belonging to the first group, whereas this angle slightly decreases in the case of sandwich-type complexes (145–164°). Thus, it can be concluded that members from both families display quasi-coplanar aromatic rings. In contrast, smaller dihedral angles of ca. 110° are found when 3d metal ions are either Ni or Co, but intramolecular centroid...centroid distances are similar in all the three groups (ca. 8 Å). For comparison, compounds **1-Ln** exhibit even smaller angles ranging from 84 to 95°, in such a way that both rings are no longer coplanar, because the empty N₂O₂ pocket allows the ligand to be considerably folded. This makes the aromatic rings to be close to each other with intramolecular centroid...centroid distances of only ca. 6.5 Å. It is worth noting that one of the aromatic groups is near (average twisting angle of ca. 15°) to the ideal mirror plane of the Keggin-type monolacunary anion with C₅ point symmetry (Figure 5.9). This configuration might be promoted by supramolecular interactions established between contiguous {Ln} units.

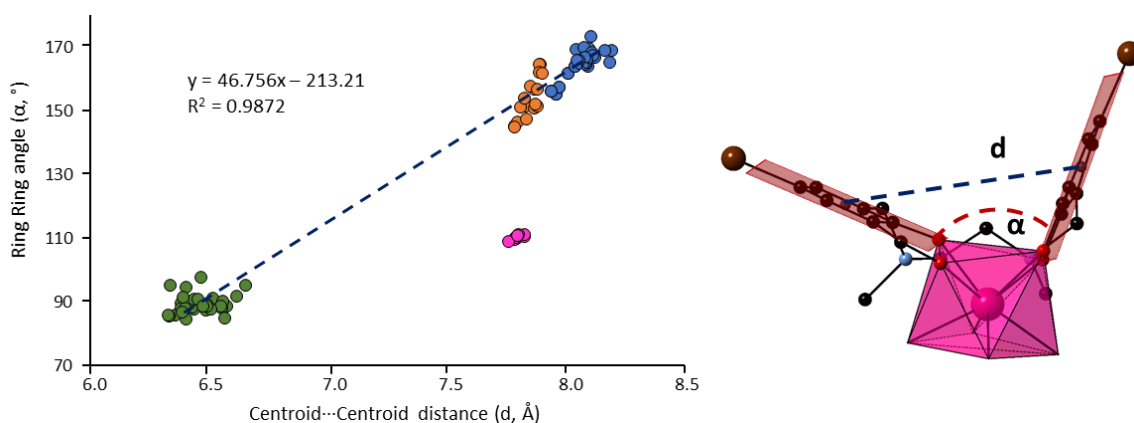


Figure 5.8. Plot of the average intramolecular C_g...C_g distances vs. dihedral angles between aromatic rings for all the crystallographically independent H₂L/L²⁻ fragments deposited in the CSD database. Fragments from heterometallic dinuclear (Ln^{III}/M^{II}) complexes are depicted in blue (M = Zn, Cu) and pink (M = Co, Ni), whereas those belonging to sandwich-type species with more than one H₂L ligand are colored in orange. Data points from compounds **1-Ln** are indicated in green.

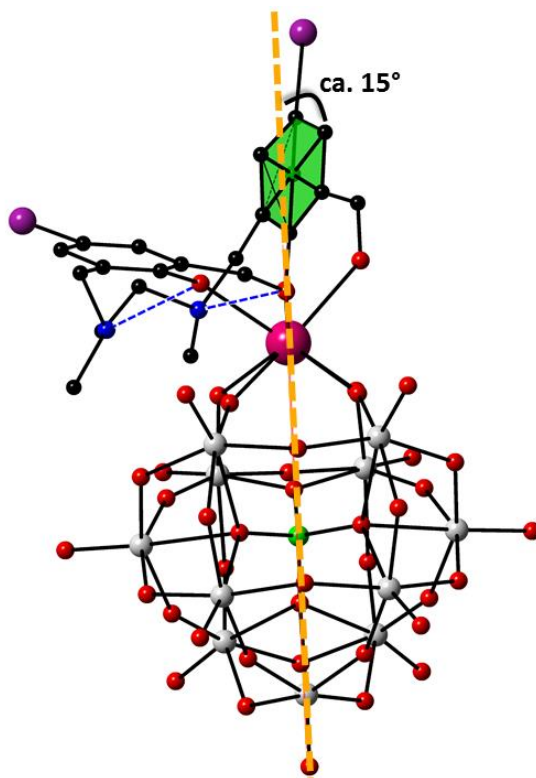


Figure 5.9. Illustration of the parallel arrangement of one of the aromatic groups with respect to the ideal mirror plane of the Keggin anion in molecular $\{Ln\}$ units represented by a dashed orange line. Intramolecular hydrogen bonds are depicted as blue dashed lines.

Lanthanide centers in **1-Ln** exhibit distorted eight-coordinated geometries that have been analyzed by continuous shape measurement (CShM) calculations. Similar CShM values have been obtained in all cases using both biaugmented trigonal prism (BTP, C_{2v} : 0.67–0.87 range) and square antiprism (SAPR, D_{4d} : 0.87–1.06 range) as reference shapes (Figure A4.8 and Table 4.2 in the Appendix 4). Comparison with other eight-coordinated reference polyhedra affords higher CShM values (above 1.4). All the lanthanide coordination polyhedra reported in this work have been scattered in the BTP vs SAPR shape map (Figure 5.10) to determine whether they follow the trend marked by the minimal distortion pathway between the two reference polyhedra. Low path deviation values in the 0.19–0.29 range, far from the upper limit of 0.5 selected by Casanova et al.,³² confirm the best description of coordination geometries as biaugmented trigonal prisms distorted towards square antiprismatic.

This type of geometry arises from the out-of-pocket coordination mode of 4f metals towards the Keggin-type monolacunary skeleton. The Ln–O bond lengths (Table A4.3 in the Appendix 4) follow the order $Ln-O_p < Ln-O_{POM} < Ln-O_a$, with average values in the 2.21–2.36, 2.27–2.45, and 2.31–2.56 Å range, respectively. As observed in some other series of lanthanide-containing POMs,^{19b} a subtle linear shortening of about 0.1 Å can be observed in these bond lengths as the atomic number of the 4f cations increases, in good agreement

CHAPTER 5

with the well-known lanthanide contraction effect (Figure 5.11). This trend is more pronounced for Ln–O_a and Ln–O_p bonds, in comparison to that of Ln–O_{POM} bonds.

Table 5.4. Continuous Shape Measurements (CShM) for the eight-coordinated lanthanide centers in compounds **1-Ln**.^[a]

	Reference Shape	1-Sm	1-Eu	1-Gd	1-Tb	1-Dy	1-Ho	1-Er	1-Tm	1-Yb	1-Lu
Ln1A	SAPR-8	0.941	1.007	0.950	0.873	0.947	0.995	0.943	0.914	0.903	0.900
	TDD-8	1.624	1.466	1.610	1.648	1.723	1.764	1.674	1.437	1.796	1.663
	JBTPR-8	1.609	1.482	1.471	1.526	1.427	1.390	1.449	1.494	1.470	1.476
	BTPR-8	0.766	0.785	0.796	0.869	0.785	0.725	0.722	0.841	0.799	0.819
Ln1B	SAPR-8	1.059	1.015	1.066	0.974	0.943	0.901	0.997	0.867	0.907	0.896
	TDD-8	1.725	1.833	1.764	1.738	1.595	1.747	1.784	1.562	1.621	1.733
	JBTPR-8	1.394	1.286	1.384	1.349	1.508	1.500	1.395	1.404	1.529	1.379
	BTPR-8	0.785	0.696	0.710	0.671	0.812	0.865	0.685	0.781	0.828	0.763
Ln1C	SAPR-8	1.052	1.034	1.004	0.917	0.965	0.904	0.983	1.041	0.911	0.889
	TDD-8	1.602	1.419	1.583	1.488	1.516	1.543	1.529	1.853	1.633	1.511
	JBTPR-8	1.456	1.546	1.439	1.529	1.468	1.433	1.525	1.442	1.479	1.415
	BTPR-8	0.857	0.837	0.766	0.809	0.762	0.776	0.720	0.776	0.823	0.804

^[a] Abbreviations. **SAPR**: square antiprism (D_{4d}); **TDD**: triangular dodecahedron (D_{2d}); **JBTPR**: Johnson biaugmented trigonal prism (C_{2v}) and; **BTPR**: biaugmented trigonal prism (C_{2v}).

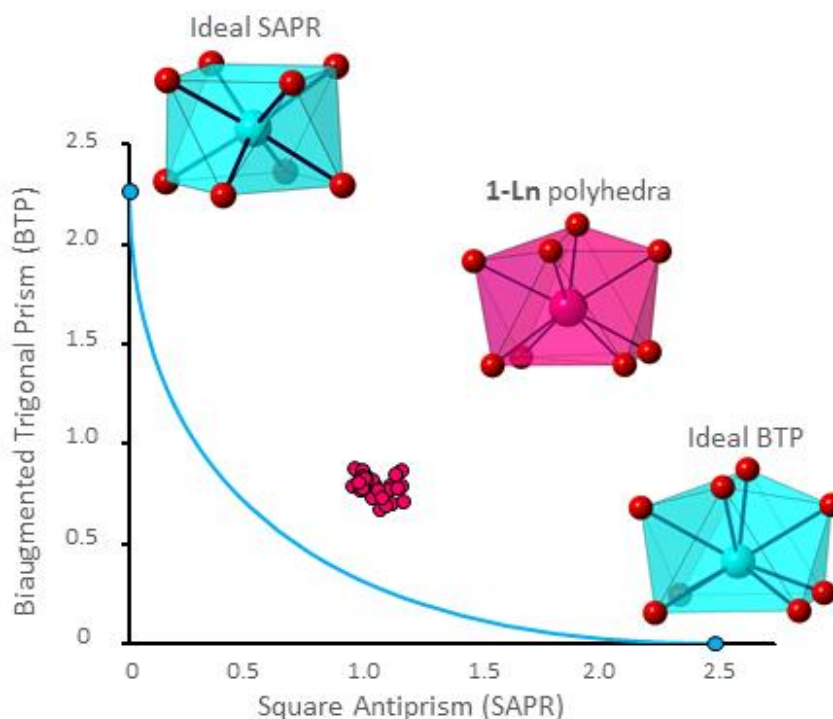


Figure 5.10. Biaugmented trigonal prism (BTP) vs. square antiprism (SAPR) shape map for the LnO₈ coordination polyhedra of 4f ions in **1-Ln**. Solid line: minimal distortion pathway between reference shapes.

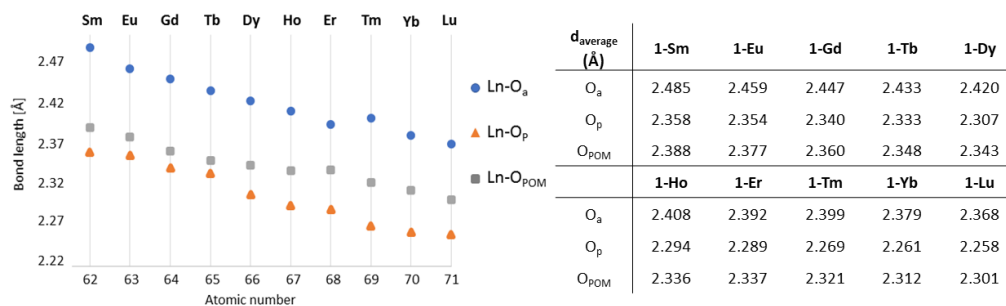


Figure 5.11. Left: Variation of average Ln–O bond length (Å) with the atomic number of the 4f metal center in compounds **1-Ln**. Right: Compilation of average Ln–O bond lengths (Å). *Abbreviations:* O_a : O atoms from the aldehyde group of the H_2L ligand; O_p : O atoms from the phenoxy group of the H_2L ligand; O_{POM} : O atoms delimiting the vacant site of the lacunary Keggin-type POM.

With regard to the crystal packing, six molecular $\{Ln\}$ hybrid POMs self-assemble into supramolecular structures in a chair-like conformation via π – π and $Br\cdots Br$ interactions (Figure 5.12). The virtual chair formed by lanthanide atoms display shortest Ln \cdots Ln distances in the 7.981(6) to 8.244(9) Å range (Figure 5.13). Aromatic rings from contiguous units contribute to the π – π stacking, which display centroid-to-centroid distances ranging from 3.52(2) to 3.618(11) Å (Table A4.4 in the Appendix 4). Additionally, only Br atoms that belong to aromatic groups parallel to the ideal symmetry plane are facing the interior of the hexamer. These six atoms correspond to alternate $\{Ln\}$ units and are disposed in two different planes with interplanar distances of about 9 Å (Figure 5.13). The 3.6465(4)–4.086(3) Å bond lengths found for the bifurcated $Br\cdots Br$ type contacts are in line with those observed for analogous interactions in the literature (Table A4.5 in the Appendix 4).³³

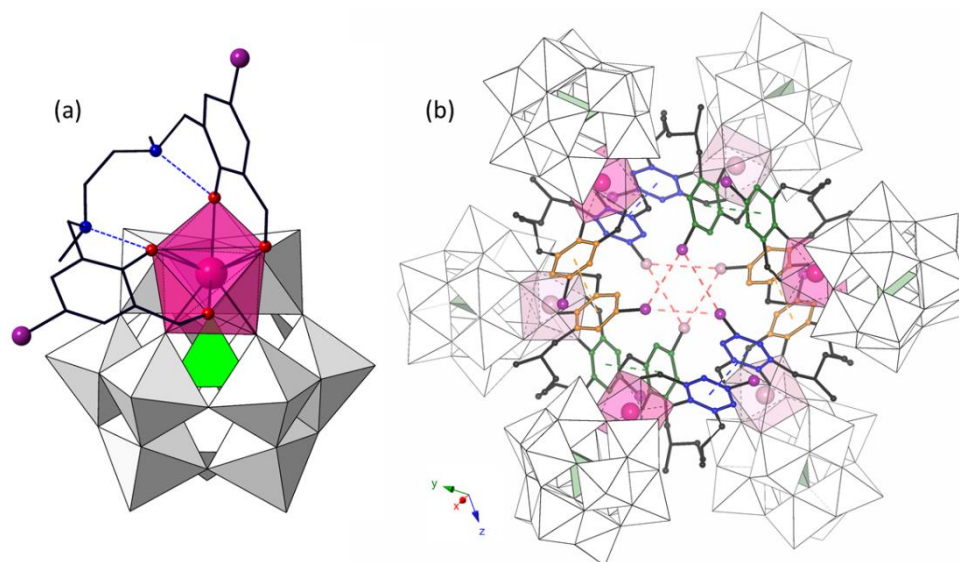
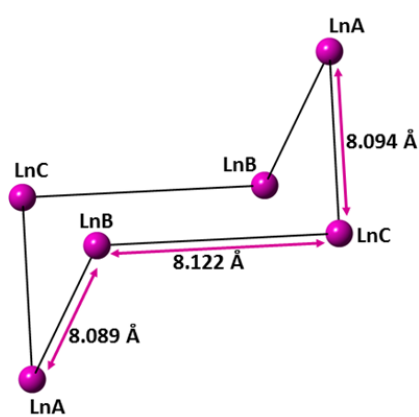


Figure 5.12. (a) Molecular Structure of hybrid $[Ln(H_2L)(\alpha\text{-SiW}_{11}\text{O}_{39})]^{5-}$ POM found in compounds **1-Ln**. Intramolecular N–H \cdots O hydrogen bonds are represented as blue dashed lines. (b) Hexameric chair-like supramolecular assemblies in **1-Ln**. Aromatic rings involved in π – π stacking interaction that belong to contiguous $\{Ln\}$ units are depicted in the same color. Intermolecular $Br\cdots Br$ contacts are represented as pink dashed lines. Color code: $\{WO_6\}$, white; $\{SiO_4\}$, green; $\{LnO_8\}$, pink; C, black; O, red; N, blue; Br, purple.

Table A4.4. Br...Br distances (Å) in compounds **1-Ln**.

	1-Sm ^[a]	1-Eu ^[b]	1-Gd ^[c]	1-Tb ^[d]	1-Dy ^[e]	1-Ho ^[f]	1-Er ^[g]	1-Tm ^[h]	1-Yb ^[i]	1-Lu ^[k]
BrA...BrB	3.706(5)	3.817(5)	3.705(5)	3.759(4)	3.677(4)	3.653(4)	3.657(5)	3.907(5)	3.645(4)	3.656(4)
BrA...BrC	3.962(6)	4.016(5)	3.958(5)	3.722(4)	3.953(4)	3.903(3)	3.882(5)	3.826(7)	3.890(4)	3.924(4)
BrB...BrC	3.960(6)	3.914(5)	3.989(4)	4.086(3)	3.923(5)	3.967(3)	3.923(5)	3.741(6)	3.945(3)	3.866(4)

Symmetry codes: [a] Br2A...Br1Bⁱ: 2-x, -y, 1-z; Br2A...Br2Cⁱⁱ: -1+x, -1+y, z; Br1B...Br2Cⁱⁱⁱ: 3-x, 2-y, 1-z; [b] Br2A...Br1B^{iv}: -x, -1-y, -z; Br2A...Br2Cⁱⁱ; Br1B...Br2C^v: 1-x, -y, -z; [c] Br2A...Br1B^{vi}: 1-x, 1-y, 1-z; Br2A...Br2Cⁱⁱ; Br1B...Br2C^{vii}: 2-x, 2-y, 1-z; [d] Br2A...Br1B^{viii}: -x, -y, -z; Br2A...Br2Cⁱⁱ; Br1B...Br2C^{ix}: 1-x, 1-y, -z; [e] Br2A...Br2B^x: 1+x, 1+y, 1+z; Br2A...Br2C^{xi}: x, y, 1+z; Br2B...Br2Cⁱⁱ; [f] Br2A...Br2B^x; Br2A...Br2C^{xi}; Br2B...Br2C^{ix}; [g] Br1A...Br1B^x; Br1A...Br1C^{xii}: 1+x, 1+y, z; Br1B...Br1C^{xiii}: x, y, -1+z; [h] Br1A...Br2B^{vi}; Br1A...Br1C^{xi}; Br2B...Br1C^{ix}; [j] Br2A...Br2B^x; Br2A...Br2C^{xi}; Br2B...Br2C^{ix}; [k] Br1A...Br2B^{xiv}: 3-x, 2-y, 2-z; Br1A...Br1C^{xii}; Br2B...Br1C^{xv}: 2-x, 1-y, 2-z.



d (Å)	1-Sm	1-Eu	1-Gd	1-Tb	1-Dy
LnA...LnB	8.096(4)	8.040(3)	8.128(3)	8.180(2)	8.123(3)
LnB...LnC	8.213(12)	8.159(8)	8.244(9)	8.177(7)	7.993(7)
LnC...LnA	8.013(7)	8.024(5)	8.050(6)	8.001(5)	8.224(12)
	1-Ho	1-Er	1-Tm	1-Yb	1-Lu
LnA...LnB	8.051(3)	8.108(4)	8.054(10)	8.059(3)	8.051(4)
LnB...LnC	7.981(6)	8.215(13)	8.044(4)	7.990(7)	8.204(13)
LnC...LnA	8.216(2)	8.018(9)	8.165(13)	8.226(12)	8.004(10)

Figure 5.13. Representation of the chair-like conformation displayed by the {Ln} molecular hybrid species in **1-Ln** compounds, represented by their Ln atoms and average Ln...Ln distances (Å) together with the table of the average distances.

5.3.3. Photoluminescent properties

Both inorganic POM fragments and the H₂L Mannich base ligand have proved to act as efficient antenna ligand to sensitize weak-emitting 4f metal centers.³⁴ In addition, an efficient emission could be *a priori* expected in the case of **1-Ln** hybrids due to the lack of any aqua ligands coordinated to lanthanide centers responsible for quenching the fluorescence through deactivation of excited states via high frequency O–H oscillators. Therefore, solid-state photophysical properties were evaluated for all **1-Ln** derivatives; **1-Sm** to **1-Dy** and **1-Tm** in the visible region and **1-Ho**, **1-Er** and **1-Yb** in the near-infrared region (NIR).

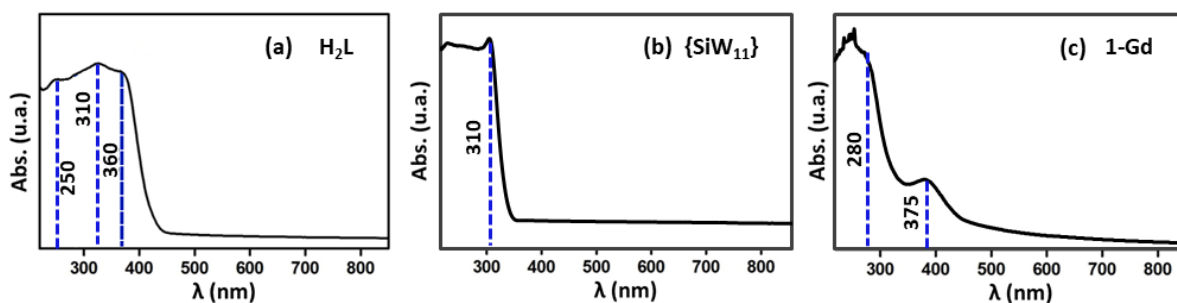


Figure 5.14. UV-vis diffuse reflectance absorption spectra of; (a) H_2L ligand, (b) $\text{K}_8[\alpha\text{-SiW}_{11}\text{O}_{39}]\cdot 13\text{H}_2\text{O}$ POM precursor, and; (c) and **1-Gd** derivative.

In the first place, the UV-vis diffuse reflectance spectrum of the H_2L ligand was measured. As shown in Figure 5.14, the H_2L organic ligand absorbs in the 220–380 nm region and displays three maxima at 250, 310 and 360 nm, which corresponds to the $\pi\text{-}\pi^*$ aromatic ring and to $n\text{-}\pi^*$ aldehyde group electronic transitions, whereas the $\text{K}_8[\alpha\text{-SiW}_{11}\text{O}_{39}]\cdot 13\text{H}_2\text{O}$ POM precursor exhibits a strong absorption below 310 nm. The related absorption in compounds **1-Ln**, as exemplified by the **1-Gd** derivative, displays two signals centered at ca. 280 and 375 nm and, thus, the analyzed samples were irradiated at these two different wavelengths using a Xe arc lamp as an excitation source.

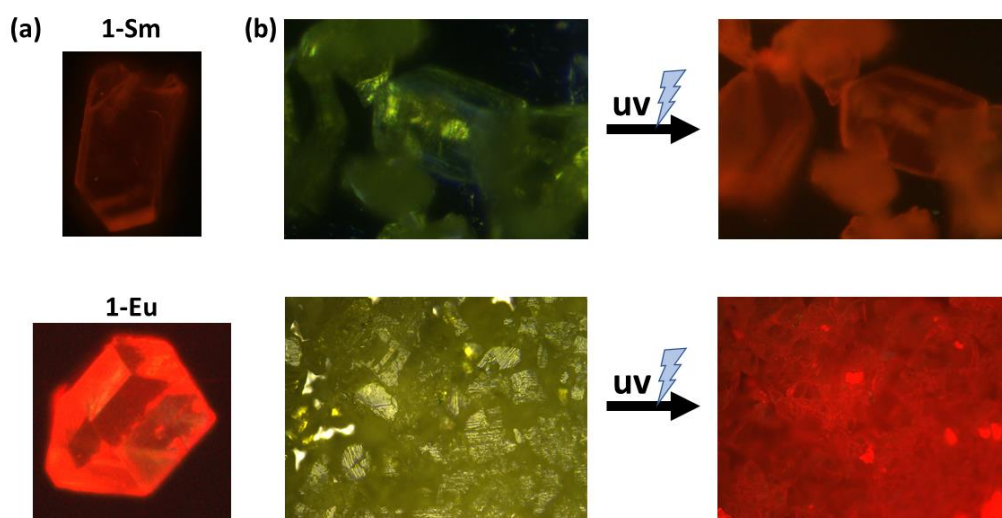


Figure 5.15. (a) Photographs of crystals of **1-Sm** (top) and **1-Eu** (bottom) under irradiation of UV light, and; (b) photographs of bulk crystalline samples before and after irradiation with UV light.

Bright orange-reddish and red photoluminescence (Figure 5.15) were observed for **1-Sm** and **1-Eu** derivatives, respectively, and their emission spectra were recorded at 10 K, 77 K, 150 K, and room temperature. Low temperature excitation spectra acquired for their more intense emission lines (600 nm for **1-Sm** and 614 nm for **1-Eu**) show a broad band in the 300–450 nm region, which is overlapped with some narrow bands arising from the intra- f^n transition of the lanthanide ions (Figure 5.16). The higher intensity of the former implies a more efficient luminescence sensitization via the excited states of the ligands, which is indicative of an antenna effect. When it comes to emission spectra, modification of

the excitation wavelength does not alter neither the position nor the fine structure of the bands arising from the splitting of J levels by the crystal field. Moreover, signals are broadened and their intensity decreases as temperature increases due to the higher kinetic energy, which promotes the radiationless thermal deactivation of excited states. Close inspection reveals that the intensity of the signals is similar for the spectra registered at 10 K and 77 K, and in turn, it undergoes a drastic decrease above 150 K.

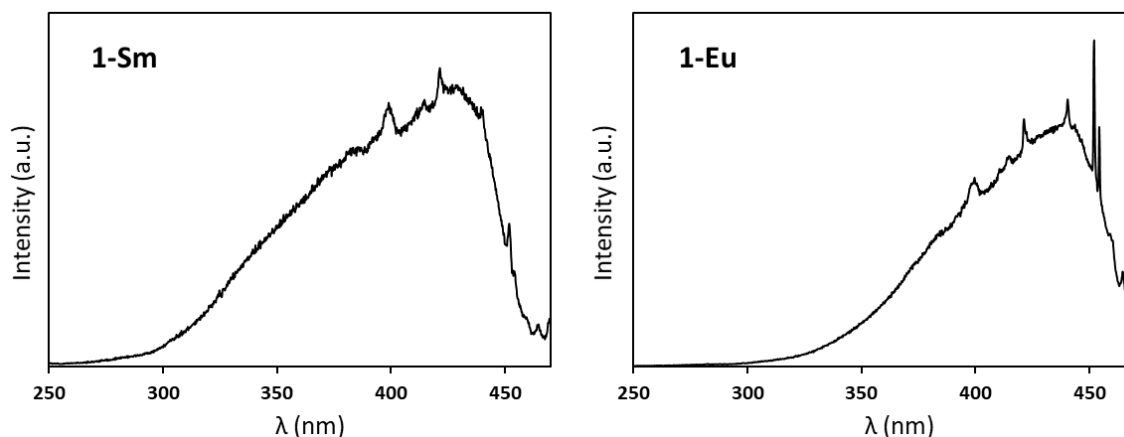


Figure 5.16. Solid state excitation spectra for **1-Sm** (left) and **1-Eu** (right) recorded at 10 K for their most intense emission bands (600 and 614 nm, respectively).

With respect to **1-Sm** derivative, the solid state luminescence spectrum (Figure 5.17) shows three group of signals with maxima at *ca.* 568, 600, and 646 nm, which correspond to ${}^4G_{5/2} \rightarrow {}^6H_J$ ($J = 5/2, 7/2$ and $9/2$, respectively) transitions.³⁵ At low temperatures, the spectra are dominated by the electric-dipole transitions ${}^4G_{5/2} \rightarrow {}^6H_{7/2}$, whereas the ${}^4G_{5/2} \rightarrow {}^6H_{9/2}$ becomes the most intense signal at room temperature. The average spin-orbit coupling parameter (λ) can be estimated from the energy difference between the centers of the emission bands ($\Delta E = J \lambda$), yielding a value of 280 cm^{-1} . In addition, the crystal field splitting of the ground state could also be tentatively calculated from the energy difference between the different M_J sublevels corresponding to the splitting of the ${}^4G_{5/2} \rightarrow {}^6H_{5/2}$ signal, which placed the energy levels of the first excited states at 125 and 272 cm^{-1} , respectively.

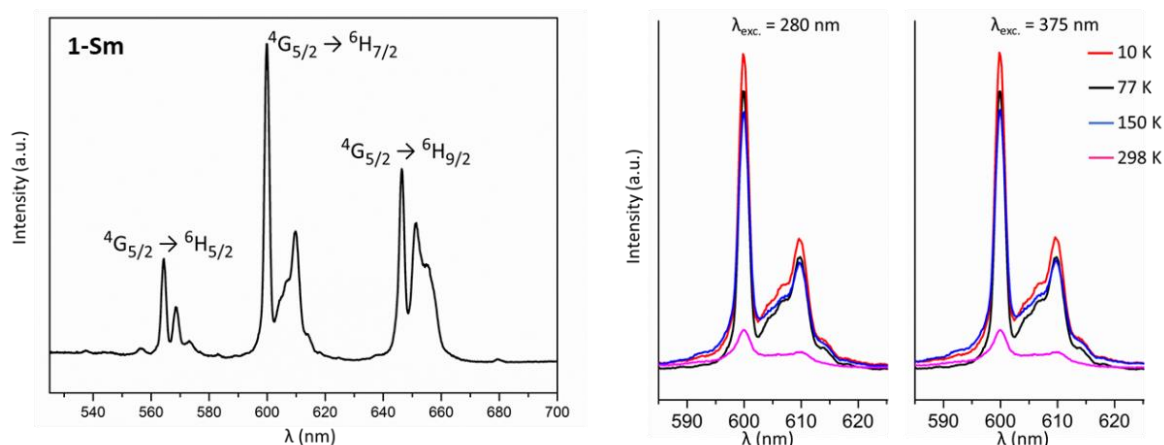


Figure 5.17. Solid state photoluminescence spectrum of **1-Sm** recorded at 10 K upon excitation at 375 nm (left). Thermal evolution of the most intense transition upon excitation at 280 and 375 nm (right).

In the case of **1-Eu**, five group of signals with peak maxima at 581, 596, 615, 653 and 703 nm are found, as it can be seen in Figure 5.18. These peaks can be assigned to characteristic ${}^5D_0 \rightarrow {}^7F_J$ ($J = 0, 1, 2, 3$ and 4) transitions. In this case, the crystal field effect allows the weak symmetry-forbidden ${}^5D_0 \rightarrow {}^7F_0$ and ${}^5D_0 \rightarrow {}^7F_3$ transitions to be observed. The former are usually not observed in molecules with high symmetry, as there would be no increment of J . However, the considerable intensity found for **1-Eu** evidences that Eu^{III} ion occupies a low symmetry site,³⁶ in good agreement with the biaugmented trigonal prismatic geometry determined by single-crystal X-ray diffraction studies for the $\{\text{EuO}_8\}$ moiety. The most dominant band corresponds to the hypertensive electric dipole ${}^5D_0 \rightarrow {}^7F_2$ transition, which displays considerably higher intensity (8:1) in comparison to the magnetic dipole allows ${}^5D_0 \rightarrow {}^7F_1$. The intensity of the former band increases with the local asymmetry. This fact can be inferred when comparing the low symmetry of the $\{\text{EuO}_8\}$ polyhedron in **1-Eu**, with the analogous square antiprismatic (D_{4d}) center in the archetypic $[\text{EuW}_{10}\text{O}_{39}]^{9-}$. In this line, the most intense ${}^5D_0 \rightarrow {}^7F_2$ transition results in bright red luminescence for **1-Eu**, whereas other Eu^{III} -containing molecules, such as the known $\text{Na}_9[\text{EuW}_{10}\text{O}_{39}] \cdot 14\text{H}_2\text{O}$ salt, emits orange fluorescence³⁷ due to the higher relative intensity of the ${}^5D_0 \rightarrow {}^7F_1$ electronic transition. The spin-orbit coupling is easy to calculate due to the well-defined signals, which results in an average value of $\lambda = 310 \text{ cm}^{-1}$ value, which is close to that calculated from magnetic susceptibility curves (see Section 5.3.4).

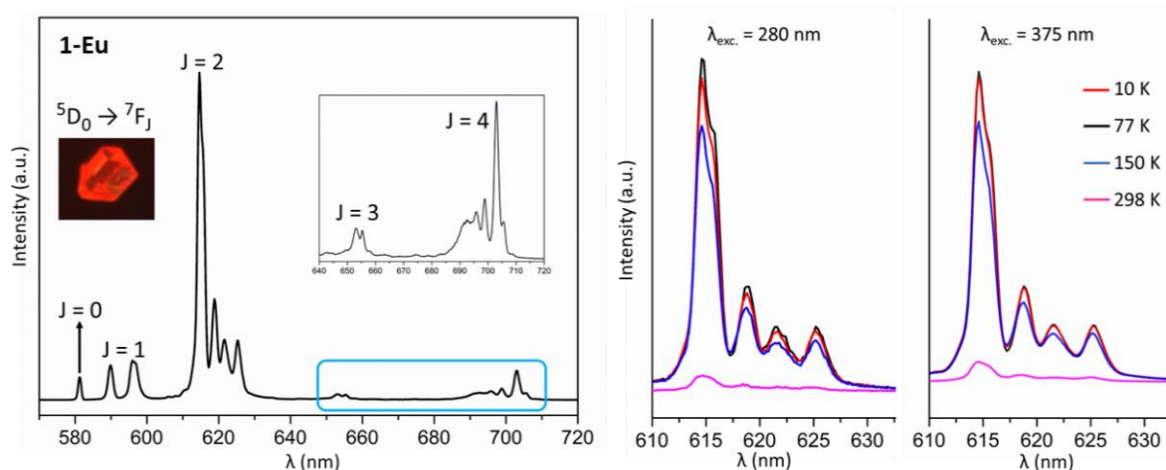


Figure 5.18. Solid state photoluminescence spectrum of **1-Eu** recorded at 10 K upon excitation at 375 nm (left). Thermal evolution of the most intense transition upon excitation at 280 and 375 nm (right).

Emission decay curves of the most intense lines for both **1-Sm** and **1-Eu** derivatives, that is, ${}^4G_{5/2} \rightarrow {}^6H_{7/2}$ at 600 nm for **1-Sm** and ${}^5D_0 \rightarrow {}^7F_2$ at 614 nm for **1-Eu**, were monitored as a function of temperature upon excitation at 280 and 375 nm. Experimental curves for **1-Sm** were fitted to a single exponential function;

$$I = A_0 + A_1 \exp\left(\frac{-t}{\tau}\right) \quad (\text{Eq. 5.1})$$

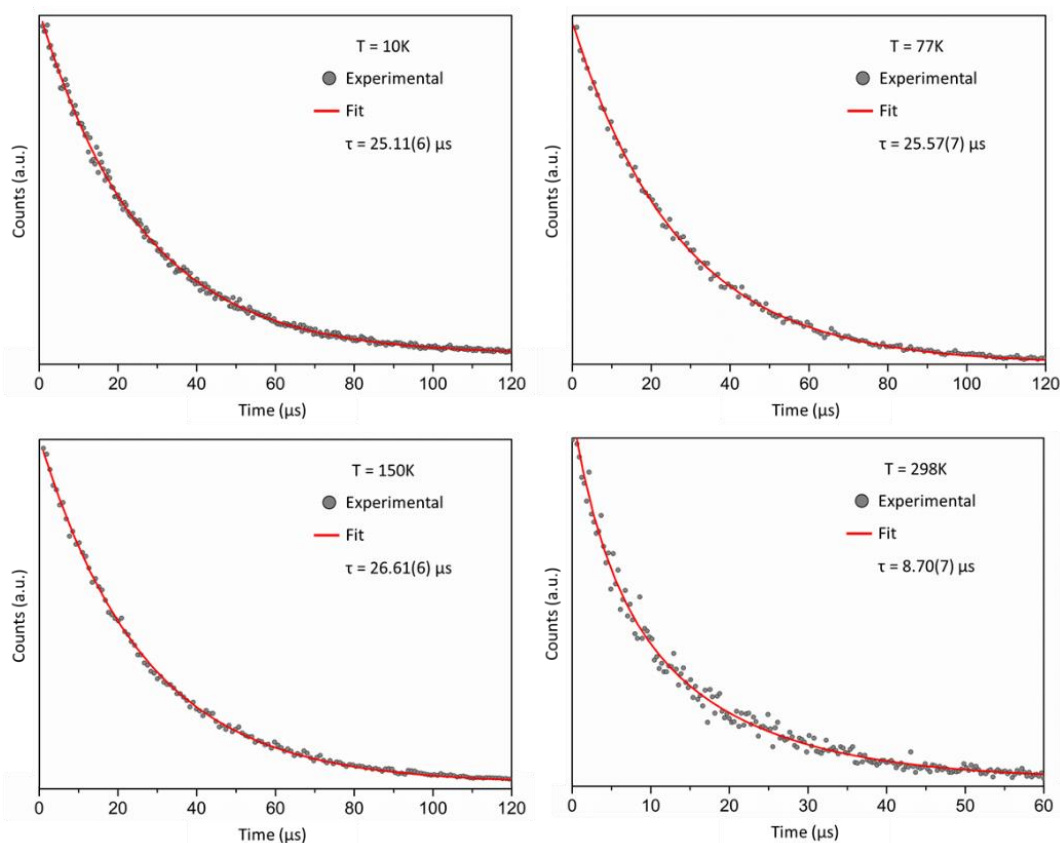
On the contrary, two decay components were fitted for the decay curves of **1-Eu**, and hence, they were fitted to a double exponential function;

$$I = A_0 + A_1 \exp\left(\frac{-t}{\tau_1}\right) + A_2 \exp\left(\frac{-t}{\tau_2}\right) \quad (\text{Eq. 5.2})$$

where τ_n is luminescence lifetime, A_0 background, and A_n weighting parameters. In the case of **1-Eu**, the second term accounts for approximately 75–80% of the total process. Moreover, luminescence lifetimes proved to be almost the same regardless of the excitation wavelength (Figures 5.19 and Figure A4.9 in Appendix 4). The fitting results showed luminescence lifetimes of *ca.* 25 μs for **1-Sm** below 150 K, which suggest the absence of any thermally activated nonradiative deactivation process, but it drastically drops at room temperature. In contrast, lifetime values at different temperatures remain almost constant at 700 μs for the principal decay component of **1-Eu**. The observed lifetimes are in line with those found in the literature for related complexes with eight coordinated Sm^{III} and Eu^{III} ions.³⁸

Table 5.6. Luminescence lifetimes of compounds **1-Sm** and **1-Eu** upon excitation at 375 nm at different temperatures.

Temperature (K)	τ_{exp} 1-Sm (μs) Em. 600 nm	τ_{exp} 1-Eu (μs) Em. 614 nm
10	25.11(6)	226(4)/735(4)
77	25.57(7)	195(3)/735(3)
150	26.61(6)	227(4)/796(3)
298	8.70(7)	181(3)/629(4)

**Figure 5.19.** Luminescence decay curves for **1-Sm** at different temperatures upon excitation at 375 nm.

On the contrary, **1-Tb**, **1-Dy** and **1-Tm** compounds display very weak ligand centered emission, which suggests an inefficient energy transfer from the ligands to lanthanide centers. To further characterize this phenomenon, the latter compounds, together with that of the **1-Gd** derivative, were irradiated with a 325 nm HeCd continuous laser and their spectra recorded at 20 K (Figure 5.20). The spectrum of **1-Gd** presents a broad band ranging from 450 nm to 650 nm and centered at 550 nm that could probably be ascribed to the emission from the first excited triplet level from the organic ligand to the ground level (*ca.* 18180 cm^{-1}). The excited levels of Gd^{III} ions (*ca.* 315 nm) usually have higher energy than those of the ligand, and hence, ligand-to-metal energy transfer is disabled. This allows the direct observation of ligand fluorescence.³⁹ A similar profile is observed in the spectra of **1-Tb**, **1-Dy** and **1-Tm**, which show additional peaks of small intensity almost shadowed by the

ligand emission that might be originated from the intraionic transitions of the metal centers. This behavior is somehow expected for **1-Dy** and **1-Tm** based on the already reported results,^{19b} which showed that H₂L does not act as a suitable antenna ligand in the case of Dy^{III} and Tm^{III} containing derivatives.

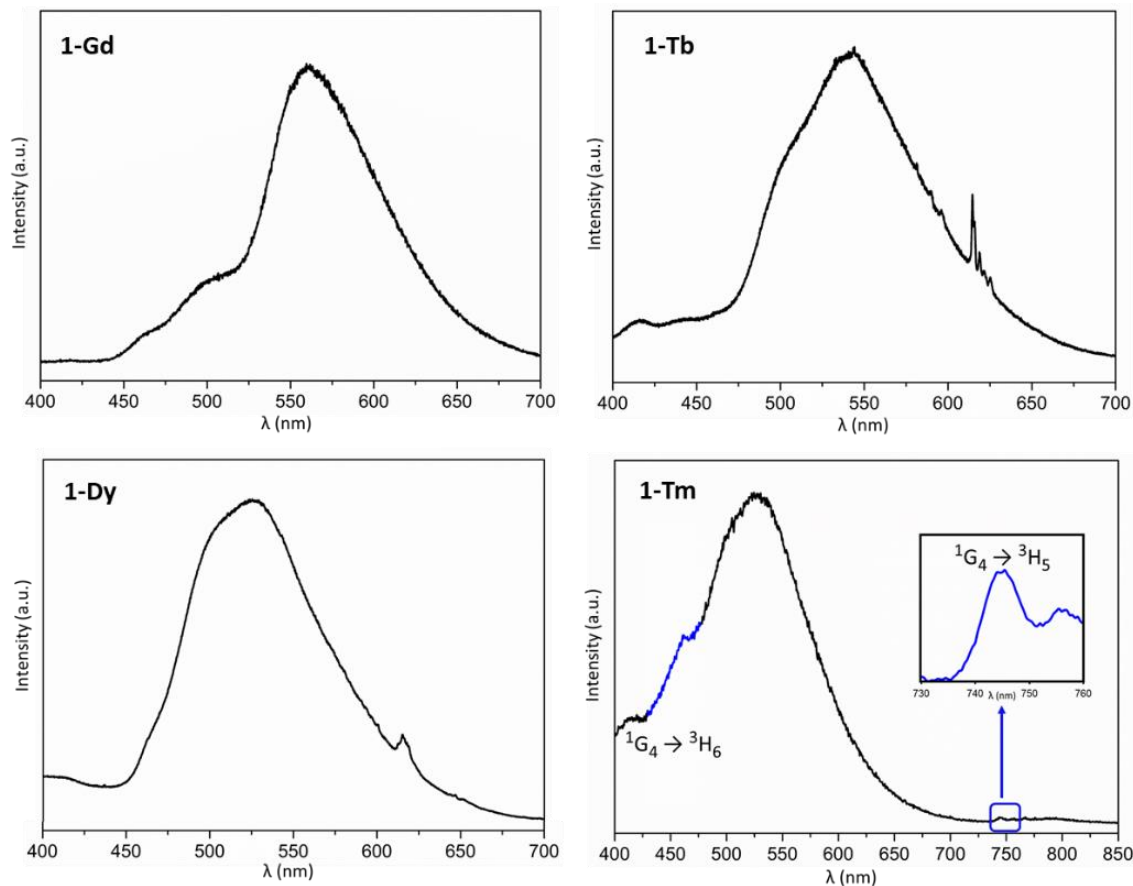


Figure 5.20. Solid state photoluminescence spectra of **1-Gd**, **1-Tb**, **1-Dy** and **1-Tm** compounds recorded at 20 K upon excitation at 325 nm.

However, considering the intense metal-centered emission displayed by the [Zn(μ -L)(μ -OAc)Tb(NO₃)₂] counterpart bearing the same organic ligand, an efficient quenching mechanism must be operative in **1-Tb**. According to Yamase's work on the luminescence of polyoxometallolanthanoates,⁴⁰ low quantum yields are usually observed for Tb^{III} derivatives due to Tb^{IV}-W^V charge transfer states and radiationless deactivation through cross-relaxation processes. The first effect can occur by the transmission of d¹ electrons to Ln^{III} ions as a result of $f\pi$ - $p\pi$ - $d\pi$ orbital mixing, but it is found to be favored only when bond angles are higher than 150°; that is, when LnO_x polyhedra share corners with WO₆ octahedra. For comparison, this mixing is much less efficient when edge-sharing takes place and Ln-O-W angles are closer to 100°. In the case of **1-Ln** complexes, each {LnO₈} polyhedron shares corners with two WO₆ units that belong to two different {W₁₀O₁₃} trimers and display Ln-O-W angles in the 153–159° range. On the contrary, the other two O_{POM} oxygens in the coordination environment of the 4f metal are those linked to two W centers

from the defective trimer. The out-of-pocket coordination mode of the lanthanide ion precludes its full incorporation to the mixed $\{\text{LnW}_2\text{O}_{13}\}$ trimer ($d_{\text{Ln}-\text{O}_c} > 3.2 \text{ \AA}$, where O_c is a central O atom from the Keggin skeleton), and therefore, **1-Ln** hybrids display angles in the $128\text{--}137^\circ$ range, which lies between the two mentioned edge- and corner-sharing modes (Figure 5.21. and Table A4.7 in the Appendix 4).

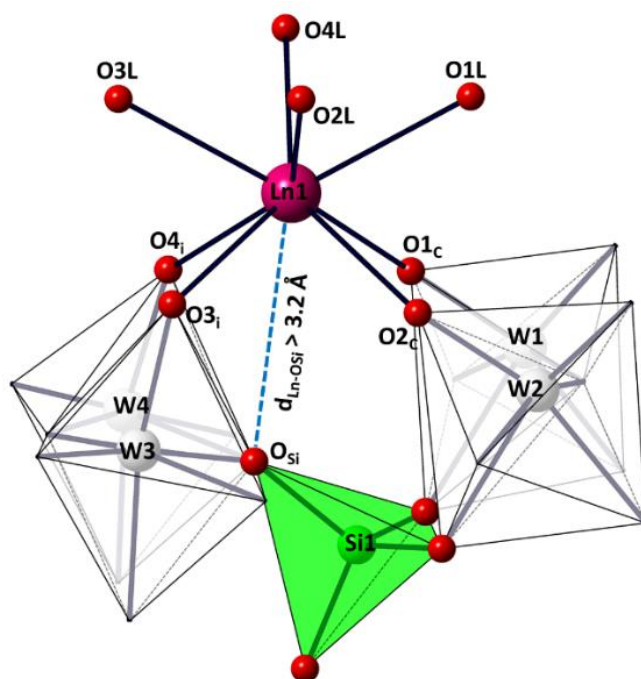


Figure 5.21. Scheme of coordination spheres of the emitting Ln centers in **1-Ln**. Abbreviations: O_c , O_i and O_{Si} denote oxygen atoms involved in corner-sharing linkage mode; those in intermediate situations between corner- and edge-sharing and central O atoms, respectively.

All in all, these effects appear to be relevant enough to completely quench the metal-centered emission in **1-Tb** but insufficient in the case of **1-Sm** and **1-Eu**, although their absolute quantum yields at room temperature have been calculated to be as low as 0.36% and $<0.01\%$, respectively. More specifically, the color of the emission originating from **1-Eu** is similar to that of the $[\text{Zn}(\mu\text{-L})(\mu\text{-OAc})\text{Eu}(\text{NO}_3)_2]$ dinuclear specie,^{19b} whereas a significant difference can be found in CIE 1931 chromaticity diagrams of the two Sm analogues (Figure 5.22). The fact that **1-Sm** emits more reddish light in contrast to the pale orange of the $[\text{Zn}(\mu\text{-L})(\mu\text{-OAc})\text{Sm}(\text{NO}_3)_2]$ counterpart is reflected in their emission spectra, in such a way that relative intensities of $^4\text{G}_{5/2} \rightarrow ^6\text{H}_{7/2}$ and $^4\text{G}_{5/2} \rightarrow ^6\text{H}_{9/2}$ electronic transitions are almost equal for the nine-coordinated Sm^{III} centers of the latter complex.

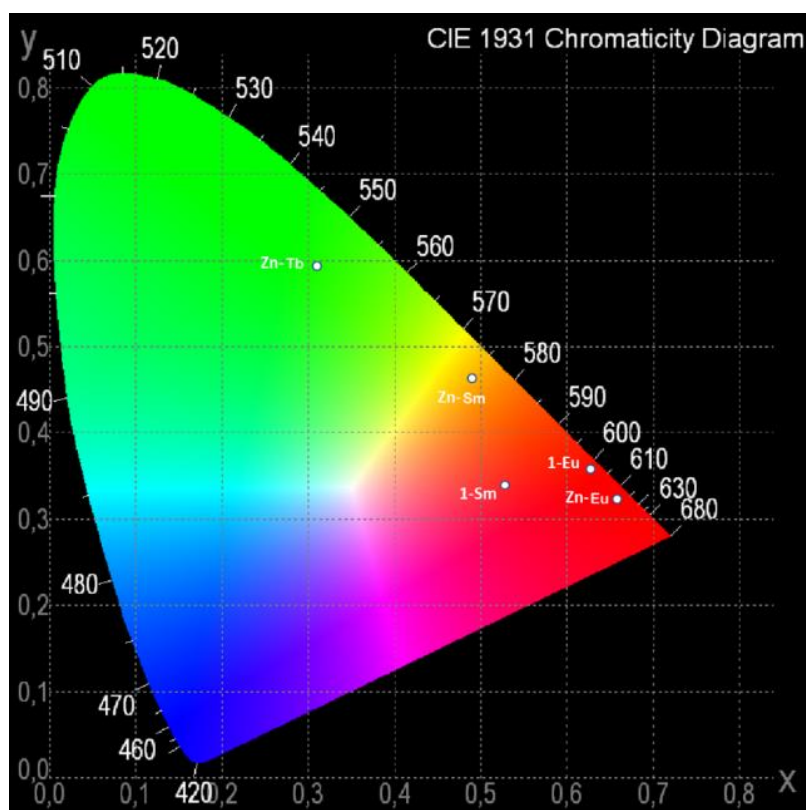


Figure 5.22. CIE 1931 x,y chromaticity coordinates as a function of the emission wavelengths for compounds **1-Ln** (Ln = Sm, Eu) compared to previously reported $[\text{Zn}(\mu\text{-L})(\mu\text{-OAc})\text{Ln}(\text{NO}_3)_2]\cdot\text{MeCN}$ (Ln = Sm, Eu, Tb) derivatives with the same H_2L ligand.^{19b}

With regard to the emission in the NIR region, this is of high interest, especially in the field of optical communications.³⁸ Spectra were only acquired at 20 K upon excitation with 325 nm HeCd continuous laser, because much lower intensities are expected in comparison to those which emit in the visible region (Figure 5.23). Compound **1-Er** exhibits a broad band in the 1475–1625 nm range with maxima at 1525 nm, which can be assigned to the $^4\text{I}_{13/2} \rightarrow ^4\text{I}_{15/2}$ transition. The **1-Yb** shows a quadruplet in the 970–1060 nm region, which is ascribed to the $^2\text{F}_{5/2} \rightarrow ^2\text{F}_{7/2}$ transition.⁴¹ This transition fits well with the expected crystal field splitting of the ground state (Kramer's doublets) for this derivative. Previous seminal work revealed that excitation mechanisms different from the antenna effect are possible in the case of Yb^{III} complexes, because there is a large energy gap between the triplet state of the ligand and the $^2\text{F}_{5/2}$ excited level of the metal.⁴² The related $[\text{Zn}(\mu\text{-L})(\mu\text{-OAc})\text{Yb}(\text{NO}_3)_2]$ dimer showed similar behavior, but no emission in the NIR region was observed for the Er^{III} derivative.^{19b} In contrast, the **1-Ho** complex does not exhibit emissive properties even at 20 K. This behavior might be due to an inefficient energy transfer from the ligand to the lanthanide center.⁴³ It is worth noting that **1-Er** and **1-Yb** represents two of the scarce examples of NIR emitting POM-based systems.⁴⁴

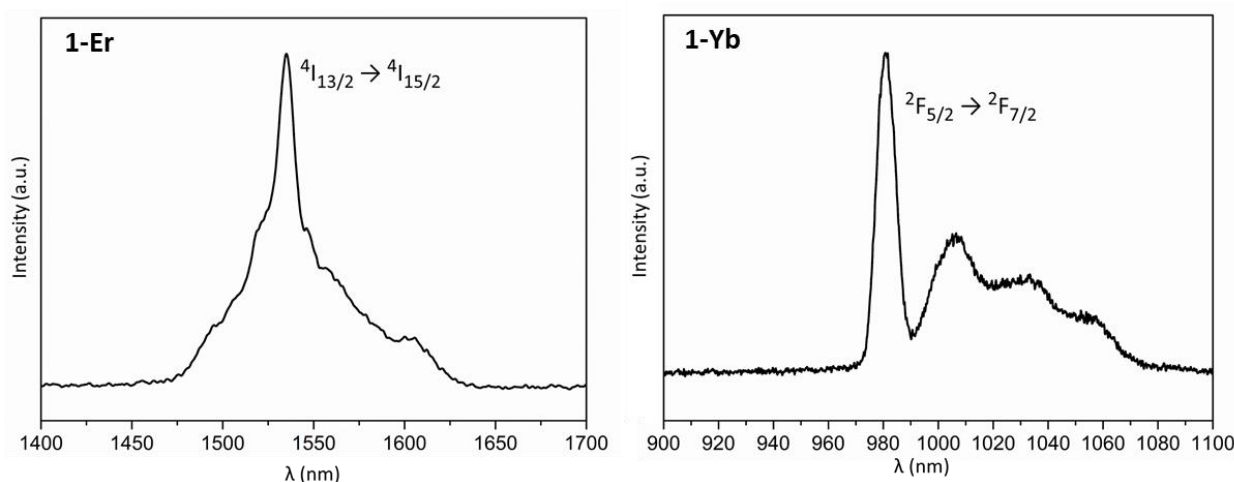


Figure 5.23. Solid state photoluminescence spectra for **1-Er** (left) and **1-Yb** (right) recorded at 20 K upon excitation at 325 nm.

5.3.4. Magnetic properties

Due to the potential of mononuclear lanthanide-substituted POMs to behave as SMMs,⁴⁵ the magnetic properties of **1-Ln** were studied in detail. Direct current (dc) magnetic susceptibilities were measured in the 2-300 K temperature range under a magnetic field of 1 kOe. Besides, field dependent ($H=0-7$ T) magnetization measurements were performed at low temperatures (2-10 K). The temperature dependence of the $\chi_M T$ product for **1-Ln** (Ln = Sm to Yb; χ_M is the molar susceptibility per Ln^{III} atom) and the magnetization vs field plots registered at 2 K are shown in Figure 5.24. The characteristics parameters are summarized in Table 5.7.

Table 5.7. Direct Current Magnetic Data for **1-Ln**.

	Ground-State of Ln ^{III} ion ^a	$\chi_M T$ (cm ³ K/mol)			M_s (μ_B)		
		theor. ^b 300 K	$\chi_M T$ exp. 300 K	$\chi_M T$ exp. 2 K	theor. ^c 2 K and 7 T	exp. at 2 K and 7 T	exp. at 10 K and 7 T
1-Sm	⁶ H _{5/2} , $g_J = 2/7$	0.09	0.33	0.04	0.71	0.21	0.05
1-Eu	⁷ F ₀ , $g_J = 0$	0	1.14	0.016	0	0.08	0.08
1-Gd	⁸ S _{7/2} , $g_J = 2$	7.88	7.88	7.90	7.0	6.99	5.77
1-Tb	⁷ F ₆ , $g_J = 3/2$	11.82	11.28	8.04	9.0	5.99	5.78
1-Dy	⁶ H _{15/2} , $g_J = 4/3$	14.17	14.24	10.70	10.0	5.41	5.20
1-Ho	⁵ I ₈ , $g_J = 5/4$	14.07	14.53	5.48	10.0	5.92	5.74
1-Er	⁴ I _{15/2} , $g_J = 6/5$	11.48	10.85	5.99	9.0	6.22	5.99
1-Tm	³ H ₆ , $g_J = 7/6$	7.14	7.09	6.10	7.0	3.77	3.51
1-Yb	² F _{7/2} , $g_J = 8/7$	2.57	1.95	1.54	4.0	1.89	1.40

$${}^b J = L - S \text{ (Sm, Eu)}; J = L + S \text{ (Tb - Yb)}; g_J = \frac{3}{2} + \frac{S(S+1) - L(L+1)}{2J(J+1)}$$

$${}^b \chi_M T = \frac{N\beta^2}{3k} \{g_J^2 J(J+1)\} \quad {}^b M_s = g_J J N \mu_B$$

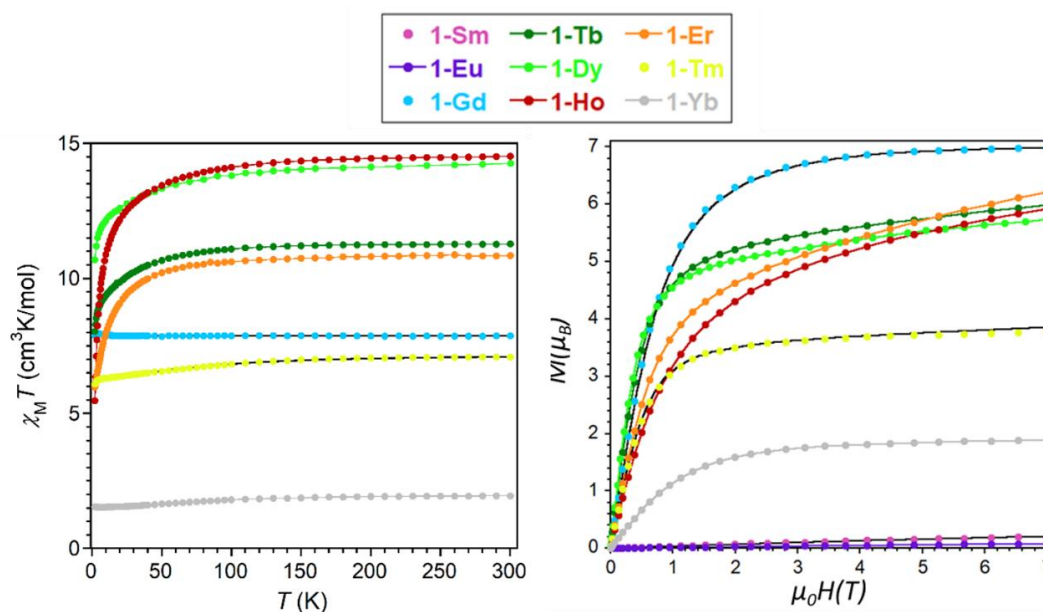


Figure 5.24. Left: Temperature dependence of the $\chi_M T$ product at 1000 Oe for complexes **1-Ln**. Right: Field dependent magnetization plots at 2 K for complexes **1-Ln**. The black solid lines represent the fitting discussed in the text. The rest of the lines are a guide for the eye.

First, the $\chi_M T$ value for **1-Sm** was found to be $0.33 \text{ cm}^3\text{K/mol}$ at 300 K, which is higher than the expected value of $0.09 \text{ cm}^3\text{K/mol}$ for a free ion with $J = 5/2$ and $g = 2/7$ (Figure 5.25). The observed behavior, though, can be ascribed to the presence of thermally populated excited states, which contribute to the magnetic susceptibility of the compound. For free Sm^{3+} and Eu^{3+} ions, the energy gap that separates the ground state from the first excited state is lower than in other ions. This favors the population of the first excited states and, consequently, the values reached by $\chi_M T$ are higher than the calculated ones at high temperatures. In the case of Sm^{III} ion, this means that the population on the first excited $J = 7/2$ state cannot be ignored. On the contrary, upon cooling, the $\chi_M T$ product goes down continuously to reach a value of $0.04 \text{ cm}^3\text{K/mol}$ at 2K. This decrease can be a consequence of the crystal field splitting of the ground state ($J = 5/2$), as it mainly affects to magnetic properties showed at low temperatures.⁴⁶

Field dependent magnetization measurements in the presence of a magnetic field $H = 0\text{-}7 \text{ T}$ and at different temperatures ($T = 2\text{-}10 \text{ K}$) represented in Figure 5.26, reveal a clear dependence of the curves with temperature, in which the highest magnetization value ($0.21 \mu_B$) is obtained at the lowest measured temperature. In this case, this value is lower than the value expected for a free Sm^{III} ion ($0.71 \mu_B$) (Table 5.7), probably due to: i) the splitting of the ground state by crystal field effects and, ii) second order Zeeman effects derived from the mixing of the ground and first excited states.

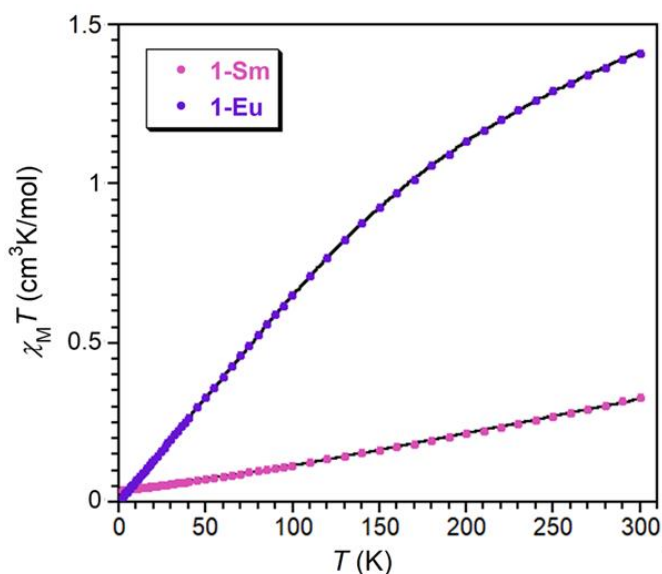


Figure 5.25. Temperature dependence of the $\chi_M T$ product at 1000 Oe for **1-Sm** and **1-Eu**. Black solid lines represent the best fit to the magnetic data.

The consideration of crystal field splitting effects in the magnetic behavior of **1-Sm** leads to a Hamiltonian that contains nine crystal field parameters (B_2^0 , B_2^2 , B_4^0 , B_4^2 , B_4^4 , B_6^0 , B_6^2 , B_6^4 , and B_6^6 , for a C_{2v} symmetry),⁴⁷ which can be simplified into the following equation to avoid over-parametrization:

$$H_{CF} = \sum (B_2^0 O_2^0 + B_4^0 O_4^0 + B_6^0 O_6^0) \quad (\text{Eq. 5.3})$$

where the O_k^q terms are equivalent Stevens operators, which are a function of the angular moments (e.g., $O_2^0 = 3L_z^2 - L^2$). Thus, Eq. 5.3 assumes a higher symmetry for the 4f center, and only considers the axial distortions and neglects transversal operators in order to be simplified.⁴⁸ The magnetic susceptibility and magnetization data were simultaneously fitted by using the Phi program⁴⁹ to the above equation, in which the spin-orbit coupling constant was fixed to the 281 cm^{-1} value estimated from luminescence studies. The best fit of the data yielded $B_2^0 = 4.997$, $B_4^0 = -0.243$, and $B_6^0 = -0.00389 \text{ cm}^{-1}$, which suggest that $M_J = \pm 1/2$ is the ground state and that the $M_J = \pm 5/2$ and $M_J = \pm 3/2$ excited states are located 153 and 310 cm^{-1} above the ground state, respectively (Figure 5.26). These results are comparable to those calculated from luminescence spectra, which places the energy levels of the first excited states at 125 and 272 cm^{-1} , respectively. Additionally, the first doublet of the first excited state ($J = 7/2$, $M_J = \pm 1/2$) is also located 1107 cm^{-1} above the ground state. A more specific representation of the crystal field splitting is displayed in Figure A4.10 in the Appendix 4.

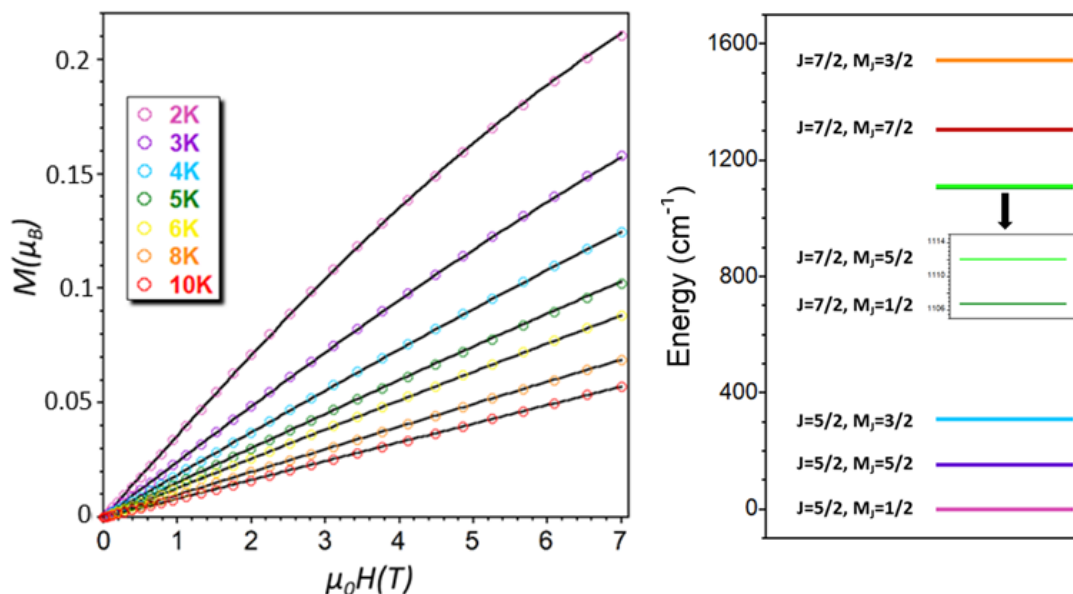


Figure 5.26. Left: Field dependent magnetization curves at different temperatures ($T = 2\text{--}10\text{ K}$) for **1-Sm**. The black lines represent the fittings discussed in the text. Right: energy level diagram for **1-Sm**.

1-Eu derivative show a similar behavior as **1-Sm**, although Eu^{III} ions should show a non-magnetic behavior as the total angular momentum is $J = 0$. Nevertheless, these ions usually present a weak magnetic response, which is normally originated by a combination between the ground state (7F_0) and the first excited state (7F_1). As mentioned before, the separation between these two levels is lower than in other ions. This behavior is known as Van Vleck paramagnetism, and it is characterized by a constant value of magnetic susceptibility at low temperatures.⁵⁰

For **1-Eu**, the $\chi_{\text{M}}T$ product at 300 K ($1.41\text{ cm}^3\text{K/mol}$) is also higher than the expected $0\text{ cm}^3\text{K/mol}$ value, although it is a common value for this ion due to the presence of thermally populated excited states (Figure 5.25). Upon cooling, the $\chi_{\text{M}}T$ product decreases continuously to $0.016\text{ cm}^3\text{K/mol}$ at 2K, which is in good agreement with an increase in the population of the $J = 0$ ground state. In the χ_{M} vs T plot (Figure 5.27) the expected Van Vleck paramagnetism can be noticed at temperatures lower than 100 K. At $T < 10\text{ K}$, however, a small paramagnetic contribution is detected, which can be probably due to a small presence of Eu^{II} ($J = 7/2$). The magnetic susceptibility curves (Figures 5.25 and 5.27) can be well modeled by an equation proposed by Kahn⁵¹ that correlates the energy of the J states with the spin-orbit coupling parameter (λ), affording $\lambda = 321\text{ cm}^{-1}$ and $\delta = 0.04\%$ (δ being the percentage of Eu^{II} impurities). This value is in good agreement with that subtracted from luminescent measurements $\lambda = 310\text{ cm}^{-1}$.

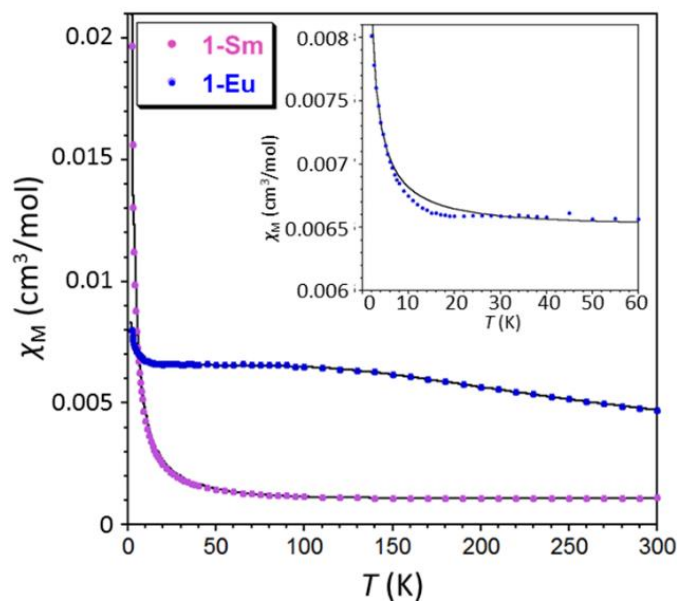


Figure 5.27. Temperature dependence of the magnetic susceptibility (χ_M) at 1000 Oe for **1-Sm** and **1-Eu**. Black solid lines represent the best fit to the magnetic data.

The calculated spin-orbit coupling value for **1-Eu** suggest that the first excited state ($J=1$) is located at around 321 cm^{-1} above the ground state $J=0$ (Figure 5.28), which implies that the magnetic contribution of that first excited state cannot be neglected. On the other hand, magnetization measurements between 2 and 10 K reveal temperature independent curves, which reach a value that is very close to $0.084 \mu_B$ at $7 T$ at all of the studied temperatures (Figure 5.28). The dependence with the field is practically linear, and no saturation is observed.

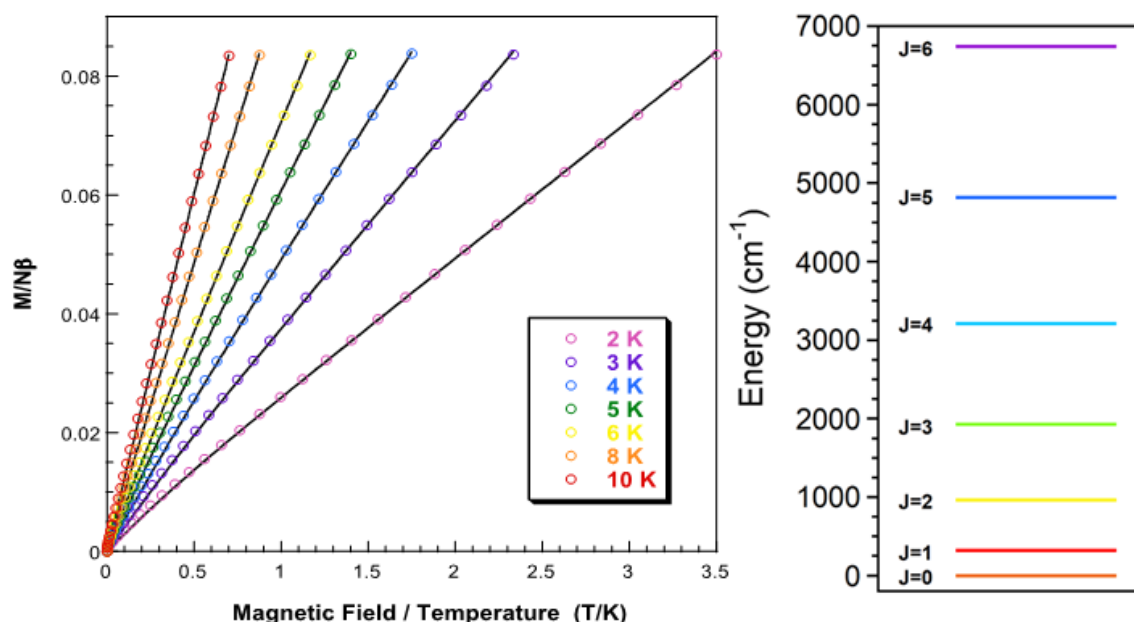


Figure 5.28. Left: Reduced field dependent magnetization curves at different temperatures for **1-Eu**. Black solid lines represent the best fit to the magnetic data. Right: Energy level diagram for **1-Eu**.

Moving to **1-Gd**, the ground state of trivalent Gd ion is $^8S_{7/2}$, with an electronic ground state presenting $L = 0$, which means that there is no first order orbital contribution. Therefore, Gd^{III} compounds should present isotropic magnetic behaviors. The experimentally observed anisotropy in some cases is usually ascribed to the interactions with neighboring ions favored by the large magnetic moment of this ion. However, crystal field effects due to distortion of the ion environment can facilitate a small mixing between the ground state and the first excited states, which leads to a second order single-ion anisotropy. In this way, the degeneracy of the four Kramer doublets of the ground octet is broken even in the absence of a magnetic field (*zero-field splitting, ZFS*).

The existence of an appreciable zero-field splitting in **1-Gd** has been confirmed by EPR spectroscopy (Figure 5.29). As usually occurs in Gd^{III} compounds the spin-lattice relaxation time is long enough that EPR signals can be easily detected at room temperature, contrary to what happens with the rest of the Ln(III) ions. Notwithstanding, the spectra are rather complex, with a high number of lines (*Fine Structure*) which reflects the perturbation caused by the ligands on the electronic states of the Gd^{III} ion. The Q-band spectrum has much better resolution and could be successfully fitted using the following Hamiltonian;

$$H = H_{Zeeman} + H_{CF} = g\beta BS + D \left[S_z^2 - \frac{1}{3} S(S+1) \right] + E(S_x^2 - S_y^2) \quad (\text{Eq. 5.4})$$

where β is the electronic Bohr magneton, B is the Raman Relaxation parameter, S is the spin and D and E are the axial and equatorial parameters of the zero-field splitting, which are related to the second-order crystal field parameters B_2^0 ($D = 3 B_2^0$) and B_2^2 ($E = B_2^2$). The best fitting to the spectrum yielded $D = 0.0802 \text{ cm}^{-1}$, $E = 0.0231 \text{ cm}^{-1}$, $g_x = 1.990$, $g_y = 1.986$ and $g_z = 1.985$. The values of D and E are in good agreement with those found in the literature for analogous systems⁵². It should be noted that the sign of the D and E parameters cannot be deduced from this study since the thermal dependence of the relative intensities is negligible between 5 and 300 K. Thus, it cannot be determined whether the ground state is the doublet $\pm 1/2$, as usually occurs, or the doublet $\pm 7/2$.

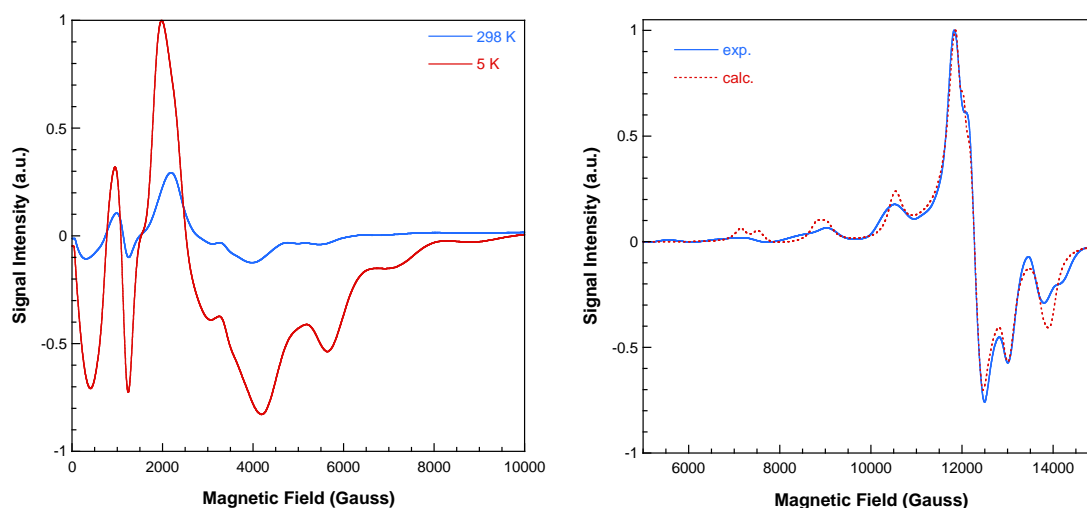


Figure 5.29. EPR spectra collected for **1-Gd**. Left: X-band. Right: Q-band.

1-Gd displays a nearly constant $\chi_M T$ value of *ca.* $7.9 \text{ cm}^3\text{K/mol}$ (Figure 5.30), close to the expected $7.88 \text{ cm}^3\text{K/mol}$ for a free ion with 7 unpaired electrons without orbital contribution to the magnetic moment. Below 10 K the $\chi_M T$ value rises slightly, up to a value of 7.98 at 4 K. As the shortest $\text{Gd}^{\text{III}}\cdots\text{Gd}^{\text{III}}$ distance is of around 8 \AA , and the Gd^{III} center is well isolated from crystal lattice, this behavior could be most likely due to the presence of impurities. But it could also be a consequence of the ZFS if the lowest energy doublet is $\pm 7/2$. The inverse of the magnetic molar susceptibility follows a Curie-Weiss law with $C_m = 7.87 \text{ cm}^3\text{K/mol}$ and $\theta = +0.1 \text{ K}$.

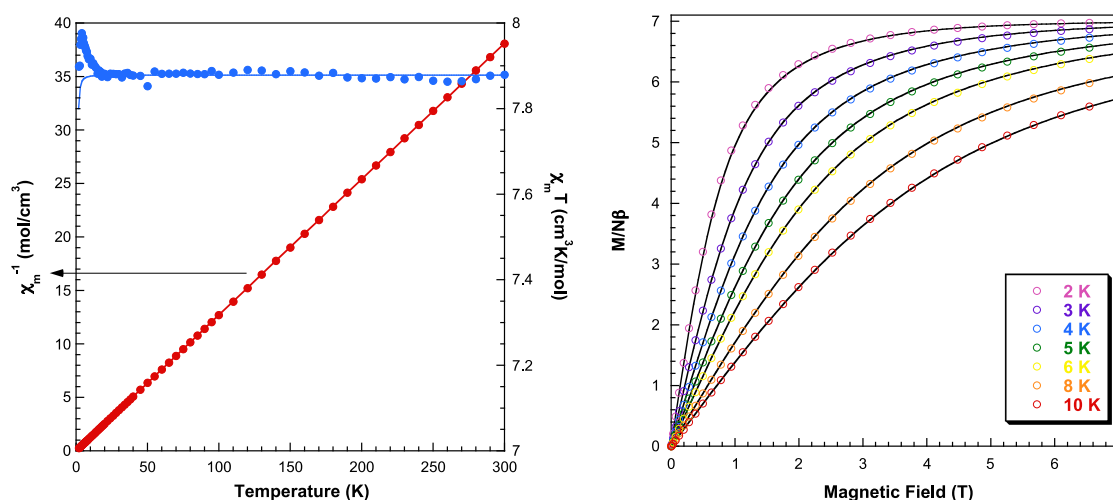


Figure 5.30. Left: Temperature dependence of the reciprocal magnetic susceptibility and the $\chi_M T$ product for **1-Gd**. Right: Field dependent magnetization curves at different temperatures. Solid lines represent the calculated curves with the zero-field splitting parameters deduced from the EPR spectra.

Field dependent magnetization data have been recorded at several temperatures between 2 and 10 K for **1-Gd**. The magnetization saturates at very low temperatures and high fields, as expected for non-interacting Gd^{III} ions (Figure 5.30). At 2 K, the magnetization grows rapidly with the applied field and practically reaches its theoretical saturation value

CHAPTER 5

of $6.99 \mu_B$ for a 7 T field. The reduced magnetization curves (M vs H/T) overlap between 2 and 10 K indicating that the magnetic anisotropy is very low in good agreement with the small values of D and E deduced from the EPR spectra. Using these values, both the susceptibility and magnetization curves can be adjusted reasonably well. Thus, according to these fitting, the ground state is fundamentally constituted by the $\pm 1/2$ doublet (71%) with a significant contribution of the $\pm 3/2$ doublet (25%) and a minor contribution of the $\pm 5/2$ doublet (4%). The first excited state is only 0.39 cm^{-1} above the ground state (Figure 5.31).

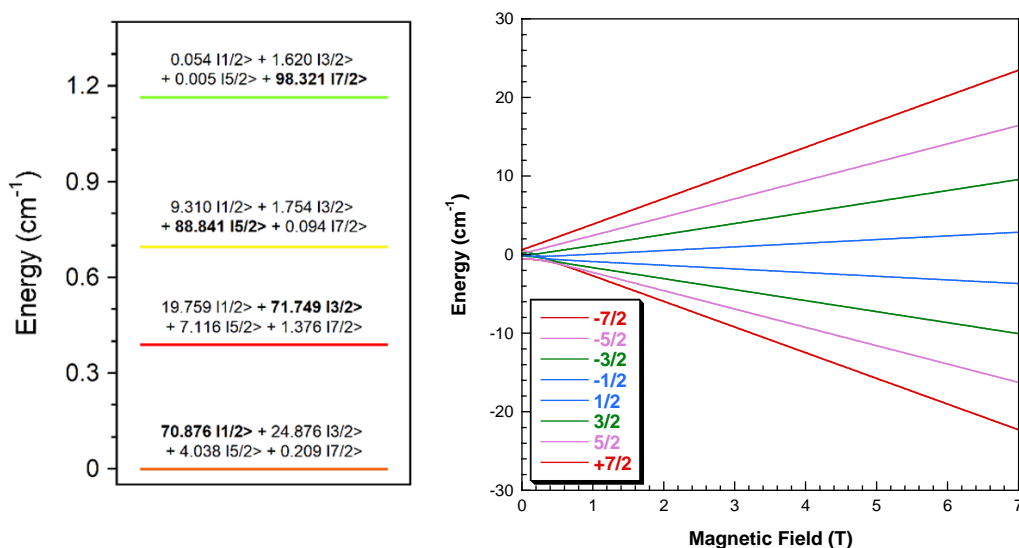


Figure 5.31. Left: Energy level diagram for **1-Gd**. Right: Zeeman splitting.

The χ_{MT} products of the remaining compounds (**1-Tb** to **1-Yb**) at room temperature (Figure 5.24 and Table 5.7) are close to the expected values for independent trivalent lanthanide ions by the free-ion approximation, which confirms that the ground states falls much lower in energy than the first excited states, thus, no significant contribution of the first excited state is considered. For instance, the theoretical spin-orbit coupling constant is near 2000 K for Tm^{III} , thus, the population of the first excited state should not be relevant in the magnetic properties of a compound containing this ion, and the magnetization and susceptibility values at room temperature should be closer to those theoretically calculated. However, in all cases the effective magnetic moment decreases continuously when lowering the temperature and sometimes, even abruptly below 100 K, as seen for **1-Tb**, **1-Dy**, **1-Ho** and **1-Er** derivatives. While the statistical population of the M_J sublevels of the ground term leads to the fulfilment of the free-ion approximation at room temperature, the splitting of the ground term by the ligand crystal field at low temperatures results in a decrease in the χ_{MT} values, and causes deviations from the Curie-Weiss law.⁴⁷ Such splitting and the resulting magnetic anisotropy are also responsible for the low magnetization values observed at 2 K and 7 T (Figure 5.24 and 5.32). In these curves, it seems that the magnetization is almost saturated at the lowest temperature (2 K) with the highest applied field; nevertheless, the experimental M_{sat} values are approximately

half of these expected for isolated ions. Upon increasing the temperature to 10 K, the dependence of the magnetization with the field is smoother. The reduction of the maximum magnetization value with increasing temperature is comparatively greater for the **1-Gd** and **1-Yb** compounds than for the rest.

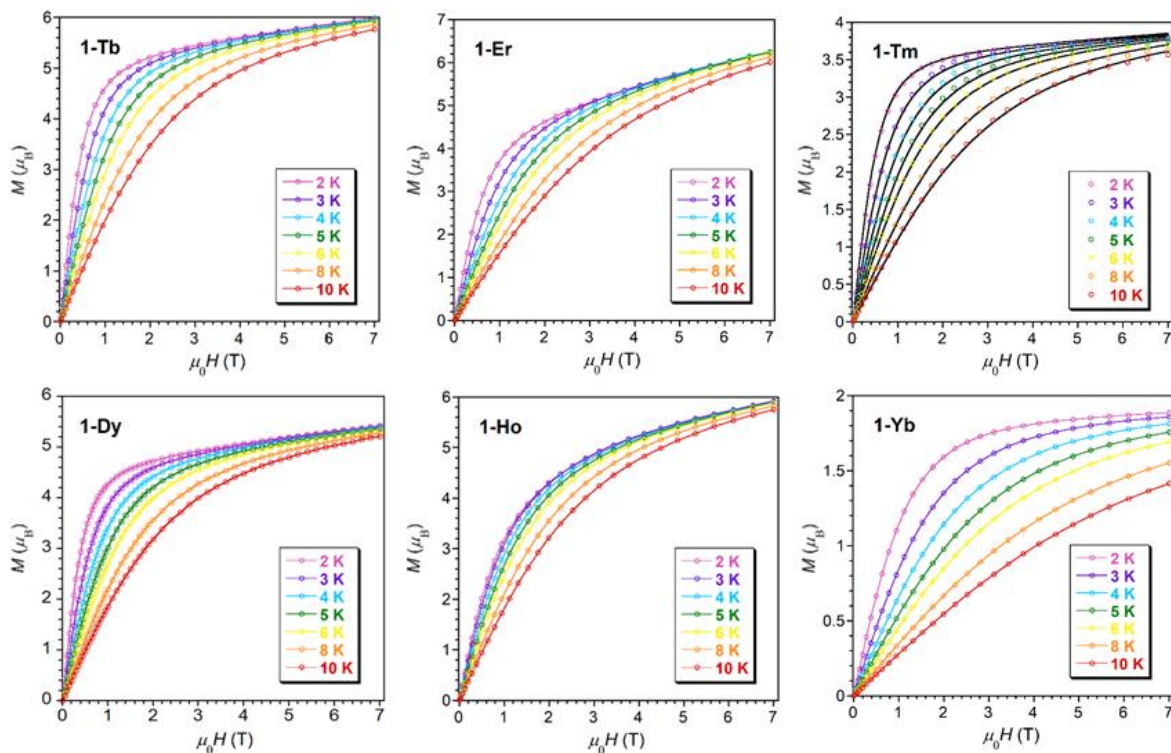


Figure 5.32. Field dependent magnetization curves at different temperatures for **1-Ln**. Black lines represent the fitting discussed in the text. The rest of the lines are a guide for the eye.

EPR spectra recorded at 4.2 K demonstrate the strong magnetic anisotropy induced by the ligand crystal field in the ground state of these compounds. In this way, **1-Dy** and **1-Er** exhibit spectra with the characteristic of an axial g tensor with perpendicular g values higher than 10 (Figure 5.33).

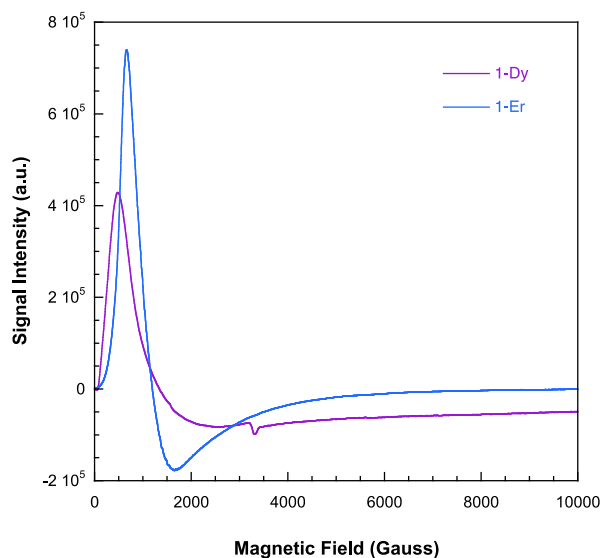


Figure 5.33. X-band EPR spectra for **1-Dy** and **1-Er** registered at 4.2 K.

The temperature dependence of the magnetic susceptibility and magnetization curves of **1-Tm** could be simultaneously fitted considering Eq. 5.3 and assuming the spin-orbit coupling of 1314 cm^{-1} , corresponding to the free-ion. In the process of fitting these parameters, the transversal components of the crystal field have not been considered in order to avoid over-parametrization, as in **1-Sm**. The best fitting with the Phi program leads to $B_2^0 = -1.529$, $B_4^0 = -0.0345$, and $B_6^0 = 0.000964 \text{ cm}^{-1}$ (Figure 5.34). These values suggest that the ground state is $M_J = \pm 6$ and that the $M_J = 0$ state is approximately 23 cm^{-1} above it, followed by ± 5 , ± 1 , ± 2 , ± 4 and ± 3 states at 51.8 , 69.8 , 176.5 and 209.3 cm^{-1} , respectively (Figure 5.35). The distribution of the energy levels found for **1-Tm** is similar to those observed in the literature for other Tm-based compounds.⁵³ Attempts to use the same methodology to fit the DC magnetic curves for the rest of the compounds (**1-Tb**, **1-Dy**, **1-Ho**, **1-Er** and **1-Yb**) were no conclusive because as they did not provide unique solutions.

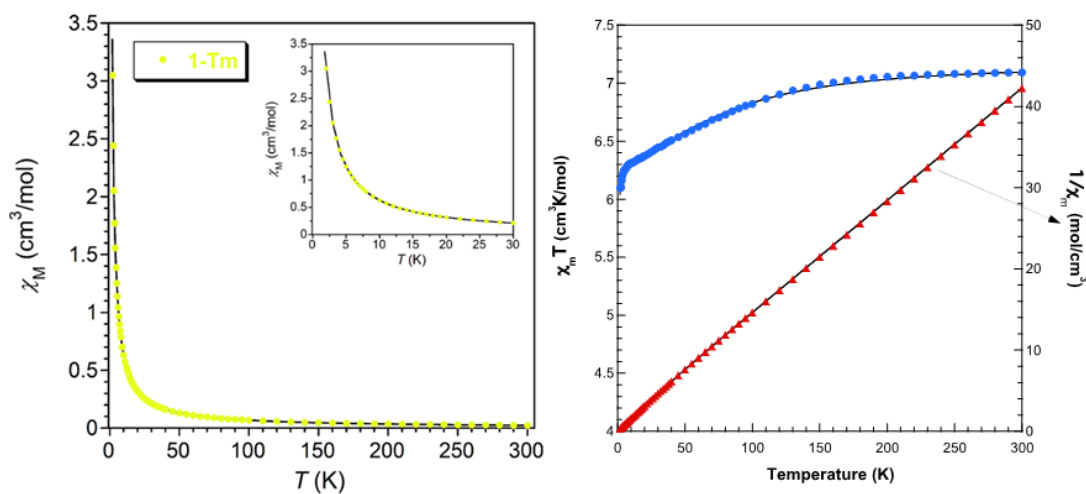


Figure 5.34. Temperature dependence of the magnetic susceptibility (χ_M) for **1-Tm**. The black solid line represents the best fit to the magnetic data as described in the main text. Right: Energy level diagram for **1-Tm**.

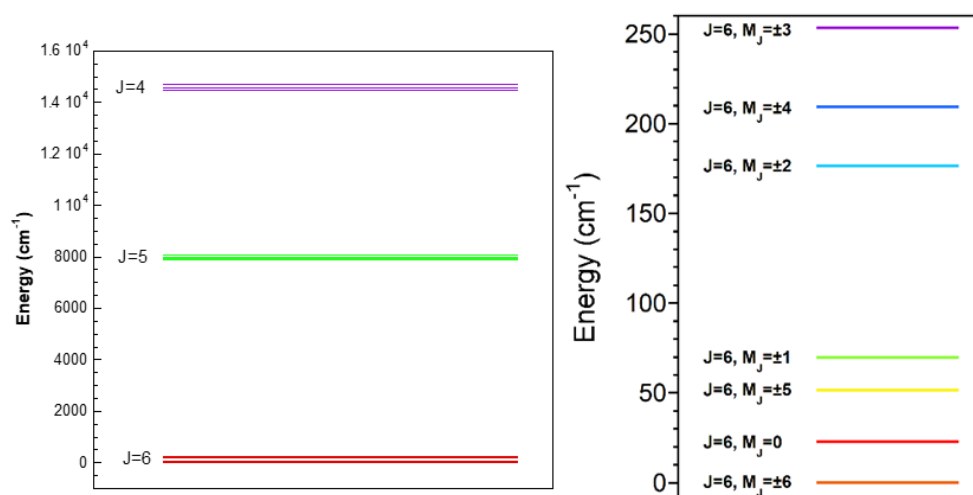


Figure 5.35. Energy level diagrams for **1-Tm**.

Additionally, alternating current magnetic susceptibility measurements were performed in order to know if the strategy of generating hybrids by grafting Ln^{III} containing complexes into lacunary-sites of the POM could lead to slow relaxation of magnetization. Dynamic *ac* data was collected for all **1-Ln** samples (except **1-Lu**), but only **1-Gd** and **1-Yb** showed a well-marked maxima in the out-of-phase susceptibility (χ_M''), below 6 K and in the presence of a 1000 Oe external magnetic field. No contribution to χ_M'' was observed at zero applied magnetic field ($H = 0$). This behavior implies that these two Gd^{III} and Yb^{III} derivatives show slow relaxation of magnetization (Figures 5.36 and 5.37). According to these results, it is demonstrated that the **1-Yb** derivative can be regarded as the first POM-based system with simultaneous NIR emission and slow magnetic relaxation behavior.

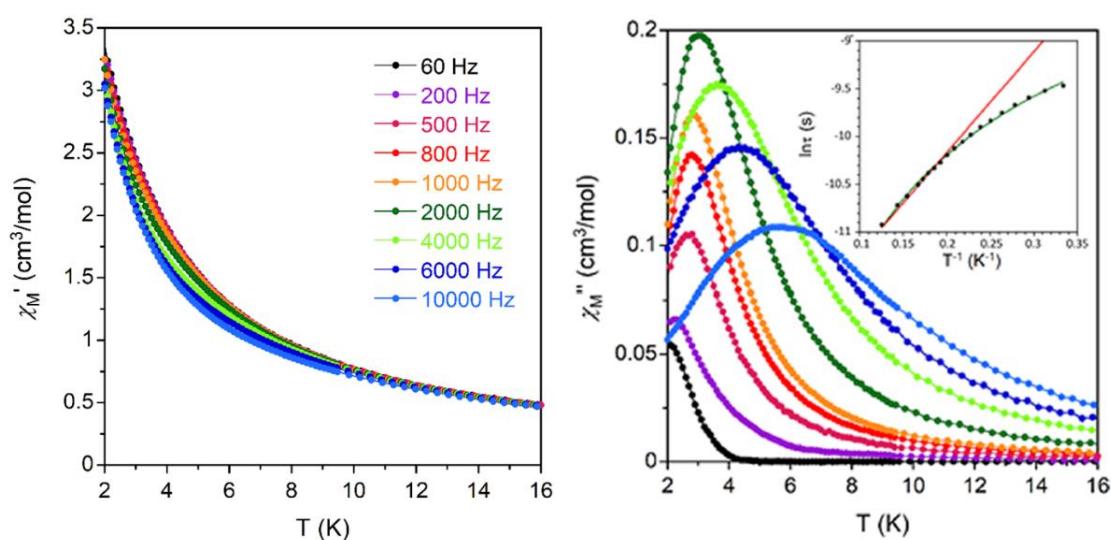


Figure 5.36. Temperature dependence of the in-phase (χ_M' , left) and out-of-phase (χ_M'' , right) components of the *ac* susceptibility for **1-Gd** under an external field of 1000 Oe. Inset: Arrhenius plot of relaxation times of **1-Gd** (red line) and best fit to Eq. 5.7 (green line).

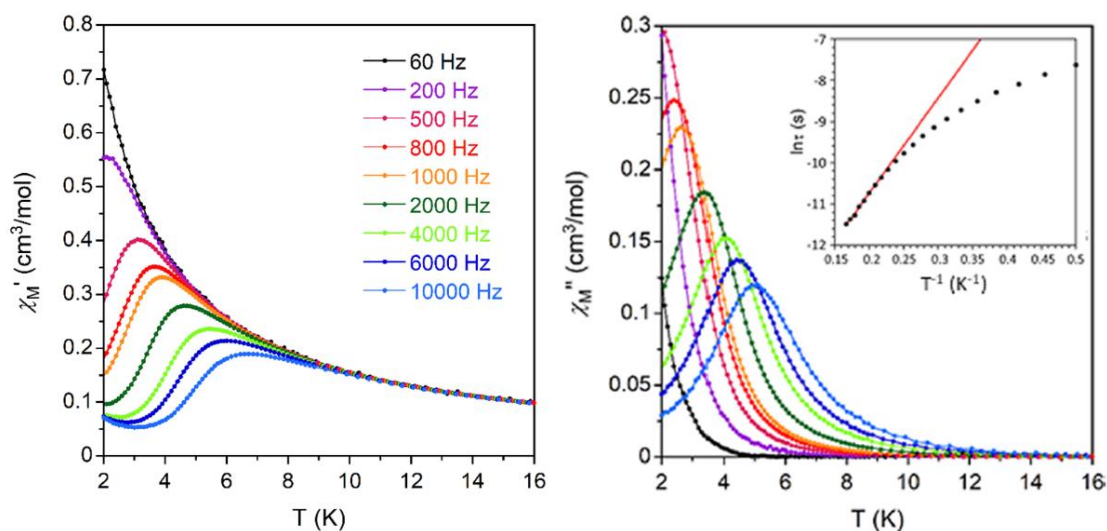


Figure 5.37. Temperature dependence of the in-phase (χ_M' , left) and out-of-phase (χ_M'' , right) components of the *ac* susceptibility for **1-Yb** under an external field of 1000 Oe. Inset: Arrhenius plot of relaxation times of **1-Yb** (red line).

The absence of similar peaks in the other compounds (**1-Sm**, **1-Eu**, **1-Tb** to **1-Tm**) could be rationalized by considering their energy level diagrams, but unfortunately, we have not been able to determine them for all the derivatives. In the case of **1-Tm**, even if the ground state is the one with the highest J ($M_J = 6$), the first excited state is $M_J = 0$, which prevents **1-Tm** from behaving as an SMM. Actually, SMM behavior in Tm^{III} based compound have been scarcely reported.⁵⁴ For **1-Tb** we have not achieved a unique fit for all the magnetic curves, but all the partial fits indicate that the ground state doublet is the $M_J = \pm 5$ combined with the $M_J = 0$ singlet, being the first excited state ($M_J = \pm 4$) at less than 10 cm^{-1} . Despite having a high $|M_J|$ ground state, this strong quantum mixture allows the system to relax, preventing the **1-Tb** complex from behaving as a SMM. The **1-Dy** derivative also displays χ_M'' signals with no maxima above 2 K (Figure 5.38) and little frequency dependence,^{19a} even if Dy^{III}-containing compounds with similar geometry have been reported before as systems with slow relaxation of magnetization.⁵⁵ The absence of any shorter Ln–O bond length in the LnO₈ coordination spheres in **1-Ln** is not appropriate for the lanthanide ions to display a ligand field that favors an axial ground state. This fact usually prevents lanthanide ions with oblate electron density such as Dy and Tb from behaving as SMMs.

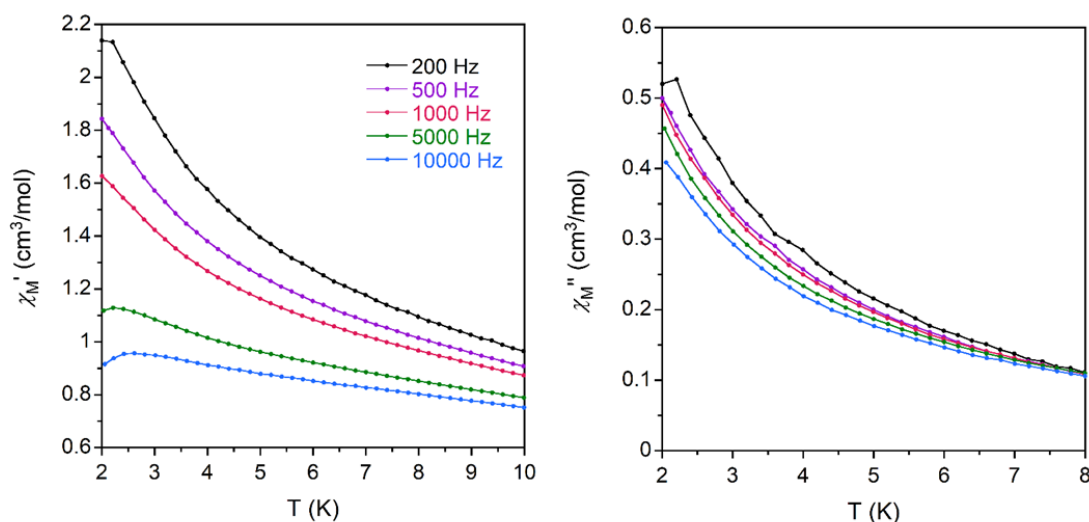


Figure 5.38. Temperature dependence of the in-phase (χ_M' , left) and out-of-phase (χ_M'' , right) components of the ac susceptibility for **1-Dy** under an external magnetic field of 1000 Oe.

In order to gain insights into the relaxation mechanisms, the frequency-dependences of in-phase and out-of-phase magnetic susceptibilities and the related Argand (Cole-Cole) plots were simultaneously fitted to the Debye model (Figures 5.39-5.41), optimizing the relaxation times (τ), the distribution of relaxation times (α), and isothermal and adiabatic susceptibilities (χ_T and χ_S , respectively).⁵⁶

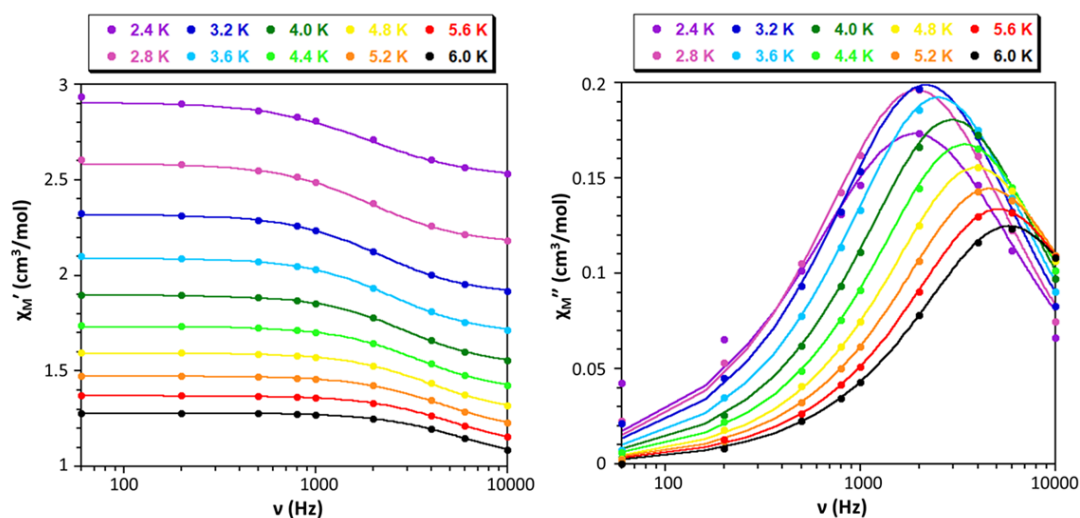


Figure 5.39. Variable temperature frequency dependence of the χ_M' (left) and χ_M'' (right) signals under 1000 Oe applied field for **1-Gd**. Solid lines represent the best fitting of experimental data to the Debye model.

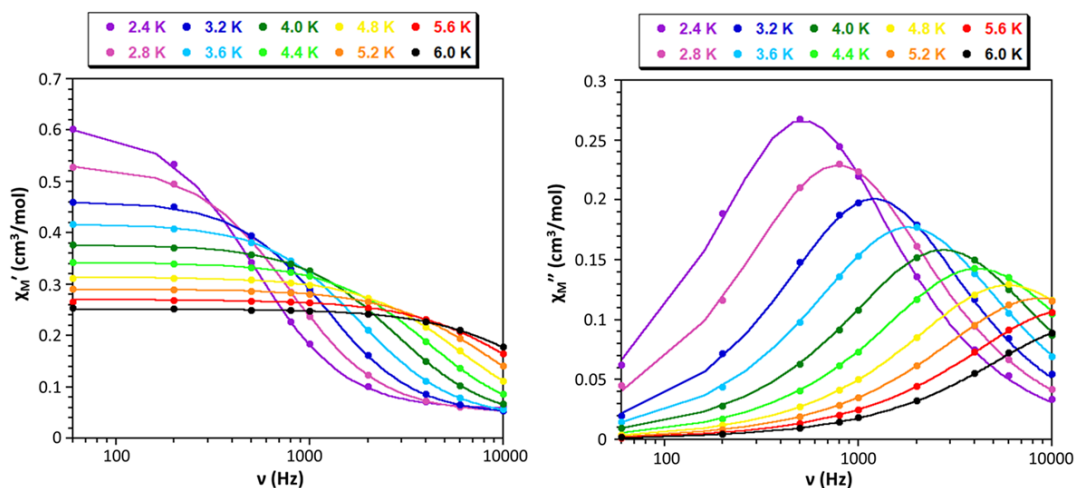


Figure 5.40. Variable temperature frequency dependence of the χ_M' (left) and χ_M'' (right) signals under 1000 Oe applied field for **1-Yb**. Solid lines represent the best fitting of experimental data to the Debye model.

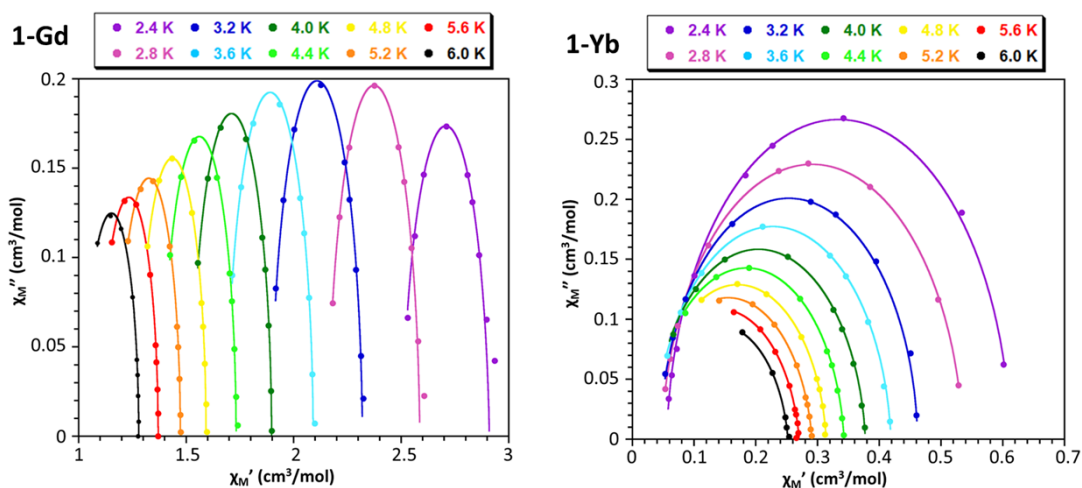


Figure 5.41. Cole-Cole plots for **1-Gd** (left) and **1-Yb** (right).

The Cole-Cole plots afford α values of 0.13 (2 K)–0.03 (6 K) for **1-Gd** and 0.04 (2 K)–0.06 (4.4 K) for **1-Yb**. These values together with the deviation of relaxation times from linearity indicate that the relaxation of the magnetization does not occur exclusively through an Orbach mechanism (Eq. 5.5). In fact, the U_{eff} (energy barrier) value obtained using Eq.5.5 for **1-Gd** (7.23 cm^{-1}) is too large for a rather isotropic ion where the energy difference between the ground and first excited state is of 0.39 cm^{-1} approximately, according to the parameters extracted from EPR measurements and direct current magnetic data (note that the Zeeman splitting of the ground state is even lower at 1000 Oe).

$$\tau^{-1} = \tau_0^{-1} \exp\left(\frac{-U_{\text{eff}}}{k_B T}\right) \quad (\text{Eq. 5.5})$$

where τ_0 is the rate of change of magnetization if there were no barrier of activation, U_{eff} the effective energy barrier of an Orbach process, T is the temperature, and k_B is Boltzmann constant.

Moreover, the relaxation times follow a power law Eq. 5.6, which leads to a $n = 1.54$ value. Such a value, significantly lower than the value expected for a Raman mechanism ($n = 7$ or 9), is between the values expected for direct processes ($n = 1$) and phonon bottleneck effects ($n = 2$), suggesting that both mechanisms could be responsible for the slow magnetic relaxation observed in **1-Gd**.⁵⁷

$$\tau^{-1} = CT^n \quad (\text{Eq. 5.6})$$

where C is a constant value and n is the Raman relaxation exponential parameter.

The application of higher external fields (*i.e.* 2000 or 3000 Oe, Figure 5.42) leads to a shift in the maximum of the χ_M'' vs T plots, in agreement with the presence of a direct mechanism. Additionally, the relaxation times reach saturation at lower temperatures upon increasing the external magnetic field (Figures 5.42 and 5.43, and Table 5.8), suggesting that QTM could be operative under certain fields. Therefore, this effect has also been considered in the final fitting of relaxation times, which follows Eq. 5.7 (inset Figure 5.36).

$$\tau^{-1} = CT^n + \tau_{QTM}^{-1} \quad (\text{Eq. 5.7})$$

where τ_{QTM} is the QTM relaxation time.

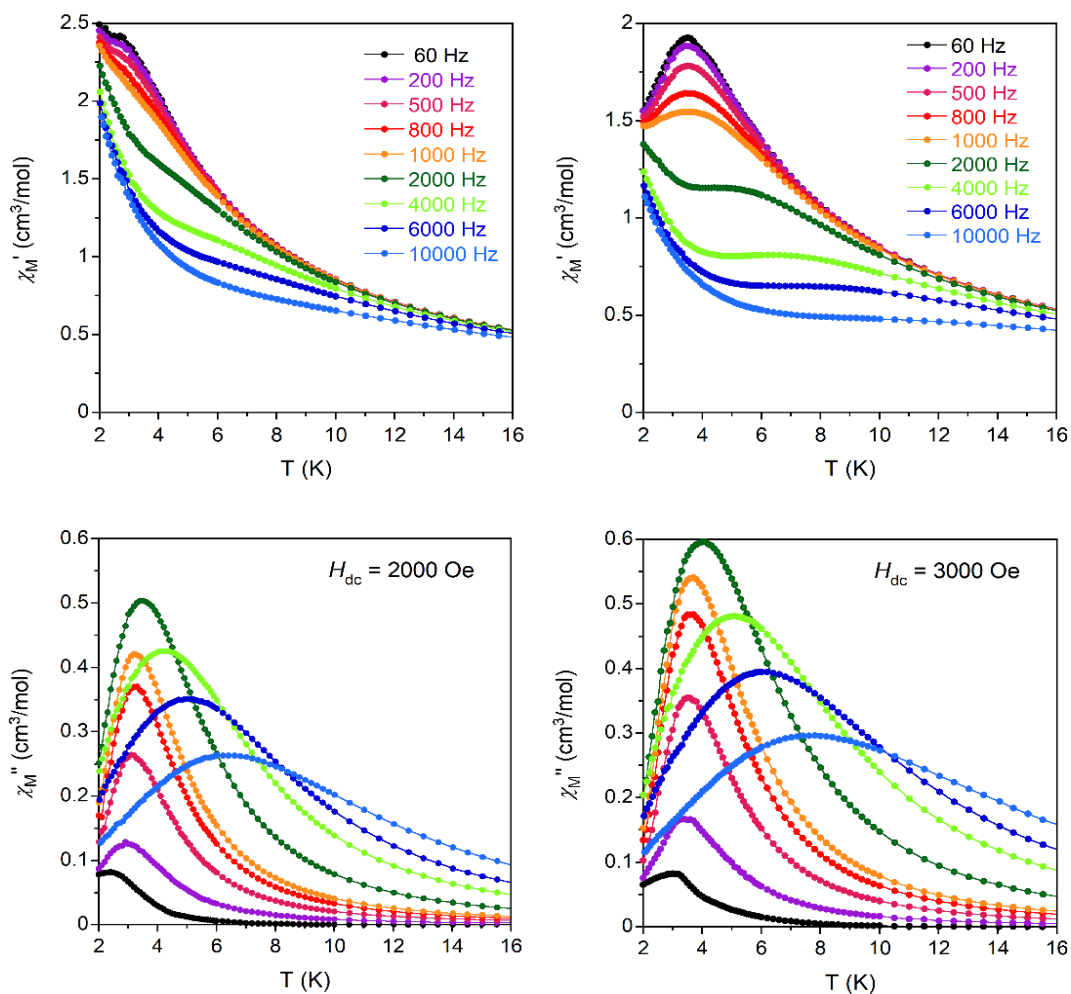


Figure 5.42. Temperature dependence of χ_M' (top) and χ_M'' (bottom) components of the *ac* susceptibility for **1-Gd** under external fields of 2000 Oe (left) and 3000 Oe (right).

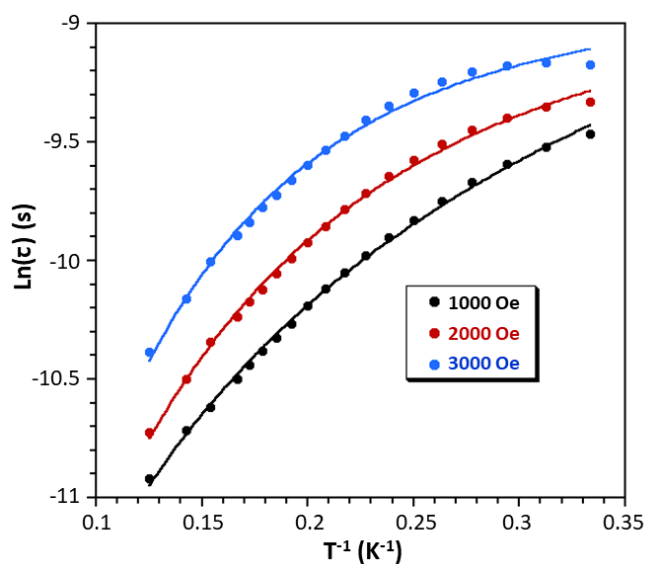


Figure 5.43. Relaxation times obtained under different applied magnetic fields for **1-Gd** with the best fitting of the data to Eq. 5.7.

Table 5.8. Values of C , n and τ_{QTM}^{-1} parameters obtained from the best fitting of relaxation times for different applied fields in **1-Gd**.

	C	n	τ_{QTM}^{-1} (s ⁻¹)
$\tau^{-1}=CT^n$ (Eq. 5.6) 1000 Oe	2217	1.54	
$\tau^{-1}=CT^n + \tau_{QTM}^{-1}$ (Eq. 5.7) 1000 Oe	1470	1.73	2540
2000 Oe	348	2.28	6474
3000 Oe	98	2.69	7144

In conclusion, the Gd^{III} single ion anisotropy, due to the mixture of states originated by the spin-orbit coupling in the second order of the perturbation theory, is large enough to induce a slow relaxation at very low temperatures in **1-Gd**.

On the other hand, the U_{eff} value of 14.8 cm⁻¹ obtained for **1-Yb** is significantly lower than the separation between the ground and first states, which is 261 cm⁻¹ deduced from the energy difference between the first two peaks in the photoluminescence spectra. Thus, a Raman relaxation process could take place in this compound, as already reported in the literature for related Yb^{III}-based compounds.^{19b}

5.3.5. Solution stability

In order to transfer the interesting properties displayed by the title compounds **1-Ln** to a bulk functional material, it is important to determine whether the hybrid assembly maintains its integrity in solution prior to its immobilization in a solid surface/matrix. Therefore, the stability of our {Ln} molecular POMs in solution was investigated by means of ¹H-NMR experiments for diamagnetic **1-Lu** as well as electrospray ionization mass spectrometry (ESI-MS) for the **1-Tm** derivative.

Figure 5.44 depicts the ESI-mass spectra of a solution of **1-Tm** in H₂O/MeCN (1:1) recorded in negative ion mode at low cone voltage. Three group of signals spanning from m/z 670 to 1500 indicate the presence of the intact {Tm} anion in the freshly prepared aqueous solution. The m/z spacing between the signals and isotopic patten inspection evidence that they match well with anionic species of similar composition, but -5 (m/z 704.8 {Tm}⁵⁻), -4 (m/z 942.7, {Tm}⁴⁻), and -3 (m/z 1434.6, {Tm}³⁻) charge states.

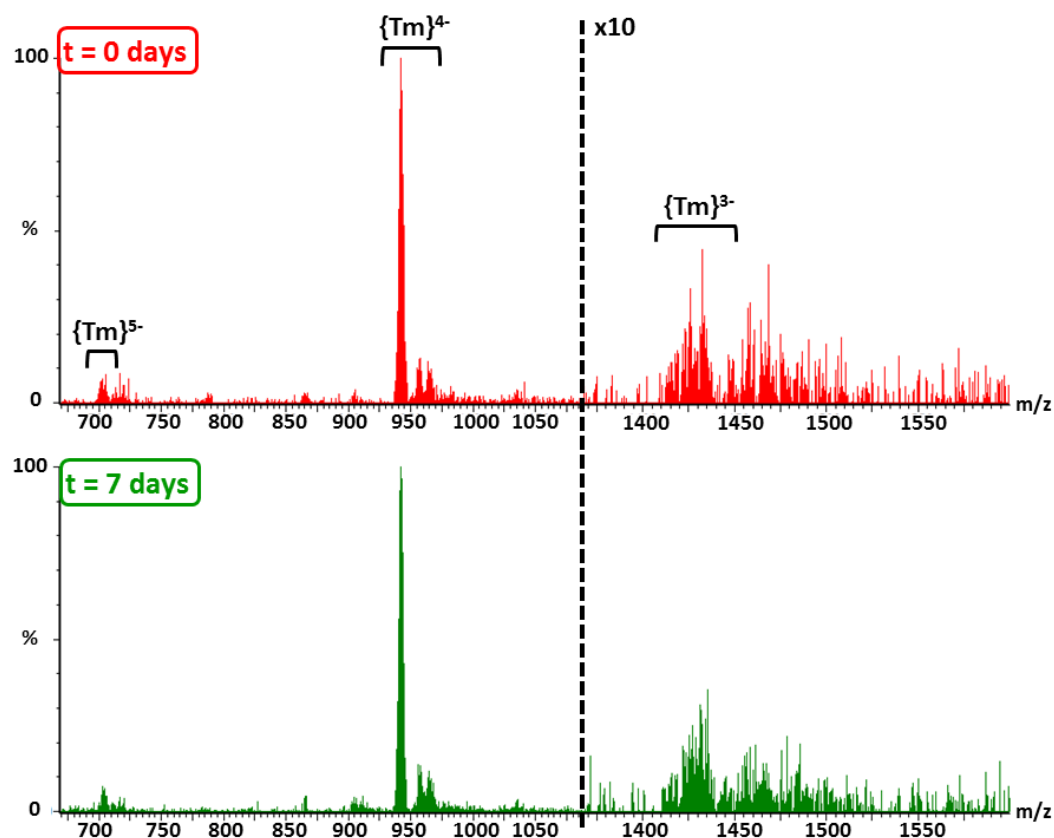


Figure 5.44. ESI-MS spectra of **1-Tm** in H₂O/MeCN (1:1) mixtures. Top, freshly prepared solution; bottom, same solution after one week. The intensity of the $m/z > 1300$ region is increased (x10) for its better visualization.

Each group of signals does not correspond to a single specific species but to a series of general formula $[\text{Tm}(\text{H}_2\text{L})(\text{SiW}_{11}\text{O}_{39}) + m\text{K}^+ + n\text{H}^+ + x\text{H}_2\text{O}]^{(5-m-n)-}$, because the high negative charge of the anion allows different extents of protonation and a variable number of associated counterion/solvent molecules to be present. This is a common fact found in the ESI-MS spectra of POM species.²⁶

Nevertheless, the experimental isotopic pattern of the most abundant group centered at m/z 942.7, compares well with that simulated for the $[\text{Tm}(\text{H}_2\text{L})(\text{SiW}_{11}\text{O}_{39}) + \text{K}^+]^{4-}$ ion, which confirms our previous assignments (Figure 5.45). The spectrum remains virtually unchanged for 1 week, and thus, it demonstrates that hybrid molecular assemblies in **1-Tm** are stable in water solution. These results can be easily extended to the remaining **1-Ln** counterparts, as indicated by the virtually identical results obtained for the **1-Tb** derivative (Figure A4.11 in the Appendix 4).

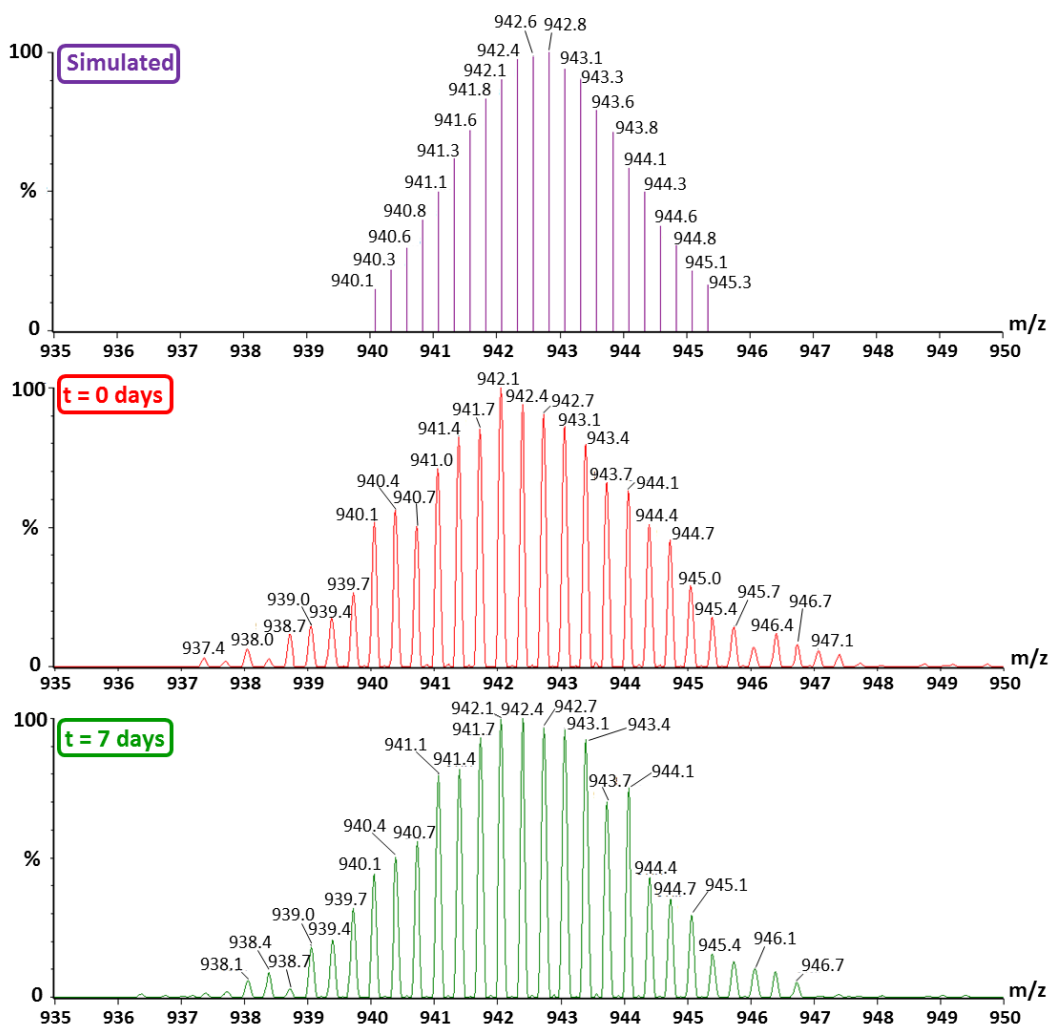


Figure 5.45. Expanded region of the most abundant signal group of the negative ESI mass spectrum for the freshly prepared solution of **1-Tm** which corresponds to the $\{\text{Tm}\}^{4-}$ series (middle), compared to that recorded one week later (bottom) and the simulated isotopic pattern for the $[\text{Tm}(\text{H}_2\text{L})(\text{SiW}_{11}\text{O}_{39}) + \text{K}^+]^{4-}$ species (top).

Immobilization of molecular $\{\text{Ln}\}$ anions could easily imply reactions in solvents other than water. Thus, their solution stability in organic media was studied by $^1\text{H-NMR}$ analyses carried out for the diamagnetic **1-Lu** derivative. Experiments were conducted in deuterated DMSO in which the H_2L ligand is soluble. Figure 5.46 compiles the spectra of the freshly prepared solution of **1-Lu** in DMSO, together with that corresponding to the H_2L ligand. The spectrum of the organic ligand is virtually identical to that recorded in CDCl_3 and shows a six-peak pattern with signals at $\delta = 2.27$ (s, 6H, N-CH_3), 2.81 (s, 4H, $-\text{CH}_2\text{CH}_2-$), 3.79 (s, 4H, $\text{Ar-CH}_2-\text{N}$); 7.64 (d, 2H, aromatic ring protons), 7.66 (d, 2H, aromatic ring protons) and 10.15 (s, 2H, $-\text{CHO}$) ppm, in good agreement with literature data.²² The coordination of the ligand to the lanthanide center in **1-Lu** does not significantly modify the positions of the signals and only small shifts ($\Delta\delta < 0.1$ ppm) can be observed upon comparison with the pristine H_2L , except for the aromatic protons which appear as only one singlet in the case of

the **1-Lu** hybrid (signals at 7.6 ppm). This fact could be related with the deprotonation of alkoxide O atoms upon coordination to lanthanide centers in line with our structural results. The additional peak of low intensity at 1.91 ppm could correspond to impurities from our acetate/acetic acid buffer solution employed in the synthesis of the complexes. Furthermore, the spectra of the freshly prepared sample of **1-Lu** and the ^1H -NMR spectra of the same sample after 7 days is virtually identical (Figure A4.12 in the Appendix 4), which indicates that the molecular hybrid POM remains stable in solution.

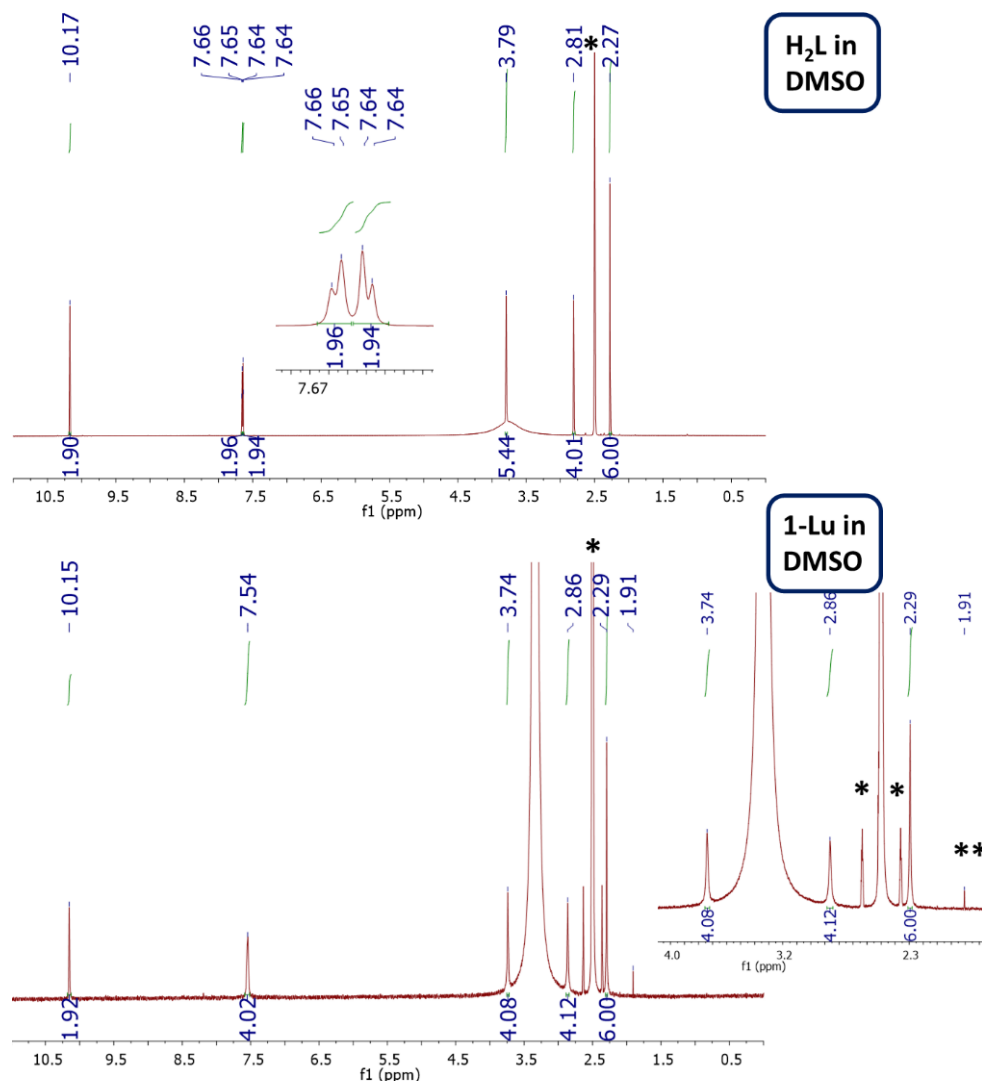


Figure 5.46. ^1H -NMR spectrum of the H_2L ligand (top) compared with that of a freshly prepared solution of **1-Lu** (bottom) in DMSO. Note that the resonance belonging to the solvent (2.50 ppm), together with its satellite peaks (2.36 and 2.63 ppm) in the spectrum of **1-Lu** (*) are pre-saturated in the spectrum of H_2L . The additional peak of low intensity at 1.91 ppm (**) could correspond to impurities from the acetate/acetic acid buffer solution employed in the synthesis of the complexes. The saturated peak at 3.30 ppm corresponds to the water molecules of hydration.

5.4. CONCLUSIONS

This work nicely exemplifies the potential of lanthanide ion/lacunary POM/aromatic multidentate organic ligand synthetic systems as dynamic libraries of building blocks with the ability to construct molecular materials with interesting optical and magnetic properties. In this chapter, the reaction of mid-to-late lanthanide(III) ions with monolacunary α -Keggin-type polyoxometalate and a compartmental organic ligand (H_2L) have resulted into ten isostructural hybrids with the general formula $K_5[Ln^{III}(H_2L)(\alpha-SiW_{11}O_{39})]\cdot 14H_2O$ ($Ln^{III} = Sm$ to Lu , **1-Ln**; $H_2L = C_{20}H_{22}Br_2N_2O_4$) which constitute some of the very scarce examples of mononuclear lanthanide complexes containing simultaneously organic and inorganic ligands. Unlike all of the metal complexes previously reported for this ligand, the empty N_2O_2 coordination site allows the folding of the organic ligand, in such a way that weak $Br\cdots Br$ and $\pi-\pi$ interactions are established between adjacent molecular units and result in supramolecular chairlike assemblies of six hybrid anions.

Compounds **1-Gd** and **1-Yb** display slow relaxation of the magnetization below ~ 6 K, which mechanistically takes place through a combination of different relaxation processes. Furthermore, the metal-centered luminescence is efficiently sensitized by the organic antenna ligand for **1-Sm** and **1-Eu** in the visible region, as well as **1-Er** and **1-Yb** in the NIR. In contrast, the quenching of the emission for **1-Tb** has been attributed to the out-of-pocket coordination mode of the lanthanide center within the POM fragment. To our knowledge, **1-Yb** compound represents the first lanthanide-containing POM-based dual magneto-luminescent material capable to exhibit simultaneous slow magnetic relaxation and NIR emission.

Finally, the stability of hybrid molecular POMs in aqueous solutions has been addressed by ESI-MS experiments, whereas similar behavior have been observed in organic DMSO medium as confirmed by 1H -NMR. Besides the multiple combinations that could arise from the accurate selection of both organic and inorganic components, the use of compartmental ligands will allow the preparation of heterometallic 3d-4f complexes. In the near future, we plan to make use of the available N_2O_2 coordination site to accommodate a transition metal ion, which might enhance the anisotropy of the system and result in improved magnetic properties.

5.5. REFERENCES

- [1] (a) Mialane, P.; Dolbecq, A.; Rivière, E.; Marrot, J.; Sécheresse, F. Functionalization of Polyoxometalates by a Negatively Charged Bridging Ligand: The Dimeric $[(\text{SiW}_{11}\text{O}_{39}\text{Ln})_2(\mu\text{-CH}_3\text{COO})_2]^{12-}$ (Ln = Gd^{III}, Yb^{III}) Complexes. *Eur. J. Inorg. Chem.* **2004**, 33-36. (b) Zhang, D.; Zhang, C.; Chen, D.; Ma, P.; Wang, J.; Niu, J. Syntheses, Structures and Properties of Dimeric Rare Earth Derivatives Based on Monovacant Keggin-Type Polyoxotungstates. *Inorg. Chim. Acta* **2012**, 391, 218-223. (c) Ma, P.; Hu, F.; Wan, R.; Huo, Y.; Zhang, D.; Niu, J.; Wang, J. Magnetic Double-Tartaric Bridging Mono-Lanthanide Substituted Phosphotungstates with Photochromic and Switchable Luminescence Properties. *J. Mater. Chem. C* **2016**, 4, 5424-5433. (d) Ma, P.; Hu, F.; Wu, H.; Liu, X.; Wang, J.; Niu, J. Luminescent Dimeric Polyoxotungstate $[\text{Ho}(\text{C}_4\text{H}_2\text{O}_6)(\alpha\text{-PW}_{11}\text{O}_{39})_2]^{16-}$ with Magnetism and Reversible Photochromism. *J. Lumin.* **2020**, 217, 116760.
- [2] Kortz, U. Rare-Earth Substituted Polyoxoanions: $[\{\text{La}(\text{CH}_3\text{COO})(\text{H}_2\text{O})_2(\alpha_2\text{-P}_2\text{W}_{17}\text{O}_{61})\}_2]^{16-}$ and $[\{\text{Nd}(\text{H}_2\text{O})_3(\alpha_2\text{-P}_2\text{W}_{17}\text{O}_{61})\}_2]^{14-}$. *J. Clust. Sci.* **2003**, 14, 205-214.
- [3] An, H.; Zhang, Y.; Hou, Y.; Hu, T.; Yang, W.; Chang, S.; Zhang, J. Hybrid Dimers Based on Metal-Substituted Keggin Polyoxometalates (metal = Ti, Ln) for Cyanosilylation Catalysis. *Dalton Trans.* **2018**, 47, 9079-9089.
- [4] (a) Mialane, P.; Dolbecq, A.; Marrot, J.; Sécheresse, F. Oligomerization of Yb(III)-Substituted Dawson Polyoxotungstates by Oxalato Ligands. *Inorg. Chem. Commun.* **2005**, 8, 740-742. (b) Zhang, S.; Wang, Y.; Zhao, J.; Ma, P.; Wang, J.; Niu, J. Two Types of Oxalate-Bridging Rare-Earth-Substituted Keggin-type Phosphotungstates $\{[(\alpha\text{-PW}_{11}\text{O}_{39})\text{RE}(\text{H}_2\text{O})_2(\text{C}_2\text{O}_4)]^{10-}$ and $\{(\alpha\text{-x-PW}_{10}\text{O}_{38})\text{RE}_2(\text{C}_2\text{O}_4)(\text{H}_2\text{O})_2\}^{3-}$. *Dalton Trans.* **2012**, 41, 3764-3772.
- [5] (a) Ritchie, C.; Moore, E. G.; Speldrich, M.; Kögerler, P.; Boskovic, C. Terbium Polyoxometalate Organic Complexes: Correlation of Structure with Luminescence Properties. *Angew. Chem. Int. Ed.* **2010**, 49, 7702-7705. (b) Ritchie, C.; Baslon, V.; Moore, E. G.; Reber, C.; Boskovic, C. Sensitization of Lanthanoid Luminescence by Organic and Inorganic Ligands in Lanthanoid-Organic-Polyoxometalates. *Inorg. Chem.* **2012**, 51, 1142-1151.
- [6] Li, F.; Guo, W.; Xu, L.; Ma, L.; Wang, Y. Two Dysprosium-Incorporated Tungstoarsenates: Synthesis, Structures and Magnetic Properties. *Dalton Trans.* **2012**, 41, 9220-9226.
- [7] Chen, H.; Sun, L.; Zhang, J.; Xiao, Z.; Ma, P.; Wang, J.; Zhang, Y.; Niu, J. Magnetic Field and Dilution Effects on the Slow Relaxation of $\{\text{Er}_3\}$ Triangle-Based Arsenotungstate Single-Molecule Magnets. *Dalton Trans.* **2020**, 49, 12458-12465.
- [8] Li, H.; Wu, H.; Wan, R.; Wang, Y.; Ma, P.; L, S.; Wang, J.; Niu, J. Utilizing the Adaptive Precursor $[\text{As}_2\text{W}_{19}\text{O}_{67}(\text{H}_2\text{O})]^{14-}$ to Support Three Hexanuclear Lanthanoid-Based Tungstoarsenate Dimers. *Dalton Trans.* **2019**, 48, 2813-2821.
- [9] Li, L.-L.; Han, H.-Y.; Wang, Y.-H.; Tan, H.-Q.; Zang, H.-Y.; Li, Y.-G. Construction of Polyoxometalates from Dynamic Lacunary Polyoxotungstate Building Blocks and Lanthanide Linkers. *Dalton Trans.* **2015**, 44, 11429-11436.
- [10] Dufaye, M.; Duval, S.; Stoclet, G.; Loiseau, T. Influence of pH on $\text{Ce}^{\text{IV}}\text{-}[\text{As}^{\text{III}}\text{W}_9\text{O}_{33}]^{9-}$ Association for the Formation of Hexanuclear Cerium(IV) Oxohydroxo-Clusters Stabilized by Trivacant Polyanions. *CrystEngComm* **2020**, 22, 371-380.
- [11] Mialane, P.; Dolbecq, A.; Lisnard, L.; Mallard, A.; Marrot, J.; Sécheresse, F. $[\epsilon\text{-PMo}_{12}\text{O}_{36}(\text{OH})_4\{\text{La}(\text{H}_2\text{O})_4\}_4]^{5+}$: The First $\epsilon\text{-PMo}_{12}\text{O}_{40}$ Keggin Ion and Its Association with the Two-Electron-Reduced $\alpha\text{-PMo}_{12}\text{O}_{40}$ Isomer. *Angew. Chem. Int. Ed.* **2002**, 41, 2398-2401.
- [12] (a) Dolbecq, A.; Mialane, P.; Lisnard, L.; Marrot, J.; Sécheresse, F. Hybrid Organic-Inorganic 1D and 2D Frameworks with ϵ -Keggin Polyoxomolybdates as Building Blocks. *Chem. Eur. J.* **2003**, 9, 2914-2920. (b) Dolbecq, A.; Mellot-Draznieks, C.; Mialane, P.; Marrot, J.; Férey, G.; Sécheresse, F. Hybrid 2D and 3D Frameworks Based on ϵ -Keggin Polyoxometallates: Experiment and Simulation. *Eur. J. Inorg. Chem.* **2005**, 3009-3018.

- [13] Cañón-Mancisidor, W. A.; Zapata-Lizama, M.; Hermosilla-Ibáñez, P.; Cruz, C.; Venegas, Yazigi, D.; Mínguez Espallargas, G. Hybrid Organic-Inorganic Mononuclear Lanthanoid Single Ion Magnets. *Chem. Commun.* **2019**, *55*, 14992-14995.
- [14] Sarwar, S.; Sanz, S.; van Leusen, J.; Nichol, G. S.; Brechin, E. K.; Kögerler, P. Phthalocyanine-polyoxotungstate lanthanide double deckers. *Dalton Trans.* **2020**, *49*, 16638-16642.
- [15] (a) Wu, H.; Yan, B.; Liang, R.; Singh, V.; Ma, P.; Wang, J.; Niu, J. An Organic Chromophore-Modified Samarium-Containing Polyoxometalate: Excitation-Dependent Color Tunable Behavior from the Organic Chromophores to the Lanthanide Ion. *Dalton Trans.* **2020**, *49*, 388-394. (b) Zapata-Lizama, M.; Hermosilla-Ibáñez, P.; Venegas-Yazigi, D.; Mínguez Espallargas, G.; Queiroz Maia, L. J.; Gasparotto, G.; De Santana, R. C.; Cañón-Mancisidor, W. A Systematic Study of the Optical Properties of Mononuclear Hybrid Organo-Inorganic Lanthanoid Complexes. *Inorg. Chem. Front.* **2020**, *7*, 3049-3062.
- [16] Fashapoyeh, M. A.; Mirzaei, M.; Eshtiagh-Hosseini, H.; Rajagopal, A.; Lechner, M.; Liu, R.; Streb, C. Photochemical and Electrochemical Hydrogen Evolution Reactivity of Lanthanide-Functionalized Polyoxotungstates. *Chem. Commun.* **2018**, *54*, 10427-10430.
- [17] Woodruff, D. N.; Winpenny, R. E. P.; Layfield, R. A. Lanthanide Single-Molecule Magnets. *Chem. Rev.* **2013**, *113*, 5110-5148.
- [18] Colacio, E. Mannich Base Ligands as Versatile Platforms for SMMs. *Top. Organomet. Chem.* **2018**, *64*, 101-162.
- [19] (a) Oyarzabal, I.; Ruiz, J.; Seco, J. M.; Evangelisti, M.; Camon, A.; Ruiz, E.; Aravena, D.; Colacio, E. Rational Electrostatic Design of Easy-Axis Magnetic Anisotropy in a Zn^{II}-Dy^{III}-Zn^{II} Single-Molecule Magnet with a High Energy Barrier. *Chem. Eur. J.* **2014**, *20*, 14262-14269. (b) Oyarzabal, I.; Artetxe, B.; Rodríguez-Diéguez, A.; García, J. A.; Seco, J. M.; Colacio, E. A Family of Acetato-Diphenoxo Triply Bridged Dimetallic Zn^{II}Ln^{III} Complexes: SMM Behavior and Luminescent Properties. *Dalton Trans.* **2016**, *45*, 9712-9726. (c) Oyarzabal, I.; Rodríguez-Diéguez, A.; Barquín, M.; Seco, J. M.; Colacio, E. The Effect of the Disposition of Coordinated Oxygen Atoms on the Magnitude of the Energy Barrier for Magnetization Reversal in a Family of Linear Trinuclear Zn-Dy-Zn Complexes with a Squareantiprism DyO₈ Coordination Sphere. *Dalton Trans.* **2017**, *46*, 4278-4286.
- [20] Feng, X.; Zhou, W.; Li, Y.; Ke, H.; Tang, J.; Clérac, R.; Wang, Y.; Su, Z.; Wang, E. Polyoxometalate-Supported 3d-4f Heterometallic Single-Molecule Magnets. *Inorg. Chem.* **2012**, *51*, 2722-2724.
- [21] Tézé, A.; Hervé, G. Early Transition Metal Polyanions. *Inorg. Synth.* **1990**, *27*, 85-96.
- [22] Yonemura, M.; Matsumura, Y.; Furutachi, H.; Ohba, M.; Okawa, H.; Fenton, D. E. Migratory Transmetalation in Diphenoxo-Bridged Cu^{II}M^{II} Complexes of a Dinucleating Macrocyclic with N(amine)₂O₂ and N(imine)₂O₂ Metal-Binding Sites. *Inorg. Chem.* **1997**, *36*, 2711-2717.
- [23] Caillet, P. Composition of Alkali Tungstate-Tungstic Anhydride Systems. *CRH Acad. Sci.* **1963**, *256*, 1986-1989.
- [24] (a) Spitsyn, V. I.; Trunov, V. K. Contribution to Study of Double Potassium Tungstates and Rare-Earth Elements (La-Lu). *Dokl. Chem.*, **1968**, *183*, 978. (b) Majer, A. A.; Provotorov, M. V.; Balashov, V. A. Double Molybdates and Tungstates of the Rare Earth and Alkali Metals. *Russ. Chem. Rev.* **1973**, *42*, 822-833.
- [25] AlDamen, M. A.; Cardona-Serra, S.; Clemente-Juan, J. M.; Coronado, E.; Gaita-Ariño, A.; Martí-Gasaldó, C.; Luis, F.; Montero, O. Mononuclear Lanthanide Single Molecule Magnets Based on the Polyoxometalates [Ln(W₅O₁₈)₂]⁹⁻ and [Ln(β₂-SiW₁₁O₃₉)₂]¹³⁻ (Ln^{III} = Tb, Dy, Ho, Er, Tm and Yb). *Inorg. Chem.* **2009**, *48*, 3467-3479.
- [26] Artetxe, B.; Reinoso, S.; San Felices, L.; Lezama, L.; Gutiérrez-Zorrilla, J. M.; García, J. A.; Galán Mascarós, J. R.; Haider, A.; Kortz, U.; Vicent, C. Cation-Directed Dimeric versus Tetrameric Assemblies of Lanthanide-Stabilized Dilacunary Keggin Tungstogermanates. *Chem. Eur. J.* **2014**, *20*, 12144-12156.

- [27] Crystal data: $\text{CsK}_2\text{Na}_2[\text{Dy}(\alpha\text{-SiW}_{11}\text{O}_{39})(\text{C}_{20}\text{H}_{22}\text{Br}_2\text{N}_2\text{O}_4)] \cdot n\text{H}_2\text{O}$ (**2-Dy**): $\text{C}_{20}\text{H}_{56}\text{Br}_2\text{CsDyK}_2\text{N}_2\text{Na}_2\text{O}_{60}\text{SiW}_{11}$; $\text{fw}=3914.52 \text{ g mol}^{-1}$; triclinic, $P\bar{1}$ (2) space group; $a=21.6434(5)$; $b=26.1841(6)$; $c=26.2379(7) \text{ \AA}$; $\alpha=64.507(3)$; $\beta=71.118(2)$; $\gamma=86.162(2)^\circ$; $V=12653.7(5) \text{ \AA}^3$; $Z=6$; $\rho_{\text{calcd}}=3.082 \text{ g cm}^{-3}$; $\mu=17.396 \text{ mm}^{-1}$; 118144 reflections collected; 55391 unique ($R_{\text{int}}=0.049$); 34704 observed ($I > 2\sigma(I)$), 1522 parameters, $R(F)=0.094$ ($I > 2\sigma(I)$), $wR(F^2)=0.241$ (all data), $\text{GoF}=1.080$.
- [28] Iijima, J.; Ishikawa, E.; Nakamura, Y.; Naruke, H. Synthesis and Structural Investigation of Sandwich Polyoxotungstates Containing Cerium (III/IV) and Mono-Lacunary Keggin Tungstophosphate Units. *Inorg. Chim. Acta* **2010**, *363*, 1500-1506.
- [29] Ruiz, J.; Mota, A. J.; Rodríguez-Diéguez, A.; Titos, S.; Herrera, J. M.; Ruiz, E.; Cremades, E.; Costes, J. P.; Colacio, E. Field and Dilution Effects on the Slow Relaxation of a Luminescent DyO_9 Low-Symmetry Single-Ion Magnet. *Chem. Commun.* **2012**, *48*, 7916-7918.
- [30] Groom, C. R.; Bruno, I. J.; Lightfoot, M. P.; Ward, S. C. The Cambridge Structural Database. *Acta Crystallogr.* **2016**, *B72*, 171-179.
- [31] (a) Oyarzabal, I.; Ruiz, J.; Ruiz, E.; Aravena, D.; Seco, J. M.; Colacio, E. Increasing the Effective Energy Barrier Promoted by the Change of a Counteranion in a Zn–Dy–Zn SMM: Slow Relaxation via the Second Excited State. *Chem. Commun.* **2015**, *51*, 12353-12356. (b) Oyarzabal, I.; Echenique-Erandonia, E.; San Sebastián, E.; Rodríguez-Diéguez, A.; Seco, J. M.; Colacio, E. Synthesis, Structural Features and Physical Properties of a Family of Triply Bridged Dinuclear 3d-4f Complexes. *Magnetochemistry* **2021**, *7*, 22-40.
- [32] Casanova, D.; Lluell, M.; Alemany, P.; Álvarez, S. The Rich Stereochemistry of Eight-Vertex Polyhedra: A Continuous Shape Measures Study. *Chem.-Eur. J.* **2005**, *11*, 1479-1494.
- [33] Cavallo, G.; Metrangolo, P.; Milani, R.; Pilati, T.; Priimagi, A.; Resnati, G.; Terraneo, G. The Halogen Bond. *Chem. Rev.* **2016**, *116*, 2478-2601.
- [34] Reinoso, S.; Giménez-Marqués, M.; Galán-Mascarós, J. R.; Victoria, P.; Gutiérrez-Zorrilla, J. M. Giant Crown-shaped Polytungstate Formed by Self-Assembly of Ce^{III} -Stabilized Dilacunary Keggin Fragments. *Angew. Chem., Int. Ed.* **2010**, *49*, 8384-8388.
- [35] Zheng, Y.; Lin, J.; Wang, Q. Emissions and Photocatalytic Selectivity of $\text{SrWO}_4:\text{Ln}^{3+}$ (Eu^{3+} , Tb^{3+} , Sm^{3+} and Dy^{3+}) Prepared by a Supersonic Microwave Co-Assistance Method. *Photochem. Photobiol. Sci.* **2012**, *11*, 1567-1574.
- [36] Binnemans, K. Interpretation of Europium(III) Spectra. *Coord. Chem. Rev.* **2015**, *295*, 1-45.
- [37] Sugeta, M.; Yamase, T. Crystal Structure and Luminescence Site of $\text{Na}_9[\text{EuW}_{10}\text{O}_{36}]\cdot 32\text{H}_2\text{O}$. *Bull. Chem. Soc. Jpn.* **1993**, *66*, 444-449.
- [38] Armelao, L.; Quici, S.; Barigelletti, F.; Accorsi, G.; Bottaro, G.; Cavazzini, M.; Tondello, E. Design of Luminescent Lanthanide Complexes: From Molecules to Highly Efficient Photo-Emitting Materials. *Coord. Chem. Rev.* **2010**, *254*, 487-505.
- [39] Lenaerts, P.; Driesen, K.; Van Deun, R.; Binnemans, K. Covalent Coupling of Luminescent Tris(2-thenoyltrifluoroacetato)lanthanide(III) Complexes on a Merrifield Resin. *Chem. Matter.* **2005**, *17*, 2148-2154.
- [40] Yamase, T. Chapter 243 Luminescence of Polyoxometallolanthanoates and Photochemical Nano-Ring Formation. In *Handbook on the Physics and Chemistry of Rare Earths*; Gschneidner, K. A., Bünzli, J.-C. G., Pecharsky, V. K., Eds.; Elsevier: Amsterdam, **2009**; pp 297-356.
- [41] (a) Pointillart, F.; le Guennic, B.; Cador, O.; Maury, O.; Ouahab, L. Lanthanide Ion and Tetrathiafulvalene-Based Ligand as a "Magic" Couple toward Luminescence, Single Molecule Magnets, and Magnetostructural Correlations. *Acc. Chem. Res.* **2015**, *48*, 2834-2842. (b) Wong, W.-K.; Liang, H.; Wong, W.-T.; Cai, Z.; Li, K.-F.; Cheah, K.-W.

Synthesis and Near-Infrared Luminescence of 3d-4f Bi-Metallic Schiff Base Complexes. *New. J. Chem.* **2002**, *26*, 275-278.

[42] Kaczmarek, A. M.; Van Hecke, K.; Van Deun, R. Low Percentage Ln³⁺ Doping in a Tetranuclear Lanthanum Polyoxometalate Assembled from [Mo₇O₂₄]⁶⁻ Polyanions Yielding Visible and Near-Infrared Luminescence. *Inorg. Chem.* **2017**, *56*, 3190-3200.

[43] (a) Zabala-Lekuona, A.; Cepeda, J.; Oyarzabal, I.; Rodríguez-Diéguez, A.; Gardía, J. A.; Seco, J. M.; Colacio, E. Rational Design of Triple-Bridged Dinuclear Zn^{II}Ln^{III}-Based Complexes: A Structural, Magnetic and Luminescence Study. *CrystEngComm* **2017**, *19*, 256-264. (b) Oyarzabal, I.; Rojas, S.; Parejo, A. D.; Salinas-Castillo, A.; García, J. Á.; Seco, J. M.; Cepeda, J.; Rodríguez-Diéguez, A. Exploring the Slow Magnetic Relaxation of a Family of Photoluminescent 3D Lanthanide–Organic Frameworks Based on Dicarboxylate Ligands. *Magnetochemistry* **2021**, *7*, 41.

[44] Liu, J.-L.; Jin, M.-T.; Chen, L.-J.; Zhao, J.-W. First Dimethyltin-Functionalized Rare-Earth Incorporated Tellurotungstates Consisting of {B- α -TeW₇O₂₈} and {W₅O₁₈} Mixed Building Units. *Inorg. Chem.* **2018**, *57*, 12509-12520.

[45] (a) Cardona-Serra, S.; Clemente-Juan, J. M.; Coronado, E.; Gaita-Ariño, A.; Camón, A.; Evangelisti, M.; Luis, F.; Martínez-Pérez, M. J.; Sesé, J. Lanthanoid Single-Ion Magnets Based on Polyoxometalates with a 5-fold Symmetry: The Series [LnP₅W₃₀O₁₁₀]¹²⁻ (Ln³⁺ = Tb, Dy, Ho, Er, Tm, and Yb). *J. Am. Chem. Soc.* **2012**, *134*, 14982-14990. (b) Vonci, M.; Boskovic, C. Polyoxometalate-Supported Lanthanoid Single-Molecule Magnets. *Aust. J. Chem.* **2014**, *67*, 1542-1552. (c) Mariichak, O. Y.; Kaabel, S.; Karpichev, Y. A.; Rozantsev, G. M.; Radio, S. V.; Pichon, C.; Bolvin, H.; Sutter, J.-P. Crystal Structure and Magnetic Properties of Peacock–Weakley Type Polyoxometalates Na₉[Ln(W₅O₁₈)₂] (Ln = Tm, Yb): Rare Example of Tm(III) SMM. *Magnetochemistry* **2020**, *6*, 53.

[46] Malik, S. K.; Vijayaraghavan, R. Crystal Field Effects on the Saturation Magnetic Moment of Sm³⁺ Ion in Ferromagnetic Samarium Compounds. *Pramana* **1974**, *3*, 122–132.

[47] Görrler-Walrand, C.; Binnemans, K. Rationalization of Crystal Field Parametrization. *In Handbook on the Physics and Chemistry of Rare Earths*; Gschneidner, K. A., Eyring, L., Jr., Eds.; Elsevier: Amsterdam, **2007**; pp 121–283.

[48] Ruiz, J.; Lorusso, G.; Evangelisti, M.; Brechin, E. K.; Pope, S. J. A.; Colacio, E. Closely-Related Zn^{II}₂Ln^{III}₂ Complexes (Ln^{III} = Gd, Yb) with Either Magnetic Refrigerant or Luminescent Single-Molecule Magnet Properties. *Inorg. Chem.* **2014**, *53*, 3586–3594.

[49] Chilton, N. F.; Anderson, R. P.; Turner, L. D.; Soncini, A.; Murray, K. S. J. PHI: A Powerful New Program for the Analysis of Anisotropic Monomeric and Exchange-Coupled Polynuclear d- and f-block Complexes. *Comput. Chem.* **2013**, *34*, 1164–1175.

[50] Takikawa, Y.; Ebisu, S.; Nagata, S. Van Vleck Paramagnetism of the Trivalent Eu ions. *J. Phys. Chem. Solids* **2010**, *71*, 1592–1598.

[51] Kahn, O. *Molecular Magnetism*; VCH: New York, **1991**.

[52] Arauzo, A.; Lazarescu, A.; Shova, S.; Bartolomé, E.; Cases, R.; Luzón, J.; Bartolomé, J.; Turta, C. Structural and Magnetic Properties of Some Lanthanide (Ln = Eu(III), Gd(III) and Nd(III)) Cyanoacetate Polymers: Field-Induced Slow Magnetic Relaxation in the Gd and Nd Substitutions. *Dalton Trans.* **2014**, *43*, 12342-12356.

[53] Jiang, S.-D.; Liu, S.-S.; Zhou, L.-N.; Wang, B.-W.; Wang, Z.-M.; Gao, S. Series of Lanthanide Organometallic Single-Ion Magnets. *Inorg. Chem.* **2012**, *51*, 3079–3087.

[54] (a) Amjad, A.; Figuerola, A.; Sorace, L. Tm(III) Complexes Undergoing Slow Relaxation of Magnetization: Exchange Coupling and Aging Effects. *Dalton Trans.* **2017**, *46*, 3848-3856. (b) Meng, Y.-S.; Qiao, Y.-S.; Zhang, Y.-Q.; Jiang, S.-D.; Meng, Z.-S.; Wang, B.-W.; Wang, Z. M.; Gao, S. Can Non-Kramers Tm^{III} Mononuclear Molecules be Single-Molecule Magnets (SMMs)? *Chem. Eur. J.* **2016**, *22*, 4707-4708.

[55] (a) Li, D.-P.; Zhang, X.-P.; Wang, T.-W.; Ma, B.-B.; Li, C.-H.; Li, Y.-Z.; You, X.-Z. Distinct Magnetic Dynamic Behavior for Two Polymorphs of the Same Dy(III) Complex. *Chem. Commun.* **2011**, *47*, 6867-6869. (b) Li, X.-L.; Chen, C.-L.; Gao, Y.-L.; Liu, C.-M.; Feng, X.-L.; Gui, Y.-H.; Fang, S.-M. Modulation of Homochiral Dy^{III} Complexes: Single-Molecule Magnets with Ferroelectric Properties. *Chem. Eur. J.* **2012**, *18*, 14632-14637. (c) Hänninen, M. M.; Mota, A. J.; Aravena, D.; Ruiz, E.; Sillanpää, R.; Camón, A.; Evangelisti, M.; Colacio, E. Two C₃-Symmetric Dy₃^{III} Complexes with Triple Di-μ-methoxy-m-phenoxo Bridges, Magnetic Ground State, and Single-Molecule Magnetic Behavior. *Chem. Eur. J.* **2014**, *20*, 8410-8420.

[56] (a) Aravena, D.; Ruiz, E. Spin Dynamics in Single-Molecule Magnets and Molecular Qubits. *Dalton Trans.*, **2020**, *49*, 9916-9928. (b) Topping, C. V.; Blundell, S. J. A.C. Susceptibility as a Probe of Low-Frequency Magnetic Dynamics. *J. Phys.: Condens. Matter* **2019**, *31*, 013001.

[57] Chen, Y. C.; Peng, Y.-Y.; Liu, J.-L.; Tong, M.-L. Field-Induced Slow Magnetic Relaxation in a Mononuclear Gd(III) Complex. *Inorg. Chem. Commun.* **2019**, *107*, 107449.

Final remarks and future perspectives

6.1. Final Remarks

6.2. Future perspectives

5.1. Final remarks

The following general conclusions can be gathered from this work:

CHAPTER 2

1. Systematic studies on the influence of the pH in the heptamolybdate/{Cu(cyclam)} synthetic system leads to the formation of POM-based hybrids with different dimensionalities, in which the nuclearity of the POM-cluster increases when adjusting the pH values to more acidic conditions.

2. Covalent attachment of {Cu(cyclam)} metalorganic complexes to heptamolybdate POM surfaces at mild pH conditions leads the formation of three porous {Mo₇O₂₄}-based POM hybrids, being one of them isostructural with compound [{Cu(cyclam)}₃(W₇O₂₄)]·15.5H₂O already reported in the literature.

3. Variable-temperature PXRD experiments on [{Cu(cyclam)}₃(Mo₇O₂₄)]·15.5H₂O show the ability of this compound to undergo solid-phase transformations under applied thermal stimuli which leads to the formation of two new partially- and fully-dehydrated compounds.

CHAPTER 3

4. The heptamolybdate /{Cu(cyclam)} synthetic system at pH values close to neutrality as well as under hydrothermal conditions, promotes the rearrangement of the well-known {Mo₇O₂₄} cluster to lead to an unprecedented octamolybdate anion within an extended POM-metalorganic hybrid framework [{Cu(cyclam)}₃(κ-Mo₈O₂₇)]·14H₂O (**1-Mo8**).

5. This work exemplifies the potential of solid-state transformations to afford novel POM clusters that have not been isolated before by classical synthetic methods in solution: Compound **1-Mo8** undergoes up to two sequential thermally triggered single-crystal-to-single-crystal transformations upon evacuation of guest water molecules. These phase transitions do not only modify the framework dimensionality through major changes in the coordination geometries of Cu^{II} centers, but also imply the isomerization of octamolybdate anions through metal migration. It worth noting that none of these three isomeric forms of octamolybdate anions have been observed before.

6. Reversible rehydration of anhydrous phases affords two additional compounds via single-crystal-to-single-crystal transformations. High-temperature anhydrous phase hydrates upon air exposure through a process that involves the condensation of one additional water molecule to the octamolybdate cluster, whereas the low temperature anhydrous phase adsorbs water without any apparent significant change in its unit cell parameters, but resulting in the same octamolybdate cluster as that in **1-Mo8**.

7. Up to three different microporous phases with accessible voids can be isolated from **1-Mo8**, which exhibit interesting water vapor sorption properties. Adsorption isotherms display an abrupt adsorption capacity at low (20-30%) relative humidity level and they are in good agreement with the structural transitions. The anhydrous phases reversibly adsorb water with one of the highest water sorption capacities reported for POM-based materials. These features, together with their high cyclability (more than 100 cycles) and appropriate sorption kinetics revealed the interest of these materials for their use in industrial applications, as they could be potentially desirable for humidity control devices in confined spaces.

9. The accessible empty channels of the thermally activated microporous materials show the capacity to adsorb N_2 and CO_2 .

10. Furthermore, these empty channels act as promising materials for selective separation of gas mixtures, specially, selective uptake of C_2H_6 over C_2H_4 , which is not a common behavior in other gas sorption materials.

CHAPTER 4

11. The use of the more bulky N4-tetradentate DMC ligand has also led to the formation of porous and extended POM-metalorganic hybrids. Unexpected rearrangement of the heptamolybdate cluster to the $[H_4CuMo_6(MoO_3)_2O_{24}]^{6-}$ anion upon its reaction with $\{Cu(DMC)\}$ results in an unprecedented POM formed by the well-known $[H_6CuMo_6O_{24}]^{6-}$ Anderson-Evans anion, to which to tetrahedral $\{MoO_4\}$ units have been condensed to central oxygen atoms from opposite faces.

12. The systematic study of the reactivity of $[H_6CrMo_6O_{24}]^{6-}$ anions with $\{Cu(DMC)\}^{2+}$ complexes leads to the formation of 6 different hybrid compounds with different dimensionalities (from 1D to 3D), which reveals the important role of the presence of different cations/anions in the aqueous reaction media.

13. TGA experiments and variable-temperature PXRD analysis revealed a thermal stability range for three of the compounds, which showed the capacity to undergo solid-phase transformation under thermal stimuli. Two of them could constitute robust frameworks as no major modification take place according to powder X-ray diffraction patterns upon thermal evacuation of guest solvent molecules.

CHAPTER 5

14. The simultaneous coordination of mid-to-late trivalent lanthanide ions to monolacunary α -Keggin-type polyoxometalate and compartmental multidentate organic ligands results effective for constructing molecular materials with interesting optical and magnetic properties. This combination results in ten isostructural compounds containing

lanthanides (from Sm to Lu), in which the Ln ion is trapped in a sandwich-type hybrid, occupying the external O₄ pocket from the organic ligand and the monolacunary vacant site of the lacunary POM anion. In this way, the empty pocket of the organic ligand confers certain flexibility that facilitates its unprecedented folding.

15. Both organic and POM inorganic ligands has proved to act as suitable antenna ligands to sensitize weak-emitting lanthanide-metal centers. Thus, metal-centered luminescence is efficiently sensitized for **Sm** and **Eu** derivatives in the visible region, as well as **Er** and **Yb** in the NIR. In contrast, the quenching of the emission for the **Tb** derivative has been attributed to the out-of-pocket coordination mode of the lanthanide center within the POM fragment.

16. Compounds containing **Gd** and **Yb** centers display slow relaxation of the magnetization below ~6 K, which mechanistically takes place through a combination of different relaxation processes.

17. The **Yb** derivative constitutes a dual magneto-luminescent material, because it represents the first lanthanide-containing POM able to simultaneously exhibit slow magnetic relaxation and NIR emission.

18. The molecular hybrids proved to be stable in solution as confirmed by ESI-MS experiments, and ¹H-NMR spectroscopy.

5.2. Future perspectives

In order to complete and improve the work carried out during this dissertation, new experiments have been planned for the near future. In addition, new research lines identified during this work are also compiled in this section:

CHAPTERS 2 and 3:

1. The crystallization of **1B-Mo7** together with **1-Mo7** compound avoid us for fully chemically characterize the first hybrid. In this sense, adjusting some synthetic parameters (temperature, the ratio of the reagents, copper source...) could facilitate the isolation of pure single-crystals **1B-Mo7**.

2. Although the determination of the single-crystal structure of thermally activated phases arising from **1-Mo7** was not achieved, the isostructurality of this compound with its tungstate-analogue was confirmed by powder XRD diffraction analyses. This could indicate the existence of an anhydrous phase with empty and available channels for the adsorption of different gases. Therefore, thermally-activated **3-Mo7** compound could be a good candidate for gas sorption measurements.

3. Studies on selective gas sorption properties for **2-Mo** and **3-Mo8** will be completed in the near future. Gas sorption properties of **6-Mo8** will also be evaluated because this compound has already demonstrate to have accessible empty pores, as confirmed by water sorption measurements.

4. The accessible voids, together with the reversible redox properties that could exhibit the molybdate-metalorganic hybrids, make them suitable candidates to be studied as electrodes for electrochemical energy storage systems like Li⁺ or Na⁺ batteries.

CHAPTER 4:

4. First of all, changes in the synthetic procedure will be considered (ration of the reagents, adjusting the pH value, hydrothermal conditions...) in order to obtain pure single-crystals of **1-CuMo8** and **1-CrMo6** in high yields. These compounds will be fully characterized in the near future and their thermostructural behavior analyzed.

5. Single-crystal XRD diffraction experiments at high temperatures will be carried out for **1Na-CrMo6**, **1NO3-CrMo6** and **1Cl-CrMo6** in order to determine if these compounds are able to undergo single-crystal-to-single-crystal transformation under thermal stimuli. The microporosity of the thermally-activated phases and their ability to adsorb gases will also be studied.

CHAPTER 5:

6. In the near future, we plan to make use of the available N₂O₂ coordination site to accommodate a transition metal ion that would allow to the preparation of heterometallic 3d-4f complexes, with the aim of enhancing the anisotropy of the system.

7. The use of different aromatic multidentate organic ligands will be also tested to modify the coordination environment of the lanthanide ions, such as; i) N,N',N''-trimethyl-N,N''-bis(2-hydroxy-3-methoxy-5-methylbenzyl)diethylene triamine and N,N'-dimethyl-N,N'-bis(2-hydroxy-3-formyl-5-bromo-benzyl)ethylenediamine exhibiting a similar structure to H₂L ligand; or, ii) smaller N,O- and O-donor ligands like picolinic or benzoic acid.

8. The change in the size of the polyanion as well as in the nature of the central heteroatom will be also studied because this could modify the coordination mode of the lanthanide to lead to an in-pocket mode.

9. New collaborations have resulted for the study of the synthesized compounds as spin qubits. Thus, relaxation times and decoherences will be studied in the near future.

Monodimensional Compounds Based on Group 6 Tetraoxometalates and Transition Metal Complexes of Cyclam Ligand

A1.1. $[\text{Ni}(\text{C}_{10}\text{H}_{24}\text{N}_4)][\text{CrO}_4]\cdot 2\text{H}_2\text{O}$ (**CrNi**)

A1.2. $[\text{M}(\text{C}_{10}\text{H}_{24}\text{N}_4)][\text{CrO}_4]\cdot 3\text{H}_2\text{O}$; M = Cu, Zn (**CrCu, CrZn**)

A1.3. $[\text{M}(\text{C}_{10}\text{H}_{24}\text{N}_4)][\text{M}'\text{O}_4]\cdot 3\text{H}_2\text{O}$; M = Ni, Zn; M' = Mo, W (**MoNi, MoZn, WNi, WZn**)

A1.4. $[\text{Cu}(\text{C}_{10}\text{H}_{24}\text{N}_4)][\text{MoO}_4]\cdot 4\text{H}_2\text{O}$ (**MoCu**)

A1.5. $[\text{Cu}(\text{C}_{10}\text{H}_{24}\text{N}_4)][\text{WO}_4]\cdot 4\text{H}_2\text{O}$ (**WCu**)

A1.6. Electron Paramagnetic Resonance (EPR)

A1.7. References

ABSTRACT: Nine new compounds have been prepared based on group 6 transition metal oxyanions with the metal-organic ligand $M''(\text{cyclam})$ ($M'' = \text{Ni}''$, Cu'' and Zn''). The compounds have been characterized by IR spectroscopy and their structure described by X-ray diffraction. All the compounds show a similar crystal packing which consist of endless chains formed by the repetition of the $\{[M(\text{cyclam})]M'\text{O}_4\}_\infty$ moieties. The chains are parallel or antiparallel between them, and with a different degree of hydration. Through C–H \cdots O, N–H \cdots O and O–H \cdots O interactions supramolecular 3D arrangements are formed in all the cases. However, these weak interactions forming the overall crystal packing prevents from studying SCSC transformations at high temperatures. Differences in the overall structure also affect to the magnetic properties, as observed in the EPR studies for **MoCu** and **WCu**.

MoCu compound was firstly obtained at alkaline pH values following the procedure indicated in Chapter 2. By changing the Mo metal source from the $\{\text{Mo}_7\text{O}_{24}\}$ precursor to Na_2MoO_4 same results were obtained. Additionally, different metal sources were used, which lead to a family of nine supramolecular 3D networks formed by the arrangement of monodimensional chains. All nine compounds exhibit the same molecular formula: $[\text{M}(\text{C}_{10}\text{H}_{24}\text{N}_4)][\text{M}'\text{O}_4] \cdot n\text{H}_2\text{O}$ ($\text{M} = \text{Ni}^{\text{II}}, \text{Cu}^{\text{II}}, \text{Zn}^{\text{II}}; \text{M}' = \text{Cr}^{\text{VI}}, \text{Mo}^{\text{VI}}, \text{W}^{\text{VI}}$). Other parameters such as the choice of nickel, copper or zinc sources (acetate, nitrate and sulphate) were also tested with no changes in the formation of the compounds.

A1.1. $[\text{Ni}(\text{C}_{10}\text{H}_{24}\text{N}_4)][\text{CrO}_4] \cdot 2\text{H}_2\text{O}$ (CrNi)

Experimental: To an aqueous solution (15 mL) of $\text{K}_2\text{Cr}_2\text{O}_7$ (0.103 g, 0.35 mmol), a solution of $\text{NiSO}_4 \cdot 6\text{H}_2\text{O}$ (0.079 g, 0.3 mmol) and cyclam (0.060 g, 0.3 mmol) in water (15 mL) was added dropwise. The pH of the mixture was adjusted to 10 with 1M NaOH and the resulting brown solution was stirred for 1 h at room temperature. Brown-orange crystal needles were obtained by slow evaporation after a week. Yield: 27 mg, 22% based on Ni. IR (Figure A1.1) (cm^{-1}): 3448 (vs), 3229 (m), 3165 (s), 2936 (m), 2864 (m), 1473 (m), 1451 (m), 1424 (m), 1388 (w), 1332 (w), 1307 (w), 1292 (m), 1264 (w), 1245 (w), 1105 (s), 1071 (w), 1051 (w), 1016 (m), 1009 (m), 949 (vs), 874 (vs), 435 (w). Elem Anal. Calcd. (%) for $\text{C}_{10}\text{H}_{28}\text{CrN}_4\text{NiO}_6$: C, 29.22%; H, 6.87%; N, 13.63%. Found: C, 28.91%; H, 6.89%; N, 13.63%.

Thermostructural behavior: Thermal stability of **CrNi** was investigated by thermogravimetric and differential thermal (TGA/DTA) analysis (Figure A1.2a), in which first a dehydration process occurs that extends up to 110 °C and accounts the two hydration water molecules (m% calcd. 8.8%; found 8.8%). The dehydration process leads to a thermal stability that extends up to 200 °C. Above this temperature, the combustion of the organic ligand takes place as an endothermic step. The final residue is obtained above 360 °C (m% calcd. for CrNiO_4 , 42.5%; found, 41.3%). Taking into account the thermal stability showed in the TGA, the thermostructural behavior of **CrNi** was studied by variable-temperature PXRD from room temperature to 210 °C every 20 °C. Figure A1.2b shows the presence of a thermal-dependent transformation at 50 °C indicated by the disappearance of the maximum at $2\theta = 13.1^\circ$ and the shift of the maxima at $2\theta = 11.0^\circ$ and 11.7° to 11.9° and 12.1° in the new phase.

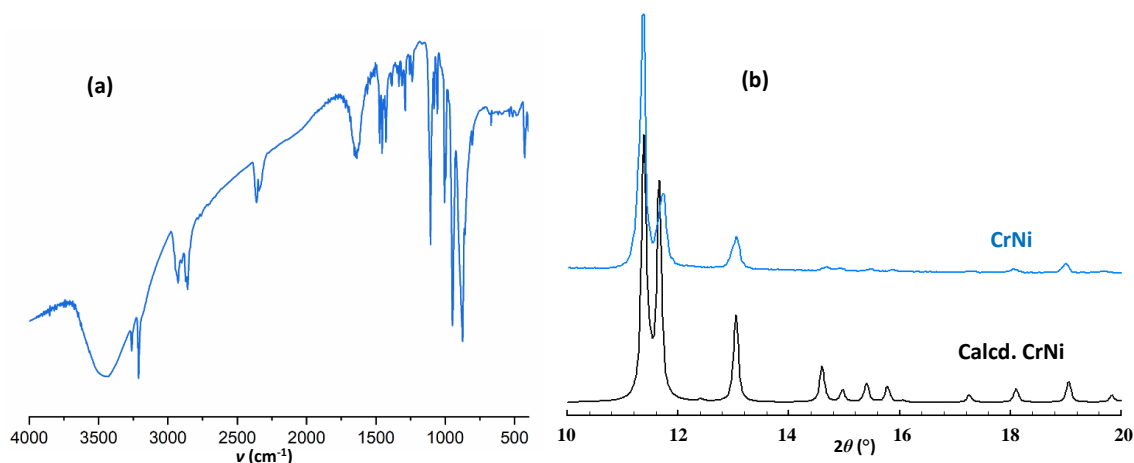


Figure A1.1. (a) FT-IR spectra of **CrNi**, and (b) comparison between the experimental powder XRD pattern of **CrNi** and that calculated from the single-crystal data.

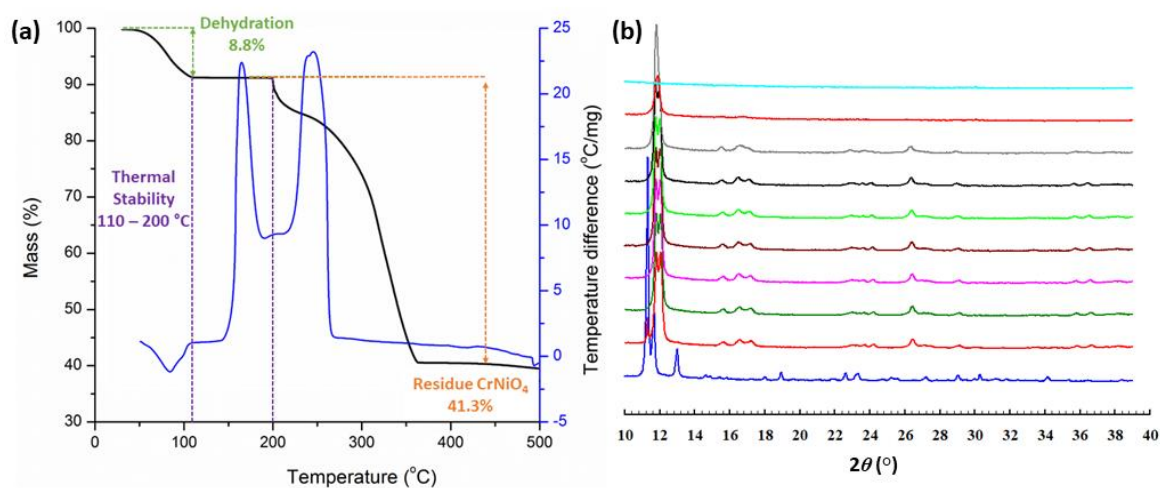


Figure A1.2. (a) TGA/DTA curves and (b) variable-temperature XRD pattern of **CrNi**.

Crystal Structure: Compound **CrNi** crystallizes in the triclinic $P-1$ space group (Table A1.1). The asymmetric unit contains a tetrahedral $[\text{CrO}_4]^{2-}$ unit, two halves of $\{\text{Ni}(\text{cyclam})\}^{2+}$ complexes and two lattice water molecules. Ni^{II} centers exhibit an octahedral geometry in which the equatorial positions are occupied by the N_4 atoms of the cyclam ligand and the axial positions by oxygen from the $\{\text{MO}_4\}$ tetrahedra. The Cr–O bond distances fall in the 1.645–1.665 Å range, which are in concordance with the reported ones.¹ In the same way, Ni–O (average distance 2.088 Å) and Ni–N (average distance 2.067 Å) bond lengths agree with the reported in literature,² and are slightly shorter from those found in chapters 2 and 3 for $\{\text{Cu}(\text{cyclam})\}^{2+}$ complexes.

The crystal packing of **CrNi** consists on monodimensional chains of $\{\text{Ni}(\text{cyclam})\}/\{\text{CrO}_4\}_\infty$ growing along the [011] direction. The chains are packed together through intermolecular N–H \cdots O interactions, forming layers parallel to the (0-11) plane. In Figure A1.3, it can be seen that no water molecules are located between the chains on a same layers. On the contrary, hydration water molecules are located between the layers,

APPENDIX 1

which help to the overall crystal packing of the $[\text{Ni}(\text{cyclam})][\text{CrO}_4]$ units through additional H-bond interactions. Even though thermostructural studies revealed the transformation of **CrNi** into an additional phase after thermal stimuli, this solid-phase transition could not be followed by single-crystal X-ray diffraction due to the loss of crystallinity of the single crystals.

Table A1.1. Crystallographic parameters of **CrNi**.

	CrNi
empirical formula	$\text{C}_{10}\text{H}_{28}\text{CrN}_4\text{NiO}_6$
fw (g mol^{-1})	411.07
crystal system	Triclinic
space group	$P\bar{1}$ (2)
a (\AA)	8.9598(6)
b (\AA)	9.1399(6)
c (\AA)	12.1365(7)
α ($^\circ$)	104.856(5)
β ($^\circ$)	92.902(5)
γ ($^\circ$)	117.785(6)
V (\AA^3)	832.91(9)
Z	2
T (K)	100.00(10)
ρ_{calcd} (g cm^{-3})	1.639
μ (mm^{-1})	1.814
collected reflns	5755
unique reflns (R_{int})	3198 (0.032)
observed reflns [$I > 2\sigma(I)$]	2739
Parameters (restraints)	218 (4)
$R(F)^a$ [$I > 2\sigma(I)$]	0.035
$wR(F^2)^b$ [all data]	0.081
GoF	1.030

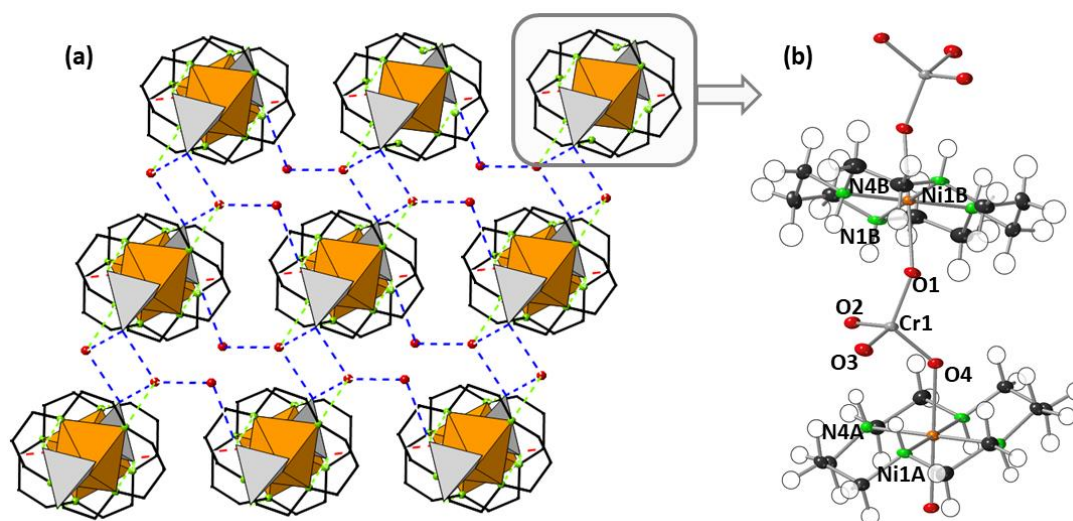


Figure A1.3. (a) Polyhedral representation of the crystal packing of **CrNi** along the $[011]$ direction, with detail of the H-bond interactions, (b) view of the monodimensional $\{\text{Ni}(\text{cyclam})\}/\{\text{CrO}_4\}_\infty$ chain with ORTEP representation. Color code: Cr, grey; Ni, orange; C, black, H, white; N, green; O, red; C–H \cdots O, N–H \cdots O and O–H \cdots O interactions, red, green and blue dashed lines, respectively.

A1.2. $[M(C_{10}H_{24}N_4)][CrO_4] \cdot 3H_2O$; M = Cu, Zn (CrCu, CrZn)

Experimental: To an aqueous solution (15 mL) of $K_2Cr_2O_7$ (0.103 g, 0.35 mmol), a solution of $MSO_4 \cdot nH_2O$ (M = Cu, 0.075 g; M = Zn, 0.0086 g, 0.3 mmol) and cyclam (0.060 g, 0.3 mmol) in water (15 mL) was added dropwise. The pH of the mixture was adjusted to 10 with 1M NaOH, and the resulting solution (Cu: brown; Zn: orange) was stirred for 1 h at room temperature. Brown (Cu) and yellow needle-shaped crystals (Zn) were obtained by slow evaporation after 10-15 days. **CrCu:** Yield: 21 mg, 16% based on Cu. IR (Figure A1.4) (cm^{-1}): 3452 (vs), 3223 (s), 3173 (s), 2938 (m), 2862 (m), 1474 (m), 1451 (m), 1431 (m), 1426 (w), 1390 (w), 1306 (m), 1290 (m), 1258 (m), 1239 (m), 1105 (s), 1067 (w), 1057 (w), 1022 (m), 1017 (m), 962 (vs), 940 (m), 886 (vs), 449 (w). Elem Anal. Calcd. (%) for $C_{10}H_{30}CrCuN_4O_7$: C, 27.68%; H, 6.97%; N, 12.91%. Found: C, 27.83%; H, 6.85%; N, 12.91%. **CrZn:** Yield: 18 mg, 14% based on Zn. IR (Figure A1.4) (cm^{-1}): 3447 (s), 3217 (s), 3144 (vs), 2936 (m), 2861 (m), 1472 (m), 1452 (m), 1425 (w), 1388 (w), 1341 (w), 1297 (w), 1259 (w), 1241 (w), 1098 (s), 1050 (w), 934 (vs), 874 (vs), 624 (m).³ Elem Anal. Calcd. (%) for $C_{10}H_{30}CrCuN_4O_7$: C, 27.56%; H, 6.94%; N, 12.86%. Found: C, 27.44%; H, 7.01%; N, 12.86%.

Thermostructural behavior: Thermal stability of **CrCu** and **CrZn** were investigated by TGA/DTA analysis (Figure A1.5). For **CrCu**, First a dehydration process occurs that extends up to 95 °C and accounts for the three hydration water molecules (m% calcd. 12.4%; found 12.5%). The dehydration process leads to a thermal stability that extends up to 190 °C. Above this temperature, the combustion of the organic ligand takes place as an endothermic step. The final residue is obtained above 320 °C (m% calcd. for $CrCuO_4$, 41.4%; found, 40.7%). Similar results were found for **CrZn** with a dehydration process that extends up to 90 °C and accounts for the three hydration water molecules (m% calcd. 12.4%; found 12.3%). The dehydration process leads to a thermal stability that extends up to 235 °C. Above this temperature, the combustion of the organic ligand takes place as an endothermic step. The final residue is obtained above 350 °C (m% calcd. for CrO_4Zn , 41.6%; found, 41.4%). Taking into account the thermal stabilities showed in the TGA, the thermostructural behavior of both compounds was studied by variable-temperature PXRD from room temperature to 210 °C every 20 °C. Figure A1.6 shows the presence of a thermal-dependent transformation at 50 °C indicated by the disappearance of the main maxima at $2\theta = 10.0^\circ$, 11.7° , 12.7° and 15.8° and the appearance of new ones at $2\theta = 11.8^\circ$, 12.5° , 15.5° and 17.3° .

APPENDIX 1

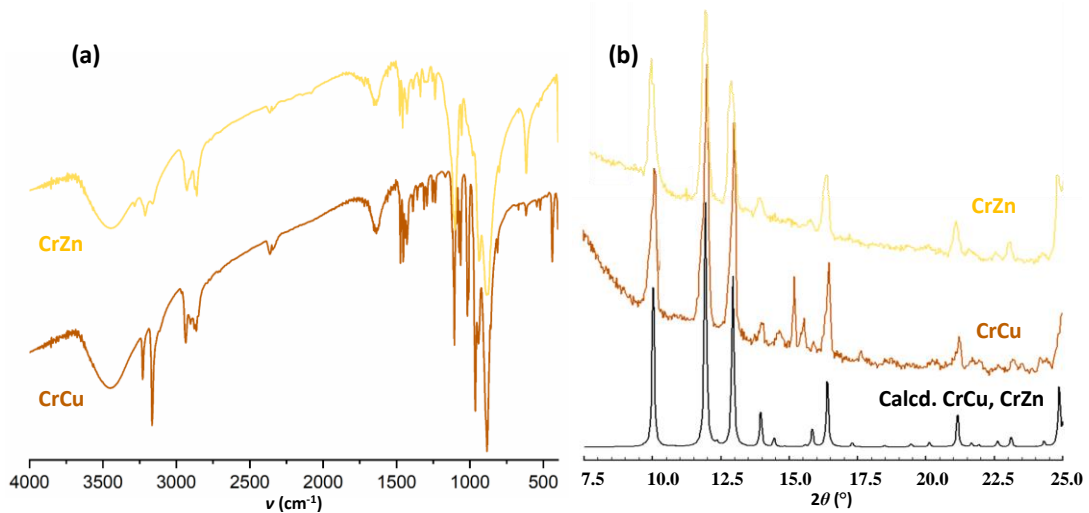


Figure A1.4. (a) FT-IR spectra of **CrCu** and **CrZn**, and; (b) comparison between the experimental powder XRD pattern of **CrCu** and **CrZn** and that calculated from the single-crystal data.

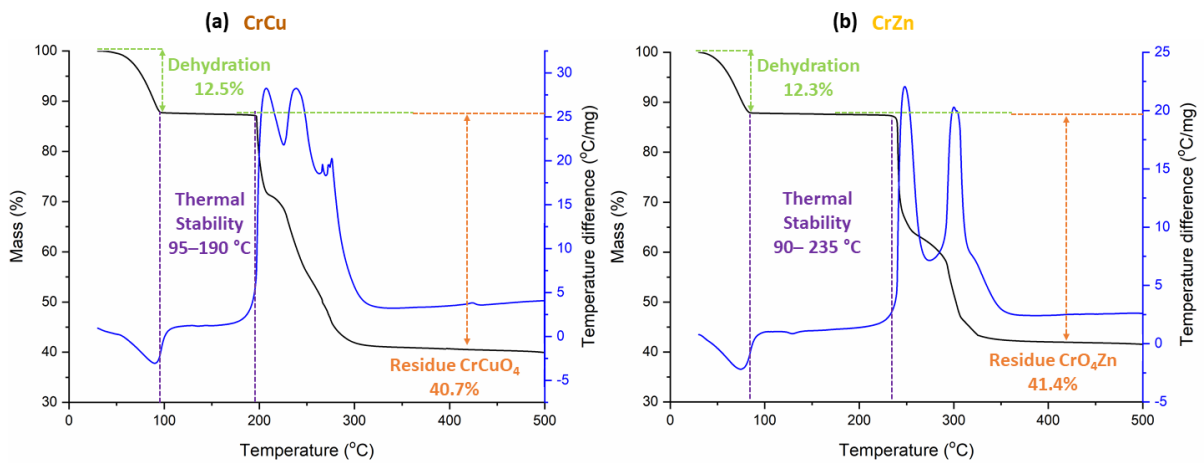


Figure A1.5. TGA/DTA curves of (a) **CrCu** and (b) **CrZn**.

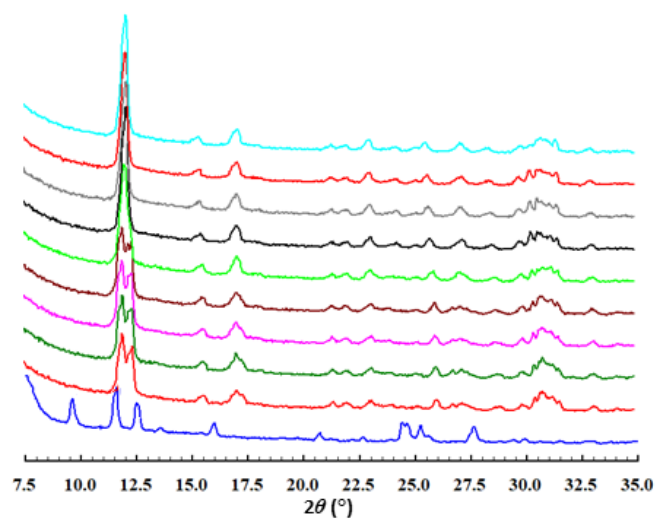


Figure A1.6. Variable temperature X-ray diffraction patterns of **CrZn** (representative of **CrCu**).

Crystal Structure: Compounds **CrCu** and **CrZn** crystallize in the monoclinic $P2_1$ space group (Table A1.2). The asymmetric unit contains two tetrahedra $[\text{CrO}_4]^{2-}$ units, two $\{\text{M}(\text{cyclam})\}^{2+}$ ($\text{M} = \text{Cu}, \text{Zn}$) complexes and six lattice water molecules. As in the previous case, the equatorial positions of the octahedral Cu^{II} and Zn^{II} centers are occupied by the cyclam ligand while the axial coordination sites are accessible for the union with O_{POM} . The Cr–O bond distances fall in the range of 1.628–1.653 Å in **CrCu** and 1.644–1.657 Å in **CrZn**, and M–O and M–N ($\text{M} = \text{Cu}, \text{Zn}$) bond lengths are in concordance with those reported along the thesis for $\{\text{Cu}(\text{cyclam})\}$ moieties.

Table A1.2. Crystallographic data for **CrCu** and **CrZn**.

	CrCu	CrZn
empirical formula	$\text{C}_{10}\text{H}_{30}\text{CrCuN}_4\text{O}_7$	$\text{C}_{10}\text{H}_{30}\text{CrN}_4\text{O}_7\text{Zn}$
fw (g mol^{-1})	433.92	435.75
crystal system	Monoclinic	Monoclinic
space group	$P2_1$ (4)	$P2_1$ (4)
a (Å)	10.47653(18)	10.39549(19)
b (Å)	13.67739(18)	13.7702(2)
c (Å)	12.5283(2)	12.3842(2)
α (°)	90.00	90.00
β (°)	102.0790(17)	103.5685(19)
γ (°)	90.00	90.00
Z	4	4
V (Å ³)	1755.46(5)	1723.29(5)
T (K)	149.99(10)	100.01(10)
ρ_{calcd} (g cm^{-3})	1.642	1.680
μ (mm^{-1})	6.952	2.061
collected reflns	7501	6416
unique reflns (R_{int})	2432 (0.027)	5477 (0.027)
observed reflns [$I > 2\sigma(I)$]	2233	4957
Parameters (restraints)	464 (17)	464 (13)
$R(F)^a$ [$I > 2\sigma(I)$]	0.023	0.027
$wR(F^2)^b$ [all data]	0.061	0.067
GoF	1.034	1.031

Regarding the crystal packing, both compounds are formed by antiparallel monodimensional chains running along the [101] direction. These chains consist on the repetition of $\{[\text{M}^{1\text{A}}][\text{Cr}^{1\text{A}}][\text{M}^{1\text{B}}][\text{Cr}^{1\text{B}}]\}_\infty$ ($\text{M} = \text{Cu}, \text{Zn}$) moieties. The chains are packed together forming corrugated layers in the (-101) plane. As seen in Figure A1.7, hydration water molecules are located between the layers, which contribute to the linking between the layers by forming an extensive hydrogen bond network. Even though thermostructural studies revealed the structural transformation of **CrCu** and **CrZn** under thermal stimuli, these solid-phase transitions could not be followed by single-crystal X-ray diffraction due to the loss of crystallinity of the single crystals.

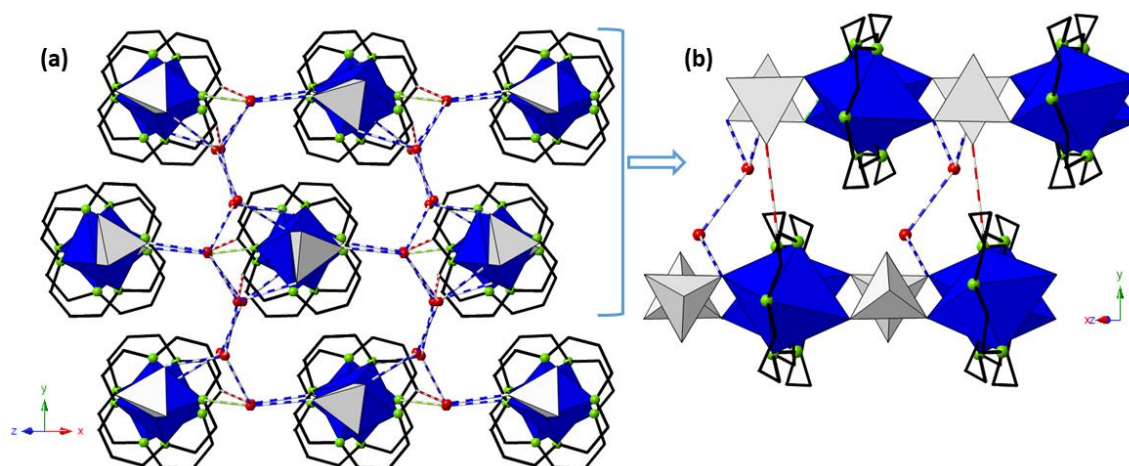


Figure A1.7. View of the (a) crystal structure of **CrCu** and **CrZn** along the [101] direction, and (b) parallel arrangement of the chains. Color code: MN_4O_2 ($M = Cu, Zn$), blue polyhedra; $C-H\cdots O$, $N-H\cdots O$ and $O-H\cdots O$ interactions, red, green and blue dashed lines, respectively.

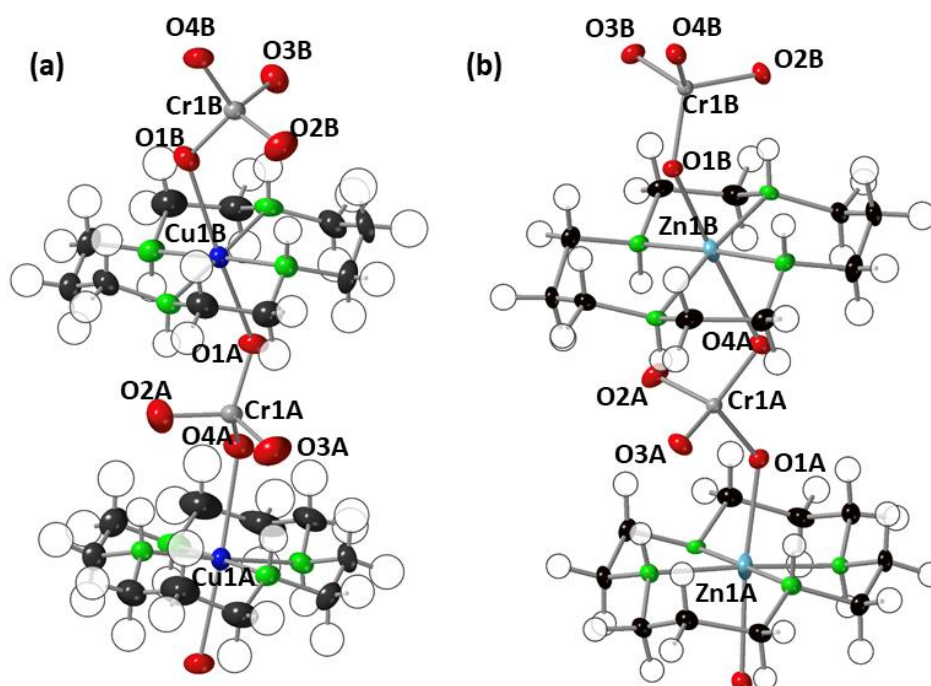


Figure A1.8. View of the monodimensional $\{M(\text{cyclam})\}/\{\text{CrO}_4\}_\infty$ ($M =$ (a) **Cu**, (b) **Zn**) chains with ORTEP representation. Color code: **Cr**, grey; **Cu**, dark blue; **Zn**, light blue.

A1.3. $[M(\text{C}_{10}\text{H}_{24}\text{N}_4)][M'\text{O}_4]\cdot 3\text{H}_2\text{O}$; $M = \text{Ni, Zn}$; $M' = \text{Mo, W}$ (**MoNi**, **MoZn**, **WNi**, **WZn**)

Experimental: To an aqueous solution (15 mL) of $\text{Na}_2M'\text{O}_4\cdot 2\text{H}_2\text{O}$ ($M' = \text{Mo}$, 0.169 g; $M' = \text{Zn}$, 0.230 g, 0.7 mmol), a solution of $\text{MSO}_4\cdot n\text{H}_2\text{O}$ ($M = \text{Ni}$, 0.079 g; $M = \text{Zn}$, 0.0086 g, 0.3 mmol) and cyclam (0.060 g, 0.3 mmol) in water (15 mL) was added dropwise. The pH of the mixture was adjusted to 10 with 1M NaOH, and the resulting solution (Ni: purple; Zn: colorless) was stirred for 1 h at room temperature. Orange (Cu) and colorless prismatic

crystals (Zn) were obtained by slow evaporation after 10-15 days. **MoNi**: Yield: 24 mg, 17% based on Ni. IR (Figure A1.9) (cm^{-1}): 3337 (s), 3254 (s), 3211 (vs), 2913 (m), 2866 (m), 2843 (m), 1472 (m), 1455 (m), 1439 (m), 1339 (w), 1317 (w), 1290 (w), 1252 (w), 1238 (w), 1103 (s), 1088 (w), 1081 (m), 1050 (m), 1001 (s), 994 (s), 898 (m), 874 (vs), 857 (vs), 831 (vs), 819 (s), 427 (m). Elem Anal. Calcd. (%) for $\text{C}_{10}\text{H}_{30}\text{MoN}_4\text{NiO}_7$: C, 25.39%; H, 6.39%; N, 11.84%. Found: C, 25.18%; H, 6.83%; N, 11.91%. **MoZn**: Yield: 11 mg, 8% based on Zn. IR (Figure A1.8) (cm^{-1}): 3390 (vs), 3209 (s), 3153 (s), 2921 (s), 2872 (s), 2854 (s), 1476 (m), 1456 (m), 1432 (m), 1348 (w), 1339 (w), 1299 (w), 1254 (w), 1241 (w), 1100 (s), 1081 (m), 1057 (m), 983 (w), 941 (s), 938 (s), 863 (vs), 852 (vs), 831 (vs), 817 (s). Elem Anal. Calcd. (%) for $\text{C}_{10}\text{H}_{30}\text{MoN}_4\text{O}_7\text{Zn}$: C, 25.04%; H, 6.30%; N, 11.68%. Found: C, 25.23%; H, 6.51%; N, 11.62%. **WNi**: Yield: 20 mg, 12% based on Ni. IR (Figure A1.8) (cm^{-1}): 3340 (vs), 3254 (vs), 3209 (vs), 3189 (vs), 2921 (s), 2853 (m), 1491 (w), 1468 (w), 1453 (m), 1427 (m), 1382 (w), 1336 (m), 1309 (w), 1290 (m), 1252 (w), 1246 (w), 1103 (s), 1085 (w), 1054 (m), 1033 (w), 1001 (m), 998 (m), 948 (s), 876 (vs), 853 (vs), 829 (vs), 426 (w), 415 (w). Elem Anal. Calcd. (%) for $\text{C}_{10}\text{H}_{30}\text{N}_4\text{NiO}_7\text{W}$: C, 21.41%; H, 5.39%; N, 10.46%. Found: C, 21.54%; H, 5.47%; N, 10.50%. **WZn**: Yield: 10 mg, 6% based on Zn. IR (Figure A1.8) (cm^{-1}): 3370 (vs), 3208 (vs), 3157 (vs), 2924 (s), 2855 (s), 1472 (m), 1454 (m), 1426 (m), 1389 (w), 1344 (w), 1314 (w), 1296 (w), 1253 (w), 1242 (w), 1101 (s), 1053 (m), 987 (w), 939 (s), 872 (vs), 852 (vs), 831 (vs). Elem Anal. Calcd. (%) for $\text{C}_{10}\text{H}_{30}\text{N}_4\text{O}_7\text{WZn}$: C, 21.16%; H, 5.33%; N, 9.87%. Found: C, 21.08%; H, 5.46%; N, 10.02%.

Thermostructural behavior: Thermal stability of **MoNi**, **MoZn**, **WNi** and **WZn** were investigated by TGA/DTA analysis (Figure A1.10). The four compounds show a similar behavior in which first a dehydration process is appreciated that extends up to 130-145 °C and accounts for the loss of three hydration water molecules (**MoNi**: m% calcd. 11.4%; found 11.3%; **MoZn**: m% calcd. 11.3%; found 11.2%; **WNi**: m% calcd. 9.6%; found 9.8%; **WZn**: m% calcd. 9.5%; found 9.7%). The dehydration process leads to a thermal stability that extends up to 235-245 °C. Above this temperature, the combustion of the organic ligand takes place as an endothermic step. The final residue is obtained above 500 °C in the case of **MoNi** and **MoZn**, and above 600 °C for **WNi** and **WZn** (**MoNi**: m% calcd. for MoNiO_4 , 46.2%; found, 46.6%; **MoZn**: m% calcd. for MoZnO_4 , 47.0%; found, 46.4%; **WNi**: m% calcd. for WNiO_4 , 54.6%; found, 54.2%; **WZn**: m% calcd. for WZnO_4 , 55.2%; found, 54.6%). Due to the thermal stabilities showed in the TGA, the thermostructural behavior of these four compounds was analyzed by variable-temperature PXRD from room temperature to 210 °C every 20 °C. Figure A1.11 shows the presence of a thermal-dependent additional phase fully transformed at 70 °C, as indicated by the clear shift of the main maxima from $2\theta = 11.6^\circ$ and 11.8° to $2\theta = 11.9^\circ$ and 12.0° .

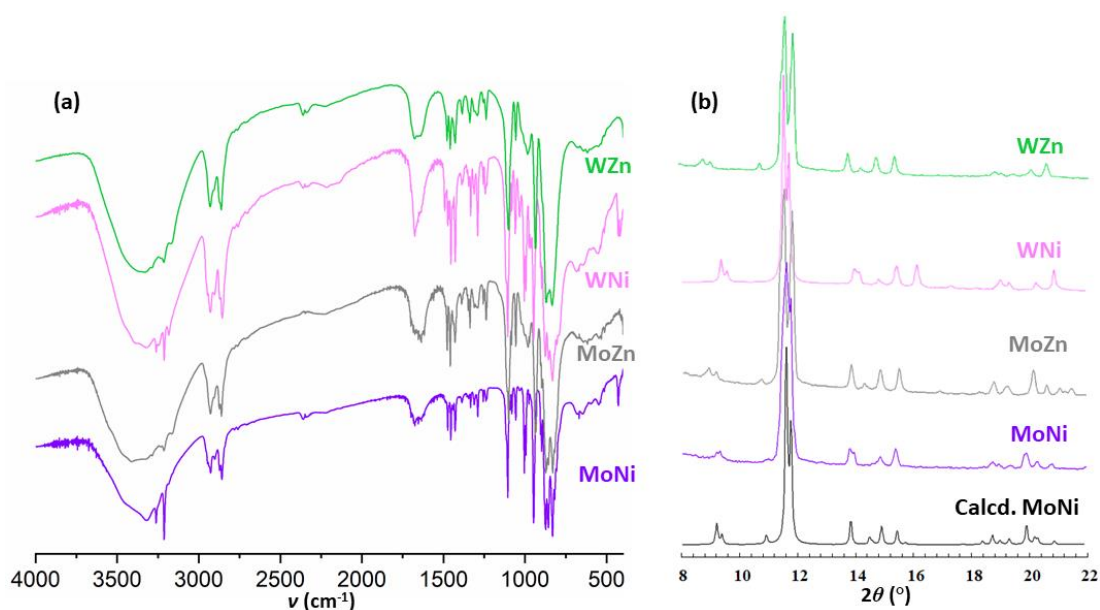


Figure A1.9. (a) FT-IR spectra of **MoNi**, **MoZn**, **WNi** and **WZn**, and; (b) comparison between the experimental powder XRD pattern of **MoNi**, **MoZn**, **WNi** and **WZn** and that calculated from the single-crystal data of **MoNi**.

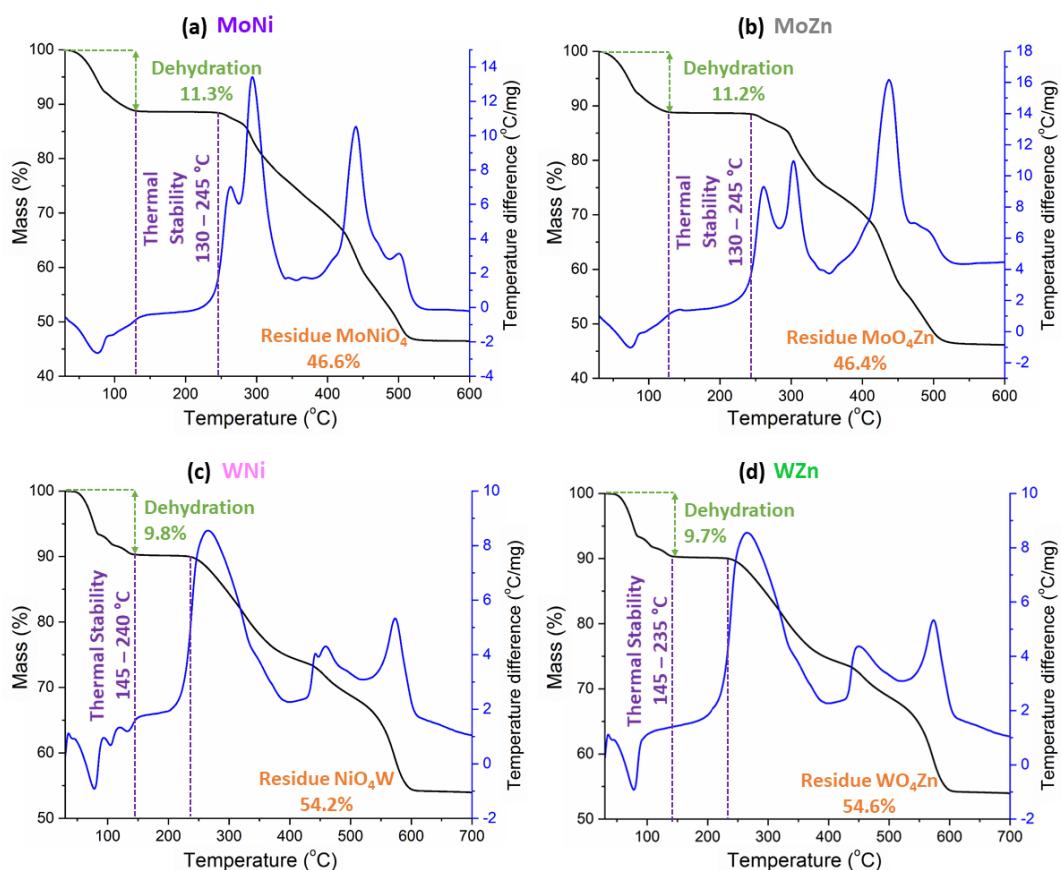


Figure A1.10. TGA/DTA curves of (a) **MoNi**, (b) **MoZn**, (c) **WNi**, and (d) **WZn**.

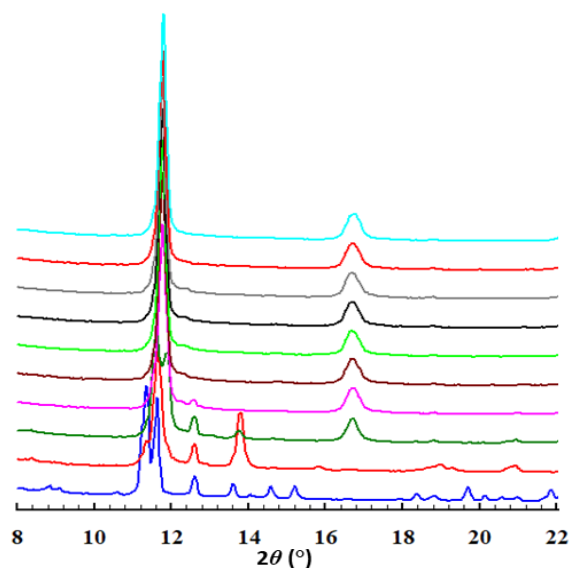


Figure A1.11. Variable temperature X-ray diffraction patterns of **MoNi** as representative of the remaining compounds, **MoZn**, **WNI** and **WZn**.

Crystal Structure: Compounds **MoNi**, **MoZn**, **WNI** and **WZn** crystallize in the monoclinic $P2_1/c$ space group (Table A1.3). The asymmetric unit contains one $[M'O_4]^{2-}$ ($M = \text{Mo}, \text{W}$) tetrahedra unit, two halves of $\{M(\text{cyclam})\}^{2+}$ ($M = \text{Ni}, \text{Zn}$) complexes and three lattice water molecules. Ni^{II} and Zn^{II} centers exhibit an octahedral geometry in which the equatorial positions are occupied by the N_4 atoms of the cyclam ligand and the axial positions by oxygen from the $\{\text{MO}_4\}$ tetrahedra. As expected, $M\text{--O}$ and $M\text{--N}$ bonds lengths found for $M = \text{Ni}$ and Zn are similar to those found along this Appendix.

Table A1.3. Crystallographic data for **MoNi**, **MoZn**, **WNI** and **WZn**.

	MoNi	MoZn	WNI	WZn
empirical formula	$\text{C}_{10}\text{H}_{30}\text{MoN}_4\text{NiO}_7$	$\text{C}_{10}\text{H}_{30}\text{MoN}_4\text{O}_7\text{Zn}$	$\text{C}_{10}\text{H}_{30}\text{N}_4\text{NiO}_7\text{W}$	$\text{C}_{10}\text{H}_{30}\text{N}_4\text{O}_7\text{WZn}$
fw (g mol^{-1})	473.03	479.69	560.94	567.60
crystal system	Monoclinic	Monoclinic	Monoclinic	Monoclinic
space group	$P2_1/c$ (14)	$P2_1/c$ (14)	$P2_1/c$ (14)	$P2_1/c$ (14)
a (\AA)	10.00594(18)	10.09829(19)	10.03179(13)	10.1344(3)
b (\AA)	15.0102(2)	14.9018(2)	15.00956(16)	14.8886(3)
c (\AA)	12.6092(2)	12.6878(2)	12.64650(15)	12.7189(4)
α ($^\circ$)	90	90	90	90
β ($^\circ$)	106.2880(18)	104.9827(19)	106.1609(13)	104.977(3)
γ ($^\circ$)	90	90	90	90
Z	4	4	4	4
V (\AA^3)	1817.78(5)	1844.38(5)	1828.97(4)	1853.92(9)
T (K)	100.01(10)	100.01(10)	100.01(10)	100.00(10)
ρ_{calcd} (g cm^{-3})	1.728	1.728	2.037	2.034
μ (mm^{-1})	1.763	2.017	2.158	7.530
collected reflns	12836	14802	10745	14804
unique reflns (R_{int})	3547 (0.029)	3594 (0.032)	3211 (0.028)	3848 (0.058)
observed reflns [$I > 2\sigma(I)$]	3227	3274	3035	3293
Parameters (restraints)	235 (6)	235 (6)	220 (18)	220 (0)
$R(F)^a$ [$I > 2\sigma(I)$]	0.021	0.022	0.023	0.033
$wR(F^2)^b$ [all data]	0.047	0.052	0.057	0.071
GoF	1.063	1.067	1.139	1.045

APPENDIX 1

The crystal packing of the four compounds consist on monodimensional chains running along the [101] direction, which are further connected through N–H···O and O_W–H_W···O_{POM} interactions to form hybrid layers (Figure A1.12b). These layers are packed forming a supramolecular 3D network through additional H-bond interactions involving hydration water molecules (Figure A1.12). As in the previous cases, even though thermostructural studies revealed the structural transformation of **MoNi**, **MoZn**, **WNi** and **WZn** under thermal stimuli, these solid-phase transitions could not be followed by single-crystal X-ray diffraction due to the loss of crystallinity of the single crystals.

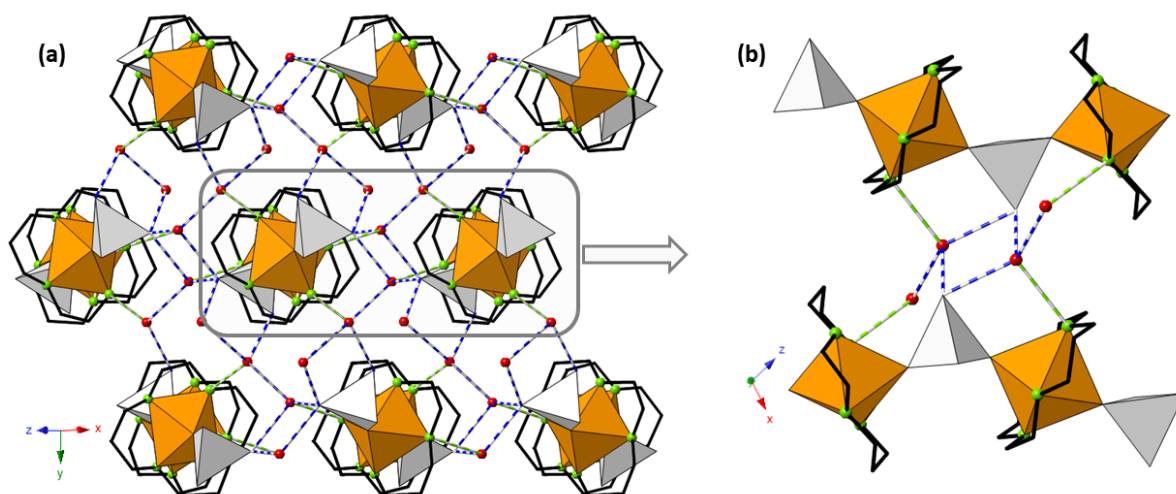


Figure A1.12. View of the (a) crystal structure of **MoNi** along the [101] direction, and (b) stacking of the monodimensional chains through H-bond interactions to form hybrid layers. Color code: MoNi₄O₂, orange polyhedra; N–H···O and O–H···O interactions, green and blue dashed lines, respectively. **MoNi** was chosen a representative of **MoZn**, **WNi** and **WZn**.

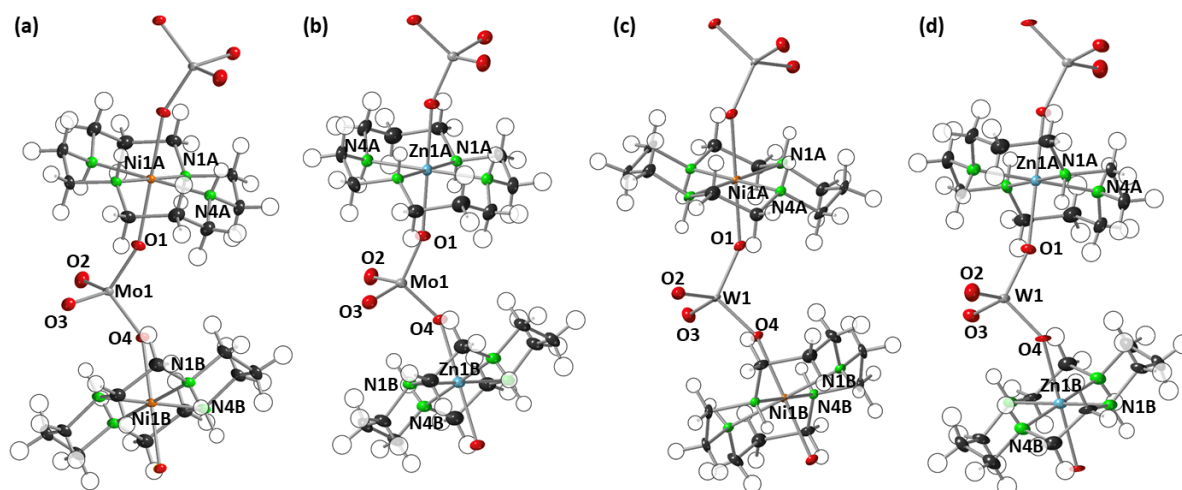


Figure 1.13. View of the monodimensional chains on **MoNi**, **MoZn**, **WNi**, and **WZn** with ORTEP representation. Color code: Mo and W, grey; Ni, orange; Zn, light blue.

A1.4. $[\text{Cu}(\text{C}_{10}\text{H}_{24}\text{N}_4)][\text{MoO}_4]\cdot 4\text{H}_2\text{O}$ (**MoCu**)

Experimental: To an aqueous solution (15 mL) of $\text{Na}_2\text{MoO}_4\cdot 2\text{H}_2\text{O}$ (0.169 g, 0.7 mmol), a solution of $\text{CuSO}_4\cdot 5\text{H}_2\text{O}$ (0.075 g, 0.3 mmol) and cyclam (0.060g, 0.3 mmol) in water (15 mL) was added dropwise. The pH of the mixture was adjusted to 10 with 1M NaOH, and the resulting purple solution was stirred for 1 h at room temperature. Purple prismatic single crystals were obtained by slow evaporation after 10-15 days. Yield: 17 mg, 11% based on Cu. IR (Figure A1.14) (cm^{-1}): 3410 (vs), 3224 (vs), 3182 (vs), 2927 (s), 2886 (s), 1471 (m), 1453 (m), 1442 (m), 1427 (m), 1374 (w), 1355 (w), 1327 (w), 1289 (w), 1253 (w), 1232 (w), 1102 (s), 1025 (m), 1016 (m), 1031 (m), 1008 (m), 961(s), 881 (vs), 852 (vs), 827 (vs), 433 (m). Elem Anal. Calcd. (%) for $\text{C}_{10}\text{H}_{32}\text{CuMoN}_4\text{O}_8$: C, 24.22%; H, 6.50%; N, 11.30%. Found: C, 24.72%; H, 6.59%; N, 11.47%.

Thermostructural behavior: Thermal stability of **MoCu** was investigated by thermogravimetric and differential thermal (TGA/DTA) analysis (Figure A1.15a), in which first a dehydration process occurs that extends up to 100 °C and accounts for four hydration water molecules (m% calcd. 14.5%; found 14.2%). The dehydration process leads to a thermal stability that extends up to almost 200 °C. Above this temperature, the combustion of the organic ligand takes place as an endothermic step. The final residue is obtained above 400 °C (m% calcd. for MoCuO_4 , 45.1%; found, 45.4%). Taking into account the thermal stability showed in the TGA, the thermostructural behavior of **MoCu** was studied by variable-temperature PXRD from room temperature to 210 °C every 20 °C. Figure A1.15b shows the presence of a thermal-dependent transformation at 70 °C indicated by the disappearance of the maximum at $2\theta = 13.1^\circ$ and the shift of the main maxima and the appearance of two new at $2\theta = 12.4^\circ$ and 15.2° .

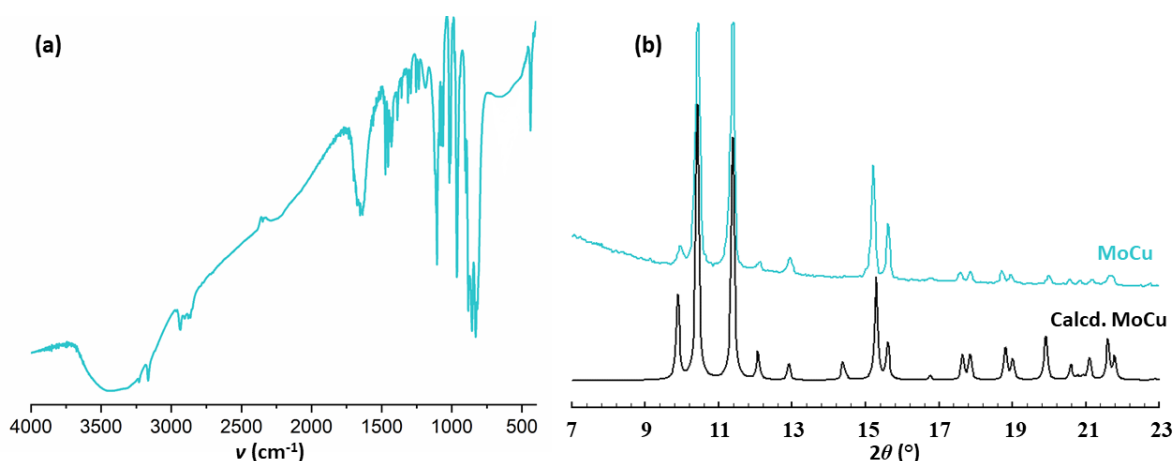


Figure A1.14. (a) FT-IR spectra of **MoCu**, and (b) comparison between the experimental powder XRD pattern of **MoCu** and that calculated from the single-crystal data.

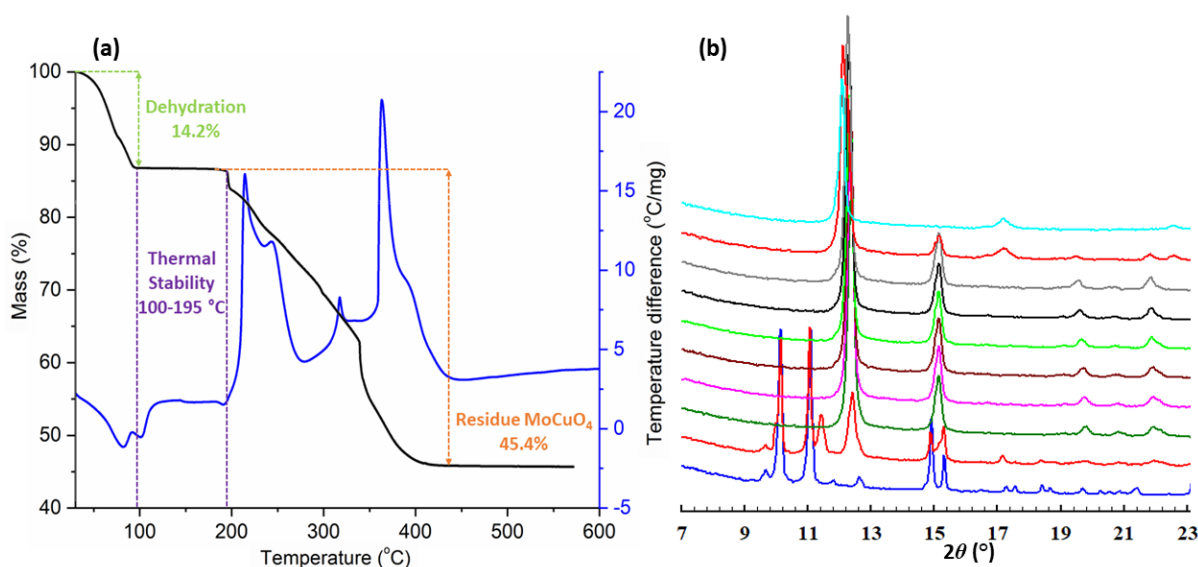


Figure A1.15. (a) TGA/DTA curves and (b) variable-temperature PXRD pattern of **MoCu**.

Crystal Structure: **MoCu** compound crystallizes in the monoclinic $P2_1/n$ space group (Table A1.4). The asymmetric unit contains one $[\text{MoO}_4]^{2-}$ tetrahedra, one octahedral $[\text{Cu}(\text{cyclam})]^{2+}$ complex and four hydration water molecules. As expected, Cu–O and Cu–N bonds lengths are fall in the range of those found for $\{\text{Cu}(\text{cyclam})\}^{2+}$ complexes along the thesis; Cu–O 2.320–2.746 Å and Cu–N 2.013–2.028 Å range.

Table A1.4. Crystallographic data for **MoCu**.

	MoCu
empirical formula	$\text{C}_{10}\text{H}_{32}\text{CuMoN}_4\text{O}_8$
fw (g mol^{-1})	495.88
crystal system	Monoclinic
space group	$P2_1/n$ (14)
a (Å)	11.3931(2)
b (Å)	14.5308(2)
c (Å)	11.6281(2)
α (°)	90
β (°)	95.0685(15)
γ (°)	90
Z	4
V (Å ³)	1917.51(6)
T (K)	100.00(10)
ρ_{calcd} (g cm^{-3})	1.718
μ (mm^{-1})	1.805
collected reflns	8550
unique reflns (R_{int})	4357 (0.030)
observed reflns [$I > 2\sigma(I)$]	3897
Parameters (restraints)	229 (0)
$R(F)^a$ [$I > 2\sigma(I)$]	0.024
$wR(F^2)^b$ [all data]	0.062
GoF	1.058

The crystal packing of **MoCu** is formed by monodimensional chains running along [010] direction, as depicted in Figure A1.16. As the chains are far enough, there are not direct hydrogen bond interactions between {Cu(cyclam)} moieties and O_{POM} atoms, therefore, individual chains are held together by H-bond interactions involving water molecules. The supramolecular arrangement shows monodimensional pores that are filled by hydration water molecules, generating hydrophilic regions growing parallel to the chains.

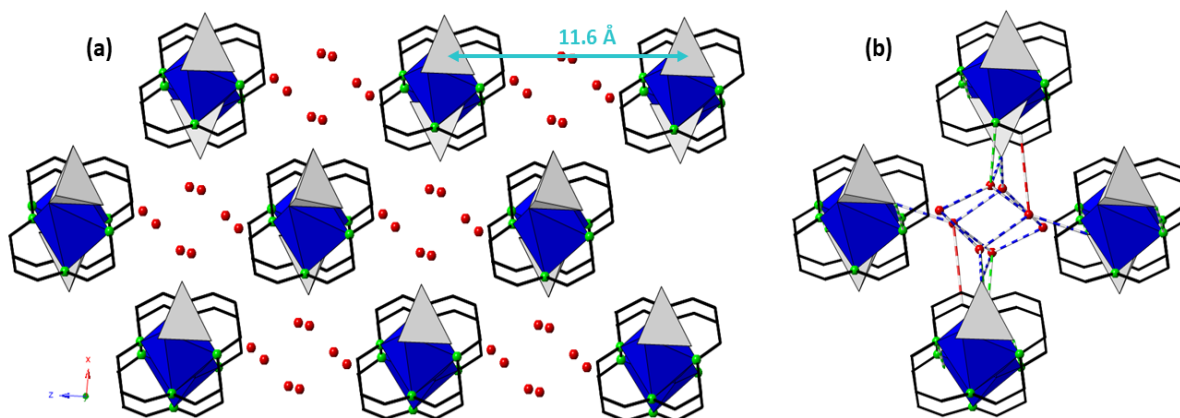


Figure A1.16. (a) Crystal packing of **MoCu** along the y axis with indication of the distance between the chains, and (b) detail of the $\text{C-H}\cdots\text{O}$, $\text{N-H}\cdots\text{O}$ and $\text{O-H}\cdots\text{O}$ interactions occurring within the water-filled channel. $\text{C-H}\cdots\text{O}$, $\text{N-H}\cdots\text{O}$ and $\text{O-H}\cdots\text{O}$ interactions, red, green and blue dashed lines, respectively.

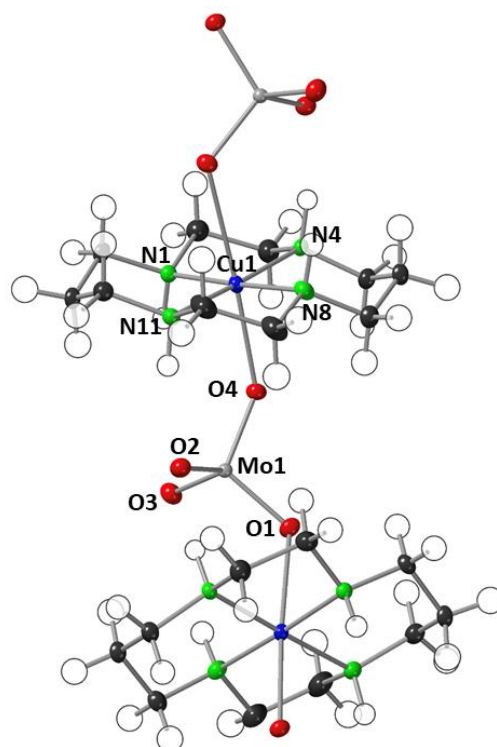


Figure 1.17. View of the monodimensional chains of **MoCu** with ORTEP representation. Color code: Mo; Cu, dark blue.

A1.5. $[\text{Cu}(\text{C}_{10}\text{H}_{24}\text{N}_4)][\text{WO}_4]\cdot 5.5\text{H}_2\text{O}$ (WCu)

Experimental: To an aqueous solution (15 mL) of $\text{Na}_2\text{WO}_4\cdot 2\text{H}_2\text{O}$ (0.230 g, 0.7 mmol), a solution of $\text{CuSO}_4\cdot 5\text{H}_2\text{O}$ (0.075 g, 0.3 mmol) and cyclam (0.060g, 0.3 mmol) in water (15 mL) was added dropwise. The pH of the mixture was adjusted to 10 with 1M NaOH, and the resulting purple solution was stirred for 1 h at room temperature. Purple prismatic single crystals were obtained by slow evaporation after 10-15 days. Yield: 15 mg, 8% based on Cu. IR (Figure A1.18) (cm^{-1}): 3410 (vs), 3231 (vs), 3159 (vs), 2944 (s), 2876 (s), 2858 (s), 1473 (m), 1452 (m), 1446 (m), 1427 (m), 1376 (w), 1359 (w), 1324 (w), 1289 (w), 1253 (w), 1231 (w), 1107 (s), 1026 (m), 1014 (m), 1019 (m), 1011 (m), 962 (s), 878 (vs), 853 (vs), 832 (vs), 438 (m). Elem Anal. Calcd. (%) for $\text{C}_{10}\text{H}_{35}\text{CuN}_4\text{O}_{9.5}\text{W}$: C, 19.66%; H, 5.78%; N, 9.17%. Found: C, 19.75; H, 5.69%; N, 9.11%.

Thermostructural behavior: Thermal stability of WCu was investigated by TGA/DTA analysis (Figure A1.19a), in which first a dehydration process occurs that extends up to 110 °C and accounts for 5.5 hydration water molecules (m% calcd. 16.2%; found 15.8%). The dehydration process leads to a thermal stability that extends up to 210 °C. Above this temperature, the combustion of the organic ligand takes place as an endothermic step. The final residue is obtained above 450 °C (m% calcd. for CuWO_4 , 51.0%; found, 50.7%).

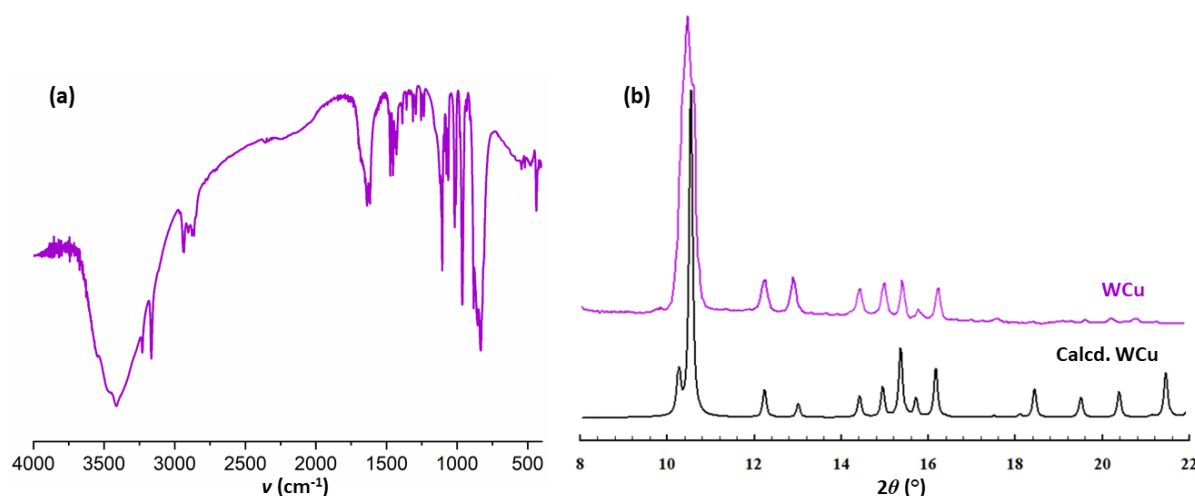


Figure A1.18. (a) FT-IR spectra of WCu, and (b) comparison between the experimental powder XRD pattern of WCu and that calculated from the single-crystal data.

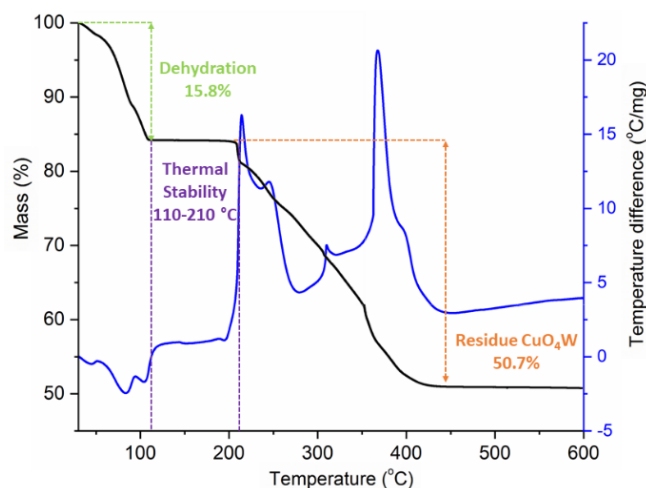


Figure A1.19. TGA/DTA curves for **WCu**.

Crystal Structure: **WCu** compound crystallizes in the orthorhombic *Pbca* space group (Table A1.5). The asymmetric unit is constituted by one $[\text{WO}_4]^{2-}$ tetrahedra, one $[\text{Cu}(\text{cyclam})]^{2+}$ metalorganic moiety and 5.5 hydration water molecules disordered in 9 positions. Cu–O and Cu–N bonds lengths are similar to those found for $\{\text{Cu}(\text{cyclam})\}^{2+}$ complexes along the thesis. Crystal packing of **WCu** can be best described as corrugated layers formed by single monodimensional chains running along the *x* axis that are hydrogen bonded between them through water molecules (Figure A1.20). The corrugated layers are further connected along [010] direction, generating cavities between the layers in which the remaining water molecules are located. The layers stack together through additional C–H \cdots O, N–H \cdots O interactions with the hydration water molecules.

Table A1.5. Crystallographic data for **WCu**.

	WCu
empirical formula	$\text{C}_{10}\text{H}_{35}\text{CuN}_4\text{O}_{9.5}\text{W}$
fw (g mol^{-1})	610.83
crystal system	Orthorhombic
space group	<i>Pbca</i>
<i>a</i> (Å)	14.2873(2)
<i>b</i> (Å)	23.1050(3)
<i>c</i> (Å)	12.3068(2)
α (°)	90
β (°)	90
γ (°)	90
<i>Z</i>	8
<i>V</i> (Å ³)	4062.57(10)
<i>T</i> (K)	100.01(10)
ρ_{calcd} (g cm^{-3})	1.961
μ (mm^{-1})	6.754
collected reflns	
unique reflns (R_{int})	4794 (0.050)
observed reflns [$I > 2\sigma(I)$]	4235
Parameters (restraints)	217 (0)
$R(F)^a$ [$I > 2\sigma(I)$]	0.043
$wR(F^2)^b$ [all data]	0.085
GoF	1.290

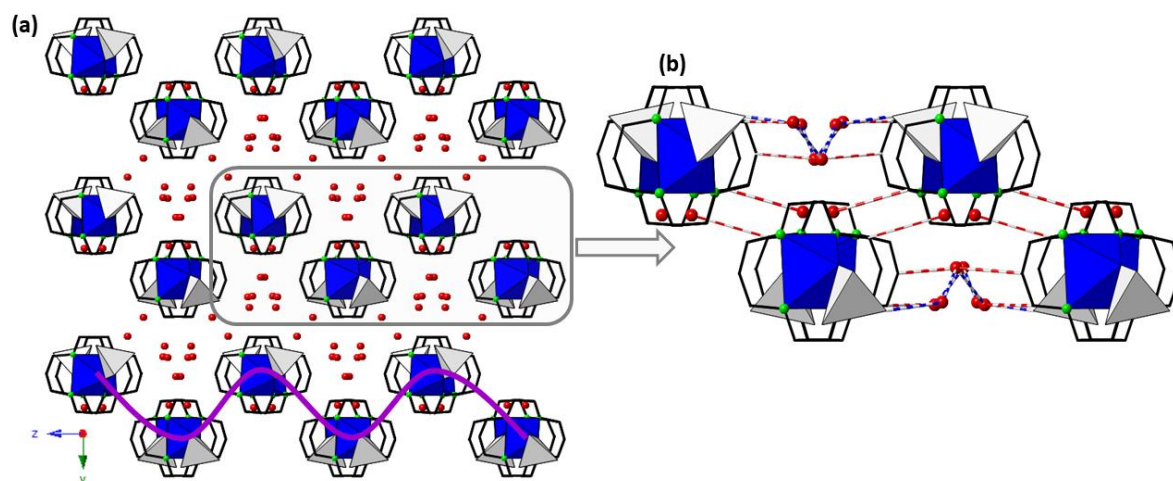


Figure A1.20. (a) Crystal packing of **WCu** along the *x* axis, and (b) detail of the C–H⋯O and O–H⋯O interactions occurring between single monodimensional chains within a corrugated layer.

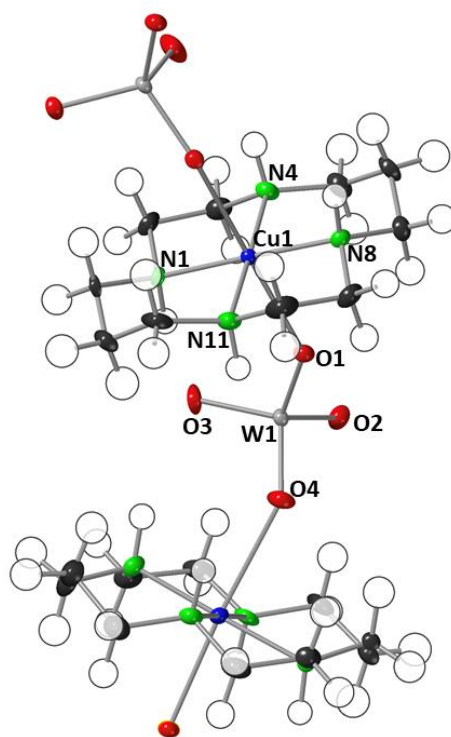


Figure 1.21. View of the monodimensional chains of **WCu** with ORTEP representation. Color code: W, grey; Cu, dark blue.

A1.6. ELECTRON PARAMAGNETIC RESONANCE (EPR)

The EPR Q-bands for compounds **MoCu** and **WCu** (Figures A1.22 and A1.23) are characteristic of an octahedral coordinated Cu^{2+} . The Q-bands show that compounds **MoCu** and **WCu** belong to the rhombic system, with an elongated octahedral or squared based pyramidal geometry (Table A1.6). Cu^{2+} has a spin $S = \frac{1}{2}$ with a nuclear spin of $I = \frac{3}{2}$ and, as it is not magnetically isolated, there is no presence of four-line hyperfine splitting.

Table A1.6. The values of "g" from the Band-Q of the EPR spectra.

	MoCu	WCu
g ₁	2.051	2.051
g ₂	2.073	2.073
g ₃	2.177	2.179

If G values are calculated by Eq. A1.1, a value of 2.85 is obtained for **MoCu** and 2.89 for **WCu**. For the obtaining G values, it has been assumed that the g_z was the g with the highest value.

$$G = \frac{g_z - 2}{\frac{g_x + g_y}{2} - 2} \quad (\text{Eq. A1.1})$$

Having a G value lower than 4 indicates that the Cu²⁺ of both compounds do not have the same orientation along the chains, what has been observed in the crystal packing for **MoCu** and **WCu** and corroborated with the distances and angles formed by the metal centers in each structure (Table A1.7) In addition, if we compared the two Q-band of both compounds, it can be seen that there is a higher difference between the g_1 and g_3 values for **WCu** than for **MoCu** (Figure A1.24). This little difference is also matches with the G values, as the value for **WCu** is a bit higher than the one for **MoCu**.

Table A1.7. M...M (M = Ni, Cu, Zn) distances and angles of M(cyclam) complexes.

	CrNi	CrZn		CrCu	
		Cr1A	Cr1B	Cr1A	Cr1B
M–Cr–M	143.8	166.4	167.9	167.2	164.2
O_{POM}–M–O_{POM}	180	175.0	173.1	174.3	176.3
M...M	6.595	7.301	7.252	7.124	7.055
	MoNi	MoZn		MoCu	
M–Mo–M	133.3	139.9		133.3	
O_{POM}–M–O_{POM}	180	173.1		180	
M...M	6.862	7.290		7.013	
	WNi	WZn		WCu	
M–W–M	133.2	131.2		133.3	
O_{POM}–M–O_{POM}	180	173.8		180	
M...M	6.891	7.185		7.033	

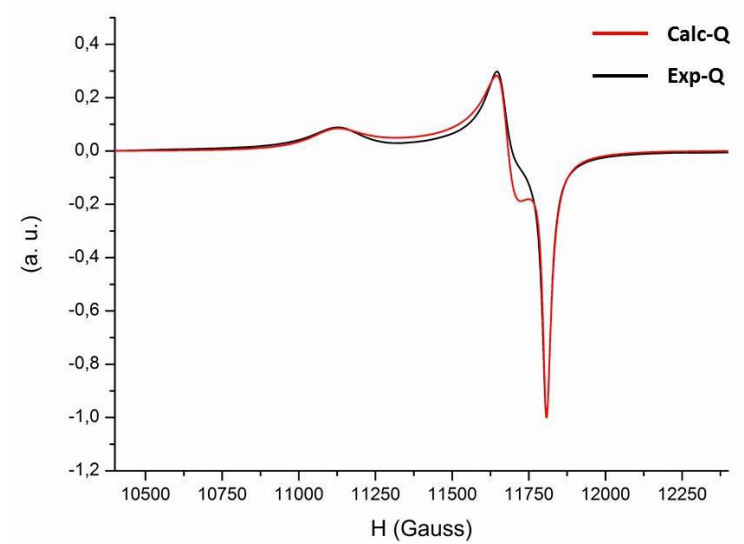


Figure A1.22. Q-band for MoCu.

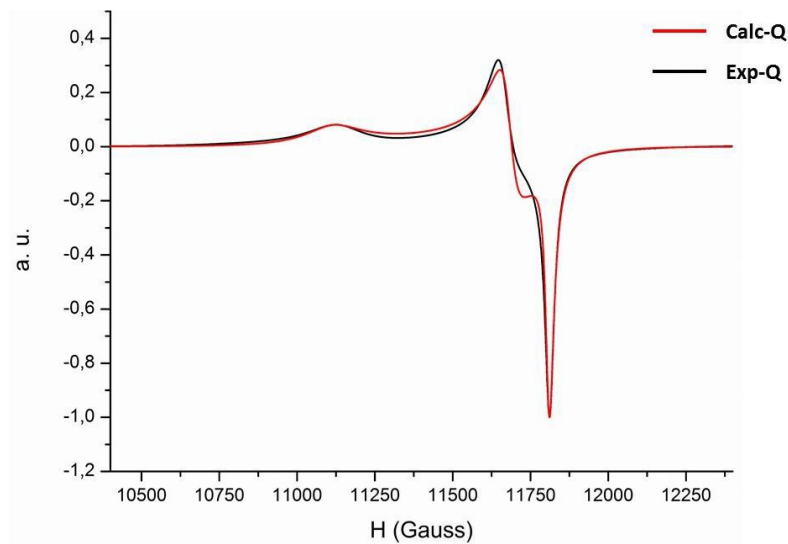


Figure A1.23. Q-band for WCu.

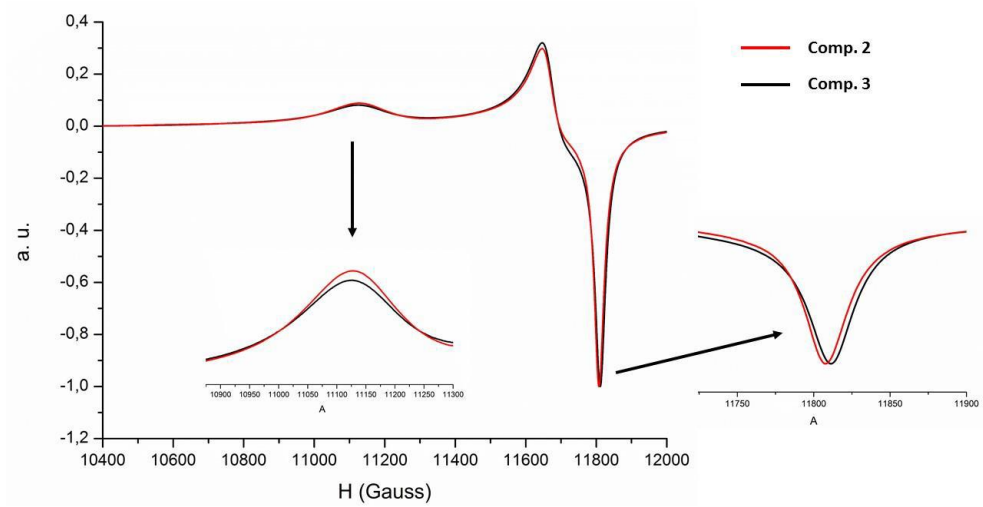


Figure A1.24. Comparison between the Q-bands of MoCu and WCu.

A1.7. REFERENCES

- [1] (a) Groysman, S.; Villagrán, D.; Nocera, D. G. Pseudotetrahedral d^0 , d^1 , and d^2 Metal-Oxo Cores within a Tris(alkoxide) Platform. *Inorg. Chem.*, **2010**, *49*, 10759-10761. (b) Sukhikh, A. S.; Khranenko, S. P.; Pishchur, D. P.; Gromilov, S. A. Jahn-Teller Effect in the $[\text{CuEn}_3]\text{CrO}_4$ Structure. *J. Struct. Chem.*, **2018**, *59*, 657-663.
- [2] (a) Hunter, T. M.; McNae, I. W.; Simpson, D. P.; Smith, A. M.; Moggach, S.; White, F.; Walkinshaw, M. D.; Parson, S.; Sadler, P. J. Configurations of Nickel-Cyclam Antiviral Complexes and Protein Recognition. *Chem. Eur. J.*, **2007**, *13*, 40-50. (b) Gavrish, S. P.; Shova, S.; Cazacu, M.; Lampeka, Y. D. Crystal Structure of the One-Dimensional Coordination Polymer Formed by the Macrocyclic $[\text{Ni}(\text{cyclam})]^{2+}$ Cation and the Dianion of Diphenylsilanediylbis(4-benzoic acid). *Acta Cryst.*, **2020**, *E76*, 929-932. (c) Tsybal, L. V.; Andriichuk, I. L.; Shova, S.; Lampeka, Y. D. Crystal Structure of $[\{\{\text{Ni}(\text{C}_{10}\text{H}_{24}\text{N}_4)\}[\text{Ni}(\text{CN})_4]\} \cdot 2\text{H}_2\text{O}]_n$, a One-Dimensional Coordination Polymer Formed from the $[\text{Ni}(\text{cyclam})]^{2+}$ Cation and the $[\text{Ni}(\text{CN})_4]^{2-}$ Anion. *Acta Cryst.*, **2021**, *E77*, 1140-1143.
- [3] Kayani, Z. N.; Iqbal, M.; Riaz, S.; Zia, R.; Naseem, S. Fabrication and Properties of Zinc Oxide Thin Film Prepared by Sol-Gel Dip Coating Method. *Mater. Sci.-Pol.*, **2015**, *33*, 515-520.

Materials and Methods

A2.1. Instrumental techniques

A2.2. Single-crystal X-ray Diffraction

A2.3. Photoluminescent analysis

A2.4. Magnetic susceptibility measurements

A2.5. Gas sorption measurements

A2.6. Dynamic vapor sorption (dvs) experiments

A2.7. References

A2.1. INSTRUMENTAL TECHNIQUES

All the experimental conditions applied for the characterization methods are described in this section. FT-IR experiments and thermal analyses were performed in the Departamento de Química Orgánica e Inorgánica (UPV/EHU), whereas the remaining analysis were carried out in Servicios Generales de Investigación (SGIker) de la UPV/EHU; powder and single-crystal X-ray diffraction measurements, elemental analysis, magnetic and susceptibility measurements, $^1\text{H-NMR}$ and ESI-MS analysis. Luminescence measurements were performed at Departamento de Física aplicada II (UPV/EHU). Gas sorption and water sorption measurements were carried out during a three-month stay at the Bernal Institute in the University of Limerick (Ireland), under the supervision of Prof. Michael Zaworotko.

A2.1.1. Elemental analysis

The C, H and N content of all the compounds was determined on a PerkinElmer 2400 CHN analyzer, employing around 10 mg of powdered crystalline samples. Metal content (lanthanides and alkaline metals of **1-Ln** (Ln = Sm to Lu) in *Chapter 5*) were analyzed using a Q-ICP-MS ThermoXSeries II analyzer coupled plasma-mass spectrometry device. Samples (50 mg) were digested in 25 mL of ultra-high purity Milli-Q water.

A2.1.2. FT-IR spectroscopy

Fourier transformed infrared (FT-IR) spectra were obtained as KBr (Aldrich, FT-IR grade) pellets on a Shimadzu FTIR-8400S spectrometer. FT-IR spectra were recorded in the 400–4000 cm^{-1} region (4 cm^{-1} resolution).

A2.1.3. Thermal analyses

Thermogravimetric and differential thermal analyses (TGA/DTA) were performed on a Mettler Toledo TGA/SDTA851^e thermobalance under a 50 $\text{cm}^3\text{min}^{-1}$ flow of synthetic air from room temperature to 800 °C at a rate of 5 °C min^{-1} . β -alumina crucibles were used for approximately 20 mg of crystalline samples.

A2.1.4. Powder X-ray diffraction

Powder X-ray diffraction (PXRD) patterns were recorded for $2\theta = 5 \leq 2\theta \leq 40^\circ$ range (0.033° step size, 30 s per step) using a Philips X'PERT PRO diffractometer operating at 40 kV/40 mA in θ - θ configuration, equipped with monochromated Cu $K\alpha$ radiation ($\lambda = 1.5418 \text{ \AA}$) and a PIXcel detector. Variable temperature PXRD patterns were collected on a Bruker D8 Advance Diffractometer operating at 30 kV/20 mA and equipped with Cu $K\alpha$ radiation, a Vantec-1 PSD detector, an Anton Parr HTK2000 high-temperature furnace, and a Pt sample holder. Temperature changes were recorded from 30 °C to 610 °C every 20 °C, for **1-Mo8**

from 30 °C to 46 °C every 2 °C and **2-Mo8** from 46 °C to 30 °C every 2 °C, with a 0.16 °C s⁻¹ heating rate between temperatures.

A2.1.6. Nuclear Magnetic Resonance Spectroscopy

¹H-Nuclear Magnetic Resonance (¹H-NMR) data as acquired for **1-Lu** sample and the H₂L starting ligand from *Chapter 5*, on a Bruker ADVANCE 500 spectrometer. For H₂L ligand, the sample was dissolved in CDCl₃ and (CD₃)₂SO, whereas **1-Lu** data was only collected in DMSO (freshly prepared and after 7 days), for solubility reasons.

A2.1.7. Electrospray ionization mass spectrometry (ESI-MS)

Electrospray ionization mass spectra (ESI-MS) of **1-Ln** (Ln = Tbⁱⁱⁱ, Tmⁱⁱⁱ) samples in *Chapter 5* were obtained on aqueous solutions of solid samples that were diluted to 10⁻⁵ M approximately on a H₂O/CH₃CN (1:1) mixture and introduced at a flow rate of 10 μL min⁻¹ using Waters SYNAPT G2 HDMS QTOF instrument with an orthogonal Z-spray electrospray interface operating with capillary voltage of 3.3 kV in the negative scan mode (V mode) and N₂ as desolvation (300 L h⁻¹) and cone gas (30 L h⁻¹). Typical desolvation (200 °C) and source block (120 °C) temperatures were used, and the cone voltage (U_c) was set to 15 V in order to control the extent of fragmentation of the detected species.

A2.2. SINGLE-CRYSTAL X-RAY DIFFRACTION

Experimental condition used on single-crystal X-ray diffraction (scXRD) studies is summarized in this section; data acquisition and reduction, solution and refinement of crystal structures; software and crystallographic databases employed for further calculations and treatment of the data.

A2.2.1. Data acquisition and reduction

Intensity data were collected on an Agilent Technologies SuperNova diffractometer equipped with either monochromated Cu Kα radiation (λ = 1.5406 Å) and an Atlas detector or Mo Kα radiation (λ = 0.71073 Å) and an Eos CCD detector. Data frames were processed (unit cell determination, analytical absorption correction with face indexing, intensity data integration, and correction for Lorentz and polarization effects) with the CrysAlis Pro¹ software package. The structures were solved using the OLEX2-1.3² program and refined by full-matrix least squares using SHELXL-2014/6, SHELXL-2018/3 and SHELXH-97.³ In all least-squares refinements, R and wR have been calculated using Eq. A2.1 and A2.2.

$$R(F) = \sum ||F_0 - F_c| | / \sum |F_0| \quad (\text{Eq. A2.1})$$

$$wR(F^2) = \{ \sum [w(F_0^2 - F_c^2)^2] / \sum [w(F_0^2)^2] \}^{1/2} \quad (\text{Eq. A2.2})$$

A2.2.3. Calculations

Final geometrical calculations were carried out with PLATON⁴ as integrated in WinGX,⁵ and their visualization was performed using Crystal-Maker. Bond Valence Sum calculations for **4-Mo8** in *Chapter 3* were carried out using the Brown & Wu method⁶ as integrated in Vesta.⁷ Both the surface of water-filled channels in porous structures as well as the solvent accessible voids present in *Chapters 2, 3* and *4*, were visualized with PyMol software.⁸

Continuous Shape Measures (CShM) calculations were performed using SHAPE programs.⁹ **CShM** structural analyses¹⁰ works by comparing the experimental polyhedra with the ideal shapes of the regular polyhedra, indicating how distorted the structure is from the reference shape. The CShM number indicates the distortion, in which the lower value is the one describing better the ideal shape.

A2.2.4. Crystallographic software and databases

Crystal Maker software¹¹ was used for the visualization and graphic representation of all the compounds. Moreover, the structural CSD and ICSD, and scientific SciFinder databases were employed in this work:

Cambridge Structural Database (CSD):¹² X-ray and neutron diffraction structures of organic, organometallic and coordination complexes are included in this database of the Cambridge Crystallographic Data Center (CCDC).

Inorganic Crystal Structure Database (ICSD):¹³ X-ray and neutron diffraction structures of completely inorganic compounds (including pure elements, minerals, metals, inorganic salts...) are included in this database of the Fachinformationszentrum (FIZ) Karlsruhe.

SciFinder:¹⁴ Multifunctional scientific database developed by the Chemical Abstract Service (CAS) for substances, reactions, and patent and journal references of chemistry and related fields.

A2.3. PHOTOLUMINESCENCE ANALYSIS

Diffuse reflectance UV–vis spectra were recorded on a UV-2600 Shimadzu spectrophotometer. Photoluminescence (PL) emission spectra were recorded for powdered crystalline **1-Ln** (Ln = Sm to Lu, *Chapter 5*) samples from 10 K to room temperature using a close cycle The cryostat contained in an Edinburgh Instruments FLS920 spectrometer equipped with a Müller-elektronik- Optik SVX1450 Xe lamp and a Kimmon IK3552R-G He: Cd continuous laser (325 nm). The lifetime measurements were performed using a μ F1 pulsed

microsecond flashlamp as an excitation source. Photographs of bulky samples were taken in a micro-PL system included in an Olympus optical microscope (Color View III camera) illuminated with an Hg lamp.

A2.4. MAGNETIC SUSCEPTIBILITY MEASUREMENTS

Magnetic susceptibilities were measured in the 2–300 K range using a Quantum Design MPMS3 SQUID magnetometer under an applied field of 0.1 T (diamagnetic corrections were estimated from Pascal's constants). Magnetization and alternating current (ac) susceptibility measurements were performed on a PPMS (Physical Property measurement System)–Quantum Design Model 6000 and the SQUID magnetometers in the 2–10 K temperature range up to a 7 T magnetic field.

Whereas magnetic susceptibilities were fitted to Van Vleck's equation (Table 5.7 in Chapter 5), the Curie-Weiss law was applied for paramagnetic regions:

$$\chi_m = \frac{C}{(T-\theta)} \quad (\text{Eq. A2.3})$$

where C is the Curie constant and θ is the Weiss temperature.

The magnetic susceptibility curves for **1-Eu** were modeled by Kahn's equation;

$$\chi(T) = \frac{Ng_j^2\beta^2J(J+1)}{3kT} + \frac{2N\beta^2(g_j-1)(g_j-2)}{3\lambda} \quad (\text{Eq. A2.4})$$

where N is the Avogadro's number, β is the Bohr magneton, k is the Boltzmann constant, g is the Landé factor, S is the spin quantum number and λ is the spin orbit coupling parameter.

The frequency-dependences of in-phase and out-of-phase magnetic susceptibilities were fitted to the Debye model;

$$\chi'(\omega) = \chi_S + (\chi_T - \chi_S) \frac{1 + (\omega\tau)^{1-\alpha} \sin\left(\frac{\pi}{2}\alpha\right)}{1 + 2(\omega\tau)^{1-\alpha} \sin\left(\frac{\pi}{2}\alpha\right) + (\omega\tau)^{2-2\alpha}} \quad (\text{Eq. A2.5})$$

$$\chi''(\omega) = (\chi_T - \chi_S) \frac{(\omega\tau)^{1-\alpha} \cos\left(\frac{\pi}{2}\alpha\right)}{1 + 2(\omega\tau)^{1-\alpha} \sin\left(\frac{\pi}{2}\alpha\right) + (\omega\tau)^{2-2\alpha}} \quad (\text{Eq. A2.6})$$

$$\chi''(\chi') = \frac{\chi_T - \chi_S}{2 \tan\left[\frac{1}{2}\pi(1-\alpha)\right]} + \left[\left(\frac{\chi_T - \chi_S}{2} \right)^2 - \left(\frac{\chi_T - \chi_S}{2 \tan\left[\frac{1}{2}\pi(1-\alpha)\right]} \right)^2 - \left(\chi' - \frac{\chi_T - \chi_S}{2} \right)^2 \right]^{\frac{1}{2}} \quad (\text{Eq. A2.7})$$

A2.4.1. Electron Paramagnetic Resonance (EPR) analysis

Electron paramagnetic resonance (EPR) spectra were recorded on powder crystalline samples Bruker ELEXSYS 500 (superhigh-Q resonator ER-4123-SHQ) and Bruker EMX (ER-510-QT resonator) continuous wave spectrometers for Q- and X-bands, respectively (magnetic calibration: NMR probe; frequency inside the cavity determined with microwave counter).

A2.5. GAS SORPTION MEASUREMENTS

Gas physisorption measurements on anhydrous samples **2-Mo8** and **3-Mo8** on Chapter 3 were carried out on the Micromeritics TriStar II PLUS 3030 instrument. The samples were first thermally activated at 50 (**2-Mo8**) and 120 °C (**3-Mo8**), and then, degassed under vacuum and at the same temperature for 4 h prior to gas sorption experiments. The PXRD analyses of the degasified samples demonstrated that the structures of the anhydrous phases retain crystallinity and remain unmodified after being exposed to vacuum conditions. Low pressure N₂ and CO₂ adsorption experiments (up to 1 bar) of **2-Mo8** and **3-Mo8** were conducted at 77 K and 195 K, respectively. This temperature was maintained by a 4 L Dewar flask filled with the mixture of acetone and dry ice. High-purity N₂ and CO₂ were used as received from BOC Gases Ireland, CP grade (99.995%). Micromeritics 3Flex surface area and pore size analyzer 3500 was used for collecting the 273 and 298 K sorption isotherms for N₂, CO₂.

Brunauer-Emmett-Teller (BET) surface areas were determined from the N₂ and CO₂ adsorption isotherms at 77 K and 195 K, respectively, using the Micromeritics Microactive Software. About 100 mg of activated samples were used for the measurements. A Julabo temperature controller was used to maintain a constant temperature in the bath throughout the experiment. The bath temperatures of 273 and 298 K were precisely controlled with a Julabo ME (v.2) recirculating control system containing a mixture of ethylene glycol and water. The low temperature at 77 K and 195 K were controlled by a 4 L Dewar filled with liquid N₂ and dry ice/acetone, respectively. Precise control of 273 and 298 K temperatures for sorption isotherms of N₂, CO₂, CH₄, C₂H₂, C₂H₄ and C₂H₆ was implemented by a dc-2006 from Ningbo Scientz Biotechnology, which contained a cyclic control system of ethylene glycol and water mixture (v/v = 1:1).

Horvath-Kawazoe (HK) Pores Size Distribution Method:¹⁵ The Horvath-Kawazoe (HK) method is based on capillary condensation is an analytic model of adsorption that is commonly used for the characterization of the pore size distribution on microporous materials.¹⁶

Calculation of Isosteric Heat of Adsorption (Q_{st}): The isosteric heat of adsorption indicates the interaction strength between the gas molecules and the adsorbent host. The Q_{st} values for **3-Mo8** in Chapter 3 were calculated from the low pressure CO₂ adsorption isotherms collected at 273 and 298 K. The Clausius-Clapeyron equation was employed for calculating Q_{st} values and virial-type equations were used to fit points in the adsorption data (Eq. 2.8). After that, the final Q_{st} values were then calculated from the virial model using Eq. 2.9. ¹⁷The plots and data for the fits are shown below (Table A2.1 and Figure A2.1)

$$Q_{st} = -R \cdot \ln\left(\frac{p_2}{p_1}\right) \left(\frac{T_1 T_2}{T_2 - T_1}\right) \quad (\text{Eq. 2.8})$$

In which R is the universal constant gas ($R = 8.314 \text{ JK}^{-1}\text{mol}^{-1}$); p is the pressure (bar), and; T is the temperature (K).

$$-Q_{st} = R \sum_{i=0}^j a_i b^i \quad (\text{Eq. 2.9})$$

In which a_i and b^i are the virial coefficients.

Table A2.1. Virial-fit parameters calculated for CO₂, CH₄, C₂H₂, C₂H₄ and C₂H₆ for **3-Mo8** in Chapter 3.

Adsorbate	C ₂ H ₂	CO ₂	C ₂ H ₄	C ₂ H ₆	CH ₄
Temperatures	273, 298 K	273, 298 K	273, 298 K	273, 298 K	273, 298 K
Adj. R ²	0.99996	1.00000	0.99992	0.99997	0.99493
a ₀	-4102.34	-2894.04	-3271.38	-3723.89	-2964.11
a ₁	376.0896	721.9293	-875.336	141.1164	13221.97
a ₂	-1111.23	-2053.44	2642.751	-2343.64	-47271.8
a ₃	-326.421	1882.093	-5158.23	-1108	-193491
a ₄	1484.386	-683.653	7136.081	7728.124	1.30E+06
a ₅	-403.97	232.6895	-2687.27	-3240.93	-1.41E+06
b ₀	23.49249	21.1802	21.40416	22.43505	23.05461
b ₁	-1.92458	-1.47199	1.71354	-1.5512	-57.7327
b ₂	8.21747	5.97802	3.22144	20.1057	387.5923
b ₃	-5.3419	-3.92305	-6.60972	-20.0097	-856.417

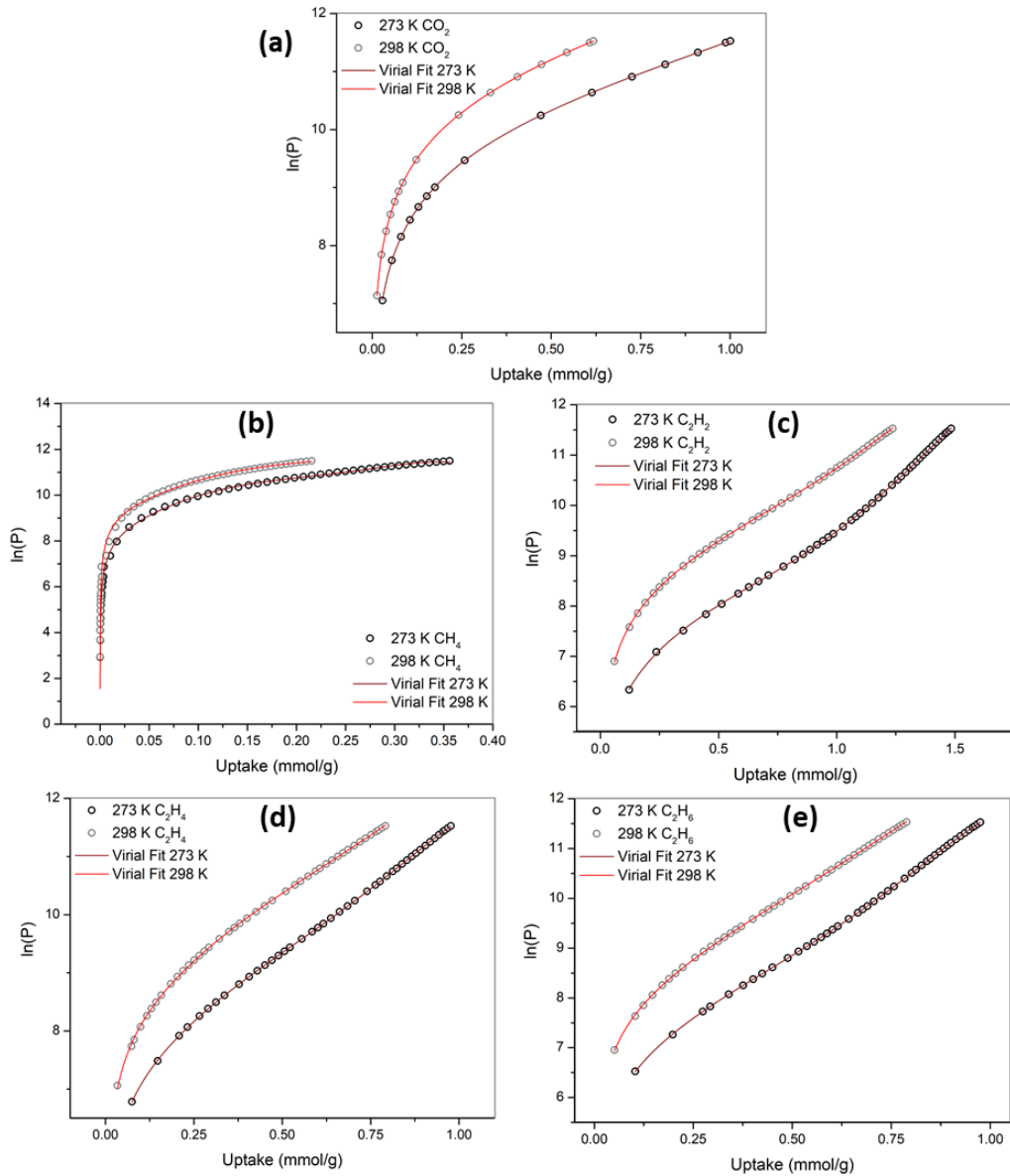


Figure A2.1. Representation of the virial-fit parameters calculated for CO₂, CH₄, C₂H₂, C₂H₄ and C₂H₆ for **3-Mo8** in Chapter 3.

Calculation of IAST Selectivity:¹⁸ Gas separation selectivities for the adsorbate mixture compositions of interest were calculated from the single-component adsorption isotherms using the Ideal Adsorbed Solution Theory (IAST) in the program IAST++.¹⁹

First, the single-component isotherms for the adsorbates at 298 K were fitted to the dual-site Langmuir-Freundlich equation.^{REF}

$$q = q_1 \frac{(K_1 P)^{n_1}}{1 + (K_1 P)^{n_1}} + q_2 \frac{(K_2 P)^{n_2}}{1 + (K_2 P)^{n_2}} \quad (\text{Eq. 2.10})$$

Where, p is the pressure of the bulk gas at equilibrium (mbar), q is the adsorbed amount per mass of adsorbent (mmol/g), q_1 and q_2 are the saturation capacities of sites 1

and 2 (mmol/g), k_1 and k_2 are the affinity coefficients of sites 1 and 2 (1/mbar), and n_1 and n_2 represent the deviations from an ideal, homogeneous surface.²⁰ Isotherm fitting parameters are summarized in Table A2.2 and all isotherms were fitted with $R^2 > 0.999$.

Table A2.2. Isotherm fitting parameters of **3-Mo8** in Chapter 3.

Adsorbate	Model	R ²	q ₁ (mmol g ⁻¹)	k ₁ (bar ⁻¹)	q ₂ (mmol g ⁻¹)	k ₂ (bar ⁻¹)
C ₂ H ₂	Dual-site Langmuir	0.999982	1.38913	5.11641	62.601	0.00107021
CO ₂	Dual-site Langmuir	0.999989	5.10039e ⁻¹¹	1.262e ⁻¹¹	1.54083	0.666305
C ₂ H ₄	Dual-site Langmuir	0.999997	0.795838	4.24502	7.02588	0.0214094
C ₂ H ₆	Dual-site Langmuir	0.999998	0.692747	8.10338	0.965212	0.215113
CH ₄	Dual-site Langmuir	0.999989	0.00735212	13.1469	2.93498	0.0784562
N ₂	Dual-site Langmuir	0.999827	7.95243e ⁻¹⁰	0.119931	0.793729	0.120284

A2.6. DYNAMIC VAPOR SORPTION (DVS) EXPERIMENTS

Dynamic water vapor sorption studies were conducted using a DVS Endeavor Surface Measurement System device, which gravimetrically measures the uptake and loss of vapor. Samples of **1-Mo8** were thermally activated at 50 (**2-Mo8**) and 120 °C (**3-Mo8**) for 1 h before performing the sorption experiments from 0 to 95% Relative Humidity (RH) in 5% incremental RH steps. The sequential steps were controlled with an equilibrium criterion of $dm/dt = 0.05 \text{ \% min}^{-1}$. The temperature was maintained constant at 298 K by enclosing the system in a temperature-controlled incubator, and pure water was used as adsorbate. After reaching a RH level of 95%, this parameter was then decreased in a similar manner to achieve a full adsorption/desorption cycle. Two complete adsorption/desorption cycles were run for **2-Mo8**, and three for **3-Mo8**. Kinetics were monitored under a constant air flow of 30 % and 60% RH, whereas 100 adsorption/desorption cycles of 15 min were used for stability studies under a constant airflow of 60 % RH.

A2.7. REFERENCES

- [1] *CrysAlisPro Software System*, Version 171.40.67; Agilent Technologies UK Ltd.: Oxford, UK, **2012**.
- [2] Dolomanov, O. V.; Bourhis, L. J.; Gildea, R. J.; Howard, J. A. K.; Puschmann, H. OLEX2: A Complete Structure Solution, Refinement and Analysis Program. *J. Appl. Crystallogr.* **2009**, *42*, 339-341.
- [3] (a) Sheldrick, G. M. Crystal Structure Refinement with SHELXL. *Acta Crystallogr., Sect. C: Struct. Chem.* **2015**, *71*, 3–8. (b) Sheldrick, G. M. Crystal structure refinement with SHELXL. *Acta Crystallogr., Sect. C: Struct. Chem.* **2014**, *71*, 3-8. (c) Sheldrick, G. M. A Short History of SHELX. *Acta Crystallogr.* **2008**, *A64*, 112–122.
- [4] Spek, A. L. Structure Validation in Chemical Crystallography. *Acta Crystallogr., Sect. D: Biol. Crystallogr.* **2009**, *65*, 148-155.

- [5] Farrugia, L. J. WinGX Suite for Small-Molecule Single-Crystal Crystallography. *J. Appl. Crystallogr.* **1999**, *32*, 837-838.
- [6] Brown, I. D.; Wu, K. K. Empirical Parameters for Calculating Cation-Oxygen Bond Valences. *Acta Crystallogr., Sect. B: Struct. Crystallogr. Cryst. Chem.* **1976**, *B32*, 1957-1959.
- [7] Momma, K.; Izumi, F. VESTA3 for Three-Dimensional Visualization of Crystal, Volumetric and Morphology Data, *J. Appl. Crystallogr.* **2011**, *44*, 1272-1276.
- [8] DeLano, W. L. The PyMOL Molecular Graphics System; DeLano Scientific: San Carlos, CA, **2002**.
- [9] Llunell, M.; Casanova, D.; Cirera, J.; Bofill, J. M.; Alemany, P.; Alvarez, S.; Pinsky, M.; Avnir, D. SHAPE, v2.1; Universitat de Barcelona: Barcelona, Spain and The Hebrew University of Jerusalem: Jerusalem, Israel, **2005**.
- [10] Cirera, J.; Ruiz, E.; Alvarez, S. Continuous Shape Measures as a Stereochemical Tool in Organometallic Chemistry. *Organometallics*, **2005**, *24*, 1556-1562.
- [11] Palmer, D. C. *Crystal Maker*; CrystalMaker Software Ltd: Oxford, UK, **2014**.
- [12] Allen, F. H. The Cambridge Structural Database: A Quarter of a Million Crystal Structures and Rising. *Acta Crystallogr.* **2002**, *B58*, 380-388.
- [13] <http://www.fiz-karlsruhe.de/icsd>
- [14] <https://scifinder.cas.org>
- [15] Horvath, G.; Kawazoe, K. Method for the Calculation of Effective Pore Size Distribution in Molecular Sieve Carbon," *J. Chem. Eng. Jpn.* **1983**, *16*, 470-475.
- [16] (a) Lastoskie, C. M. A Modified Horvath-Kawazoe Methods for Micropore Size Analysis. *Stud. Surf. Sci. Catal.* **2000**, *128*, 475-484. (b) Dombrowski, R. J.; Lastoskie, C. M.; Hyduke, D. R. The Horvath-Kawazoe Method Revised. *Colloids Surf. A Physicochem. Eng. Asp.* **2001**, *187-188*, 23-29.
- [17] Nuhnen, A.; Janiak, C. A Practical Guide to calculate the Isotheric Heat/Enthalpy of Adsorption via Adsorption Isotherms in Metal-Organic Frameworks, MOFs. *Dalton Trans.* **2020**, *49*, 10295-10307.
- [18] Cessford.; N. F.; Seaton, N. A.; Düren, T. Evaluation of Ideal Adsorbed Solution Theory as a Tool for the Design of Metal-Organic Framework Materials. *Ind. Eng. Chem. Res.* **2012**, *51*, 4911-4921.
- [19] Simon, C. M.; Smit, B.; Haranczyk, M. pylAST: Ideal Adsorbed Solution Theory (IAST) Python Package. *Comput. Phys. Commun.* **2016**, *200*, 364-380.
- [20] Bojdys, M. J. Prediction of Gas Adsorption Selectivity by Ideal Adsorption Solution Theory (IAST). **2013**.

SUPPLEMENTARY MATERIAL FOR CHAPTER 3

APPENDIX 3

Table A3.1. Cu–O and Cu–N bond lengths (Å) in compounds 1-Mo8–5-Mo8.

1-Mo8		2-Mo8		3-Mo8	
Cu1A		Cu1A		Cu1A	
Cu1A–O11	2.310(5)	Cu1A...O12	3.446(7)	Cu1A–O1 ^{ix}	2.504(9)
Cu1A–O6 ⁱ	2.876(5)	Cu1A...O12 ^v	3.446(7)	Cu1A–O7	2.540(9)
Cu1A–N1A	1.997(8)	Cu1A–N1A	2.005(10)	Cu1A–N1A	2.020(12)
Cu1A–N4A	2.009(7)	Cu1A–N4A	1.998(9)	Cu1A–N4A	1.997(13)
Cu1A–N8A	2.006(8)	Cu1A–N1A ^v	2.005(10)	Cu1A–N8A	2.003(13)
Cu1A–N11A	2.002(7)	Cu1A–N4A ^v	1.998(9)	Cu1A–N11A	2.013(12)
Cu1B		Cu2A		Cu2A	
Cu1B–O77	2.336(7)	Cu2A–O6	2.283(8)	Cu2A–O66	2.377(9)
Cu1B–O22 ⁱⁱ	2.595(6)	Cu2A–O6 ^{vi}	2.283(8)	Cu2A–O66 ^x	2.377(9)
Cu1B–N1B	2.009(9)	Cu2A–N21A	2.023(9)	Cu2A–N21A	1.999(13)
Cu1B–N4B	2.009(9)	Cu2A–N24A	2.013(9)	Cu2A–N24A	2.027(13)
Cu1B–N8B	2.010(8)	Cu2A–N21A ^{vi}	2.023(9)	Cu2A–N21A ^x	1.999(13)
Cu1B–N11B	2.006(8)	Cu2A–N24A ^{vi}	2.013(9)	Cu2A–N24A ^x	2.027(13)
Cu1C		Cu1B		Cu1B	
Cu1C–O44	2.358(5)	Cu1B–O22	2.393(6)	Cu1B–O22	2.249(11)
Cu1C–O44 ⁱⁱⁱ	2.358(5)	Cu1B–O22 ^{iv}	2.393(6)	Cu1B...O46 ^{xi}	3.625(9)
Cu1C–N1C	2.034(7)	Cu1B–N1B	2.009(9)	Cu1B–N1B	2.015(11)
Cu1C–N4C	2.020(7)	Cu1B–N4B	2.006(9)	Cu1B–N4B	2.030(13)
Cu1C–N1C ⁱⁱⁱ	2.034(7)	Cu1B–N1B ^{iv}	2.009(9)	Cu1B–N8B	2.026(13)
Cu1C–N4C ⁱⁱⁱ	2.020(7)	Cu1B–N4B ^{iv}	2.006(9)	Cu1B–N11B	2.009(13)
Cu2C		Cu2B		Cu1C	
Cu2C–O8	2.302(7)	Cu2B–O77	2.270(7)	Cu1C–O88	2.602(9)
Cu2C–O8 ^{iv}	2.302(7)	Cu2B–O77 ^{vii}	2.270(7)	Cu1C–O88 ^{viii}	2.602(9)
Cu2C–N21C	2.013(16)	Cu2B–N21B	2.030(10)	Cu1C–N1C	2.038(11)
Cu2C–N24C	1.969(16)	Cu2B–N24B	2.025(9)	Cu1C–N4C	2.011(11)
Cu2C–N21C ^{iv}	2.013(16)	Cu2B–N21B ^{vii}	2.030(10)	Cu1C–N1C ^{vii}	2.038(11)
Cu2C–N24C ^{iv}	1.969(16)	Cu2B–N24B ^{vii}	2.025(9)	Cu1C–N4C ^{vii}	2.011(11)
Cu2C–N31C	1.96(3)				
Cu2C–N34C	2.06(3)				
Cu2C–N31C ^{iv}	1.96(3)				
Cu2C–N34C ^{iv}	2.06(3)				
		Cu1C			
		Cu1C–O8	2.563(8)		
		Cu1C–O4 ^{viii}	2.592(8)		
		Cu1C–N1C	1.974(11)		
		Cu1C–N4C	1.993(12)		
		Cu1C–N8C	2.017(15)		
		Cu1C–N11C	2.024(12)		

Symmetry codes: i) $\frac{1}{2}-x, -1/2+y, 3/2-z$; ii) $3/2-x, \frac{1}{2}+y, 3/2-z$; iii) $1-x, 1-y, 2-z$; iv) $1-x, 1-y, 1-z$; v) $1-x, -y, 1-z$; vi) $1-x, -y, -z$; vii) $1-x, 1-y, -z$; viii) $1+x, y, z$; ix) $-1/2+x, 3/2-y, -1/2+z$; x) $1-x, 2-y, -z$; xi) $\frac{1}{2}-x, -1/2+y, \frac{1}{2}-z$; xii) $-x, -y, 2-z$; xiii) $x, y, 1+z$; xiv) $-x, 1-y, 2-z$; xv) $-x, 1-y, 3-z$; xvi) $2-x, 1-y, 1-z$; xvii) $-1+x, y, z$; xviii) $2-x, -y, 2-z$; xix) $2-x, -y, 1-z$; xx) $2-x, 1-y, 2-z$.

Table A3.1 (continuation). Cu–O and Cu–N bond lengths (Å) in compounds 1-Mo8–5-Mo8.

4-Mo8		5-Mo8	
Cu1A		Cu1A	
Cu1A–O11	2.46(3)	Cu1A–O11	2.386(12)
Cu1A–O11 ^{xii}	2.46(3)	Cu1A–O11 ^{xvi}	2.386(12)
Cu1A–N1A	2.05(4)	Cu1A–N1A	2.015(16)
Cu1A–N4A	2.02(4)	Cu1A–N4A	2.036(16)
Cu1A–N1A ^{xii}	2.05(4)	Cu1A–N1A ^{xvi}	2.015(16)
Cu1A–N4A ^{xii}	2.02(4)	Cu1A–N4A ^{xvi}	2.036(16)
Cu1B		Cu1B	
Cu1B–O2 ^{xiii}	2.70(3)	Cu1B–O6	2.559(14)
Cu1B–O2 ^{xiv}	2.70(3)	Cu1B–O22 ^{xvii}	2.455(14)
Cu1B–N1B	1.99(5)	Cu1B–N1B	1.99(2)
Cu1B–N4B	1.97(3)	Cu1B–N4B	2.02(2)
Cu1B–N1B ^{xv}	1.99(5)	Cu1B–N8B	2.00(2)
Cu1B–N4B ^{xv}	1.97(6)	Cu1B–N11B	2.02(2)
Cu1B–N21B	2.01(7)		
Cu1B–N21B	2.01(7)		
Cu1C		Cu2B	
Cu1C–O4	2.70(3)	Cu2B–O77	2.340(15)
Cu1C–O4 ⁱⁱⁱ	2.70(3)	Cu2B–O77 ^{xviii}	2.340(15)
Cu1C–N1C	1.96(4)	Cu2B–N21B	2.04(2)
Cu1C–N4C	1.91(5)	Cu2B–N24B	1.96(3)
Cu1C–N1C ⁱⁱⁱ	1.96(4)	Cu2B–N21B ^{xviii}	2.04(2)
Cu4C–N4C ⁱⁱⁱ	1.94(5)	Cu2B–N24B ^{xviii}	1.96(3)
		Cu1C	
		Cu1C–O44	2.370(14)
		Cu1C–O44 ^{xix}	2.370(14)
		Cu1C–N1C	2.009(17)
		Cu1C–N4C	2.01(2)
		Cu1C–N1C ^{xix}	2.009(17)
		Cu1C–N4C ^{xix}	2.01(2)
		Cu2C	
		Cu2C–O8	2.351(17)
		Cu2C–O8 ^{xx}	2.351(17)
		Cu2C–N21C	2.04(2)
		Cu2C–N24C	2.04(2)
		Cu2C–N21C ^{xx}	2.04(2)
		Cu2C–N24C ^{xx}	2.04(2)

Symmetry codes: i) $\frac{1}{2}-x, -1/2+y, 3/2-z$; ii) $3/2-x, \frac{1}{2}+y, 3/2-z$; iii) $1-x, 1-y, 2-z$; iv) $1-x, 1-y, 1-z$; v) $1-x, -y, 1-z$; vi) $1-x, -y, -z$; vii) $1-x, 1-y, -z$; viii) $1+x, y, z$; ix) $-1/2+x, 3/2-y, -1/2+z$; x) $1-x, 2-y, -z$; xi) $\frac{1}{2}-x, -1/2+y, \frac{1}{2}-z$; xii) $-x, -y, 2-z$; xiii) $x, y, 1+z$; xiv) $-x, 1-y, 2-z$; xv) $-x, 1-y, 3-z$; xvi) $2-x, 1-y, 1-z$; xvii) $-1+x, y, z$; xviii) $2-x, -y, 2-z$; xix) $2-x, -y, 1-z$; xx) $2-x, 1-y, 2-z$.

APPENDIX 3

Table A3.2. Geometrical parameters of the intermolecular N–H...O and C–H...O hydrogen bonds in compounds **1-Mo8–5-Mo8**.

Donor–H...Acceptor	D–H	H...A	D...A	D–H...A
1-Mo8				
N24C–H24C...O14W ⁱ	0.91	2.27	3.01(2)	137
C10A–H10B...O15W ⁱ	0.97	2.44	3.160(16)	130
C10B–H10D...O15W ⁱⁱ	0.97	2.44	3.404(17)	170
C13B–H13D...O13W ⁱⁱⁱ	0.97	2.40	3.34(3)	164
C14A–H14A...O12W ^{iv}	0.97	2.58	3.43(2)	147
C23C–H23A...O14W ⁱ	0.97	2.38	3.00(3)	121
C27C–H27A...O9W ⁱ	0.97	2.56	3.46(2)	154
2-Mo8				
N1A–H1A...O1 ^v	0.98	1.89	2.856(11)	168
N4A–H4A...O3 ^{vi}	0.98	2.48	3.234(11)	134
N4A–H4A...O134 ^{vi}	0.98	2.11	3.004(11)	150
C2A–H2AB...O3 ^{vi}	0.97	2.47	3.182(13)	130
C2A–H2AB...O23 ^{vi}	0.97	2.49	3.331(14)	145
C5A–H5AA...O2 ^v	0.97	2.48	3.300(15)	142
C7A–H7AA...O2 ^{vi}	0.97	2.47	3.285(15)	142
C7A–H7AA...O23 ^{vi}	0.97	2.48	3.335(13)	147
3-Mo8				
N1B–H1B...O6 ^{vii}	0.98	2.54	3.251(15)	130
N1B–H1B...O56 ^{vii}	0.98	2.11	3.015(15)	153
N1C–H1C...O8 ^{viii}	0.98	1.94	2.910(17)	171
N4A–H4A...O12 ^{ix}	0.98	2.12	2.944(15)	141
N8A–H8A...O4 ^{ix}	0.98	2.27	3.124(16)	145
N8A–H8A...O134 ^{ix}	0.98	2.48	3.300(16)	142
N11B–H11B...O5 ^{vii}	0.98	2.53	3.320(16)	138
N11B–H11B...O145 ^{vii}	0.98	2.26	3.136(17)	148
C3B–H3BA...O46 ^{vii}	0.97	2.48	3.317(19)	144
C7B–H7BB...O4 ^{vii}	0.97	2.33	3.27(2)	164
C13B–H13A...O5 ^{vii}	0.97	2.54	3.304(19)	135
C13B–H13A...O56 ^{vii}	0.97	2.40	3.219(19)	141
C2A–H2AB...O12 ^{ix}	0.97	2.39	3.111(19)	131
C6A–H6AA...O134 ^{ix}	0.97	2.43	3.283(19)	147
4-Mo8				
N1B–H1B...O12 ^x	0.98	2.24	3.18(7)	160
C5B–H5BB...O3W ^{xi}	0.97	2.47	3.33(10)	148
C3C–H3CB...O3W ^{xii}	0.97	2.27	3.18(9)	154
5-Mo8				
N24C– H24C...O11W ^{xiii}	0.98	2.04	2.97(3)	157

SUPPLEMENTARY MATERIAL FOR CHAPTER 5

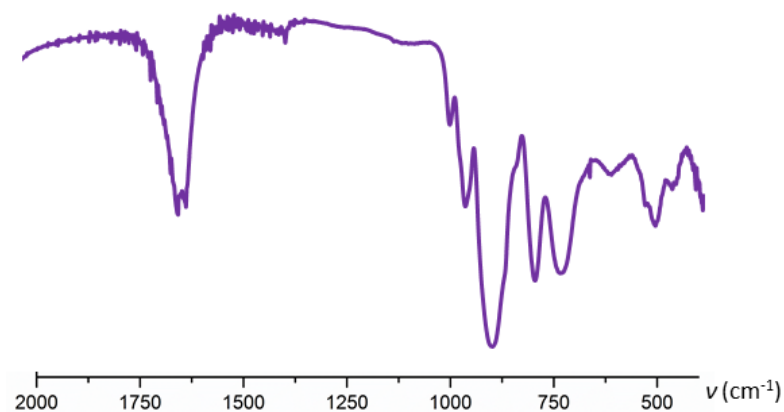


Figure A4.1. FT-IR spectra of the $K_8[\alpha\text{-SiW}_{11}\text{O}_{39}]\cdot 13\text{H}_2\text{O}$ Keggin-type precursor.

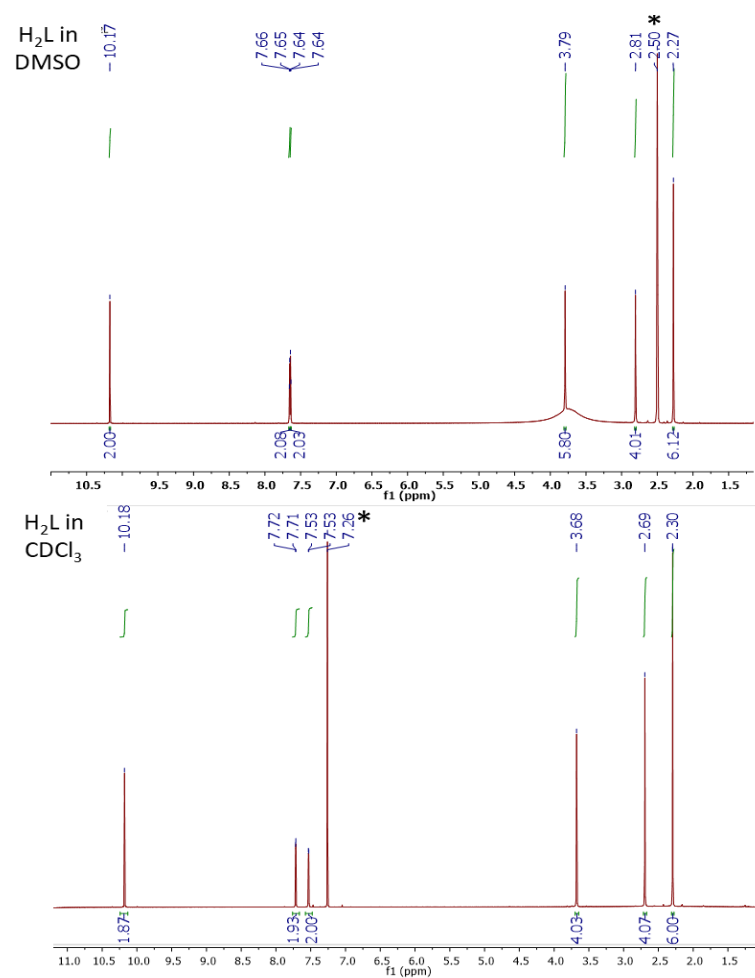


Figure A2.2. Comparison between $^1\text{H-NMR}$ spectra of H_2L ligand in DMSO (top) and CDCl_3 (bottom). Signals belonging to the solvent (2.50 ppm for DMSO and 7.26 ppm for CDCl_3) are marked (*).

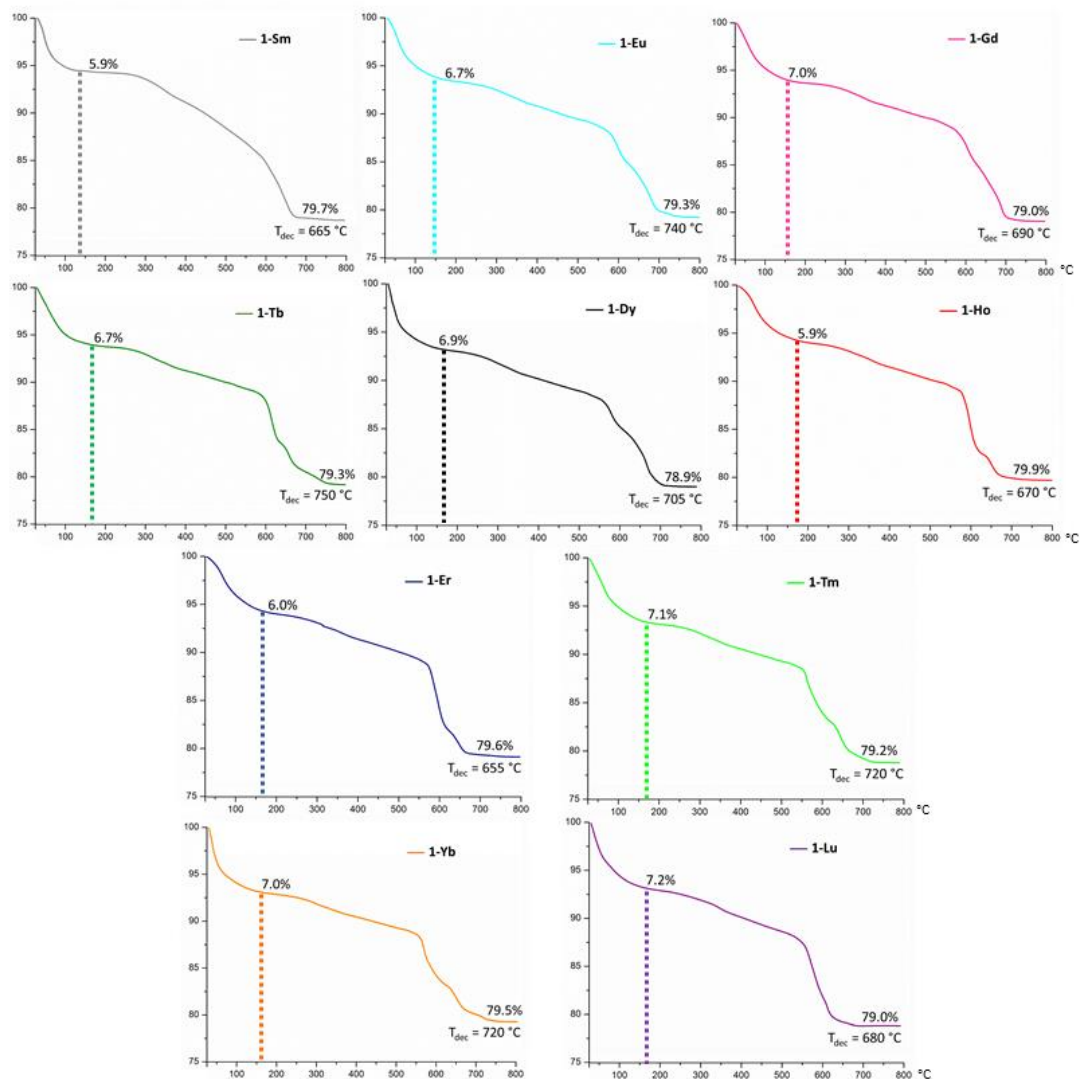


Figure A4.3. TGA curves of compounds **1-Ln** (Ln = Sm to Lu).

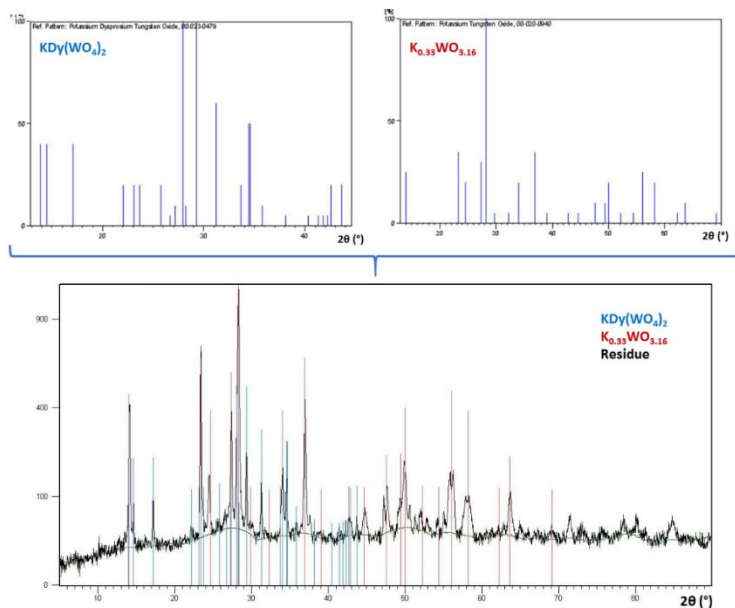


Figure A4.4. Identification of the final residue from the thermal decomposition of **1-Dy** by PXRD analyses.

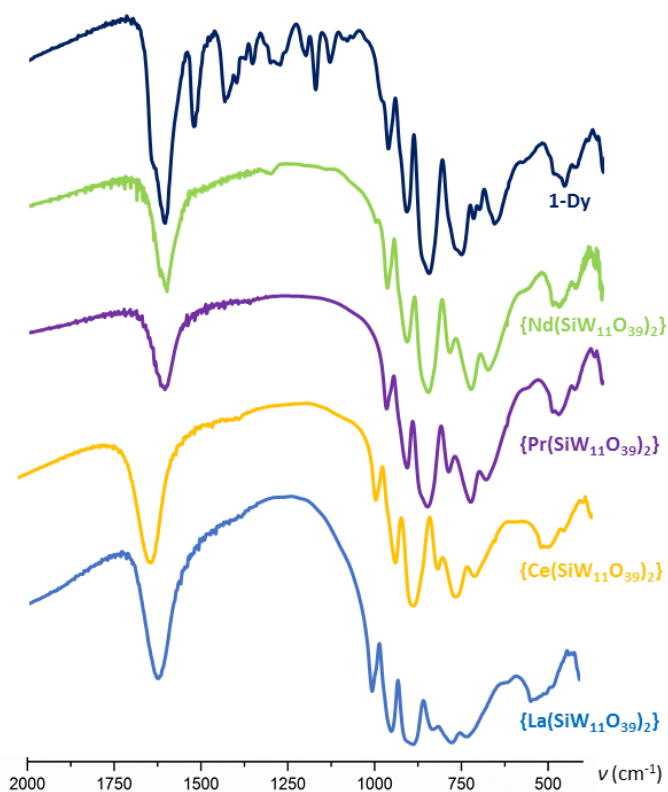


Figure A4.5. FT-IR spectrum of **1-Dy** compared to those recorded for crystals obtained in analogous reactions but using early lanthanide ions (La to Nd). The latter has been identified as Peacock-Weakley type $[\text{Ln}^{\text{III}}(\text{SiW}_{11}\text{O}_{39})_2]^{13-}$ sandwich POMs.

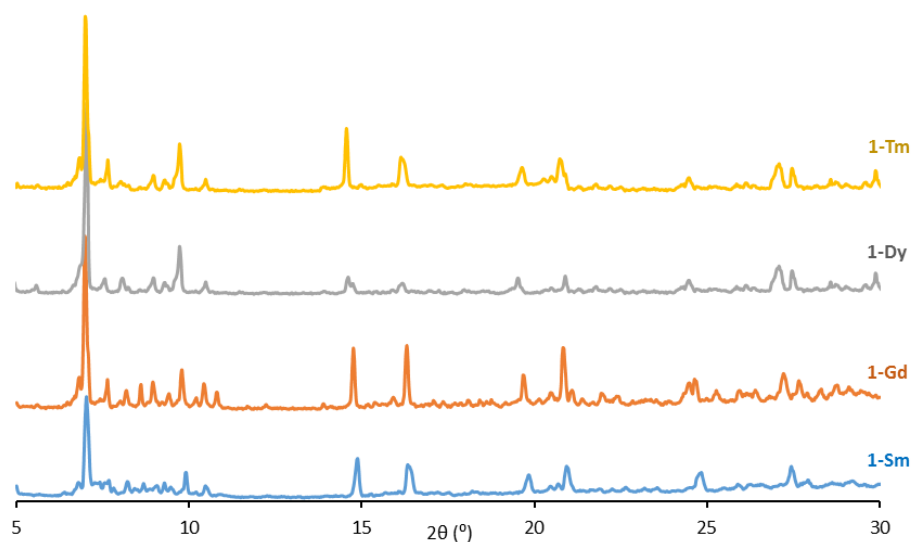


Figure A4.6. Experimental powder X-ray diffraction patterns of the freshly filtered crystals.

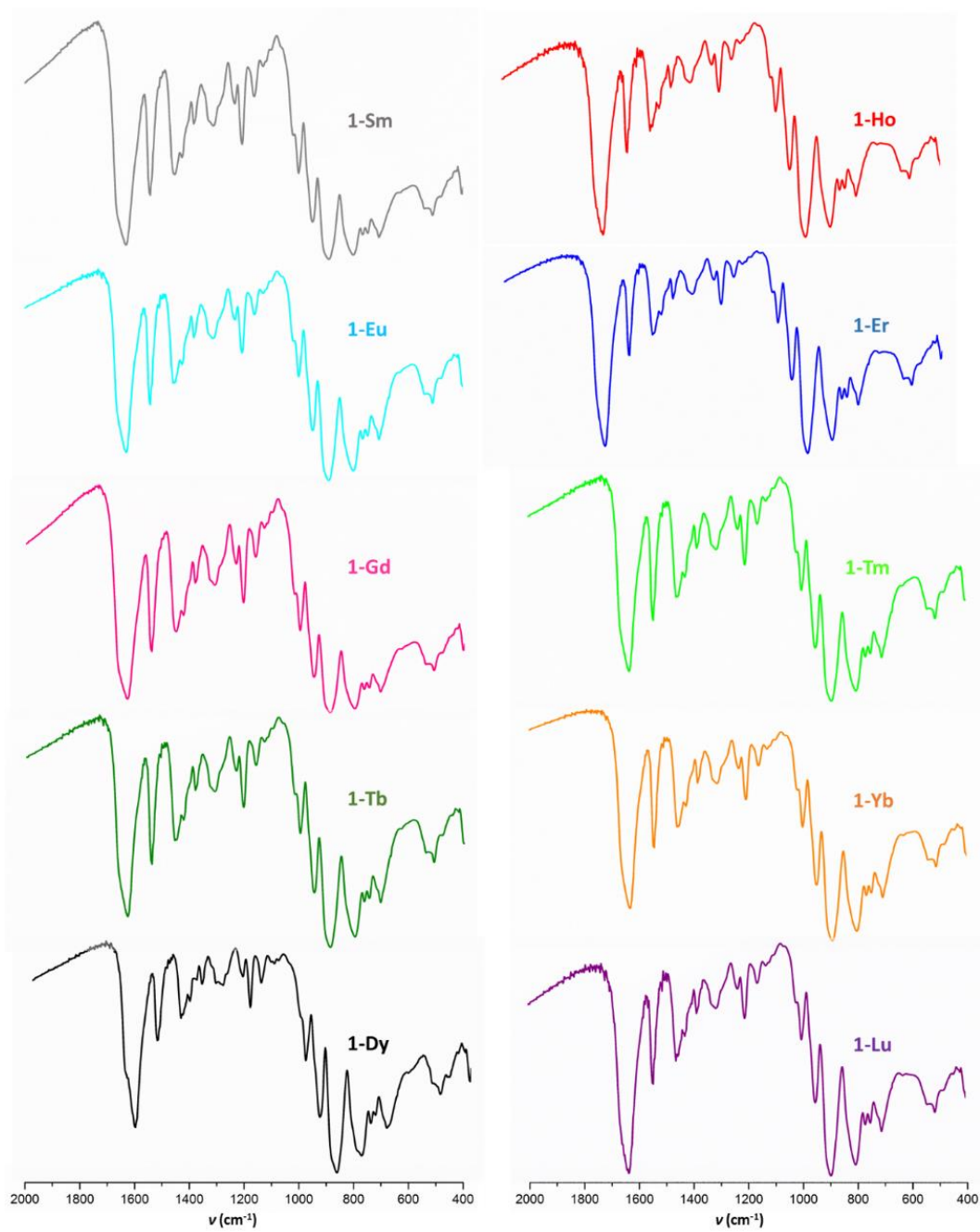


Figure A4.7. FTIR spectra of 1-Ln (Ln = Sm to Lu).

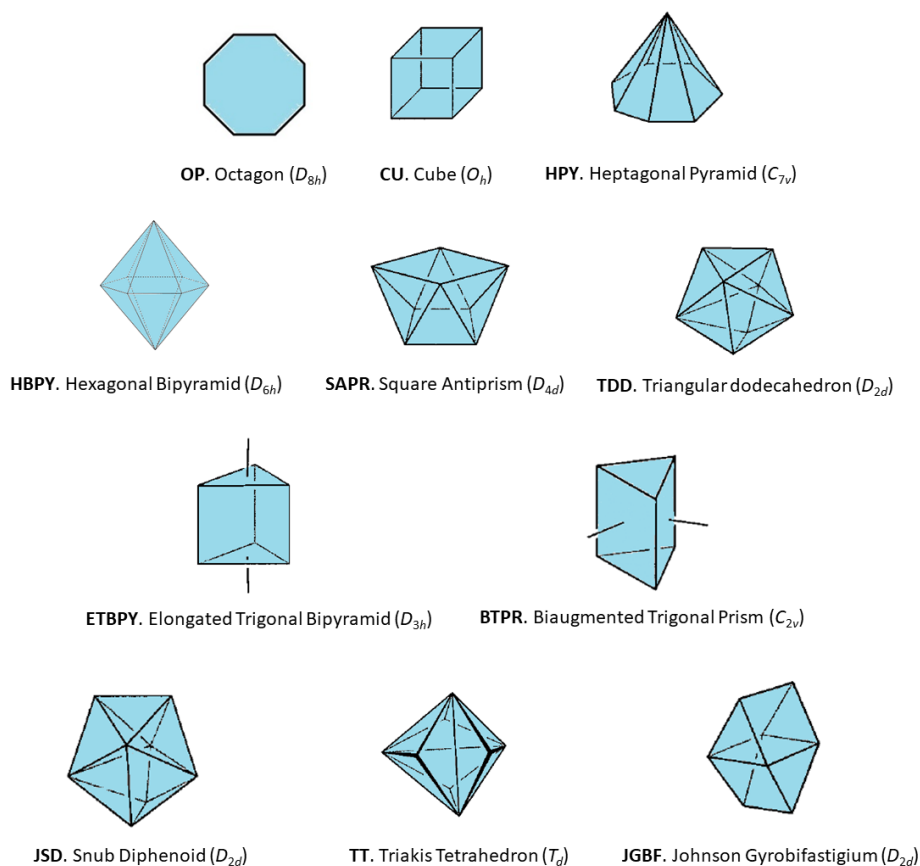


Figure A4.8. Structural representation of ideal polyhedra used for determining CShM measurements.

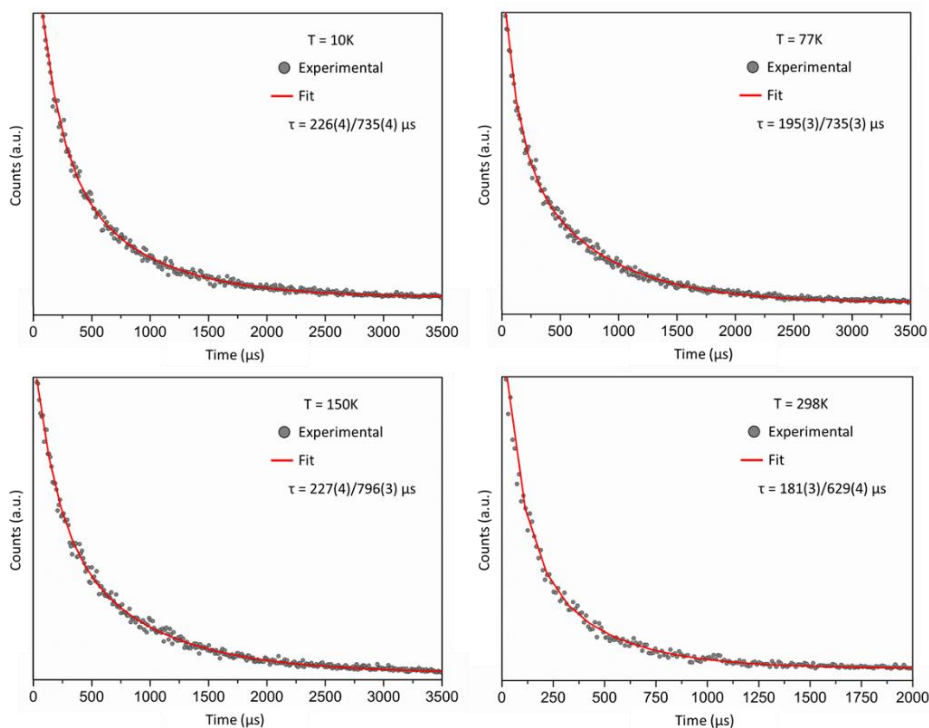


Figure A4.9. Luminescence decay curves for **1-Eu** at different temperatures upon excitation at 375 nm.

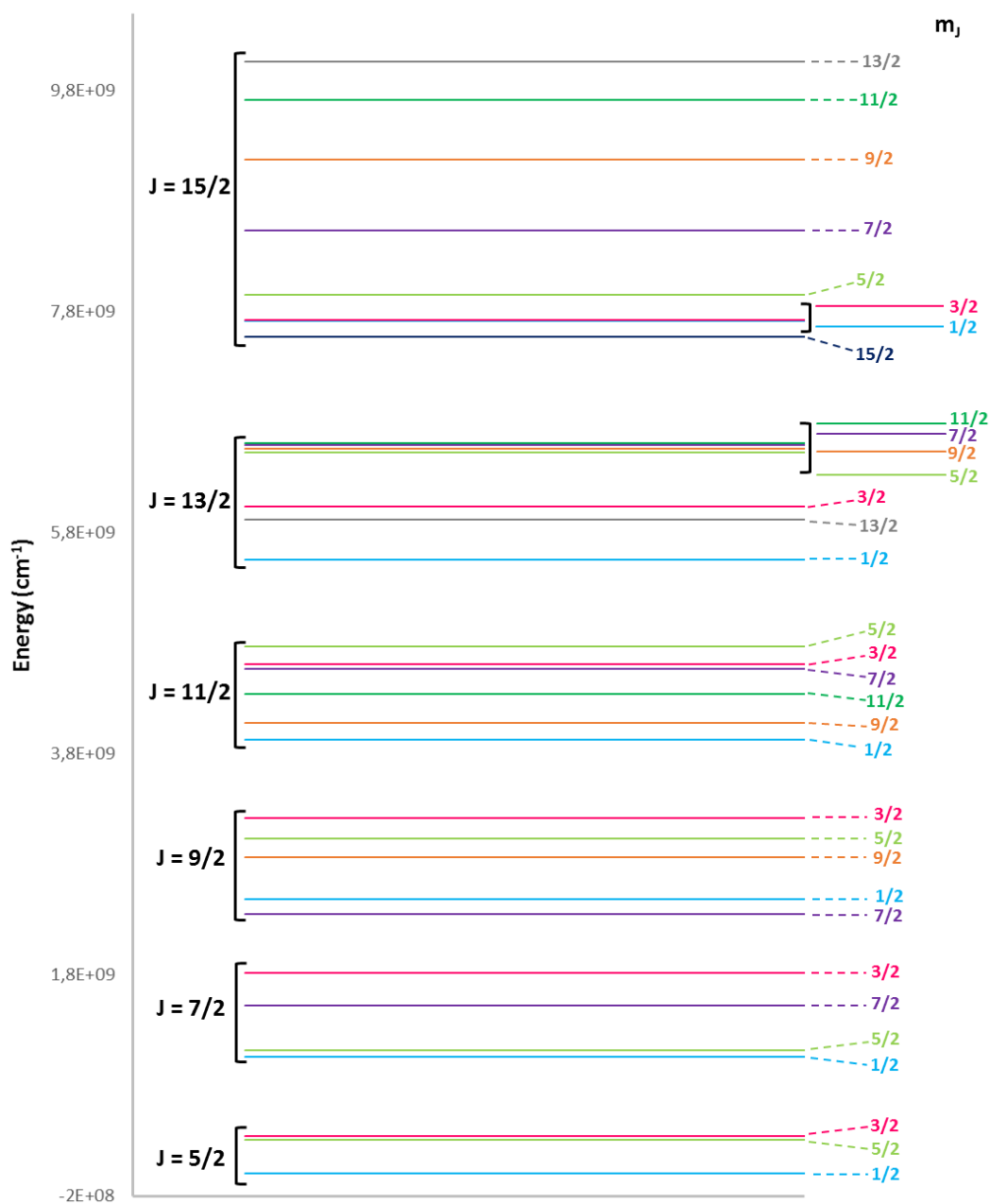


Figure A4.10. A more specific representation of the sublevels generated by the crystal field splitting in 1-Sm compound.

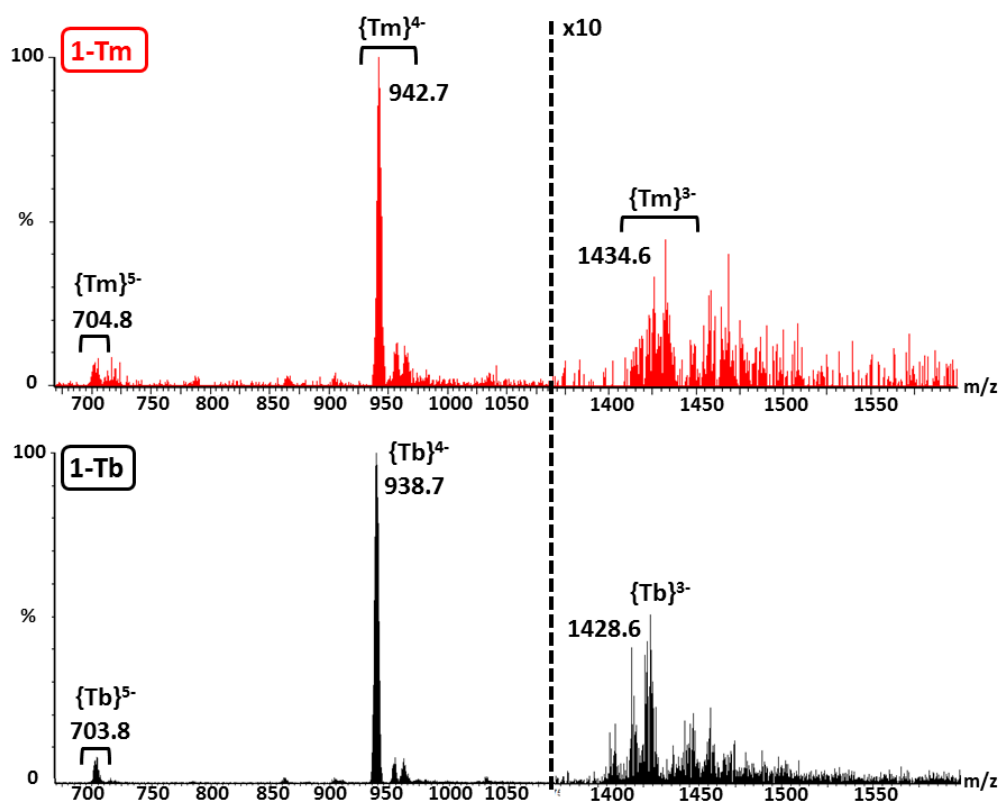


Figure A4.11. Negative ESI-MS spectra of **1-Tm** in $H_2O/MeCN$ (1:1) mixture compared to that acquired for **1-Tb** derivative. The intensity of the $m/z > 1300$ region is increased (x10) for its better visualization.

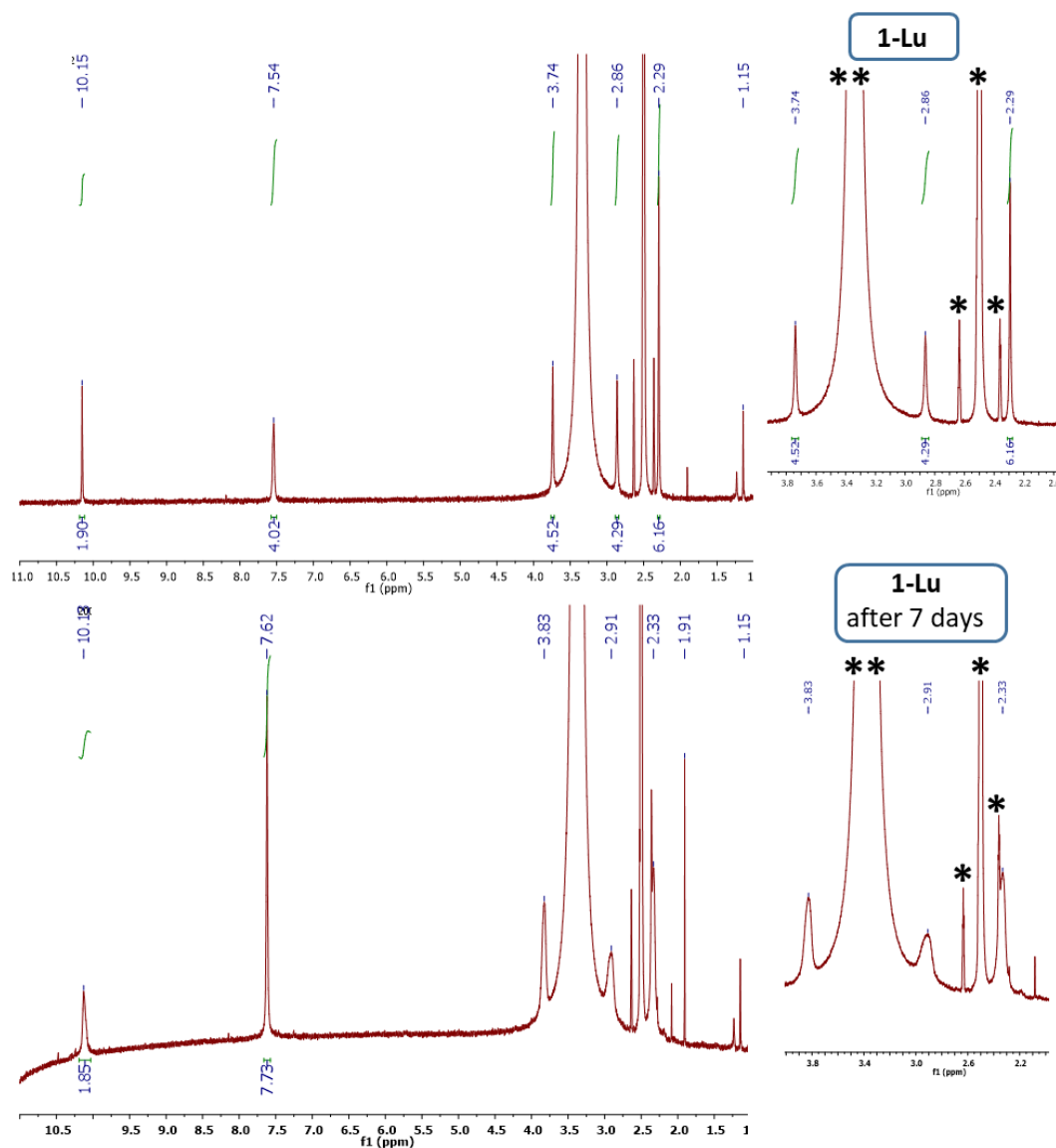


Figure A4.12. $^1\text{H-NMR}$ spectrum of a freshly prepared **1-Lu** sample in DMSO (top), and the same solution after one week (bottom). Note that the resonance belonging to the solvent (2.50 ppm), together with its satellite peaks (2.36 and 2.63 ppm) in the spectrum of **1-Lu** are marked (*). The additional peaks of lower intensities (as 1.91 ppm) could correspond to impurities from the acetate/acetic acid buffer solution employed in the synthesis of the complexes. The saturated peak at 3.30 ppm (**) corresponds to the water present on the molecule.

APPENDIX 4

Table 4.1. Selected geometrical parameters for all the structures containing the H₂L ligand and lanthanide ions included in the CSD database: Intramolecular centroid...centroid (C_g...C_g) distances (Å) and dihedral angles (°) between aromatic rings.

1 Ligand			2 Ligands (Sandwich-type)			This work					
Refcode	Cg...Cg distance	Ring...ring angle	Refcode	Cg...Cg distance	Ring...ring angle	Cg...Cg distance	Ring...ring angle				
<i>Ln/Zn system</i>			<i>Ln/M system (M = Cu, Zn)</i>								
BIPFIS	8.066	168.5	DONSAC	7.898	164.4	1-Sm	6.502	88.7			
BIPFOY	8.050	168.8		7.837	151.3		6.471	97.3			
BIPFUE	8.104	169.3	DONSEG	7.815	150.8		6.660	95.0			
BIPGAL	8.080	169.6		7.893	164.2	6.578	88.5				
BIPGEP	8.112	173.1	GALBUT	7.871	156.5	1-Eu	6.522	91.0			
BIPGIT	8.192	164.8		7.895	161.6		6.621	91.7			
BIQBIP	8.074	165.2	KAVXIR	7.856	157.5	1-Gd	6.442	87.6			
	8.097	163.6		7.790	145.0		6.410	84.3			
BIQBOV	8.062	165.1	KAVXOX	7.801	146.0		6.559	87.8			
	8.090	164.2		7.838	147.1	6.363	85.5				
BIQBUB	7.965	154.9	KAVXUD	7.833	153.7	1-Tb	6.492	87.3			
	7.977	157.1		7.788	144.5		6.561	90.1			
BIQCAI	8.017	161.3	KAVYAK	7.884	156.5	1-Dy	6.409	94.4			
	7.945	155.8		7.908	161.6		6.435	88.2			
IFUCER	8.045	163.7	KAWKOL	7.874	150.6		6.554	88.5			
REJFIY	8.197	168.5		7.884	151.0	6.386	89.4				
REJFOE	8.168	168.5	YUDVOK	7.878	151.9	1-Ho	6.444	90.5			
REJGAR	8.126	166.5					6.572	84.8			
REJGEV	8.113	167.9				6.388	87.7				
REJGIZ	8.118	166.9				1-Er	6.339	85.4			
REJGOF	8.094	165.9					6.514	87.5			
REJGUL	8.086	166.4				1-Tm	6.496	89.0			
REJHAS	8.062	165.4					6.460	90.4			
REJHEW	8.054	165.5					6.406	87.8			
<i>Ln/Cu system</i>									1-Yb	6.341	94.8
IMAGEL	8.096	164.3								6.397	91.1
IMAGIP	8.087	164.1							6.495	88.5	
IMAGUB	8.072	164.0							1-Lu	6.391	86.5
IMAJAK	8.056	164.0								6.333	85.5
<i>Ln/M system (M = Co, Ni)</i>										6.478	88.3
IMAGOV	7.792	108.6									
IMAHAI	7.763	109.9									
IMAHEM	7.793	110.1									
IMAHOW	7.830	110.8									
IMAHUC	7.788	109.2									
IMAJEO	7.799	109.8									
IMAJIS	7.833	110.4									
IMAJUE	7.803	110.6									
IMAKAL	7.806	110.8									

Table 4.2. Continuous Shape Measurements (CSM) for the eight coordinated lanthanide atoms in compounds **1-Ln**.^[a]

Atom	Shape	1-Sm	1-Eu	1-Gd	1-Tb	1-Dy	1-Ho	1-Er	1-Tm	1-Yb	1-Lu
Ln1A	SAPR-8	0.941	1.007	0.950	0.873	0.947	0.995	0.943	0.914	0.903	0.900
	TDD-8	1.624	1.466	1.610	1.648	1.723	1.764	1.674	1.437	1.796	1.663
	JBTPR-8	1.609	1.482	1.471	1.526	1.427	1.390	1.449	1.494	1.470	1.476
	BTPR-8	0.766	0.785	0.796	0.869	0.785	0.725	0.722	0.841	0.799	0.819
Ln1B	SAPR-8	1.059	1.015	1.066	0.974	0.943	0.901	0.997	0.867	0.907	0.896
	TDD-8	1.725	1.833	1.764	1.738	1.595	1.747	1.784	1.562	1.621	1.733
	JBTPR-8	1.394	1.286	1.384	1.349	1.508	1.500	1.395	1.404	1.529	1.379
	BTPR-8	0.785	0.696	0.710	0.671	0.812	0.865	0.685	0.781	0.828	0.763
Ln1C	SAPR-8	1.052	1.034	1.004	0.917	0.965	0.904	0.983	1.041	0.911	0.889
	TDD-8	1.602	1.419	1.583	1.488	1.516	1.543	1.529	1.853	1.633	1.511
	JBTPR-8	1.456	1.546	1.439	1.529	1.468	1.433	1.525	1.442	1.479	1.415
	BTPR-8	0.857	0.837	0.766	0.809	0.762	0.776	0.720	0.776	0.823	0.804

^[a] Abbreviations. **SAPR**: square antiprism (D_{4d}); **TDD**: triangular dodecahedron (D_{2d}); **JBTPR**: Johnson biaugmented trigonal prism (C_{2v}) and; **BTPR**: biaugmented trigonal prism (C_{2v}).

APPENDIX 4

Table 4.3. Lanthanide-Oxygen bond lengths (Å) and Ln...Ln distances (Å) in compounds 1-Ln.

		1-Sm	1-Eu	1-Gd	1-Tb	1-Dy
Ln1A-O1LA	O _a	2.46(2)	2.50(2)	2.491(16)	2.476(13)	2.474(16)
Ln1A-O4LA		2.431(18)	2.405(15)	2.414(13)	2.406(10)	2.379(17)
Ln1A-O2LA	O _p	2.36(2)	2.36(2)	2.341(15)	2.325(13)	2.297(16)
Ln1A-O3LA		2.38(2)	2.372(18)	2.377(14)	2.355(12)	2.330(16)
Ln1A-O1A	O _{POM}	2.40(2)	2.35(2)	2.370(15)	2.325(11)	2.324(16)
Ln1A-O2A		2.389(19)	2.363(19)	2.367(16)	2.309(11)	2.336(17)
Ln1A-O3A		2.435(18)	2.412(16)	2.391(15)	2.376(11)	2.360(16)
Ln1A-O4A		2.353(17)	2.360(17)	2.352(15)	2.339(11)	2.351(16)
Ln1B-O1LB	O _a	2.451(19)	2.399(18)	2.402(15)	2.381(12)	2.447(18)
Ln1B-O4LB		2.556(18)	2.522(16)	2.492(13)	2.476(13)	2.378(16)
Ln1B-O2LB	O _p	2.372(16)	2.393(18)	2.352(14)	2.353(11)	2.286(18)
Ln1B-O3LB		2.339(18)	2.322(17)	2.313(14)	2.315(12)	2.331(16)
Ln1B-O1B	O _{POM}	2.363(18)	2.386(16)	2.345(12)	2.334(10)	2.330(17)
Ln1B-O2B		2.369(19)	2.367(17)	2.329(14)	2.321(11)	2.337(16)
Ln1B-O3B		2.387(17)	2.372(14)	2.368(13)	2.349(10)	2.382(16)
Ln1B-O4B		2.423(17)	2.399(17)	2.392(14)	2.395(10)	2.325(17)
Ln1C-O1LC	O _a	2.56(3)	2.51(2)	2.485(18)	2.457(13)	2.46(2)
Ln1C-O4LC		2.45(2)	2.42(2)	2.396(15)	2.399(12)	2.381(17)
Ln1C-O2LC	O _p	2.331(16)	2.329(15)	2.310(13)	2.303(10)	2.286(16)
Ln1C-O3LC		2.364(17)	2.348(17)	2.344(14)	2.345(10)	2.313(15)
Ln1C-O1C	O _{POM}	2.363(16)	2.364(15)	2.335(13)	2.333(10)	2.319(16)
Ln1C-O2C		2.34(2)	2.351(18)	2.334(14)	2.330(11)	2.323(16)
Ln1C-O3C		2.45(2)	2.43(2)	2.378(18)	2.396(11)	2.39(2)
Ln1C-O4C		2.379(18)	2.364(15)	2.353(17)	2.373(10)	2.336(17)
O _a (average)		2.485	2.459	2.447	2.433	2.420
O _p (average)		2.358	2.354	2.340	2.333	2.307
O _{POM} (average)		2.388	2.377	2.360	2.348	2.343
LnA...LnB		8.096(4)	8.040(3)	8.128(3)	8.180(2)	8.123(3)
LnB...LnC		8.213(12)	8.159(8)	8.244(9)	8.177(7)	7.993(7)
LnC...LnA		8.013(7)	8.024(5)	8.050(6)	8.001(5)	8.224(12)

Abbreviations: O_a: O atoms from the aldehyde group of the H₂L ligand; O_p: O atoms from the phenoxy group of the H₂L ligand; O_{POM}: O atoms delimiting the vacant site of the lacunary Keggin-type POM.

Table 4.3 (continuation). Geometrical parameters (\AA , $^\circ$) of intermolecular π - π interactions in 1-Ln.

		1-Ho	1-Er	1-Tm	1-Yb	1-Lu
Ln1A-O1LA	O_a	2.466(13)	2.33(2)	2.34(2)	2.430(13)	2.320(13)
Ln1A-O4LA		2.358(15)	2.428(17)	2.46(2)	2.339(15)	2.383(18)
Ln1A-O2LA	O_p	2.277(13)	2.315(18)	2.264(18)	2.250(13)	2.288(16)
Ln1A-O3LA		2.319(14)	2.28(2)	2.257(18)	2.280(14)	2.225(18)
Ln1A-O1A	O_{POM}	2.327(12)	2.32(2)	2.28(2)	2.289(13)	2.274(17)
Ln1A-O2A		2.336(14)	2.33(2)	2.289(18)	2.311(14)	2.283(15)
Ln1A-O3A		2.375(13)	2.331(19)	2.295(19)	2.354(13)	2.288(15)
Ln1A-O4A		2.350(13)	2.377(17)	2.38(2)	2.308(14)	2.331(14)
Ln1B-O1LB	O_a	2.439(16)	2.36(2)	2.46(2)	2.401(16)	2.436(13)
Ln1B-O4LB		2.364(13)	2.46(2)	2.329(18)	2.328(13)	2.308(15)
Ln1B-O2LB	O_p	2.277(15)	2.310(16)	2.26(2)	2.253(15)	2.258(17)
Ln1B-O3LB		2.325(13)	2.30(2)	2.291(19)	2.283(14)	2.290(14)
Ln1B-O1B	O_{POM}	2.304(13)	2.325(18)	2.31(2)	2.290(15)	2.300(16)
Ln1B-O2B		2.290(13)	2.35(2)	2.28(2)	2.285(14)	2.309(15)
Ln1B-O3B		2.389(13)	2.332(18)	2.360(19)	2.345(13)	2.322(14)
Ln1B-O4B		2.315(14)	2.344(19)	2.30(2)	2.307(13)	2.315(14)
Ln1C-O1LC	O_a	2.455(16)	2.365(19)	2.34(2)	2.433(16)	2.335(16)
Ln1C-O4LC		2.364(14)	2.41(3)	2.466(18)	2.341(15)	2.426(18)
Ln1C-O2LC	O_p	2.252(13)	2.276(17)	2.28(2)	2.225(13)	2.277(13)
Ln1C-O3LC		2.312(13)	2.25(2)	2.26(2)	2.273(13)	2.211(13)
Ln1C-O1C	O_{POM}	2.305(13)	2.320(19)	2.307(19)	2.281(13)	2.286(16)
Ln1C-O2C		2.325(14)	2.313(18)	2.31(2)	2.280(14)	2.282(13)
Ln1C-O3C		2.379(15)	2.32(2)	2.358(19)	2.372(15)	2.290(15)
Ln1C-O4C		2.338(13)	2.38(2)	2.387(19)	2.322(13)	2.328(15)
O_a (average)		2.408	2.392	2.399	2.379	2.368
O_p (average)		2.294	2.289	2.269	2.261	2.258
O_{POM} (average)		2.336	2.337	2.321	2.312	2.301
LnA...LnB		8.051(3)	8.108(4)	8.054(10)	8.059(3)	8.051(4)
LnB...LnC		7.981(6)	8.215(13)	8.044(4)	7.990(7)	8.204(13)
LnC...LnA		8.216(2)	8.018(9)	8.165(13)	8.226(12)	8.004(10)

Abbreviations: O_a : O atoms from the aldehyde group of the H_2L ligand; O_p : O atoms from the phenoxy group of the H_2L ligand; O_{POM} : O atoms delimiting the vacant site of the lacunary Keggin-type POM.

APPENDIX 4

Table 4.4. Geometrical parameters (Å, °) of intermolecular π - π interactions in **1-Ln**.

Centroids	Cg...Cg	ANG	Slippage	Centroids	Cg...Cg	ANG	Slippage
1-Sm				1-Ho			
Cg1...Cg3 ⁱ	3.52(2)	6	0.860	Cg1...Cg6 ^{xii}	3.564(11)	5	1.148
Cg2...Cg5 ⁱⁱ	3.531(18)	4	0.549	Cg2...Cg3 ^{xiii}	3.535(13)	5	0.547
Cg3...Cg1 ⁱⁱⁱ	3.52(2)	6	0.512	Cg3...Cg2 ^{xiii}	3.536(13)	5	0.821
Cg4...Cg6 ^{iv}	3.538(15)	5	1.153	Cg4...Cg5 ^{xiv}	3.540(12)	2	0.605
Cg5...Cg2 ⁱⁱ	3.529(18)	4	0.762	Cg5...Cg4 ^{xiv}	3.540(12)	2	0.750
Cg6...Cg4 ^v	3.538(15)	5	0.907	Cg6...Cg1 ^{xii}	3.563(11)	5	0.888
1-Eu				1-Er			
Cg1...Cg3 ⁱ	3.550(17)	3	0.788	Cg1...Cg6 ^{xii}	3.532(18)	4	0.582
Cg2...Cg5 ^{vi}	3.539(16)	3	0.592	Cg2...Cg3 ^{vii}	3.524(19)	7	1.006
Cg3...Cg1 ⁱⁱⁱ	3.551(17)	3	0.600	Cg3...Cg2 ^{vii}	3.526(19)	7	0.576
Cg4...Cg6 ^{iv}	3.540(14)	4	1.034	Cg4...Cg5 ^{xiv}	3.552(17)	6	1.168
Cg5...Cg2 ^{vi}	3.538(16)	3	0.774	Cg5...Cg4 ^{xiv}	3.552(17)	6	0.852
Cg6...Cg4 ^v	3.540(14)	4	0.813	Cg6...Cg1 ^{xii}	3.532(18)	4	0.809
1-Gd				1-Tm			
Cg1...Cg3 ⁱ	3.576(15)	7	0.921	Cg1...Cg6 ^{ix}	3.539(17)	5	0.853
Cg2...Cg5 ^{vii}	3.550(14)	4	0.578	Cg2...Cg4 ^{xv}	3.527(18)	5	0.855
Cg3...Cg1 ⁱⁱⁱ	3.576(15)	7	0.494	Cg3...Cg5 ⁱ	3.56(2)	3	0.803
Cg4...Cg6 ^{iv}	3.591(11)	6	1.198	Cg4...Cg2 ^{xvi}	3.528(18)	5	0.601
Cg5...Cg2 ^{vii}	3.550(14)	4	0.776	Cg5...Cg3 ⁱⁱⁱ	3.56(2)	3	0.612
Cg6...Cg4 ^v	3.593(11)	6	0.852	Cg6...Cg1 ^{ix}	3.541(17)	5	1.097
1-Tb				1-Yb			
Cg1...Cg3 ⁱ	3.568(11)	6	1.012	Cg1...Cg6 ^{xii}	3.589(12)	7	1.210
Cg2...Cg5 ^{viii}	3.618(11)	6	0.473	Cg2...Cg3 ^{xiii}	3.551(13)	6	0.518
Cg3...Cg1 ⁱⁱⁱ	3.568(11)	6	0.672	Cg3...Cg2 ^{xiii}	3.551(13)	6	0.869
Cg4...Cg6 ^{iv}	3.589(9)	5	1.088	Cg4...Cg5 ^{xiv}	3.541(13)	4	0.598
Cg5...Cg2 ^{viii}	3.618(11)	6	0.779	Cg5...Cg4 ^{xiv}	3.540(13)	4	0.834
Cg6...Cg4 ^v	3.589(9)	5	0.784	Cg6...Cg1 ^{xii}	3.588(12)	7	0.874
1-Dy				1-Lu			
Cg1...Cg6 ^{ix}	3.575(13)	6	1.189	Cg1...Cg6 ^{xvii}	3.532(14)	4	0.587
Cg2...Cg3 ^x	3.577(17)	6	0.589	Cg2...Cg4 ⁱⁱⁱ	3.564(15)	5	0.907
Cg3...Cg2 ^x	3.577(17)	6	0.976	Cg3...Cg5 ^v	3.570(13)	6	1.191
Cg4...Cg5 ^{xi}	3.542(16)	4	0.529	Cg4...Cg2 ⁱ	3.563(15)	5	0.607
Cg5...Cg4 ^{xi}	3.540(16)	4	0.773	Cg5...Cg3 ^{iv}	3.569(13)	6	0.874
Cg6...Cg1 ^{ix}	3.576(13)	6	0.854	Cg6...Cg1 ^{xvii}	3.533(14)	4	0.790

Cg_i = Centroid of the aromatic ring defined by the following atoms:

i = 1: C2A, C3A, C4A, C5A, C6A, C7A; i = 2: C12A, C13A, C14A, C15A, C16A, C17A; i = 3: C2B, C3B, C4B, C5B, C6B, C7B; i = 4: C12B, C13B, C14B, C15B, C16B, C17B; i = 5: C2C, C3C, C4C, C5C, C6C, C7C; i = 6: C12C, C13C, C14C, C15C, C16C, C17C.

Cg...Cg = distance between centroids; ANG = dihedral angle between planes containing both rings; Slippage = distance between one centroid and its perpendicular projection to the plane containing the second ring.

Symmetry codes: (i) x, -1+y, z; (ii) 3-x, 1-y, 1-z; (iii) x, 1+y, z; (iv) -1+x, y, z; (v) 1+x, y, z; (vi) 1-x, -1-y, -z; (vii) 2-x, 1-y, 1-z; (viii) 1-x, -y, -z; (ix) 1-x, 2-y, 1-z; (x) -x, 1-y, 1-z; (xi) -x, 1-y, -z; (xii) 2-x, 1-y, 2-z; (xiii) 1-x, -y, 2-z; (xiv) 1-x, -y, 1-z; (xv) x, 1+y, 1+z; (xvi) x, -1+y, -1+z; (xvii) 2-x, 2-y, 2-z.

Table 4.5. Br...Br distances (Å) in compounds **1-Ln**.

	1-Sm ^[a]	1-Eu ^[b]	1-Gd ^[c]	1-Tb ^[d]	1-Dy ^[e]	1-Ho ^[f]	1-Er ^[g]	1-Tm ^[h]	1-Yb ^[j]	1-Lu ^[k]
BrA...BrB	3.706(5)	3.817(5)	3.705(5)	3.759(4)	3.677(4)	3.653(4)	3.657(5)	3.907(5)	3.645(4)	3.656(4)
BrA...BrC	3.962(6)	4.016(5)	3.958(5)	3.722(4)	3.953(4)	3.903(3)	3.882(5)	3.826(7)	3.890(4)	3.924(4)
BrB...BrC	3.960(6)	3.914(5)	3.989(4)	4.086(3)	3.923(5)	3.967(3)	3.923(5)	3.741(6)	3.945(3)	3.866(4)

Symmetry codes: [a] Br2A...Br1Bⁱ: 2-x, -y, 1-z; Br2A...Br2Cⁱⁱ: -1+x, -1+y, z; Br1B...Br2Cⁱⁱⁱ: 3-x, 2-y, 1-z; [b] Br2A...Br1B^{iv}: -x, -1-y, -z; Br2A...Br2C^v; Br1B...Br2C^{vi}: 1-x, -y, -z; [c] Br2A...Br1B^{vii}: 1-x, 1-y, 1-z; Br2A...Br2C^{viii}; Br1B...Br2C^{ix}: 2-x, 2-y, 1-z; [d] Br2A...Br1B^x: -x, -y, -z; Br2A...Br2C^{xi}; Br1B...Br2C^{xii}: 1-x, 1-y, -z; [e] Br2A...Br2B^{xiii}: 1+x, 1+y, 1+z; Br2A...Br2C^{xiv}: x, y, 1+z; Br2B...Br2C^{xv}; [f] Br2A...Br2B^{xvi}; Br2A...Br2C^{xvii}; Br2B...Br2C^{xviii}; [g] Br1A...Br1B^{xix}; Br1A...Br1C^{xx}: 1+x, 1+y, z; Br1B...Br1C^{xxi}: x, y, -1+z; [h] Br1A...Br2B^{xxii}; Br1A...Br1C^{xxiii}; Br2B...Br1C^{xxiv}; [j] Br2A...Br2B^{xxv}; Br2A...Br2C^{xxvi}; Br2B...Br2C^{xxvii}; [k] Br1A...Br2B^{xxviii}: 3-x, 2-y, 2-z; Br1A...Br1C^{xxix}; Br2B...Br1C^{xxx}: 2-x, 1-y, 2-z.

Table 4.6. Ln–O_{POM}–W bond angles in **1-Ln**. Note the difference between oxygen atoms involved in corner sharing (O_c) and those in intermediate situations between corner and edge sharing (O_i).

	1-Sm	1-Eu	1-Gd	1-Tb	1-Dy
Ln–O1A _c –W1A	155.1(10)	155.6(19)	153.6(7)	156.4(6)	155.7(10)
Ln–O2A _c –W2A	156.1(11)	157.2(11)	156.0(8)	157.3(6)	157.4(10)
Ln–O3A _i –W3A	128.3(11)	130.3(10)	130.9(9)	131.4(6)	132.7(9)
Ln–O4A _i –W4A	133.1(7)	134.3(8)	133.8(7)	133.9(5)	134.2(9)
Ln–O1B _c –W1B	156.5(11)	156.2(9)	156.7(7)	156.8(6)	155.7(9)
Ln–O2B _c –W2B	156.1(11)	155.0(10)	155.4(8)	154.6(6)	157.6(9)
Ln–O3B _i –W3B	133.7(10)	132.2(8)	132.0(7)	133.0(5)	130.5(9)
Ln–O4B _i –W4B	131.5(9)	130.3(8)	131.2(7)	129.7(5)	135.7(7)
Ln–O1C _c –W1C	155.2(9)	154.6(9)	156.0(8)	155.3(5)	155.0(9)
Ln–O2C _c –W2C	158.0(11)	155.6(9)	155.9(9)	156.9(6)	157.1(9)
Ln–O3C _i –W3C	131.4(8)	130.7(8)	130.4(8)	131.5(5)	131.5(8)
Ln–O4C _i –W4C	133.9(10)	134.7(10)	133.8(9)	133.8(5)	134.5(9)
	1-Ho	1-Er	1-Tm	1-Yb	1-Lu
Ln–O1A _c –W1A	156.5(7)	156.6(13)	158.5(12)	156.7(7)	157.9(9)
Ln–O2A _c –W2A	156.7(8)	154.0(10)	157.8(11)	156.8(8)	157.0(8)
Ln–O3A _i –W3A	132.0(7)	133.7(9)	136.1(10)	132.9(7)	136.5(7)
Ln–O4A _i –W4A	134.0(7)	132.2(9)	132.3(9)	135.6(8)	134.1(9)
Ln–O1B _c –W1B	156.3(7)	157.9(11)	153.7(11)	157.9(8)	154.4(9)
Ln–O2B _c –W2B	157.0(8)	154.1(13)	157.2(12)	158.0(8)	156.8(8)
Ln–O3B _i –W3B	131.8(8)	132.7(9)	132.8(11)	132.3(8)	133.2(8)
Ln–O4B _i –W4B	135.5(7)	132.0(10)	135.2(10)	136.2(7)	135.6(8)
Ln–O1C _c –W1C	155.1(7)	158.5(13)	158.0(11)	156.9(8)	156.7(8)
Ln–O2C _c –W2C	155.7(8)	154.5(9)	156.4(12)	156.5(7)	154.7(9)
Ln–O3C _i –W3C	130.5(7)	134.3(10)	135.2(11)	131.8(7)	135.6(8)
Ln–O4C _i –W4C	135.3(7)	131.4(11)	131.5(10)	135.2(7)	133.0(7)

CURRICULUM VITAE

Estibaliz Ruiz Bilbao

Departamento de Química Orgánica e Inorgánica
Facultad de Ciencia y Tecnología
Universidad del País Vasco/Euskal Herriko Unibertsitatea (UPV/EHU)
Campus de Leioa, B° Sarriena s/n
48940, Leioa, Spain.
e-mail: *estibaliz.ruiz@ehu.eus*

RESEARCH TOPICS

My scientific interest is focused on polyoxometalate (POM) chemistry: i) characterization of new inorganic clusters and organic-inorganic hybrids based on POMs (single-crystal and powder XRD, FTIR, TGA, ESI-MS) ii) synthesis of POM-based porous materials and their stimuli-responsive structural transitions (gas and water sorption and separation) and; iii) 4f-metal containing POMs with interesting optical and magnetic properties.

EDUCATION

PhD University of the Basque Country UPV/EHU (2018-PRESENT)

Thesis Polyoxometalate-Based Hybrids with 3d- and 4f-Metal Complexes Bearing Multidentate Organic Ligands. From Magnetoluminescent Molecular Species to Extended Frameworks with Sorption Ability

Supervisors Prof. Luis Lezama Diago (UPV/EHU)
Dr. Beñat Artetxe Arretxe (UPV/EHU)

M. Ed. Profesorado de Educación Secundaria Obligatoria, Bachillerato, Formación Profesional y Enseñanza de Idiomas en la especialidad de Física y Química. Universidad Internacional de Valencia (VIU) (2018-2019).

M.Sc. Polymers, Colorants and Fine Chemicals
University of Leeds (UK) (2016-2017)

B.Sc. Chemistry
University of the Basque Country UPV/EHU (2004-2009)

RESEARCH STAYS ABROAD

Study of gas and vapor sorption properties in porous extended POM-based organic-inorganic hybrids. University of Limerick, Limerick, Ireland. 2022 (Three months) Supervisor: Prof. Michael Zaworotko.

SCIENTIFIC PUBLICATIONS

1. **Ruiz-Bilbao, E.**; Iturrospe, A.; Reinoso, S.; Artetxe, B.; Beobide, G.; San Felices, L.; Lezama, L.; Gutiérrez-Zorrilla, J. M.; Darwish, S.; Sensharma, D.; Zaworotko, M. J. Consecutive Single-Crystal-to-Single-Crystal Isomerizations of Unprecedented Octamolybdate Anions within a Microporous Hybrid Framework with Robust Water Sorption Properties. *Submitted*.
2. **Ruiz-Bilbao, E.**; Pardo-Almanza, M.; Oyarzabal, I.; Artetxe, B.; San Felices, L.; García, J. A.; Seco, J. M.; Colacio, E.; Lezama, L.; Gutiérrez-Zorrilla, J. M. Slow Magnetic Relaxation and Luminescent Properties of Mononuclear Lanthanide-Substituted Keggin-Type Polyoxotungstates with Compartmental Organic Ligands. *Inorg. Chem.* **2022**, *61*, 2428-2443.
3. **Ruiz-Bilbao, E.**; Fernández-Navarro, L.; Artetxe, B.; Gutiérrez-Zorrilla, J.M. (2022) "Chapter 1. General Principles and Structural Chemistry of Polyoxometalates" in Polyoxometalates: Advances, Properties and Applications. Ruiz Rubio, L.; Vilas Vilela, J. L.; Artetxe, B.; Gutiérrez-Zorrilla, J. M.; Eds. Jenny Stanford Publishing, New York, USA.
4. Vitoria, P.; Wéry, A. S. J.; San Felices, L., Bravo-García, L.; **Ruiz-Bilbao, E.**; Laza, J. M.; Vilas, J. L.; Gutiérrez-Zorrilla, J. M. Reversible First-Order Single Crystal to Single Crystal Thermal Phase Transition in $[(\text{CH}_3)_3\text{CNH}_3]_4[\text{V}_4\text{O}_{12}]$. *Materials* **2022**, *15*, 5663.
5. Fernández-Navarro, L.; Nunes-Collado, A.; Artetxe, B.; **Ruiz-Bilbao, E.**; San Felices, L.; Reinoso, S.; Wéry, A. S. J.; Gutiérrez-Zorrilla, J. M. Isolation of the elusive Heptavanadate Anion with Trisalkoxide Ligands. *Inorg. Chem.* **2021**, *60*, 5442-5445.
6. Dissem, N.; Artetxe, B.; San Felices, L.; Beobide, G.; Castillo, O.; **Ruiz-Bilbao, E.**; Lezama, L.; Vivanco, M. dM.; Haddad, A.; Gutiérrez-Zorrilla, J. M. Single-Crystal-to-single-Crystal Cluster Transformation in a Microporous Molybdoarsenate(V)-Metalorganic Framework. *Inorg. Chem.* **2021**, *60*, 14913-14923.
7. Fernández-Navarro, L.; Iturrospe, A.; Reinoso, S.; Artetxe, B.; **Ruiz-Bilbao, E.**; San Felices, L.; Gutiérrez-Zorrilla, J. M. Thermally Induced Structural Transitions between Single-Crystalline States in the First Hybrid Compound Combining Keggin-Type Clusters with Metal-Cyclam Complexes: From Two-Dimensional Covalent Assemblies to Discrete Molecular Species. *Cryst. Growth Des.* **2020**, *20*, 3499-3509.
8. Artetxe, B.; Iturrospe, A.; Vitoria, P.; **Ruiz-Bilbao, E.**; Garitaonandia, J. S.; Gutiérrez-Zorrilla, J. M. A Charge-Transfer Salt Based on Ferrocene/Ferrocenium Pairs and Keggin-Type Polyoxometalates. *Molecules* **2018**, *23*, 3150.

CONTRIBUTIONS TO MEETINGS

1. Flash-Presentation at *FMOCS VII. Frontiers in Metal Oxide Cluster Science*. Tarragona, Spain, 2023.
2. Poster Presentation at *8th European Chemistry Society (EuChemS) Congress*. Lisbon, Portugal, 2022.
3. Poster Presentation at *XXXVIII Reunión Bienal de la Sociedad Española de Química (RSEQ)*. Granada, Spain, 2022.
4. Poster Presentation at *Virtual Congress of the American Chemical Society (ACS Fall)*. Atlanta, USA, 2021.
5. Oral communication at *VII. Jornadas de Investigación de la Facultad de Ciencia y Tecnología*. Leioa, Spain, 2020.
6. Poster Presentation at *XXXVII Reunión Bienal de la Sociedad Española de Química (RSEQ)*. Donostia, Spain, 2019.
7. Poster Presentation at *7th European Chemistry Society (EuChemS) Congress*. Liverpool, UK, 2018.
8. Oral communication at *VI. Jornadas de Investigación de la Facultad de Ciencia y Tecnología*. Leioa, Spain, 2018.
9. Oral communication at *BCMaterials Workshop: New Materials for a Better Life*. Leioa, Spain, 2018.

TEACHING AND MANAGEMENT ACTIVITIES

1. Official teaching in the Degree of Chemistry, UPV/EHU. Courses: Basic Laboratory Operations and Inorganic Chemistry II (Lab practicals), 180 h, at UPV/EHU, 2019-2022.
2. Supervisor of the cooperation program "External Academic Practices for students", at UPV/EHU, 2021.
3. Management Committee and Electoral Commission as representative of the collective of M.Sc. and Doctoral students, at UPV/EHU, 2021-2022.
4. Organizing committee of the XXXV Basque Chemistry Olympics organized by the Real Sociedad Española de Química (RSEQ), 2022-2023.
5. Participation as teacher in the XVIII and XIX edition of "Weeks of Science, Technology and Innovation", organized by UPV/EHU, 2019-2020.

6. Dissemination in Basque language: **Ruiz-Bilbao, E.**; Fernández-Navarro, L.; Artetxe, B.; San Felices, L.; Reinoso, S. Polioxometalatoak ingurune urtsuan: egitura esanguratsuenak. *Ekaia* **2021**, *42*, 139-154.
7. Dissemination in Basque language: Fernández-Navarro, L., **Ruiz-Bilbao, E.**; Artetxe, B.; San Felices, L.; Iturrospe, A.; Reinoso, S. Monokristal-monokristal eraldaketak polioxometalatoetan oinarritutako sistemetan: termikoki aktibatutako zenbait adibide. *Ekaia* **2019**, *36*, 239-254.